DENOISING AND SEGMENTATION OF ULTRASOUND MEDICAL IMAGES

Ph.D. THESIS

by

DEEP GUPTA

DEPARTMENT OF ELECTRICAL ENGINEERING
INDIAN INSTITUTE OF TECHNOLOGY ROORKEE
ROORKEE – 247667 (INDIA)

NOVEMBER, 2014

DENOISING AND SEGMENTATION OF ULTRASOUND MEDICAL IMAGES

A THESIS

Submitted in partial fulfilment of the requirements for the award of the degree

of

DOCTOR OF PHILOSOPHY

in

ELECTRICAL ENGINEERING

by

DEEP GUPTA

DEPARTMENT OF ELECTRICAL ENGINEERING
INDIAN INSTITUTE OF TECHNOLOGY ROORKEE
ROORKEE – 247667 (INDIA)

NOVEMBER, 2014

INDIAN INSTITUTE OF TECHNOLOGY ROORKEE
ROORKEE

CANDIDATE'S DECLARATION

I hereby certify that the work which is being presented in this thesis entitled **"DENOISING AND SEGMENTATION OF ULTRASOUND MEDICAL IMAGES"** in partial fulfilment of the requirements for the award of the Degree of Doctor of Philosophy and submitted in the Department of Electrical Engineering of the Indian Institute of Technology Roorkee is an authentic record of my own work carried out during a period from July, 2011 to November, 2014 under the supervision of Dr. R.S. Anand, Professor and Dr. Barjeev Tyagi, Associate Professor, Department of Electrical Engineering, Indian Institute of Technology Roorkee.

The matter presented in this thesis has not been submitted by me for the award of any other degree of this or any other Institute.

(**DEEP GUPTA**)

This is to certify that the above statement made by the candidate is correct to the best of our knowledge.

(R.S. Anand)
Supervisor

(Barjeev Tyagi)
Supervisor

Date: _____

ABSTRACT

In the field of medical imaging technologies, ultrasound imaging (US) has an important role in the diagnosis of several diseases because of its safe application for patients, low cost and portability. In usual, the diagnostic procedures based on the perception of medical images are performed in a subconscious way which is based on the conclusion drawn upon how the clinicians understand and interpret them. It is only since the last couple of years that computers have been used to process the images digitally in the equipment to some extent and thus help the clinician in their diagnostic decision. However, it is a difficult task in the case of US images because of the presence of speckles and other artifacts. The image segmentation is also a key step in several computer aided diagnosis systems used to identify a particular region of interest such as the tumor, lesion and other abnormalities, to measure the growth of tumors and to help in treatment planning.

Speckle considered as multiplicative noise is a prime factor that degrades the contrast resolution and masks the meaningful texture information present in the US images. This makes accurate identification of object boundaries and contours of anatomical structures a challenging task. Hence, the image denoising can be considered as a fundamental task to improve the quality of the US images by suppressing the speckle noise without affecting the edge information. Thus, in the above perspective, the image denoising algorithms should fulfil the following three principal criteria:

1. The algorithm must be capable of suppressing the maximum amount of noise from a particular region.
2. The true tissue information, including the edges and other fine details should also be preserved and if possible, may be enhanced.
3. The denoising algorithm must be computationally efficient, stable and robust.

With the above background, the main objective of the present research work has been to design and develop the effective algorithms to achieve the improved performance in image denoising and segmentation. To obtain these objectives, it has been necessary to analyze and identify better approaches among the existing remarkable denoising and segmentation approaches and also it necessitated to improve the performance of the best identified approach, either by modifying the earlier algorithm or by suggesting a new algorithm. Accordingly, the entire research work has been planned and carried out in the following three different steps.

1. Comparison of several existing image denoising methods has been carried out under two major categories, i.e. spatial domain category and transform domain category, and an optimum approach suitable for the US medical images has been identified.
2. Based on the post-analysis of the approaches from two major categories mentioned above, new suitable denoising approaches have been designed and implemented to

improve the quality of the US images by suppressing the noise and preserving the edges.

3. A comparative evaluation of several existing segmentation approaches used for the US medical images have been carried out and new segmentation algorithms for the US images have been designed and implemented.

In order to achieve the first objective of the initial phase of work, the performance of various existing denoising methods namely, adaptive weighted median filter (AWMF), wiener filter (WF), maximum homogeneity over a pixel neighborhood filter (MHOPNF), anisotropic diffusion filter (ADF), speckle reducing anisotropic diffusion (SRAD), nonlinear complex diffusion filter (NCDF), total variation filter (TVF), nonlocal means filter (NLMF) in spatial domain, while wavelet, ridgelet, curvelet and shearlet based methods in the transform domain category, have been evaluated on the test images degraded by different types of noise such as speckle and Gaussian noise and on real US images. Their performance is not only analyzed and evaluated in terms of visual perception, but also in terms of different performance measures such as the peak signal to noise ratio (PSNR), signal to noise ratio (SNR), structural similarity index metric (SSIM), figure of merit (FOM) and edge keeping index (EKI). Besides the above parameters, mean to variance ratio (MVR) has also been used for the quantitative analysis of the US images because of the nonavailability of the reference US images. From the experimental results, it is observed for all noise levels that the TVF, NLMF, curvelet and shearlet based approaches are able to suppress good amount of noise with better edge preservation in terms of quantitative measures, but in curvelet based method, some visual distortion like oscillations occur in the denoised images. For some images, ridgelet based approach also provides a competitive performance than others, but further it leads to some visual distortion. Moreover, diffusion based and the TVF approaches suffer from the loss of edge information. It is also observed that the better perceptual quality is obtained by the TVF, NLMF and shearlet based approaches. The diffusion, ridgelet and curvelet based approaches are also suitable to provide better denoising performance, but at the cost of blurring the edges and introducing some visual distortion.

Under the second objective, six different algorithms are proposed in the present work. Based on the results obtained from the above comparative analysis, the first denoising approach based on M-band ridgelet transform is proposed in the present work. It utilizes the features of M-band wavelet transform in place of the 2-band wavelet transform (WT) used in the implementation of the ridgelet transform. The proposed approach utilizes the variation of the frequency resolution feature of the À trous algorithm by which a noisy image has been decomposed into different scales. NeighShrink (NS) thresholding is also utilized in the proposed approach to provide the approximated modified image coefficients that also

improve the noise reduction efficiency. Based on the experimental results, it is observed that the proposed M-band ridgelet thresholding (MBRT) approach is able to produce better results by suppressing a sufficient amount of the speckle noise with more edges being preserved.

It is observed on the basis of the findings obtained from the first objective, that the curvelet based approach also produces better denoising results. Curvelet transform (CVT) uses a parabolic scaling law to resolve the two dimensional singularities along C^2 curves. It also overcomes the limitation of the wavelet and ridgelet, which are less efficient to represent the sharp transition like line and curve singularities available in the images. To represent the edges more efficiently, ripplet transform (RT) has been evolved by incorporating two new additional parameters. It also provides a new tight frame with a sparse representation for the source images with discontinuities along the C^d curves, where $d = 2$ refers to parabolic scaling same as the curvelets and for $d = 3$, ripplet has the cubic scaling and so forth. Based on the literature review and comparative evaluation performed earlier, the WT thresholding approach has improved its performance by incorporating some spatial domain techniques. Considering their merits, two different nonlinear filtering approaches in ripplet domain have been proposed here using the NS and BlockShrink (BS) thresholding approach that are named as the RTNLF-1 and the RTNLF-2, respectively. Nonlinear bilateral filtering (NLBF) is applied to the low frequency ripplet coefficients. The performance of these proposed denoising methods depend on the decomposition levels, different parameters of the RT and NLBF approach. The optimal values of these parameters have been decided by conducting the several experiments on the available test image datasets for the different levels of speckle noise with several combinations of these parameters. The results of the proposed RTNLF-1 and RTNLF-2 methods are compared with the bilateral, wavelet based NeighShrink (WT-NS), wavelet based NeighShrink using the NLBF (WT-NLBF-NS), wavelet based BlockShrink (WT-BS), linear homogeneous mask area filter (LHMAF), ADF, Fourth order PDE filter (FOPDEF), SRAD, NCDF, improved nonlinear complex diffusion (INCDF), wavelet based approach using generalized Gaussian distribution (WT-GGD), squeez box filter (SBF) and TVF approach. It is observed from their comparative results that proposed RTNLF-1 and RTNLF-2 methods provide better quality of images by suppressing more speckle noise as compared to others. Moreover, the RTNLF-2 approach performs better than the RTNLF-1. The higher SNR and PSNR values with larger EKI and SSIM values obtained by the proposed approaches indicate that the noise suppression is neither at the cost of blurring the edges nor at the loss of edge information.

From the analysis of experimental results obtained earlier, it is observed that the TVF approach is quite good and has the ability to suppress the noise, but it performs noise reduction with the loss of edge information which means that some edge information is lost

within the noise residual. Thus, a remnant approach for adaptive fusion based noise filtering (RBAF) is proposed using the TVF and shearlet thresholding using cycle spinning (CSST) approach. The proposed RBAF approach fuses three different images processed by the (a) TVF approach, (b) CSST approach and (c) extracted edges structured information (ESI) from the remnant of TVF approach and processed by the CSST approach. The proposed RBAF approach fuses these images based on the 3×3 block variance map evaluated for all three above processed images. The RBAF approach improves both the perceptual quality and the detectability of real US images and several test images corrupted with the speckle and Gaussian noise of different levels (characterized by their standard deviation and variance). To assess the performance of the proposed RBAF approach, the results of other methods such as the TVF, TI-WT, curvelet thresholding using cycle spinning (CSCVT) approach, CSST, CVT with the TVF approach (CVT-TVF) are considered. It is observed from the analysis of all the experimental results that the higher values of EKI and FOM with improved values of the SNR, PSNR and SSIM are obtained for the proposed RBAF approach. Further, it indicates that the improved noise suppression provided by the proposed RBAF approach does not produce the blurred edges. Besides this improved performance, the proposed RBAF approach also helps to suppress the staircase/blocking effects produced by the TVF method and the fuzzy edges introduced by the CVT and ST based methods.

Based on the outcomes of the different experiments performed earlier and the literature, it is observed that anisotropic diffusion is widely used for denoising of the US image, but it suffers from the loss of edges information available in the images that are also very important for visual perception. To represent more edges, nonsubsampled shearlet transform (NSST) has been presented by providing both the multiscale and direction analysis of an image. Further, two different noise filtering approaches using the modified nonlinear adaptive anisotropic diffusion (NADF) equations in the NSST domain and thresholding approach (similar to the CVT and ST thresholding) have also been proposed. In the modified diffusion process, an adaptive gray variance is also incorporated with the gradient information of eight connected neighboring pixels to preserve the edges, effectively in the first proposed approach and named as the NSST-NADF. Motivated by the better noise reduction results of the NLMF presented in the first comparative analysis, the nonlocal pixel information is also incorporated to evaluate the gradient of eight connected neighboring pixels with an adaptive gray variance in the second proposed approach and is named as the NSST-NLNADF. Their denoising performance is also compared with all aforementioned existing methods, including the speckle reducing bilateral filter. The proposed methods are also adapted to both the speckle and Gaussian noise. Based on the experimental results, it is observed that the proposed NSST-NLNADF approach ensures an improvement in noise reduction and preservation of more edges by providing higher SNR, PSNR, FOM, SSIM and

EKI values than the NSST-NADF approach and others and thus providing the processed images with better visual quality.

In order to achieve the next objective of the present work, two different segmentation methods are proposed to delineate the region of interest in the US medical images using clustering and level set methods. Based on the literature, the performance of the traditional active contour segmentation methods is subjected to appropriate and accurate contour initialization and optimal configuration of the contour propagation controlling parameters, which also require extensive manual intervention. Therefore, two different segmentation approaches, namely hybrid edge-based active contour model (EBACM) with the kernel fuzzy c-mean clustering (KFCM) and region-based active contour model (RBACM) with the Gaussian kernel fuzzy clustering (GKFCM) have been proposed here to segment the US medical images.

In the first proposed segmentation approach, the features of both the edge-based active contour model using the distance regularized level set and the KFCM clustering are merged to detect the abnormalities from the US images. In the proposed approach, the fuzzy membership function from the variants of KFCM with spatial constraints, i.e. KFCM_S1 and KFCM_S2 clustering, is employed to initialize the curve that evolves to extract the desired object of interest. In addition to contour initialization, the results of the fuzzy clustering are also used for further evaluation of the contour propagation controlling parameters. Thus, two different segmentation approaches, namely the EBACM-KFCM_S1 and EBACM-KFCM_S2 are proposed, which start with the KFCM_S1 and KFCM_S2 methods, respectively, to initialize the curve and evaluate the curve evolution controlling parameters. The segmentation results of both the EBACM-KFCM_S1 and EBACM-KFCM_S2 methods are compared with the different variants of fuzzy c-means using spatial constraints (FCM_S1 and FCM_S2), KFCM_S1, KFCM_S2, geodesic active contour (GAC), region-based active contour driven by region scalable fitting (ACMRSF), edge-based active contour model (EBACM) applied on the large database of the US images. Their performances are estimated, quantitatively in terms of different performance measures such as true positive (TP), false positive (FP), accuracy (ACC), Jaccard similarity index (JSI), dice coefficient (DC) and Hausdorff distance (HD). The quantitative analysis shows that the results of the proposed segmentation methods provide higher segmentation accuracy compared to the others. It also provides better values of other performance metrics such as the TP, FP, JSI, DC and HD. For the proposed EBACM-KFCM_S2 method, when tested on the US images, the averaged performance measures such as the TP, ACC, JSI, and DC are higher than the EBACM-KFCM_S1 method. The proposed approaches also help to remove the need of manual intervention and decrease the processing time.

In the second proposed segmentation approach, the features of the RBACM driven by the RSF energy and the two different variants of the Gaussian kernel fuzzy c-mean clustering with spatial information such as the GKFCM_S1 and GKFCM_S2 are utilized. In addition to the previously described methods in the earlier paragraph, two more hybrid segmentation methods using the RBACM approach have been proposed, which starts with the GKFCM_S1 and GKFCM_S2 approach, individually. The proposed approaches utilize the GKFCM_S1 and GKFCM_S2 clustering, individually, not only to initialize the contour, but also to estimate the several contour propagation controlling parameters. These proposed approaches are named as the RBACM-GKFCM_S1 and RBACM-GKFCM_S2. In these segmentation approaches, the intensity information in the local regions as against the global regions in conventional RBACM approach, are utilized to drive the motion of contour toward the desired object boundaries. The RSF formulation is also responsible for attracting the contour toward the object boundaries, thus increasing the speed of the contour propagation. The effectiveness of the proposed approaches is illustrated through several experiments performed on the similar US images, synthetic test images and also compared with the results of the above segmentation methods, including the RBACM using spatial fuzzy clustering (RBACM-SFCM) approach. From the experimental results, it is observed that the segmented images obtained by the proposed approaches are approximately similar to that of the manually delineated region compared to others. It is further observed that the proposed approaches achieve higher segmentation accuracy than the GAC, ACMRSF, RBACM-SFCM and EBACM, which itself signifies improvement in the results of the proposed approaches. These proposed methods also take comparatively less time to segment the image.

For the purpose of implementing and evaluating the performance of the above discussed proposed methods, the US images were acquired from the image database available at (http://rad.usuhs.edu/medpix/parent.php3?mode=home_page), (http://ultrasonics.bioenggineering.illinois.edu), (http://www.ultrasoundcases.info/), (http://radiologyinfo.org/en/photocat/), (http://thelivercarefoundation.org) and from the database of GE, Phillips and Siemens.

ACKNOWLEDGEMENTS

I express my gratitude to my supervisors Dr. R.S. Anand and Dr. Barjeev Tyagi, Department of Electrical Engineering, IIT Roorkee, for their guidance and suggestions for the completion of this study.

I express my sincere thanks to the members of my research committee Prof. M.L. Dewal, Prof. G.N. Pillai, Department of Electrical Engineering, IIT Roorkee and Prof. Manoj Misra, Department of Computer Science and Engineering, IIT Roorkee for their constructive discussions and valuable suggestions during the meetings of my research committee. I am thankful to Prof. Pramod Agarwal, Dean Academics, IIT Roorkee and Prof. S.P. Srivastava, H.O.D. Department of Electrical Engineering, IIT Roorkee for providing necessary support and facilities throughout this study and in the submission of this thesis. I am equally indebted to Prof. Vinod Kumar, Dean Faculty Affairs and Coordinator, Instrumentation and Signal Processing group, Department of Electrical Engineering, IIT Roorkee, who has always been my source of motivation for me and pursuance of my work. I am also thankful to all other faculty members of the Department of Electrical Engineering, IIT Roorkee for their support.

I am thankful to Mr. Rajeev Kumar, Mr. Dinesh Sharma, Mr. Aamir Ahmed, Mr. Rishab, Mr. Mohan Singh and the staff of Applied Instrumentation Lab, Biomedical Lab and office of the Department of Electrical Engineering for their co-operation and assistance. I extend thanks to all non-teaching staff, Department of Electrical Engineering, IIT Roorkee for their day to day co-operation.

I am extremely thankful to Dr. S.L. Rao, Assistant Professor, National Institute of Technology Karnataka for his every help and invaluable support rendered during my research work. I am also grateful to the reviewers for their constructive suggestion and invaluable advice for improving the quality of my publications derived from this work.

I am highly thankful to my friends and fellow researchers Dr. Jainy Sachdeva, Dr. Yatindra Kumar, Mr. Sanjay Kumar for their necessary help during the work. I am also thankful to my fellow researchers Mr. K.S. Sajan, Mr. N.M. Biradar, Mr. Arun Balodi, Mr. Jayendra Kumar, Mr. Yogesh Sariya, Mr. Pankaj Pratap Singh, Mr. Sachin Singh and Mr. Arvind Yadav for their kind support during this work.

I cannot forget my best friends Mr. Himanshu Sharma and his wife who never hesitated to render their help at the time of some critical difficulties and spared their time whenever required during my Ph.D. work. I express my thanks for their help in need. I also extend my thanks to all those whom I have missed to mention.

I also sincerely acknowledge the financial support and assistantship provided by the MHRD, Government of India, for this study.

I am indebted to my beloved parents and in-laws for their pains, encouragements and consistently supports during my Ph.D. work. They are my pillars and without their support

this work was not possible to conclude. I express my deepest appreciation for my sister and my well wishers whose blessings helped me reach this end. I owe greatly to my wife 'Sneha' for her unwavering patience, understanding and encouragement, as the present work is finally concluded, because of her personal sacrifices and supports for which I shall ever remain indebted.

Last but not the least, I am thankful to the Almighty who gave me the strength and health for completing the work.

(Deep Gupta)

CONTENTS

LIST OF FIGURES

LIST OF TABLES

LIST OF ABBREVIATIONS

ACC	Accuracy
ACM	Active Contour Model
ACMRSF	Active Contour Model using RSF
AWMF	Adaptive Weighted Median Filter
ADF	Anisotropic Diffusion Filter
AVG	Average
BCFCM	Bias Corrected Fuzzy C-Means
BS	BlockShrink
CV	Chan-Vese
COV	Coefficient of Variation
CT	Computed Tomography
CW	Continuous Wave
CVT	Curvelet Transform
CS	Cycle Spinning
CSCVT	Cycle Spinning Based Curvelet Thresholding
CSST	Cycle Spinning Based Shearlet Thresholding
DPAD	Detail Preserving Anisotropic Diffusion
DC	Dice Coefficient
D	Dimensional
DFB	Directional Filter Bank
DRLSE	Distance Regularized Level Set Evolution
EBACM	Edge-Based Active Contour Model
EKI	Edge Keeping Index
ESI	Edge Structured Information
FP	False Positive
FFT	Fast Fourier Transform
FOM	Figure of Merit
FOPDEF	Fourth Order Partial Differential Equation Filter
fMR	Functional Magnetic Resonance
FCM	Fuzzy C-Means
FLIFCM	Fuzzy Local Information C-Means
GKFCM	Gaussian Kernel Based Fuzzy C-Means
GKFCM_S1	Gaussian KFCM with Spatial Constraints using Mean Filter
GKFCM_S2	Gaussian KFCM with Spatial Constraints using the Median Filter
GGD	Generalized Gaussian Distribution

GAC	Geodesic Active Contour
GVF	Gradient Vector Flow
HD	Hausdorff Distance
HF	High Frequency
INCDF	Improved Nonlinear Complex Diffusion Filter
ISRAD	Improved Speckle Reducing Anisotropic Diffusion
ICOV	Instantaneous Coefficient Of Variation
JSI	Jaccard Similarity Index
KFCM	Kernel Fuzzy C-Means
KFCM_S1	Kernel Fuzzy C-Means with Spatial Constraints using Mean Filter
KFCM_S2	Kernel Fuzzy C-Means with Spatial Constraints using the Median Filter
LP	Laplacian Pyramid
LSF	Level Set Function
LHMAF	Linear Homogeneous Mask Area Filter
LF	Low Frequency
MR	Magnetic Resonance
MHOPNF	Maximum Homogeneity over A Pixel Neighborhood Filter
MBRT	M-band Ridgelet Thresholding
MVR	Mean to Variance Ratio
MAD	Median Absolute Deviation
NS	NeighShrink
NADF	Nonlinear Adaptive Diffusion Filter
NLBF	Nonlinear Bilateral Filter
NCDF	Nonlinear Complex Diffusion Filter
NLNADF	Nonlocal Based Nonlinear Adaptive Diffusion Filter
NLMF	Nonlocal Means Filter
NSLP	Nonsubsampled Laplacian Pyramid
NSST	Nonsubsampled Shearlet Transform
OCT	Optical Coherence Tomography
OSRAD	Oriented Speckle Reducing Anisotropic Diffusion
PDE	Partial Differential Equation
PSNR	Peak Signal to Noise Ratio
PNVI	Percentage Normalized Variance Image
PM	Perona and Malik
PET	Positron Emission Tomography
PDF	Probability Density Function
PW	Pulse Wave

RBACM	Region-Based Active Contour Model
RSF	Region Scalable Fitting
RBAF	Remnant Based Adaptive Fusion
RTNLF	Ripplet Domain Nonlinear Filtering
RT	Ripplet Transform
RDPAD	Robust Detail Preserving Anisotropic Diffusion
RSRAD	Robust Speckle Reducing Anisotropic Diffusion
ShF	Shearing Filter
ST	Shearlet Transform
SNR	Signal to Noise Ratio
SPECT	Single Photon Emission Computed Tomography
SFCM	Spatial Fuzzy C-Means
SRAD	Speckle Reducing Anisotropic Diffusion
SRBF	Speckle Reducing Bilateral Filter
SBF	Squeeze Box Filter
STD	Standard Deviation
SURE	Stein's Unbiased Risk Estimate
SSIM	Structural Similarity Index Metric
S-L	Sylvester-Lyapunov
SAR	Synthetic Aperture Radar
TGC	Time Gain Compensation
TVF	Total Variation Filter
TI-WT	Translation Invariant Wavelet Transform
TP	True Positive
US	Ultrasound
WT	Wavelet Transform
WF	Wiener Filter

CHAPTER 1: INTRODUCTION

This chapter presents an introduction to the research work carried out in this thesis. It starts with some background on medical imaging and different imaging modalities in which ultrasound imaging is most commonly used because of its advantages compared to the others. This chapter also presents an exhaustive review of the work done on different image denoising and segmentation algorithms for the ultrasound images. The objectives for present study have been decided on the basis of these reported works. The organization of the present thesis is also given at the end of this chapter.

1.1 Motivation

A large number of diseases have become an important public health issue in the world today. The diagnosis of some diseases is delayed or missed because of absence of generally no symptoms until the disease has reached an advanced stage. Also, the symptoms may vary from patient to patient. In addition, some symptoms may not be very specific to a particular disease and may resemble with the symptoms of other diseases. This needs some hidden information from the human body where medical imaging plays an important role. The clinical examination and the various branches of the pathology are the other constituents. Several imaging modalities used for taking the medical images of patients' internal body parts are now available for the diagnosis of different diseases. These include X-ray, computed tomography (CT), magnetic resonance (MR), ultrasound (US), positron emission tomography (PET), single photon emission computed tomography (SPECT), functional magnetic resonance (fMR) and angiography etc. The US imaging is widely used in the medical diagnosis because of its cost effectiveness, portability, acceptability and safety. Moreover, the applications of the medical imaging are not only limited to the diagnosis, but also open surgery is being replaced by minimum invasive procedures and image guided intervention is becoming more common.

Any diagnosis is based on the perception of these images obtained by different imaging modalities in a subconscious way, which can be stated that it is a conclusion drawn upon what we see, understand and interpret. But to achieve these objectives, the image needs to be noise free as much as possible. Thus, image denoising is considered as a fundamental step among the various image processing tasks such as compression, segmentation and feature extraction. Besides the image denoising, image segmentation is the key step in several computer aided diagnosis systems which results in partitioning of the image into distinct regions that have some specific clinical meaning. Although manual segmentation done by the experts remains superior in quality and accuracy, but it has two main drawbacks. The first is that producing a manual segmentation is time consuming and second is that the segmentation is subject to variations between both the inter-observers and intra-observer. The computer aided systems for the accurate segmentation of the medical images allow more precise and less time consuming process and also help the medical

practitioner in making the speedy decisions. These motivations motivated to search for better denoising and segmentation approaches that may be helpful in better diagnosis.

1.2 Medical Imaging Modalities: A Brief Overview

Medical imaging plays a prominent role in the diagnosis and treatment of diseases. The challenging problem of extracting the clinically useful information about anatomical structures imaged through different imaging modalities has received enormous attention. There is no single imaging modality which suits for the radiological applications and requirements. In addition, each medical imaging modality is limited by the respective physics of energy interaction with cells of the human body, instrumentation and physiological constraints. Medical imaging modalities that do not make the incision physically are noninvasive. The noninvasive imaging techniques are used for the detection of a disease during a mass screening and to gather important information such as its shape and size, but in the few cases, biopsy as invasive approach is also used in diagnosis especially for tissue genocity. Biopsy brings useful information by removing a small amount of tissue, but it's quite difficult to be accepted by the patients because of its invasiveness and also its possible side effects (pain in one third of the patient, severe complications in 0.3% and even death in 0.03%). There are various different medical imaging modalities that are based on the different types of energy sources used in imaging process and provides the internal views of the anatomical structure, where a radiologist/clinician examine and analyze the images. This categorization of different medical imaging modalities with respect to the energy sources used in the imaging process is shown in Table 1.1 [74].

Table 1.1 Classification of different medical imaging modalities based on the types of energy sources used for imaging

Imaging modalities	Energy sources used
(1) X-ray radiography, X-ray mammography, X-ray computed tomography (2) Ultrasound imaging (3) Optical transmission and Trans-illumination imaging	External energy source
(1) Nuclear Medicine: Single photon emission tomography (SPECT) (2) Nuclear Medicine: Positron emission tomography (PET)	Internal energy source
(1) Magnetic resonance imaging, MRI, fMRI (2) Optical fluorescence imaging	Combined: Internal and external energy source

In the case of the external energy source, X- ray is commonly used imaging technique for anatomical structure that is based on the energy of ionized radiations. This imaging

modality develops an image according to the attenuation coefficients of radiation passing through the body that are further based on the density of tissue or part of the body being imaged [74]. This radiation based technique also includes X-ray radiographs, mammography and computed tomography imaging. X-ray mammography is a specialized radiographic imaging approach that is utilized for breast imaging (diagnosis of breast disease). X-ray computed tomography (CT) is another radiographic inspection technique that utilizes a computer to gather the multiple images of a cross sectional plane of an object.

Another technique of external energy sources based imaging is the US imaging that relies on reflected sound waves to generate an image. A common medical US device sends the US waves into the tissue and analyzes the reflecting waves in order to obtain the images. The standard US image represents a spatial map of the tissue region of interest with different acoustic properties. When the US passes through different tissues, echoes are produced at the boundaries that describe or separate them. For example, tumors may produce echoes that are different from the echoes made by healthy tissues.

For trans-illumination imaging, the use of laser light to produce images of tissue continues to be explored for its possible applications in cancer detection. This method, sometimes referred to as laser optical tomography and is similar to an X-ray CT, except that the light in the near-infrared region (700–1200 nm), rather than X-rays, is used as the energy probe [74].

Nuclear medicine imaging modalities utilize an internal energy source through an emission process to image the human body which provides useful metabolic information about the physiological functions of the organs. In this approach, radioactive pharmaceuticals are injected into the patient's body to interact with selected body matter/tissue to generate an internal source of radioactive energy and to emit gamma ray with photon energy (140 KeV) used for imaging. At this energy level, photons penetrate well through the tissue, and the same can still be effectively detected. For SPECT imaging technique, the gamma camera is mounted on a rotational gantry and is used as an area detector [74]. The acquired data are topographically reconstructed to produce 2D slices.

Furthermore, MR imaging or MRI is a procedure that utilizes a powerful magnet and radio waves to generate detailed images of the body's organs and structures. This type of imaging is done without use of X-rays or other radiation. The images produced by the MR imaging show the exact details of inside the body. The MRI allows acquisition of images with excellent anatomical details and high contrast of soft tissue.

Another emerging imaging modality is fluorescence imaging that utilizes an external ultraviolet energy source to stimulate the internal biological molecules of interest, which absorbs the ultraviolet energy, become an internal source of energy and then emit the energy at visible electromagnetic radiation wavelengths.

As there is no perfect common imaging modality for all radiological applications, there is a need to choose the best suitable modality for a particular application. The choice of the best imaging modality to solve any particular clinical problem is actually based on the factors such as resolution, contrast, mechanism, speed, convenience, acceptability and safety. For imaging the soft tissues, US imaging scores high for all of these factors [250]. Further, the US imaging has following advantages over the CT, MR and other imaging techniques.

1. The US imaging is a most popular and primarily used technique in developing countries for the detection of several diseases because of its low cost and real time imaging capabilities. The CT and MRI are of higher cost in comparison to the US and incur huge costs to patients. Therefore, these imaging techniques put more financial burden to the patients in a country like India, where most of the patients generally come from rural environment. Moreover, it is very difficult for those patients to frequently go through the sequence of costly imaging procedures. Thus, the US imaging is preferred in developing countries on account of its least expensiveness as one of the qualities.
2. The US imaging is used for initial diagnosis, while the CT and MRI are utilized as a method of characterization and evolution of the diseases. Moreover, the amount of the information obtained from the CT and MRI is very large and it is very difficult for the inexperienced radiologist to interpret all these images in a short duration of time, whereas the US examination is relatively simpler than the CT and MRI. Therefore, the clinical relevance of the US examination is high worldwide due to the versatility and widespread availability of the US systems, and the relative simplicity of performing the US examination in comparison to the CT and MRI.
3. The US imaging is recognized as one of the most risk free system to diagnose any disease in the soft tissue of human body. For example, the US is the initial examination performed in most of the patients clinically suspected having a liver mass as compared to the CT and MRI.
4. All the US, CT and MR are noninvasive imaging modalities. But, on the electromagnetic and radiation level, the CT and MRI are quite invasive. From the high energy photons in X-ray CT, to the 2+ Tesla coils of an MR imaging device, these modalities alter the physical and chemical reactions of the body in order to obtain data [167]. On the other hand, no harmful effects on the tissues as a result of the US examination have ever been observed at the doses and energies used in today's clinical practice. Sonography uses high frequency pressure waves and thus affects and measures the total kinetic energy of the molecules in the tissue rather than the internal energy of their electrons or nuclei. The fact that the US is noninvasive allows the radiologist to obtain several images of human anatomy which is of particular interest, and no special precautionary measures to be taken.

5. The logistics of storage and installation of US machines are easier than the CT and MRI, since ultrasound machines are smaller and lighter. Further by obtaining a real time image, a working diagnosis could be made without delay using the US.

Although, the US imaging is an attractive medical imaging technique in general, because of its several advantages. The diagnostic accuracy of the US used for the detection purpose is estimated to be lower than the CT and MR. The MR imaging has the highest diagnostic accuracy. Furthermore, the limitation with US imaging is operator dependent, but it is overcome once the observer is trained. Speckle is another factor that affects the quality of the US images. Due to the presence of these speckles, an expert may not be able to extract the most useful information from the images. Thus, the interpretation of the different experts/radiologist may be different from the same US image. Regardless of all the limitations, the US imaging is preferred imaging in India on account of its widespread availability and low cost. Therefore, in this thesis, the US images have been chosen for study.

1.3 Ultrasound Imaging

Ultrasound imaging is a procedure in which high energy acoustic waves with a frequency greater than 20 KHz are bounced off from internal organ or tissues of a human body and make echoes [167]. These echo patterns are shown on the screen of the US machine, forming a picture of body tissue called a sonogram or ultrasonography. The basic principle of the US imaging is the transmission of high frequency acoustic waves into the patient's body followed by its reception, processing and display of echoes reflected back from the tissue's structures or medium within the body [167]. It has been recognized as a highly useful and powerful tool for the diagnosis and evaluation of the several clinical entities. In order to take the US image, it is very essential to understand how the US imaging system works and how acoustic wave is converted into an image.

In the US imaging process, the radiologist/clinician scans the desired portion of the body/organ by properly locating a medical ultrasound probe on the surface of the body. In order to provide a good acoustic contact, the skin is smeared with a jelly like substance [158]. Very short pulses are transmitted approximately 500 times each second by a piezoelectric transducer of material such as lead zirconate titanate, barium titanate that is able to convert electric signal into mechanical waves. The similar transducer also acts as a receiver that can also receive the sound echoes reflected back from the body tissues/organs and then converted back into the electrical signal. Due to different arrangements of the piezoelectric elements and the different shape of the transducer, transducers are classified into three different types such as a linear array (side by side arrangement of the elements), convex array (the elements are arranged into a sector like field) and phased array (each element fires the acoustic beam in proper order).

Low frequency transducers (3.0-3.5 MHz) are utilized for viewing large structures that are not close to the transducer, while the high frequency transducer (5-10 MHz) are used for those structures, which are close to the transducer [158]. The ideal transducer used for the US imaging would be perfectly matched to the human body with respect to shape and size; would also have high efficiency as a transmitter and high sensitivity as a receiver, a wide dynamic range and a wide frequency response for pulse operation. The pulse echo method depends on the measurement of time elapsed between the transmission of a pulse of US and the reception of its echo from a reflecting or scattering target, and measurement of the amplitude of its echo returned back from the target [158]. The amplitude of an echo provides the information about the depth of penetration of US waves and the effect of attenuation of US by the tissue. Further, if the transducer is moved across the patient's body while all the echoes are recorded and maintained on a video screen, a two dimensional image (B scan) will be generated. This is termed as brightness mode scanning. It modulates the brightness of a dot to denote the amplitude of a signal displayed at the location of the interface. The spot shown on the screen become brighter with stronger echo signal. Changes in the echo amplitude between maximum and minimum can be made to produce perceptible changes in the image brightness. Each pixel's brightness is displayed as one of 256 gray levels in black and white represented by 0 and 255, respectively. Black pixels represent fluid filled structures while white pixels refer to the dense tissues that reflect the major portion of incident sound beam. The spatial resolution of the image in US imaging depends upon the ultrasonic frequency as explained in the following subsections.

1.3.1 Propagation of ultrasonic waves through biological tissues

The Figure 1.1 shows the operation of ultrasonic transducer being used in medical imaging with an aperture that is usually in the form of a circle or a rectangle. The continuous wave excitation of a transducer produces effects in the near and far field and is given by the following equation [214].

$$I_d/I_0 = sin^2\left\{\left(\frac{\pi}{\lambda}\right)\left[(a^2 + d^2)^{1/2} - d^2\right]\right\} \quad (1.1)$$

where I_0 is the intensity at the surface of the transducer, I_d refers to the intensity at a distance d from the transducer along the central axis of the beam, a refers to the radius of the transducer and λ is the wavelength. In the near field, the beam is roughly cylindrical, with a series of axial maxima and minima of decreasing complexity, moving away from the transducer, whereas in the far field, the last maxima is formed at $d = \frac{a^2}{\lambda}$; $if\ a^2 >> d^2$.

The Eqn. (1.1) characterizes the intensity of wave along the depth of penetration and its relation with respect to the ratio of the wavelength and the size of the transducer. Similarly, the speed of the US wave depends upon the medium through which, it propagates. With the elasticity of the medium (κ) and the density of the medium (ρ), the speed (c) of the

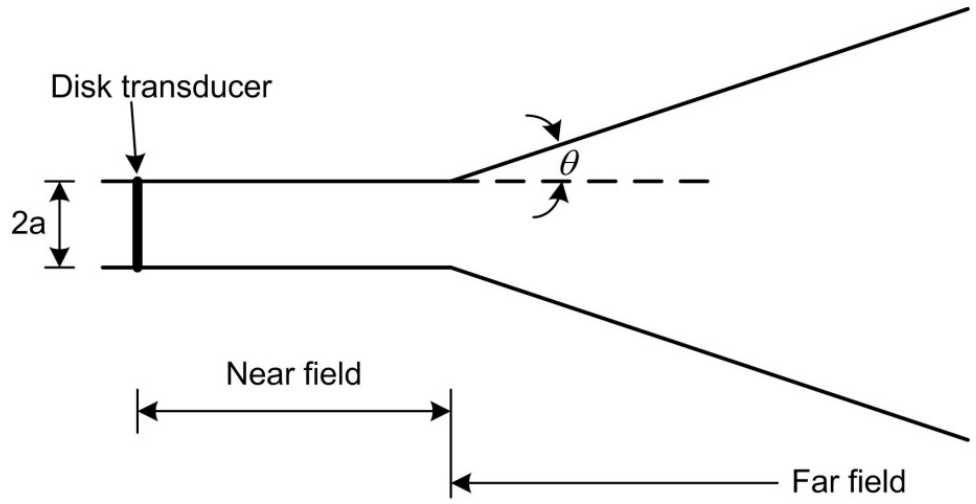

Figure 1.1 Propagation of the US beam produced by a disc transducer in the homogeneous medium [214]

US waves is given by

$$c = \sqrt{\kappa/\rho} \tag{1.2}$$

At a plane boundary between two media where the speed changes from c to c', relationship is given by

$$c' = \left(\frac{\sin\theta_t}{\sin\theta_i}\right) c \tag{1.3}$$

where θ_t and θ_i are the angles of refraction and incidence of the US waves, respectively.

At the normal incidence, with heterogeneous boundary having acoustical impedances of the two mediums as the Z_1 and Z_2, intensity of reflected waves is given by

$$I_r = I_i \left(\frac{Z_2 - Z_1}{Z_2 + Z_1}\right)^2 \tag{1.4}$$

where I_i and I_r are the intensities of the incident and reflected waves, respectively. The acoustic impedances are characterized by the material properties. The impedance is defined by the product of the density of a material and the speed of sound. For different biological materials, the impedance values with its attenuation effects are shown in Table 1.2 [249].

The Eqn. (1.2) shows the effect of different biological material constant such as κ and ρ on the speed of US waves whereas the Eqn. (1.4) gives the effects of acoustical impedances on the intensity of reflected waves. In addition, different biological materials exhibit different acoustical impedances. From the Eqn. (1.4), it is evident that the reflection of an incident wave is stronger, if the difference of acoustic impedance between two tissues at the interface is high. Reflection at a smooth boundary interface that has a diameter greater than that of the US beam is known as specular reflection [158]. The air has a low value of acoustic impedance. The sound is to be reflected entirely at a tissue air interface. Thus, if any air bubble exists along the propagation path of the US wave, a dark spot has appeared on the screen during the US scan. Moreover, the attenuation of the US energy is very high in the air

and thus, no reflection will be received by the transducer, when the US beams propagate through the air. Thus, coupling gel is required to put on the skin surface at the spot where the clinicians put the transducer during the US scanning. The best coupling agents are water soluble gels, but water is suitable for very short examination. The common coupling gel is a composition of 10 g Carbomer, 0.25 g ethylenediamine tetraacetic acid (EDTA), 75 g propylene glycol, 12.5 g trolamine and up to 500 ml demineralized water [158].

Table 1.2 Properties of some materials and body parts related to the US imaging

Material	Propagation speed c (ms^{-1})	Impedance Z $(10^6\ kg\ m^{-2}\ s^{-1})$	Attenuation coefficients α at 1 MHz $(dB\ cm^{-1})$
Air	330	0.0004	1.2
Blood	1570	1.61	0.2
Brain	1540	1.58	0.9
Fat	1450	1.38	0.6
Liver	1550	1.65	0.9
Muscles	1590	1.7	1.5 to 3.5
Skull bone	4000	7.8	13
Soft tissue (mean value)	1540	1.63	0.6
Water	1480	1.48	0.002

The boundaries of tissue including the organ surface and vessel walls are not smooth, but are seen rough by the US beam, i.e. there are irregularities at a scale similar to the wavelength of the US. These interfaces causes nonspecular reflection, called as backscattering, over a large angle [158]. Some of these reflections will reach the transducer and contribute to the construction of the image. The apparent conclusion is that the spatial resolution improves as the wavelength is decreased or the frequency is increased.

1.3.2 Typical medical ultrasound imaging system

A block diagram of a typical medical US imaging system is shown in Figure 1.2. A typical medical US device sends the US waves into the tissue using a piezoelectric crystal based transducer and analyzes the reflecting waves in order to obtain images of the structure of interest or mechanical parameters of the tissue. As the acoustic waves are transmitted into the body, it is reflected at the junction of different tissues, some of them are absorbed by the tissue, some of them will continue the propagation into deeper tissue of the body, some of them are diffracted as well as scattered into the different directions and some are reflected at the interface of media with different acoustic impedances. The strong absorption and scattering of acoustic waves in tissues indicate that the US imaging has quite poor signal to noise ratio compared to the others. The reflected echoes from different depths of the body are received by the transducer. The depth of each reflector can be estimated

from the time recorded between the transmission of US pulse and the reception of its echo using pulse echo method.

The US imaging system presented in Figure 1.2 consists a transducer of piezoelectric material, control panel with pulse generation and timing circuit, computer processing and display system. Furthermore, the US machine has several control knobs which are very important to control the image. For example, gain control is utilized to control to adjust the sensitivity of a signal. Gain is the ratio of the output of electrical power to input. Time gain compensation (TGC) is provided to compensate the decreased signal strengths of deeper tissues to the greater attenuation over a long path.

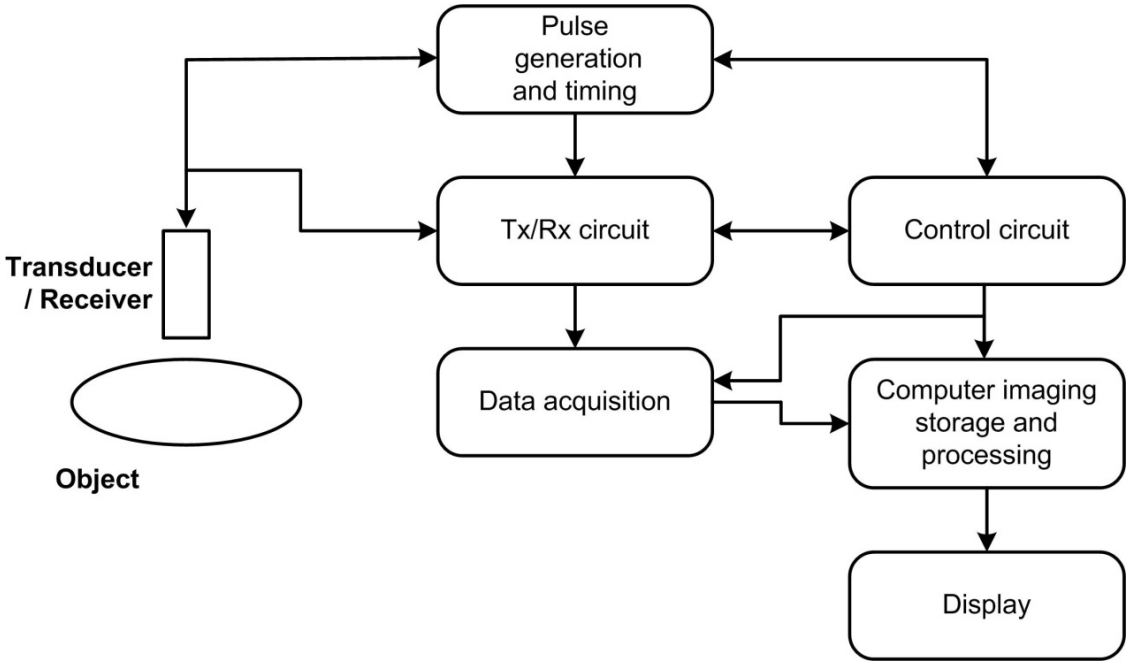

Figure 1.2 Block diagram of a conventional ultrasound imaging system [74]

The following four different modes of the US imaging are used in medical applications:

A-mode: This is the simplest US imaging mode in which a single transducer probe is used and the echoes are plotted on a screen along the distance (time) axis as peaks proportional to the amplitude (intensity) of each signal. This method is rarely used today, as it conveys limited information as a measurement of distance [158].

B-mode: B-mode (brightness) is a similar approach, but the echoes are displayed as points of different grayscale or brightness corresponding to the amplitude (intensity) of each signal [158, 197]. The B-mode of the US imaging provides a two dimensional image representing the changes in acoustic impedance of the tissue. To obtain a two dimensional image of the tissue structure, the transducer is pivoted at a point about an axis and is used to provide a V-shaped imaging region. Using the computer processing system, several versions of the acquired data can be displayed to show the acoustic characteristics of the tissue structure and its medium. The returned echoes are processed with proper pre-amplification and

adaptive gain amplifiers for acquiring the raw data that are converted into an image for display. Dynamic B-mode scanners provide real time US images using multiple transducer arrays and computer controlled data acquisition and display systems.

M-mode: In the M-mode (time motion), the depth in tissue is displayed along the one axis while the other axis represents time [158]. It is used to analyze moving structures such as heart valves. The echoes generated by a stationary transducer are recorded continuously over time.

Doppler mode: Doppler US imaging techniques include the capability of accurately measuring velocities of moving material, such as blood in arteries and veins. Doppler capability is most often combined with B-mode scanning to produce the images of blood vessels from which blood flow can be directly measured. This technique is used extensively to investigate heart valve defects, arteriosclerosis, and hypertension, particularly in the heart, but also in the abdominal aorta and the portal vein of the liver. Various types of Doppler systems such as continuous wave (CW) Doppler, pulse wave (PW) Doppler, spectral Doppler and color flow duplex are used in medical diagnosis [158].

1.3.3 Image quality and resolution

The image quality is the thing that keeps the clinicians more concerned. As the quality of US image is in best phase, the physicians get more diagnostic information from the images. There are few theoretical issues that affect the image quality. The quality of the US images depends on the image resolution such as axial and lateral. For different organs, different transducers with different frequencies are chosen. A higher frequency allows a higher axial and lateral resolution. Resolution refers to the minimum distance between two points at which they can be represented as distinct.

The axial resolution represents as the ability to differentiate between two points along the direction of the US propagation (axial direction) [158]. It depends on the pulse length and makes better, if the pulse length shortens. A transducer having high transmission bandwidth with high frequency (3-7 MHz) are more suitable for providing short acoustic pulses and then better axial resolution. Higher the frequency or smaller the wavelength ($f \propto 1/\lambda$) refers to the better axial resolution.

The lateral resolution is observed in a direction at right angle to the axis of the US wave propagation [158]. It depends on the diameter of an US beam. It is determined by measuring the width of the main lobe of a beam pattern at either -3dB or -6dB. A large transducer provides a narrower beam because of diffraction, but the size of the transducer is limited by some certain applications. A narrower beam can be accomplished at the cost of large side lobes that also reduce the contrast in an image because of interference of the reflections from the main lobes and side lobes. Good lateral resolution is achieved by focusing the transducer at a point within the certain depth.

Another important factor affecting the quality of an image is contrast resolution that is also decreased by inducting the noise in the image because of the multiple reflections (reverberation) of the US pulse [172]. The other factor is the penetration depth which is also related to the frequency as well as the wavelength. The higher frequencies are attenuated by tissue more than lower frequencies in the tissue medium. Higher frequency denotes lower wavelength and greater resolution, but lower depth of penetration. Normally, clinicians use lower frequencies for adults and higher frequency for children. Therefore, there is a trade off between the necessary depth of penetration and the desired image resolution.

1.3.4 Speckle

The US speckle is a granular pattern caused by constructive and destructive coherent interference of backscattered echoes from the randomly distributed scatters that are smaller in size. Because of the existence of these speckles, the US images become very complex to decipher. Speckle is also a main factor that limits the contrast resolution in the US imaging, thereby limiting the detectability of small, low contrast region and making the US images generally difficult for the non-specialist to interpret. In fact, due to the presence of speckle, even US experts with sufficient experience may not be able to extract correct and useful information from the speckled images. Speckle noise also limits the effective application of the image processing and analysis algorithms. Therefore, speckle is most often considered a dominant source of noise that is multiplicative in nature. Speckle occurs especially with images of liver and kidney whose underlying structures are too small to be resolved by large US wavelength [167].

The phenomenon of speckle occurs when a coherent source and a noncoherent detector are used to interrogate a medium. Several microscopic tissue components smaller than the spatial resolution of technique act together to reflect the sound waves incoherently. Speckle is manifested in a granular pattern due to image formation under coherent waves that are backscattered by the targeted surfaces and arrive out of phase at the transducer. When waves of a single wavelength are reflected from a rough surface, each point on the surface effectively behaves as a source of spherical waves [35]. These numerous spherical waves will have many different phases that will cause the waves to interact constructively at a few points in space and destructively at other points. If the surface is rough enough to cause a phase difference greater than 2π then the resultant intensity pattern will be random [35, 167]. The maximum possible intensity would be the sum of the amplitudes of a large number of large amplitude spherical waves, whereas the minimum intensity when all the waves interact destructively, would be zero. In the regions of low average signal intensity, constructive interactions will produce only medium or low amplitudes, while higher amplitude waves are present in the region of high average signal intensity. The overall result is that the random noise signal will have an average amplitude that increases with overall signal

intensity. In an image this appears as many bright specks in the lighter regions. This is speckle noise. In contrast to Gaussian 'additive noise', speckle is called multiplicative noise [35]. Finally, it can be said that the speckle is a complex phenomenon in the US imaging. Besides the speckles available in US images, different artifacts are also introduced in the US images because of the poor nature of machines, the human operator error such as wrong selection of the gain and incorrect placement of the transducer and other physiological and pathological conditions of the human body. Therefore, the US images are characterized by the speckle which makes the interpretation of these images very difficult.

1.4 Need of Image Denoising

The US imaging is one of the most important and cheapest instruments used for the diagnostic purpose among the clinicians. Due to inherent limitations of the acquisition methods and systems, the US images are degraded by the multiplicative speckle noise. As mentioned earlier, speckle is considered as a prime factor that degrades the quality of US images and most importantly meaningful texture information present in the US images. It has an undesirable interference effect on the images that obscure fine details in the images such as lesions with the faint gray value transition and small details and makes the US images generally difficult for the nonspecialist to interpret. In fact, the experts with a lot of experience may not be able to draw the final conclusions from these images. The presence of these speckles affects human interpretation of the images as well as computer assisted method also. Apart from this, the other image processing tasks such as segmentation, feature extraction, analysis, recognition, quantitative measurement etc. may also become difficult.

The detection and enhancement of the boundaries between different cavities and organs are of great need in the US imaging and are considered as a challenging problem. Although, image acquisition techniques yield an ever-improving quality, the presence of the noise introduced by the image formation process, image recording and transmission etc. is unavoidable. Hence, there is a need of image denoising for most of the post processing algorithms. To improve the quality of the images, the most important issue is the reduction of speckle noise. Sometimes, the noise reduction process may suppress the important details of the images. Thus, the noise reduction approach should be designed in such a manner that they can suppress the noise as much as possible without any significant loss of (boundary) edge information [5, 20, 25, 51, 166, 167, 210, 253, 277]. So, it becomes more difficult and challenging task to design and develop the image denoising approaches with edge preservation that simultaneously fulfil three different criteria such that the approach must be capable to suppress the maximum amount of the noise from the region of interest with the preservation of edge information and it must be stable and robust. Image denoising may also become a preprocessing step for the different image processing applications.

1.5 Need of Image Segmentation

Ultrasound image segmentation is an important issue in medical image analysis and visualization. The main objective of image segmentation is to change the representation of an image into more meaningful clinical information extracted from the US images and easier to analyze. In other words, image segmentation approach is used to partition the given image into several parts or different anatomical structures such as blood vessels and liver tumors from their background. Boundary identification, which is resultant of segmentation, is important for deriving the morphological information of the US image, which often serves as a crucial descriptor in both quantitative and qualitative US image analysis.

Furthermore, image segmentation is required for several other purpose such as localization of tumor, lesion and other abnormalities, measure the tissue volume to measure the growth of tumors (also recession in tumor size with treatment) and to help in treatment planning prior to radiation therapy, in radiation dose calculation. The accurate segmentation provides more meaningful and useful information from the US images used for clinical purpose. For example, in quantitative examination, instead of using only the diameter to quantify the scale of tumor, area and the boundary of tumor may be added for a more comprehensive characterization. In qualitative analysis, segmentation of the US image may provide better visualization of surface for a particular region of interest [250]. Segmentation accuracy determines the eventual success or failure of the computerized analysis algorithms. Moreover, the segmentation of US image is a challenging task because of its poor resolution, weak edges, the presence of speckle noise/artifacts and patient movement. Therefore, it is an area of prime concern for researchers and still there is a need of segmentation approach for the US images that can accurately provide the segmented images used for clinical purpose and analyze these image for the extraction of features of interest involving edges, regions and texture for further analysis [75].

1.6 Literature Review

The US images are very difficult to diagnose because of the existence of speckle, which hampers the perception and extraction of fine details from the image. In literature, many researchers have proposed the image denoising and segmentation methods for the US medical images; a review of the work reported, is being presented here.

1.6.1 Developments in image denoising aspects

A variety of the noise reduction/image enhancement algorithms for the US images have been implemented in previous years. Bamber and Daft [18] reported that the lesion detectability gets reduced by approximately a factor of eight due to the presence of speckle in the image. They proposed a noise reduction filter that changes the amount of the smoothing according to the ratio of local variance to local mean. Consequently, the most of

the enhancement algorithms to improve the visual quality of the US image are relied on speckle reduction treating speckles as a random noise. The noise reduction methods can be primarily classified as image averaging (compounding) and image filtering (post-acquisition) [168]. Compounding methods are based on the average of multiple images which are obtained by sampling the same object at different time, from different views, or with different frequencies and thus, reduce speckle up to limit. This approach has been proposed in the majority of the speckle noise suppression techniques [148, 178, 197]. Donnell et al. [178] made incoherent averaging of measurements at different view and direction, which are used to reduce speckle noise in the US images. In their work, an analytic expression for the correlation between two measurements made at different spatial positions is derived. Thus, the optimum aperture displacement for efficient incoherent averaging is computed using their derived expression and found to be equal to approximately one half of the aperture length [178]. However, the image averaging methods suffer from the loss of spatial resolution.

Filtering methods have the advantage that they are not affected by the acquisition procedure. Filtering methods present a practical alternative for most of the clinical applications. Filtering methods can be classified as single scale spatial filtering such as linear [157, 192], nonlinear adaptive methods [103], multiscale spatial filtering such as diffusion based methods [11, 33, 140, 142, 168, 176, 186, 266] and several multiscale methods in different transform domain such as pyramid [88], wavelet [80, 92, 234], ridgelet [174, 194], and curvelet [13, 225] based approaches. In the category of filtering approach, there has been a continuous research in both the domain such as spatial and frequency domain. The various popular filters used in the spatial domain are wiener filter [103, 126], proximity based filters [228, 262] and order statistic filters [163, 183]. Wiener filter applied to an image tailors itself to the local image variance from the neighborhood of each pixel, so as to perform little smoothing wherever the variance is large, and vice versa. This filter works best when the noise is of constant-power additive noise, such as Gaussian noise. The widely used proximity based filters though do not require a prior knowledge about the image like wiener filter; they help to remove noise at the cost of blurring the edges. Simple mathematical linear spatial filters such as mean filter degrade sharp details such as line and edges [103, 254], because in these filters neighboring pixels are averaged together at the cost of resolution. Most popular nonlinear nonadaptive filters such as median filter [122], which is a specific case of an order statistic filter, are applied to all the pixels whether they are corrupted or not. Nonlinear filter, e.g. the weighted median filter [36] is also used to retain the edges as compared to classical median filter, but it results in a loss of resolution by suppressing fine details. Another approach is adaptive filtering that entails a trade-off between smoothing efficiency and the preservation of discontinuities. An example of adaptive filtering is the adaptive weighted median filter [157]. It is an enhanced version of the weighted

median filter for suppressing the speckle in the US images. The weighted median of a window is defined as the median of an extended sequence formed by replicating pixels in such region by an amount estimated from their distance from the central pixel and an estimation of the local homogeneity. Singh et al. [217] proposed an adaptive rank ordered mean filter that is also able to reduce the impulse noise and preserve the image details. Other stochastic approach used for speckle reduction in the US image has been proposed in [232] and known as a squeeze box filter (SBF). It is a local averaging method that removes the local extreme assumed to be outliers in a robust statistical estimation framework [69]. Rayleigh-maximum likelihood (R-ML) filter has been proposed using similar methodological tools in [17].

Most widely cited filters used for speckle noise reduction in the statistical category include the filters proposed by Lee [142, 143], Frost [96] and Kuan [139]. These filtering approaches are not based on the mean or median filtering rather they depend on the coefficient of variation (COV). The lee filter attempts to distinguish whether a pixel is a noisy pixel or an image detail. Both the Lee and Kuan filters provide an output image by computing a linear combination of the center pixel intensity in a filter window with the average intensity of the window. Therefore, the filter achieves a balance between straightforward averaging (in homogeneous regions) and the identity filter (where edges and point features exist). This balance depends on the COV inside the moving neighboring window. The Frost filter also strikes a balance between averaging and the all pass filter. In this case, the balance has been achieved by forming an exponentially shaped filter kernel. These filters are sensitive to the size and shape of the filter window and provide over smoothing and blurring the edges, if the size of the window is too large, while in case of the small window's size, it is not able to completely suppress the speckle noise. Motivated by the relationship between a Gaussian operator and a linear diffusion equation, Perona and Malik [186] suggested an approach based on the nonlinear anisotropic diffusion filter. Based on the work presented in [186], several researchers [1, 7, 11, 33, 53, 88, 112, 128, 138, 152, 154, 160, 168, 216, 227, 231, 266, 274] proposed anisotropic diffusion methods, where the anisotropic diffusion equations provide the approach for selective image smoothing. Black et al. [33] described that the anisotropic diffusion can be seen as a robust estimation procedure which estimates a piecewise smooth image from a noisy input image. Abd-Elmoniem et al. [1] introduced a nonlinear coherent diffusion model for speckle reduction and coherence enhancement of the US image. Yu and Acton [266] provided the derivation of speckle reducing anisotropic diffusion (SRAD). This method has adopted the concept of Lee and Frost filtering approaches into anisotropic diffusion algorithm by exploiting the instantaneous coefficient of variation that also serves as the edge or high contrast feature detector in the speckled image [167]. The SRAD approach makes fine details to be more visible in the image; still it has a

limitation in preserving subtle features such as small cysts and lesions in the US images because of blurring of the edges. Later on, several variants such as robust SRAD (RSRAD) [231], detail preserving anisotropic diffusion (DPAD) [11], oriented SRAD (OSRAD) [138], improved SRAD (ISRAD) [227] and robust DPAD (RDPAD) [154]. In RSRAD, the relations between anisotropic diffusion and robust statistics are described. Tabuer [231] presented a new edge stopping function based on Tukey's biweight robust estimator that also provides sharper boundaries and improves the stopping criterion of the diffusion process. In DPAD approach, Fernández et al. [11] modified the SRAD algorithm to rely on the Kuan filter instead of the Lee filter. The OSRAD is used to perform directional filtering of the image by adding a nonscalar component to the SRAD algorithm. The ISRAD makes use of an alternative diffusion threshold estimator for better preservation of low contrast features in the image, while the RDPAD approach is a modified version of the DPAD algorithm using Tukey's error norm and is able to provide better preservation of detail in the diffused image. It is also less sensitive to the number of iterations. However, it suffers from the over diffusion problem. Giloba et al. [100] proposed nonlinear complex diffusion filter (NCDF) used for image enhancement that is further utilized by Salinas and Fernandez [208] for suppressing the speckle in optical coherence tomography images (OCT). Bernards et al. [20] has also proposed an improved and adaptive version of the NCDF approach named as INCDF and applied to the OCT images. Yu et al. [273] also introduced another variant of the anisotropic diffusion using the SUSAN edge detector [218] instead of gradient edge detector as used in the conventional diffusion model. The PDE based diffusion methods provide better denoising effect. However, they tend to overblur the image with many edge/texture details getting lost.

Another PDE based approach is the total variation filtering (TVF) used for image denoising that has been proposed by Rudin et al. [204] and named as ROF model. It is based on a total variation iterative algorithm where the total variation norm of the image is minimized subject to the constraints estimated from the noise statistics. These constraints are imposed using Lagrange multipliers. The ROF model is solved using this minimization problem through PDE-based schemes. Several approaches have been proposed to minimize the total variation of the ROF model such as a nonlinear projection based approach proposed by Chambolle [47]. However, the TV based methods have to undergo several iterations for denoising and also fine structures, details and textures are not properly preserved by these methods [25]. The TV minimization approach has also been adapted to the US imaging in [3, 25, 27, 76, 159]. Unlike the previous adaptive filters, all the considered PDE based filtering techniques are iterative and provide smooth images while preserving the edges. Nevertheless, most importantly structural details are unfortunately suppressed during iterations [69]. In the recent years, a particular attention paid to another nonlinear bilateral filter (NLBF) is proposed by Tomasi and Manduchi [237] to take into account local structure

in addition to intensity and geometric feature [162] and used in several image processing applications [119, 188, 280]. Several authors [203, 229, 239, 272, 280, 281] also utilized the NLBF approach either in spatial domain or transform domain using the hybrid filtering technique for the noise reduction purpose. However, it has a tendency to oversmooth and sharpen edge and texture. An adaptive fast bilateral filter has also been proposed by Shao and Paul [213] for suppressing the speckle in case of US images. In this approach a local histogram is introduced to speed up the processing of bilateral filter. Similarly, Buades et al. [37] proposed a nonlocal means filtering (NLMF) approach in which each pixel is estimated by the weighted averaging of other pixels whose neighborhood have similar geometrical configuration. Initially, it is developed for the additive Gaussian noise. In Coupe et al. [69], the nonlocal mean theory has been adapted for speckle reduction in the US medical images. In another approach, Zhang et al. [283] proposed a two directional nonlocal variation model used for image denoising. This approach consists of three components such as a scaled version of the original image and other two are estimated using the similarities. Further, the nonlocal denoising approaches are moment based [127] or group similar block by block matching and then apply 3D transform domain filtering [71, 72]. Another iterative weighted maximum likelihood filter has also been employed for reducing the speckle noise with probabilistic patch based weights [73].

In another category of multiscale denoising, initially spatial information of the image is transformed into frequency domain using one of the transformation techniques such as wavelet, ridgelet, contourlet, curvelet etc. Later such information is processed for better image enhancement. Presently, lots of research work on image processing is concentrated in transform domain. In that series, there has been considerable interest in using the wavelet transform (WT) as a powerful tool for image denoising [5, 6, 28, 51, 79, 80, 82, 111]. The first wavelet based method for speckle reduction was reported by Gao et al and Guo et al.[99, 105]. Donoho et al. [79-82] proposed wavelet thresholding approach, which is a true signal estimation technique that exploits the capabilities of the WT for signal denoising [31, 79, 111]. The well known thresholding methods include VisuShrink [82] and SureShrink [81]. In wavelet thresholding approach, a signal is decomposed into low frequency (LF) component (approximation subband) and high frequency (HF) components (detail subbands); since approximation subband has most of the signal information and detail subband are processed with the thresholding approach. These thresholding procedures generally result some artifacts in the denoised image [94]. To over this limitation, BayesShrink approach is introduced by Chang et al. [51], which determines the threshold value in Bayesian framework through modelling the distribution of the wavelet coefficients as Gaussian [281]. Fodor and Kamath [92] also presented an empirical study on the image denoising by wavelet shrinkage such as soft, hard, garrote and semisoft and also showed that SureShrink and BayesShrink

give better results. In 2006, Saad et al. [205] proposed a comparison between two multi-resolution approaches such as soft thresholding and power law used for speckle reduction in the US images. The method of enhancement uses a wavelet approach for soft threshold and power law with nonlinear upper and lower cut-off. All the standard wavelet thresholding methods assume that the noise is white Gaussian noise and independent of noise-free signal. However, these techniques become ineffective when applied to medical US image degraded by speckle noise. Therefore, the wavelet domain despeckling techniques are applied to the image logarithm, since after the logarithmic transformation, speckle noise becomes approximately additive Gaussian noise. These techniques are called homomorphic speckle filtering techniques [5, 19, 28, 94, 104, 111, 155] in which the WT coefficients of the logarithm of speckled image are considered. These coefficients are subsequently shrunk or adaptively thresholded [97].

In this category, initially, the researchers [5, 52] applied statistical approach such as the Bayesian approach for image denoising. This approach has been extended by the researchers in [6, 28, 70, 94, 111, 136, 166] by considering various noise models for the distribution of noisy wavelet coefficients like hidden Markov model [70], Gaussian [95], Fisher-Tippet [166], Rayleigh [111]. Dependency of these approaches to a specific noise model decreases their flexibility. In [209], the Bayesian based approach using Sylvester-Lyapunov (S-L) equation has been presented for both additive Gaussian and multiplicative noise. Further, some of the researchers [189, 190, 198, 199] proposed a mixture of statistical model which has additional computational complexity. For example, Rabbani et al. [199] proposed a mixture of Laplacian and Gaussian model for estimating noise free wavelet coefficients and mixture of Gaussian and Rayleigh model. Apart from these denoising methods used in the WT domain, Cai and Silverman [38] presented two different thresholding methods such as Neighblock and Neighcoeff for one dimensional signal using overlapping block rather than individual wavelet coefficients. In 2005, Chen et al. [56] motivated and applied Neighcoeff to image denoising and named as NeighShrink approach that has a basic limitation of using universal threshold and constant window size for all the wavelet coefficients. Further, it is improved by Dengwen and Wengang [289] and this approach is used an optimal threshold and window's size estimated by minimizing the Stein's unbiased risk estimate (SURE). Several thresholding approaches [19, 31, 39, 173, 189, 282] were also proposed for image denoising purpose.

The main strength of wavelet based approaches is its capability to treat the different subbands of an image separately [203]. However, the WT based method may introduce many visual artifacts in the denoised images. The WT is able to efficiently represent a function with one dimensional point singularity. However, it is less efficient in representing the sharp transition like line and curve singularities due to its limitation of direction. To

overcome the limitation of the WT, ridgelet transform has been evolved to provide the information about the orientation of linear edges [77]. However, it is unable to represent the curve singularities effectively. Ridgelet transform provides the information about the orientation of the linear edges. Donoho et al. [225] presented curvelet transform (CVT) used to represent two dimensional singularities with the smooth curve and also provides better denoising with edge preservation results. However, the CVT does not provide a multi-resolution representation of the geometry and the curvelet is also not built directly in the discrete domain [106, 165]. Contourlet transform proposed by Vetterli et al. [78] performs well in noise reduction due to the application of multiscale Laplacian pyramid (LP) followed by directional filter banks. However, it has less directional features than curvelets. To represent the edges more efficiently, Labate et al. [106, 141] proposed a new multiscale analysis tool named as shearlet. The decomposition of shearlet is similar to the contourlets except that there is no limitation on the number of directions. Presently, it is also utilized in different image processing applications [83] such as edge detection [264], denoising [57, 58, 84, 118, 149, 285] and fusion [60, 165, 246] and quoted that it provides better results than the others.

Later efforts in this area have suggested that the perceptual quality obtained in the WT domain could be substantially improved using further spatial operation. Therefore, the aforementioned approaches can be combined in order to utilize both the features and to take advantage of the different paradigms. For such purpose, some researchers [14, 239, 281] proposed wavelet transform based bilateral filtering approach. It provides better denoising and also effectively preserves the edges. In addition, Yu et al. [272] have proposed trivariate shrinkage in the wavelet domain and joint bilateral filter in the spatial domain. Some authors [27, 76, 84, 149, 159] proposed several denoising methods using the TVF approach with the different transformation techniques with their advantages. In another approach, Abrahim et al. [3] presented a wavelet based total variation filtering approach for suppressing the speckle noise in the US image in which noisy image undergoes several iterations for suppressing the noise, but it leads to blurring effect. To overcome such limitation, the fusion of the noisy images processed by total variation and curvelet based approach are presented in [25]. This method is applied to the CT medical images and shows a better denoising method by providing better results, but it also suffers from the limitations of curvelet. Most of the recent work [88, 89, 128, 176, 200] on speckle suppression techniques are also based on fusion of diffusion and multiscale techniques. Moreover, Yap et al. [263] conducted a survey on a group of non-radiologists and a group of proficient radiologists to envision the effect of computer processed images in improving human performance in the US breast cancer detection. They concluded that the condition of computer processed images beside the original US images; considerably improve the detection tasks of nonradiologist, but only

marginal improvements are shown in the detection and classification tasks of the group of proficient radiologist. These surveillances clearly proved the effectiveness of using imaging algorithms in computer-assisted diagnosis systems.

1.6.2 Developments in image segmentation aspects

Image segmentation is an important step for quantitative and qualitative analysis of the medical image. An accurate segmentation provides more meaningful information of the medical images. The US image segmentation is a very difficult task due to speckle and weak edges of a particular object of interest. In past years, several researchers proposed different segmentation methods based on either discontinuity (edge based) or similarity criterion (thresholding, region growing, region split and merge, watershed) [103, 181]. The traditional edge detection techniques are susceptible to spurious responses when applied to the US image. Image thresholding is a basic approach used for segmentation purpose. It is spatially blind image segmentation technique [241] in which the partitioning of object from background area is performed by the choice of the proper range of gray scales [117]. This approach is very convenient and easy for segmentation, but due to the noise and artifacts present in the US images, accurate segmentation is not achieved. The region boundary obtained by such type of techniques provides false interpretation of the object shape. Another spatial blind image segmentation approach is clustering, which is utilized to partition a given set of objects within a given set of cluster [130, 241]. The clustering, particularly fuzzy c-means (FCM) clustering and its different variants are widely used for image segmentation purpose and it is able to retain much more information [187]. However, it is very sensitive to noise and other imaging artifacts because it does not consider any spatial context. To overcome this problem, Ahmed et al. [9] proposed an improved FCM called as the bias corrected FCM (BCFCM) by incorporating the spatial neighborhood term and successfully applied on the MR images. It works well by providing better segmented images than the conventional FCM approach, but it takes too much time than the FCM. To solve this problem, Chen and Zhang [222] modified the cost function of the BCFCM by incorporating the kernel induced distance instead of Euclidean distance and named as kernel FCM. These methods are also highly affected by their parameters. Yang and Tsai [260] introduced a Gaussian kernel based FCM (GKFCM) with spatial information. Chuang et al. [63] presented another variant of the FCM approach by incorporating the spatial information into the membership function for clustering purpose. Kang et al. [129] also proposed a novel modified FCM approach in which spatial neighborhood information is incorporated into the conventional FCM algorithm with an adaptive weighted averaging filter. It also improves the segmentation results. Krinidis and Chatzis [137] proposed a robust fuzzy local information c-means approach (FLIFCM) that includes a fuzzy factor into the cost function of the FCM and the local spatial information.

Presently, several fuzzy based methods used for the image segmentation purpose can be found [116, 130, 131, 156, 175, 191, 258].

In another category of image segmentation approach, region and energy-based techniques are spatially guided approaches that are dependent upon the spatial relationship of the pixels used for image segmentation. They include region growing, split and merge and hybrid growing-merging in the region-based approach while energy based approach includes active contour, graph-based, watershed and marker-based watershed segmentation methods. Region growing segmentation approach starts from a single pixel or some predefined labelled set of pixels called a seed based on the homogeneity criterion and it stops, when pixels satisfying the homogeneity criterion, are no longer found. Using this method, the segmentation performance totally depends upon the seed pixels. Several authors [2, 8, 86, 87, 233] developed different segmentation approaches using region growing method. But, this method suffers from the problem of oversegmentation. Another region-based approach is region split and merge that is initiated with the repetitively split until segments satisfying a particular homogeneity criterion are obtained [23, 40]. In the category of energy and contour based segmentation, watershed is a popular approach used for segmentation purpose that utilizes image morphology [103, 241]. It utilizes region as well as contour information for the image segmentation. The main advantages of the watershed segmentation approach are that it is very simple and always provides a complete division of the image [22, 123]. It is highly sensitive to noise and suffers from the problem of oversegmentation. Some authors also tried to use the watershed approach for the hybrid image segmentation purpose [114, 115, 211, 215, 286]. In one hybrid watershed segmentation approach, both morphological and region merging are used to detect the objects. Though, it overcomes the problem of the watershed, but still oversegmentation, poor detection of thin structures, poor detection of significant areas with low contrast boundaries and missing of boundaries are the prominent limitations because of the existence of speckles in US images. The active contour model is based on the energy minimization and gives closed contour shape of the object. It can be categorized based on their implementation as being either parametric or geometric [241]. Active contour model or snake model proposed by Kass et al. [133] in 1988 and proved to be an efficient framework for delineating an object boundary from a noisy two dimensional image. The main problem associated with this model is the initialization and poor convergence in noisy image. It is also a time consuming process. The snake model is also successfully applied to the echocardiographic US images, but in case of the liver US images, it is very difficult to segment because of the high concentration of blood vessel in the liver. The gradient vector flow (GVF) algorithm [255] is proposed to overcome the convergence problem in Kass model. The authors also presented their performance on twelve different US images of liver tumors having different sizes. To

overcome the problems of snake model, Osher and Sethian [180] modelled the propagating curve as the specific levels of higher dimensional surface. The surface can change to take on the desired shape with time. This surface is called level set function (LSF) and the middle front is called zero level set. In 1995, Malladi et al. [161] used the levels set techniques proposed by Osher and Sethian for shape recovery. To increase the robustness, Gong et al. [102] proposed a hybrid level set approach by incorporating the shape constraints into a region-based contour evolution. The active contour model in the level set formulation is further categorized as edge-based and region-based approach. Edge-based level set models utilize image gradient of a given image for stopping and evolution purpose of the curve.

Geodesic active contour (GAC) model is most popular edge based segmentation method that utilizes edge-based stopping term and a balloon force term employed for controlling the moving curve [45, 182, 248], but it is very difficult to design the balloon force. Furthermore, it is usually sensitive to noise and suffers from initializing the curve. In the conventional level set methods, some irregularities occur during the evolution of the level set function. In conventional level set approaches, it is a prime requirement to keep the moving curve close to signed distance function [64, 185]. Re-initialization is the process which is used to provide a stable curve motion and better segmentation results. Many researchers [179, 185, 212, 248] have tried to re-initialize the regularity of the level set function (LSF) and make it stable. However, sometimes it moves the zero LSF away from the estimated position. In order to solve this problem, Li et al. [64] introduced a variational formulation for the GAC with a penalty term that drives the level set function to be close to the signed distance function. This method completely eliminates the periodic re-initialization process of the level set function during the evolution process by considering the variational energy function as a combination of the internal and external energy term, where the external energy forces the zero level set function to the expected position while internal energy is used to penalize the deviation of the LSF from a signed distance function. However, some unwanted side effects are produced on the level set function because of the penalty term and thus it may affect the segmentation accuracy. Furthermore, Li et al. [65] extended their previous method and introduced a new distance regularization term and external energy term that forces the motion of contour toward the expected position. This distance regularizing term completely eliminates the requirement of re-initialization and also helps to avoid the undesirable effects introduced by the penalty term in their previous approach.

Besides the edge-based active contour models, region-based models aim to identify each region of interest in the given image by incorporating the region based information into their energy functional. Region-based active contour models have shown many advantages over the edge-based active contour models such as the unrestricted position of the initial contour, the automatic detection of estimated boundaries and effective reasonable

segmentation because of global energy minimization based on the statistical properties inside and outside the evolving contour on which it evolves the deformable shapes and keeps the regularity of the active contour. Chan and Vese [48] proposed a region-based active contour model that is named as CV model used for segmentation purpose. It is based on the Mumford and Shah model [169] to extract the object of interest whose boundaries are not detected by the gradient. The CV model provides better performance than the GAC model because of its ability to obtain a large convergence rate. However, image segmentation using the CV model depends on the placement of initial contour. Due to improper initialization of contour, different results may be obtained using different contours selected for a similar image. To overcome this limitation of the CV model, many researchers [202, 221, 242, 265, 268] have tried to introduce some efficient techniques. Solem et al. [221] propsoed the initialization methods for contour which is estimated using a search method. It is also a time consuming process and often fails during the small difference between the object and its background. In [202], initializing curve is generated by iteratively connecting edge points estimated by the canny detector and morphological filter, while in [265, 268], these schemes are introduced without solving the PDE's. However, these are still sensitive to initialization of contour and noise. Further, Li et al. [66] introduced a variational level set formulation for image segmentation that works on the region scalable fitting (RSF) energy function and regularization function. The RSF function is capable to obtain the intensity information in the local regions at a fixed scale to compute the two fitting functions and drives the contour toward the estimated boundaries of the object. The regularity term available in this model is used to control the length of the object boundaries and prevents the oversegmentation. Currently, several researchers [236, 275, 276, 278] tried to utilize these methods for the US image segmentation purpose. Moreover, Zhang et al. [279] presented another region-based active control model that utilizes both the features of the GAC and the CV model. In this approach, signed pressure function has been used instead of edge stopping function to control the direction of the curve evolution. Several quantitative evaluations have been performed on this approach and it has been reported that it performs better than the conventional level set methods.

In another graph based model [91] used for image segmentation, firstly graph is constructed by considering each vertex corresponding to a pixel in the image and the edge connects the pixel to its neighbor. After constructing the graph, the different subgraphs of similar intensity levels are now merged and produce larger subgrpah. Finally, by repeating the merging process, an image is segmented into the larger homogenous region. It produces better segmented images with higher accuracy; however, it is sensitive to the parameter selection. Recently, several approaches based on graph theory have been employed by many researchers [120, 121, 184] for the segmentation of the US images. In the present

work, only edge-based and region-based active contour models and clustering approaches are considered to implement the proposed approaches. Besides all these aforementioned segmentation approaches, many other algorithms such as Markov random field [34, 108], neural network [125, 251], fuzzy logic [2], cell-competition [54], fast marching [43] are also presented by several researchers.

1.7 Objectives of the Present Study

The main objective of the present study is to develop the denoising and segmentation methods for the US medical images. It has been recognized and emphasized in the previous sections that speckle noise reduction and simultaneously edge preservation improve the perception of the US images. Therefore, edge preserved denoising of US images has been targeted as a problem here under consideration. Another main problem is the accurate segmentation of the US medical images. For achieving these two objectives, different techniques have been proposed by several researchers as summarized in the previous section. With these objectives, initially it has been necessary to analyze and identify a better approach among the existing popular denoising and segmentation approaches. After identification of the suitable approaches, the task has been to improve the performance of the identified approach, either by modifying the earlier algorithm or by suggesting a new approach. Thus, based on the above observation following objectives have been identified for this study:

1. Comparative analysis of the speckle reduction performance provided by the several existing approaches and identification of an optimum approach for the denoising of US medical images.
2. Design, development and implementation of image denoising methods.
   In order to achieve this objective, different denoising approaches are proposed in the present study that also leads to further different sub-objectives. For such purpose, efforts have been made for the improvement in their computational performances such as robustness, stability and efficiency, and finally targeted to make the superior performance of image denoising approach for the qualitative and quantitative measures like noise suppression and most importantly edge preservation while denoising.
3. Design, development and implementation of image segmentation algorithms for the US medical images.
   To fulfil this objective, two different edge-based and region-based active contour segmentation methods are proposed in the present study.

1.8 Organization of the Thesis

The research work carried out here in this thesis is reported under two different aspects. The first aspect refers to the denoising of US medical images, while the second

deals with the segmentation of US medical images. This thesis comprises of eight chapters. The present chapter 1 introduces the topic and states the objectives. The rest of the thesis is organized as follows:

Chapter 2 presents the details of an effort to evaluate the performance of various existing denoising approaches on the US images. The quantitative and qualitative analysis of these approaches is carried out in terms of noise suppression and edge preservation. At the end of this chapter, the detailed description of the proposed M-band ridgelet based thresholding approach is provided with a comparative analysis of the denoising results obtained by the different approaches. Based on the quantitative analysis, advantages and limitations of the approaches are mentioned at the end.

Chapter 3 provides details of developed two nonlinear filtering approaches in ripplet domain using a bilateral filter and thresholding methods such as NeighShrink and BlockShrink. The denoising performance of the proposed approaches is evaluated for both the test and real US images quantitatively and qualitatively. A comparative analysis of the denoising results provided by the proposed and other existing approaches is also presented at the end of the chapter.

Chapter 4 presents the proposed remnant approach for adaptive fusion based noise filtering in the US images that fuses the images denoised by the TVF, shearlet thresholding using cycle spinning (CSST) approach, separately and edge information extracted from the remnant of TVF and processed by the CSST approach. The denoising results and behavior of the proposed approach are explained at the end of this chapter.

Chapter 5 introduces two different denoising approaches developed based on nonsubsampled shearlet transform (NSST) using modified nonlinear diffusion equations. The first approach is based on the modified diffusion equations by incorporating an adaptive gray variance with the gradient information for increased template size, while in the second approach, nonlocal pixel information is incorporated to evaluate the gradient with an adaptive gray variance. The improved performance of the proposed approaches is compared with the others and discussed in this chapter.

Chapter 6 presents the proposed hybrid segmentation technique for the US images using two approaches, i.e. kernel fuzzy clustering and edge-based active contour model. The proposed approach starts with kernel fuzzy clustering and then the results of clustering method are employed to initialize the curve and to estimate the several controlling parameters. To provide in-depth insight, a comparison is also made between the segmentation results obtained by the proposed and other approaches.

Chapter 7 introduces another hybrid segmentation approach for the US medical images by utilizing both the features of the Gaussian kernel fuzzy clustering and region-

based active contour segmentation approach. At the end of this chapter, a comparative analysis of the segmentation performance obtained by the proposed and other existing methods is presented for both the synthetic test images and real US images.

Chapter 8 concludes the work stating the important features and advantages of the proposed schemes. The outlook for future work is also given at the end of this chapter.

CHAPTER 2: VARIOUS DENOISING APPROACHES AND THEIR PERFORMANCE EVALUATION

This chapter describes different types of noise present in the ultrasound medical images. These noises such as Gaussian and speckle can have a significant impact on the quality of ultrasound images. In this chapter, the work is concentrated on speckle noise known as multiplicative noise considered as a most prominent factor that affects the human interpretation and accuracy of computer- assisted methods for processing of ultrasound medical images. Based on the noise model introduced in this chapter, several denoising approaches are derived and explained in detail. The performance of these denoising methods is also discussed, qualitatively and quantitatively in terms of different performance evaluation parameters whose mathematical formulations are presented in this chapter. In the last part of this chapter, one of the proposed approach has been extensively analyzed, evaluated and compared with the others based on various performance measures.

2.1 Introduction

Currently, the research in medical imaging has produced many different imaging modalities for the clinical purpose. Among the different imaging modalities, the US imaging is of a particular interest in the medical diagnosis of neck, chest, liver, abdominal cavity, gallbladder, pancreas, spleen, adrenal glands, kidney, prostate and scrotum. The main advantages of the US imaging, besides, there being no tissue damage in the process, are that it allows faster and accurate procedures due to its real time capabilities and low cost of the scan. However, the US images are of relatively poor quality because of various noises and artifacts present in them. These are the main factors that limit the contrast resolution in the US imaging that also affect the detection of small and low contrast regions and thus, making the US images difficult to interpret for the specialist. In fact, due to the presence of these noises, even the US experts may not be able to extract the correct and useful information from the images. This also limits the effective application of the image processing and analysis algorithms. Among all the noises and artifacts present in the US images, speckle is considered as one of the most prime sources of noise. Speckle occurs especially with the liver and kidney images whose underlying structures are too small to be resolved by the large US wavelength. Sometimes, the US images also suffer from the random additive Gaussian noise. Therefore, these noises should be filtered out [145, 154, 155, 166, 209].

In the above context, Image denoising is mostly considered as the first step required before the image is studied. The detection and enhancement of the boundaries between different cavities and organs are in great need in US images and is also considered as a challenging problem because of some limitations of the image denoising methods such as the blurring of edges and loss of some detailed information present in the US images. To overcome such denoising problems, many researchers have introduced several denoising algorithms in last two decades [7, 31, 128, 145, 174, 231, 232, 266, 274]. Each approach has

its assumptions, advantages and limitations. Thus, denoising and particularly, edge preserved denoising algorithms should be designed in such a manner that they suppress the noise as much as possible without any significant loss of information present in the US images. Therefore, it is an area of prime concern for the researcher and still there is a need of denoising methods that can efficiently remove the noise, retain sharp features of the images from the blurred one, and simultaneously enhance its clinical useful features.

In the following sections of this chapter, after introducing the sources of noise present in the US images and their noise models in the initial parts of the chapter, efforts have been made to describe the various denoising methods and evaluate their performance on the basis of their noise reduction and edge preservation capability. In the later part of this chapter, one of the proposed approach is analyzed and evaluated based on the different performance measure as discussed in this chapter.

2.2 Sources of Noise

Most of the images are assumed to have one or more sources of noise in different imaging modalities. Information and awareness about the sources of noise present in the original image play an important role in the development of image denoising model. When we are aware about the information on the degradation effect of noise and its model, the inverse process can be applied on the noisy image to restore back in its original form. Therefore, the basic sources of the noise in US imaging and its effects on the digital image are discussed here.

The US medical images largely show the noise variation and spatial resolution degradation that completely depends on the different patient because of a heterogeneous mixture of fat, muscles, parenchymatic and connective tissue presented in the propagation path of US waves. Figure 2.1 presents the simulated wave propagation of 7.5 MHz pulse excitation from a focused circular transducer with a diameter of 4.8 mm.

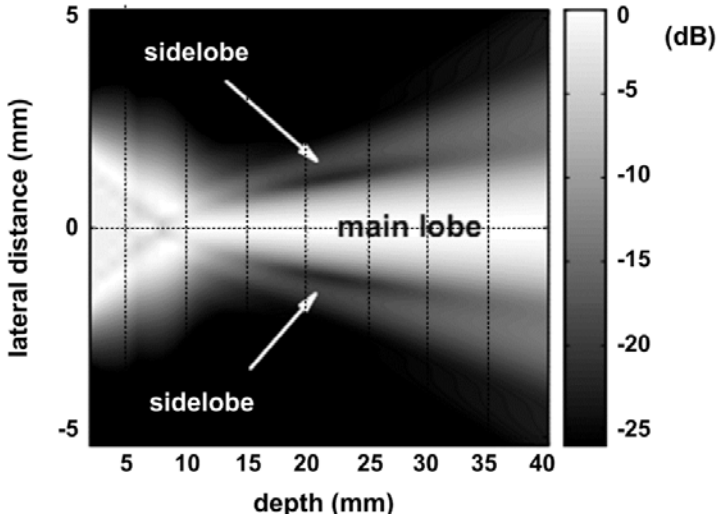

Figure 2.1 Simulated beam propagation of 7.5 MHz pulse excitation from a focused circular transducer with the diameter of 4.8 mm [171]

Three main important factors causing noise in the US images are as follows [171]:

1. *Aberration:* Aberration takes place due to the variation of the tissue parameter in space that affects the US wave propagation. It happens because of the variation in velocity of the wave propagation due to the inhomogeneous speed of sound. This actually distorts the focusing of the US beam that also leads further strengthening of side-lobes. This leads to a reduction of both the spatial and contrast resolution because of widening the width of main lobe and increasing the side lobe energy, respectively and resulting in blurring of the image [171].
2. *Reverberation:* A large number of multiple scattering of a transmitted pulse because of non-homogeneous nature of tissue medium produces noise, named as reverberation. This scattering follows and appears as an additive noise in the image. This also leads to reduce the contrast resolution and builds the false copies of interfaces at deeper depth than the exact location of the original one, which makes it harder to distinguish the real structure being imaged [172].
3. *Attenuation:* The term attenuation refers to decrease in energy, amplitude and intensity of the transmitted pulse when it propagates. It happens because of two prominent mechanisms such as scattering and absorption. The attenuation in the different tissues has a relation to the distance travelled by the US pulse and the frequency of the US pulse that is transmitted. Higher attenuation comes with the higher frequency US waves than the lower frequency. Hence, it becomes necessary to decrease the frequency and resolution, where structures are larger and need greater depth of penetration.

In addition, because of the finite size of aperture, beam side lobe appears in a beam pattern around the beam main lobe as shown in Figure 2.1. They also affect the contrast resolution. By incorporating the apodization, the side lobe level gets decreased by reducing the amplitude of vibration at the edge of the transducer. This also leads to increase the contrast resolution, but the width of the main lobe widens and thus reducing the spatial resolution. Hence, there is a trade-offs between spatial resolution and side lobe levels for selecting an appropriate apodization profile or window function [223]. Sometimes improper interface of transducer probe also introduces the random noise.

2.3 Types of Noise and Noise Models

The noise commonly present in an image generated by the different sources can be classified into two categories:

1. Additive noise, found in most of the imaging application.
2. Multiplicative speckle noise, observed in the US, laser and SAR images.

In general, digital images such as digital photographs, videos consist of discrete samples of scalar or vector functions defined on the Cartesian grids in multidimensional domain. The black and white photographs and gray scale images consist of scalar data on a two dimensional grid, whereas colour images contain three dimensional data (the RGB colour) on a two dimensional grid. Moreover, the colour videos consist three dimensional information on a three dimensional grid rather than two dimensional where the third dimension acts as a time grid [103]. Most of the medical images are of gray scale or colour images having pixel value in terms of gray intensity of two and three dimensional data (RGB), respectively on two dimensional grid [16]. Let us consider, its representation as a two dimensional array of data $g(x, y)$, where (x, y) refers to the pixel location. The pixel value corresponds to the gray intensity value of the image at a pixel location (x, y).

2.3.1 Additive noise

The common noise model such as a Gaussian, uniform and impulse can be grouped into the category of additive noise that is defined by the following mathematical formulations.

$$s(x, y) = f(x, y) + n(x, y) \tag{2.1}$$

where $s(x, y)$ is the noisy image, $f(x, y)$ is the noise free image and $n(x, y)$ represents the additive noise.

From Eqn. (2.1), it is clear that additive types of noise are not dependent on the original pixel values of the image. The original pixel values are randomly modified by adding the random gray levels of noise. Different researchers modelled these types of noise by the probability density function (PDF) of the gray value distribution in the spatial domain. Among such PDF distribution, the most common type of noise model is Gaussian noise, according to which every noisy image pixel is a combination of the original pixel value and a randomly distributed Gaussian noise value which has a bell shaped PDF and is represented as follows:

$$F(s) = \frac{1}{\sqrt{2\pi\sigma}} e^{-(s-\mu)^2/2\sigma} \tag{2.2}$$

where μ and σ refer to the mean and variance of the noise, respectively.

2.3.2 Multiplicative noise

The US images are very complex to diagnose because of the existence of speckle, which restrains the extraction of fine details from the image. It is a granular pattern developed in the image due to the noise produced from the different sources. Speckle is manifested in a granular pattern due to the image formation under coherent waves which are backscattered by the targeting surfaces and arrived out of phase at the sensor. The speckle is also modelled as multiplicative noise that represents one of the major sources of image quality degradation and reduces the ability of human observer to interpret the fine details in diagnostic examination.

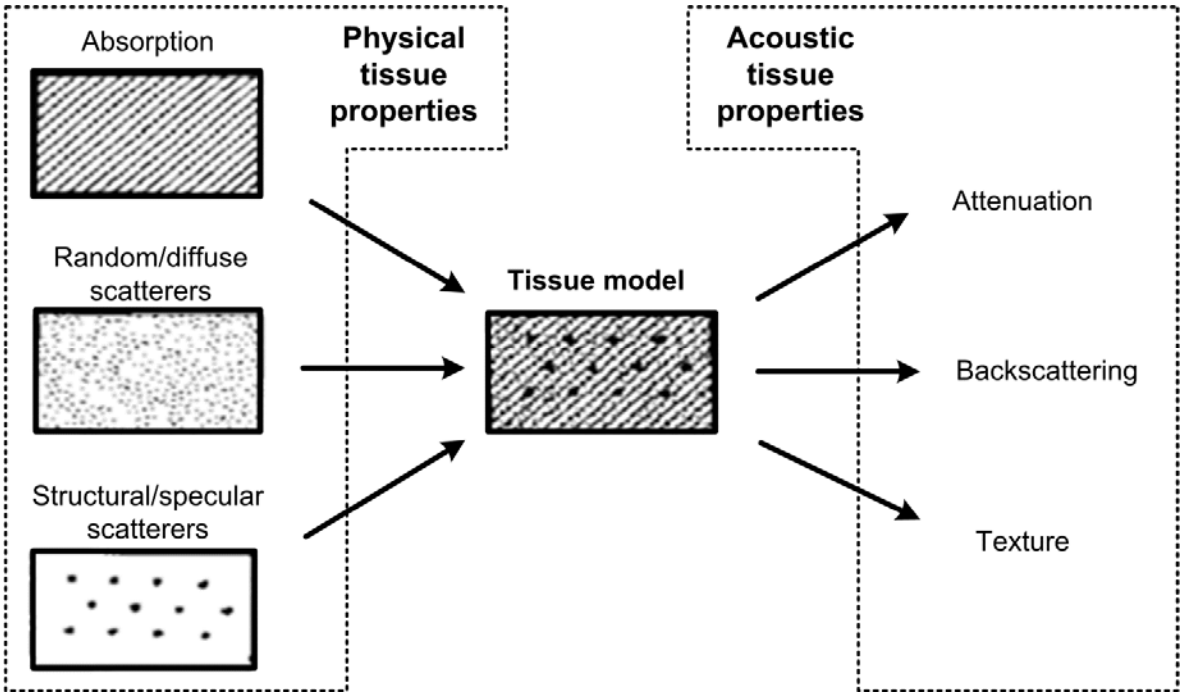

Figure 2.2 Block diagram of an 'acoustic tissue model' and kind of information that can be derived with ultrasonic characterization [235]

The most commonly used diagram to explain the effects that are present when a tissue is intensified, is depicted in Figure 2.2. A universally agreed upon definition of a model still seems to be lacking. Nevertheless, a number of possible mathematical formulations exist, whose feasibility needs to be verified by their practical use. Therefore, the most relevant noise model useful for the US image denoising cannot be easily represented. Besides this, if the speckle is fully developed, it follows the Rayleigh distribution [17, 243, 271]. Some studies also demonstrated that the speckle follows the K-distribution [288], Fisher-Tippett distribution [209] and Gamma distribution [200]. Another multiplicative speckle model has been presented by Achim et al. [5, 28]. The noisy speckled image in spatial domain can be mathematically expressed as

$$s(x,y) = f(x,y)g(x,y) + n(x,y) \tag{2.3}$$

where $s(x,y)$ refers to the noisy image, $f(x,y)$ is the noise free image and $g(x,y)$ and $n(x,y)$ refer to the multiplicative and additive noise (sensor noise) functions, respectively. This model has been successfully used in both the US and SAR imaging. The additive term has a lesser effect than the multiplicative one. Thus, only multiplicative noise term is considered in case of the US images [5]. Therefore, the Eqn. (2.3) can be formulated by ignoring the additive component as follows:

$$s(x,y) = f(x,y)g(x,y) \tag{2.4}$$

The statistical properties of the speckle noise have also been studied by Goodman [104]. This noise model was developed in [5, 104] and utilized in [28, 29, 111, 153, 164, 166, 234,

277] to design the useful denoising method for speckle reduction in the US images. The wave received at the US sensor is a combination of the multiple reflected waves from the target interface. The mathematical expression defined for a signal observed at any point is given as follows:

$$O(x,y) = \sum\sum s(x,y)\,.\,h\big(x - x_1, y - y_{1,}\big) \tag{2.5}$$

where $h(x,y)$ refers to the impulse response of the acquisition system, $s(x,y)$ is the scattered signal and $O(x,y)$ is an observed signal. At this point, the intensity $I(x,y)$ defined in the multiplicative form is given below:

$$I(x,y) = \big\|O(x,y)\big\|^2 = s(x,y)^2.g(x,y) \tag{2.6}$$

where $g(x,y)$ represents noise, independent from the useful signal. This model also offers a good approximation for the US images within the homogeneous region. Besides this, Loupas et al. [157] presented a signal dependent noise model by considering the proportional relation of the mean and variance, directly rather than the standard deviation. Furthermore, this empirical model has also been employed to implement the speckle reduction algorithms [113, 132].

$$s = f + n\sqrt{f} \tag{2.7}$$

where s is the observed signal, f is the true signal and n is the speckle noise. In this model, a uniform area has been assumed. The variance of the observed signal (σ) is equal to the $f\sigma_1$, where σ_1 refers to the noise variance. If the arithmetic mean μ of the output signal is utilized as an expectation of f, then the $\sigma = \mu\sigma_1$. In such a way, the ratio σ/μ can be used to describe the baseline noise level in the homogeneous region. Figure 2.3 and Figure 2.4 show the gray-level histograms for uniform speckle regions in a real US image. In this chapter, while analyzing and evaluating the different denoising approaches, same model has been used for simulating the speckle in the test images. The performance of different approaches has been evaluated based on several performance measures as given in the next section.

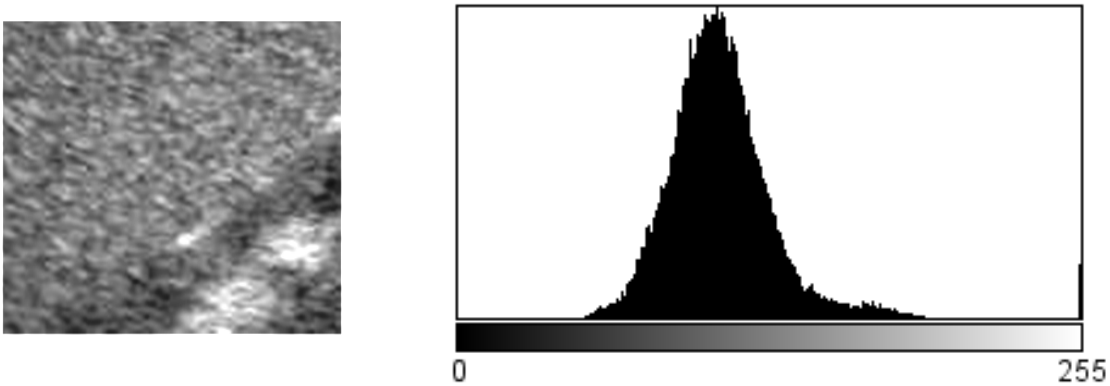

(a) (b)

Figure 2.3 Uniform speckle ultrasound image (a) Original image (b) Gray level histogram

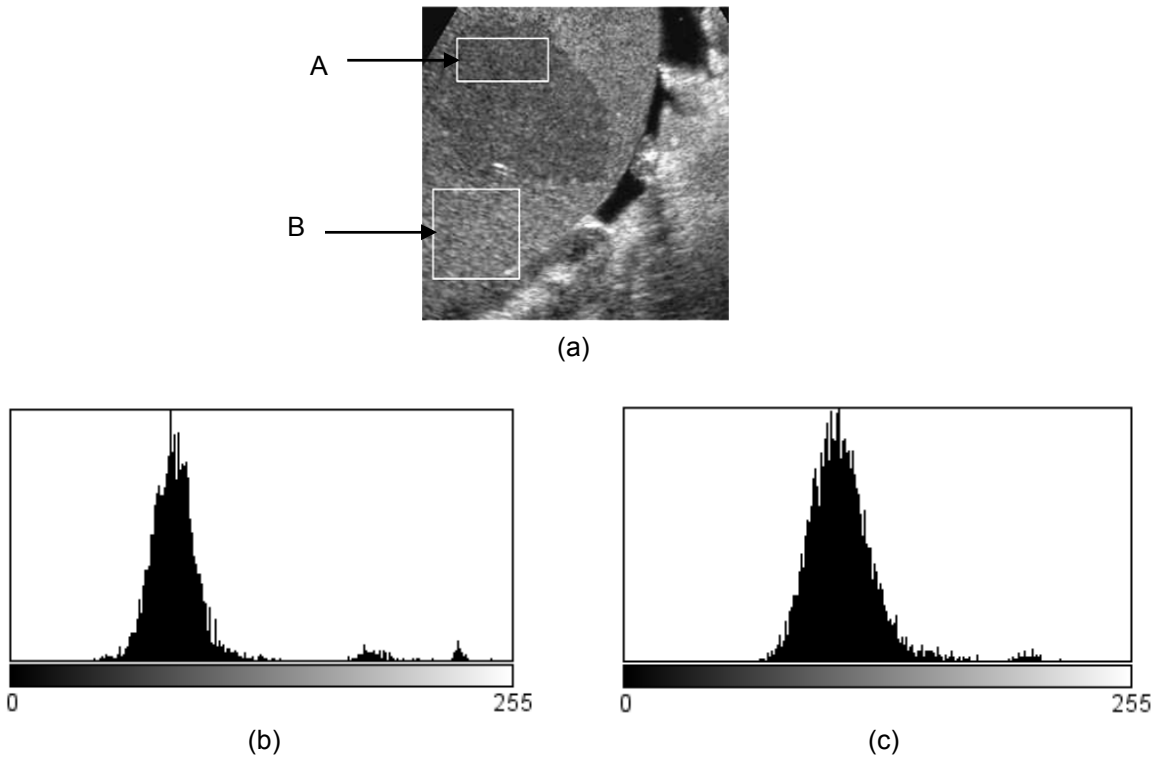

Figure 2.4 (a) Original ultrasound image. Gray level histogram of (b) Region A (c) Region B

2.4 Performance Measures

In the medical imaging context, where the ultimate use of an image is their visual assessment and interpretation, subjective and diagnostic evaluation methods are the most appropriate. However, they demand time consuming procedures and are largely dependent on the specific task. Quantitative evaluations are often used to facilitate the conclusions by computing some numerical values and quantify the quality of denoised images in comparison to original one. They are very easy to compute and also applicable to all types of images regardless of the nature of applications. Therefore, our main emphasis in this study is to improve the following two principal performance of denoising.

(1) Noise suppression performance

(2) Edge preservation performance

For quantitative evaluation of the performance achieved for these two objectives, different performance measures have been used in the different sections of the thesis. The peak signal to noise ratio, and signal to noise ratio [112] are commonly used performance indices to measure the noise suppression capability of the denoising methods. However, they are not sufficient to reflect the performance for visual perception and edge preservation capability. Therefore, additional performance metric like structural similarity index metric [247] has been used as a measure of overall performance of noise suppression and visual perception. Besides these, Pratt's figure of merit [112, 192] and edge keeping index [30, 88, 168] are also used to evaluate the edge preservation capability. The mathematical formulations for the aforementioned performance measures are given as follows:

(a) *Peak signal to noise ratio* (PSNR): The PSNR analysis uses a standard mathematical model to measure an objective difference between two images. It estimates the noise suppression performance in the reconstructed image with respect to an original image. The PSNR is defined as given below:

$$PSNR = 20log_{10}\left(\frac{MAX}{\sqrt{MSE}}\right) \tag{2.8}$$

where MAX is the maximum pixel value of the image and MSE is the mean squared error which is equal to the mean difference between the original and the restored image. The MSE is evaluated as

$$MSE = \frac{1}{MN}\sum_{x=1}^{M}\sum_{y=1}^{N}(s(x,y) - \hat{s}(x,y))^2 \tag{2.9}$$

where $s(x,y)$ is original image and $\hat{s}(x,y)$ is denoised image of size $M \times N$.

(b) *Signal to noise ratio* (SNR): The SNR is a commonly used measure to quantify the noise suppression quality of denoised image. It gives a better indication of signal preservation. A higher SNR value indicates a better image denoising capability. The SNR is the ratio of the variance of noise free image to noise variance. It is defined as given below:

$$SNR = 10\,log_{10}\left(\frac{variance(noisefree\ image)}{variance(remaining\ noise)}\right) \tag{2.10}$$

(c) *Structural similarity index metric* (SSIM): The SSIM index is used to study the structural and perceptual closeness between the original and filtered image. For the default value of K_1=0.01 and K_2=0.03 and the dynamic range (L) of the pixel is 255, the SSIM is evaluated as

$$SSIM = \frac{(2\mu_s \times \mu_{\hat{s}} + C_1)(2\sigma_{s,\hat{s}} + C_2)}{(\mu_s^2 + \mu_{\hat{s}}^2 + C_1)(\sigma_s^2 + \sigma_{\hat{s}}^2 + C_2)} \tag{2.11}$$

where $C_1 = (K_1 \times L)^2$ and $C_2 = (K_2 \times L)^2$, $\sigma_{s,\hat{s}} = \frac{1}{L-1}\sum_{k=1}^{L}(s_k - \mu_s)(\hat{s}_k - \mu_{\hat{s}})$ is the covariance in moving template, s is the original image and $\hat{s}$ is the denoised image with mean μ_s , $\mu_{\hat{s}}$ and variance σ_s and $\sigma_{\hat{s}}$, respectively. If the value is closer to 1, then denoised image is closer to original one.

(d) *Pratt's Figure of merit* (FOM): The FOM is most commonly used to quantitatively estimate the edge preservation. The FOM is defined as given below:

$$FOM = \frac{1}{max(s_D, s_I)}\sum_{i=1}^{s_D}\left(\frac{1}{1+\alpha d_i^2}\right) \tag{2.12}$$

where s_D is the number of detected edge pixels, s_I is the number of ideal edge pixels, d_i is the deviation or Euclidean distance between the i^{th} detected edge pixel and the nearest ideal edge pixel and α is the positive scaling factor, typically set to 1/9. The FOM ranges between 0 and 1, and as it is closer to one, it indicates better ability of the denoising method to preserve the edges. The Canny edge operator is used to locate the edges in all the processed results with the threshold of 0.5 [138, 266].

(d) *Edge keeping index* (EKI): The EKI is used as another objective criterion to evaluate the edge preservation capability of denoising methods, and is evaluated as

$$EKI = \frac{I\left(\Delta s - \overline{\Delta s}, \Delta \hat{s} - \overline{\Delta \hat{s}}\right)}{\sqrt{I(\Delta s - \overline{\Delta s}, \Delta s - \overline{\Delta s}) \cdot I\left(\Delta \hat{s} - \overline{\Delta \hat{s}}, \Delta \hat{s} - \overline{\Delta \hat{s}}\right)}} \tag{2.13}$$

where Δs and $\Delta \hat{s}$ represent the high pass filtered versions of s and $\hat{s}$, respectively, calculated by 3×3 standard approximation of a Laplacian operator with the mean intensity value as $\overline{\Delta s}$ and $\overline{\Delta \hat{s}}$. The function I is defined as $I(s_1, s_2) = \sum_{x=1}^{M} \sum_{y=1}^{N} s_1(x, y) s_2(x, y)$, where M×N is the size of the image. This quantitative performance measure should be close to unity for better preservation of edges.

2.5 Overview of Denoising Methods

The image denoising plays a significant role in modern applications of various fields, including medical imaging and pre-processing for computer vision. This is because of noise and artifacts that are introduced in the US images due to inherent limitations of its acquisition techniques and systems. The term denoising is always a trade-off between noise reduction and loss of significant information from the clinical point of view. The denoising process is, therefore, attractive to retain the important information as much as possible. So, it is very difficult to suggest a robust technique for noise suppression which is also equally useful for the US images. This section presents an overview of some existing remarkable denoising methods which are also implemented here for their qualitative and quantitative performance evaluation on the US images.

2.5.1 Adaptive weighted median filter

The median filter [122] is a nonlinear filter that is employed to all the pixels whether they are corrupted or not. In this approach, the value of middle pixel is replaced with the median value of its neighboring pixels in a moving template. Loupas et al. [157] presented an adaptive weighted median filter (AWMF) that also originates from the median by incorporating the weighted coefficients. Usually, the weighted median of a region $\Re(x, y)$ is defined as an extended sequence which is formed by replicating each term $T(x)$ within the region for $[m(x)]$ times, where $m(x)$ is the corresponding weight coefficients. For example, if $m(1) = 3$, $m(2) = 4$ and $m(3) = 2$, then the weighted median of the sequence $[T(1), T(2), T(3)]$ is given by

$$Y = median[T(1), T(1), T(1), T(2), T(2), T(2), T(2), T(3), T(3)] \tag{2.14}$$

Adapting filtering techniques have also been developed for feature detection in the US images and to evaluate the filter output at each pixel using appropriately shaped and sized local filtering kernels surrounding the pixel of interest [21]. The main concept behind the AWMF is to select the weights that decrease as one moves away from the center pixel of a

given template, and the decreasing rate is also controlled by the local image content [157]. In the AWMF, signal preservation is inversely proportional to noise reduction. The main advantage of the AWMF is that the ratio of variance and mean can characterize the local image content using weighted median filtering with the weights adjusted according to the local statistics of the image. This results not only in the maximum noise reduction in uniform areas, but also preserves the resolvable structures and can be given as

$$m(x,y) = [m(k+1,k+1) - sd\sigma^2/\mu]_+ \quad (2.15)$$

where s is a scaling constant, d is the distance of the point from the center pixel within the template $(k+1,k+1)$. The parameters μ and σ^2 are the local mean and variance inside the template of size $(2k+1)\times(2k+1)$. The AWMF parameters like scaling constant and window size are selected experimentally in terms of the quality of the processed image. In the above equation, the sign '+' means the nearest integer to the quantity within the bracket, if the quantity is positive, otherwise it becomes zero.

2.5.2 Wiener filter

The wiener filter (WF) uses a pixel wise adaptive method based on the first order statistics such as mean and variance that are estimated from a local neighborhood of the pixels within a moving template. The filter may use the following equation for the reconstruction of an image [139, 140, 155].

$$\hat{s}(x,y) = \mu_{s(x,y)} + K(x,y)\big(s(x,y) - \mu_{s(x,y)}\big) \quad (2.16)$$

where $s(x,y)$ is the noisy pixel value, $\hat{s}(x,y)$ is the denoised pixel value and $\mu_{s(x,y)}$ is the local mean of the pixel values in a moving template. The parameter $K(x,y)$ is a weighting factor that is a function of local statistics within a moving template and having the value in between 0 and 1. It can be estimated as [142]

$$K(x,y) = (\sigma^2 - \sigma_n^2)/\sigma^2 \quad (2.17)$$

where σ^2 and σ_n^2 refer to the variance in the moving template and the variance of noise in the whole image, respectively. The noise variance σ_n^2 can be estimated as given below:

$$\sigma_n^2 = \sum_{x=1}^{p} \sigma_p^2/\mu_{s_p} \quad (2.18)$$

where σ_p^2 is the variance and μ_{s_p} is the mean of noise in a pre-defined template, respectively. The parameter p is an index for all templates in the whole image [1]. Here, the template size 5×5 is selected for evaluating the denoising performance.

2.5.3 Maximum homogeneity over a pixel neighborhood filter

The maximum homogeneity over a pixel neighborhood filter (MHOPNF) is based on the estimation of most homogenous neighborhood around every pixel of an image [12, 155, 210]. The MHOPNF operates by considering only those pixel values that fall in the processed

neighborhood within a moving template. It uses the following equation to reconstruct the output filtered image.

$$\hat{s}(x,y) = [\alpha(x,y)s(x,y)]/\sum_{i,j}\alpha(x,y) \tag{2.19}$$

$$\alpha(x,y) = \begin{cases} 1 & (1-2\sigma_n)\mu_{s(x,y)} \le s(x,y) \le (1+2\sigma_n)\mu_{s(x,y)} \\ 0 & otherwise \end{cases} \tag{2.20}$$

where $s(x,y)$ is the noisy pixel value, $\hat{s}(x,y)$ is the denoised pixel value and $\mu_{s(x,y)}$ is the local mean of the pixel values in a moving template. There is no need to tune any thresholds or parameters for implementing the MHOPNF approach and thus it makes it a suitable filter for interpretation.

2.5.4 Anisotropic diffusion filter

The diffusion methods are derived from the concept of partial differential equations (PDE) based methodology. The PDE based noise suppression method allows the generation of an image scale space due to filter window size and shape [186]. The PDE based technique offers two types of the diffusion such as linear and nonlinear diffusion. Between these formulations, linear diffusion has its own limitations such as it diffuse the data equally in all the directions so that it not only removes unwanted noise, but also affects important features of the image by blurring and dislocation of the edges. On the other hand, the anisotropic diffusion filter (ADF) introduced by Perona and Malik (PM) [186] provides a multiscale nonlinear diffusion technique that offers a good compromise between noise removal and edge preservation. The main idea behind the ADF is to differentiate the edges and noise by incorporating the image gradient operator and then iteratively eliminate small variations due to noise and meanwhile preserve large variations due to the edges [274]. The mathematical formulation of the ADF was based on the heat equation that is given as

$$\frac{\partial s(x,y;t)}{\partial t} = div(g(\|\nabla s(x,y;t)\|).\nabla s(x,y;t)) \tag{2.21}$$

where div is the divergence operator, $g(\cdot)$ is the diffusion parameter. The coefficients $g(\|\nabla s(x,y;t)\|)$ varying normally in the range of [0, 1] allows the controlling of the diffusion regularization process more accurately. If g is a constant parameter, i.e. independent of image positions (x,y) or time t, it leads to a linear diffusion equation as written below:

$$\frac{\partial s}{\partial t} = div\big(g.\nabla s(x,y;t)\big) = g\nabla^2 s(x,y;t) \tag{2.22}$$

To preserve the edges, Perona and Malik also suggested two diffusion parameters that can be expressed as

$$g(\|\nabla s(x,y;t)\|) = \frac{1}{\left[1+\left(\frac{\|\nabla s(x,y;t)\|}{K}\right)^2\right]} \tag{2.23}$$

$$g(\|\nabla s(x,y;t)\|) = exp\left(-\left[\frac{\|\nabla s(x,y;t)\|}{K}\right]^2\right) \tag{2.24}$$

where K is the edge magnitude parameter on which the behavior of the ADF depends. If $\|\nabla s(x,y;t)\| \gg K$, then the diffusion coefficient becomes zero ($g(\|\nabla s(x,y;t)\|) \to 0$) and we achieve all pass filter. On the other hand, if $\|\nabla s(x,y;t)\| \ll K$, then the diffusion coefficient becomes one ($g(\|\nabla s(x,y;t)\|) \to 1$) and becomes isotropic diffusion.

2.5.5 Speckle reducing anisotropic diffusion

In case of the images containing speckles, isotropic diffusion will actually enhance the speckles instead of suppressing the noise [231]. Therefore for speckle reduction, an alternative adaptive filtering approach based on the PDE is proposed and named as speckle reducing anisotropic diffusion (SRAD) [266]. This method has adopted an idea of Lee's adaptive filtering [144] into anisotropic diffusion algorithm by exploiting the instantaneous coefficient of variation (ICOV). The SRAD method is outlined by first representing the discrete form of the anisotropic diffusion equation by replacing the diffusion coefficient $g\big((\nabla s\ (x,y;t))_p\big)$ with the ICOV and it can be written as below [266]:

$$s(x,y;t+\Delta t) = s(x,y;t) + \frac{\Delta t}{|\eta_{i,j}|}\sum_{p\in\eta_{i,j}} g\big((ICOV\ (x,y;t))_p\big)\cdot\big((\nabla s(x,y;t))_p\big) \tag{2.25}$$

and

$$g(ICOV) = \frac{1}{1+\left(\frac{ICOV^2-ICOV_0^2}{ICOV_0^2+ICOV_0^4}\right)} \tag{2.26}$$

$$g(ICOV) = exp\left[-\left(\frac{ICOV^2-ICOV_0^2}{ICOV_0^2+ICOV_0^4}\right)\right] \tag{2.27}$$

where $|\eta_{i,j}|$ is the total number of the pixels in the spatial neighborhood of the pixel $(\eta_{i,j})$ and Δt is the time step parameter. The $ICOV_0$ is speckle scale function that effectively controls the amount of smoothing applied to an image by the SRAD. The ICOV estimated in terms of the approximations to the derivatives of s in the given 3×3 template can be written as

$$ICOV = \sqrt{\frac{\left(\frac{1}{2}\right)\left(\frac{\|\nabla s\|}{s}\right)^2-\left(\frac{1}{4}\right)^2\left(\frac{\nabla^2 s}{s}\right)^2}{\left[1+\left(\frac{1}{4}\right)\left(\frac{\nabla^2 s}{s}\right)\right]^2}} \tag{2.28}$$

This ICOV combines a normalized gradient magnitude operator and a normalized Laplacian operator to act like an edge detector for a noisy image. High relative gradient magnitude and low relative Laplacian tend to indicate an edge. The speckle scale function is also estimated by

$$ICOV_0 = \frac{1.4826\times MAD(\nabla I)}{\sqrt{2}} \tag{2.29}$$

where MAD stands for the median absolute deviation [11, 267]. The divergence can be iteratively calculated as follows with the time step size of Δt and sufficiently small spatial step size of $d = 1$ in x and y directions within a template having size of 3×3 at iteration t.

$$f(x,y;t)=\frac{1}{d^2}\begin{bmatrix} g(x+1,y;t)\big(s(x+1,y;t)-s(x,y;t)\big) \\ +g(x-1,y;t)\big(s(x-1,y;t)-s(x,y;t)\big) \\ +g(x,y+1;t)\big(s(x,y+1;t)-s(x,y;t)\big) \\ +g(x,y-1;t)\big(s(x,y-1;t)-s(x,y;t)\big) \end{bmatrix} \tag{2.30}$$

The final SRAD update function results in

$$s(x,y;t+1)=s(x,y;t)+\frac{\Delta t}{4}f(x,y,t) \tag{2.31}$$

2.5.6 Nonlinear complex diffusion filter

Nonlinear complex diffusion filter (NCDF) [100] is derived from the concept of the PM formulation by extending the analysis from real axis to the complex domain and becomes a process with complex value diffusion coefficient. This method is based on the combination of diffusion equations and the free Schrödinger equation and offers a generalized form of the linear scale space in the complex domain. The mathematical formulation of the NCDF method is expressed as

$$\frac{\partial s}{\partial t}=\nabla\cdot\big(g\big(Im(s)\big)\nabla s\big) \tag{2.32}$$

where g refers to the diffusion coefficient and $Im(\cdot)$ denotes the imaginary values. The coefficient of diffusion can be estimated by [100, 208]

$$g\big(Im(s)\big)=e^{j\theta}\Big/\left[1+\left(\frac{Im(s)}{\kappa\theta}\right)^2\right] \tag{2.33}$$

where θ refers to the phase angle of the diffusion coefficient and it should be a small value $(\theta \ll 1)$ and κ refers to the threshold parameter. This choice of the small value of $\theta \to 0$ relies on the fact that the imaginary part can be considered as smoothed second derivative of the initial signal; factored by θ and time [100, 160, 208].

$$\lim_{\theta\to 0}\frac{Im(s)}{\theta}=t\Delta G_{\tilde{\sigma}} * s_0 \tag{2.34}$$

where $G_{\tilde{\sigma}}$ refers to a Gaussian kernel with $\lim_{\theta\to 0}\sigma=\sqrt{2t}$ and Δ represents a second order derivative (Laplacian) offers the zero crossing points. The diffusion process becomes easier for the smooth region and attenuated at edge points present in an image because the evaluation of the diffusion coefficient does not consider the image derivatives [20]. This is the main advantage of the NCDF compared to the real diffusion coefficients because the estimation of the image derivatives is highly ill-posed at the early stages, if the noise is present [20]. The authors [100] has already mentioned that the imaginary part of the initial signal is considered as a smooth function of its second derivative and the ratio $(Im(s)/\theta)$ is proportional to its Laplacian. Another benefit of the NCDF method is that it removes noise from edges and also avoids the staircasing effects. The parameters $\theta=\pi/3$ and $\kappa=20$ are used for evaluating the performance of the NCDF method. The NCDF method helps to remove more noise. However, the time step and threshold parameter are constant in the

NCDF. Therefore, Bernardes et al. [20] improved the NCDF model by modifying the adaptive time step and threshold parameter and named as improved NCDF (INCDF).

2.5.7 Total variation filter

Total variation filter (TVF) proposed by Rudin, Osher and Fatemi (ROF) [204] is an iterative- based constrained optimization approach that is also known as the ROF method on the basis of the first letter of their authors' name. It is able to suppress the noise by smoothing the homogenous region present in the images. The TVF is based on minimization of the total variation norm of the image subject to some constraints that are estimated from the noise statistics. The constraints are imposed using the Lagrange multipliers. The ROF model is solved using the minimization problem through the PDE based schemes which are also numerically intensive. The regularization criterion used for image denoising is given below:

$$min_{\hat{s}\in X}\frac{\|s-\hat{s}\|^2}{2\lambda}+J(\hat{s}) \tag{2.35}$$

where $s=s(x,y)$ is the noisy image and $\hat{s}=\hat{s}(x,y)$ refers to the approximated image of the same size of original image; X denotes the Euclidean space $\mathbb{R}^{M\times M}$, $\|\cdot\|^2$ is the Euclidean norm in and $\lambda>0$ is a Lagrange multiplier. The function $J(\hat{s})$ is the discrete total variation of $\hat{s}$ and is given as

$$J(\hat{s})=\sum_{1\le x,y\le M}|\nabla s(x,y)| \tag{2.36}$$

where

$$\nabla s(x,y)=\left[\nabla s_x(x,y)\nabla s_y(x,y)\right] \tag{2.37}$$

$$\nabla s_x(x,y)=s(x+1,y)-s(x,y) \text{ and } \nabla s_y(x,y)=s(x,y+1)-s(x,y) \text{ for } x,y=1,2,\dots,M \tag{2.38}$$

Several different methods have been presented for the minimization of the ROF function. One of them is Chambolle's approach [47] that is a projection based approach used in the present study to minimize the ROF function and solved the above mentioned function as given below:

$$\hat{s}=s-\lambda div\left(p^i\right) \tag{2.39}$$

where $div\left(p^i\right)$ refers to the nonlinear projection in two dimensions and an algorithm is used to compute the optimal solution p^i as follows. Let $p^0=0$ and the step size is taken $0<\tau<0.25$ to ensure the convergence of the $\lambda div\left(p^i\right)$

$$p^{i+1}(x,y)=\frac{p^i(x,y)+\tau\left(\nabla\left(div\left(p^i\right)-s/\lambda\right)\right)(x,y)}{1+\tau\left|\left(\nabla\left(div\left(p^i\right)-s/\lambda\right)\right)(x,y)\right|} \tag{2.40}$$

2.5.8 Non local means filter

Non local means filter (NLMF) proposed by Buades et al. [37] is one of the most prominent denoising algorithm that considers both the image geometries either local or

nonlocal. The denoising process is performed using the NLMF by replacing each pixel in the degraded image by a weighted average of all the other pixel intensities and averaging is performed over a smaller window centered on a pixel of interest [230, 270]. The mathematical formulation of the NLMF can be represented as [37, 69]

$$NLM\big(s(x)\big) = \sum_{y \in s} \omega(x,y) s(y) \tag{2.41}$$

with

$$0 \leq \omega(x,y) \leq 1 \text{ and } \sum_y \omega(x,y) = 1 \tag{2.42}$$

where $s(x)$ and $s(y)$ refer to the denoised image pixel and noisy image pixel, respectively. x and y are the image pixel counts and s is the set of all the image pixels. $\omega(x,y)$ refers to the weights that are based on the similarity between the square neighborhood $N(x)$ and $N(y)$ of a fixed size centered at pixels x and y, respectively. The similarity $\omega(x,y)$ is evaluated as

$$\omega(x,y) = \frac{1}{Z(x)} exp\left(\frac{-\alpha(x,y)}{h^2}\right) \tag{2.43}$$

$$\alpha(x,y) = \kappa_a^G \left\| s\big(N(x)\big) - s\big(N(y)\big) \right\|^2 \tag{2.44}$$

$$Z(x) = \sum_y exp\left(\frac{-\alpha(x,y)}{h^2}\right) \tag{2.45}$$

where $c(N(x))$ and $c(N(y))$ are the intensity gray level vectors, κ_a^G is the Gaussian kernel, $a > 0$ represents the standard deviation and the parameter h acts as a degree of filtering that controls the decay of the exponential function. For the computational efficiency, the NLMF algorithm is restricted to a predefined search window that has much smaller size than the original image size. Pierrick et al. [69] also presented an optimized Bayesian NLMF with block-wise approach for the particularly log compressed images. In the present work, the NLMF approach is used with the search window $S = 15 \times 15$, square local neighborhood $N = 5 \times 5$, and $h = 10 \times \sigma$, where both the N and S are nonlocal template's size.

2.5.9 Wavelet based method

Wavelet based denoising proposed by several authors [3, 28, 111, 216, 220, 234] is another class of methods by decomposing an image into different wavelet coefficients such as approximation (low frequency (LF) subband) and detail (high frequency (HF) subband) coefficients. Firstly, the concept of soft thresholding proposed by Donoho [79] is used to suppress the speckles in the US images and is also explored by other researchers [5, 31, 111, 234]. This method makes an effort to suppress the noise by using thresholding methods named as wavelet shrinkage such as hard and soft thresholding. These thresholding methods are investigated on a logarithmic scale for despeckling of the US images since after the logarithmic transformation. This technique is called homomorphic speckle filtering technique in which the wavelet transform (WT) coefficients of the logarithm of a noisy image are considered. For an estimated threshold value (T), the wavelet coefficients $s^{WT}(x,y)$ of an

image $s(x,y)$ are modified using hard and soft thresholding as follows:

$$s_{Hard}^{WT}(x,y) = \begin{cases} s^{WT}(x,y) & |s^{WT}(x,y)| > T \\ 0 & otherwise \end{cases} \quad (2.46)$$

$$s_{Soft}^{WT}(x,y) = \begin{cases} s^{WT}(x,y) - T & s^{WT}(x,y) > T \\ s^{WT}(x,y) + T & s^{WT}(x,y) < -T \\ 0 & |s^{WT}(x,y)| < T \end{cases} \quad (2.47)$$

where $s_{Hard}^{WT}(x,y)$ and $s_{Soft}^{WT}(x,y)$ represents the modified wavelet coefficients using a hard and soft threshold, respectively. In this method, the main task is to choose the threshold value that is called universal threshold and is estimated as

$$T = \sigma\sqrt{2\log(n)} \quad (2.48)$$

where n is the length of signal coefficients and σ is an estimated noise variance that is computed using the median of absolute value [289] as mentioned above. Besides these schemes, various shrinkage methods such as SureShrink [92], BayesShrink [92], NeighShrink [56], ProbShrink [189] have also been proposed by several researchers and shows their success in a range of situations where many previous non wavelet methods have met partial success [92]. Generally, hard thresholding is useful to preserve the features present in an image, while soft thresholding provides the smoothing, but it may lead to some oscillations [155, 257]. To minimize these oscillation, translation invariant wavelet transform (TI-WT) has been proposed in [196] and proved the ability to provide better noise reduction performance than wavelet. In this study, bior6.8 wavelet filter with four levels decomposition is used to perform the experiments. The reason of selecting bior6.8 wavelet filter is that it provides better edge preservation [30, 234].

2.5.10 Ridgelet based method

In literature, wavelet plays a dominant role in any frequency domain analysis. It also provides good results with the different thresholding and other denoising algorithms as mentioned above. The WT is able to efficiently represent a function with one dimensional point singularity. Similarly, if the line and curve edges are present in the images, then the entire wavelet coefficient gets affected. It means that the WT is less efficient in representing the sharp transitions. For such type of transitions, the WT generates a large number of wavelet coefficients even at the finer scales and is repeated at the scale after scale. Therefore, it is said that the reconstruction of the edges performed by the WT based thresholding methods gets affected. The concept of the ridgelet transform [77] has been evolved to overcome the limitation of the wavelet transform. Ridgelet transform is implemented by applying one dimensional WT to the slices of radon transform that can also be obtained by evaluating one dimensional inverse Fourier transform to the two dimensional Fourier transform of function restricted to radian lines through the origin. For a given integrable bivariate signal $s\,(x,y)$, continuous ridgelet coefficients (CRT) are defined as

below [77]:

$$CRT(a,b,\theta) = \int_{\mathbb{R}^2} s(x,y)\psi_{a,b,\theta}(x,y)dxdy = \int_{\mathbb{R}} \psi_{a,b}(t)R_a(\theta,t)dt \quad (2.49)$$

where the bivariate ridgelet $\psi_{a,b,\theta}$ in two dimensional is defined from a wavelet function in one dimensional $\psi(x)$ as follows:

$$\psi_{a,b,\theta}(x,y) = a^{-1/2}\psi((x\,cos\theta + y\,sin\theta - b)/a) \quad (2.50)$$

This function $\psi_{a,b,\theta}(x,y)$ has constant value along the lines $x\,cos\theta + y\,sin\theta = K$, and the radon transform $R_a(\theta,t)$ is defined as

$$R_a(\theta,t) = \int_{\mathbb{R}^2} s(x,y)\,\delta(xcos\theta + ysin\theta - t)dxdy \quad (2.51)$$

The discrete version of the ridgelet transform has also been developed by several researchers [77, 252] and also applied to image denoising problem using thresholding methods as similar to the WT [101, 159, 174]. In the present work, the Neighcoeff thresholding approach [56] is used with the ridgelet transform as mentioned in [101]. This method provides good results by thresholding the ridgelet coefficients based on the universal threshold and sum of squares of all the ridgelet coefficients within a square neighborhood template, as expressed below:

$$\hat{s}^{Ridgelet}(x,y) = \left(1 - \frac{T^2}{S^2(x,y)}\right)_+ s^{Ridgelet}(x,y) \quad (2.52)$$

$$S^2(x,y) = \sum_{(a,b)\in W(x,y)}\left[s^{Ridgelet}(a,b)\right]^2 \quad (2.53)$$

where T refers to threshold value obtained using the universal threshold, $s^{Ridgelet}(x,y)$ and $\hat{s}^{Ridgelet}(x,y)$ represent the ridgelet coefficients of noisy image and modified noise free ridgelet coefficients after thresholding process.

2.5.11 Curvelet based method

The concept of the curvelet transform (CVT) is evolved to overcome the limitations of the wavelet and ridgelet transform and to represent a curve as a superposition of the functions of various lengths and widths obeying the scaling law [225]. It is performed by decomposing the image into different sub-images using two dimensional wavelet transform and then each subimages are analyzed using a local ridgelet transform. The curvelet function is defined as

$$\gamma_{a,\vec{b},\theta} = \gamma_{a,\vec{0},0}\left(R_\theta(\vec{x} - \vec{b})\right) \quad (2.54)$$

where $R_\theta = \begin{bmatrix} cos\theta & sin\theta \\ -sin\theta & cos\theta \end{bmatrix}$ represents a rotation matrix that rotates θ radians. $\vec{x}$ and $\vec{b}$ are the two dimensional vectors, $\gamma_{a,\vec{0},0}$ is the element curvelet function. The curvelet family has another parameter to provide directional information, including the position and scaling information as compared to the wavelet. Like the ridgelet, curvelet occur at all the scales, positions and orientations. Curvelets have a variable length and width in comparison to

ridgelet that have a global length and variable width. In the curvelet functions, parabolic scaling is used to provide the effective length and width of the region $(width = length^2)$ that leads to anisotropic behavior of curvelets and ensures for capturing the curve singularities for which the WT and ridgelet transform are not efficient. Due to this feature, very few coefficients of curvelet transform are required for capturing the arbitrary waveforms like line and curve singularity. The anisotropic property is also illustrated in Figure 2.5 that implies that a very few non-zero coefficients are sufficient to capture the curve edges than the wavelet. It ensures that the handling capacity of curvelet for capturing the curve is better than the others.

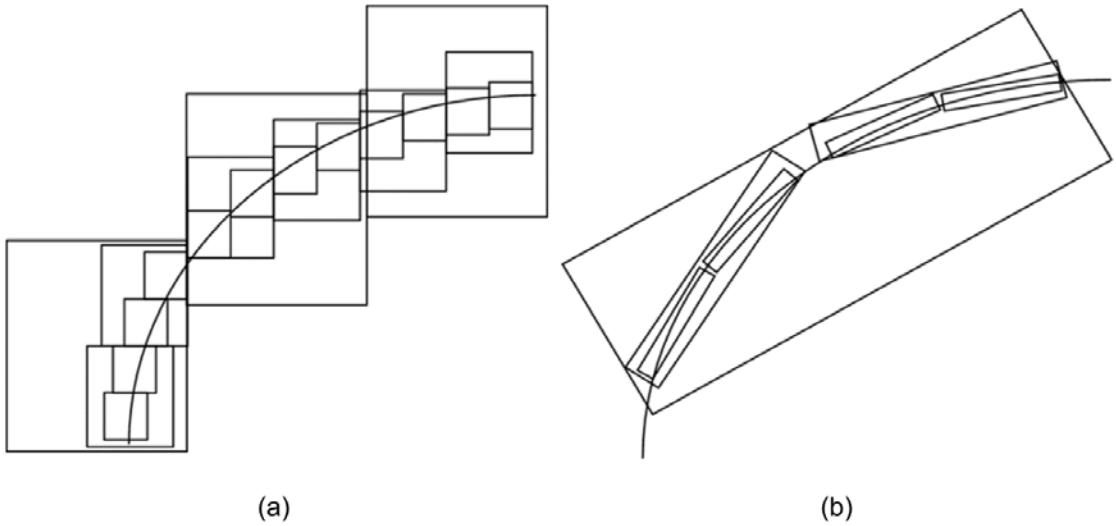

Figure 2.5 Comparative representations of curve discontinuity by the (a) WT (b) CVT [13]

Candes et al. [41] proposed the two efficient and generalized versions of the CVT for image denoising. The one successful image denoising approach has also been introduced by Stark et al. [225] and they extended their method for another application of the contrast enhancement of gray scale and colour image [224]. They also reported that thresholding of the CVT coefficients is easy and effective for image denoising with better edge preservation due to anisotropic property of the CVT. Saevarsson et al [207] introduced the time invariant image denoising approach using the CVT named as curvelet based cycle spin (CS) denoising algorithm and showed better edge preservation results. Based on this conclusion, another denoising approaches have been proposed with the CVT for additive Gaussian noise [10]. In the first method, hard thresholding function is employed and in another, cycle spinning approach is combined with the curvelet (CSCVT). The author also presented that the CSCVT provides good denoising and edge preservation results. Therefore, in this study, the noisy image is processed using the CVT based hard thresholding developed in [225] and cycle spinning approach in the same manner as the WT based thresholding approach. The thresholding function can be written as

$$\hat{s}_\lambda^{CVT}(x,y) = \begin{cases} s_\lambda^{CVT}(x,y) & \left|s_\lambda^{CVT}(x,y)\right|/\sigma > K\sigma_\lambda \\ 0 & otherwise \end{cases} \tag{2.55}$$

where K is the scale dependent constant parameter that is taken 4 for first scale and 3 for the others. The parameter σ_λ is the individual standard deviation of noisy subimage coefficients at each scale decomposed using the CVT. Here, $s_\lambda^{CVT}(x,y)$ and $\hat{s}_\lambda^{CVT}(x,y)$ represent the noisy curvelet coefficients and approximated noiseless curvelet coefficients.

2.5.12 Shearlet based method

To efficiently represent more edges, Labate et al. [106, 107, 141] introduced the concept of shearlet transform (ST). It has all the properties such as multiscale, localization, anisotropy and directionality similar to the other multiscale geometric analysis tools. The decomposition of ST consists of multiscale and multidirectional decomposition, which are similar to contourlets introduced by Do and Vetterli [78] except that there is no limitation on the number of directions. The ST overcomes the limitation of other transforms and also provides the sparse representation for the objects. It can also be constructed in discrete domain which is the major limitation of the CVT because of introducing the two different discrete implementations of the CVT by the researchers [41, 225]. The ST combines the multi-scale and direction analysis, separately. Firstly, Laplacian pyramid is used to decompose the noisy image into high and low frequency components, then direction filtering is used to get different subbands and different direction shearlet coefficients. Direction filtering is achieved using the shear matrix. Hence, the shearlet transform as given in [85], is defined as below:

$$\psi_{j,k,m}^{(0)}(x) = 2^{j\frac{3}{2}}\psi^{(0)}\left(S_0^k D_0^j x - m\right) \text{ and } \psi_{j,k,m}^{(1)}(x) = 2^{j\frac{3}{2}}\psi^{(1)}\left(S_1^k D_1^j x - m\right) \quad (2.56)$$

where $j \geq 0, -2^j \leq k \leq 2^j - 1, m \in \mathbb{Z}^2$,

$\hat{\psi}^{(0)}(\xi) = \hat{\psi}^{(0)}(\xi_1, \xi_2) = \hat{\psi}_1(\xi_1)\hat{\psi}_2(\xi_2/\xi_1)$ and $\hat{\psi}^{(1)}(\xi) = \hat{\psi}^{(1)}(\xi_1, \xi_2) = \hat{\psi}_1(\xi_2)\hat{\psi}_2(\xi_1/\xi_2)$

where D and S refer to the anisotropic and shear matrix, respectively, j and, k and m are scale, direction and shift parameter, respectively. The symbols D and S both denote 2×2 invertible matrices with $det|S| = 1$. The detailed explanation of ST will be discussed in Chapter 4.

In this study, the noisy image is processed using the similar approach of the hard thresholding as discussed above in the curvelet based method using the CS approach. For the decomposed noisy shearlet coefficients $s_\lambda^{ST}(x,y)$, the estimated denoised coefficient $\hat{s}_\lambda^{ST}(x,y)$ is computed by similar Eqn. (2.55).

$$\hat{s}_\lambda^{ST}(x,y) = \begin{cases} s_\lambda^{ST}(x,y) & \left|s_\lambda^{ST}(x,y)\right| > K\sigma\sigma_\lambda \\ 0 & otherwise \end{cases} \quad (2.57)$$

2.6 Experimentation

To analyze the noise suppression and edge preservation capability of the denoising approaches introduced above, different quantitative performance measures are used. To assess the performance of these denoising methods, three different experiments are

conducted on the several test images degraded by different noises such as multiplicative speckle noise and additive Gaussian noise and various real US images.

Experiment 1: *Denoising of simulated test images corrupted by multiplicative speckle noise* - To perform this experiment, two sets of the simulated images acquired from http://field - ii.dk/examples and a two dimensional phantom image are considered as noise free images. The testing gray scale images of kidney, fetus and phantom images are corrupted with the multiplicative speckle noise of three different noise levels that were used by setting the different variance of noise ($\sigma = 0.1,\ 0.2$ and 0.3) to analyze and compare the performance of the aforementioned denoising methods. The original noise free images are shown in Figure 2.6 and Figure 2.7 shows the noisy kidney, fetus and phantom images contaminated by speckle noise with their variance $\sigma = 0.1,\ 0.2$ and 0.3, respectively.

Experiment 2: *Denoising of additive Gaussian noise in standard test images* - To investigate the robustness of above mentioned denoising methods, three different standard test images such as Lena, Girl and Boat images are also taken to evaluate the performance of denoising approaches for additive Gaussian noise reduction. For such purposes, these three test images are degraded with the Gaussian noise by setting different noise standard deviation like $\sigma_n = 10, 20$ and 30. Figure 2.8 shows the original Lena, girl and boat images and their noisy version with $\sigma_n = 20$ are shown in the Figure 2.9.

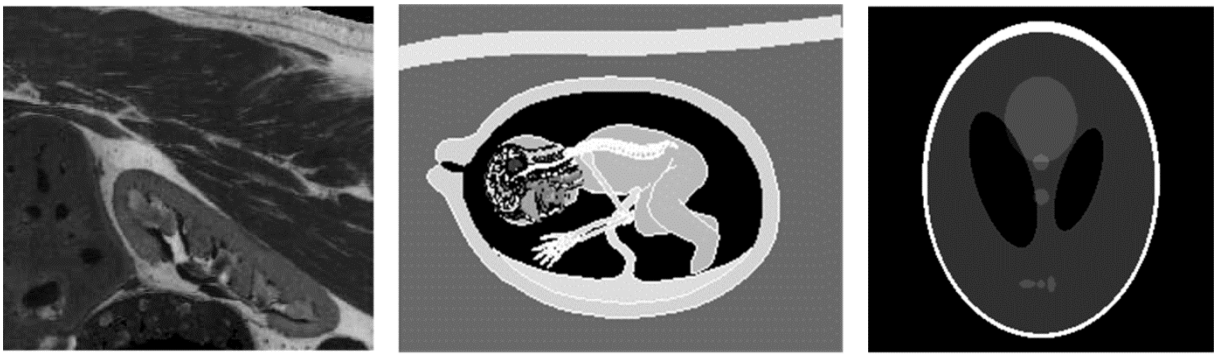

Figure 2.6 Original test images used to investigate the performance of denoising methods by suppressing the multiplicative speckle noise (a) Kidney (b) Fetus (c) Phantom image

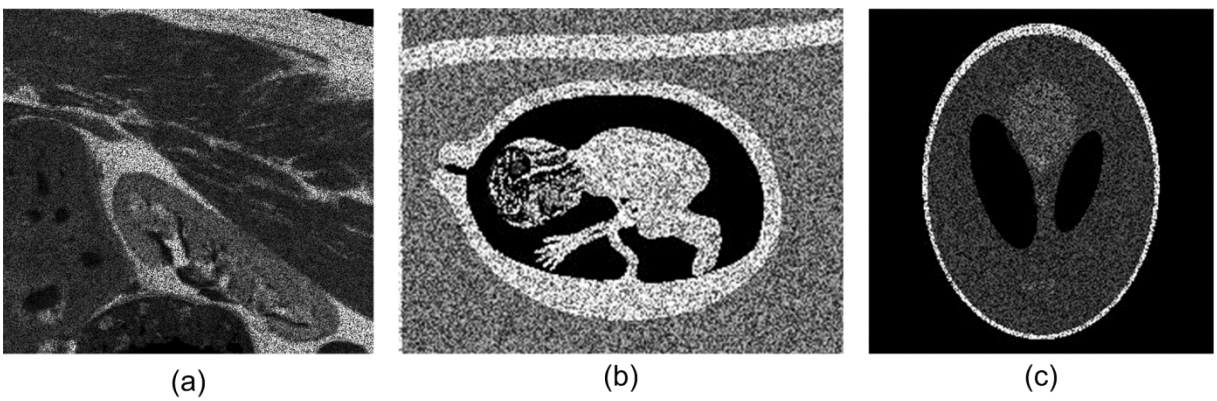

Figure 2.7 (a) Kidney (b) Fetus (c) Phantom image corrupted by speckle noise with the noise level of different variance σ = 0.1, 0.2 and 0.3, respectively

(a) (b) (c)

Figure 2.8 Standard test images used to investigate the performance of denoising methods by reducing the additive Gaussian noise (a) Lena image (b) Girl image (c) Boat image

(a) (b) (c)

Figure 2.9 (a) Lena (b) Girl (c) Boat images corrupted by Gaussian noise with a noise level of $\sigma_n = 20$

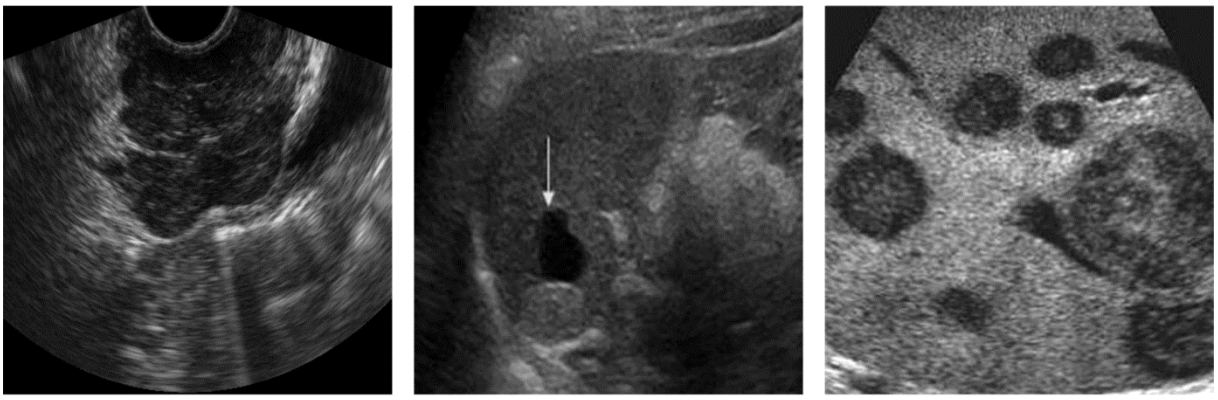

(a) (b) (c)

Figure 2.10 Original ultrasound images (a) Prostate (b) splenic cyst (c) Multiple liver masses ultrasound images

Experiment 3: *Denoising of the real US medical images for speckle reduction* - In this experiment, several real US images acquired from the open image source database (http://rad.usuhs.edu/medpix/parent.php3?mode=home_page), (http://ultrasonics.bioenggineering.illinois.edu),(http://thelivercarefoundation.org) and (http://www.ultrasoundcases.info/) are used to evaluate the performance of the denoising methods. Dr. T.S.A. Geertsma, Netherland also granted to utilize the different US medical images of different patients. All the denoising

methods are tested on several US images. Out of them, three US images such as prostate, splenic cyst and multiple liver masses US images are shown in Figure 2.10 and considered to present the validation results obtained from the different denoising methods, qualitatively and quantitatively in the present and next three subsequent chapters.

2.7 Results and Discussions

Experiment 1: To validate the experimental objectives, the denoised kidney, fetus and phantom images corresponding to their noisy version images are shown in Figure 2.11, Figure 2.12 and Figure 2.13, respectively, and their results from (a)-(l) also illustrate the denoised images obtained by the AWMF, WF, MHOPNF, ADF, SRAD, NCDF, TVF, NLMF, TI-WT, ridgelet, curvelet and shearlet transform based methods, respectively. From the Figure 2.11; it is observed that the denoised kidney images obtained from the TVF, NLMF and shearlet based methods provide better denoising results compared to the others in terms of visual quality. Moreover, the diffusion based methods such as ADF, SRAD and NCDF approaches also produce good results by reducing the speckle, but it also leads to remove the edge details present in the images. By comparing the visual analysis of the results produced by the diffusion based method, the NCDF method seems to be good similar to the SRAD for suppressing the speckles. On the other hand, the TVF and NLMF provide the best denoising results among all of them. However, the TVF suffers from the loss of the edge information. As mentioned in the literature about the transform domain approaches, in curvelet based methods, some visual distortion like oscillations occur in the denoised kidney images. Shearlet based method is also able to reduce a good amount of speckle than CVT and remove the limitations of the TI-WT and CVT based methods.

In case of the denoised fetus images shown in Figure 2.12**,** the same denoising methods achieve good performance in accordance with the visual results except for the TI-WT and ridgelet based method. The ridgelet based method also provides a competitive performance as compared to other remarkable denoising methods, but in addition, it leads to some visual distortion similar to curvelet based methods. The TVF and NLMF approaches generate much better denoised images for the phantom images as shown in Figure 2.13 as compared to the others. The WF method does not produce a satisfactory result in reducing the speckle, while the AWMF generates better results than the WF, but it is also not able to remove sufficient amount of speckle noise. Moreover, the shearlet based method also yields better denoising performance with good edge preservation results. These subjective outcomes mentioned above are validated with the various quantitative evaluations. These quantitative outcomes are also supported by four metrics such as PSNR, SNR, SSIM and EKI and mentioned in Table 2.1 for the processed kidney image.

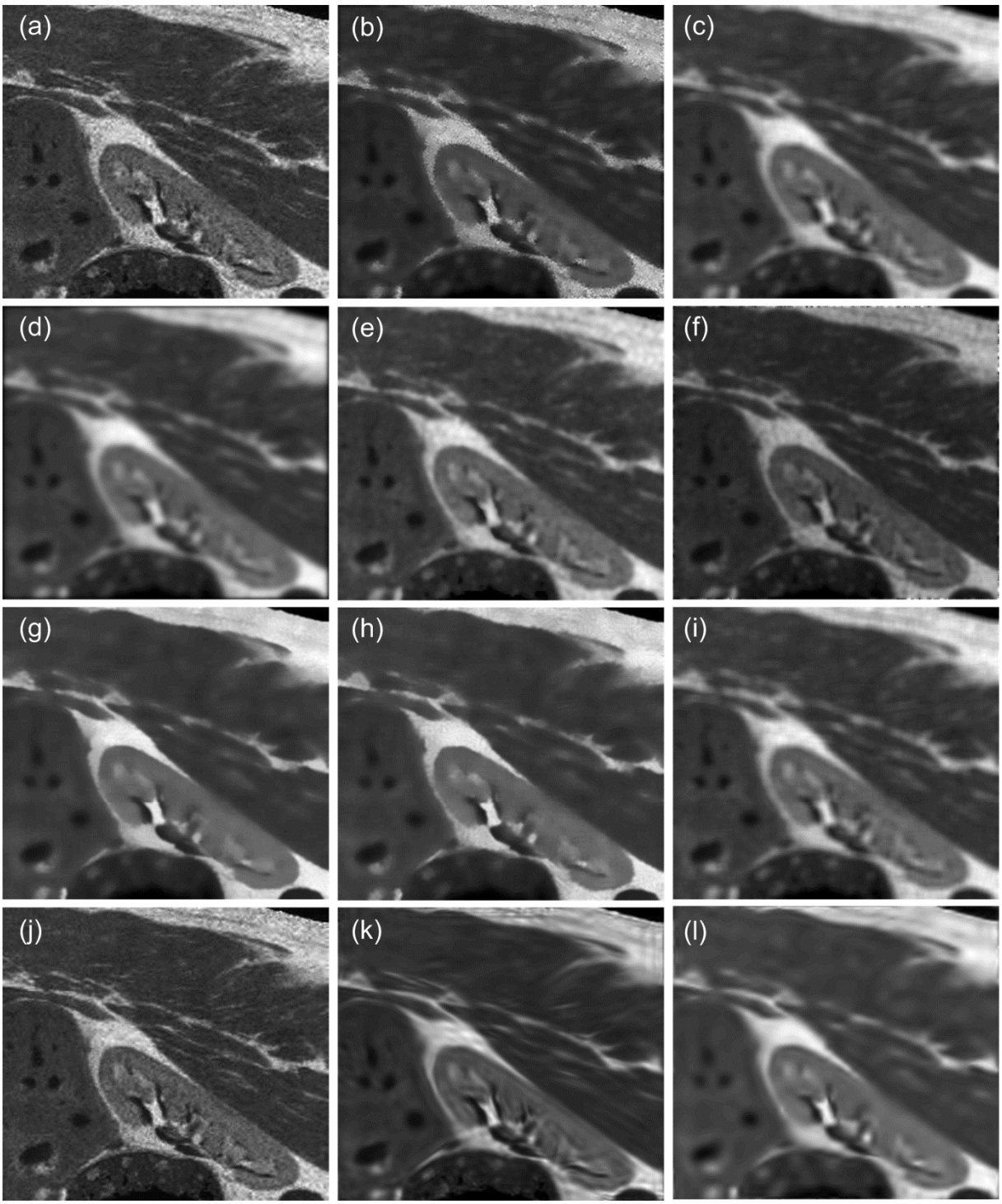

Figure 2.11 Visual comparison of various noise reduction methods applied to kidney image degraded by speckle noise (a) AWMF (b) WF (c) MHOPNF (d) ADF (e) SRAD (f) NCDF (g) TVF (h) NLMF (i) TI-WT (j) Ridgelet (k) Curvelet (l) Shearlet

From the results mentioned in Table 2.1, it is observed that the NLMF method produces better noise suppression performance for low level noise, but for noise level $\sigma = 0.3$, shearlet based method gains higher values of the SNR and PSNR as 16.43 and 27.05, respectively. This also achieves competitive structural similarity and edge preservation performance compared to the NLMF approach that provides the best denoising performance among all the above mentioned methods. Curvelet and ridgelet based methods

exhibit similar performance as mentioned in the literature. Another quantitative assessment is done to fetus image, processed by the different aforementioned methods and shown in Table 2.2. The NLMF approach behaves similar to previous assessments and provides better results than others. After that, shearlet also provides satisfactory and competitive results than the NLMF. Obviously, it achieves better noise suppression performance with edge preservation performance by achieving higher EKI values than others. The ridgelet based method which adopts a Neighcoeff thresholding approach, provides better speckle reduction performance with more edge preservation in case of low level noise and also gains a competitive PSNR and SNR values with larger edge preservation than the wavelet and curvelet based methods at higher noise level.

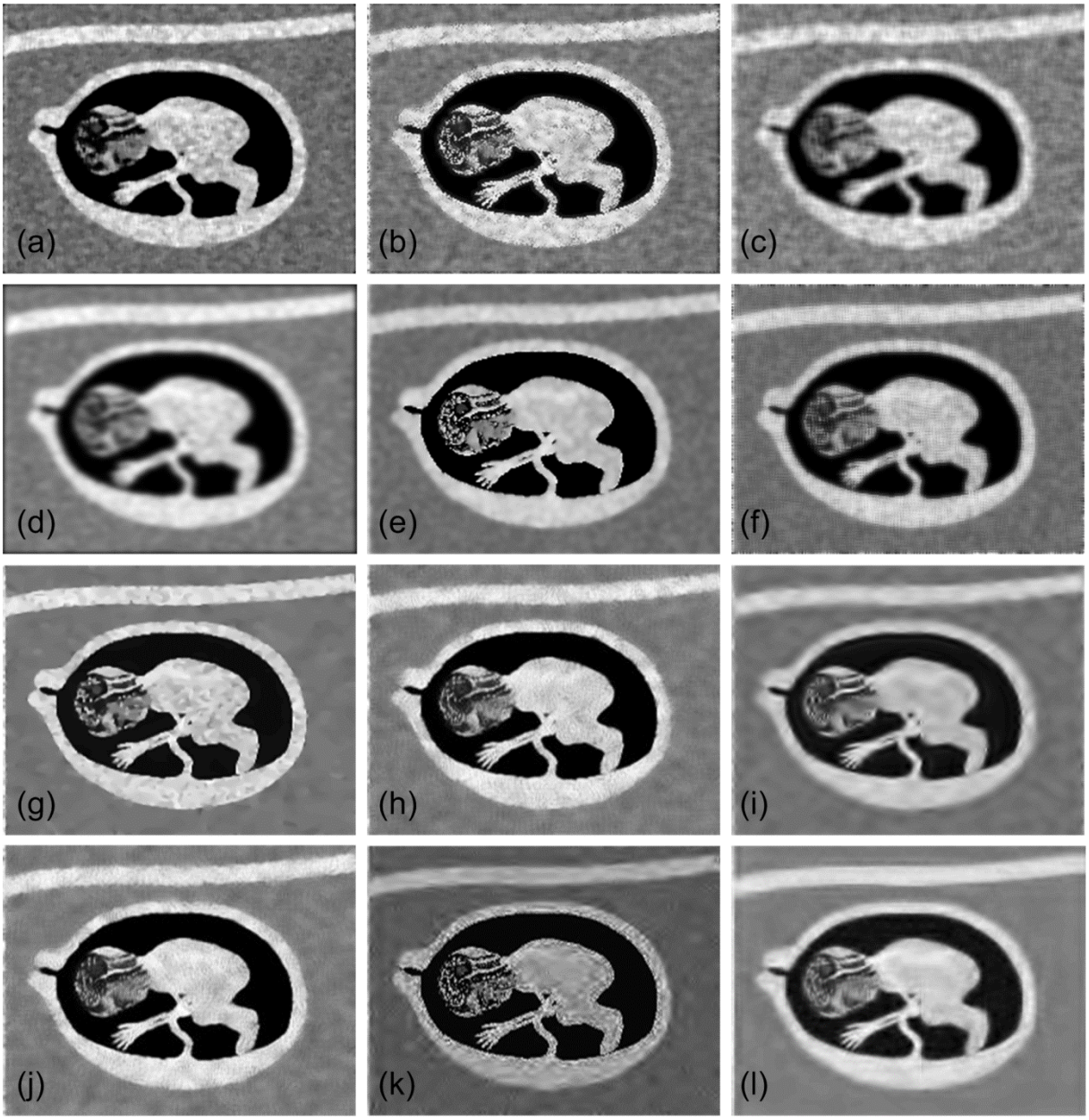

Figure 2.12 Visual comparison of various noise reduction methods applied to fetus image degraded by speckle noise (a) AWMF (b) WF (c) MHOPNF (d) ADF (e) SRAD (f) NCDF (g) TVF (h) NLMF (i) TI-WT (j) Ridgelet (k) Curvelet (l) Shearlet

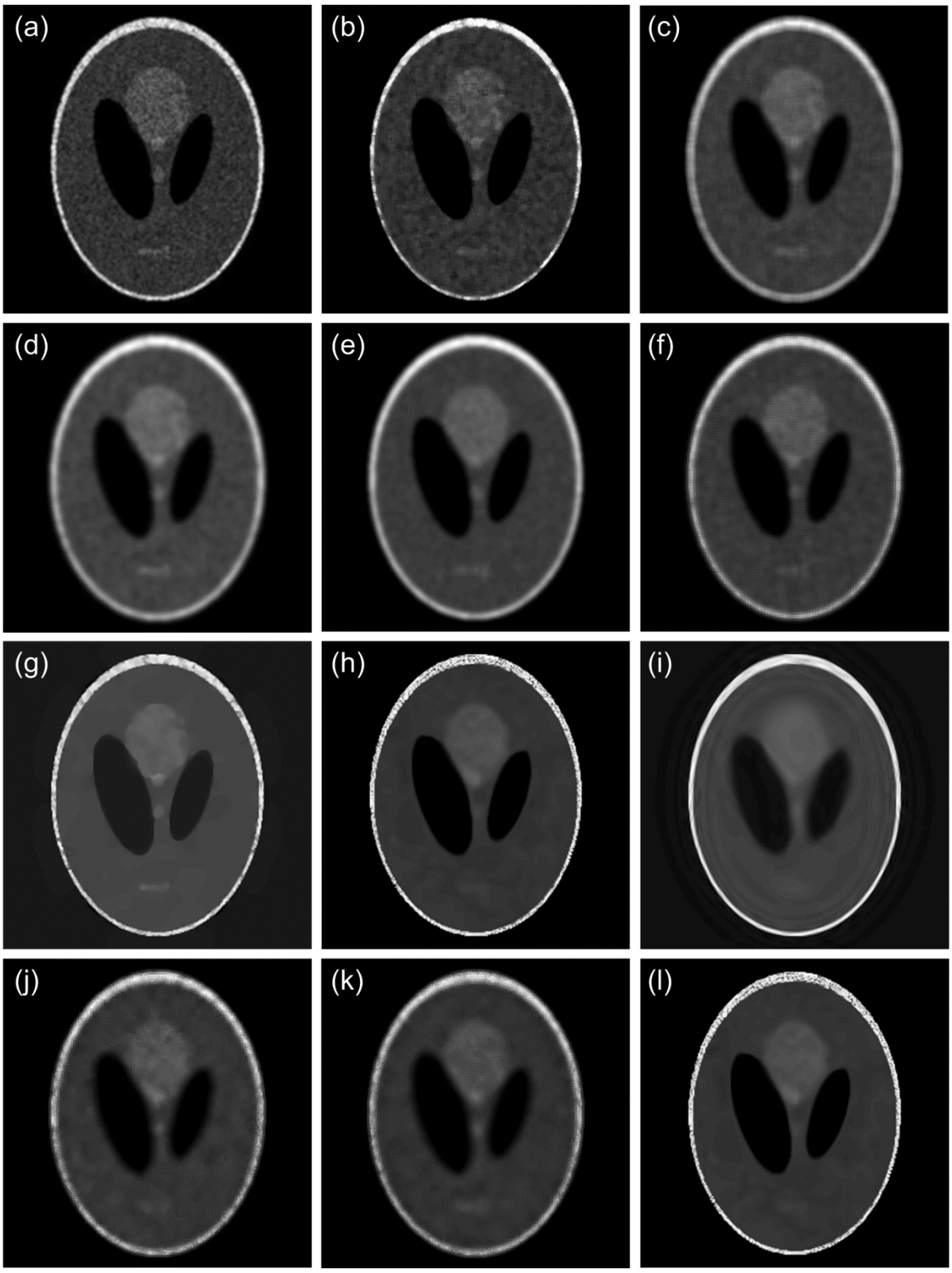

Figure 2.13 Visual comparison of various noise reduction methods applied to 2D phantom image degraded by speckle noise (a) AWMF (b) WF (c) MHOPNF (d) ADF (e) SRAD (f) NCDF (g) TVF (h) NLMF (i) TI-WT (j) Ridgelet (k) Curvelet (l) Shearlet

Besides these, the diffusion based methods like the ADF, SRAD and NCDF methods also produce good values of the SNR and PSNR, but the EKI values provided by these methods are less in comparison to others, which is also reflected in the visual analysis of the

denoised images as illustrated above. In the case of phantom image, all the assessment parameters are evaluated for all noise levels and given in the Table 2.3. From the results mentioned in Table 2.3, the TVF method extends its capability to reduce the speckle noise by producing higher SNR and PSNR values as 13.69 and 25.86, respectively than the shearlet method for noise level $\sigma = 0.1$. In case of high noise level $(\sigma = 0.3)$, the shearlet based method produces higher SNR and PSNR values as 11.31 and 23.48, respectively. The ridgelet based method also shows good noise suppression performance with better edge preservation than the curvelet based method for $\sigma = 0.1$ and for high noise levels, it produces the competitive values.

Table 2.1 Comparative speckle reduction performance of twelve denoising methods for kidney image

Metrics	$\sigma = 0.1$				$\sigma = 0.2$				$\sigma = 0.3$			
Methods	PSNR	SNR	SSIM	EKI	PSNR	SNR	SSIM	EKI	PSNR	SNR	SSIM	EKI
AWMF	21.39	10.77	0.7376	0.4388	20.69	10.07	0.7068	0.4209	20.95	10.33	0.6896	0.3260
WF	20.05	9.44	0.7119	0.4058	19.76	9.14	0.6937	0.3899	19.35	8.74	0.6792	0.3187
MHOPNF	20.49	9.87	0.7435	0.3301	20.11	9.48	0.7161	0.3235	19.19	8.57	0.6847	0.3226
ADF	21.74	11.11	0.7610	0.3181	20.79	10.17	0.7190	0.3041	20.46	9.84	0.6974	0.3011
SRAD	25.86	15.24	0.7197	0.4598	25.04	14.42	0.6944	0.3332	24.69	14.07	0.6873	0.3211
NCDF	25.22	14.61	0.6869	0.4277	24.27	13.65	0.6368	0.3139	23.54	12.92	0.6256	0.3024
TVF	25.85	15.23	0.6747	0.4149	25.65	15.03	0.6527	0.4036	25.52	14.90	0.6331	0.3931
NLMF	28.37	17.75	0.7829	0.4827	27.37	16.75	0.7797	0.4519	26.20	15.58	0.7612	0.4236
TI-WT	27.48	16.86	0.7412	0.4319	27.31	16.69	0.7391	0.4307	26.91	16.29	0.7353	0.4218
Ridgelet	24.54	13.93	0.7375	0.4136	23.75	13.13	0.7325	0.3782	22.09	11.47	0.7146	0.3672
Curvelet	26.77	16.15	0.7666	0.4340	26.57	15.95	0.7633	0.4318	26.27	15.65	0.7407	0.4193
Shearlet	27.54	16.92	0.7603	0.4567	27.28	16.66	0.7548	0.4349	27.05	16.43	0.7560	0.4231

Table 2.2 Comparative speckle reduction performance of twelve denoising methods for fetus image

Metrics	$\sigma = 0.1$				$\sigma = 0.2$				$\sigma = 0.3$			
Methods	PSNR	SNR	SSIM	EKI	PSNR	SNR	SSIM	EKI	PSNR	SNR	SSIM	EKI
AWMF	16.89	11.90	0.5382	0.5408	14.42	9.43	0.4485	0.4321	14.52	9.53	0.4005	0.3287
WF	16.93	11.93	0.6691	0.5014	13.98	9.01	0.5762	0.5538	11.11	6.13	0.5009	0.3360
MHOPNF	15.73	10.75	0.5635	0.3451	13.29	8.31	0.5110	0.2975	10.82	5.83	0.4732	0.2773
ADF	17.06	12.08	0.5925	0.3572	15.72	10.73	0.5375	0.3246	15.58	10.59	0.4978	0.3092
SRAD	18.33	13.34	0.6286	0.3828	16.66	11.67	0.5512	0.3866	15.39	10.40	0.4445	0.3625
NCDF	17.63	12.64	0.5683	0.3337	16.11	11.12	0.4789	0.3498	15.56	10.57	0.4334	0.3131
TVF	17.84	12.85	0.5854	0.3696	17.01	12.02	0.5631	0.3531	16.13	11.14	0.5325	0.3105
NLMF	19.56	14.57	0.6800	0.6336	18.13	13.14	0.6369	0.5454	17.91	12.92	0.5752	0.4541
TI-WT	18.31	13.32	0.6077	0.3785	17.40	12.41	0.5758	0.3579	16.50	11.51	0.5445	0.3167
Ridgelet	18.71	13.69	0.6001	0.5242	16.71	11.72	0.5678	0.4824	16.21	11.22	0.5412	0.3951
Curvelet	18.03	13.04	0.6381	0.4277	17.15	12.16	0.6164	0.4089	16.38	11.39	0.5816	0.3730
Shearlet	18.80	13.81	0.6490	0.4387	17.75	12.76	0.5764	0.4192	16.82	11.83	0.5095	0.3879

Table 2.3 Comparative speckle reduction performance of twelve denoising methods for phantom image

Metrics	$\sigma = 0.1$				$\sigma = 0.2$				$\sigma = 0.3$			
Methods	PSNR	SNR	SSIM	EKI	PSNR	SNR	SSIM	EKI	PSNR	SNR	SSIM	EKI
AWMF	21.71	9.55	0.7590	0.5327	20.75	8.58	0.7264	0.4738	20.02	7.86	0.6222	0.2413
WF	22.23	10.06	0.7563	0.4696	21.18	9.01	0.6718	0.4208	20.19	8.02	0.6954	0.3775
MHOPNF	22.67	10.49	0.7367	0.7034	20.54	8.37	0.7266	0.5361	19.13	6.95	0.7143	0.4341
ADF	21.98	9.81	0.7650	0.7381	21.12	8.95	0.7451	0.5159	19.98	7.81	0.7305	0.3945
SRAD	22.74	10.57	0.8035	0.5995	22.31	10.14	0.7855	0.5939	22.10	9.92	0.7686	0.5909
NCDF	23.23	11.06	0.7726	0.6998	22.74	10.57	0.7079	0.6086	22.25	10.08	0.6636	0.5376
TVF	25.86	13.69	0.6883	0.6452	24.07	11.90	0.6944	0.5878	23.20	11.03	0.6986	0.5354
NLMF	27.31	15.14	0.8492	0.7933	24.69	12.53	0.8135	0.6326	23.14	10.97	0.7829	0.6180
TI-WT	24.71	12.54	0.7920	0.5930	23.64	11.47	0.7680	0.5600	23.12	10.95	0.7529	0.5312
Ridgelet	24.14	11.97	0.7894	0.6834	22.21	10.03	0.7548	0.5239	20.11	7.93	0.7347	0.4585
Curvelet	25.01	12.84	0.7970	0.6121	24.12	11.95	0.7923	0.5799	23.38	11.22	0.7813	0.5521
Shearlet	25.55	13.39	0.8365	0.6850	24.44	12.27	0.7974	0.6267	23.48	11.31	0.7823	0.5397

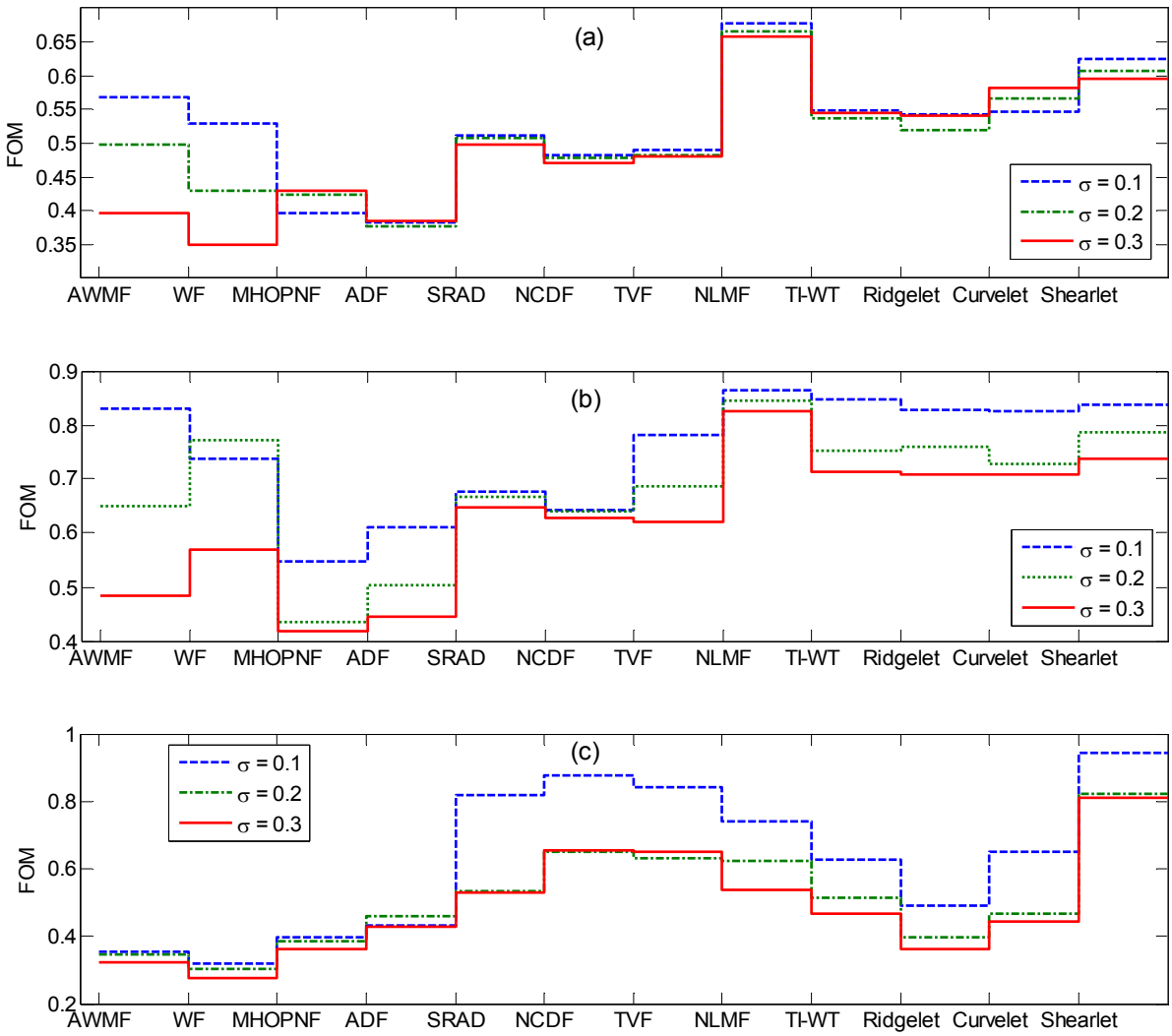

Figure 2.14 Comparative performance of the FOM values obtained by different denoising methods applied to speckled (a) Kidney image (b) Fetus image (c) Phantom Image

Besides all the performance measure such as the PSNR, SNR, SSIM and EKI measured for all the speckled images, another performance metric such as the FOM is also measured and represented in Figure 2.14 for all three images corrupted by all three noise levels. From Figure 2.14 (a), it is observed that NLMF and shearlet based methods achieve higher FOM value compared to the others for all three noise levels. It means more edge preservation by the NLMF and shearlet based methods than the others. The diffusion based methods also have a competitive value of the FOM with the TVF method. Similarly, in Figure 2.14 (b), the shearlet based method gains higher FOM values than other transform based methods (such as TI-WT, ridgelet and curvelet), especially for higher noise level. In the Figure 2.14 (c), shearlet method also shows larger FOM values than others. For low level noise, the NCDF, TVF and NLMF methods provides good FOM values, but fail to maintain its consistency to achieve the higher FOM values. Therefore, it can be said that the transform based method such as shearlet, ridgelet, curvelet and the TVF, NLMF or their integration can reflect as a good option for denoising.

Experiment 2: In this experiment, different images degraded with additive Gaussian noise are considered to investigate the robustness of all denoising techniques. The denoised images corresponding to noisy Lena, girl and boat images shown in Figure 2.9 are illustrated in Figure 2.15, Figure 2.16 and Figure 2.17, respectively. From these figures, it is observed that the WF approach works better than the AWMF. The MHOPNF method provides better noise reduction performance, but it leads to loss of edge information. The diffusion based method does not work better to remove the Gaussian noise and the edges available in the original images are completely lost in the denoised images because of smoothing of the edges, which leads to blurred images. The TVF and NLMF methods present their ability to suppress the noise, but edge information is also lost, if the noise level is increased. Sometimes, the TVF method shows the blocking effect in the images because of loss of the important image information that goes out with the residual of the denoised images. In additive noise reduction, most of the edges are preserved by the transform based denoising methods. In context to transform based denoising method, curvelet based method are able to preserve more edges than the wavelet and ridgelet based methods as mentioned in the literature. However, it leads to some visual distortion as seen in the denoised Lena, girl and boat images. The ST becomes an alternative that produces the denoised images of better visual quality than the curvelet based method with the preservation of more edges. In the denoised images produced by the shearlet based method, the problem of visual distortion occurred with the CVT based method becomes less, but it is not completely removed. Furthermore, based on the visual quality of the denoised images, it is observed that shearlet and curvelet based methods provide better results by preserving the image information. Moreover, the TVF/NLMF method can also be a suitable method for more noise suppression.

Figure 2.15 Visual comparison of various noise reduction methods applied to Lena image corrupted by Gaussian noise (a) AWMF (b) WF (c) MHOPNF (d) ADF (e) SRAD (f) NCDF (g) TVF (h) NLMF (i) TI-WT (j) Ridgelet (k) Curvelet (l) Shearlet

The objective outcomes are listed in Table 2.4 corresponding to a noisy Lena image corrupted by additive Gaussian noise. From the results mentioned in Table 2.4, it is clear that the NLMF and shearlet based methods outperform the others in terms of noise suppression

and edge preservation by providing higher SNR, PSNR, SSIM and EKI values. The curvelet based method and TVF also behave like a competitor with these denoising methods.

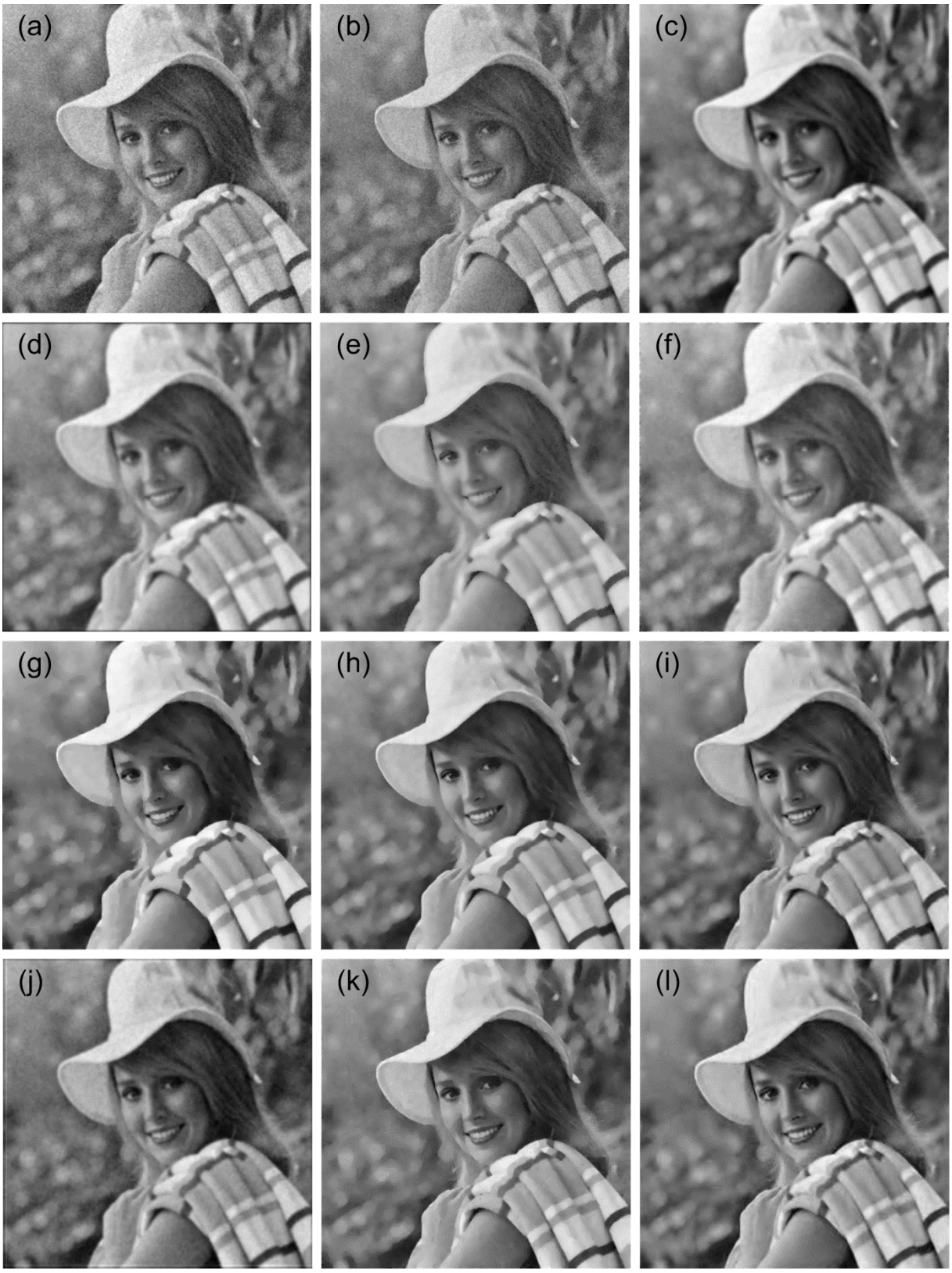

Figure 2.16 Visual comparison of various noise reduction methods applied to Girl image corrupted by Gaussian noise (a) AWMF (b) WF (c) MHOPNF (d) ADF (e) SRAD (f) NCDF (g) TVF (h) NLMF (i) TI-WT (j) Ridgelet (k) Curvelet (l) Shearlet

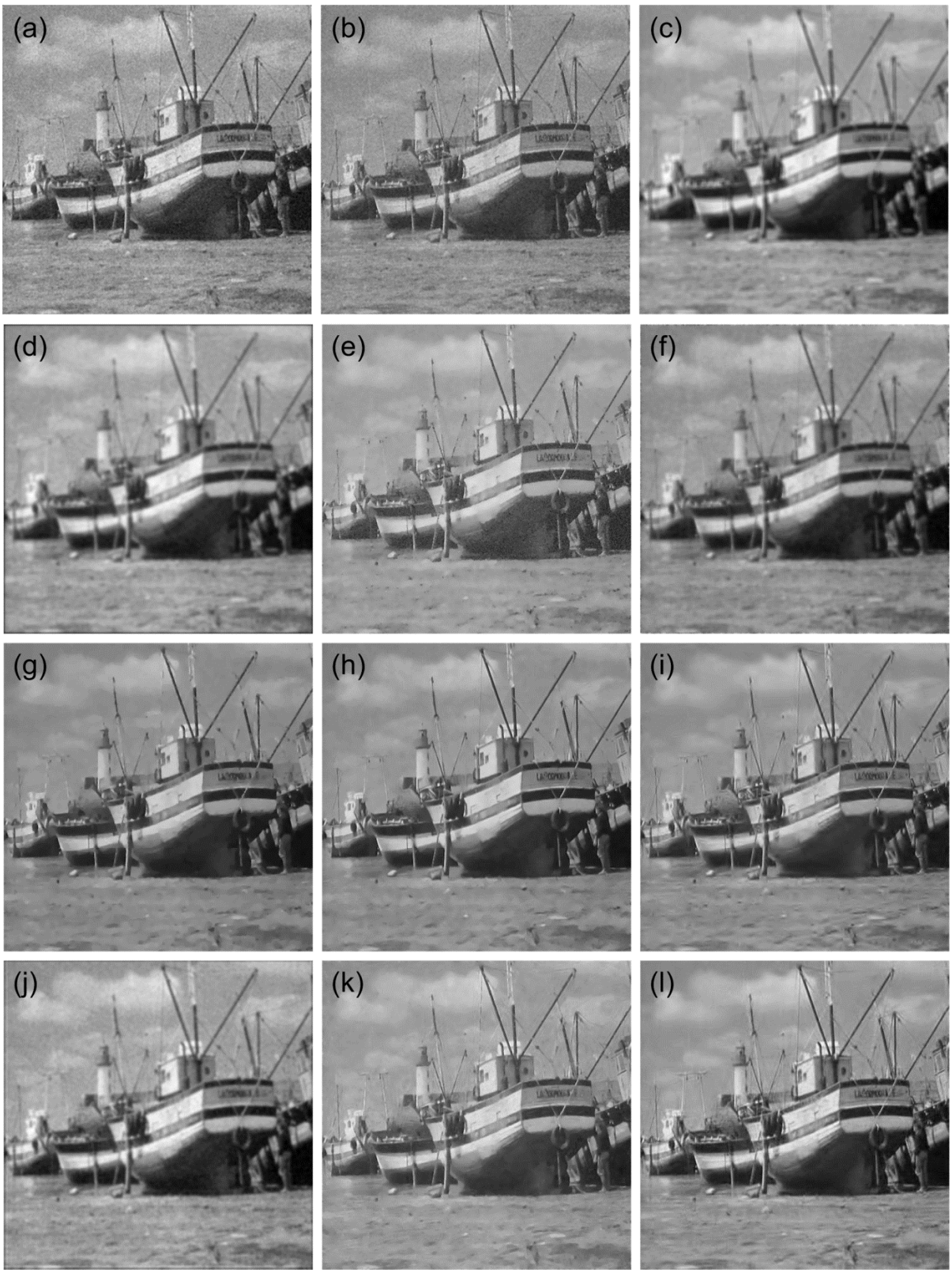

Figure 2.17 Visual comparison of various noise reduction methods applied to boat image corrupted by Gaussian noise (a) AWMF (b) WF (c) MHOPNF (d) ADF (e) SRAD (f) NCDF (g) TVF (h) NLMF (i) TI-WT (j) Ridgelet (k) Curvelet (l) Shearlet

The quantitative results obtained from the denoised girl images are given in Table 2.5. From the results mentioned in Table 2.5, the NLMF method achieves higher PSNR and SNR values as 34.17 and 29.61, respectively, for $\sigma_n = 10$, but for high noise level, shearlet based

thresholding gains higher PSNR and SNR values than the NLMF. For higher level of noise, the TVF approach is also able to achieve a competitive value of SNR and PSNR in comparison to the NLMF and shearlet method. Moreover, the shearlet based denoising method also outperforms the others in case of phantom image as mentioned in Table 2.6. From the results given in Table 2.6, it is observed that both the NLMF and shearlet methods have approximately same PSNR and SNR values for $\sigma_n = 10$, but the shearlet method shows its superiority over the NLMF for higher noise level. The TVF also acts as a good noise suppressing method, if the noise level gets increased, but at the cost of losing the edge information available in the source images. By considering, all the results mentioned in all three tables, the wiener filter can also be a good denoising option, if the noise level is too low otherwise, the transform based denoising methods may be better options.

Table 2.4 Comparative denoising performance of twelve different approaches applied to Lena image corrupted by additive Gaussian noise

Metrics	$\sigma_n = 10$				$\sigma_n = 20$				$\sigma_n = 30$			
Methods	PSNR	SNR	SSIM	EKI	PSNR	SNR	SSIM	EKI	PSNR	SNR	SSIM	EKI
AWMF	32.42	26.77	0.9265	0.6336	28.49	22.83	0.8032	0.4319	25.62	19.97	0.6815	0.3002
WF	33.04	27.38	0.9439	0.6582	29.13	23.47	0.8265	0.5236	25.81	20.15	0.7026	0.3532
MHOPNF	27.56	21.90	0.8724	0.5750	27.32	21.67	0.8207	0.4599	26.98	21.33	0.7986	0.4360
ADF	26.82	21.16	0.9105	0.5908	25.09	19.43	0.8333	0.4729	23.85	18.19	0.8060	0.3970
SRAD	27.82	22.17	0.8963	0.2914	23.85	18.20	0.8397	0.3338	21.89	16.23	0.7992	0.3396
NCDF	27.75	22.09	0.8826	0.4791	26.90	21.25	0.8654	0.3198	25.70	20.04	0.8348	0.2199
TVF	29.99	24.33	0.8767	0.7216	29.98	24.33	0.8837	0.6863	29.45	23.79	0.8751	0.6520
NLMF	35.52	29.87	0.9600	0.8447	32.13	26.47	0.9203	0.7348	29.91	24.26	0.8802	0.6130
TI-WT	35.15	29.49	0.9609	0.8244	31.53	25.88	0.9204	0.6701	29.44	23.78	0.8833	0.5442
Ridgelet	28.30	22.64	0.9113	0.6061	27.97	22.31	0.8784	0.6013	27.49	21.83	0.8338	0.5934
Curvelet	34.83	29.17	0.9569	0.8313	31.66	26.01	0.9178	0.7386	29.73	24.07	0.8805	0.6724
Shearlet	35.63	29.98	0.9643	0.8509	32.65	26.99	0.9300	0.7536	30.77	25.12	0.8932	0.6748

Table 2.5 Comparative denoising performance of twelve different approaches applied to girl image corrupted by additive Gaussian noise

Metrics	$\sigma_n = 10$				$\sigma_n = 20$				$\sigma_n = 30$			
Methods	PSNR	SNR	SSIM	EKI	PSNR	SNR	SSIM	EKI	PSNR	SNR	SSIM	EKI
AWMF	32.12	27.56	0.8244	0.5483	28.44	23.89	0.7091	0.3794	25.59	21.04	0.6858	0.2616
WF	33.24	28.69	0.8391	0.6601	28.99	24.44	0.7314	0.4702	25.69	21.13	0.7074	0.3252
MHOPNF	28.70	24.15	0.8872	0.6133	28.34	23.79	0.8686	0.6003	27.82	23.26	0.8391	0.5696
ADF	27.02	22.47	0.9201	0.6152	25.23	20.68	0.8617	0.5249	23.96	19.41	0.8419	0.4590
SRAD	21.35	16.79	0.8656	0.3391	20.39	15.85	0.8188	0.3144	19.58	15.03	0.7770	0.3072
NCDF	29.43	24.87	0.8999	0.5552	28.24	23.69	0.8854	0.3775	26.67	22.12	0.8555	0.2786
TVF	30.55	25.99	0.8660	0.6806	30.73	26.18	0.8769	0.6406	30.17	25.62	0.8684	0.6075
NLMF	34.17	29.61	0.9436	0.7309	32.04	27.49	0.9098	0.6694	30.41	25.86	0.8784	0.5859
TI-WT	33.73	29.18	0.9420	0.7232	31.24	26.68	0.9023	0.6021	29.63	25.07	0.8696	0.5088
Ridgelet	29.23	24.68	0.9206	0.6018	28.81	24.26	0.8922	0.5988	28.18	23.63	0.8494	0.5923
Curvelet	33.42	28.87	0.9370	0.7195	31.27	26.72	0.8971	0.6559	29.83	25.28	0.8657	0.6201
Shearlet	34.02	29.47	0.9371	0.7325	32.14	27.59	0.9112	0.6686	30.84	26.29	0.8808	0.6208

Table 2.6 Comparative denoising performance of twelve different approaches applied to boat image corrupted by additive Gaussian noise

Metrics	$\sigma_n = 10$				$\sigma_n = 20$				$\sigma_n = 30$			
Methods	PSNR	SNR	SSIM	EKI	PSNR	SNR	SSIM	EKI	PSNR	SNR	SSIM	EKI
AWMF	29.68	24.33	0.9238	0.5696	27.09	21.75	0.8236	0.4034	24.79	19.45	0.7165	0.2835
WF	32.14	26.79	0.9455	0.6774	28.37	23.02	0.8549	0.5925	25.36	20.01	0.7450	0.4212
MHOPNF	25.51	20.17	0.8248	0.4656	25.40	20.05	0.7887	0.4568	23.24	17.90	0.7323	0.4387
ADF	24.79	19.45	0.8549	0.5358	23.33	17.99	0.7838	0.4162	22.31	16.97	0.7247	0.3761
SRAD	26.47	21.12	0.8314	0.5590	23.55	18.19	0.7934	0.4865	21.16	15.82	0.7348	0.4056
NCDF	25.43	20.09	0.8132	0.4899	24.95	19.61	0.8033	0.3371	24.21	18.87	0.7829	0.2488
TVF	27.48	22.14	0.8079	0.6637	27.43	22.09	0.8203	0.6395	27.12	21.77	0.8223	0.6084
NLMF	33.31	27.97	0.9480	0.8659	29.82	24.48	0.8816	0.7662	27.71	22.37	0.8265	0.6363
TI-WT	33.26	27.92	0.9540	0.8523	29.36	24.02	0.8940	0.7021	27.47	22.12	0.8395	0.5612
Ridgelet	25.66	20.32	0.7468	0.4340	25.47	20.13	0.7693	0.4317	25.20	19.85	0.7619	0.4261
Curvelet	32.71	27.37	0.9488	0.8495	29.49	24.15	0.8893	0.7445	27.49	22.15	0.8357	0.6475
Shearlet	33.32	27.98	0.9568	0.8613	30.01	24.66	0.9056	0.7521	28.19	22.85	0.8568	0.6535

Table 2.7 Comparative denoising performance of some existing approaches based on the PSNR values for Lena image degraded by different noise levels

S. No.	Methodology	PSNR for various noise levels		
		$\sigma_n = 10$	$\sigma_n = 20$	$\sigma_n = 30$
1	Soft shrinkage using universal threshold [92]	28.10	22.14	18.62
2	Hard shrinkage using universal threshold [92]	30.49	27.49	25.93
3	Visu shrinkages using universal threshold [82]	28.76	26.46	25.14
4	Sure shrinkages (sub band adaptive of visu shrinkage version) [79]	33.38	30.22	28.18
5	Bayes shrinkage [51]	33.32	30.17	27.13
6	Probshrinkage [189]	33.80	30.49	---
7	Zhang's shrinkage with TNN [282]	33.60	30.49	28.62
8	Shrinkage function by Nasri et al. with TNN [173]	33.82	30.56	28.77
9	Image denoising based on statistical modeling 7X7 [136]	34.24	30.92	---
10	HMT [70]	33.84	30.39	28.35
11	BLS-GSM [190]	34.19	30.89	29.06
12	Laplacian mixture shrinkage (7x7) using WT [199]	34.18	30.88	28.99
13	Image denoising in steerable pyramid domain 7x7 (SoftLMAP) [198]	34.19	30.94	29.14
14	Bivariate shrinkages with adaptive dual Tree complex wavelet packet [259]	34.73	31.43	29.37
15	Pointwise shape-adaptive DCT for high-quality denoising [93]	35.58	32.60	**30.86***
16	WTTNN approach [31]	34.21	30.72	28.88
17	WT based thresholding neural network with adapting learning rate [31]	34.33	30.91	29.04
18	Adaptive thresholding function using WT with db8 [29]	34.27	30.81	28.97
19	Adaptive thresholding function using WT with bior 6.8 [29]	34.36	30.93	29.06
20	Subband adaptive thresholding function using PSO [32]	34.34	30.94	---
21	WT domain with Trivariate shrinkage and joint bilateral filter [272]	**35.70**	**32.80**	**31.08**
22	Adaptive fusion using wavelet and curvelet transform [30]	35.59	32.33	30.38
23	RADWT based nonlinear filtering [109]	33.80	30.39	28.37
24	Curvelet based thresholding using cycle spinning approach	34.83	31.66	29.73
25	Shearlet based thresholding using cycle spinning approach	**35.63***	**32.65***	30.77

Apart from all the comparisons between the performance of all the twelve denoising methods, another comparative quantitative performance is used with some other existing approaches based on the PSNR values achieved for the denoised Lena images, as presented in Table 2.7. From the quantitative results, it has been observed that the PSNR values achieved by the shearlet based methods are better in almost all the approaches except for the approach presented in [272] and [93] (for $\sigma_n = 30$). In case of the methodology mentioned in [272], the PSNR values are higher because of the usage of additional spatial domain filtering. In case of method mentioned in [93], some additional computational complexity occurs. Thus, to analyze the performance of the curvelet and shearlet based methods along with all others denoising methods on the real US images, another experiment is performed and presented in the next section of this chapter in which the performance evaluation of speckle reduction performed by the various aforementioned denoising methods is addressed.

Experiment 3: As mentioned above in the experimental section, different US images are considered to conduct this experiment and processed by all the aforementioned denoising methods. Out of them, the denoised prostate US images are illustrated in Figure 2.18. In case of the diffusion based method, the process is stopped automatically when the residual error, defined as mean square error of the image between two iterations is smaller than 0.01. The time step is set to 0.25 for the ADF and SRAD methods. The parameters are set similar to those as previous one. The subjective outcomes of two other US images such as splenic cyst and multiple liver masses are shown in Figure 2.19 and Figure 2.20, respectively. From these results, it is evident that the NLMF output gives better speckle reduction performance for prostate and splenic cyst US images, but all the edge information is lost, while reducing the speckle. The similar thing happens with the third US images that the SRAD outperforms the others by reducing the speckle from the US image, but all the fine details and edge information that have also some clinical meaning, are lost during the smoothing of the image. The ADF method shows some blurring effect in the image because of smoothing the edges and fine details, but the NCDF provide better results than the ADF. The transform domain methods also introduce some false edges in all the processed US images. Besides these, the ridgelet based method using Neighcoeff approach is able to suppress the speckles with preserving some edge information. In all these methods, the shearlet method produces the despeckled US images with good visual quality and it has also capability to capture more edges during the denoising process. The amount of the visual distortion or fuzzy edges that are introduced in the other transform based methods, becomes very less in case of the shearlet transform.

Apart from the visual assessments, any denoising performance requires a support of the objective evaluations for the validation purposes, but it is very difficult to analyze the

denoising results of the real US images processed with different denoising methods in terms of different performance measures, since there are no noise free reference images.

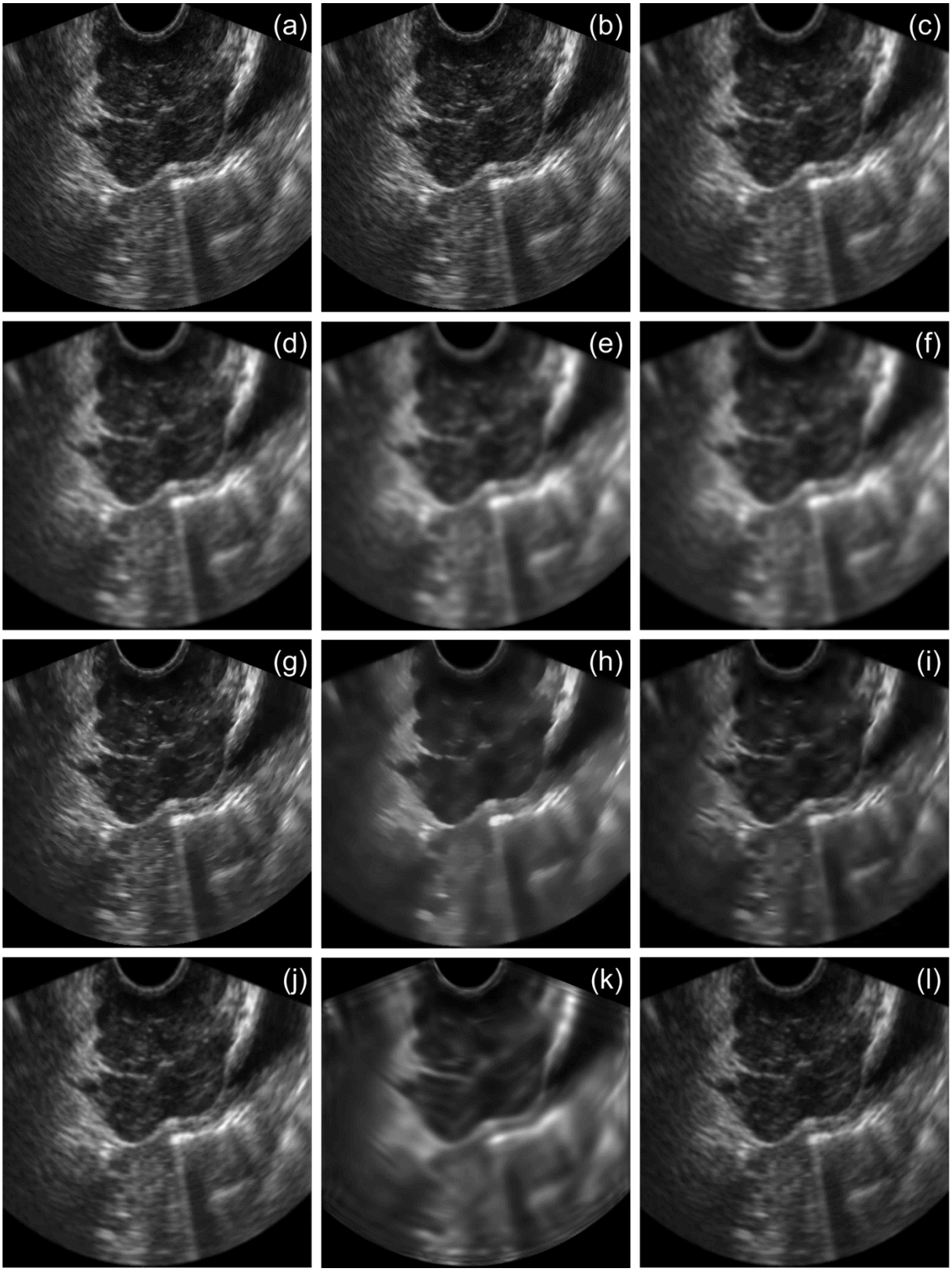

Figure 2.18 Visual comparison of various denoising methods applied to prostate ultrasound image (a) AWMF (b) WF (c) MHOPNF (d) ADF (e) SRAD (f) NCDF (g) TVF (h) NLMF (i) TI-WT (j) Ridgelet (k) Curvelet (l) Shearlet

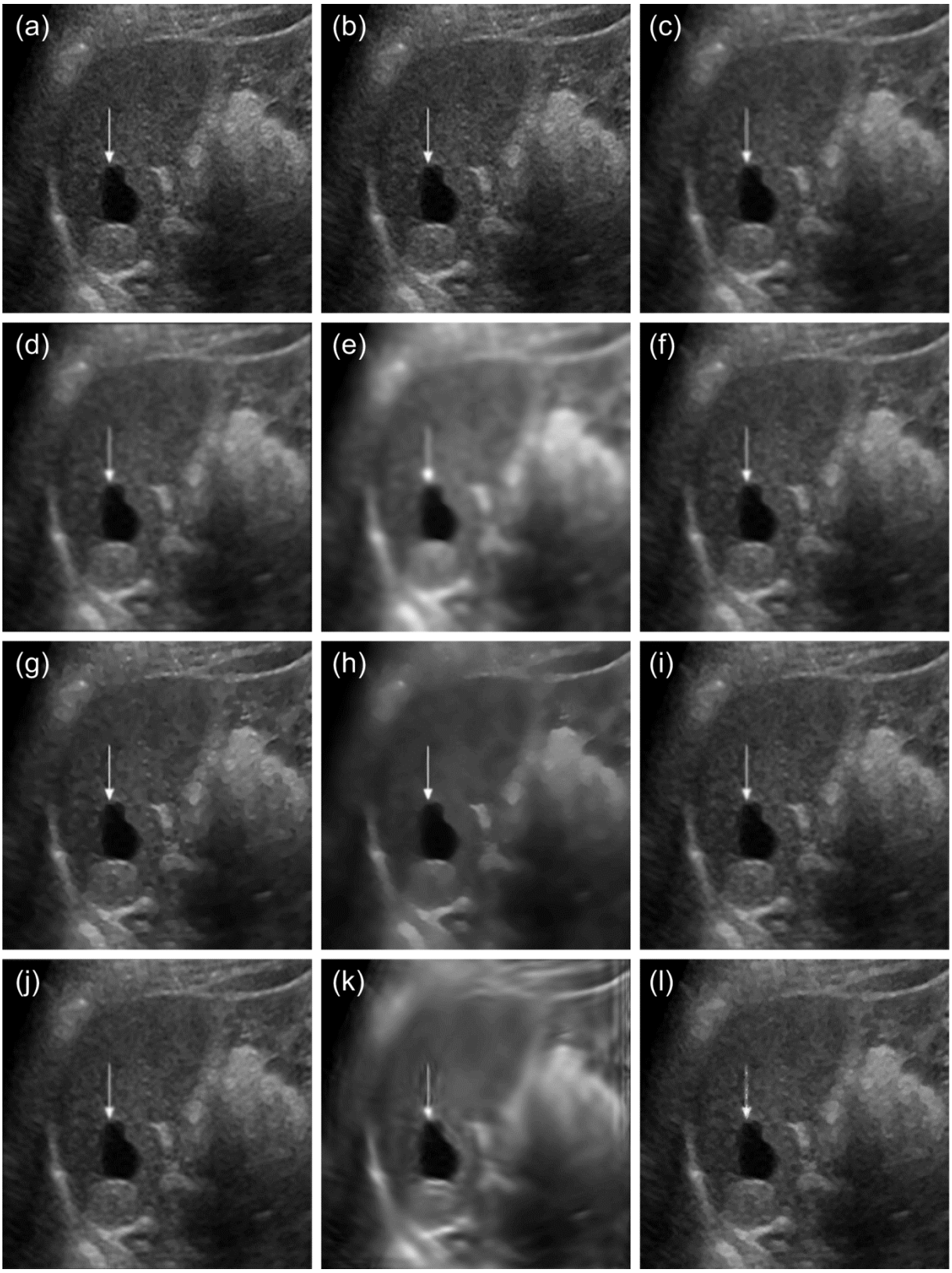

Figure 2.19 Visual comparison of various denoising methods applied to splenic cyst ultrasound image (a) AWMF (b) WF (c) MHOPNF (d) ADF (e) SRAD (f) NCDF (g) TVF (h) NLMF (i) TI-WT (j) Ridgelet (k) Curvelet (l) Shearlet

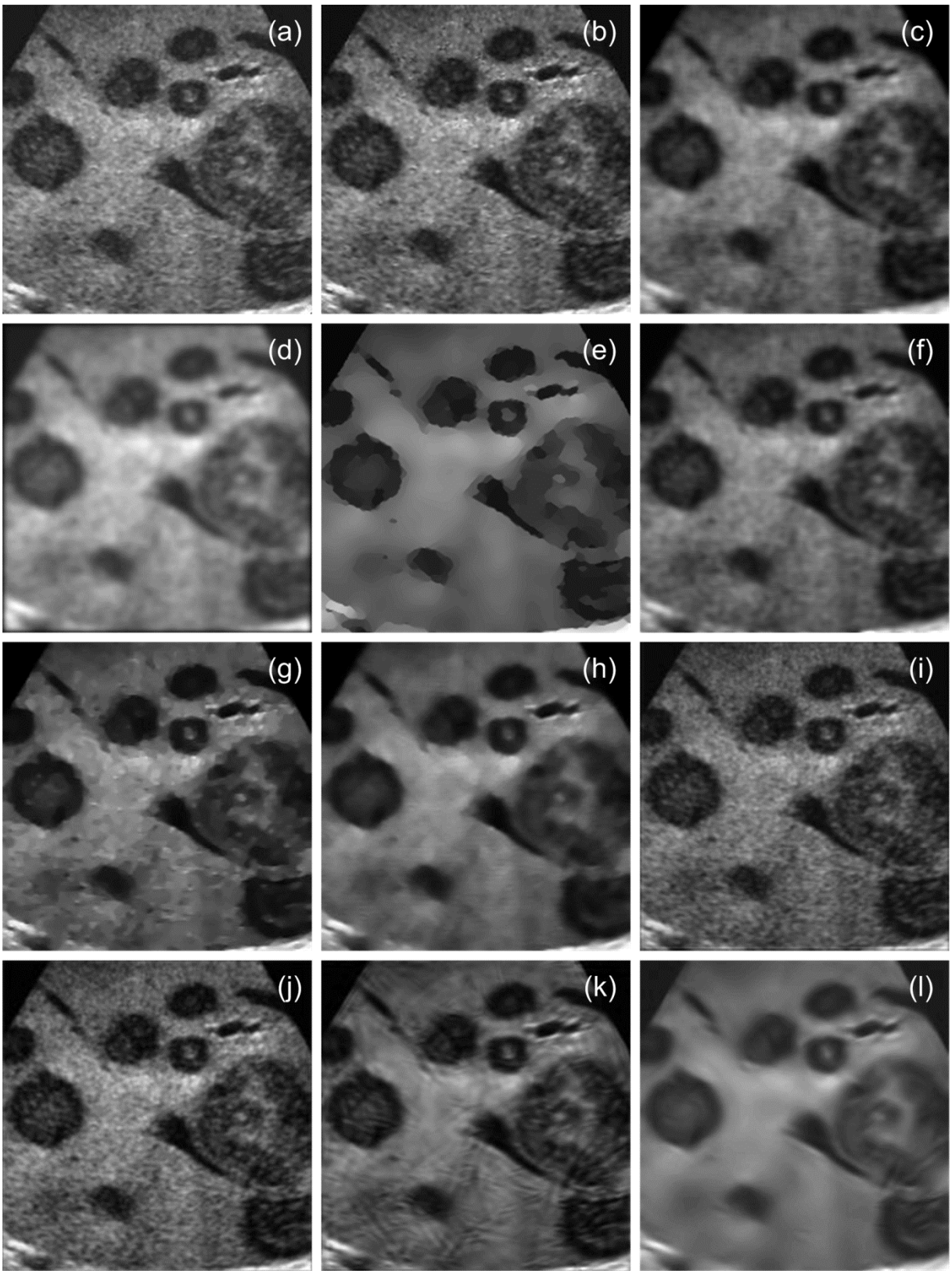

Figure 2.20 Visual comparison of various denoising methods applied to multiple liver masses ultrasound image (a) AWMF (b) WF (c) MHOPNF (d) ADF (e) SRAD (f) NCDF (g) TVF (h) NLMF (i) TI-WT (j) Ridgelet (k) Curvelet (l) Shearlet

Therefore, mean to variance ratio (MVR) is used as an index for estimating the speckle noise level in the US images over different image regions. A larger value of the MVR

represents a better quantitative performance of the different denoising methods on existing real US images. For such purpose, four different US images out of the dataset are presented in Figure 2.21. In this figure, two different image regions are marked with the red and blue rectangle on each US image for the quantitative analysis. Red and blue rectangles represent region 1 and region 2, respectively. The MVR values obtained for both the regions 1 and 2 as MVR 1 and MVR 2, respectively, are shown in Figure 2.22 (a)-(d). From the MVR values as mentioned in Figure 2.22, the TVF, NCDF and shearlet based methods achieve larger MVR values which means that these methods outperform the others exhibited in terms of speckle suppression by obtaining higher MVR values.

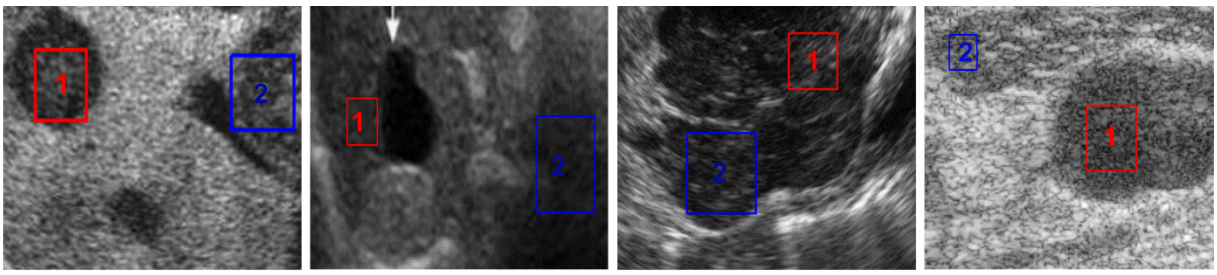

(a) (b) (c) (d)

Figure 2.21 Real ultrasound images with two selected image regions as Region 1 and 2 for the quantitative measure of MVR. Region 1 is marked as red rectangle and Region 2 as blue

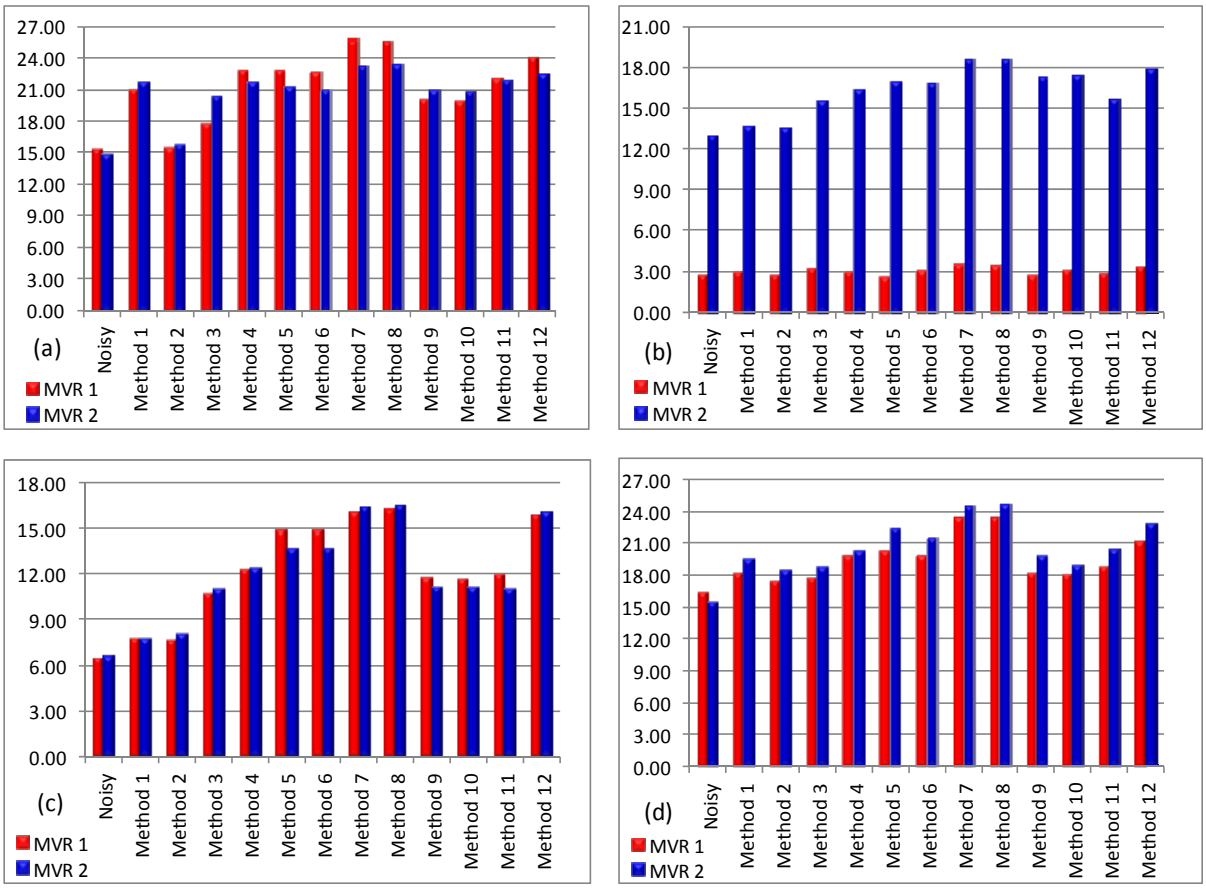

Figure 2.22 Plot of MVR values obtained by the different denoising methods for two image regions shown in the Figure 2.21 (a)-(d). Here, methods 1-12 refer to the AWMF, WF, MHOPNF, ADF, SRAD, NCDF, TVF, NLMF, TI-WT, Ridgelet, Curvelet and Shearlet, respectively

Table 2.8 Performance comparison of the various denoising methods using the averaged MVR values over 100 different regions obtained on 50 ultrasound images

S. No.	Methodology	MVR
1	Noisy	14.04 ± 3.04
2	AWMF	16.27 ± 4.69
3	WF	15.64 ± 3.42
4	MHOPNF	16.70 ± 3.49
5	ADF	18.26 ± 4.23
6	SRAD	19.45 ± 3.97
7	NCDF	19.32 ± 3.69
8	TVF	21.45 ± 4.95
9	NLMF	21.51 ± 4.13
10	TI-WT	18.16 ± 3.14
11	Ridgelet based method	17.47 ± 3.69
12	Curvelet based method	18.22 ± 4.57
13	Shearlet based method	20.94 ± 3.88

In addition, to further assess the performance of aforementioned denoising methods, 100 measurements are taken on fifty different US images, in which two measurements at the different locations for each image, to evaluate the MVR values. Table 2.8 shows the averaged MVR values obtained for different denoising techniques. The results presented in Table 2.8 also show the superiority of the TVF, NLMF and shearlet based methods to provide the effective noise suppression as compared to the others.

2.8 Proposed M-band Ridgelet Based Thresholding Approach

The M-band ridgelet transform overcomes the limitations of ordinary ridgelet transform by replacing the 2-band WT to analyze the edges and features present in the images. As mentioned above, to provide a solution for the limitations of the WT, ridgelet transform has been introduced as a representation of multidimensional signals which is used to map the line singularities to the point singularities using radon transform and after that the WT is used to provide better performance for characterizing the point singularities in the Radon transform [77]. Although, ridgelet transform provides better result and breaks the limitation of the wavelets, however, 2-band WT must be performed in radon domain to complete the ridgelet transform. It also derives another shortcoming of the standard wavelet. They are only capable to analyze low frequency signals, not for high frequency signals [194, 226]. Therefore, in this section, M-band ridgelet transform is used for reducing the speckle present in the US images using M-band wavelet decomposition in radon domain. The decomposition using M-band ridgelet transform also helps to enlarge the high frequency components.

2.8.1 M-band ridgelet transform

Consider there is a univariate function $\psi: \mathbb{R} \to \mathbb{R}$ which satisfy the admissibility condition as [225]

$$\int \left|\hat{\psi}(\xi)\right|^2 / |\xi|^2 \, d\xi < \infty \tag{2.58}$$

where $\hat{\psi}$ denotes the Fourier transform of the univariate function ψ which has a vanishing mean $\int \psi(t)dt = 0$. For each $a > 0$, $b \in R$ and $\theta \in [0,2\pi]$, the bivariate ridgelet $\psi_{a,b,\theta}: \mathbb{R}^2 \to \mathbb{R}^2$ is defined as follows:

$$\psi_{a,b,\theta}(x,y) = a^{-1/2}\psi((x\,cos\theta + y\,sin\theta - b)/a) \tag{2.59}$$

This function $\psi_{a,b,\theta}(x,y)$ has constant value along the lines $x\,cos\theta + y\,sin\theta = K$.

where K is constant, $a > 0$ is the scale parameter, b is the location parameter and θ is an orientation parameter. For a given integrable bivariate signal $s(x,y)$, ridgelet coefficients (R_T) are defined as

$$R_T(a,b,\theta) = \int_{\mathbb{R}^2} s(x,y)\psi_{a,b,\theta}(x,y)dxdy \tag{2.60}$$

Due to

$$\psi_{a,b,\theta}(x,y) = \int_{\mathbb{R}} \psi_{a,b}(t)\,\delta(xcos\theta + ysin\theta - t)dt \tag{2.61}$$

where $\psi_{ab}(t) = a^{-1/2}\psi((t-b)/a)$ and

$$R_T(a,b,\theta) = \int_{\mathbb{R}^2} s(x,y)\left[\int_{\mathbb{R}} \psi_{a,b}(t)\,\delta(xcos\theta + ysin\theta - t)dt\right]dxdy \tag{2.62}$$

$$R_T(a,b,\theta) = \int_{\mathbb{R}^2} \int_{\mathbb{R}} s(x,y)\psi_{a,b}(t)\,\delta(xcos\theta + ysin\theta - t)dxdy\,dt \tag{2.63}$$

$$R_T(a,b,\theta) = \int_{\mathbb{R}} \psi_{a,b}(t) \int_{\mathbb{R}^2} s(x,y)\,\delta(xcos\theta + ysin\theta - t)dxdydt \tag{2.64}$$

$$R_T(a,b,\theta) = \int_{\mathbb{R}} \psi_{a,b}(t)R_a(\theta,t)dt \tag{2.65}$$

where $R_a(\theta,t)$ refers to the radon transform of the signal $s(x,y)$ and is given as follows:

$$R_a(\theta,t) = \int_{\mathbb{R}^2} s(x,y)\,\delta(xcos\theta + ysin\theta - t)dxdy \tag{2.66}$$

Thus, the ridgelet transform is evaluated by applying one dimensional wavelet transform to the slices of radon transform. For a 2D signal, the radon transform can be obtained with the fast Fourier transform (FFT) as per following three steps:

1. Compute the two dimensional FFT of a given image.
2. Cartesian to polar conversion using an interpolation scheme that means we can obtain the samples on a polar grid by substituting from nearby samples at square grid as shown in Figure 2.23. It is the intersection between the set of 2M radial lines and that of Cartesian lines parallel to the axes for an image of size M × M.
3. Evaluate the one dimensional inverse FFT on each angular line.

Yu et al. reported the M-band ridgelet transform for texture classification [194] in which one dimensional 2-band WT is replaced by the M-band WT along the radial and angular lines

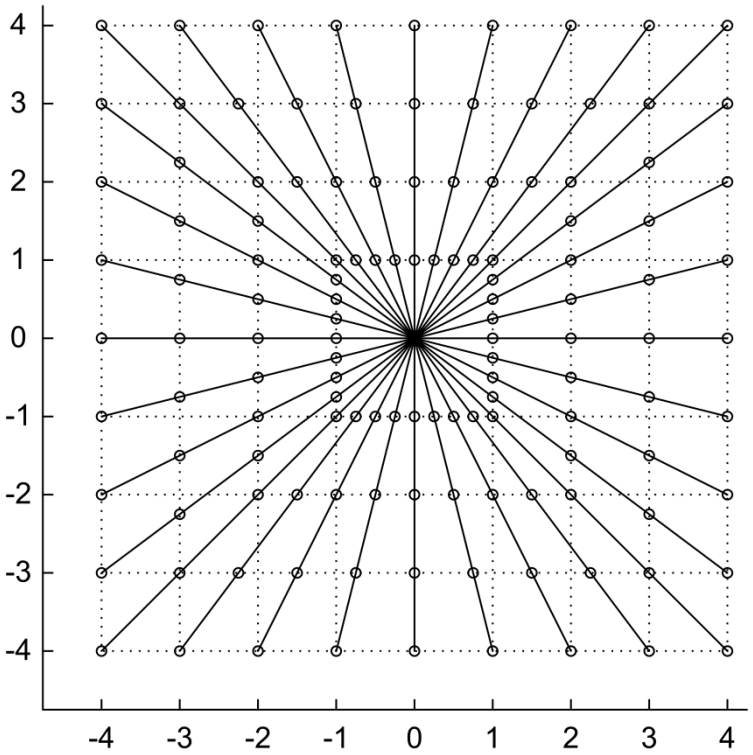

Figure 2.23 An illustration of the rectopolar grid in the frequency domain for an 8×8 image

separately. The M-band wavelet transform is used to decompose the signal into M×M channels that are also capable to zoom the noisy subimage coefficients. At the initial stage, the À trous algorithm is employed to decompose the data in different scales and obtain the low frequency part which has the same size as the original image.

2.8.2 NeighShrink thresholding

Various thresholding schemes are provided in the literature. The thresholding scheme provides the modified coefficients by comparing the transformed coefficients against a threshold to remove the noise from a signal while preserving the important information of the original signal. The subband containing high frequency coefficients is processed with the thresholding techniques such as soft and hard thresholding, but sometimes they carry the edges and features with large magnitude. The main task of thresholding approach is the proper selection of the threshold value (T). Now, thresholding is concentrated on the neighborhood thresholding, called as NeighShrink (NS) which has been improved further by Zhou et al. [289]. Several quantitative evaluations have been performed and shown that the NS approach performs better than the other existing methods. The performance of the M-band ridgelet filtering algorithm is evaluated by denoising the high frequency coefficients using soft and the NS thresholding algorithms. Soft thresholding is used to approximate the noisy M-band ridgelet coefficients $s_M^{Ridgelet}(x, y)$ of the signal [79]. The coefficients, whose absolute values are lower than the particular threshold (T), are first set to zero and then scaling the nonzero coefficients having values greater than the threshold (T).

To achieve the threshold coefficient, an improved NS algorithm based on the Stein's unbiased risk estimate (SURE) is presented. Therefore, for the noisy coefficient $s_M^{Ridgelet}(x,y)$ to be thresholded, consider a square window $w(x,y)$ centered at a noisy coefficient. Let $S^2(x,y) = \sum_{(k,l)\in w(x,y)}\left(s_M^{Ridgelet}(k,l)\right)^2$ and the thresholding expression is given by

$$\hat{s}_M^{Ridgelet}(x,y) = \left(1 - \frac{T^2}{S^2(x,y)}\right)_+ s_M^{Ridgelet}(x,y) \tag{2.67}$$

where $\hat{s}_M^{Ridgelet}(x,y)$ is the estimator of the unknown noiseless coefficient and thresholding factor.

$$\emptyset = (1 - T^2/S^2(x,y))_+ \tag{2.68}$$

Here, the '+' sign means to keep only the positive values while it is set to zero when it is negative and T is the threshold value. The optimal value of the threshold T and window size l is determined for every subband using SURE by minimizing the mean squared error or risk of the corresponding subband. Stein showed that for almost fixed estimator $\hat{s}_M^{Ridgelet} = \hat{s}_M^{Ridgelet}(x,y)$ based on the data $s_M^{Ridgelet} = s_M^{Ridgelet}(x,y)$, the risk $\mathrm{E}\left\{\left\|\hat{s}_M^{Ridgelet} - s_M^{Ridgelet}\right\|^2\right\}$ can be estimated.

$$E\left\{\left\|\hat{s}_M^{Ridgelet} - s_M^{Ridgelet}\right\|^2\right\} = E\{SURE(s_M^{Ridgelet}, T, l)\} \tag{2.69}$$

where $SURE(s_M^{Ridgelet}, T, l) = N + E\left\{\left\|G\left(s_M^{Ridgelet}\right)\right\|^2 + 2\nabla \cdot G\left(s_M^{Ridgelet}\right)\right\}$

and $G\left(s_M^{Ridgelet}\right) = \{G(i)\}_{i=1}^n = \hat{s}_M^{Ridgelet} - s_M^{Ridgelet}$, n is the number of the noisy coefficients in a subband, arranged in 1D vector. This is the expected risk estimated on a particular subband for a square neighboring window. The optimal threshold T and neighboring window size l for different subband minimize $SURE(s_M^{Ridgelet}, T, l)$. Accordingly,

$$(T,l) = argmin[SURE\left(s_M^{Ridgelet}, T, l\right)] \tag{2.70}$$

2.8.3 Implementation steps

For the noise reduction and implementing the above aspects, the proposed algorithms are formulated as follows:

Step 1: Start with the noisy image $s(x,y)$ and apply the À trous algorithm [284] with $k = 3$ scales. The decomposition of an image using À trous algorithm is considered as a superposition of the form.

$$s^{AT}(x,y) = s_{nr}(x,y) + \sum_{k=1}^{nr} d_k\,(x,y) \tag{2.71}$$

A summary of the À trous algorithm is as follows

1. Start with an image $s(x,y)$ and initialize k to 0.
2. Evaluate the coarser approximation $s_{k-1}(x,y)$ of the original image by computing a convolution of the data with the help of 2D low pass filter:

$$h = \frac{1}{256}\begin{pmatrix} 1 & 4 & 6 & 4 & 1 \\ 4 & 16 & 24 & 16 & 4 \\ 6 & 24 & 36 & 24 & 6 \\ 4 & 16 & 24 & 16 & 4 \\ 1 & 4 & 6 & 4 & 1 \end{pmatrix} \quad (2.72)$$

This filter leads to an iterative convolution with a template of 5×5.

3. Compute the difference between two consecutive approximations.

$$d_k(x,y) = s_{k-1}(x,y) - s_k(x,y) \quad (2.73)$$

4. Go to step 2, if $k < nr$, where nr is the number of resolutions for evaluating the approximations.

5. $d_k(x,y)$ includes the information of the two successive approximations.

$$d_k(x,y) = \{d_0(x,y), d_1(x,y), \dots, d_{nr}(x,y)\} \quad (2.74)$$

Step 2: Evaluate the radon transform on each detail subbands of k scale as mentioned above.

Step 3: Apply M-band wavelet transform on radon coefficients to compute the M-band ridgelet coefficients $s_M^{Ridgelet}(x,y)$. Here, 3-band wavelet transform is used to implement the above aspects.

Step 4: After getting the coefficients from step 3, calculate the optimal value of the threshold (T) corresponding to minimize the risk as per Eqns. (2.69) and (2.70).

Step 5: Apply the threshold on the M-band ridgelet coefficients $s_M^{Ridgelet}(x,y)$ obtained from the step 3, to compute the approximated or threshold coefficients $\hat{s}_M^{Ridgelet}(x,y)$ using Eqns. (2.67) and (2.68).

Step 6: Reconstruct the denoised image $\hat{s}(x,y)$ with the approximated coefficients, obtained from step 5.

2.8.4 Results and discussions

In order to investigate the results of the proposed M-band ridgelet using the NS thresholding approach, same test images such as kidney, fetus and phantom images and the US images such as prostate, splenic cyst and multiple liver masses US images are used to investigate the performance of the M-band ridgelet based denoising approach. For all three different noise levels, the denoised images produced by the proposed M-band ridgelet thresholding (MBRT) approach are illustrated in Figure 2.24, which shows the speckle reduction capability of the proposed MBRT approach. From the visual results of these images processed by the proposed MBRT approach, it is seen that this method is capable to produce good quality images by suppressing the speckle noise with more edge preservation. Among all three different images, this method seems to provide better speckle reduction performance in fetus images.

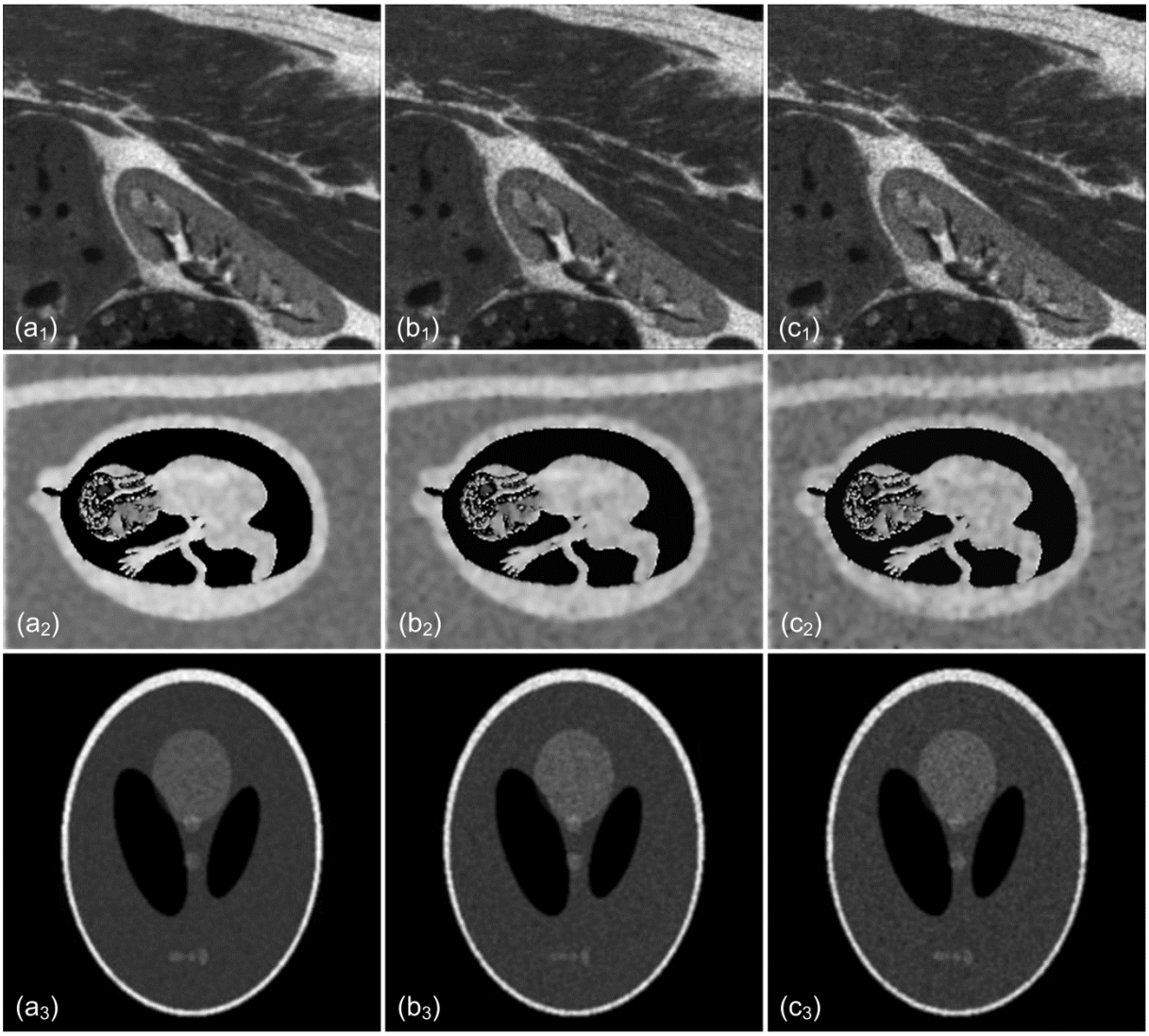

Figure 2.24 Visual results of denoised images obtained by the proposed MBRT approach. a, b and c represent the denoised images corresponding to σ = 0.1, 0.2 and 0.3, respectively. 1, 2 and 3 shows the kidney, fetus and phantom image, respectively

Table 2.9 Speckle reduction performance obtained by the proposed MBRT approach applied to kidney, fetus and phantom images illustrated in Figure 2.6

Images	Noise level	PSNR	SNR	SSIM	FOM	EKI
Kidney image	$\sigma = 0.1$	27.49	16.88	0.8184	0.7578	0.4601
	$\sigma = 0.2$	26.35	15.73	0.7714	0.7553	0.4417
	$\sigma = 0.3$	25.88	15.26	0.7696	0.7381	0.4319
Fetus image	$\sigma = 0.1$	19.68	14.69	0.6391	0.9199	0.5257
	$\sigma = 0.2$	18.73	13.73	0.5866	0.7872	0.5026
	$\sigma = 0.3$	18.01	13.02	0.5519	0.7163	0.4164
Phantom image	$\sigma = 0.1$	25.46	13.29	0.8227	0.8496	0.7766
	$\sigma = 0.2$	23.56	11.39	0.8052	0.8259	0.6862
	$\sigma = 0.3$	22.25	10.08	0.7803	0.7519	0.6346

Apart from the visual assessment, the performance has been extensively analyzed and evaluated using the different performance measures as mentioned in Table 2.9. The quantitative results are evaluated for all the images corrupted by multiplicative speckle noise of different variance 0.1, 0.2 and 0.3 as mentioned above. In these objective results, PSNR and SNR values show the speckle reduction capability of the proposed MBRT approach, while SSIM values present the structural similarity of the denoised and reference images with the noise suppression performance. The edge preservation capability is also described by the higher FOM and EKI values, i.e. closer to unity value. It is observed from the Table 2.9 that the SSIM and FOM achieve the value approx between 0.6-0.8 and 0.7-0.9, respectively, which indicates that the proposed MBRT approach is producing more detailed images in which most of the structural features are preserved. To investigate the superiority of the denoising methods two different experiments are performed as follows:

Experiment 1: *Comparative performance analysis of speckle reduction obtained by the proposed MBRT approach and others for simulated kidney, fetus and phantom images* - To compare the despeckling ability of the proposed MBRT approach, some other remarkable methods such as the ADF, SRAD, TVF, wavelet-NS and ridgelet-NS approaches are used, in which, wavelet and M-band ridgelet transform are integrated with the NS approach [289]. Table 2.10 shows the comparative evaluation of six different denoising methods based on the values of different objective indices. From Table 2.10, it is observed that the proposed method provides higher PSNR (27.49, 26.35 and 25.88) and SNR (16.88, 15.73 and 15.26) values for kidney images as compared to the others. Similarly, for fetus images, the proposed MBRT approach produces better noise suppression results by providing higher SNR and PSNR values. In case of the phantom images, the SNR and PSNR values obtained by the TVF approach as 25.86, 24.07, 23.20 and 13.69, 11.90, 11.03, respectively are higher than the proposed MBRT approach. Moreover, the proposed method gains the competitive values of the PSNR as 25.46, 23.56, 22.25 and SNR as 13.29, 11.38, 10.08 with higher SSIM, FOM and EKI values as compared to all the other denoising methods. From these results, it can be observed that the proposed approach is not only better in computational efficiency but also gives better performance of denoising reflected in all performance indices used here. There is a significant improvement in edge preservation performance in all the test images used for speckle reduction purpose. The TVF approach can also be utilized as another option for denoising in its similar or some modified form and integrating with an appropriate transform based approach.

Experiment 2: *Comparative analysis of real US images processed by the proposed MBRT and other approaches* - For such comparison, similar denoising methods are considered to compare the speckle reduction capability of the proposed MBRT approach applied to the real US images.

Table 2.10 Comparison between the quantitative results obtained by the proposed MBRT with other methods

Noise level	Methods	Kidney image					Fetus image					Phantom image				
		PSNR	SNR	SSIM	FOM	EKI	PSNR	SNR	SSIM	FOM	EKI	PSNR	SNR	SSIM	FOM	EKI
$\sigma = 0.1$	ADF [186]	21.74	11.11	0.7610	0.3831	0.3181	17.06	12.08	0.5925	0.6121	0.3572	21.98	9.81	0.7650	0.4311	0.7381
	SRAD [266]	25.86	15.24	0.7197	0.5124	0.4598	18.33	13.34	0.6286	0.6758	0.3828	22.74	10.57	0.8035	0.8202	0.5995
	TVF [47]	25.85	15.23	0.6747	0.4893	0.4149	17.84	12.85	0.5854	0.7819	0.3696	25.86	13.69	0.6883	0.8426	0.6452
	Wavelet-NS [289]	23.15	12.53	0.7305	0.4973	0.3962	18.38	13.39	0.6243	0.7627	0.4883	23.52	11.34	0.7734	0.4931	0.6825
	Ridgelet [101]	24.54	13.93	0.7375	0.5432	0.4136	18.71	13.69	0.6001	0.8269	0.5242	24.14	11.97	0.7894	0.4915	0.6834
	Proposed MBRT	27.49	16.88	0.8184	0.7578	0.4601	19.68	14.69	0.6391	0.9199	0.5257	25.46	13.29	0.8227	0.8496	0.7766
$\sigma = 0.2$	ADF [186]	20.79	10.17	0.7190	0.3776	0.3041	15.72	10.73	0.5375	0.5037	0.3246	21.12	8.95	0.7451	0.4601	0.5159
	SRAD [266]	25.04	14.42	0.6944	0.5087	0.3332	16.66	11.67	0.5512	0.6681	0.3866	22.31	10.14	0.7855	0.5337	0.5939
	TVF [47]	25.65	15.03	0.6527	0.4822	0.4036	17.01	12.02	0.5631	0.6876	0.3531	24.07	11.90	0.6944	0.6328	0.5878
	Wavelet-NS [289]	21.68	11.05	0.7293	0.5131	0.3493	16.54	11.55	0.5572	0.6010	0.3755	21.11	8.93	0.7597	0.3554	0.4641
	Ridgelet [101]	23.75	13.13	0.7325	0.5201	0.3782	16.71	11.72	0.5678	0.7586	0.4824	22.21	10.03	0.7548	0.3957	0.5239
	Proposed MBRT	26.35	15.73	0.7714	0.7553	0.4417	18.73	13.73	0.5866	0.7872	0.5026	23.56	11.38	0.8052	0.8259	0.6862
$\sigma = 0.3$	ADF [186]	20.46	9.84	0.6974	0.3851	0.3011	15.58	10.59	0.4978	0.4447	0.3092	19.98	7.81	0.7305	0.4267	0.3945
	SRAD [266]	24.69	14.07	0.6873	0.4972	0.3211	15.39	10.40	0.4445	0.6472	0.3625	22.10	9.92	0.7686	0.5291	0.5909
	TVF [47]	25.52	14.90	0.6331	0.4802	0.3931	16.13	11.14	0.5325	0.6210	0.3105	23.20	11.03	0.6986	0.6494	0.5354
	Wavelet-NS [289]	19.74	9.12	0.7148	0.5132	0.3323	15.53	10.55	0.5367	0.6458	0.3650	19.66	7.49	0.7389	0.2614	0.4386
	Ridgelet [101]	22.09	11.47	0.7146	0.5404	0.3672	16.21	11.22	0.5412	0.7097	0.3951	20.11	7.93	0.7347	0.3613	0.4585
	Proposed MBRT	25.88	15.26	0.7696	0.7381	0.4319	18.01	13.02	0.5519	0.7163	0.4164	22.25	10.08	0.7803	0.7519	0.6346

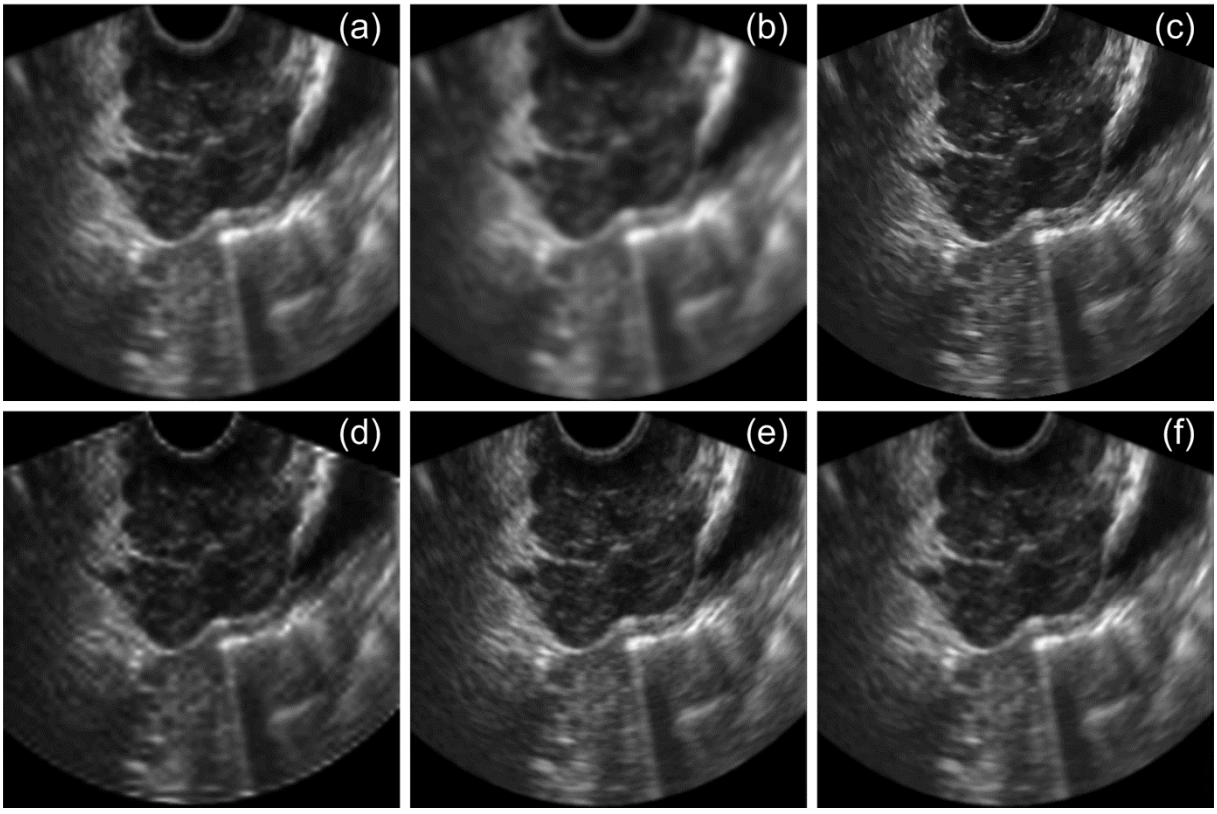

Figure 2.25 Comparative visual analysis of prostate ultrasound image, processed by (a) ADF (b) SRAD (c) TVF (d) Wavelet-NS (e) Ridgelet (f) Proposed MBRT approach

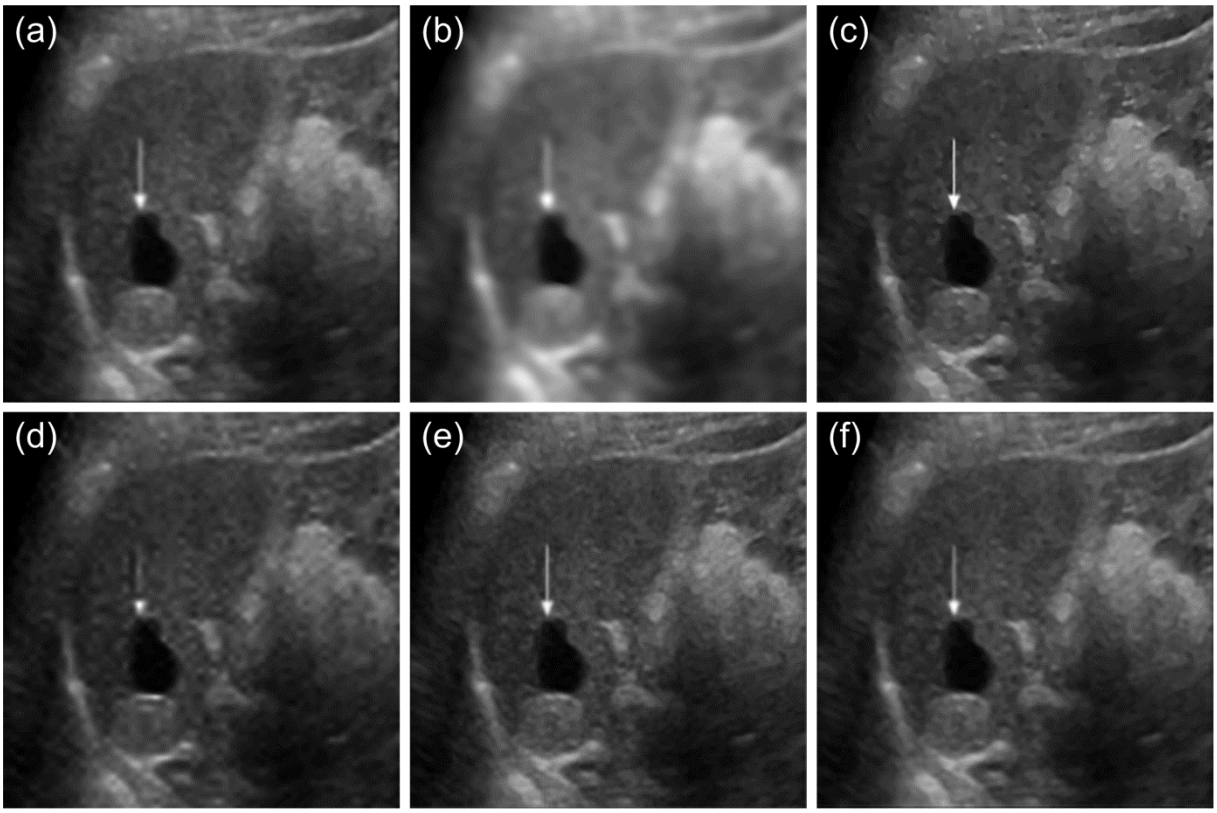

Figure 2.26 Comparative visual analysis of splenic cyst ultrasound image, processed by (a) ADF (b) SRAD (c) TVF (d) Wavelet-NS (e) Ridgelet (f) Proposed MBRT approach

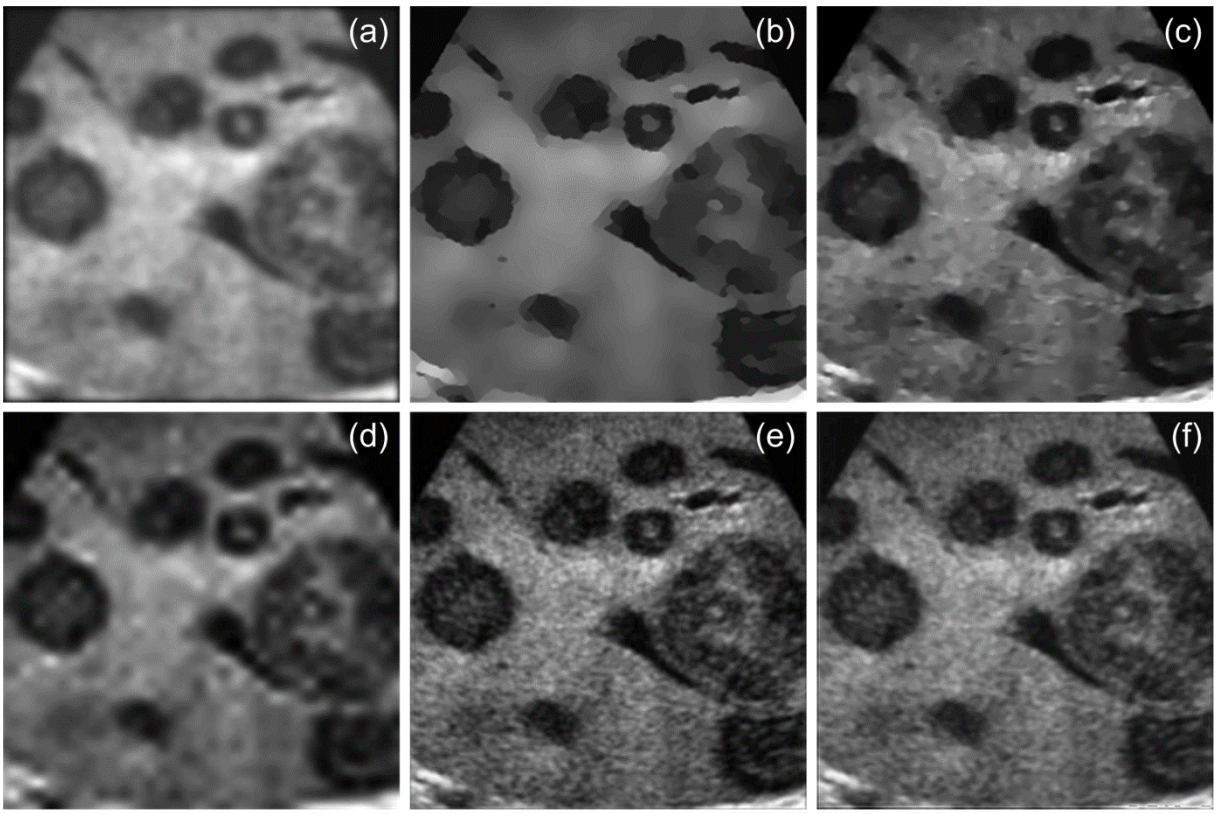

Figure 2.27 Comparative visual analysis of multiple liver masses ultrasound image, processed by (a) ADF (b) SRAD (c) TVF (d) Wavelet-NS (e) Ridgelet (f) Proposed MBRT approach

In this experiment, visual assessments are done with the processed prostate, splenic cyst and multiple liver masses US images. The denoised prostate US image produced by different methods is shown in Figure 2.25. From the results, it is observed that diffusion based approach produces a blurring effect in the images because of smoothing of the edges. Thus, the edge and other image information are lost during the smoothing process. On the other side, wavelet based approach does not produce a good denoised image. Moreover, in the processed prostate US images obtained by the wavelet method does not show its capability of capturing the edge information, but introduces some visual distortion in the resultant image. The proposed method and the TVF approach provide good quality of image that is also evident by presenting the processed splenic cyst US image in Figure 2.26. From the results presented in Figure 2.26, it is observed that the diffusion based ADF and SRAD approaches are able to suppress the noise, but at the cost of losing the edge information. Similarly, another US image processed by the proposed and other methods are shown in Figure 2.27 and approximately similar results are found with respect to speckle reduction in US images, except one change that the SRAD method provides better noise reduction performance. However, all the edges information, which are clinically relevant, are lost during speckle reduction process, but for further analysis using image processing techniques, it may be useful.

For performing another comparative analysis, a liver cyst US image acquired from the

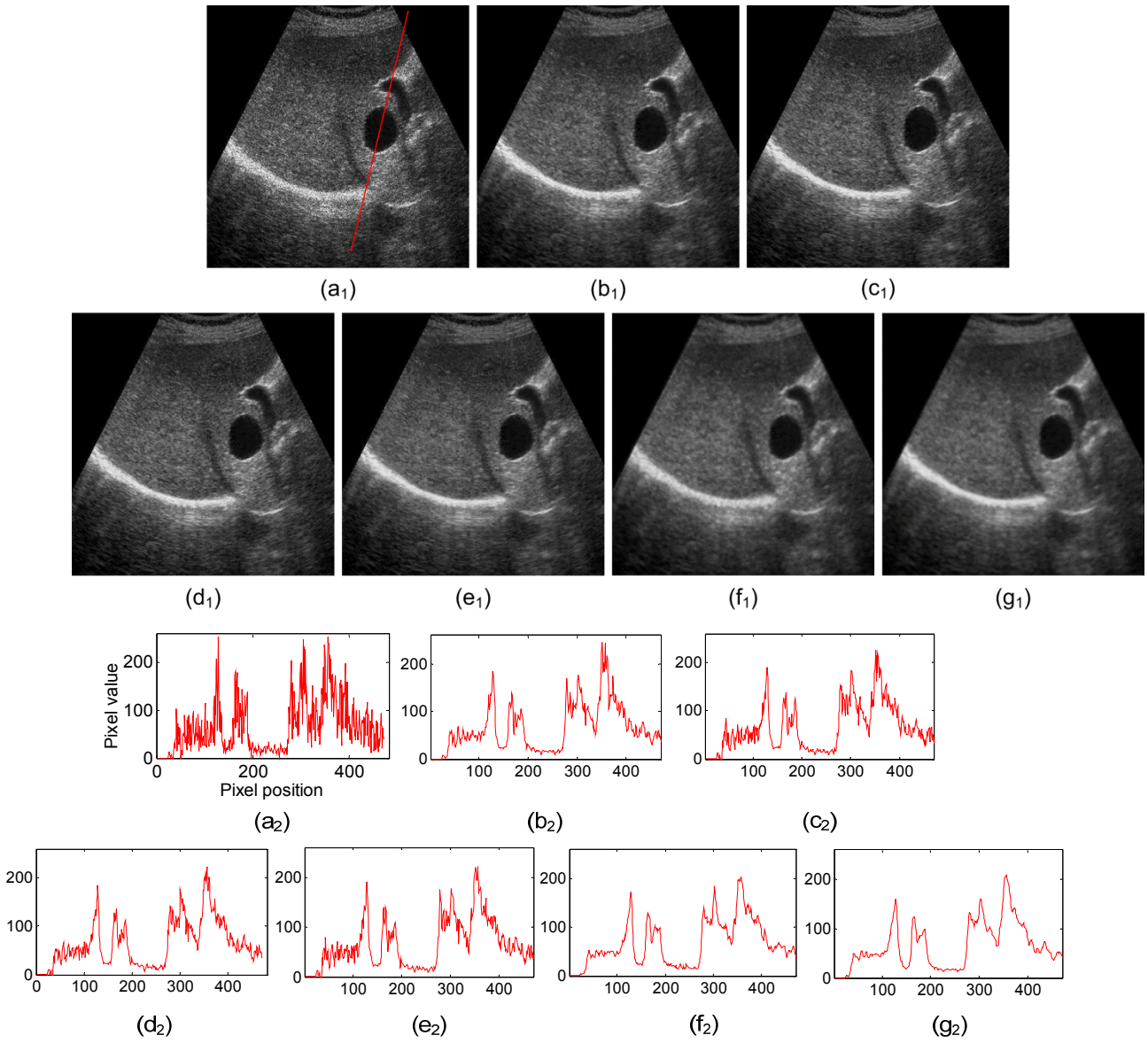

Figure 2.28 Despeckling results of considered (a) Ultrasound image with marked red line. Results processed by (b) Wavelet-WF (c) Wavelet-NS (d) Wavelet-BF-NS (e) Wavelet-TVF (f) Ridgelet (g) Proposed MBRT approach. Here, 1 indicates the image results after processed by these mentioned methods and 2 refers to the line profile corresponding to the results obtained from (a)-(g)

samsung medison website (www.medison.ru/uzi/eho156.htm) and shown in Figure 2.28 (a), is considered which is processed by other integrated denoising methods different from previous mentioned methods. The despeckled images obtained by the different denoising methods such as wavelet-WF, wavelet-NS [289], wavelet transform with the NS and bilateral filter (wavelet-BF-NS) [14], the TVF with wavelet transform (wavelet-TVF) [3], ridgelet based method (similar as mentioned above), are shown in Figure 2.28 (a_1)-(g_1), respectively. Another analysis is also done based on the line profile that indicates the gray level intensities across a predefined line marked by red on the US image. It is also observed from the line profile analysis as shown in Figure 2.28 (a_2)-(g_2) that the content of the image are well preserved and the transitions of the despeckled US images are smoother than noisy image.

Table 2.11 Averaged PSNR, SNR, SSIM and EKI measured by various approaches for the test images degraded by speckle noise

Noise level	Denoising methods	PSNR	SNR	SSIM	EKI
σ = 0.1	AWMF	19.99 ± 2.69	10.74 ± 1.18	0.6783 ± 0.1218	0.5041 ± 0.0567
	WF	19.74 ± 2.66	10.48 ± 1.29	0.7124 ± 0.0436	0.4589 ± 0.0487
	MHOPNF	19.63 ± 3.55	10.37 ± 0.45	0.6812 ± 0.1020	0.4595 ± 0.2113
	ADF	20.26 ± 2.77	11.01 ± 1.14	0.7062 ± 0.0985	0.4711 ± 0.2320
	SRAD	22.31 ± 3.78	13.05 ± 2.35	0.7173 ± 0.0875	0.4807 ± 0.1099
	NCDF	22.03 ± 3.94	12.77 ± 1.78	0.6759 ± 0.1026	0.4871 ± 0.1901
	TVF	23.18 ± 4.63	13.92 ± 1.21	0.6495 ± 0.0559	0.4765 ± 0.1477
	NLMF	25.08 ± 4.81	15.82 ± 1.69	0.7707 ± 0.0853	0.6365 ± 0.1553
	TI-WT	23.50 ± 4.70	14.24 ± 2.30	0.7136 ± 0.0952	0.4678 ± 0.1117
	Ridgelet	22.46 ± 3.26	13.19 ± 1.07	0.7090 ± 0.0978	0.5404 ± 0.1356
	Curvelet	23.27 ± 4.62	14.01 ± 1.86	0.7339 ± 0.0843	0.4913 ± 0.1047
	Shearlet	23.96 ± 4.58	14.71 ± 1.93	0.7486 ± 0.0943	0.5268 ± 0.1373
	Proposed MBRT	24.21* ± 4.05	14.95* ± 1.81	0.7601* ± 0.1048	0.5875* ± 0.1669
σ = 0.2	AWMF	18.62 ± 3.64	9.36 ± 0.75	0.6272 ± 0.1551	0.4423 ± 0.0279
	WF	18.31 ± 3.81	9.05 ± 0.08	0.6472 ± 0.0625	0.4548 ± 0.0871
	MHOPNF	17.98 ± 4.07	8.72 ± 0.66	0.6512 ± 0.1216	0.3857 ± 0.1309
	ADF	19.21 ± 3.03	9.95 ± 0.91	0.6672 ± 0.1131	0.3815 ± 0.1168
	SRAD	21.34 ± 4.27	12.08 ± 2.17	0.6769 ± 0.1181	0.4379 ± 0.1377
	NCDF	21.04 ± 4.34	11.78 ± 1.64	0.6079 ± 0.1172	0.4241 ± 0.1608
	TVF	22.24 ± 4.60	12.98 ± 1.77	0.6367 ± 0.0670	0.4481 ± 0.1235
	NLMF	23.39 ± 4.75	14.14 ± 2.28	0.7434 ± 0.0937	0.5433* ± 0.0904
	TI-WT	22.78 ± 5.01	13.52 ± 2.78	0.6943 ± 0.1036	0.4495 ± 0.1024
	Ridgelet	20.89 ± 3.70	11.63 ± 1.55	0.6850 ± 0.1021	0.4615 ± 0.0751
	Curvelet	22.61 ± 4.89	13.35 ± 2.25	0.7240* ± 0.0943	0.4735 ± 0.0928
	Shearlet	23.16* ± 4.88	13.89* ± 2.41	0.7095 ± 0.1172	0.4936 ± 0.1155
	Proposed MBRT	22.88 ± 3.86	13.62 ± 2.17	0.7211 ± 0.1177	0.5435 ± 0.1273
σ = 0.3	AWMF	18.49 ± 3.48	9.24 ± 1.26	0.5708 ± 0.1513	0.2987 ± 0.0497
	WF	16.88 ± 5.02	7.63 ± 1.35	0.6252 ± 0.1079	0.3441 ± 0.0302
	MHOPNF	16.38 ± 4.82	7.12 ± 1.38	0.6241 ± 0.1315	0.3447 ± 0.0807
	ADF	18.67 ± 2.69	9.41 ± 1.44	0.6419 ± 0.1259	0.3349 ± 0.0517
	SRAD	20.73 ± 4.79	11.46 ± 2.27	0.6335 ± 0.1686	0.4248 ± 0.1453
	NCDF	20.45 ± 4.28	11.19 ± 1.52	0.5742 ± 0.1234	0.3844 ± 0.1328
	TVF	21.62 ± 4.89	12.36 ± 2.21	0.6214 ± 0.0837	0.4130 ± 0.1138
	NLMF	22.42* ± 4.19	13.16* ± 2.31	0.7064 ± 0.1142	0.4986 ± 0.1046
	TI-WT	22.18 ± 5.27	12.92 ± 2.93	0.6776 ± 0.1156	0.4232 ± 0.1073
	Ridgelet	19.47 ± 2.99	10.21 ± 1.98	0.6635 ± 0.1064	0.4069 ± 0.0468
	Curvelet	22.01 ± 5.09	12.75 ± 2.51	0.7012* ± 0.1055	0.4481 ± 0.0929
	Shearlet	22.45 ± 5.19	13.19 ± 2.82	0.6826 ± 0.1505	0.4502 ± 0.0795
	Proposed MBRT	22.05 ± 3.94	12.79 ± 2.59	0.7006 ± 0.1289	0.4943* ± 0.1218

* means the second highest value of the each performance measure in the table.

Besides all the performance analysis of various denoising methods with one proposed MBRT approach, a new comparative analysis is also done by evaluating all the performance measures such as PSNR, SNR, SSIM and EKI (mean ± standard deviation) obtained by all the denoising methods applied to all test images. The averaged performance of the PSNR, SNR, SSIM and EKI are presented in Table 2.11. From the results mentioned in Table 2.11, it is observed that the averaged values of all the performance measure obtained by the NLMF, shearlet and proposed MBRT approaches produce higher values than the others. For low level noise variance $\sigma = 0.1$, the proposed MBRT approach provides better results by providing higher averaged SNR, PSNR, SSIM and EKI values such as 14.95, 24.21, 0.7601 and 0.5875, respectively, than the other methods except the NLMF method. For noise variance $\sigma = 0.2$ and 0.3, the NLMF is still able to produce higher values of performance measures than the shearlet and the proposed MBRT methods, but the EKI values obtained using the proposed MBRT approach are still higher than the NLMF and shearlet for noise level $\sigma = 0.2$. It also provides the competitive values of other performance measures to the NLMF, TVF and shearlet based methods for $\sigma = 0.3$. From the analysis of all these performance indices, it can be summarized that the MBRT approach obviously outperforms the other methods. In addition, proposed method gains approx 19.25-21.11%, 22.64-30.63%, 23.33-34.62%, 18.1-19.5%, 6.37-8.52%, 7.82-9.9%, 1.99-4.44%, 0.44-3.02%, 7.79-13.25% and 0.18-4.04% higher PSNR values (in dB) than the AWMF, WF, MHOPNF, ADF, SRAD, NCDF, TVF, TI-WT, ridgelet and curvelet methods, respectively. Only the NLMF method outperforms in terms of PSNR by 1.68-3.59%. The proposed method also provides the stable SNR value with approx 38.42-45.51%, 42.65-67.63%, 11.61-36.88%, 3.48-7.4% higher than the AWMF, WF, diffusion based approaches and the TVF method. The proposed MBRT approach outperforms the ridgelet based approach by obtaining approx 13.34-25.27%, 5.27-7.21% and 8.72-21.48% higher SNR, SSIM and EKI values. Besides this, the NLMF method shows better noise suppression performance by achieving higher SNR (2.89-5.82%) and SSIM values (0.83-3.09%) than the proposed approach. Sometimes; it leads to loss of edge information reflected in the EKI values. For noise variance $\sigma = 0.2$ and 0.3, the shearlet also produces the competitive values of the PSNR, SNR, SSIM and EKI to the NLMF and the proposed method. By analyzing the results mentioned in Table 2.11, it is observed that the NLMF, TVF and diffusion based approach along with the transform based methods such as shearlet, proposed MBRT can be available as the better option for suppressing the speckle as much as possible depending upon the applications.

2.9 Summary

The denoising is a most important step in the image processing applications and especially in case of the US images having speckles as it is difficult to extract the relevant clinical information from the US images in the presence of speckle. Firstly, a comparative

analysis is performed to investigate the noise suppression (speckle as well as Gaussian) performance of the twelve denoising methods on both the test images and real US images. Based on the results obtained from this comparative analysis, one method is also proposed using M-band ridgelet transform as described in the last part of this chapter. This method also exploits the features of the M-band WT in place of 2-band WT. The proposed approach utilizes the variation of the frequency resolution feature of the À trous algorithm by which a noisy speckled image has been decomposed into different scales. Thresholding provides the approximated modified image coefficients that also improve the despeckling efficiency. The proposed method is also able to produce better results by suppressing sufficient amount of the speckle noise with more edge preservation. Few methods such as the TVF, NLMF, curvelet and shearlet based approach exhibit better speckle reduction performance than others. However, it leads to some limitations also such as the TVF and NLMF suffer from losing the edges in case of higher noise level, The TVF method also produces some blocking effects in the denoised images. Anisotropic diffusion is also able to smooth the US images, but at the cost of blurring the edges. The curvelet based method has some visual distortion in the denoised images rather than providing good quality images. Shearlet method has less distortion than the curvelet based method. The NS thresholding used with the proposed M-band ridgelet transform also provides better noise reduction results with good edge preservation. One important point can be observed in the comparative PSNR analysis of the Lena image that the transform based method with spatial domain processing achieves better noise suppression performance. Based on all the analysis, it is concluded that transform based methods outperform others by preserving more edges with the sufficient amount of noise suppression and the diffusion and TVF approaches provide a considerable amount of noise suppression at the cost of losing the edges, which must be preserved in the denoised images as much as possible.

CHAPTER 3: RIPPLET DOMAIN NONLINEAR FILTERING APPROACH

This chapter presents two different approaches for reducing the speckle in ultrasound medical images. For such purpose, two nonlinear filtering approaches have been used in the ripplet domain that is employed to provide an effective representation of the noisy image coefficients. In this chapter, the methodologies used to present the proposed methods are explained in detail and based on this; the design steps of ripplet domain nonlinear filtering approaches are discussed. The performance of these speckle reduction algorithms are discussed in both the subjective and objective manner and a detailed comparative analysis has also been presented in the last section of this chapter for assessing the performance of speckle reduction obtained by the proposed methods.

3.1 Introduction

It has been analyzed and emphasized in the previous chapter that the noise reduction along with the preservation of more edge information available in the source images is able to improve the visual assessment of the US images. Currently, lots of research work on image denoising methods is concentrated in the transform domain, which is already observed in previous chapter 2, where ridgelet, curvelet and shearlet transform have been used for speckle reduction. The performance of ridgelet transform has also been improved using the M-band ridgelet transform. Each transform has its own advantages and limitations that are also discussed in chapter 2, where a detailed comparative analysis of several existing denoising methods was carried out on the US images. Based on the subjective and objective outcomes of that comparative analysis, it was observed that the curvelet and shearlet based methods produce better denoising results. Along with these observations, one more comparative analysis has been performed in which the WT thresholding method improved its performance by incorporating some spatial domain techniques [272]. These outcomes have motivated to address and utilize the transformation technique with some spatial domain approaches.

Recently, many researchers tried to explore the applications of the ridgelet and CVT for image denoising because of their anisotropic property. The WT is less efficient in representing the sharp transition like line and curve singularities due to its limitation of direction. The ridgelet transform is able to perfectly capture the line singularities of the images, but it is not able to efficiently represent the curve singularities. Further, the CVT has been introduced by Starck et al. [225] to represent two dimensional singularities with arbitrary shaped curve because most of the images inherently have gray level transitions or discontinuities along the curve. The main idea of the curvelets is to represent a curve as a superposition of the functions of various lengths and widths obeying the scaling law. To represent the edges more efficiently in images, Jun et al. [256] introduced a new multiscale geometric analysis tool called ripplet transform (RT) type I that presents a generalized version of the CVT with two new additional parameters for providing the anisotropy

capability. This guarantees to effectively represent the singularities along the arbitrary shaped curves. The RT with their different features such as anisotropy, localization, directionality, multiscale and multiresolution is employed to provide effective representation of the image coefficients. The RT also overcomes the limitations of other transforms and provides the sparse representation for the objects [256]. With the RT, a nonlinear bilateral filter (NLBF) approach is used to propose two denoising approaches using the NeighShrink (NS) and BlockShrink (BS) thresholding after decomposing an image into different subbands.

In the following sections of this chapter, after introducing the overview of the RT and its decomposition structure, some efforts have been made to explain an idea of the NLBF and thresholding approaches used in the proposed methods. Next section illustrates the proposed method. Many efforts have been made to evaluate and compare their denoising performance with others in terms of speckle reduction with retention of more edges.

3.2 Ripplet Transform

The RT is a higher dimensional generalization of the CVT and is capable to represent the two dimensional signals at the different scales and different directions. To realize anisotropic directionality, the CVT uses a parabolic scaling law as mentioned in the previous chapter. From this perspective, the anisotropic properties of the CVT guarantees to resolve the two dimensional singularities along C^2 curves [225]. On the other side, the RT also provides a new tight frame with sparse representation for the source images with discontinuities along C^d curves [256]. If $d = 1$, then ripplet does not show the anisotropy behavior. For $d = 2$, it has parabolic scaling same as the curvelets and for $d = 3$, ripplet has the cubic scaling and so forth. The anisotropic capabilities of RT type-1 are capable to efficiently represent the singularities along the arbitrary shaped curves because of these added new parameters support c and degree d. The RT is a generalized version of the CVT with the parameters $c = 1$ and $d = 2$. Thus, the CVT is just a special case of ripplet.

3.2.1 Continuous ripplet transform

The continuous RT is defined as inner product of two dimensional integrable function $s(\vec{x})$ and ripplets $p_{a,\vec{b},\theta}(\vec{x})$ as follows [256]:

$$R(a,\vec{b},\theta) = \langle s, p_{a,\vec{b},\theta} \rangle = \int s(\vec{x})\, \overline{p_{a,\vec{b},\theta}(\vec{x})} d\vec{x} \tag{3.1}$$

where $R(a,\vec{b},\theta)$ is the ripplet coefficients and $\overline{(\cdot)}$ shows the conjugate operation. The ripplet function is defined as

$$p_{a,\vec{b},\theta}(\vec{x}) = p_{a,\vec{0},0}\left(R_\theta(\vec{x} - \vec{b})\right) \tag{3.2}$$

where $p_{a,\vec{0},0}(\vec{x})$ is a ripplet element function, $R_\theta = \begin{bmatrix} cos\theta & sin\theta \\ -sin\theta & cos\theta \end{bmatrix}$ is a rotation matrix, which rotates θ radians. $\vec{x}$ and $\vec{b}$ are two dimensional vectors.

The $p_{a,\vec{0},0}(\vec{x})$ can also be represented in the frequency domain as follows:

$$\hat{p}_a(r,\omega) = \frac{1}{\sqrt{c}} a^{\frac{1+d}{2d}} W(a \cdot r) V\left(\frac{a^{1/d}}{c \cdot a} \cdot \omega\right) \quad (3.3)$$

where $\hat{p}_a(r,\omega)$ is the Fourier transform of the ripplet element function $p_{a,\vec{0},0}(\vec{x})$ in polar co-ordinate. a, $\vec{b}$ and θ are the scale, position and rotation parameter, respectively. $W(r)$ and $V(\omega)$ represent the radial window and angular window having compact supports on [1/2, 2] and [-1, 1], respectively, that satisfy the two admissibility conditions as follows:

$$\int_{1/2}^{2} W^2(r) \frac{dr}{r} = 1 \text{ and } \int_{-1}^{1} V^2(t)\, dt = 1 \quad (3.4)$$

These two windows divide the polar frequency domain into wedges shown in Figure 3.1 (a). The main issue with the continuous ripplet transform is that it can only capture the behavior of the high frequency components of the original signal. So the full continuous ripplet transform is established by the combination of finer scale RT and coarse scale isotropic WT which represent the characteristic of the high and low frequency components, respectively. The approximated image can be reproduced by the inverse of the ripplet transform and it is expressed as given below [256]:

$$s(\vec{x}) = \int R\left(a, \vec{b}, \theta\right) p_{a,\vec{b},\theta}(\vec{x}) da d\vec{b} d\theta / a^3 \quad (3.5)$$

where R is a ripplet coefficient of the input signal, a is the scale parameter, $\vec{b}$ is a positional parameter and θ is a rotation parameter.

3.2.2 Discrete ripplet transform

In the field of digital image processing, discrete transforms are needed for their computerized algorithm implementation. So, discrete RT is evaluated by discretizing the parameters of ripplets. The parameter a is sampled at dyadic intervals whereas $\vec{b}$ and θ are sampled at equally spaced intervals. The scale parameter (a), the position parameter (b) and rotation parameter (θ) are substituted with a_j, $\vec{b}_k$ and θ_l, respectively, that satisfy $a_j = 2^{-j}$, $\vec{b}_k = [c \cdot 2^{-j} \cdot k_1, 2^{-j/d} \cdot k_2,]^T$ and $\theta_l = (2\pi/c) \cdot (2^{-[j(1-1/d)]}) \cdot l$, where $\vec{k} = [k_1\, k_2\,]^T$, $(\cdot)^T$ denotes the transpose of a vector and $j, k_1, k_2, l \in \mathbb{Z}$. The frequency response of ripplet function is given as

$$\hat{p}_j(r,\omega) = \frac{1}{\sqrt{c}} a^{\frac{1+d}{2d}} W(2^{-j} \cdot r) V\left(\frac{2^{-j(1/d-1)}}{c} \cdot \omega - l\right) \quad (3.6)$$

where W and V satisfy the following conditions.

$$\sum_{j=0}^{\infty} \left|W(2^{-j} \cdot r)\right|^2 = 1 \text{ and } \sum_{l=-\infty}^{\infty} \left|V\left(\frac{2^{-j(1/d-1)}}{c} \cdot \omega - l\right)\right|^2 = 1 \quad (3.7)$$

For a fixed value of c, degree d is used to control the resolution in the directions at each high pass band. For given a fixed value of d, parameter c controls the number of directions at all high pass bands. The c and d in combination are used to determine the final number of

directions at each band together. The discrete ripplet transform of the two dimensional signal $s(x,y)$ with size $M \times N$ is given by ripplet coefficients $R_{j,\vec{k},l}$.

$$R_{j,\vec{k},l} = \sum_{x=0}^{M-1} \sum_{y=0}^{N-1} s(x,y)\overline{p_{j,\vec{k},l}(x,y)} \tag{3.8}$$

An approximated image $\hat{s}(x,y)$ can be reconstructed through inverse discrete RT as given below:

$$\hat{s}(x,y) = \sum_j \sum_{\vec{k}} \sum_l R_{j,\vec{k},l} p_{j,\vec{k},l}(x,y) \tag{3.9}$$

Figure 3.1 (b) shows a real ultrasound image and decomposition of the image processed using the RT is illustrated in Figure 3.1 (c).

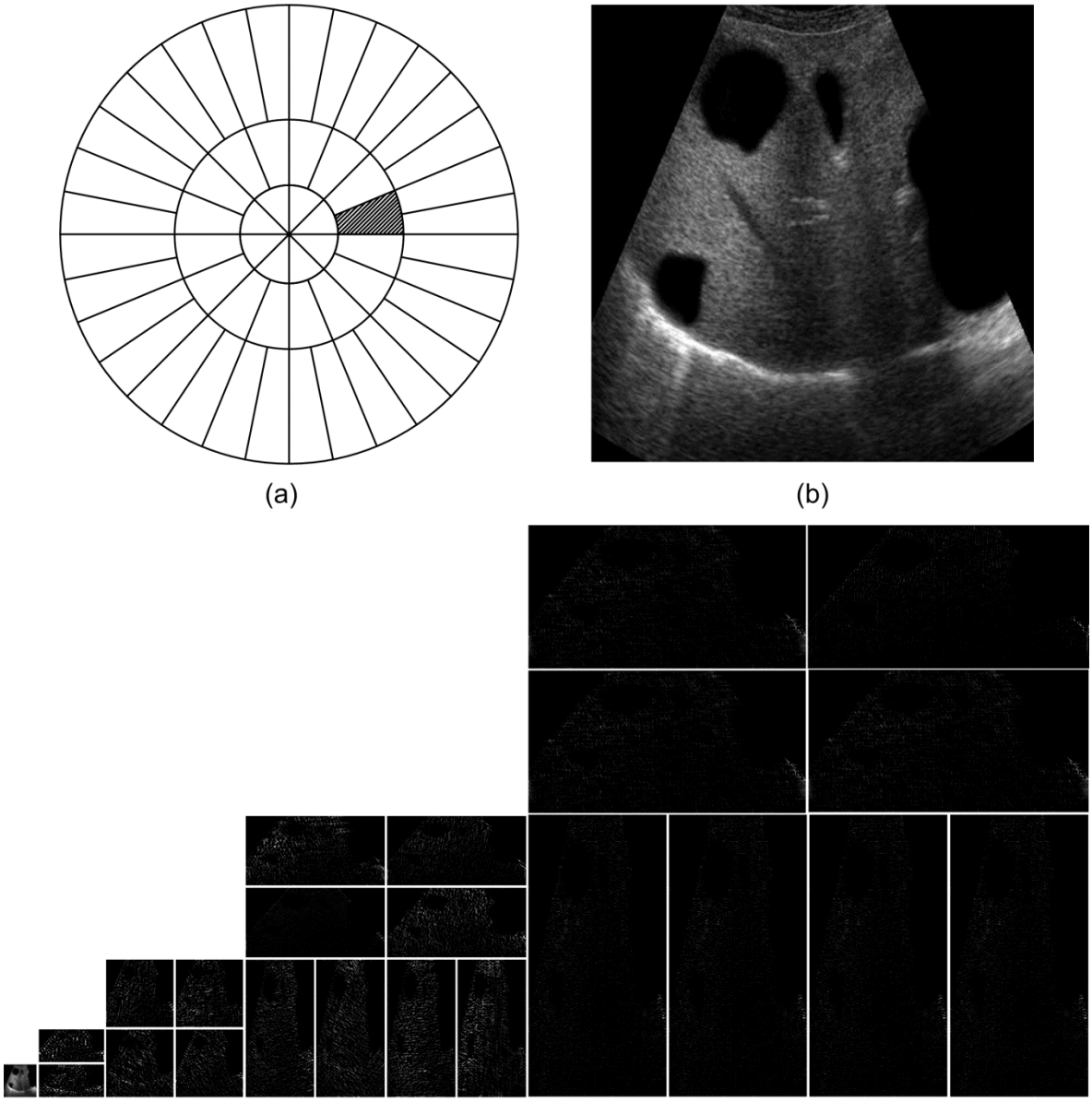

(a) (b)

(c)

Figure 3.1 (a) The tiling of the polar frequency domain. The dashed wedge corresponds to the frequency transform of the element function. (b) Original ultrasound image (c) Different subbands after decomposition using ripplet transform with support (c=1) and degree (d=4).

3.3 Nonlinear Bilateral Filter

Bilateral filter is a nonlinear filtering approach to perform the edge preserved denoising within the spatial domain [14, 237, 239, 280]. Bilateral filter replaces the pixel values by a weighted sum of the pixels in a local neighborhood. It is achieved by the combination of two Gaussian filters, spatial (domain) and intensity (range) filter. The range filter coefficients are proportional to the intensity distance $\big(s(y) - s(x)\big)$ around the local neighborhood of a pixel. The domain filter coefficients are proportional to the spatial distance $(y - x)$ of the pixel in approximation subband coefficients around its neighborhood. Thus, at a pixel location x, the response of the NLBF can be computed as [281]

$$\hat{s}(x) = \frac{1}{h}\sum_{y\in N_s(x)} D_f(x,y)\, R_f(x,y) s(y) \tag{3.10}$$

where x and y are the coordinate vectors, $D_f(x,y)$ and $R_f(x,y)$ are spatial and intensity filter components of the bilateral filter, respectively. They are defined as

$$\left.\begin{aligned} D_f(x,y) &= exp\left[\frac{-\|y-x\|^2}{2\sigma_d^2}\right] \\ R_f(x,y) &= exp\left[\frac{-\|s(y)-s(x)\|^2}{2\sigma_r^2}\right] \end{aligned}\right\} \tag{3.11}$$

$N_s(x)$ is the spatial neighborhood and h is the normalization constant defined as

$$h = \sum_{y\in N_s(x)} D_f(x,y)\, R_f(x,y) \tag{3.12}$$

where both the spatial and intensity domain behaviors are characterized by the σ_d and σ_r, respectively.

In bilateral filter, the choice of the parameters σ_d and σ_r is very important. These parameters have been analyzed as a function of noise variance, but the optimal value of σ_d is relatively insensitive to noise variance while σ_r value changes, significantly by changing the noise variance [229, 281]. Therefore, the optimal values of the NLBF parameters are selected by repeating the experiments for different combinations of the σ_d and σ_r for a constant noise variance. In the case of additive model, it works as a good filter, but in the presence of the speckle noise, the relationship between σ_r and noise variance (σ) is not established because of the multiplicative nature. This problem can be solved by the modified range filter which is given below:

$$R_f(x,y) = exp\left[\frac{-\|s(y)-s(x)\|^2}{2\|s(x)\|^2\sigma_r^2}\right] \tag{3.13}$$

More noise components are suppressed with a larger value of σ_r. However, some artifacts may also be introduced with the increasing value of σ_r.

3.4 Thresholding Approaches

In recent years, the thresholding schemes are considered in many studies for image denoising purpose. The most important task is to select a proper threshold value by which the decomposed image coefficients are compared and result in the modified thresholded

coefficients. For such purposes, soft and hard thresholding is generally used for evaluating the threshold value using the universal threshold as mentioned in chapter 2. However, they also carry the edges and features with large magnitude. The two other important thresholding methods such as the NeighShrink (NS) and BlockShrink (BS) have been introduced and further improved by Dengwen et al [289, 290] and Cai et al. [39]. They have reported better denoising results than the other existing methods using WT. The performance of the proposed methods mentioned in this chapter is evaluated by suppressing the speckle noise of high frequency coefficients using soft with NeighShrink (in scheme-1) and BlockShrink (in scheme-2) thresholding algorithms.

3.4.1 NeighShrink thresholding

The NS thresholding approach based on Stein's unbiased risk estimate (SURE) is discussed in chapter 2. After estimating the noisy ripplet coefficients, a threshold value (T) is required. The thresholding function is given as

$$\hat{s}^{RT}(x,y) = \left(1 - \frac{T^2}{\sum_{(k,l)\in w(x,y)}(s^{RT}(k,l))^2}\right)_+ s^{RT}(x,y) \tag{3.14}$$

where $s^{RT}(x,y) = s^{RT}$ is the noisy ripplet coefficients and $\hat{s}^{RT}(x,y) = \hat{s}^{RT}$ refers to approximated ripplet coefficients after thresholding process; $w(x,y)$ is a squared template that is centered at noisy coefficients. Here '+' sign means to keep only the positive values and put zero in case of negative values. The optimal value of the threshold is estimated by minimizing the SURE risk of the corresponding subimage coefficients obtained after decomposing the image using the RT as mentioned in Eqns. (2.69) and (2.70) (in subsection 2.8.2). In this mathematical expressions, $s_M^{Ridgelet}$ and $\hat{s}_M^{Ridgelet}$ are replaced by the s^{RT} and $\hat{s}^{RT}$, respectively.

3.4.2 BlockShrink thresholding

To evaluate the noise free ripplet coefficients, an improved data driven BS thresholding approach is introduced that is based on the SURE [39, 290]. For the noisy ripplet coefficients $s^{RT}(x,y)$ to be threshold, Let $S^2_{w_1,w_2}(x,y) = \sum_{x\in xw_1, y\in yw_2}(s^{RT}(x,y))^2$ and the thresholding expression now on $w_1 \times w_2$th block is given as below:

$$\hat{s}^{RT}(x,y) = s^{RT}(x,y)\left(1 - \frac{T}{S^2(x,y)}\right)_+ \quad \text{for } x \in xw_1 \text{ and } y \in yw_2 \tag{3.15}$$

where $xw_1 = \{x: (w_1-1)l_b + 1 \le x \le w_1 l_b\}$ and $yw_2 = \{y: (w_2-1)l_b + 1 \le y \le w_2 l_b\}$. $\hat{s}^{RT}(x,y)$ is the estimator of the unknown noiseless ripplet coefficients, w_1 and w_2 are the number of blocks in x and y direction, respectively, and the thresholding factor $\phi = \left(1 - \frac{T}{S^2(x,y)}\right)_+$. The optimal values of threshold (T) and block size are determined for every subband by minimizing the SURE risk of the corresponding subband. Stein showed that for

almost any estimator $\hat{s}^{RT} = \hat{s}^{RT}(x, y)$ based on data $s^{RT} = s^{RT}(x, y)$, the SURE risk can be estimated as

$$SURE\left(s^{RT}, T, {l_b}^2\right) = \sum_{w_1, w_2=1}^{N/l_b} SURE\left(s^{RT}(w_1, w_2), T, l_b^2\right) \quad (3.16)$$

where

$$SURE\left(s^{RT}(w_1, w_2), T, l_b^2\right) = l_b^2 + \left(\frac{T^2 - 2T(l_b^2 - 2)}{S_{w_1, w_2}^2}\right)\Big|_{S_{w_1, w_2}^2 > T} + \left(S_{w_1, w_2}^2 - 2 \times l_b^2\right)\Big|_{S_{w_1, w_2}^2 \leq T} \quad (3.17)$$

The value of optimal threshold T and block size l_b is obtained by minimizing $SURE\left(s^{RT}, T, l_b^2\right)$. Accordingly,

$$(T, l_b) = argmin SURE\left(s^{RT}, T, l_b^2\right) \quad (3.18)$$

3.5 Proposed Ripplet Domain Nonlinear Filtering Approach

For reducing speckle in the US medical images and implementing the above aspects, the proposed filtering approaches using two different thresholding schemes are formulated in three following steps.

1. Choose the optimal values of the ripplet parameters c and d and compute the ripplet coefficients from the speckled images.
2. Select and perform the appropriate filtering method on these ripplet speckled coefficients to get the modified ripplet coefficients.
3. Finally, estimate the reconstructed signal by taking the inverse RT of these modified ripplet coefficients.

The process flow of the proposed filtering approach is given in Figure 3.2. In this figure, two different filtering approaches are proposed in which the NS thresholding algorithm is used in the first approach named as the RTNLF-1 (approach-1) and the BS thresholding is utilized in the RTNLF-2 (approach-2). Both the thresholding methods are applied to only the high frequency subband coefficients after performing the ripplet decomposition. In conventional thresholding using any transformation technique, low frequency coefficients named as the approximation or coarser coefficients are left as similar as it is obtained after the decomposition, but in the proposed methods, the NLBF is applied to the low frequency ripplet coefficients before taking the inverse of RT of modified noise free ripplet coefficients. In the proposed approaches, homomorphic filtering technique is adapted in which the RT is applied on the log transformed image coefficients rather than the original one and finally, approximate the despeckled image by applying an exponential operator.

Implementation steps

Based on all these aspects, the proposed filtering approach is formulated in the following implementation steps.

Step 1: Start with the speckled images and apply the log transformation on these images.

Step 2: The multiscale decomposition is performed on the log-transformed image using the RT to obtain the speckled ripplet coefficients. After applying the RT at different scales, it is decomposed into a set of the ripplet coefficients as a vector consisting of different subbands $(L+1)$ with the different spectral resolution such as,

$$s^{RT}(x,y) = RT\big(s'(x,y)\big) = [l^s, h_i^s], \text{ where } i = 1, 2, \ldots, \mathrm{L} \quad (3.19)$$

where l^s and h_i^s refer to the low and high frequency ripplet coefficients, respectively.

Step 3: *For RTNLF-1 (approach-1)*

(a) For applying the NS algorithms, firstly, calculate the optimal value of the threshold by minimizing the SURE risk as mentioned in chapter 2 using Eqns. (2.69) and (2.70).

For RTNLF-2 (approach-2)

(b) For implementing the BS algorithm on the high frequency subimage ripplet coefficients, estimate the optimal value of the threshold and block size by minimizing the risk as per Eqns. (3.16)- (3.18)

Step 4: *For RTNLF-1 (approach-1)*

(a) Now apply the threshold on ripplet coefficients obtained from step 2, to compute the approximated or threshold coefficients using Eqn. (3.14)

$$rh_i^s(x,y) = NS\big(h_i^s(x,y)\big) \quad (3.20)$$

For RTNLF-2 (approach-2)

(b) Apply the threshold on noisy ripplet coefficients obtained from step 2.

$$rh_i^s(x,y) = BS\big(h_i^s(x,y)\big) \quad (3.21)$$

where rh_i^s refers to the threshold ripplet high frequency subband coefficients.

Step 5: *For RTNLF-1 and RTNLF-2*

The approximation i.e. low frequency ripplet coefficients (l^s) are processed using the NLBF approach to get the filtered coefficients after estimating the optimal values of the bilateral filter parameters i.e. σ_d and σ_r.

$$rl^s(x,y) = NLBF\big(l^s(x,y)\big) \quad (3.22)$$

Step 6: After applying above filtering methods, the modified ripplet coefficients are given as below:

$$\hat{s}^{RT}(x,y) = [rl^s, rh_i^s] = [rl^s, rh_1^s, rh_2^s, rh_3^s, \ldots, rh_{\mathrm{L}}^s] \quad (3.23)$$

Step 7: The filtered approximated ripplet coefficients are processed with inverse ripplet transform to obtain the estimate of $s'(x,y)$.

$$\hat{s}'(x,y) = RT^{-1}(\hat{s}^{RT}(x,y)) \quad (3.24)$$

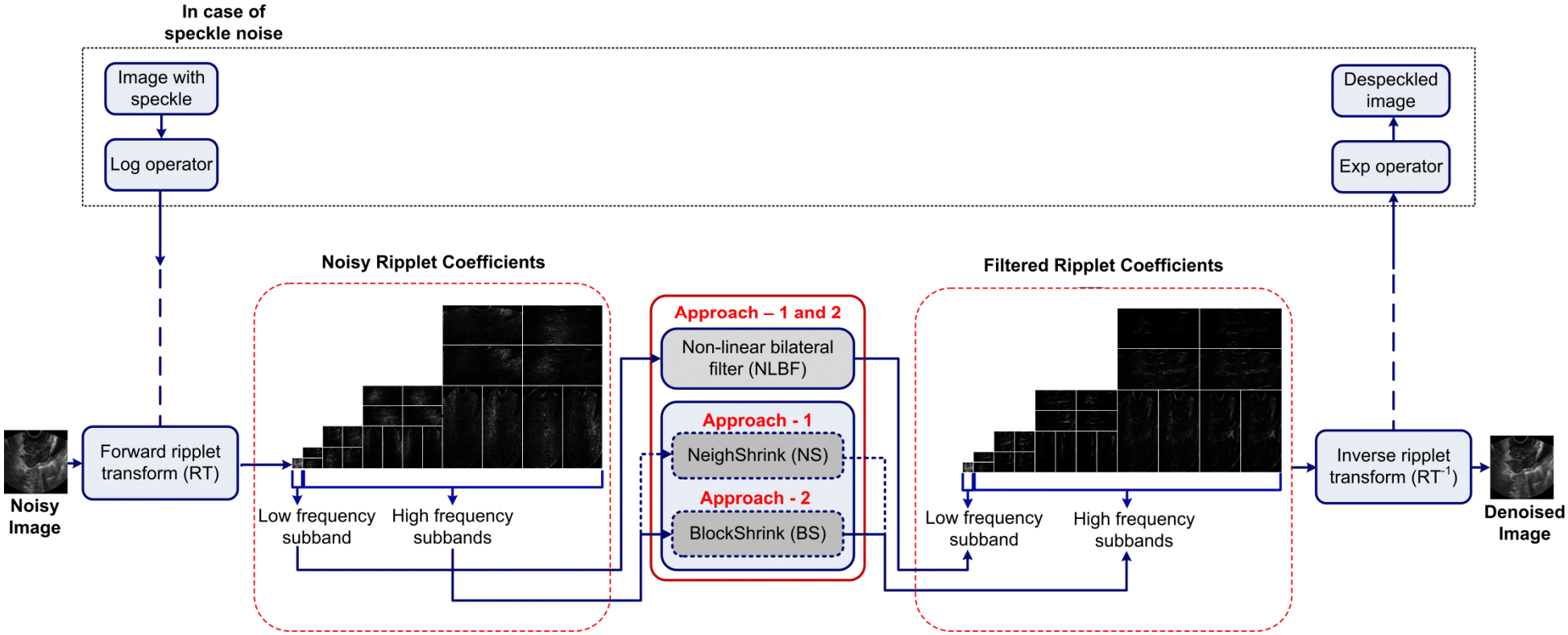

Figure 3.2 Process flow of the proposed nonlinear filtering approaches in ripplet domain

Step 8: Finally, reconstruct the enhanced despeckled image $\hat{s}(x,y)$ with the modified coefficients obtained from steps 4 and 5 by taking the exponential of the estimated image $\hat{s}'(x,y)$

3.6 Experimentation

Three different experiments are conducted on the given test images and real US images for analyzing the performance of their speckle reduction with the preservation of more and more edges information. For presenting the performance of the proposed denoising approaches based on the RT, same dataset as mentioned in chapter 2 such as kidney, fetus and phantom images synthesized using MATLAB and prostate, splenic cyst, multiple liver masses US images, are used here. The performance measures used for assessing the performance of the proposed methods quantitatively are also discussed in chapter 2. The experiments are discussed below:

Experiment 1: Analysis and evaluation of the proposed RTNLF-1 approach.

1.1: Estimation of the optimal values of the NLBF parameters.

1.2: Denoising of simulated test images corrupted by multiplicative speckle noise.

1.3: Denoising of real US medical images for speckle reduction.

Experiment 2: Analysis and evaluation of the proposed RTNLF-2 approach.

2.1: Estimation of the optimal values of the NLBF parameters.

2.2: Denoising of simulated test images degraded by multiplicative speckle noise.

2.3: Denoising of real US medical images for speckle reduction.

Experiment 3: Comparative evaluation of the proposed approaches.

3.1: Comparison of the proposed RTNLF approach-1 and 2 with other methods for denoising in noisy test images.

3.2: Comparison of the proposed RTNLF approach-1 and 2 with other methods for speckle reduction in existing real US images

3.7 Results and Discussions

3.7.1 Experiment 1: Analysis and evaluation of the proposed RTNLF-1 approach

In order to validate the experimental objective, it is further decomposed into three different sub experiments as listed below:

1.1: *Estimation of the optimal values of the NLBF parameters* - The performance of the proposed RTNLF-1 depends on the decomposition levels and the parameters (window size (w_s), σ_d and σ_r) of the NLBF. The optimal values of these parameters have been decided by conducting the several experiments on the available noise free dataset for different noise levels. Table 3.1 shows the comparative analysis for various combinations of the ripplet parameters (c and d) using the average values of different performance

measures. From Table 3.1, it is observed that the PSNR and SNR have obtained higher values for the parameters $c = 1$ and $d = 5$. However, the edge preservation factors FOM and EKI have larger values for parameters $c = 1$ and $d = 4$. Also, the computed averaged values of PSNR and SNR do not show a large difference for the decomposition of images with ripplet parameters $d = 4$ and $d = 5$. If the value of the parameter d goes higher, it leads to edge loss with less noise suppression. Based on the experimental results shown in Table 3.1, the ripplet parameters $c = 1$ and $d = 4$ have been chosen for further analysis.

The optimal parameters involved in the NLBF approach are selected by evaluating the various combinations of the σ_d, σ_r and window size. The several combinations of parameters are selected as: $1 \leq \sigma_d \leq 5$, $1 \leq \sigma_r \leq 8$ and $3 \leq$ window size ≤ 15 at regular interval of 0.2, 1 and 2, respectively. All these experiments have been performed for the different noise levels. The SNR and EKI values are obtained for all the combinations as shown in Table 3.2. It provides the average values of SNR and EKI obtained for the different combinations of the window size and various noise levels. As shown in Table 3.2, the SNR and EKI (in %) achieve higher values within the range of window size 11 to 15. The obtained values of SNR and EKI did not show a large difference over this range of any values of σ_d and σ_r. Therefore, the optimal value of the window size for a particular value of the σ_d and σ_r can be considered for the other values of σ_d and σ_r. Based on the result of Table 3.2, the window size =11 has been chosen for the next analysis.

Table 3.1 Averaged PSNR, SNR, FOM and EKI values obtained for various combinations of ripplet parameters (c and d) and the NLBF parameters (window size $= 9$, $\sigma_d = 5$, $\sigma_r = 2\sigma$)

Ripplet parameters		Decomposition	PSNR	SNR	FOM	EKI
$c = 1$	$d = 3$	[1, 2, 4, 4, 8]	24.17	14.91	0.86208	0.70394
$c = 1$	$d = 4$	[1, 2, 4, 8, 8]	24.95	15.69	0.87919	0.71251
$c = 1$	$d = 5$	[1, 2, 4, 8, 16]	24.98	15.72	0.87785	0.70884
$c = 1$	$d = 6$	[1, 2, 4, 8, 16]	24.82	15.56	0.87371	0.70014

Table 3.2 Averaged SNR and EKI values obtained for various window sizes, $\sigma_d = 3$ and $\sigma_r = 2\sigma$

Noise level	Metrics	Window size						
		3	5	7	9	11	13	15
$\sigma = 0.1$	SNR	16.0018	16.0053	16.0103	16.0120	16.0127	16.0127	16.0127
	EKI (%)	71.1974	71.3454	71.3464	71.4614	71.7684	71.8644	71.7664
$\sigma = 0.2$	SNR	14.5810	14.5817	14.5820	14.5822	14.5832	14.5831	14.5831
	EKI (%)	61.6120	61.6340	61.6370	61.9010	62.1300	62.1330	62.1300
$\sigma = 0.3$	SNR	12.9898	12.9899	12.9900	12.9900	12.9910	12.9909	12.9909
	EKI (%)	57.8853	57.9963	58.0283	58.0533	58.0583	58.0583	58.0553

To choose the optimal values of σ_d and σ_r, the similar experiments have been performed in the various combinations for σ_d, σ_r and at the different noise levels. The different performance measures such as the PSNR, SNR, FOM and EKI are evaluated for each combination. The average values of performance measures are given in Table 3.3. As shown in Table 3.3, the optimal range of σ_d values is approx $[1.4 - 2.0]$ for which the PSNR, SNR, FOM (%) and EKI (%) values are higher under varying noise levels (σ). Also, the evaluated values of PSNR and SNR do not vary significantly on larger values of σ_d. However, the EKI values decrease on larger values of σ_d. Therefore, $\sigma_d = 1.8$ has been selected for the present study.

The optimal choice of σ_r value is obtained by successive experiments for varying noise levels and the optimal values of $\sigma_d = 1.8$ and window size $= 11$. Figure 3.3 gives the plot of average values of the SNR and EKI (in %) obtained from the different values of σ_r at different noise levels (σ). Based on the performance comparison as shown in Figure 3.3, the optimal range of the parameter σ_r has been identified between 1σ to 3σ for which the SNR and EKI values get higher for different noise levels. Therefore, the parameter $\sigma_r = 2\sigma$ has been chosen to investigate the performance of the proposed method. Based on all these outcomes obtained by performing this experiment discussed earlier, the following parameters such as $c = 1$, $d = 4$, window size $= 11, \sigma_d = 1.8$ and $\sigma_r = 2\sigma$ are selected for the proposed denoising approach-1.

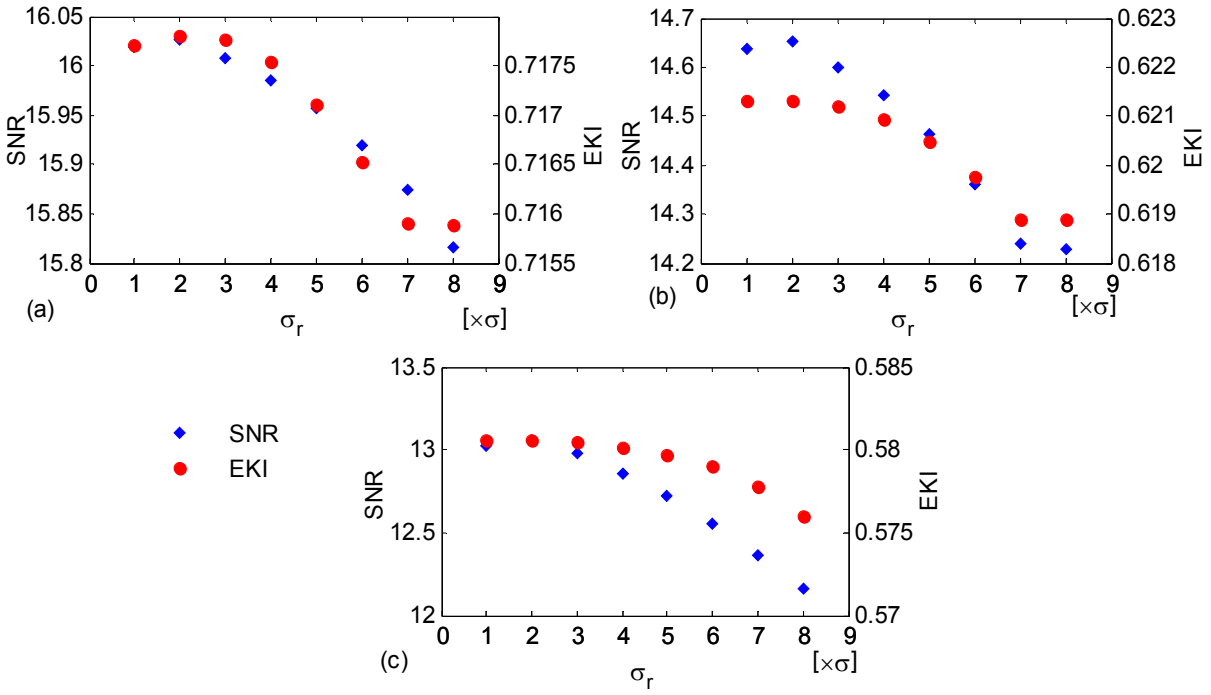

Figure 3.3 Comparative performance of the SNR and EKI obtained for different values of σ_r, $\sigma_d = 1.8$, window size$= 11$ and different noise variance (a) 0.1 (b) 0.2 (c) 0.3

Table 3.3 Averaged PSNR, SNR, FOM (%) and EKI (%) values obtained from different values σ_d, $\sigma_r = 2\sigma$ and window size = 11

σ_d	$\sigma = 0.1$				$\sigma = 0.2$				$\sigma = 0.3$			
	PSNR	SNR	FOM (%)	EKI (%)	PSNR	SNR	FOM (%)	EKI (%)	PSNR	SNR	FOM (%)	EKI (%)
1	25.2943	16.0310	88.4089	71.7746	23.8719	14.6086	84.6335	62.1309	22.2784	13.0151	83.5854	58.0614
1.2	25.2990	16.0357	88.4644	71.7773	23.8785	14.6153	84.5463	62.1316	22.2859	13.0226	83.5855	58.0618
1.4	25.3124	16.0491	88.5069	71.7789	23.8892	14.6259	84.6623	62.1319	22.2955	13.0325	83.6164	58.0624
1.6	25.3049	16.0416	88.6599	71.7798	23.9010	14.6380	84.7190	62.1319	22.3076	13.0446	83.6551	58.0628
1.8	25.2900	16.0267	88.2633	71.7800	23.9166	14.6533	85.0700	62.1330	22.3233	13.0600	83.7067	58.0630
2	25.2863	16.0233	88.4459	71.7793	23.8657	14.6024	84.8432	62.1317	22.3429	13.0796	83.5930	58.0627
2.2	25.2838	16.0205	88.2214	71.7779	23.8612	14.5982	84.7937	62.1314	22.2728	13.0096	83.2826	58.0622
2.4	25.2814	16.0181	88.2521	71.7759	23.8562	14.5929	84.7153	62.1311	22.2665	13.0032	83.0734	58.0614
2.6	25.2790	16.0160	88.2548	71.7735	23.8525	14.5892	84.7462	62.1307	22.2618	12.9986	82.9296	58.0604
2.8	25.2775	16.0142	88.1445	71.7710	23.8493	14.5860	84.7084	62.1304	22.2578	12.9945	82.9974	58.0594
3	25.2760	16.0127	88.2602	71.7684	23.8465	14.5832	84.5813	62.1300	22.2543	12.9910	83.1282	58.0583

1.2: *Denoising of simulated test images corrupted by multiplicative speckle noise* - To investigate the performance of the proposed RTNLF-1, all three simulated kidney, fetus and phantom images are used that are corrupted by the speckle noise with the noise level characterized by the noise variance. The denoising results are also compared with the bilateral filter [229] with $\sigma_d = 1.8$ and $\sigma_r = 2\sigma$, WT-NS [289], WT-NLBF-NS [14], ridgelet [101], curvelet [10] based methods. The denoised kidney images processed by all these methods are shown in Figure 3.4. From these figures, it is observed that the proposed RTNLF-1 provides much better results in comparison to the others. The bilateral filter and WT-NLBF-NS method also provide better noise suppression results, but still the preservation of more edges becomes a problem. The quantitative outcomes obtained by these methods are listed in Table 3.4. Besides the visual assessments, the results in Table 3.4 show that the RTNLF-1 also produces better noise suppression and edge preservation results by estimating higher PSNR, SNR SSIM, FOM and EKI values as compared to others. For low level noise, bilateral filter and curvelet has a competitive noise suppression performance with lower edge preservation performance than the proposed RTNLF-1, while in case of the high level noise $\sigma = 0.3$, the RTNLF-1 achieves higher edge preservation results with the competitive value of noise suppression performance parameters than the curvelet based method.

For another visual assessment of the denoising techniques, the denoised fetus images corresponding to $\sigma = 0.2$ and a synthetic 2D phantom image corresponding to $\sigma = 0.3$ are shown in Figure 3.5 and Figure 3.6, respectively. From visualizing these denoised images, the RTNLF-1 provides better quality of images than others by suppressing a good amount of the speckle noise with better edge preservation. This is also validated by the evaluation of image quality measures for three different noise levels. From Figure 3.5 (f), it is visualized

that the proposed method generates the most similar result as the noise free image. From the results mentioned in Table 3.5, it is also observed that the SNR, PSNR, SSIM, FOM and EKI values obtained by the proposed RTNLF-1 are higher than others in all the cases.

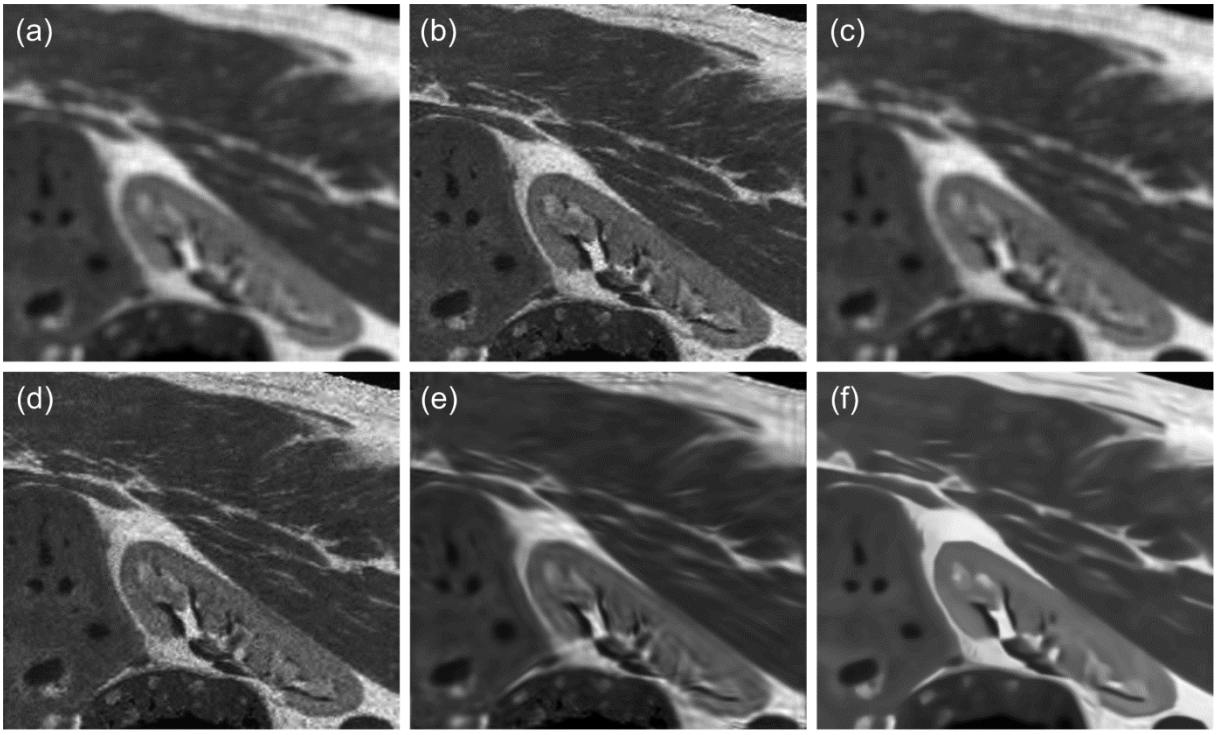

Figure 3.4 Visual comparison of simulated kidney image denoised by (a) Bilateral filter (b) WT-NS (c) WT-NLBF-NS (d) Ridgelet (e) Curvelet (f) Proposed RTNLF-1

Table 3.4 Performance comparison between the proposed RTNLF-1 approach with others for kidney image degraded by speckle noise

Noise level	Methods	PSNR	SNR	SSIM	FOM	EKI
$\sigma = 0.1$	Bilateral	26.05	15.43	0.7186	0.5387	0.4685
	WT-NS	23.15	12.53	0.7305	0.4973	0.3962
	WT-NLBF-NS	25.96	15.34	0.7596	0.6572	0.4304
	Ridgelet	24.54	13.93	0.7375	0.5432	0.4136
	Curvelet	26.77	16.15	0.7666	0.5460	0.4340
	Proposed RTNLF-1	28.10	17.47	0.7981	0.7924	0.5175
$\sigma = 0.2$	Bilateral	25.11	14.49	0.7114	0.5248	0.3284
	WT-NS	21.68	11.05	0.7293	0.5131	0.3493
	WT-NLBF-NS	24.73	14.12	0.7426	0.6151	0.3916
	Ridgelet	23.75	13.13	0.7325	0.5201	0.3782
	Curvelet	26.57	15.95	0.7633	0.5663	0.4318
	Proposed RTNLF-1	27.41	16.79	0.7852	0.7891	0.4811
$\sigma = 0.3$	Bilateral	24.83	14.21	0.7045	0.5134	0.3387
	WT-NS	19.74	9.12	0.7148	0.5132	0.3323
	WT-NLBF-NS	23.15	12.53	0.7221	0.5862	0.4322
	Ridgelet	22.09	11.47	0.7146	0.5404	0.3672
	Curvelet	26.27	15.65	0.7407	0.5828	0.4193
	Proposed RTNLF-1	25.84	15.22	0.7621	0.7551	0.4743

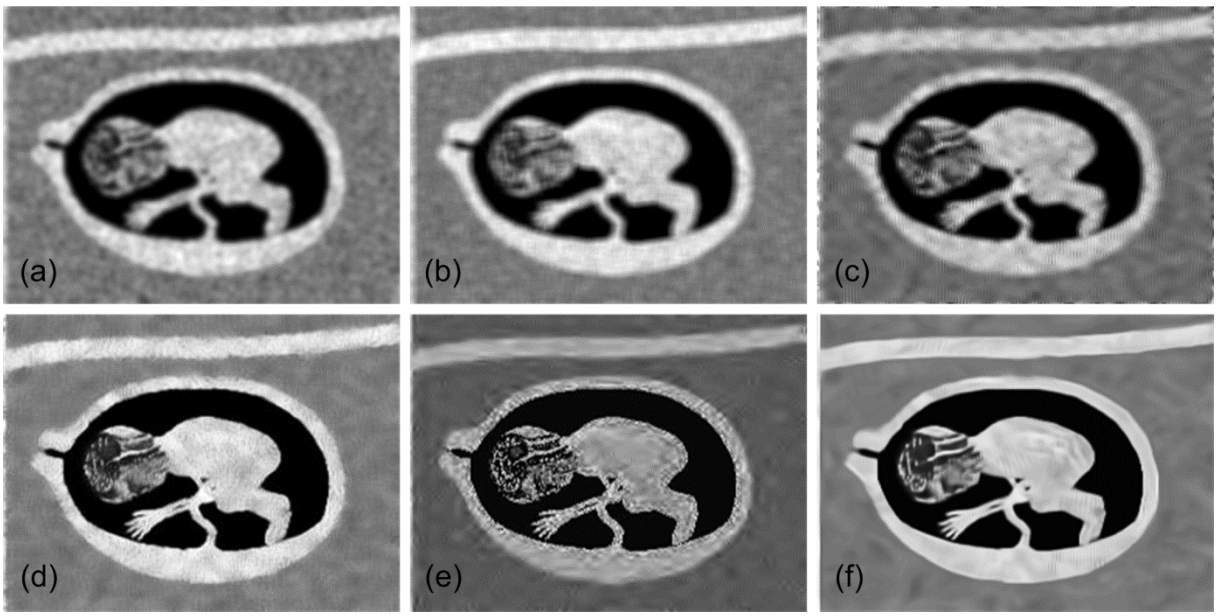

Figure 3.5 Visual comparison of fetus image denoised by (a) Bilateral filter (b) WT-NS (c) WT-NLBF-NS (d) Ridgelet (e) Curvelet (f) Proposed RTNLF-1

Table 3.5 Performance comparison between the proposed RTNLF-1 approach with others for fetus image degraded by speckle noise

Noise level	Methods	PSNR	SNR	SSIM	FOM	EKI
$\sigma = 0.1$	Bilateral	18.58	13.60	0.6157	0.6847	0.3758
	WT-NS	18.38	13.39	0.6243	0.7627	0.4883
	WT-NLBF-NS	18.43	13.44	0.6558	0.7673	0.5268
	Ridgelet	18.71	13.69	0.6001	0.8269	0.5242
	Curvelet	18.03	13.04	0.6381	0.8258	0.4277
	Proposed RTNLF-1	20.59	15.60	0.6712	0.9102	0.7174
$\sigma = 0.2$	Bilateral	16.72	11.75	0.5689	0.6741	0.3951
	WT-NS	16.54	11.55	0.5572	0.6010	0.3755
	WT-NLBF-NS	16.68	11.69	0.6236	0.7561	0.5036
	Ridgelet	16.71	11.72	0.5678	0.7586	0.4824
	Curvelet	17.15	12.16	0.6164	0.7276	0.4089
	Proposed RTNLF-1	19.38	14.39	0.6397	0.9006	0.6587
$\sigma = 0.3$	Bilateral	16.54	11.55	0.4763	0.6698	0.3609
	WT-NS	15.53	10.55	0.5367	0.6458	0.3650
	WT-NLBF-NS	15.79	10.81	0.5661	0.7085	0.4495
	Ridgelet	16.21	11.22	0.5412	0.7097	0.3951
	Curvelet	16.38	11.39	0.5816	0.7086	0.3730
	Proposed RTNLF-1	18.31	13.32	0.6085	0.8970	0.5464

In case of phantom image shown in Figure 3.6, bilateral and curvelet methods also produce good denoised images; the proposed RTNLF-1 outperforms the other methods. It is supported by some objective evaluations as listed in Table 3.6. From these results, it is seen that bilateral and WT-NLBF-NS methods achieve competitive EKI values to the RTNLF-1, but in case of noise suppression performance exhibited by the SNR and PSNR values, the WT-NLBF-NS and curvelet based methods are better. Moreover, the proposed RTNLF-1 shows

better noise suppression and edge preservation by providing higher SNR, PSNR, SSIM, FOM and EKI values than the bilateral, WT-NLBF-NS and curvelet based methods.

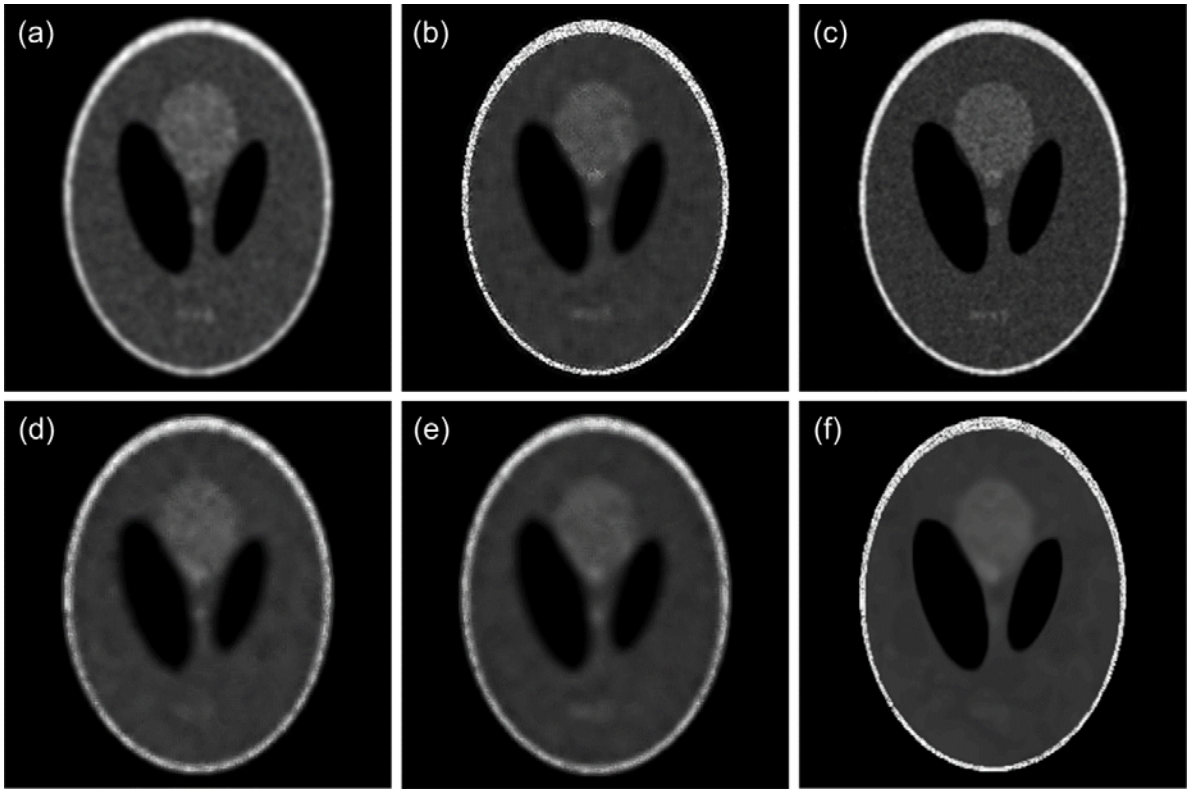

Figure 3.6 Visual comparison of phantom image denoised by (a) Bilateral filter (b) WT-NS (c) WT-NLBF-NS (d) Ridgelet (e) Curvelet (f) Proposed RTNLF-1

Table 3.6 Performance comparison between the proposed RTNLF-1 approach with others for phantom image degraded by speckle noise

Noise level	Methods	PSNR	SNR	SSIM	FOM	EKI
$\sigma = 0.1$	Bilateral	23.59	11.41	0.7865	0.8698	0.6885
	WT-NS	23.52	11.34	0.7734	0.4931	0.6825
	WT-NLBF-NS	25.12	12.94	0.8026	0.8894	0.6862
	Ridgelet	24.14	11.97	0.7894	0.4915	0.6834
	Curvelet	25.01	12.84	0.7970	0.6494	0.6121
	Proposed approach-1	27.18	15.01	0.8436	0.9653	0.9185
$\sigma = 0.2$	Bilateral	22.93	10.76	0.7389	0.6922	0.6123
	WT-NS	21.11	8.93	0.7597	0.3554	0.4641
	WT-NLBF-NS	22.23	10.06	0.7918	0.8212	0.6135
	Ridgelet	22.21	10.03	0.7548	0.3957	0.5239
	Curvelet	24.12	11.95	0.7923	0.4688	0.5799
	Proposed approach-1	24.95	12.78	0.8192	0.8624	0.7242
$\sigma = 0.3$	Bilateral	22.41	10.23	0.7104	0.6472	0.5469
	WT-NS	19.66	7.49	0.7389	0.2614	0.4386
	WT-NLBF-NS	21.83	9.66	0.7872	0.6941	0.5631
	Ridgelet	20.11	7.93	0.7347	0.3613	0.4585
	Curvelet	23.38	11.22	0.7813	0.4435	0.5521
	Proposed approach-1	22.81	10.64	0.7889	0.8591	0.7212

1.3: *Denoising of real US medical images for speckle reduction* - In order to investigate the performance of the proposed RTNLF-1 approach on the real US images, the same images are taken as shown in chapter 2 to conduct this experiment. Out of them, the prostate US images processed by the different denoising methods as discussed in the previous section are presented in Figure 3.7. As mentioned earlier in the previous chapter, the curvelet method adds some fuzzy edges in the form of visual distortion in the US images. By visualizing all the images shown in Figure 3.7, the bilateral filter and the WT-NLBF-NS methods are also capable to remove the speckle but some edges are lost during the despeckling process. Among all these images, it is observed that the proposed RTNLF-1 approach produces better quality images with more edges than others.

For another investigation, the despeckling results of the splenic cyst US images are shown in Figure 3.8. Also from the results illustrated in Figure 3.8, similar patterns of all the denoising methods as mentioned before are observed in which the proposed RTNLF-1 approach is able to produce better visual quality of the splenic cyst image. Besides this, the WT-NLBF-NS approach is also a good competitor to the bilateral approach.

Another US image of multiple liver masses processed by all the methods is shown in Figure 3.9. From the visual results of Figure 3.9, it is observed that the results obtained from the WT-NS and WT-NLBF-NS methods are blurred and large amount of edge information is also lost. Besides this, ridgelet method is able to remove sufficient amount of the speckle noise, while the bilateral produces the results by reducing considerable amount of speckle

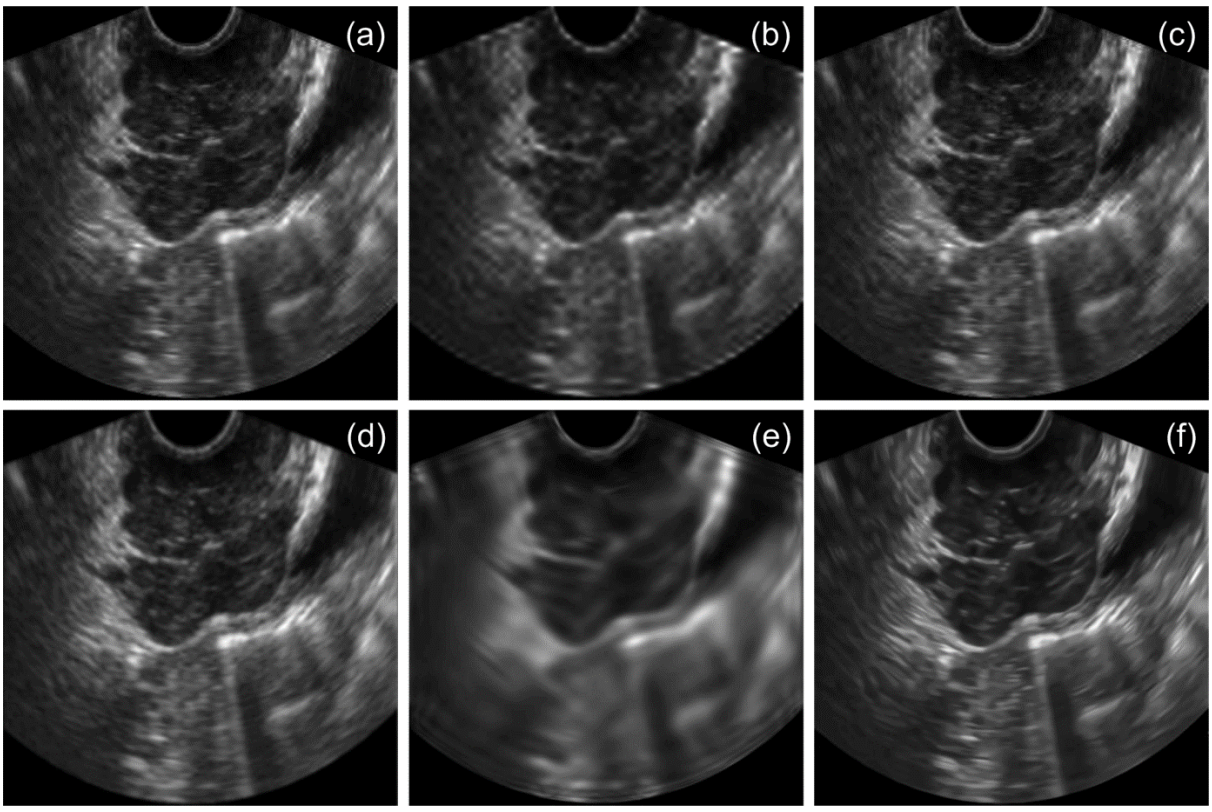

Figure 3.7 Visual comparison of prostate ultrasound image, processed by (a) Bilateral filter (b) WT-NS (c) WT-NLBF-NS (d) Ridgelet (e) Curvelet (f) Proposed RTNLF-1

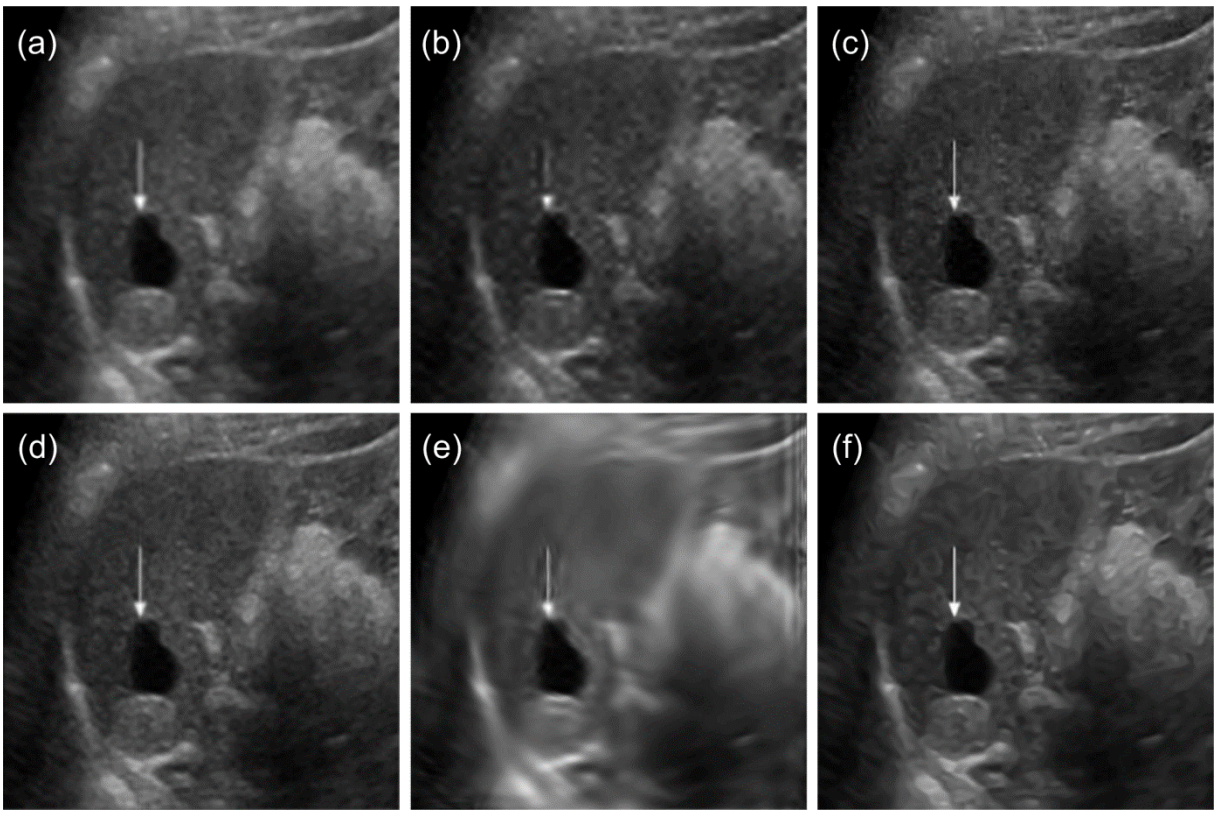

Figure 3.8 Visual comparison of splenic cyst ultrasound image, processed by (a) Bilateral filter (b) WT-NS (c) WT-NLBF-NS (d) Ridgelet (e) Curvelet (f) Proposed RTNLF-1

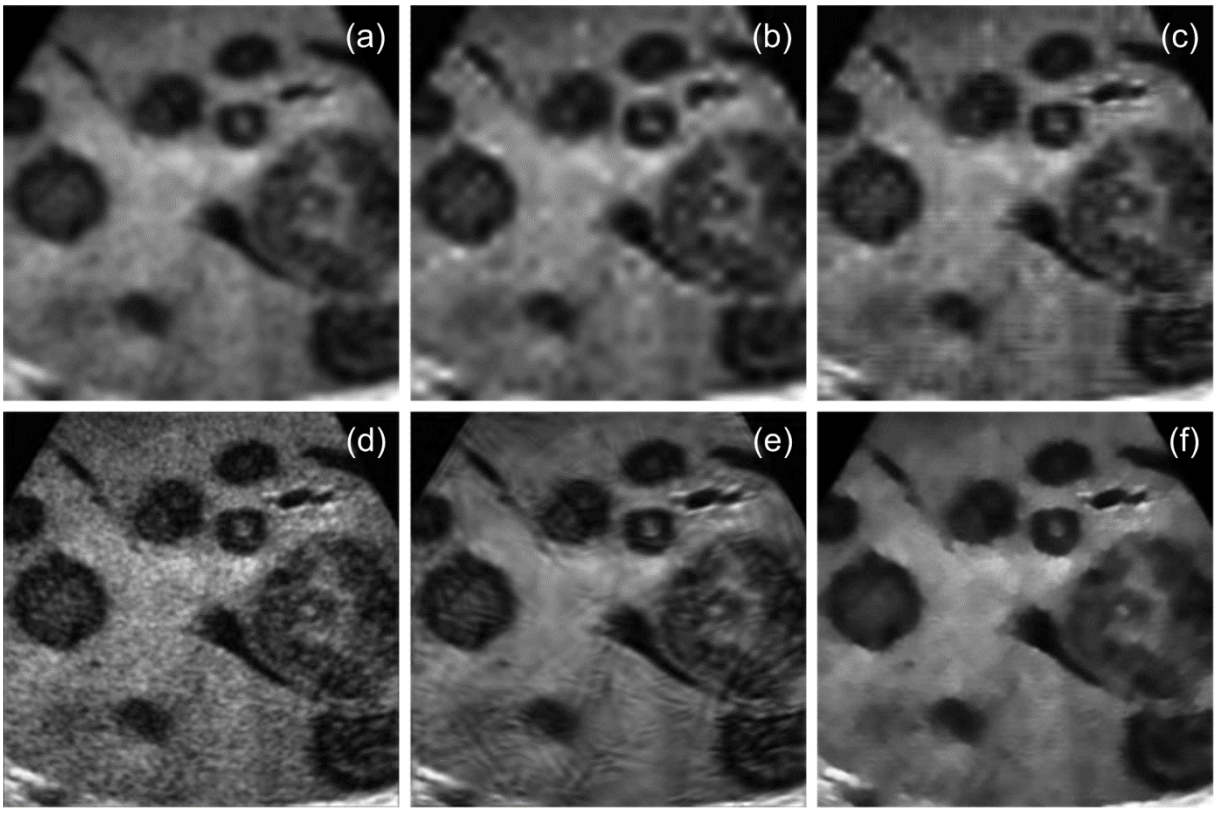

Figure 3.9 Visual comparison of multiple liver masses ultrasound image, processed by (a) Bilateral filter (b) WT-NS (c) WT-NLBF-NS (d) Ridgelet (e) Curvelet (f) Proposed RTNLF-1

in the US images. The proposed RTNLF-1 approach produces good quality of denoising results with more edge preservation than the others. As mentioned in the previous chapter, the quantitative analysis of the denoising process is too much difficult in case of the US images because of non-availability of the reference noise free images. To achieve this objective, the MVR values are evaluated for the different regions marked on each US image of our datasets as shown in Figure 2.21. The estimated MVR values for both the regions of four different US images are shown in Figure 3.10 (a)-(d), respectively. From the bar graph presented in the Figure 3.10, it is observed that the proposed RTNLF-1 approach achieves higher value of the MVR for both the regions, which also describes the better speckle reduction performance of the proposed RTNLF-1 approach than the others. Besides the proposed RTNLF-1 approach, the approximately similar MVR values are obtained for both the bilateral and WT-NLBF-NS methods. Moreover, the proposed RTNLF-1 approach outperforms the others in terms of speckle suppression in the existing real US images.

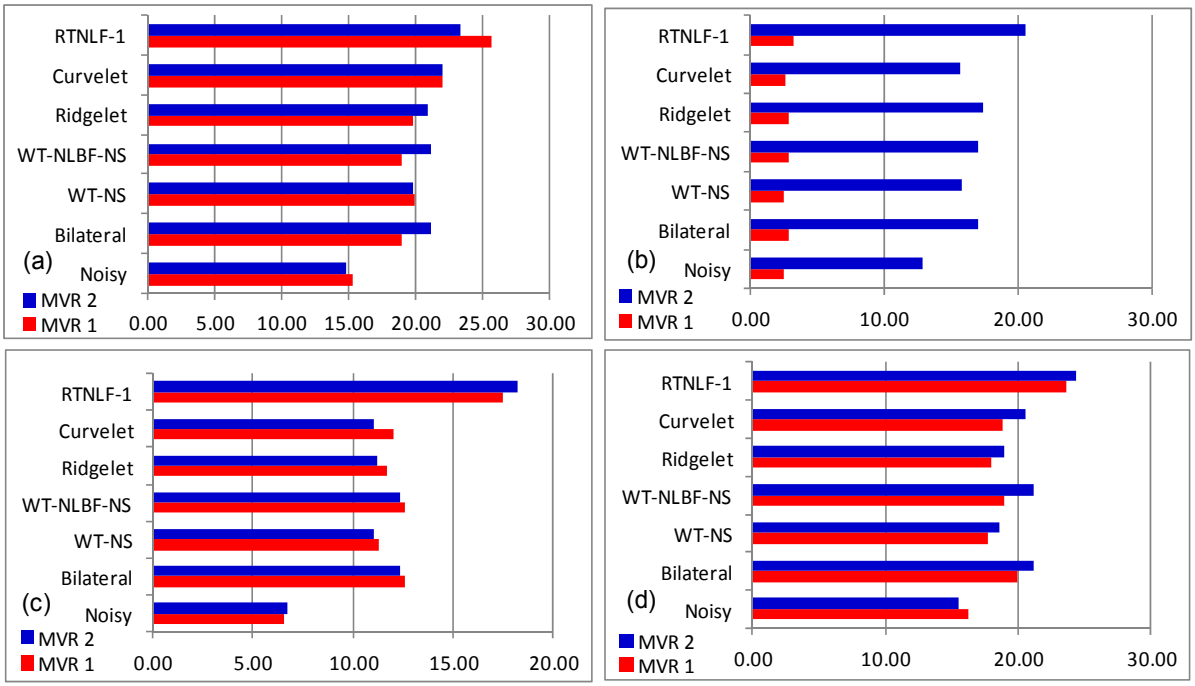

Figure 3.10 Plot of the MVR values obtained from the different denoising methods for two image regions shown in Figure 2.21

Apart from all these performances of the proposed RTNLF-1 approach, 100 different subsequent measurements are taken on two different image regions of each US image to evaluate the MVR values. The averaged values of the MVR are shown in Table 3.7. The results presented in Table 3.7 also show the superiority of the proposed RTNLF-1 approach.

Table 3.7 Performance comparison of the denoising methods with the proposed RTNLF-1 using the averaged MVR values over 100 different regions marked on 50 ultrasound images

Methods	Noisy	Bilateral	WT-NS	WT-NLBF-NS	Ridgelet	Curvelet	Proposed Approach -1
MVR	14.04 ± 3.04	19.69 ± 3.23	16.97 ± 4.21	17.89 ± 3.83	17.47 ± 3.69	18.22 ± 4.57	21.98 ± 3.93

3.7.2 Experiment 2: Analysis and evaluation of the proposed RTNLF-2 approach

To validate the experimental objective of the proposed RTNLF-2 approach, three different experiments are considered. These sub-experimental objectives are listed as below:

2.1: *Estimation of the optimal values of the NLBF parameters* - As mentioned in the previous subsection 1.1 of section 3.7.1, the optimal value of the NLBF and ripplet parameters are decided by the successive experiments on the test image dataset. For choosing the optimal values of the ripplet parameters c and d, the performance measures are obtained for different values of the c and d with the window size $(w_s) = 9$, $\sigma_d = 5$ and $\sigma_r = 2\sigma$. Table 3.8 shows that the PSNR and SNR have obtained higher mean values for the parameters $c = 1$ and $d = 5$. However, the edge dislocation and preservation factor such as the FOM have higher mean value for the parameters $c = 1$ and $d = 3$ and the SSIM and EKI have larger mean value for $c = 1$ and $d = 4$. Furthermore, the evaluated mean values of PSNR and SNR do not exhibit a large difference for the decomposition of images with ripplet parameter $d = 4$, $d = 5$ and $d = 6$. Similarly, Table 3.8 does not show a large difference between the FOM, SSIM and EKI values for $d = 3$ and $d = 4$. If the value of the parameter d goes higher, it leads to edge loss with less noise suppression. Based on the results shown in Table 3.8, ripplet parameters $c = 1$ and $d = 4$ are used for the next analysis.

Now by selecting different combinations as $1 \leq \sigma_d \leq 5$, $1 \leq \sigma_r \leq 7$ and $3 \leq w_s \leq 15$ at regular interval of 0.2-0.4, 1 and 2, respectively, the optimal parameters of the NLBF are chosen. For such purpose, Table 3.9 shows the average values of the SNR, SSIM (%) and EKI (%) for different w_s and fixed $\sigma_d = 3$ and $\sigma_r = 2\sigma$. From these results, it is observed that the values of the SNR, SSIM and EKI achieve higher values within $9 \leq w_s \leq 15$. The average values of SNR, SSIM and EKI shown in Table 3.9 did not show a large difference over $11 \leq w_s \leq 15$ for different values of σ_d and σ_r. Therefore, the optimal value of the window size for the particular values of σ_d and σ_r can be considered for other values of σ_d and σ_r. Based on the result of Table 3.9, we chose the window size $w_s = 11$ for the next evaluation.

For choosing the optimal values of σ_d and σ_r, Table 3.10 shows the average values of the performance measures evaluated for different values of the σ_d with optimal value of the $w_s = 11$ and $\sigma_r = 2\sigma$. The optimal range for the σ_d value is approx [1.4-2.0] for which the values of PSNR, SNR, SSIM, FOM, and EKI are higher under varying noise levels (σ).

Table 3.8 Performance measures obtained for several combinations of ripplet parameters (c and d) and the NLBF parameters (window size $= 9$, $\sigma_d = 5$ and $\sigma_r = 2\sigma$)

Ripplet parameters		Decomposition	PSNR	SNR	SSIM	FOM	EKI
$c = 1$	$d = 3$	[1, 2, 4, 4, 8]	24.92	15.66	0.78718	0.88517	0.71817
$c = 1$	$d = 4$	[1, 2, 4, 8, 8]	25.08	15.82	0.78752	0.88102	0.71856
$c = 1$	$d = 5$	[1, 2, 4, 8, 16]	25.27	16.01	0.78617	0.87823	0.70075
$c = 1$	$d = 6$	[1, 2, 4, 8, 16]	25.14	15.88	0.73911	0.83621	0.65182

Table 3.9 The SNR, SSIM and EKI values obtained for various window sizes, $\sigma_d = 3$ and $\sigma_r = 2\sigma$

Noise level	Metrics	Window size						
		3	5	7	9	11	13	15
$\sigma = 0.1$	SNR	16.4616	16.4727	16.4648	16.4699	16.4727	16.4729	16.4729
	SSIM (%)	78.8037	78.8041	78.8041	78.8045	78.8046	78.8014	78.8012
	EKI (%)	72.7587	72.9298	73.0376	73.1442	73.3531	73.3527	73.3511
$\sigma = 0.2$	SNR	14.8836	14.8850	14.8852	14.8854	14.8866	14.8865	14.8865
	SSIM (%)	74.9851	74.9851	74.9854	74.9857	74.9857	74.9856	74.9847
	EKI (%)	63.8569	63.8569	63.8569	63.8458	63.8569	63.8559	63.8552
$\sigma = 0.3$	SNR	13.4862	13.4865	13.4866	13.4877	13.4877	13.4873	13.4873
	SSIM (%)	72.0179	72.0182	72.0185	72.0185	72.0187	72.0184	72.0173
	EKI (%)	59.0378	59.0378	59.0378	59.0389	59.0399	59.0399	59.0391

Therefore, $\sigma_d = 2$ has been selected for further study.

Figure 3.11 gives a plot of average values of the SNR and EKI obtained from the different values of σ_r at different noise levels and the optimal values of $\sigma_d = 2$ and $w_s = 11$. Based on the results presented in Figure 3.11, the optimal range of the parameter σ_r is identified between 1σ to 3σ for which the SNR and EKI values rise higher for different noise levels. Therefore, the parameter $\sigma_r = 2\sigma$ is chosen to analyze the performance of the proposed method. Based on all the experiments presented earlier, the following parameters are selected for the proposed method: $c = 1$, $d = 4$, $w_s = 11$, $\sigma_d = 2$ and $\sigma_r = 2\sigma$.

Table 3.10 Performance measures obtained from the different values of σ_d, $\sigma_r = 2\sigma$ and window size = 11

Noise level	Metrics	σ_d						
		1	1.4	1.8	2	2.4	2.8	3
$\sigma = 0.1$	PSNR	25.7557	25.7583	25.7510	25.7464	25.7381	25.7309	25.7327
	SNR	16.4957	16.5016	16.4910	16.4867	16.4781	16.4742	16.4727
	SSIM (%)	78.8129	78.8146	78.8184	78.8134	78.8112	78.8059	78.8046
	FOM (%)	89.6799	89.7344	89.7969	89.5333	89.5248	89.4145	89.5302
	EKI (%)	73.3562	73.3605	73.3614	73.3616	73.3609	73.3551	73.3531
$\sigma = 0.2$	PSNR	24.1786	24.1893	24.2011	24.2167	24.1613	24.1494	24.1466
	SNR	14.9187	14.9293	14.9414	14.9567	14.9016	14.8894	14.8866
	SSIM (%)	75.0169	75.1015	75.2123	75.3767	75.2548	75.0158	74.9857
	FOM (%)	85.4668	85.3796	85.5523	85.9033	85.6270	85.1940	85.1262
	EKI (%)	64.0073	64.0079	64.0089	64.0100	63.9988	63.8912	63.8569
$\sigma = 0.3$	PSNR	22.7725	22.7779	22.8010	22.8134	22.7566	22.7509	22.7444
	SNR	13.5125	13.5179	13.5413	13.5567	13.4999	13.4912	13.4877
	SSIM (%)	72.1141	72.1324	72.1875	72.2467	72.1846	72.1274	72.0187
	FOM (%)	84.2463	84.2697	84.3084	84.3600	83.7267	83.5829	84.3096
	EKI (%)	59.1074	59.1084	59.1092	59.1100	59.1074	59.0410	59.0399

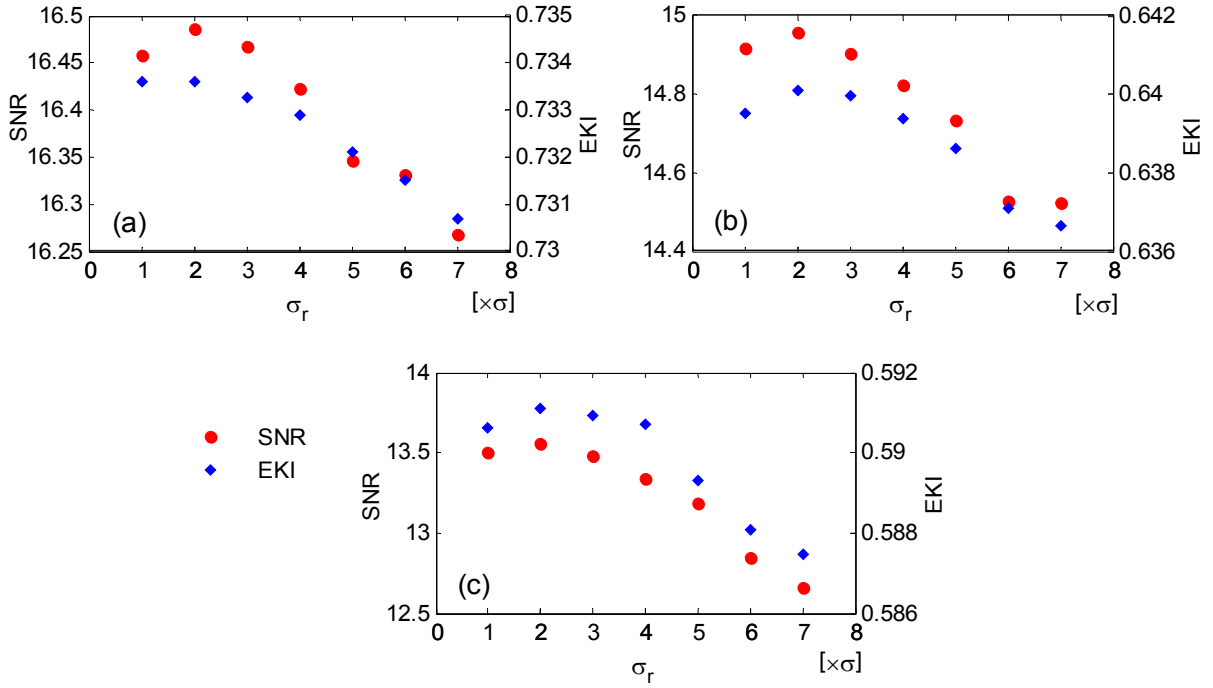

Figure 3.11 Comparative performance of the SNR and EKI obtained for the different values of σ_r, $\sigma_d = 1.8$, window size= 11 and different noise variance (a) 0.1 (b) 0.2 (c) 0.3

2.2: *Denoising of simulated test images degraded by multiplicative speckle noise* - In order to assess the denoising performance of the RTNLF-2, similar test images are considered as in the section 3.7.1. The denoised images of all three different test images degraded by multiplicative speckle noise of noise variance $\sigma = 0.1$, 0.2 and 0.3, respectively are shown in Figure 3.12. In the Figure 3.12, four different remarkable denoising methods such as bilateral filter approach [229], WT-BS [39, 290], curvelet [10] and the proposed RTNLF-2 approach are considered. From these figures, it is observed that the proposed RTNLF-2 approach provides much better denoising results of kidney and fetus images as compared to the others. Another assessment of the visual quality of the phantom image, the WT-BS method also provides the denoised image of good quality along with the proposed RTNLF-2 approach. Furthermore, it is concluded from these results that the proposed RTNLF-2 approach outperforms the other existing methods considered in the present work. These visual results are also validated by the quantitative results as shown in Table 3.11. From the results mentioned in Table 3.11, it is seen that the proposed RTNLF-2 approach achieves approx 6.48-10.23%, 14.09-17.94% and 3.21-17.5% larger PSNR values, 11.33-17.67%, 16.47-25.36% and 7.23-36.28% higher SNR values, 8.7-15.28%, 11.3-28.13% and 8.1-11.88% higher SSIM values and 15.8-50%, 54.8-94.7% and 21.26-34.57% higher EKI values than bilateral filter approach for simulated kidney, fetus and phantom images, respectively. The proposed RTNLF-2 approach also gains approx 20.95-31.22%, 10.56-19.2% and 14.72-16.47% higher PSNR values, 38.15-66%, 14.37-28.04% and, 31.89-42.65% higher SNR values than the WT-BS approach with the approx 35.9-45.69%, 48.3-66.5% and 35.6-65.7%

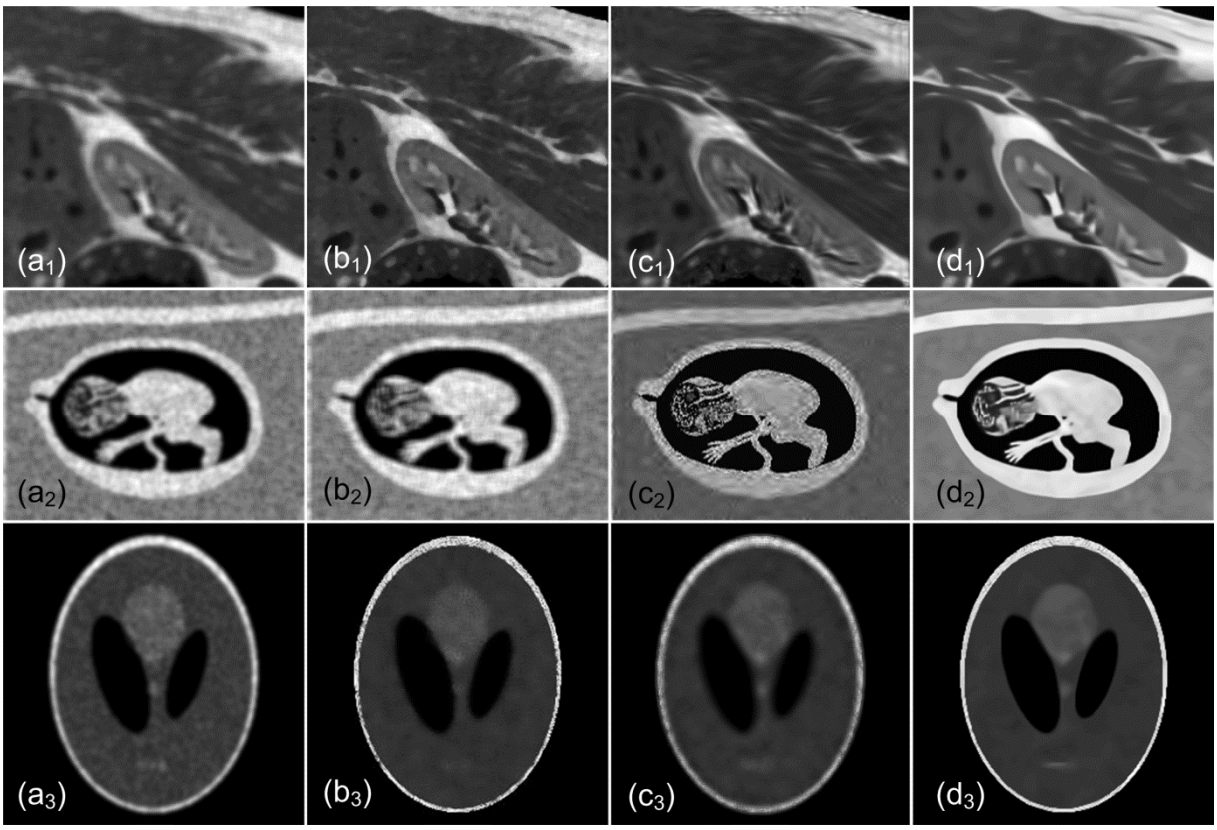

Figure 3.12 Visual comparison of kidney, fetus and phantom images denoised by (a) Bilateral filter (b) WT-BS (c) Curvelet (f) Proposed RTNLF-2. Here, 1, 2 and 3 refer to kidney, fetus and phantom images, respectively

higher EKI values for all three different noisy images corrupted by the different noise levels. Sometimes, the curvelet method produces approx 1-2% higher SNR and PSNR values than the proposed RTNLF-2 approach in the case of phantom image. Moreover, the performance measures such as the PSNR, SNR, SSIM, FOM and EKI values obtained from the RTNLF-2 are increased by approx 0.65-7.17%, 1.09-11.89%, 3.39-8.06%, 31.67-46.28% and 14.08-25% for kidney images, 14.99-15.3%, 21.13-21.86%, 4.33-7.4%, 11.54-27.04% and 49.79-71.08% for fetus images and 4.68-10.84%, 9.54-21.11%, 1.28-6.74%, 48.78-94.63%, 28.04-51.36% for phantom images than the curvelet based method.

2.3: *Denoising of real US medical images for speckle reduction* - For analyzing the performance of the proposed RTNLF-2 approach on the real US images, same US images as presented in section 3.7.1 are considered to conduct this experiment. The processed prostate, splenic cyst and multiple liver masses US images are shown in Figure 3.13. By analyzing the visual results illustrated in Figure 3.13, it is visualized that the proposed RTNLF-2 approach produces better quality images than the others with retention of more edge information. Besides this, the MVR values are also calculated for two different image regions marked on the several US images by the same approach as used in previous section and a comparison between all the denoising methods is also shown in Figure 3.14. From this

Table 3.11 Performance comparison between the proposed RTNLF-2 approach with others

Images	Noise Level	Metrics	Denoising methods			
			Bilateral	WT-BS	Curvelet	Proposed approach-2
Kidney image	$\sigma = 0.1$	PSNR	26.05	23.72	26.77	28.69
		SNR	15.43	13.08	16.15	18.07
		SSIM	0.7186	0.7341	0.7666	0.8284
		FOM	0.5387	0.5197	0.5460	0.7987
		EKI	0.4685	0.3991	0.4340	0.5425
	$\sigma = 0.2$	PSNR	25.11	22.13	26.57	27.68
		SNR	14.49	11.51	15.95	17.05
		SSIM	0.7114	0.7342	0.7633	0.7915
		FOM	0.5248	0.5312	0.5663	0.7958
		EKI	0.3284	0.3556	0.4318	0.4926
	$\sigma = 0.3$	PSNR	24.83	20.15	26.27	26.44
		SNR	14.21	9.53	15.65	15.82
		SSIM	0.7045	0.7174	0.7407	0.7658
		FOM	0.5134	0.5372	0.5828	0.7674
		EKI	0.3387	0.3318	0.4193	0.4834
Fetus image	$\sigma = 0.1$	PSNR	18.58	18.84	18.03	20.83
		SNR	13.6	13.85	13.04	15.84
		SSIM	0.6157	0.6254	0.6381	0.6853
		FOM	0.6847	0.7921	0.8258	0.9211
		EKI	0.3758	0.4935	0.4277	0.7317
	$\sigma = 0.2$	PSNR	16.72	16.67	17.15	19.72
		SNR	11.75	11.69	12.16	14.73
		SSIM	0.5689	0.5716	0.6164	0.6431
		FOM	0.6741	0.7154	0.7276	0.9076
		EKI	0.3951	0.4115	0.4089	0.6852
	$\sigma = 0.3$	PSNR	16.54	15.83	16.38	18.87
		SNR	11.55	10.84	11.39	13.88
		SSIM	0.4763	0.5372	0.5816	0.6103
		FOM	0.6698	0.6631	0.7086	0.9002
		EKI	0.3609	0.3715	0.3730	0.5587
Phantom image	$\sigma = 0.1$	PSNR	23.59	23.97	25.01	27.72
		SNR	11.41	11.79	12.84	15.55
		SSIM	0.7865	0.7754	0.7970	0.8507
		FOM	0.8698	0.4992	0.6494	0.9662
		EKI	0.6885	0.6831	0.6121	0.9265
	$\sigma = 0.2$	PSNR	22.93	22.01	24.12	25.25
		SNR	10.76	9.84	11.95	13.09
		SSIM	0.7389	0.7618	0.7923	0.8267
		FOM	0.6922	0.3631	0.4688	0.8737
		EKI	0.6123	0.5084	0.5799	0.7425
	$\sigma = 0.3$	PSNR	22.41	19.86	23.38	23.13
		SNR	10.23	7.69	11.22	10.97
		SSIM	0.7104	0.7452	0.7813	0.7913
		FOM	0.6472	0.3126	0.4435	0.8632
		EKI	0.5469	0.4412	0.5521	0.7312

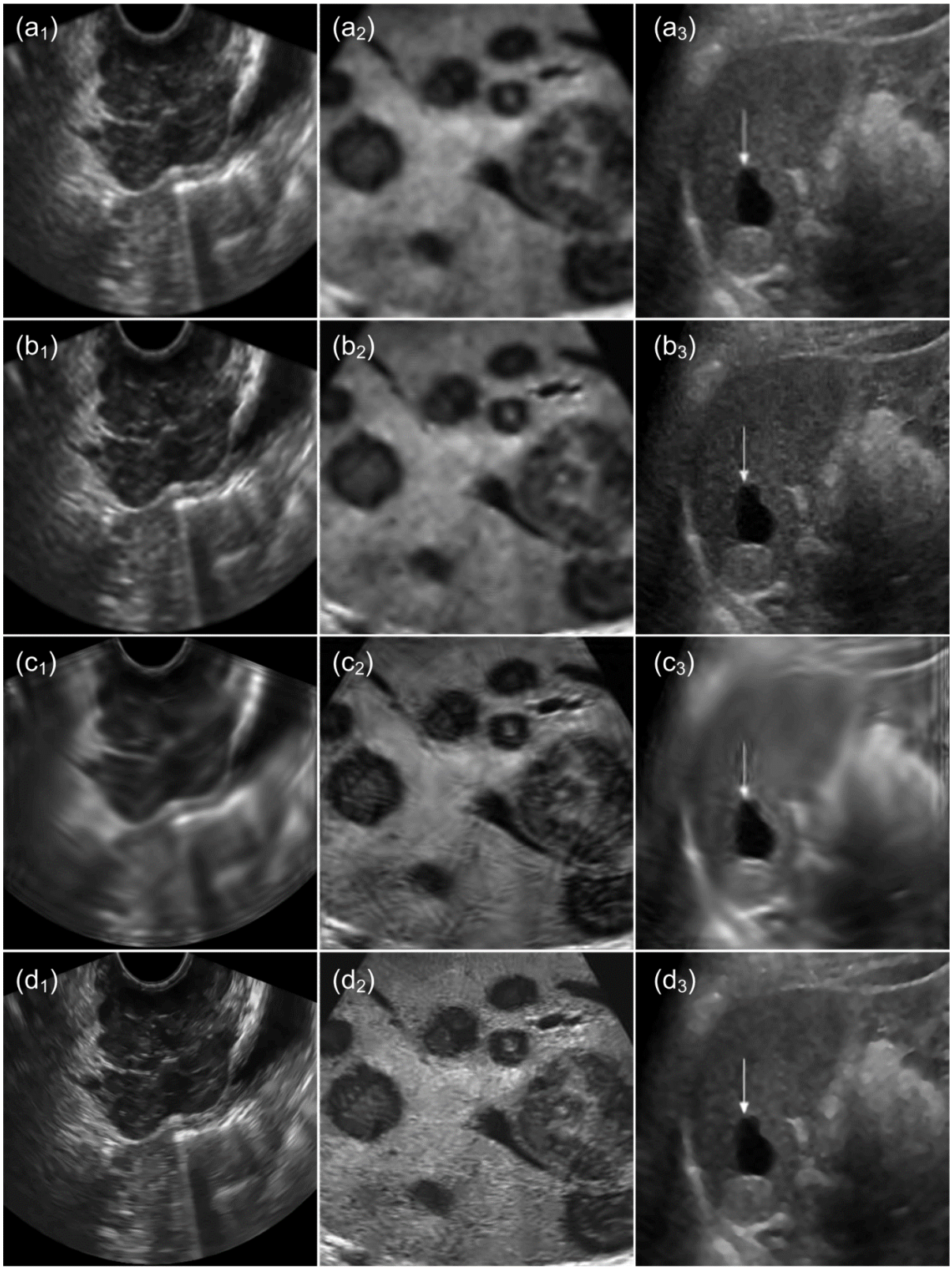

Figure 3.13 Visual comparison of three different ultrasound images, processed by (a) Bilateral filter (b) WT-NS (c) Curvelet (d) Proposed RTNLF-2 approach. Here, 1, 2 and 3 refer to prostate, splenic cyst and multiple liver masses ultrasound images, respectively

comparison illustrated in Figure 3.14, it is observed that the MVR values are also higher produced by the proposed RTNLF-2 approach than others. The averaged MVR value obtained by the RTNLF-2 is 22.17, which is also higher than others including RTNLF-1.

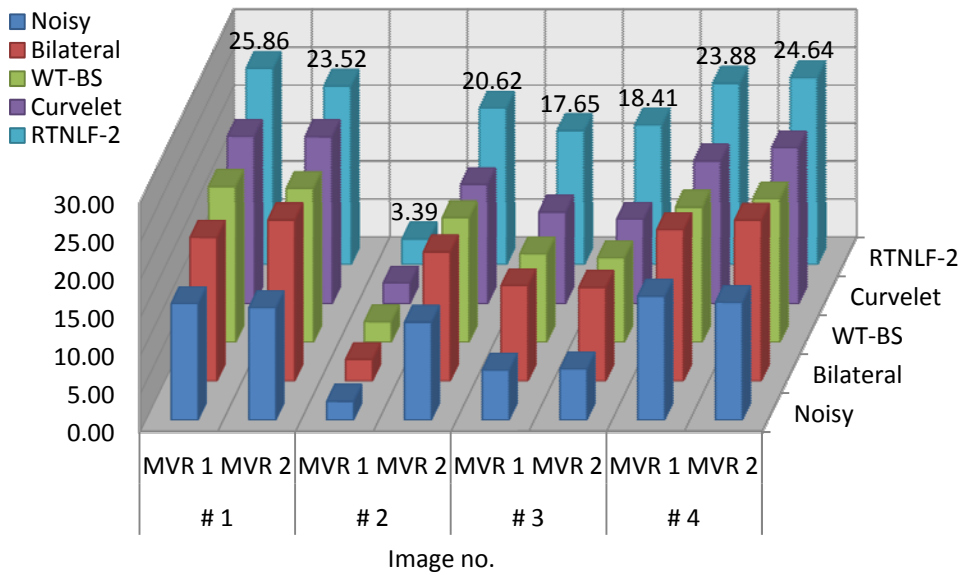

Figure 3.14 Plot of a comparison of the MVR values obtained from the denoising techniques for two different image regions shown in Figure 2.21

3.7.3 Experiment 3: Comparative evaluation of the proposed approaches

In order to investigate the performance of both the proposed approaches, two subsequent experimental objectives are considered, which are presented as follows:

3.1: *Comparison of the proposed RTNLF approach-1 and 2 with other methods for denoising in noisy test images* - In this section, a detailed comparison of the denoising performance of both the proposed RTNLF-1 and RTNLF-2 approaches with existing methods are presented for aforementioned all three different test images that are used to analyze the performance of these methods. The denoising methods used for such purpose are given below:

Method 1: The linear homogeneous mask area filter (LHMAF) as described in [170, 210] with 5×5 square neighborhood window and 15 iterations.

Method 2: The Kuan filter as described in [139].

Method 3: Anisotropic diffusion filter (ADF) as described in [186] with 50 iterations and $\tau = 0.25$.

Method 4: Fourth order PDE filter (FOPDEF) as described in [269] with 250 iterations, $k = 0.5$ and time step $\Delta t = 0.25$.

Method 5: The SRAD (speckle reducing anisotropic diffusion) approach as discussed in [266] with second diffusivity equation, 35 averaged iterations and $\tau = 0.2$.

Method 6: Nonlinear complex diffusion filter (NCDF) as described in [100] with $\theta = \pi/30$ and $\kappa = 20$.

Method 7: Improved adaptive complex diffusion (INCDF) as described in [20] with $\tau_{max} = 10s$, $\kappa_{min} = 2$, $\kappa_{max} = 28$, and $\theta = \pi/30$.

Method 8: A wavelet thresholding approach based on generalized Gaussian distribution (WT-GGD) assumption for noise free coefficients of a logarithmic transformed medical image with

the threshold parameter (T) which depends on the standard deviation of noise and subband variance [111]. Four level decomposition is considered using bior 6.8 wavelet [234]

Method 9: The squeez box filter (SBF) as described in [232] with 7×7 square window and 500 iterations.

Method 10: A nonlinear total variation filtering approach (TVF) [47] as described in chapter 2.

Method 11: The proposed RTNLF-1 as discussed in this chapter.

Method 12: The proposed RTNLF-2 as discussed in this chapter.

To perform this experiment, same kidney, fetus and phantom images are used as testing images degraded by three different noise levels $\sigma = 0.1,\ 0.2$ and 0.3, respectively. The outcomes of kidney images processed by the various denoising methods corresponding to $\sigma = 0.1$ are presented in Figure 3.15. From these figures, it is observed that the proposed RTNLF-1 and RTNLF-2 methods provide better quality of images by suppressing a good amount of the speckle noise compared to others. With the proposed method, the TVF method also produces a considerable quality of image, but some information is lost during the TVF process. Apart from the visual assessment, Table 3.12 summarizes all the performance measures evaluated by all the twelve different methods at three different noise levels. From the objective results listed in Table 3.12, it is observed that the proposed RTNLF-1 achieves approx 45.67%, 28-37%, 26.3-31.84%, 11.72-18.4%, 4.46-8.66%, 9.77-11.42%, 3.4-9.07%, 5.6-8.7%, 4.32-7.83% and 1.25-8.7% higher PSNR values and 100%, 55.7-78.43%, 54.67-65.09%, 21.66-33.89%, 8.17-16.44%, 17.8-23%, 5.92-15.71%, 9.97-14.71%, 7.64-13.37% and 2.15-14.71% higher SNR values than the LHMAF, Kuan, ADF, FOPDEF, SRAD, NCDF, INCDF, WT-GGD, SBF and TVF methods, respectively. The proposed RTNLF-1 approach also achieves approx 7.76-11.71%, 5.07-24.87%, 4.88-9.28%, 5.7-8.99%, 10.9-13.08%, 16.19-23.3%, 4.26-9.54%, 5.37-5.94%, 6.5-7.3% and 18.29- 20.4%

Table 3.12 Image quality measures obtained by different denoising techniques for the processed kidney images

Metrics	$\sigma = 0.1$				$\sigma = 0.2$				$\sigma = 0.3$			
Methods	PSNR	SNR	SSIM	EKI	PSNR	SNR	SSIM	EKI	PSNR	SNR	SSIM	EKI
LHMAF	19.29	8.67	0.7406	0.3235	18.55	7.94	0.7151	0.3177	18.07	7.44	0.6822	0.3177
Kuan	21.84	11.22	0.7596	0.3333	20.03	9.41	0.6770	0.3150	19.37	8.75	0.6103	0.3046
ADF	21.74	11.11	0.7610	0.3181	20.79	10.17	0.7190	0.3041	20.46	9.84	0.6974	0.3011
FOPDEF	23.95	13.33	0.7323	0.3734	23.15	12.54	0.7249	0.3293	23.13	12.51	0.7208	0.3291
SRAD	25.86	15.24	0.7197	0.4598	25.04	14.42	0.6944	0.3332	24.69	14.07	0.6873	0.3211
NCDF	25.22	14.61	0.6869	0.4277	24.27	13.65	0.6368	0.3139	23.54	12.92	0.6256	0.3024
INCDF	26.84	16.22	0.7286	0.4962	25.13	14.51	0.7531	0.3234	24.99	14.37	0.7197	0.4029
WT-GGD	25.85	15.23	0.7574	0.4664	25.74	15.12	0.7412	0.4305	24.47	13.84	0.7215	0.4294
SBF	26.23	15.61	0.7438	0.3719	25.42	14.81	0.7371	0.3397	24.77	14.14	0.7123	0.3242
TVF	25.85	15.23	0.6747	0.4149	25.65	15.03	0.6527	0.4036	25.52	14.90	0.6331	0.3931
RTNLF-1	28.10	17.47	0.7981	0.5175	27.41	16.79	0.7852	0.4811	25.84	15.22	0.7621	0.4743
RTNLF-2	28.69	18.07	0.8284	0.5425	27.68	17.05	0.7915	0.4926	26.44	15.82	0.7658	0.4834

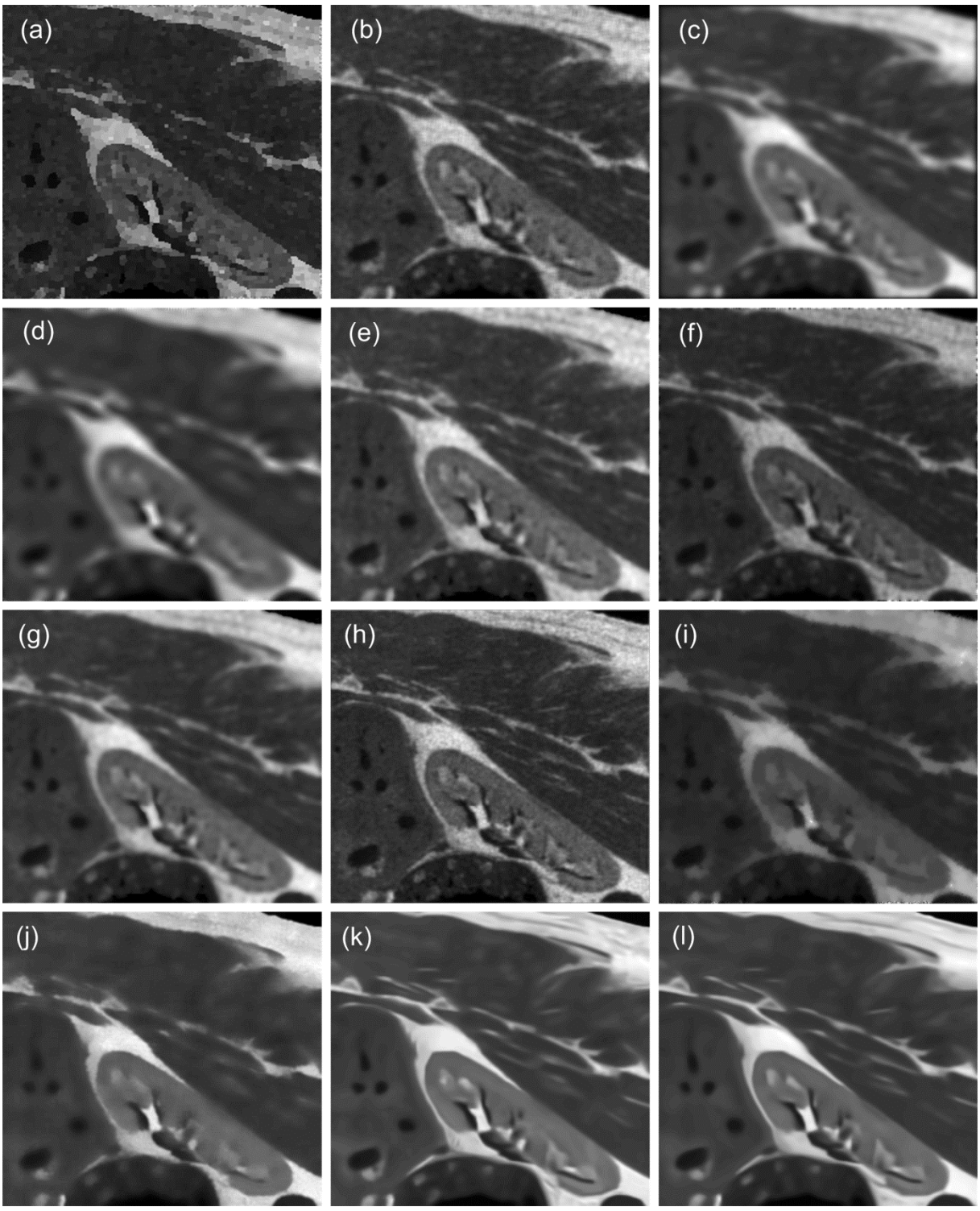

Figure 3.15 Visual comparison of kidney image denoised by (a) LHMAF (b) Kuan (c) ADF (d) FOPDEF (e) SRAD (f) NCDF (g) INCDF (h) WT-GGD (i) SBF (j) TVF (k) Proposed RTNLF-1 (l) Proposed RTNLF-2

higher SSIM values and 49.29-59.97%, 52.73-55.71%, 57.52-62.68%, 38.59-46.1%, 12.55-47.71%, 21-56.85%, 4.29-48.76%, 10.46-11.75%, 39.15-46.3% and 19.2-24.73% larger the EKI values than the methods 1-10, respectively. From these results, it is also observed that the diffusion based methods, WT-GGD, SBF and TVF method are capable to suppress the noise at each level, but the problem of losing edge information still exists and it becomes

larger, if noise level is increased. Besides this, the proposed RTNLF-2 method produces 0.99-2.32%, 1.55-3.94%, 0.8-3.8%, 1.92-4.83% higher the PSNR, SNR, SSIM and EKI values than the RTNLF-1 method.

In another assessment of fetus image illustrated in Figure 3.16, the WT-GGD method produces a good quality of fetus image in comparison to the proposed methods. The output image produced by the SBF is blurred. By visualizing the denoised fetus images, it is seen that the proposed RTNLF-2 approach is more capable to provide better quality of images than the RTNLF-1. The diffusion methods are also reliable to remove the speckles, but at the cost of removing the edge information. All these subjective outcomes are supported by some objective measures as listed in Table 3.13. By analyzing these results, it is observed that the

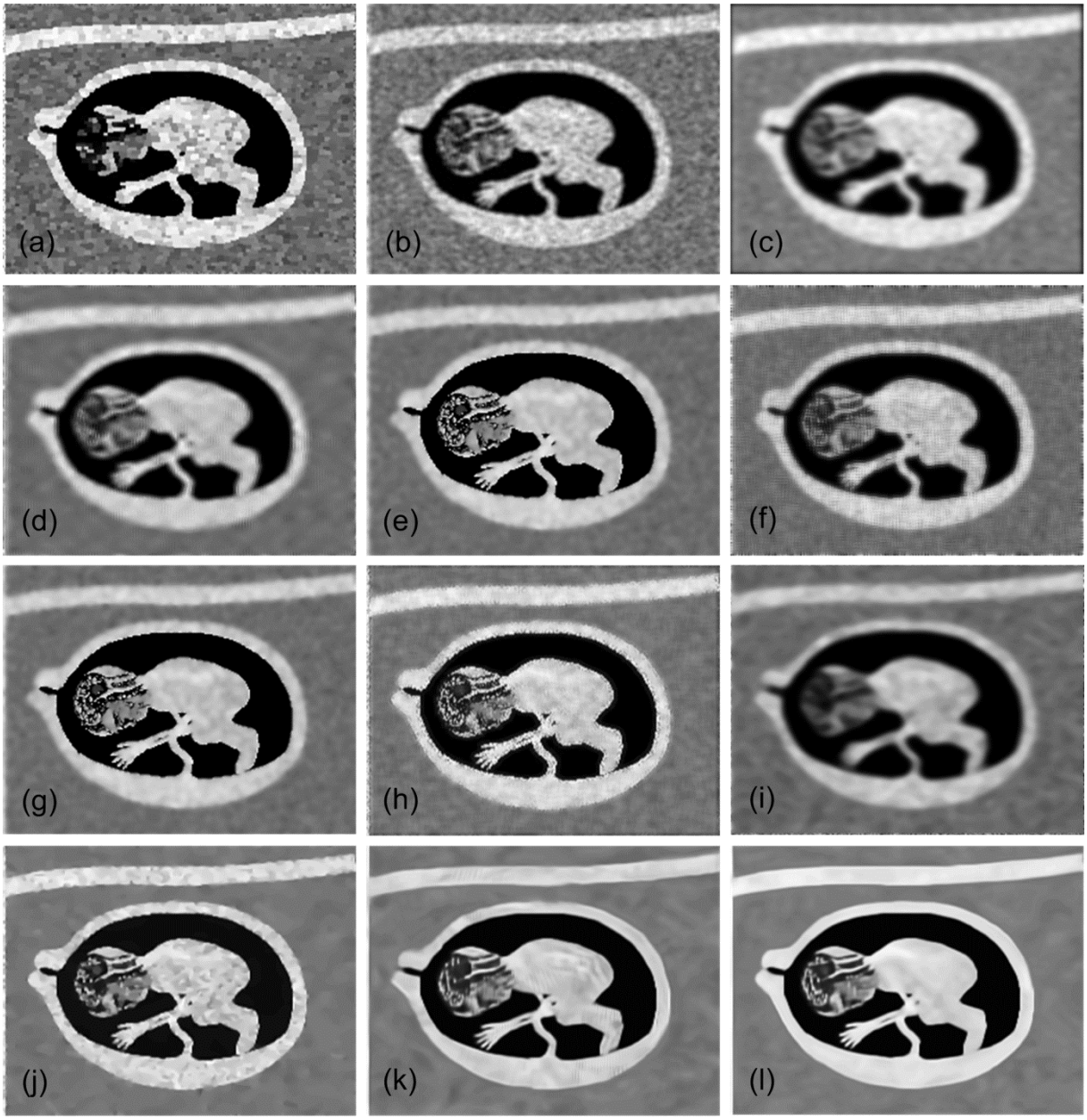

Figure 3.16 Visual comparison of fetus image denoised by (a) LHMAF (b) Kuan (c) ADF (d) FOPDEF (e) SRAD (f) NCDF (g) INCDF (h) WT-GGD (i) SBF (j) TVF (k) Proposed RTNLF-1 (l) Proposed RTNLF-2

proposed RTNLF-2 approach produces approx 1.17-3.06%, 1.54-4.2%, 0.3-2.1% and 1.99-4.02% higher PSNR, SNR, SSIM and EKI values than the RTNLF-1 approach. The RTNLF-2 also achieves approx 80-95% higher EKI value than the SBF and TVF methods. It also gains approx 5.91-8.95%, 8.15-12.48%, 3.49-8.06%, 19.12-56.06% higher PSNR, SNR, SSIM and EKI values than the WT-GGD method. Apart from this, the proposed RTNLF-1 also gains better results than other aforementioned denoising methods 1-10 such as diffusion, WT_GGD, SBF and TVF based approaches.

The subjective results of another investigation of the phantom image degraded by speckle noise with $\sigma = 0.3$, processed by all these methods are shown in Figure 3.17. From the visual results, it is observed that the ADF, SRAD, INCDF, WT-GGD and TVF methods are capable to remove the speckle noise along with the proposed methods. As the noise level $\sigma = 0.3$ is concerned, the TVF method provides better quality images than the proposed RTNLF-1 and 2 approaches. This is also reflected in the quantitative results that are shown in Table 3.14. At the noise level $\sigma = 0.3$, the PSNR and SNR values obtained by the TVF method are approx 1.7% and 3.67% higher than the proposed RTNLF-2 method, but the SSIM and EKI values are approx 11.45% and 25.76% lower than the RTNLF-2 approach that reflects the loss of edge information in the TVF process. Besides this, the proposed RTNLF-2 method gains approx 1.2-1.99%, 2.43-3.6%, 0.3-0.92% and 0.87-2.53% higher PSNR, SNR, SSIM and EKI values than the proposed method-1 that also provides approx 5.1%, 9.64%. 22.56%, 42.36% and 3.66%, 7.39%, 17.97%, 23.21% higher PSNR, SNR, SSIM, EKI values than the TVF method for the noise level $\sigma = 0.1$ and 0.2, respectively. Furthermore, both the proposed RTNLF-1 and 2 methods produce 0.7-4.57%, 1.28-9.79%, 0.32-5.38%, 4.64-20.27% and 2.7-5.83%, 4.93-12.46%, 0.62-6.27%, 7.28-21.3% higher PSNR, SNR, SSIM and EKI values than the WT-GGD, respectively.

Table 3.13 Image quality measures obtained by different denoising techniques for the processed fetus images

Metrics	$\sigma = 0.1$				$\sigma = 0.2$				$\sigma = 0.3$			
Methods	PSNR	SNR	SSIM	EKI	PSNR	SNR	SSIM	EKI	PSNR	SNR	SSIM	EKI
LHMAF	15.21	10.22	0.5249	0.3334	12.89	7.91	0.4345	0.3120	10.79	5.81	0.3804	0.2952
Kuan	17.12	12.13	0.4722	0.3580	16.22	11.23	0.3945	0.2944	15.17	10.18	0.3536	0.2754
ADF	17.06	12.08	0.5925	0.3572	15.72	10.73	0.5375	0.3246	15.58	10.59	0.4978	0.3092
FOPDEF	17.63	12.64	0.6573	0.4603	16.39	11.41	0.6200	0.3540	15.82	10.81	0.5344	0.3188
SRAD	18.33	13.34	0.6286	0.3828	16.66	11.67	0.5512	0.3866	15.39	10.40	0.4445	0.3625
NCDF	17.63	12.64	0.5683	0.3337	16.11	11.12	0.4789	0.3498	15.56	10.57	0.4334	0.3131
INCDF	18.69	13.71	0.6381	0.4714	16.85	11.86	0.5893	0.4066	15.94	10.95	0.5079	0.3863
WT-GGD	19.20	14.21	0.6537	0.5722	18.62	13.62	0.6214	0.5752	17.32	12.34	0.5648	0.3580
SBF	17.95	12.97	0.6482	0.4072	16.79	11.80	0.6194	0.3646	16.34	11.36	0.5613	0.3154
TVF	17.84	12.85	0.5854	0.3696	17.01	12.02	0.5631	0.3531	16.13	11.14	0.5325	0.3105
RTNLF-1	20.59	15.60	0.6712	0.7174	19.38	14.39	0.6397	0.6587	18.31	13.32	0.6085	0.5464
RTNLF-2	20.83	15.84	0.6853	0.7317	19.72	14.73	0.6431	0.6852	18.87	13.88	0.6103	0.5587

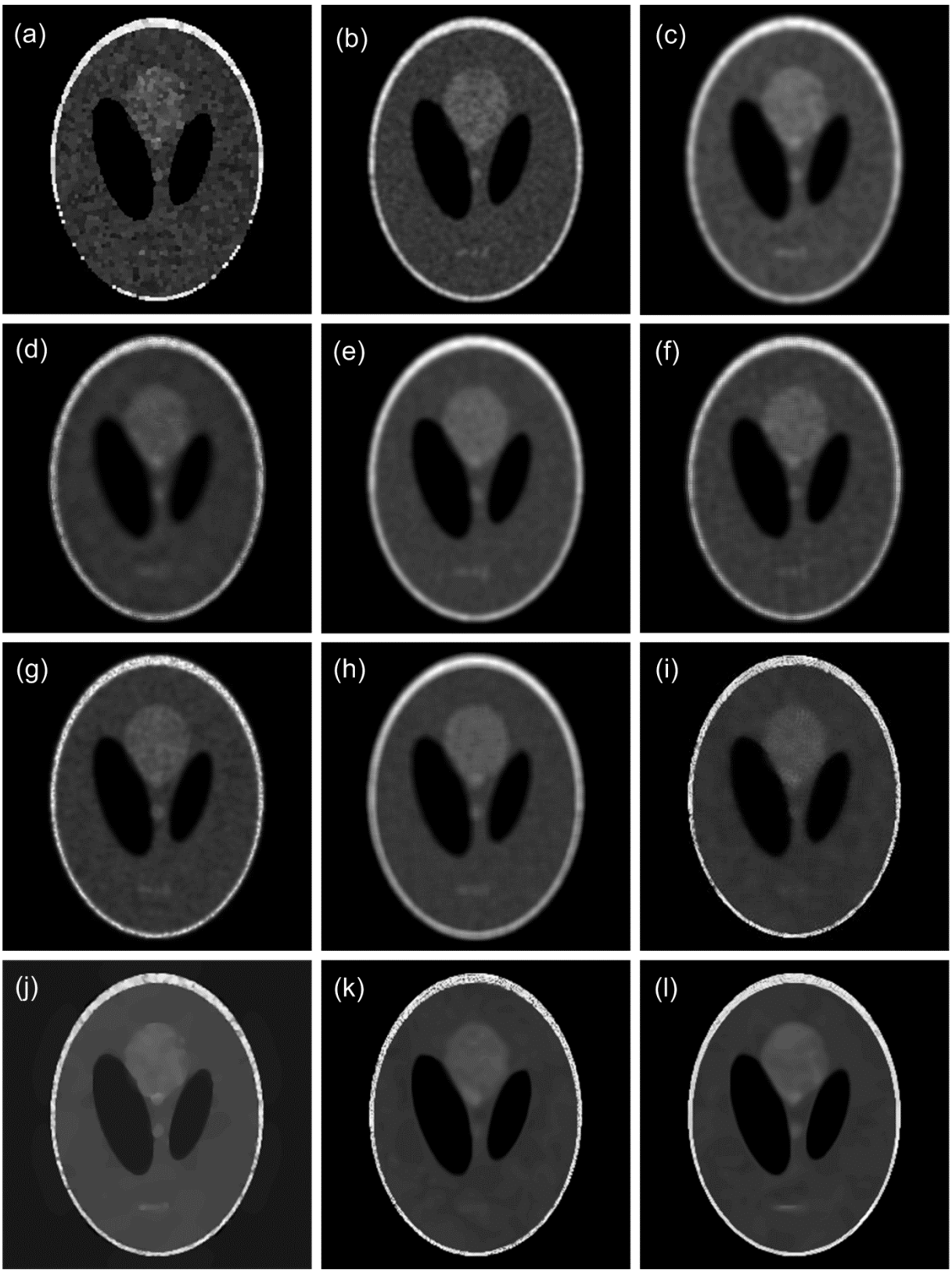

Figure 3.17 Visual comparison of phantom image denoised by (a) LHMAF (b) Kuan (c) ADF (d) FOPDEF (e) SRAD (f) NCDF (g) INCDF (h) WT-GGD (i) SBF (j) TVF (k) Proposed RTNLF-1 (l) Proposed RTNLF-2

Moreover, both the proposed RTNLF-1 and 2 achieve better noise suppression and edge preservation performance, but the RTNLF-2 approach outperforms the RTNLF-1.

Table 3.14 Image quality measures obtained by different denoising techniques for the phantom images

Metrics	$\sigma = 0.1$				$\sigma = 0.2$				$\sigma = 0.3$			
Methods	PSNR	SNR	SSIM	EKI	PSNR	SNR	SSIM	EKI	PSNR	SNR	SSIM	EKI
LHMAF	21.51	9.33	0.7553	0.3729	19.85	7.67	0.6827	0.3334	18.71	6.55	0.6282	0.3177
Kuan	21.62	9.45	0.7039	0.4476	20.27	8.09	0.6418	0.3391	19.82	7.65	0.6062	0.2978
ADF	21.98	9.81	0.7650	0.7381	21.12	8.95	0.7451	0.5159	19.98	7.81	0.7305	0.3945
FOPDEF	22.43	10.26	0.7760	0.5911	22.07	9.91	0.7614	0.5779	21.81	9.64	0.7599	0.4505
SRAD	22.74	10.57	0.8035	0.5995	22.31	10.14	0.7855	0.5939	22.10	9.92	0.7686	0.5909
NCDF	23.23	11.06	0.7726	0.6998	22.74	10.57	0.7079	0.6086	22.25	10.08	0.6636	0.5376
INCDF	24.52	12.35	0.8224	0.6932	23.68	11.51	0.8071	0.6470	23.06	10.88	0.7718	0.5857
WT-GGD	26.99	14.82	0.8005	0.7637	23.86	11.64	0.7893	0.6921	22.24	10.07	0.7864	0.6162
SBF	24.41	12.24	0.7967	0.5872	22.41	10.26	0.7911	0.5603	21.89	9.71	0.7834	0.5389
TVF	25.86	13.69	0.6883	0.6452	24.07	11.90	0.6944	0.5878	23.20	11.03	0.6986	0.5354
RTNLF-1	27.18	15.01	0.8436	0.9185	24.95	12.78	0.8192	0.7242	22.81	10.64	0.7889	0.7212
RTNLF-2	27.72	15.55	0.8507	0.9265	25.25	13.09	0.8267	0.7425	23.13	10.97	0.7913	0.7312

3.2: *Comparison of the proposed RTNLF approach-1 and 2 with other methods for speckle reduction in the real US images* - In this experiment, another detailed comparison is done for real US images as utilized in chapter 2, but processed by all twelve denoising methods as discussed above. The processed prostate US images are shown in Figure 3.18. Another two denoised splenic cyst and multiple liver masses US images are shown in Figure 3.19 and Figure 3.20, respectively. From these visual results, it is observed that the proposed RTNLF-1 and RTNLF-2 methods produce better quality of the US images than others. The outcomes of the diffusion based methods get blurred and the resolution of the processed US images is very poor, but in case of the multiple liver masses, the SRAD achieves good noise suppression results, but all the edge information is lost during the smoothing process. The resultant US images obtained from the WT-GGD are not able to produce good results. Besides it, the TVF approach is capable to remove speckles from the US images, but it suffers from the loss of information that is also more important for the clinical diagnosis. The proposed RTNLF-2 approach outperforms the others, including the proposed RTNLF-1 approach. The validation of the visual results of the US images processed by the different denoising methods is very difficult as discussed in the previous chapter. Moreover, for the validation of the visual results, the MVR values as discussed in the previous chapters are estimated for all the US images with two different image regions marked on them. Out of them, the four different US images are considered to evaluate the MVR values for both the regions 1 and 2 marked by the red and blue rectangle, respectively shown in Figure 2.21 as MVR1 and MVR2. The results are presented in a bar graph as shown in Figure 3.21. From the bar graphs, it is observed that the proposed RTNLF-1 and RTNLF-2 methods gain higher

MVR values than the others. Moreover, the proposed RTNLF-2 exhibits its superiority by providing the highest MVR value.

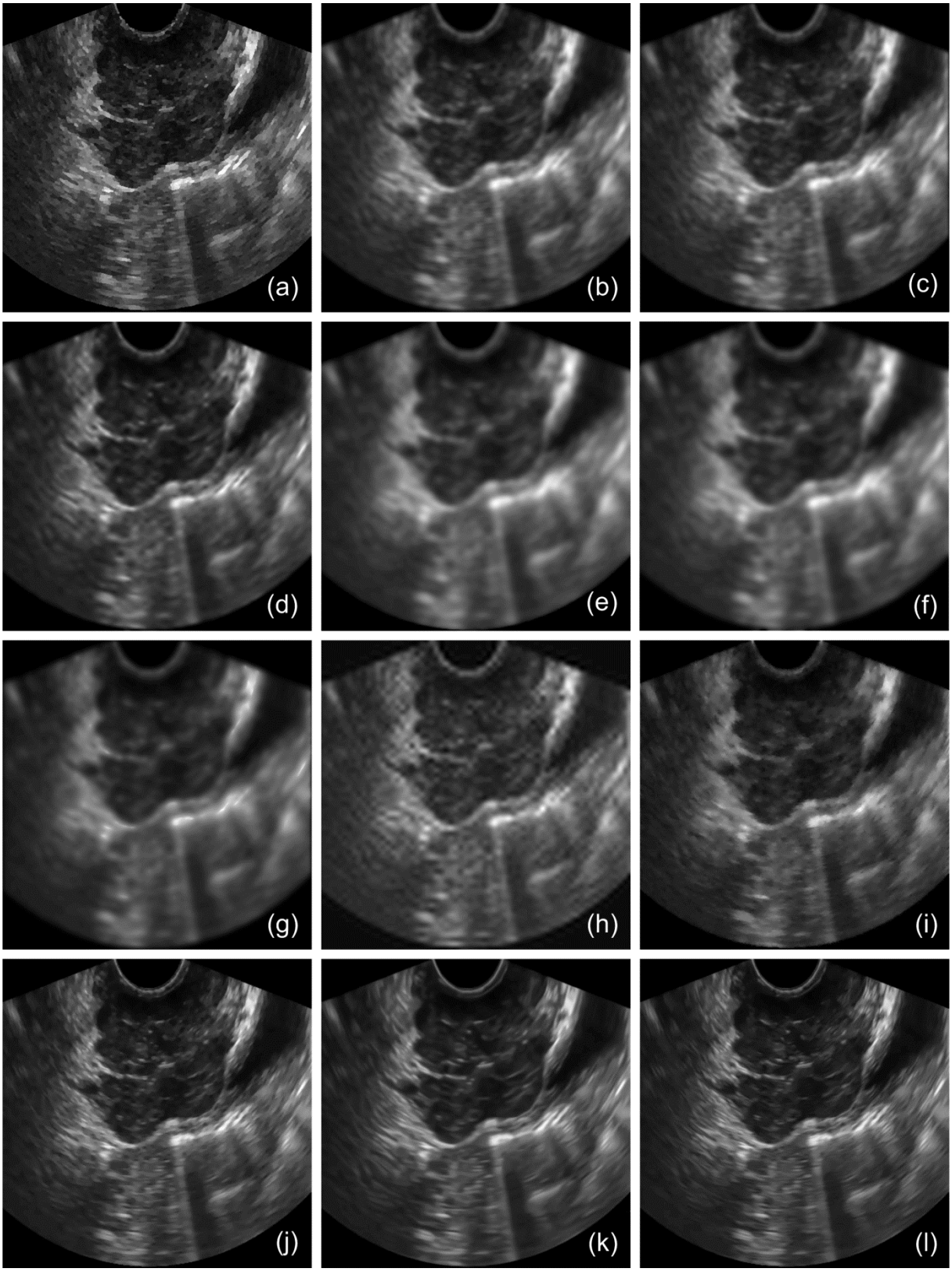

Figure 3.18 Visual comparison of prostate ultrasound image processed by the (a) LHMAF (b) Kuan (c) ADF (d) FOPDEF (e) SRAD (f) NCDF (g) INCDF (h) WT-GGD (i) SBF (j) TVF (k) Proposed RTNLF-1 (l) Proposed RTNLF-2

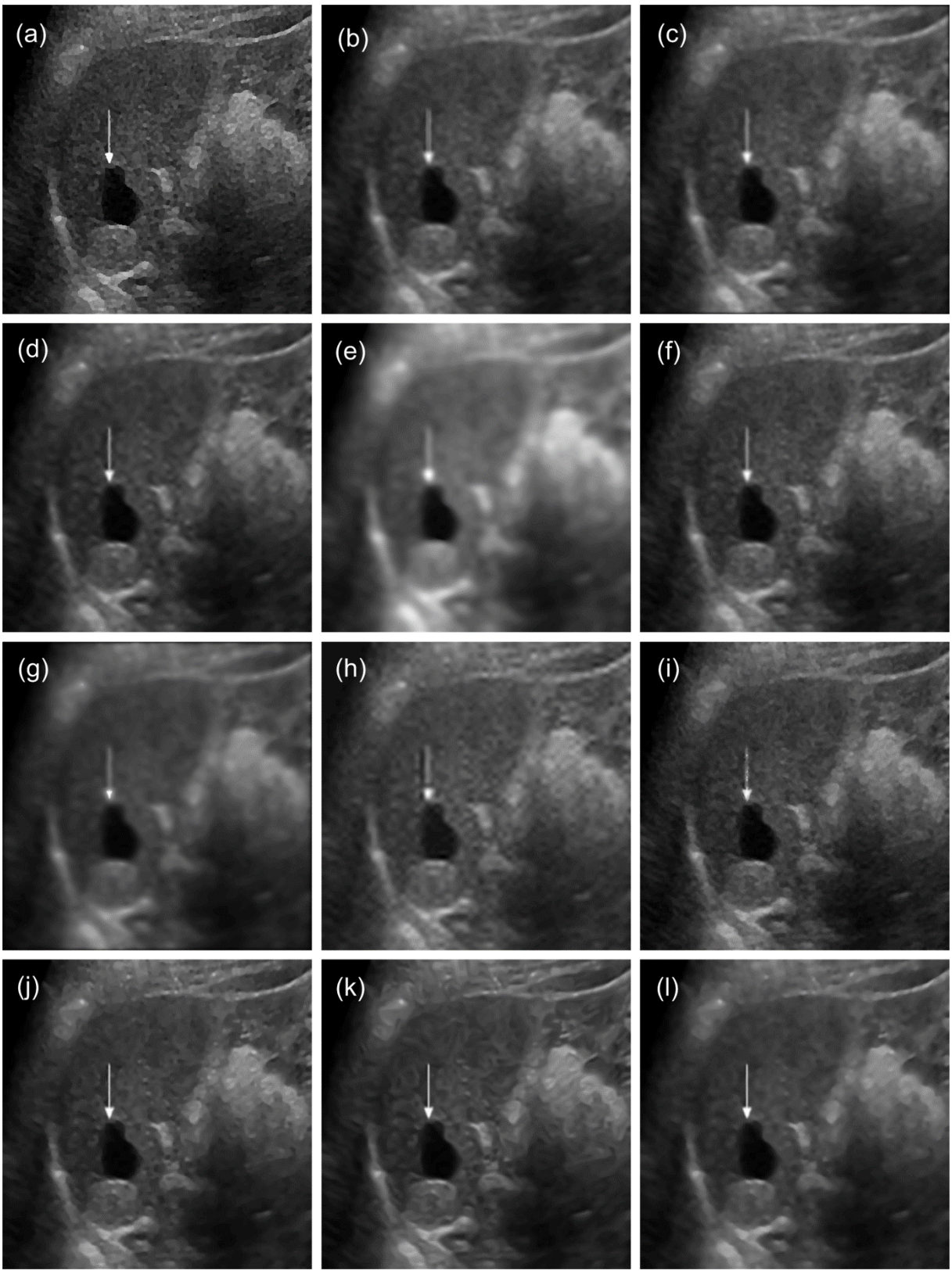

Figure 3.19 Visual comparison of splenic cyst ultrasound image processed by the (a) LHMAF (b) Kuan (c) ADF (d) FOPDEF (e) SRAD (f) NCDF (g) INCDF (h) WT-GGD (i) SBF (j) TVF (k) Proposed RTNLF-1 (l) Proposed RTNLF-2

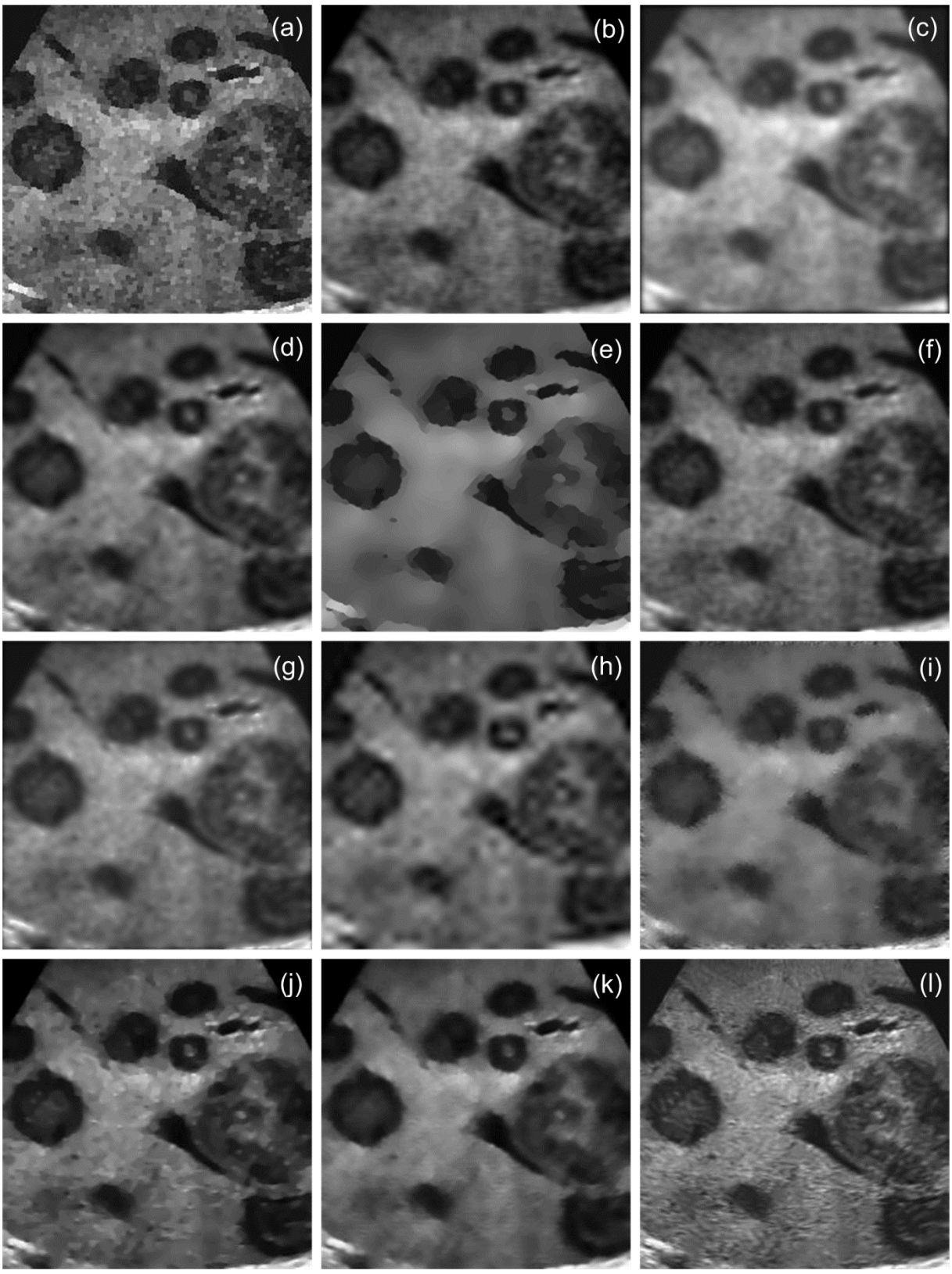

Figure 3.20 Visual comparison of multiple liver masses ultrasound image processed by the (a) LHMAF (b) Kuan (c) ADF (d) FOPDEF (e) SRAD (f) NCDF (g) INCDF (h) WT-GGD (i) SBF (j) TVF (k) Proposed RTNLF-1 (l) Proposed RTNLF-2

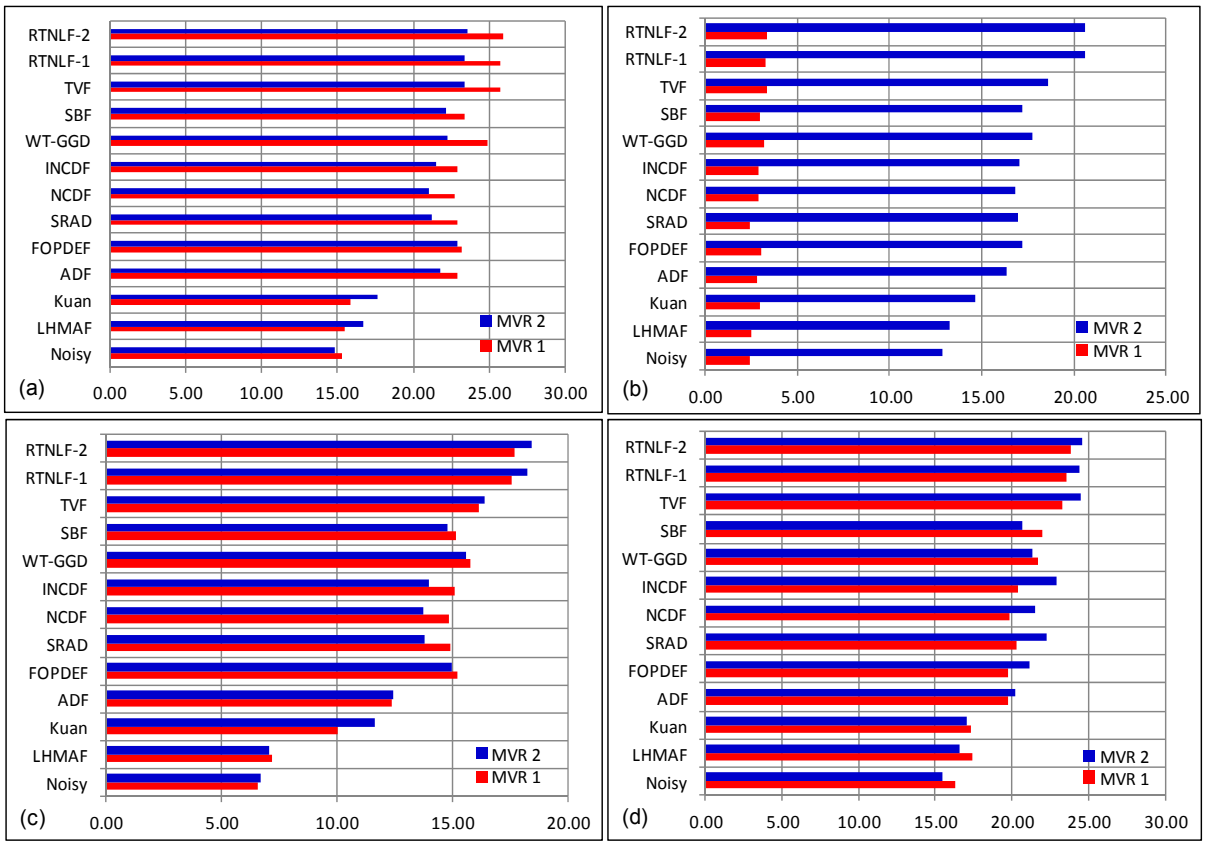

Figure 3.21 Comparison between the MVR values obtained from the different denoising methods for two image regions shown in Figure 2.21

In addition, Table 3.15 shows the MVR values (mean ± standard deviation) estimated for all 100 measurements that are conducted on fifty different US images in which two measurements at two different regions for each images are considered and the results mentioned in Table 3.15 exhibit the superiority of the proposed methods in the effective speckle reduction as compared to the others.

Table 3.15 Performance comparison of the various denoising methods with both the proposed RTNLF approaches-1 and 2 using the averaged MVR values over 100 different regions marked on 50 different ultrasound images

S. No.	Methodology	MVR
1	Noisy	14.04 ± 3.04
2	LHMAF	15.19 ± 3.46
3	Kuan	16.56 ± 4.98
4	ADF	18.26 ± 4.23
5	FOPDEF	19.27 ± 4.46
6	SRAD	19.45 ± 3.97
7	NCDF	19.32 ± 3.69
8	INCDF	21.05 ± 3.15
9	WT-GGD	20.49 ± 4.57
10	SBF	20.12 ± 4.87
11	TVF	21.45 ± 4.95
12	Proposed approach-1	21.98 ± 3.93
13	Proposed approach-2	22.17 ± 4.33

3.8 Summary

In this chapter, two different denoising approaches are proposed using the NLBF and thresholding methods such as the NS and BS algorithms, named as RTNLF-1 and RTNLF-2, respectively. In the proposed methods, the features of the RT are used that also provides the multiscale and direction analysis of the images. Besides it, the features of the bilateral filter applied on the low frequency approximation coefficients are utilized to suppress the large amplitude noise components and thresholding approaches provide the approximated threshold coefficients which improve the denoising efficiency with better edge preservation. The proposed method is also analyzed to improve not only the perceptual quality of the images, but also to preserve more edge information. From the experimental results, it is observed that the proposed approaches do not only achieve higher SNR and PSNR values but also improves the SSIM and EKI values. The higher SNR and PSNR values with larger EKI and SSIM values indicate that the noise suppression is neither at the cost of blurring the edges nor the loss of edge information. A detailed comparative study with the proposed RTNLF-1 and 2 is also presented in the last section of this chapter, which depicts the superiority of the proposed approaches. But in all the experimental results, one pattern is observed that among all the other denoising methods, the TVF approach is good. This method has an ability to suppress the speckle noise, but noise reduction is performed with the loss of edge information that means some edge information is lost within the noise residual. Furthermore, it is concluded that the proposed method ensures an improvement in effective suppression of speckle noise and preservation of more edges, thus providing the despeckled images with good visual appearance.

CHAPTER 4: REMNANT APPROACH FOR ADAPTIVE FUSION BASED NOISE FILTERING

This chapter presents a remnant approach for adaptive fusion based noise filtering, which is used to suppress the speckle noise in the ultrasound images. The present method utilizes both the features of the shearlet transform and total variation algorithm. In the proposed method, three different denoised images processed by the total variation approach, shearlet thresholding, separately and the edge structured information recovered from the remnant of the total variation filtering approach, are fused adaptively. For such purpose, different weights are evaluated from the different variance map of individual denoised image and the edge extracted information from the remnant of total variation approach. The performance of the proposed remnant approach are discussed in both the subjective and objective manner and a comparative study has also been presented in the last section of this chapter for investigating the noise reduction performance obtained by the proposed method.

4.1 Introduction

Imaging systems and sub-resolution scatterers are two main factors that degrade the quality of the US medical images and thus cause a problem for the radiologist to discriminate the fine details of the images during the diagnostic examinations. As a result, image processing for reducing the speckle noise and blurring is a critical pre-processing step. From the previous chapters, it is analyzed that the noise reduction with better edge preservation improves the quality of the US images, thus leads to increase the accuracy of the diagnostic process. In the chapter 3, two different approaches have been discussed with their despeckling performances. Based on both the subjective and objective analysis, it is observed that the proposed approaches presented in the chapter 3 have produced better denoising results. However, at a higher noise level, the TVF approach outperforms them in terms of noise suppression parameters such as the SNR and PSNR values, but it suffers from the loss of edge information by achieving lower EKI values. Based on the comparative analysis of several denoising methods presented in chapter 2, the ST produces better denoising results, especially in terms of edge preservation than the curvelet and other methods. The ST based method also produces less visual distortion (fuzzy edges) near the original edges or in the homogeneous region than the CVT based methods. These outcomes concluded from the previous chapters have motivated to address and utilize both the features of the TVF and ST based method in one common remnant based adaptive fusion (RBAF) approach used for noise reduction in the US medical images.

With this motivation, a new concept has been evolved that the disturbed homogenous region by the curvelet and shearlet domain may result in more effective edge preserved image denoising [30]. In chapter 2, the performance of TVF approach has been discussed with the observation of better denoised homogenous region of the image. Thus, it has become a suitable choice for fusing the homogeneous region of the image. Accordingly, in

this chapter, the RBAF approach is introduced to overcome the limitations of the TVF and the ST. In the proposed approach, a fusion algorithm is presented to fuse the information of the images obtained by the TVF approach and ST based method, separately and extracted edges structured information (ESI) from the remnant of the TVF method after denoising by the ST based method.

The subsequent part of this chapter is structured as follows. Next two sections provide the brief idea of ST and TVF methods used to implement the proposed RBAF approach. After that, the proposed RBAF approach and its implementation are discussed. The performance of the proposed RBAF method is also analyzed in the presence of speckle as well as Gaussian noise. Many efforts have been made to evaluate and compare the denoising performance with others in terms of noise suppression and edge preservation.

4.2 Shearlet Transform

To address the limitations of other transformation techniques such as difficult to handle the different singularities available in the images, the ST has been applied to different application in the last few years [57, 83, 84, 149, 153, 264, 285]. Shearlet transform combines the multiscale and direction analysis, separately. Shearlet is very similar to the contourlets introduced by Vetterli et al. [78] except that there is no limitation of the directions like contourlets. Shearlet can also be constructed in discrete domain realized by the combination of Laplacian pyramid (LP) and directional filters bank (DFB) [85, 141, 151]. Firstly, Laplacian pyramid is used to decompose the noisy image into high and low frequency components, then direction filtering is utilized to get the different subbands and different direction shearlet coefficients. Direction filtering is achieved using the shear matrix. In two dimensional space, shearlets are defined as

$$A_{DS} = \{\psi_{j,k,m}(x) = |det\ D|^{j/2}\psi(S^k D^j x - m): j,k \in \mathbb{Z}, m \in \mathbb{Z}^2\} \quad (4.1)$$

where D refers to the anisotropic matrix, S denotes the shear matrix and j, k and m are scale, direction and shift parameter, respectively, ψ refers to a generating function. The D and S both are 2×2 invertible matrices and $|\det S| = 1$. The elements of the system are called composite wavelet, if it forms a Parseval frame for $L^2(\mathbb{R}^2)$, which is also an affine like system. For any $f \in L^2(\mathbb{R}^2)$

$$\sum_{j,k,m} |\langle f, \psi_{j,k,m}\rangle|^2 = \|f\|^2 \quad (4.2)$$

The anisotropic dilation matrix $\begin{bmatrix} d & 0 \\ 0 & d^{1/2} \end{bmatrix}$ or $\begin{bmatrix} d^{1/2} & 0 \\ 0 & d \end{bmatrix}$, where $d > 0$ controls the scale of shearlets, which ensures that the frequency support of shearlets becomes increasingly stretched at finer scales. The shear matrix $S = \begin{bmatrix} 1 & s \\ 0 & 1 \end{bmatrix}$ or $\begin{bmatrix} 1 & 0 \\ s & 1 \end{bmatrix}$ controls only the direction of shearlets. The shearlet transform function is

$$\psi_{j,k,m}^{(0)}(x) = 2^{j\frac{3}{2}}\psi^{(0)}\left(S_0^k D_0^j x - m\right) \tag{4.3}$$

$$\psi_{j,k,m}^{(1)}(x) = 2^{j\frac{3}{2}}\psi^{(1)}\left(S_1^k D_1^j x - m\right) \tag{4.4}$$

where $j \geq 0, -2^j \leq k \leq 2^j - 1, m \in \mathbb{Z}^2$, $\hat{\psi}^{(0)}(\xi) = \hat{\psi}^{(0)}(\xi_1, \xi_2) = \hat{\psi}_1(\xi_1)\hat{\psi}_2(\xi_2/\xi_1)$ and $\hat{\psi}^{(1)}(\xi) = \hat{\psi}^{(1)}(\xi_1, \xi_2) = \hat{\psi}_1(\xi_2)\hat{\psi}_2(\xi_1/\xi_2)$

For any $(\xi_1, \xi_2) \in D_0$, $D_0 = \left\{(\xi_1, \xi_2) \in \widehat{\mathbb{R}}^2 : |\xi_1| \geq \frac{1}{8}, |\xi_2/\xi_1| \leq 1\right\}$ and $D_1 = \left\{(\xi_1, \xi_2) \in \widehat{\mathbb{R}}^2 : |\xi_2| \geq \frac{1}{8}, |\xi_1/\xi_2| \leq 1\right\}$ consist of supports of $\psi_{j,k,m}^{(0)}(x)$ and $\psi_{j,k,m}^{(1)}(x)$. The decomposition of the US images in both the horizontal and vertical cone is shown in Figure 4.1 (a) and (b), respectively.

4.3 Shearlet Thresholding

In the recent years, various thresholding (shrinkage) schemes are considered for image denoising. The thresholding scheme provides the threshold coefficients by comparing the transformed coefficients against a threshold to remove the noise from a signal, while preserving the most important information of the original signal. In the present study, the hard thresholding is performed using the ST and the cycle spinning (CS) approach, independently in each noisy shearlet coefficient. The fundamental principle of hard thresholding using the ST is same as the thresholding used with the WT and CVT. To achieve the threshold coefficients from the noisy ST coefficients $s^{ST}(x, y)$, the thresholding expression is given as

$$\hat{s}^{ST}(x, y) = \begin{cases} s^{ST}(x, y), & |s^{ST}(x, y)| \geq K\sigma_1\sigma_2 \\ 0, & \text{otherwise} \end{cases} \tag{4.5}$$

where $\hat{s}^{ST}(x, y)$ is the estimator of unknown noiseless coefficients using the hard thresholding, σ_1 is the standard deviation of the noisy images, σ_2 is the standard deviation of noisy subband at each scale decomposed using the ST. The noise variance of each subband is estimated from the noisy shearlet coefficients using Monte Carlo technique [225].

$$\sigma_2 = \sqrt{\frac{1}{L_a L_b}\sum_{x=1}^{L_a}\sum_{y=1}^{L_b} s^{ST}(x, y)s^{ST*}(x, y)} \tag{4.6}$$

where $s^{ST*}(x, y)$ is the complex conjugate of $s^{ST}(x, y)$ and $L = L_a \times L_b$ is the size of the subband at each scale. For each high frequency shearlet subbands, the scale dependent parameter K is chosen as 4 for first scale and 3 for others.

In this present study, hard thresholding combined with the concept of CS approach [10] is applied to every detailed coefficients of shearlet decomposition for denoising purpose. Firstly, the CS approach is applied to the noisy image to get the shifted version of a noisy image within a specified range of circular shifts that depend on the length of the input vector scale $\gamma(i)$. The total number of translations along the horizontal axis is equal to 2^{L-i} and $2^{L-\gamma(i)}$ for the vertical axis, respectively, where *L* denotes the length of the input vector, $\gamma(i)$

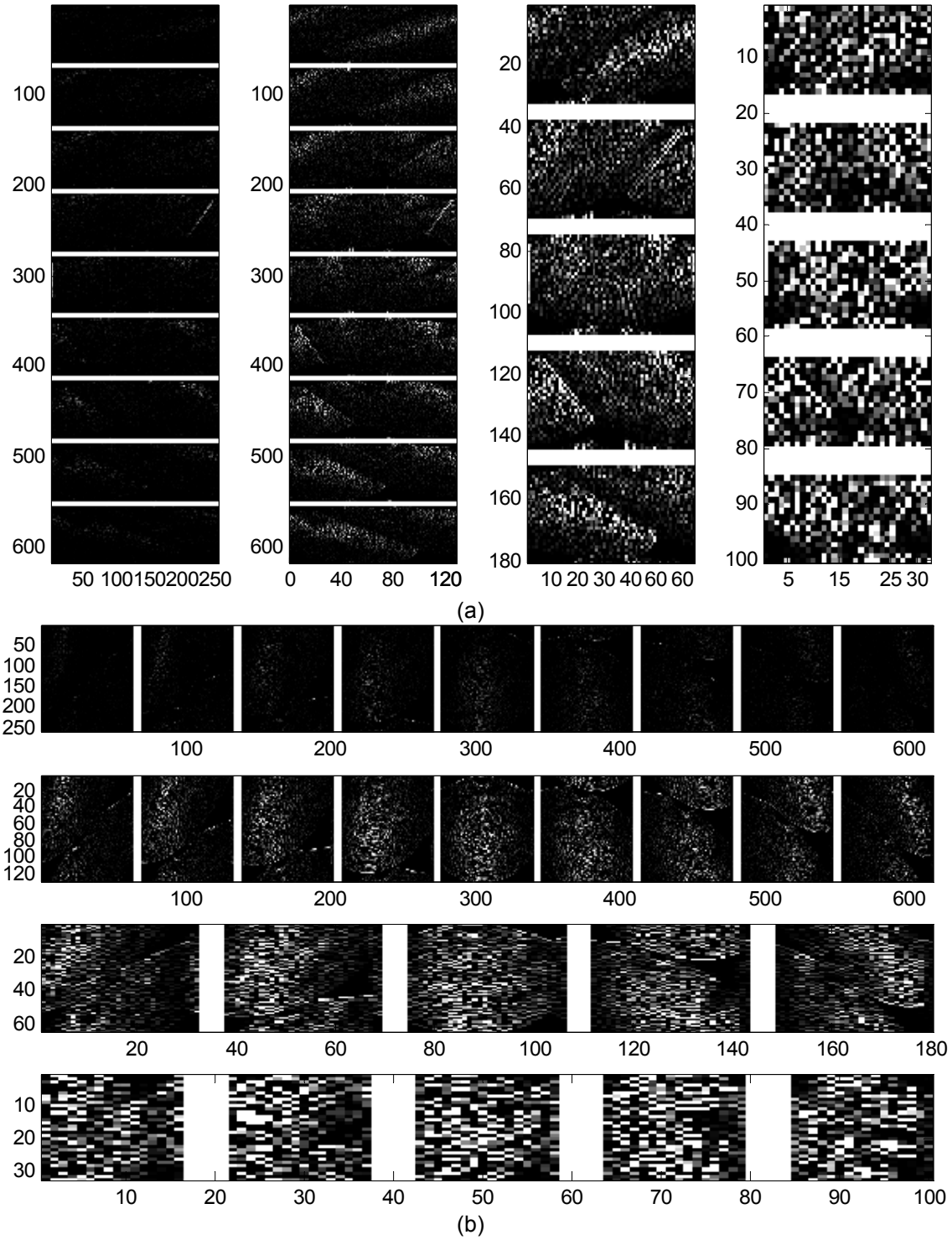

Figure 4.1 Shearlet decomposed coefficients of an ultrasound image for the (a) Horizontal cone (b) Vertical cone

refers to the size of the shearlet along the scale i.e. scale value and i represents as an index. Subsequently, the ST is applied to the shifted version of the noisy image $s(x, y)$ to get noisy shearlet coefficients $s^{ST}(x, y)$. After applying the thresholding scheme on the noisy shearlet coefficients, the inverse ST is applied on the threshold coefficients and finally resulting denoised images are shifted back to original position and the results are averaged out. In the case of multiplicative noise, such process is applied on the log transformed image and at

last, exponential operator is applied to reconstruct the denoised image. A summary of the algorithm is given as follows:

Step 1: Apply the circular shifts on the noisy image.

$$s'(x,y) = circular\_shift\big(s(x,y), [x_{shift}, y_{shift}]\big) \quad (4.7)$$

The number of shifts depends on the length of the input vector scale.

Step 2: Perform the multiscale decomposition of the shifted version of an image using the ST to obtain the noisy ST coefficients.

$$s^{ST}(x,y) = ST\big(s'(x,y)\big) \quad (4.8)$$

Step 3: Apply the thresholding scheme on the noisy ST coefficients to get the threshold ST coefficients.

$$\hat{s}^{ST}(x,y) = \Theta_{thr}\big(s^{ST}(x,y)\big) \quad (4.9)$$

Step 4: Invert the multiscale decomposition to reconstruct the denoised image.

$$\hat{s}'(x,y) = ST^{-1}\big(\hat{s}^{ST}(x,y)\big) \quad (4.10)$$

Step 5: After taking the ST^{-1}, the inverse shift is performed and resulting denoised image are shifted back to the original position and then the translated results are averaged to get the approximated image.

$$\hat{s}(x,y) = circular\_shift\big(\hat{s}'(x,y), [-x_{shift}, -y_{shift}]\big) \quad (4.11)$$

4.4 Total Variation Filtering

As discussed in section 2.5.7 of chapter 2, the TVF algorithm proposed by Rudin, Osher and Fatemi is used as a regularization criterion for image denoising [204]. Several methods have been presented for the minimization of the ROF function. In the present study, a projection based approach presented by Chambolle [47] is used to minimize the ROF function. All the mathematical formulations involved in the implementation of the TVF method have already been presented in the chapter 2. In the implementation of the TVF method, the most important task is to estimate the weighting parameter (λ). In the present work, the simple automatic approach for the selection of this parameter has been used. To estimate the parameter λ, the implementation of the TVF algorithm is given as follows:

Step 1: Start with the noisy image $s = s(x,y)$, a weighting parameter $(\lambda > 0)$ and algorithm tolerance $(T > 0)$.

Step 2: Initialize $p^0 = 0$.

Step 3: Calculate the values $a = \nabla\left(div\big(p^i - s/\lambda\big)\right)$ for all the pixel values (x,y) in the image.

Step 4: Update the values of $p^{i+1} = \frac{p^i + \tau a}{1 + \tau|a|}$ for all the pixel values (x,y) in the image.

Step 5: Evaluate $\hat{s} = s - \lambda div(p^{i+1})$ and $b = s - \hat{s} = \lambda div(p^{i+1})$.

Step 6: Update the values of λ using $c = \|b\| = \|s - \hat{s}\|$ and $\lambda' = \left(\frac{\sqrt{\sigma L}}{c}\right)\lambda$, where L refers to the total number of pixels and σ denotes the noise variance.

Step 7: Evaluate the value of $\left(p^{i+1} - p^{i}\right)$ and check if $\left(p^{i+1} - p^{i}\right) > T$, update $s = \hat{s}$ and $\lambda = \lambda'$.

Step 8: Repeat the procedure from step 3 to 7.

In the present work, some experiments are performed on the different images and processed by the TVF algorithm for different noises. Figure 4.2 (a)-(f) represent the remnant of the denoised images by the TVF method. It can be observed from Figure 4.2 (a)-(f) that some texture and edge information are lost in the remnant of the denoised image obtained by the TVF method. To extract the edge information from the remnant of the denoised image by the TVF method, shearlet denoising is used as mentioned above.

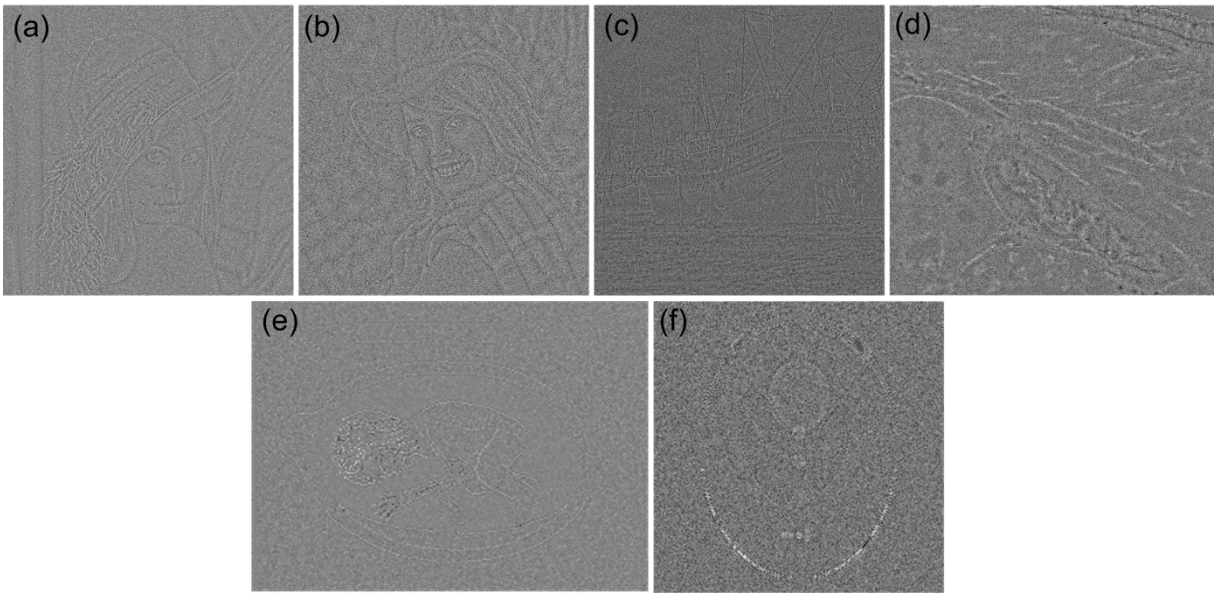

Figure 4.2 The edge information lost in denoised images (a) Lena image (b) Girl image (c) Boat image (d) Kidney image (e) Fetus image (f) Phantom image

4.5 Proposed Remnant Approach for Adaptive Fusion Based Noise Filtering

In the proposed RBAF noise filtering approach, the fusion algorithm is presented to fuse the information of images which are processed with the TVF, ST thresholding using cycle spinning (CSST) approach, separately and extracted edges from the remnant of TVF method. Figure 4.3 shows the ESI extracted from the different methods such as the TI-WT, CVT and ST based methods for the Lena, girl and boat images degraded by the additive noise. Similarly, Figure 4.4 also shows the extracted ESI from the aforementioned denoising methods for kidney, fetus and phantom image corrupted by multiplicative speckle noise. Firstly, such noisy images are processed by the TVF algorithm and shearlet thresholding using cycle spinning (CSST) approach. It is also observed from Figure 4.2 that the edge information is lost during the TVF method. The remnants of the denoised images by the TVF

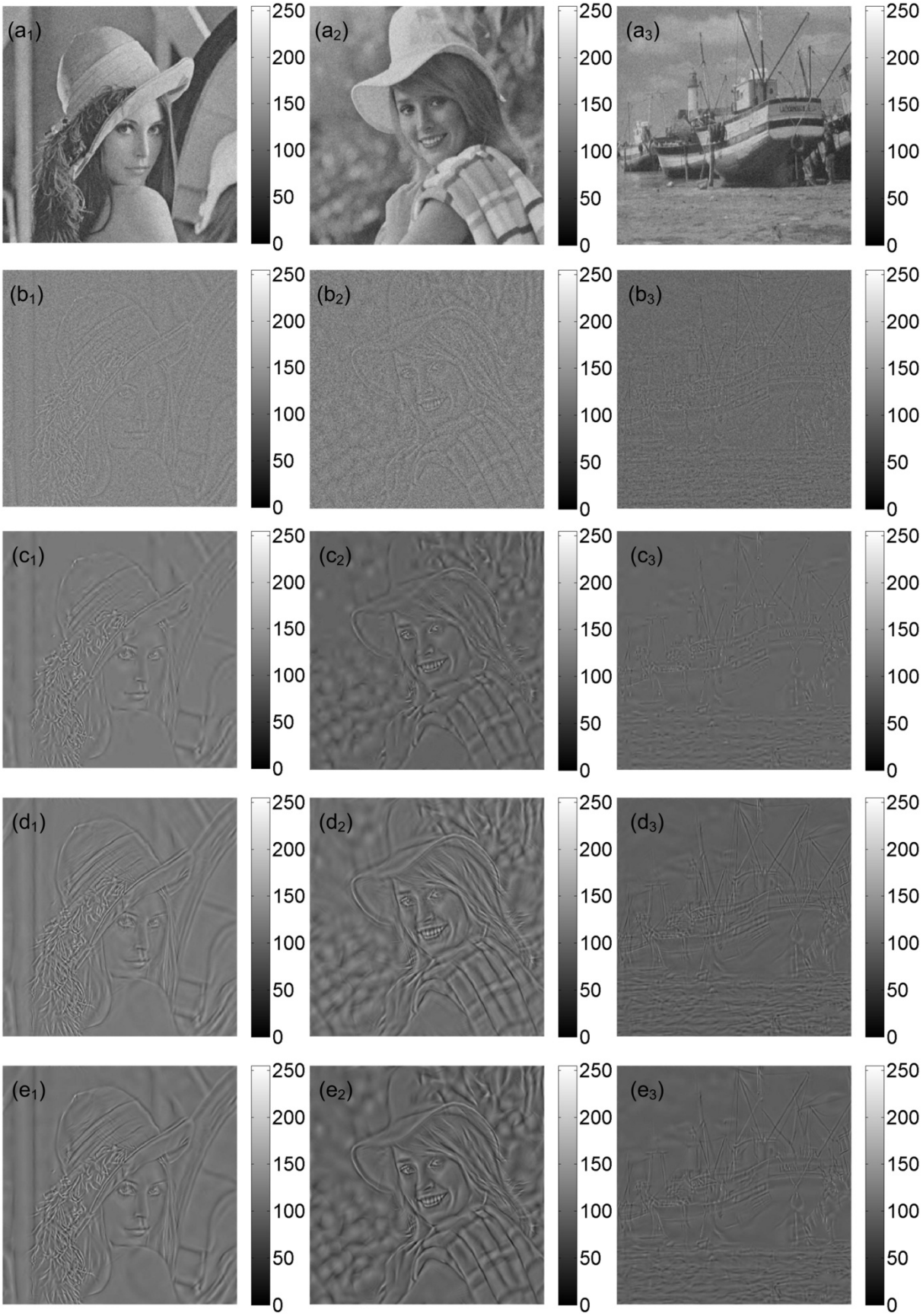

Figure 4.3 (a) Image contaminated with Gaussian noise (b) Remnant of the denoised images by TVF approach. Extracted edge structured information from (c) TI-WT method (d) CVT based method (e) ST based method. Here, 1, 2 and 3 represent Lena, girl and boat images, respectively

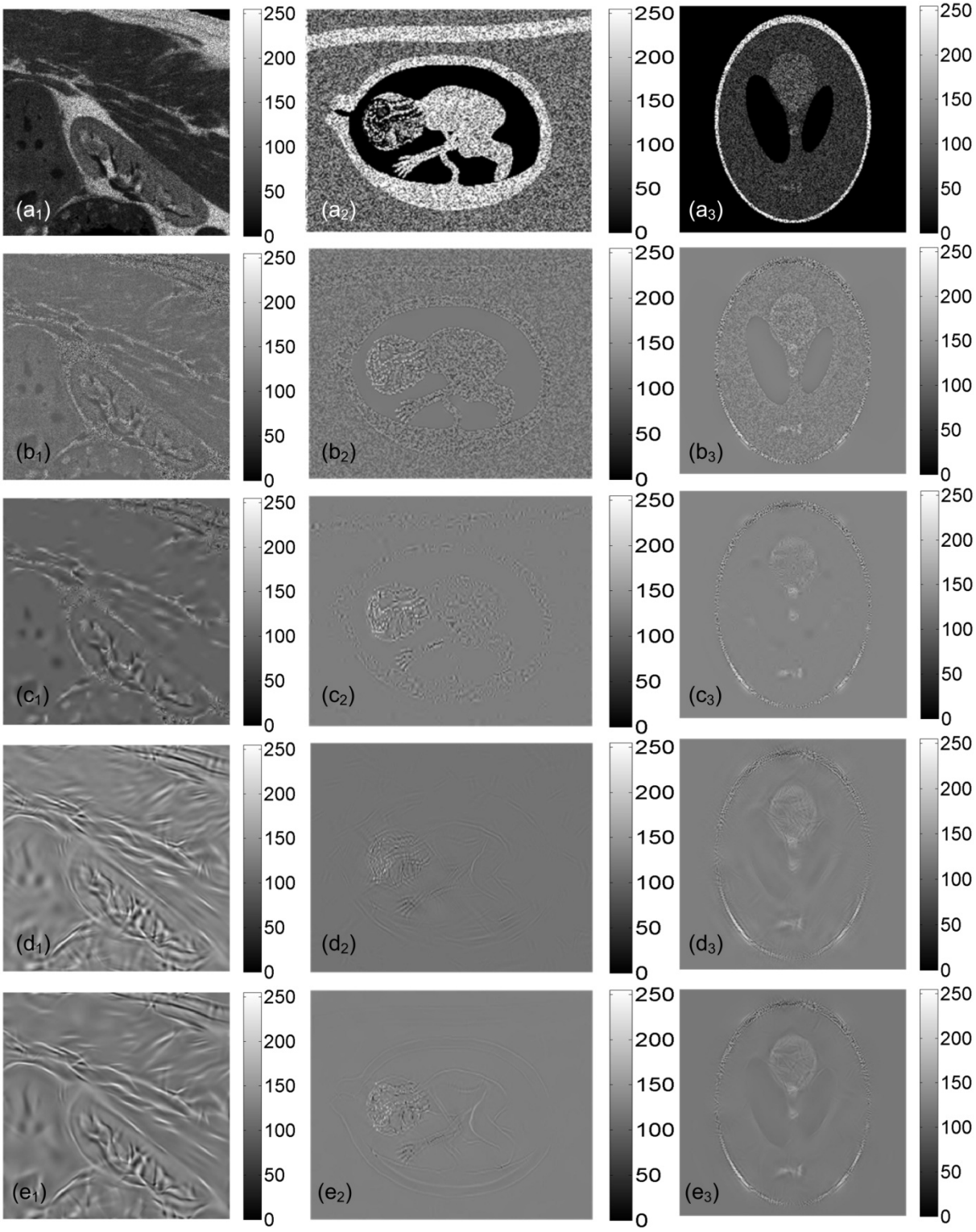

Figure 4.4 (a) Image contaminated with speckle noise (b) Remnant of the denoised images by TVF method. Extracted edge structured information from (c) TI-WT method (d) CVT based method (e) ST based method. Here, 1, 2 and 3 represent kidney, fetus and phantom images, respectively

approach are obtained and shown in Figure 4.3 (b) and Figure 4.4 (b). Furthermore, the ESI shown in Figure 4.3 (c)-(e) and Figure 4.4 (c)-(e) are extracted back by processing the remnant of the TVF method by TI-WT, CSCVT and CSST methods, respectively. It is also observed from both the figures that the edges extracted by the TI-WT does not tend to give

better performance and also provides less edge information as compared to others. The ESI extracted by the CSCVT provides better results than the TI-WT method. To investigate and compare the performance of the CSST, it is utilized to recover the ESI as shown in Figure 4.3 (e) and Figure 4.4 (e) for additive and multiplicative noise corrupted images, respectively. The results mentioned in both the above figures also show that it provides more ESI from the remnant of the denoised image obtained by the TVF method.

Finally, the concept of fusing the information in the denoised image is carried out in three different denoised images by (a) TVF approach (b) CSST approach and (c) the ESI recovered by the CSST method from the remnant of the denoised image by the TVF approach. Although, the edge information has been extracted from the remnant of the TVF method, but it cannot be added directly in the denoised image obtained by CSST method. It does not provide good performance. Therefore, for better edge preservation, it is proposed to fuse all the denoised images by an adaptive fusion algorithm. The process flow involved in the implementation of adaptive fusion based denoising method is shown in Figure 4.5.

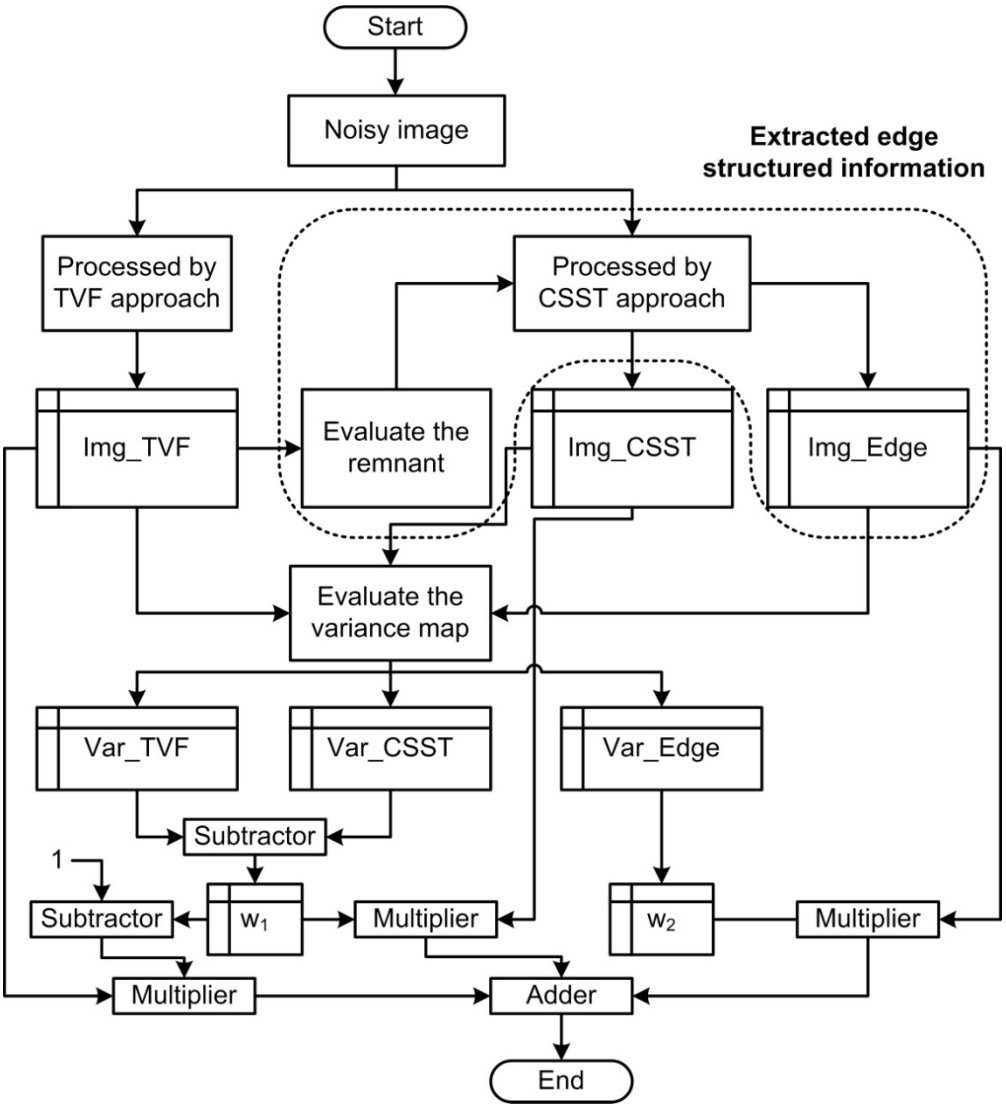

Figure 4.5 Process flow of the proposed RBAF approach

In Figure 4.5, Img_TVF, Img_CSST and Img_Edge refer to the images processed with the TVF approach, CSST approach and the ESI extracted from the remnant of TVF method using CSST approach, respectively. After getting these images, variance map of the denoised images and extracted edge information have been estimated by taking the 3×3 block variance at each pixel of the above results (Img_TVF, Img_CSST and Img_Edge) and then it has been normalized. Now, the three different variance maps Var_TVF, Var_CSST and Var_Edge are obtained. By subtracting the Var_TVF and Var_CSST, w_1 is evaluated and w_2 is estimated directly from Var_Edge. Both w_1 and w_2 are used as weight factors for the fusion process. Finally, all the three images are fused as follows,

$$\text{Output} = (1 - w_1) \times \text{Img\_TVF} + w_1 \times \text{Img\_CSST} + w_2 \times \text{Img\_Edge} \quad (4.12)$$

Implementation steps

Based on the above discussed concept, the main frame of denoising based on the proposed RBAF approach is formulated in the following implementation steps:

Step 1: Perform the TVF and the CSST approach on a noisy image, separately.

Step 2: Compute the remnant of the TVF approach in which edge information is lost during the TVF denoising.

Step 3: Apply the CSST method for extracting the edge information from the remnant of TVF approach obtained from step 2.

Step 4: By taking the 3×3 block variance at each pixel of the denoised images obtained from the TVF, CSST and the edge information extracted from step 3, variance of these images are obtained.

Step 5: Convert the variance images obtained from step 4 into percentage normalized variance images (PNVI's) by multiplying with (100/ maximum value of the variance of the respective images) then the PNVIs are converted into binary by MATLAB command im2bw. Now, three different variance images such as the Var_TVF, Var_CSST and Var_Edge are obtained for the image processed by the TVF method, CSST method and extracted edge information by the CSST approach, respectively.

Step 6: Compute the difference between the PNVI's of denoised images processed with the TVF and CSST method. This difference value is used as a weight factor w_1 for the Img_CSST and the value of $(1 - w_1)$ is used for Img_TVF.

Step 7: The PNVI value of the extracted edge information is used as a weight factor w_2 for the edge information Img_Edge.

Step 8: Perform the fusion with adaptive weight factors within 3×3 template and reconstruct the image using Eqn. (4.12).

4.6 Experimentation

In this section, three different experiments are conducted to assess the performance of

the proposed RBAF noise filtering approach. For such purpose, the same test images are considered as used in the chapter 2 for Gaussian and speckle noise removal. The performance measures such as the SNR, PSNR, SSIM, FOM and EKI used for investigating the performance of the proposed RBAF method quantitatively are also considered similarly as used in chapter 2 and 3. Three different experiments are discussed as given below:

Experiment 1: To analyze and evaluate the performance obtained by the proposed RBAF method for multiplicative speckle noise removal.

Experiment 2: To analyze and evaluate the performance obtained by the proposed RBAF method for suppressing the additive Gaussian noise.

Experiment 3: To analyze and evaluate the proposed RBAF approach for real US images.

4.7 Results and Discussions

Experiment 1: *Analysis and evaluation of the RBAF approach for speckle noise removal* - In order to validate the experimental objectives, the same three different images such as the kidney, fetus and phantom images are considered as in the previous chapters. To asses and compare the performance of the proposed RBAF noise filtering approach, another set of different remarkable denoising methods are considered as follows:

Method 1: A nonlinear TVF approach as described above.

Method 2: The TI-WT based thresholding approach as discussed in chapter 2.

Method 3: The CSCVT approach as described in [10] and also in chapter 2. In this experiment, scale dependent constant parameter is chosen as k=4 for the first scale and k=3 for the others.

Method 4: The CSST approach as discussed above and also in [110].

Method 5: The TVF with CVT approach (CVT-TVF) as described by Bahdauria et al. in [25].

Method 6: The proposed RBAF noise filtering approach as discussed above. In the proposed approach, the denoised images processed with the TVF and CSST approach, separately and extracted ESI from the remnant of TVF are fused together based on the 3×3 block variance map evaluated for all three processed images. From the variance images, it is observed that the images which have more edge information show the higher variance values within 3×3 block. Based on this concept, the weight factor w_2 achieves higher value than w_1 for speckled images. For the additive noise, the weight factor w_1 gains higher values than w_2 for some regions within 3×3 block.

Based on all the aforementioned denoising methods, the processed images of noisy version of kidney, fetus and phantom images are presented in Figure 4.6, Figure 4.7, and Figure 4.8, respectively. From the results shown in these figures, it is observed that the proposed RBAF noise filtering approach is more capable to reflect more edges after denoising process. From the visual assessment, it is observed that the proposed RBAF

approach gets much better visual results than the TVF, TI-WT, CSCVT methods and provides a significant improvement in noise reduction than the CSST and TVF-CVT methods for the speckle noise. Further, it gets much better edge preservation performance than the CSST and TVF-CVT method. For kidney images illustrated in Figure 4.6, the image processed by the CSST method reflects better results than the CVT-TVF method, but in case of fetus and phantom images, it becomes reversed. The CVT-TVF method provides more noise suppression performance than the CSST method. Moreover, the proposed RBAF outperforms both the CSST and CVT-TVF methods for all the images. The results of visual assessment are also validated by evaluating the different objective measures as presented in the previous chapter. The quantitative outcomes are listed in Table 4.1 corresponding to all these images.

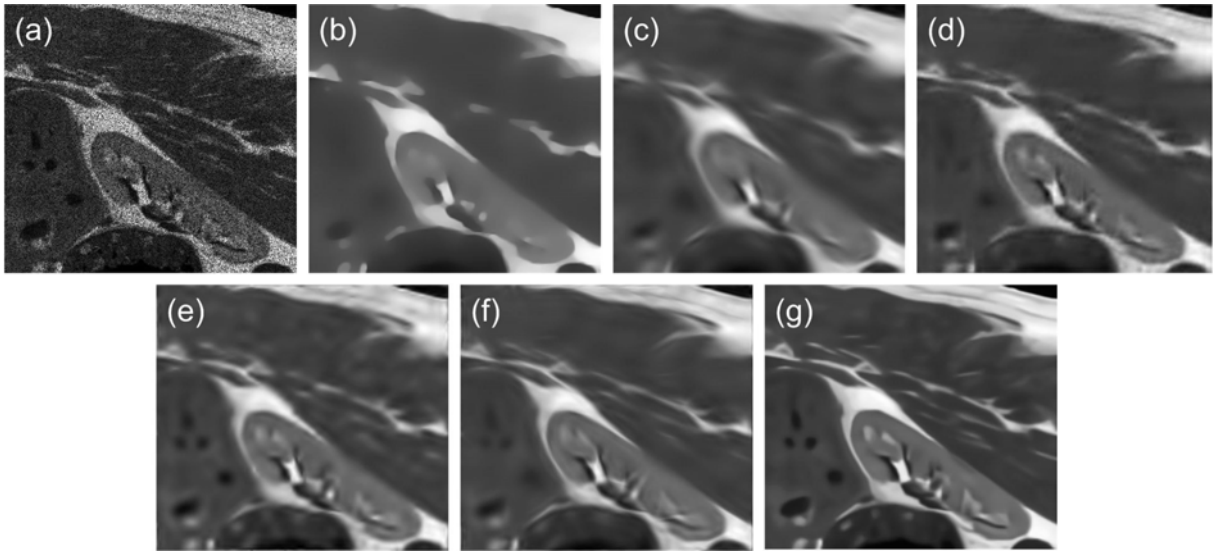

Figure 4.6 Visual comparison of the denoising methods for (a) Kidney image corrupted by speckle noise (b) Method 1 (c) Method 2 (d) Method 3 (e) Method 4 (f) Method 5 (g) Method 6 (Proposed RBAF)

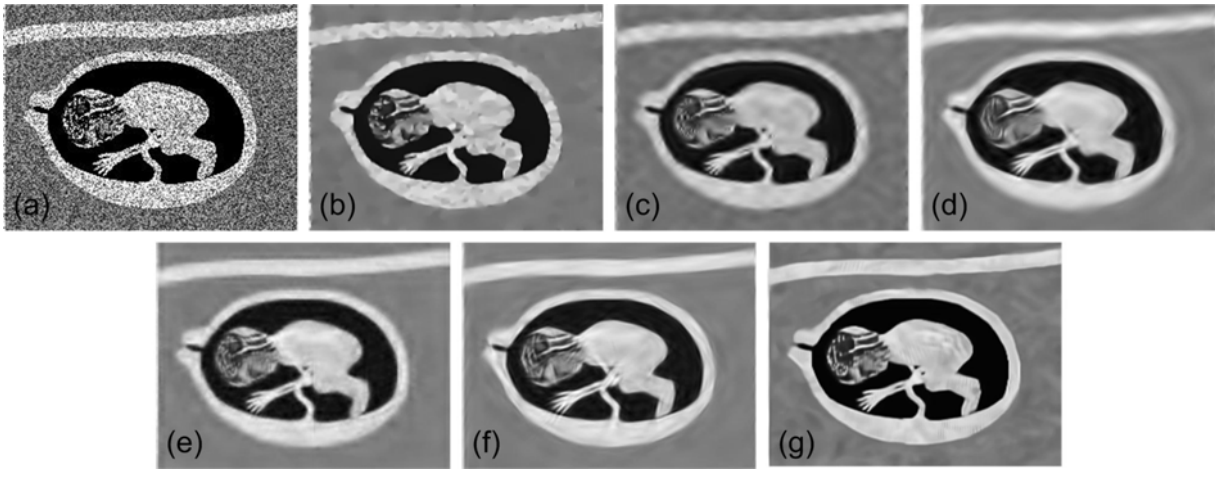

Figure 4.7 Visual comparison of the denoising methods for (a) Fetus image corrupted by speckle noise (b) Method 1 (c) Method 2 (d) Method 3 (e) Method 4 (f) Method 5 (g) Method 6 (Proposed RBAF)

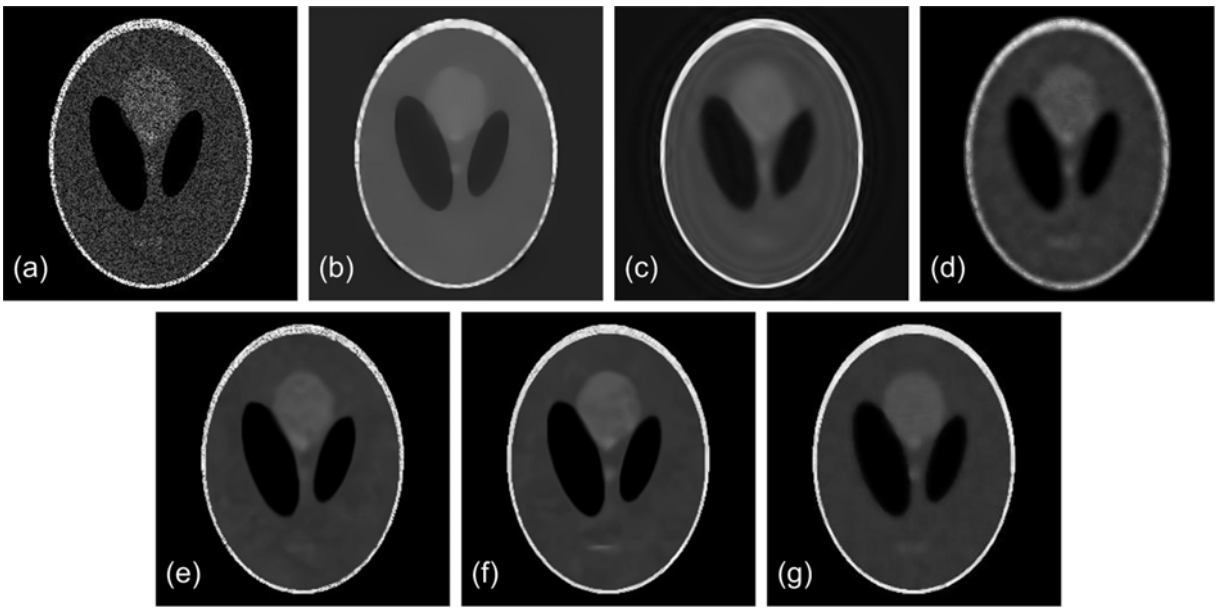

Figure 4.8 Visual comparison of the denoising methods for (a) Phantom image corrupted by speckle noise (b) Method 1 (c) Method 2 (d) Method 3 (e) Method 4 (f) Method 5 (g) Method 6 (Proposed RBAF)

From the results mentioned in Table 4.1, it is observed that the noise reduction performance of the proposed RBAF method achieves approx 6.11-16.09%, 0.63-9.21%, 3.08-12.10%, 0.11-8.97% and 1.23-4.31% higher PSNR than the TVF, TI-WT, CSCVT, CSST and CVT-TVF methods, respectively for kidney image. With higher SNR values, the RBAF approach also gains approx 10.47-27.31%, 1.04-15.01%, 5.18-20.06%, 0.18-14.60% and 2.1-6.83% higher SNR values than the methods 1-5, respectively. It also achieves approx 12.22-17.91%, 7.80-9.89%, 7.28-10.54%, 1.95-9.55% and 4.09-6.60% larger EKI values than the TVF, TI-WT, CSCVT, CSST and CVT-TVF methods, respectively. For fetus image, the RBAF method also produces higher PSNR (8.06-16.93%, 5.6-13.93%, 6.41-15.70%, 3.63-10.96% and 1.04-1.56%), SNR (11.67-23.50%, 8.08-19.14%, 9.22-21.70%, 5.16-14.92% and 1.55-2.06%), SSIM (15.44-16.89%, 12.60-12.89%, 5.27-7.24%, 5.44-20.65% and 2.61-3.07%) and EKI values (50.56-84.31%, 47.62-79.97%, 25.34-59.27%, 20.5-55.3% and 2.67-10.97%) than the TVF, TI-WT, CSCVT, CSST and CVT-TVF methods, respectively. Similarly, the proposed method shows better noise reduction performance than the CSST and CVT-TVF methods in terms of higher PSNR (0.77-4.81% and 1.05-1.90%) and SNR values (1.59-9.11%, 2.06-3.54) for the denoised phantom images. It also produces larger EKI values approx 6.11-20.19% and 0.38-1.22% than the CSST and CVT-TVF methods. Moreover, the quantitative results show that with low levels of noise, the proposed RBAF approach produces competitive edge preservation results as compared to the others and outperforms the others with better noise suppression. In case of high levels of noise, the RBAF approach produced the competitive noise suppression results compared to others with better edge preservation performance. Furthermore, the proposed approach outperforms all the other methods. This is also reflected visually that the proposed RBAF approach is able to

Table 4.1 Image quality measures obtained by the different denoising methods for kidney, fetus and phantom images corrupted by multiplicative speckle noise

Images	Noise level	Metrics	Method 1	Method 2	Method 3	Method 4	Method 5	Proposed RBAF
Kidney image	$\sigma = 0.1$	PSNR	25.85	27.48	26.77	27.54	28.77	30.01
		SNR	15.23	16.86	16.15	16.92	18.15	19.39
		SSIM	0.6747	0.7412	0.7666	0.7603	0.8164	0.8432
		EKI	0.4149	0.4319	0.4340	0.4567	0.4473	0.4656
	$\sigma = 0.2$	PSNR	25.65	27.31	26.57	27.28	27.53	28.11
		SNR	15.03	16.69	15.95	16.66	16.91	17.49
		SSIM	0.6527	0.7391	0.7633	0.7548	0.7711	0.7962
		EKI	0.4036	0.4307	0.4318	0.4349	0.4383	0.4655
	$\sigma = 0.3$	PSNR	25.52	26.91	26.27	27.05	26.75	27.08
		SNR	14.90	16.29	15.65	16.43	16.13	16.46
		SSIM	0.6331	0.7353	0.7407	0.7560	0.7606	0.7679
		EKI	0.3931	0.4218	0.4193	0.4231	0.4348	0.4635
Fetus image	$\sigma = 0.1$	PSNR	17.84	18.31	18.03	18.80	20.54	20.86
		SNR	12.85	13.32	13.04	13.81	15.55	15.87
		SSIM	0.5854	0.6077	0.6381	0.6490	0.6639	0.6843
		EKI	0.3696	0.3785	0.4277	0.4387	0.6635	0.6812
	$\sigma = 0.2$	PSNR	17.01	17.40	17.15	17.75	18.66	18.90
		SNR	12.02	12.41	12.16	12.76	13.67	13.91
		SSIM	0.5631	0.5758	0.6164	0.5764	0.6324	0.6489
		EKI	0.3531	0.3579	0.4089	0.4192	0.5346	0.5652
	$\sigma = 0.3$	PSNR	16.13	16.50	16.38	16.82	17.25	17.43
		SNR	11.14	11.51	11.39	11.83	12.25	12.44
		SSIM	0.5325	0.5445	0.5816	0.5095	0.5979	0.6147
		EKI	0.3105	0.3167	0.3730	0.3879	0.4213	0.4675
Phantom image	$\sigma = 0.1$	PSNR	25.86	24.71	25.01	25.55	26.28	26.78
		SNR	13.69	12.54	12.84	13.39	14.11	14.61
		SSIM	0.6883	0.7920	0.7970	0.8365	0.8440	0.8500
		EKI	0.6452	0.5930	0.6121	0.6850	0.8202	0.8233
	$\sigma = 0.2$	PSNR	24.07	23.64	24.12	24.44	24.79	25.05
		SNR	11.90	11.47	11.95	12.27	12.62	12.88
		SSIM	0.6944	0.7680	0.7923	0.7974	0.8314	0.8302
		EKI	0.5878	0.5600	0.5799	0.6267	0.6799	0.6870
	$\sigma = 0.3$	PSNR	23.20	23.12	23.38	23.48	23.97	23.66
		SNR	11.03	10.95	11.22	11.31	11.80	11.49
		SSIM	0.6986	0.7529	0.7813	0.7823	0.7884	0.7831
		EKI	0.5354	0.5312	0.5521	0.5397	0.5658	0.5727

suppress the speckle noise along with the preservation of more edges.

Apart from the analysis of the SNR, PSNR, SSIM and EKI values, another index such as the FOM is used to investigate the robustness of edge preservation performance for all methods stated above. The FOM values closer to 1, indicate better edge preservation and less edge dislocation in the denoised images. Figure 4.9 shows a comparative analysis of the FOM values for the images corrupted by the multiplicative speckle noise. From the Figure 4.9, it is clear that the proposed RBAF method achieves higher FOM values (approx 0.7-0.8) than all the other existing methods as mentioned above. The TVF-CVT method gains an improvement in the FOM values than the TVF, TI-WT, CSCVT and CSST methods. In case of phantom image, the FOM values approx 0.82 obtained by the CSST and CVT-TVF methods are similar. Moreover the proposed RBAF methods also show a significant improvement in the FOM values produced by the CVT-TVF method that indicates better edge preservation performance of the proposed method.

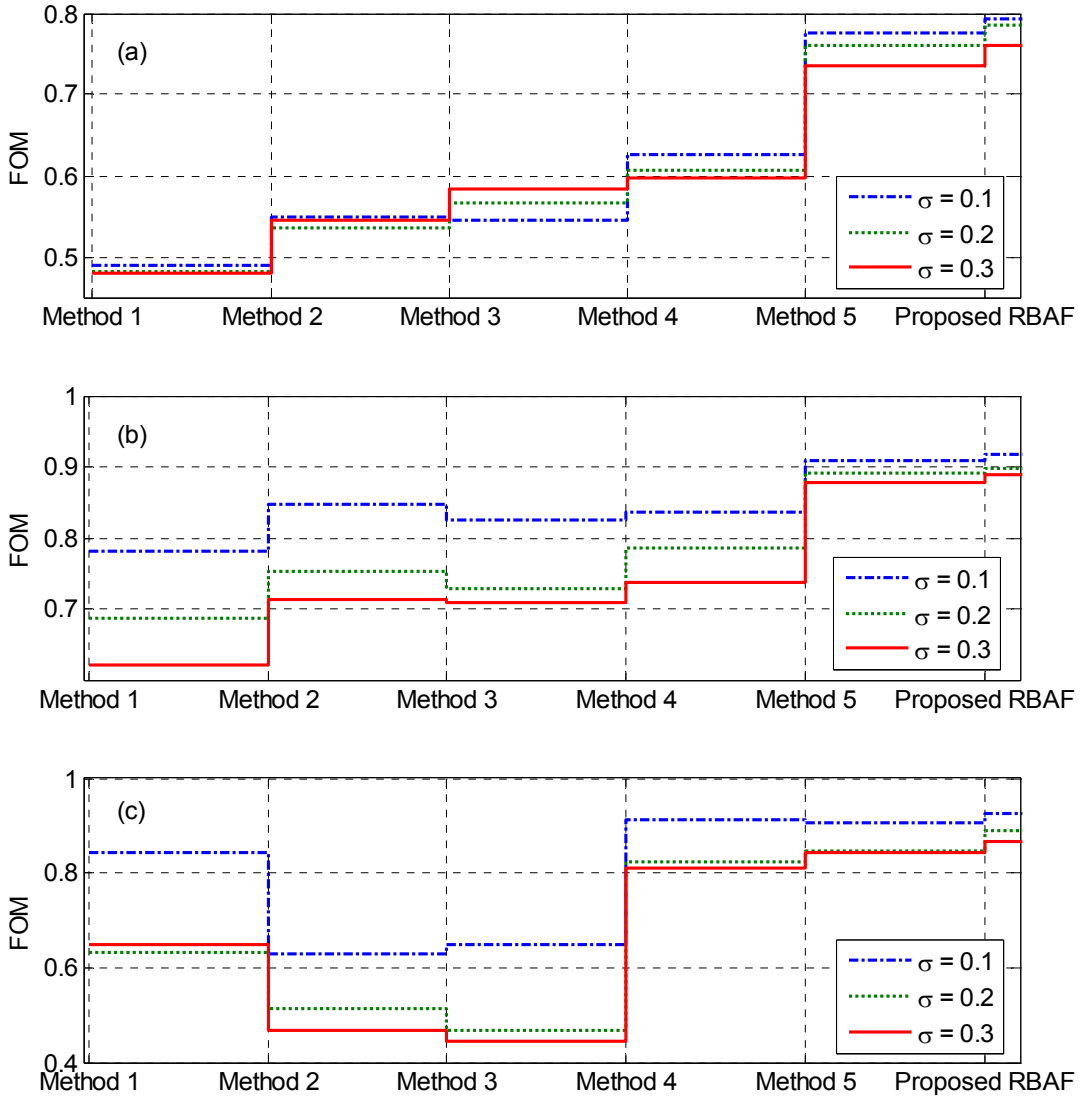

Figure 4.9 Comparative performance of the FOM values produced by different denoising methods applied to (a) Kidney image (b) Fetus image (c) Phantom image

Finally, it can be concluded from Table 4.1 and Figure 4.9 that there is a considerable improvement in noise suppression with higher values of the PSNR and SNR that is not at the cost of edge loss shown by the higher values of EKI and FOM.

Experiment 2: *Analysis and evaluation of the RBAF approach for Gaussian noise removal* - In order to investigate the robustness of the proposed RBAF approach, Lena, girl and boat images with additive Gaussian noise model are considered. Different levels of noise are added by setting different standard deviation of noise $\sigma_n = 10,\ 20$ and 30 to investigate the performance of different methods. The denoised images corresponding to noisy Lena,

Figure 4.10 Visual comparison of the denoising methods for (a) Lena image corrupted by Gaussian noise (b) Method 1 (c) Method 2 (d) Method 3 (e) Method 4 (f) Method 5 (g) Method 6 (Proposed RBAF)

Figure 4.11 Visual comparison of the denoising methods for (a) Girl image corrupted by Gaussian noise (b) Method 1 (c) Method 2 (d) Method 3 (e) Method 4 (f) Method 5 (g) Method 6 (Proposed RBAF)

girl and boat image are shown in Figure 4.10, Figure 4.11 and Figure 4.12, respectively. From the visual assessment of these results, it is observed that the CSST method produces better quality of images by capturing more edges than the TVF, TI-WT and CSCVT methods. It is also capable to reduce the fuzzy edges produces by the CVT method. The TVF-CVT is also a better competitor of the CSST that shows a considerable amount of improvement in the SNR/PSNR and EKI values. Furthermore, the proposed RBAF method is capable to effectively retain the edges and thus, providing better quality images with good resolution. The outcomes of the methods supported by four different parameters are listed in Table 4.2. From the results mentioned in Table 4.2 for denoised kidney images, the proposed RBAF method produces better noise suppression as compared to the TVF, TI-WT, CSCVT, and CSST methods with improved edge preservation performance. The RBAF noise filtering approach also achieves better edge preservation performance by providing higher EKI values and a competitive noise suppression performance than the CVT-TVF approach. Besides this, it produces approx 0.37-1.85%, 0.43-2.28% higher PSNR and SNR values, respectively, with approx 0.61-2.91 larger EKI values than the CVT-TVF method. Similarly, in case of girl image, the proposed RBAF approach gains approx 2.49-13%, 2.34-4.35%, 3.29-3.65%, 0.26-1.47% and 1.14-2.28% higher PSNR values than the TVF, TI-WT, CSCVT, CSST, and CVT-TVF methods with higher SNR, SSIM and EKI values. It achieves approx 0.3-1.7%, 1.38-2.67% higher SNR, 0.3-1.13%, 0.18% higher SSIM values and 0.51-8.05%, 0.66-4.10% larger EKI values than the CSST and CVT-TVF methods for girl image. Similarly, the proposed method produces an improved performance for a boat image. From the objective results mentioned in Table 4.2, it is concluded that the proposed method improves its edge preservation performance with approx 13.33-31.35%, 2.29-22.87%, 2.62-6.48%, 1.2

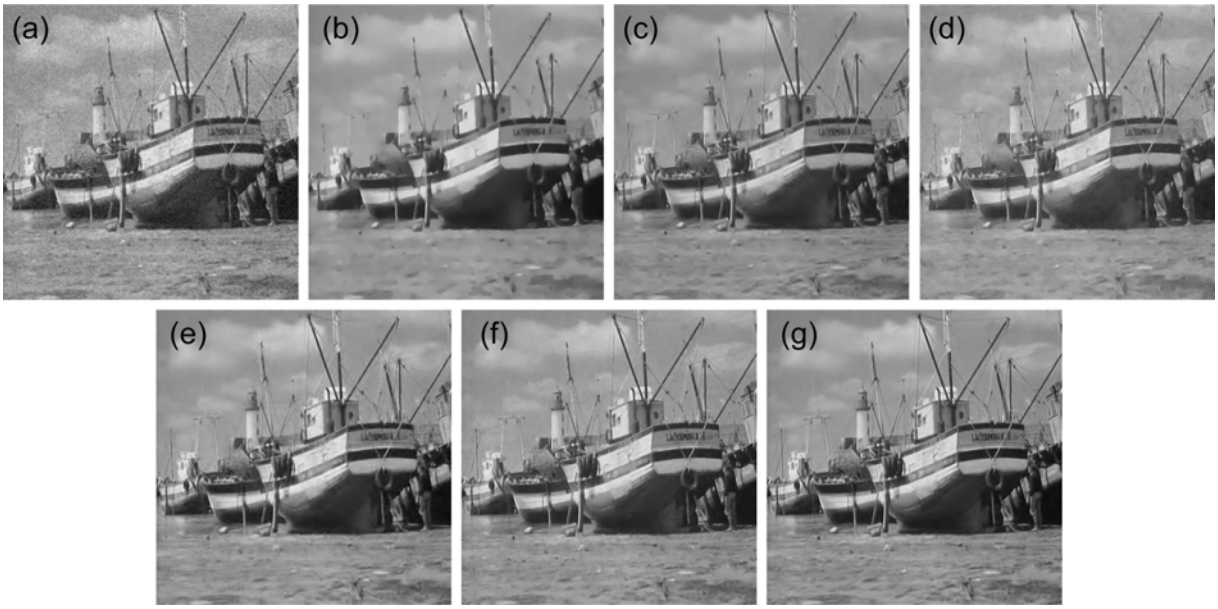

Figure 4.12 Visual comparison of the denoising methods for (a) Boat image corrupted by Gaussian noise (b) Method 1 (c) Method 2 (d) Method 3 (e) Method 4 (f) Method 5 (g) Method 6 (Proposed RBAF)

Table 4.2 Image quality measures obtained by the different denoising methods for Lena, girl and boat images corrupted by additive Gaussian noise

Images	Noise level	Metrics	Method 1	Method 2	Method 3	Method 4	Method 5	Proposed RBAF
Lena image	$\sigma_n = 10$	PSNR	29.99	35.15	34.83	35.63	35.61	35.74
		SNR	24.33	29.49	29.17	29.98	29.96	30.09
		SSIM	0.8767	0.9609	0.9569	0.9643	0.9646	0.9652
		EKI	0.7216	0.8244	0.8313	0.8509	0.8505	0.8557
	$\sigma_n = 20$	PSNR	29.98	31.53	31.66	32.65	32.32	32.66
		SNR	24.33	25.88	26.01	26.99	26.66	27.00
		SSIM	0.8837	0.9204	0.9178	0.9300	0.9348	0.9349
		EKI	0.6863	0.6701	0.7386	0.7536	0.7728	0.7845
	$\sigma_n = 30$	PSNR	29.45	29.44	29.73	30.77	30.26	30.82
		SNR	23.79	23.78	24.07	25.12	24.61	25.17
		SSIM	0.8751	0.8833	0.8805	0.8932	0.9051	0.9061
		EKI	0.6520	0.5442	0.6724	0.6748	0.7144	0.7352
Girl image	$\sigma_n = 10$		30.55	33.73	33.42	34.02	33.75	34.52
		SNR	25.99	29.18	28.87	29.47	29.19	29.97
		SSIM	0.8660	0.9420	0.9370	0.9371	0.9470	0.9477
		EKI	0.6806	0.7232	0.7195	0.7325	0.7314	0.7362
	$\sigma_n = 20$	PSNR	30.73	31.24	31.27	32.14	31.86	32.39
		SNR	26.18	26.68	26.72	27.59	27.31	27.84
		SSIM	0.8769	0.9023	0.8971	0.9112	0.9156	0.9139
		EKI	0.6406	0.6021	0.6559	0.6686	0.6809	0.6874
	$\sigma_n = 30$	PSNR	30.17	29.63	29.83	30.84	30.57	30.92
		SNR	25.62	25.07	25.28	26.29	26.01	26.37
		SSIM	0.8684	0.8696	0.8657	0.8808	0.8883	0.8899
		EKI	0.6075	0.5088	0.6201	0.6208	0.6444	0.6708
Boat image	$\sigma_n = 10$	PSNR	27.48	33.26	32.71	33.32	33.25	33.61
		SNR	22.14	27.92	27.37	27.98	27.90	28.27
		SSIM	0.8079	0.9540	0.9488	0.9568	0.9610	0.9691
		EKI	0.6637	0.8523	0.8495	0.8613	0.8654	0.8718
	$\sigma_n = 20$	PSNR	27.43	29.36	29.49	30.01	29.81	30.26
		SNR	22.09	24.02	24.15	24.66	24.47	24.92
		SSIM	0.8203	0.8940	0.8893	0.9056	0.9139	0.9161
		EKI	0.6395	0.7021	0.7445	0.7521	0.7631	0.7665
	$\sigma_n = 30$	PSNR	27.12	27.47	27.49	28.19	28.23	28.40
		SNR	21.77	22.12	22.15	22.85	22.89	23.05
		SSIM	0.8223	0.8395	0.8357	0.8568	0.8594	0.8693
		EKI	0.6084	0.5612	0.6475	0.6535	0.6796	0.6895

-5.52% and 0.45-1.46% higher EKI values than the methods 1-5, respectively. Moreover, the proposed RBAF method outperforms all other denoising techniques for the different noise levels in terms of noise reduction and edge preservation as much as possible.

Experiment 3: *Analysis and evaluation of the RBAF approach for speckle reduction in the existing real US images* - In order to fulfil the experimental objective, prostate US image is considered. The denoised prostate US images obtained by the various aforementioned methods are shown in Figure 4.13. From the visual assessment of the results illustrated in Figure 4.13, it is observed that the TVF and TI-WT methods are able to suppress the speckle, but some edges that are available in the original US image are lost during the filtering process. Besides it, the CSST method produces better noise suppression performance by preserving more edges presented in prostate US images than the TVF, TI-WT and CSCVT methods, but the CVT-TVF approach produces denoised images with better visual quality than the CSST approach. Furthermore, the proposed RBAF approach provides better results in terms of speckle reduction than both the CSST and CVT-TVF approach.

For another visual assessment of the performance obtained by the proposed approach, a liver US image is taken and processed by all the denoising methods as mentioned above. The denoised liver US images are shown in Figure 4.14, by which it is observed that the proposed RBAF approach provides better results than others as similar to the previous results. Besides these results, the quantitative evaluation of the MVR values is performed in support of the visual results obtained by the different denoising methods. A larger value of MVR represents a better quantitative performance of denoising methods. For such purpose, four different bar graphs are presented in Figure 4.15 for two different image regions marked

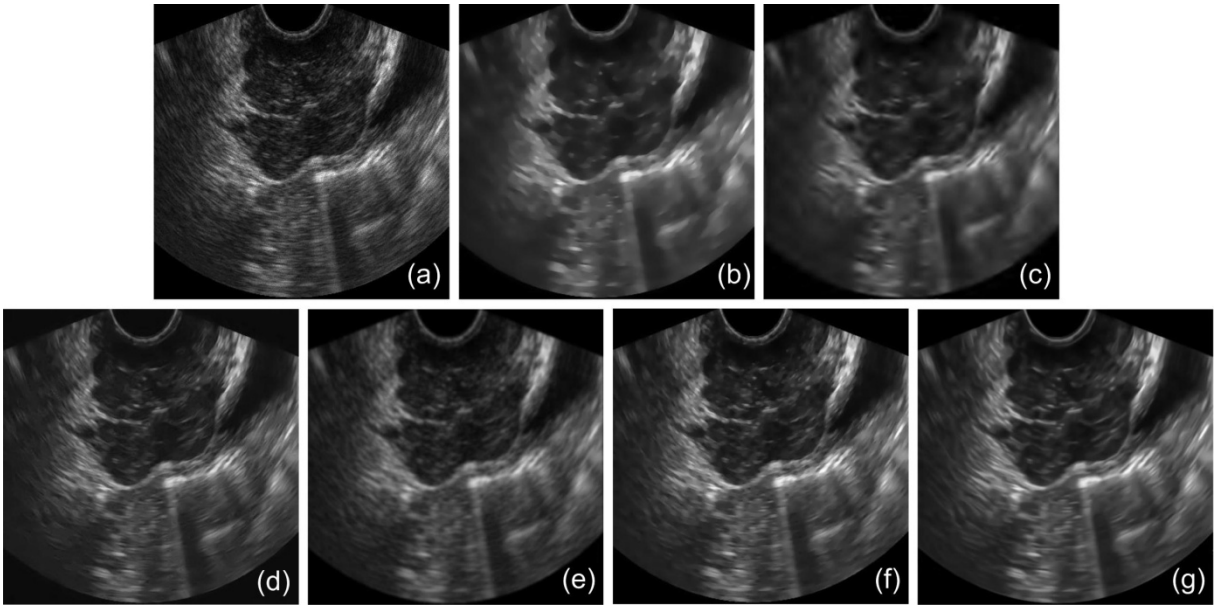

Figure 4.13 Visual comparison of the (a) Prostate ultrasound image, processed by different denoising methods (b) Method 1 (c) Method 2 (d) Method 3 (e) Method 4 (f) Method 5 (g) Method 6 (Proposed RBAF)

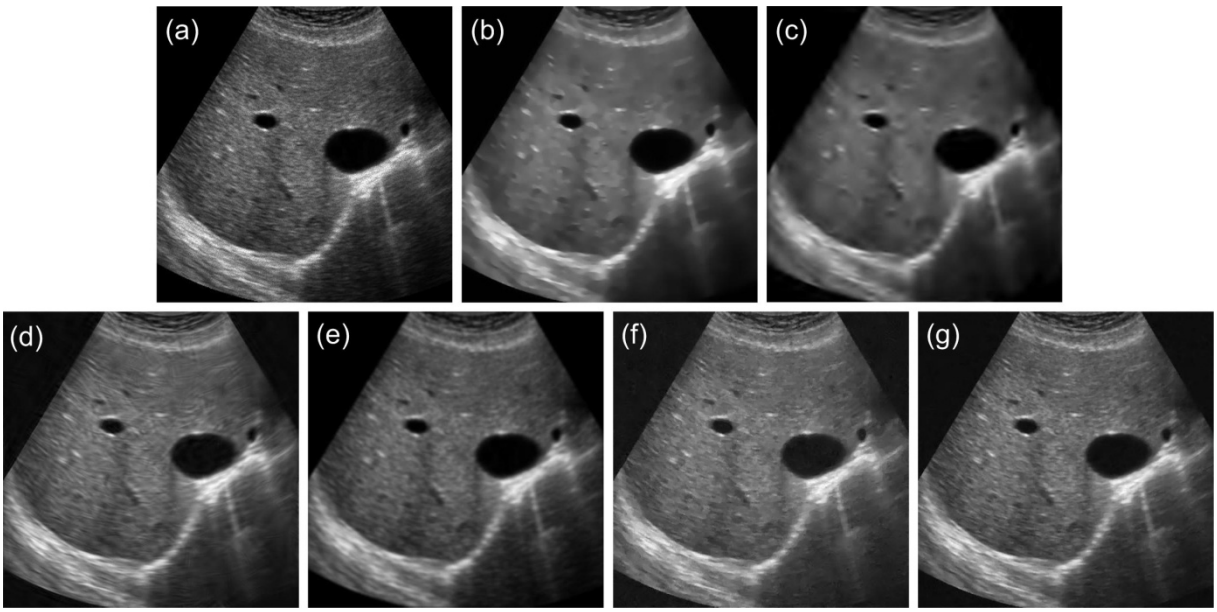

Figure 4.14 Visual comparison of the (a) Liver ultrasound image, processed by different denoising methods (b) Method 1 (c) Method 2 (d) Method 3 (e) Method 4 (f) Method 5 (g) Method 6 (Proposed RBAF)

on four different US images illustrated in Figure 2.21. From the MVR values shown in Figure 4.15, it is observed that the CVT-TVF approach provides larger MVR values than the TVF, TI-WT CSCVT, and CSST method and also produce the competitive MVR values to the proposed RBAF approach for some images. Moreover, the proposed RBAF approach outperforms the CVT-TVF method as well as others by producing higher MVR values.

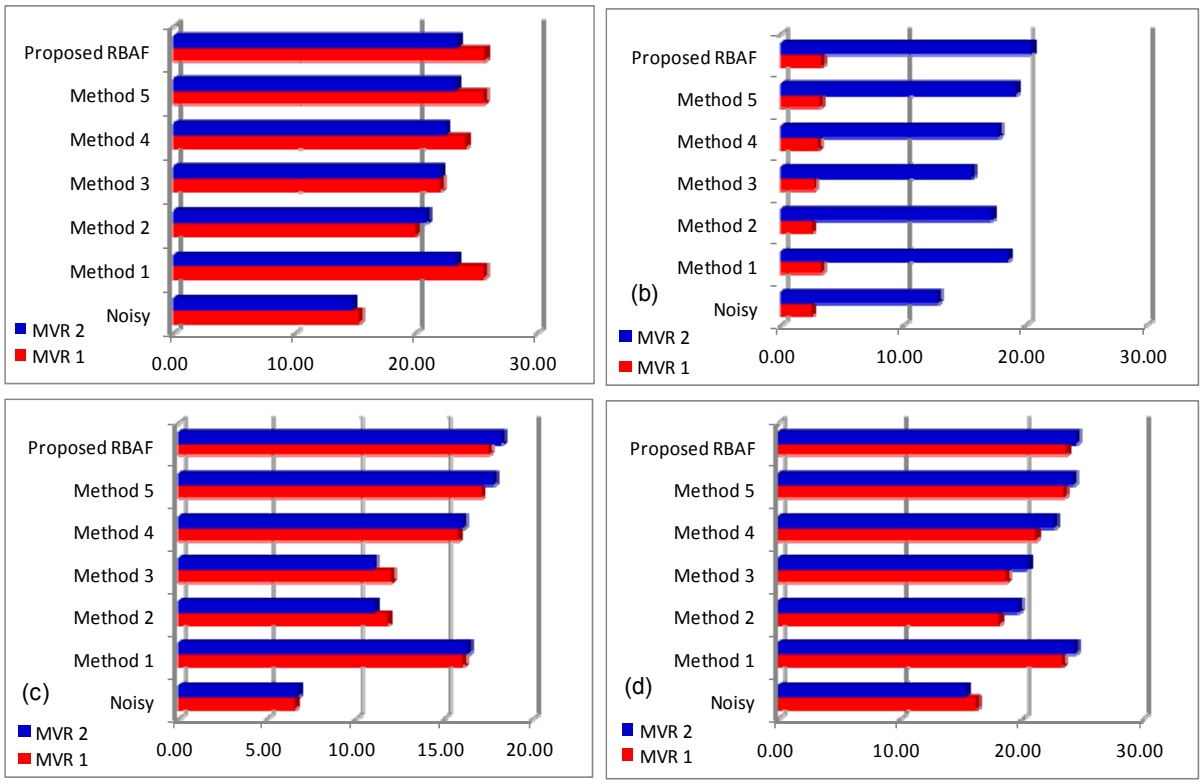

Figure 4.15 Comparison between the MVR values obtained from the different denoising methods for two different image regions illustrated in Figure 2.21

Table 4.3 Performance comparison of the denoising methods with the proposed RBAF approach using averaged MVR values over 100 different image regions on 50 ultrasound images

Methods	Noisy	Method 1	Method 2	Method 3	Method 4	Method 5	Proposed RBAF
MVR	14.04 ± 3.04	21.45 ± 4.95	18.16 ± 3.14	18.22 ± 4.57	20.94 ± 3.88	21.31 ± 4.85	22.23 ± 3.98

In addition, to further assess the performance of different denoising methods, Table 4.3 shows the averaged MVR values for each denoising method including the proposed RBAF method applied on two different locations of fifty different US images. In this way, 100 different observations (two measurement for each image) are considered to present the averaged (average ± standard deviation) MVR values. The results of Table 4.3 show the superiority of the proposed RBAF method in terms of effective noise reduction performance by providing higher average MVR value (22.23) compared to the others.

4.8 Summary

This chapter presents a hybrid noise reduction technique using a remnant approach based on adaptive fusion by the TVF and ST based methods and named as the RBAF noise filtering approach. This hybrid approach takes the advantage of both the TVF method for noise suppression and the ST based method for denoising and recovering of edges which have been lost during the TVF method. The three denoised images are fused adaptively by varying the weights of the denoised image by the TVF method, shearlet denoising and extracted edges from the remnant of the denoised image by TVF method. The proposed RBAF approach also helps to suppress the staircase or blocking effects produced by the TVF method and the fuzzy edges introduced by the CVT and ST based methods. The denoising capabilities of the proposed RBAF approach are also compared with others using a number of standard test images corrupted with Gaussian noise, simulated speckled images and real US images. Experimental results show a significant improvement in the PSNR and SNR values obtained by the proposed RBAF approach as compared to others. The improved values of EKI also indicate that the improvement in the PSNR and SNR values is not at the cost of blurring the edges of denoised image. The proposed method also tends to efficiently retain the structural similarity and edges as can be seen from the results of SSIM and FOM values. Finally, it is concluded that the proposed RBAF approach does not only ensure an improvement in the visual appearance of enhanced regions, but also exhibits the improved performance in terms of edge preserved noise reduction in the images.

CHAPTER 5: NOISE FILTERING USING ADAPTIVE ANISOTROPIC DIFFUSION EQUATIONS IN NONSUBSAMPLED SHEARLET DOMAIN

In this chapter, two different approaches are discussed for removing the different types of noises. For such purpose, the anisotropic diffusion equations are modified and used in the nonsubsampled shearlet domain that is employed to provide the effective representation of the image coefficients. The modified diffusion equations are applied to the noisy coarser nonsubsampled shearlet coefficients to improve the noise reduction efficiency and effectively preserve the edge features. The methodologies used to present the proposed approaches are also discussed in this chapter. The performance of the proposed methods is also assessed for both the additive Gaussian and multiplicative speckle noise, qualitatively and quantitatively. A detailed comparative analysis has also been done and presented in the last section of this chapter for assessing better performance of the noise reduction produced by the proposed methods.

5.1 Introduction

It has been analyzed and emphasized in previous chapters that the image denoising is an important process in image processing, but it becomes more important in any image denoising process that there is no blurring effect produced in the denoised image with no edge dislocations. As mentioned in previous three chapters that are based on noise filtering in the transform domain, each method has some advantages and limitations. From a comparative analysis presented in chapter 2, it has been analyzed that the PDE based methods also serve the same denoising purpose, but at the cost of some blurring effects introduced in the processed images. Besides this, it is also recognized from chapter 3 that the transformation techniques such as the CVT, ST and RT are able to represent the singularities present in the images, but it generally leads to shift variance and pseudo-Gibbs oscillations. Thus, some visual distortions are reflected in the denoised images. To overcome such limitations, chapter 4 presented an RBAF approach using the TVF algorithm and shearlet based method. Shearlet can be reconstructed in the discrete domain realized by the combination of the LP and DFB, but still the lack of shift invariance problem cannot be overcome. Although, some methods based on shearlet have also been presented for the different applications [57, 58, 84, 149, 153, 285]. To solve this problem, Easley et al. [85] introduced a nonsubsampled ST (NSST) to provide both the multiscale and direction analysis for an image. The NSST is realized using nonsubsampled Laplacian pyramid (NSLP) followed by several shearing filters. The NSST also provides flexible directional selectivity and shift invariance [85, 98, 118]. Thus, in the present study, the NSST is used to decompose an image into finer and coarser coefficients. The NSST thresholding is also applied on the high frequency finer NSST subimage coefficients as similar to the CVT and ST thresholding. Besides the NSST thresholding, the PDE based method such as nonlinear anisotropic diffusion is also used to improve the denoising performance.

In the present work, the modified adaptive anisotropic diffusion model is applied to the noisy coarser NSST subimage coefficients rather than keeping the coarser subimage coefficients unchanged. In the modified diffusion process, an adaptive gray variance is also incorporated with the gradient information of eight connected neighboring pixels to preserve the edges, effectively in one approach. Motivated from better noise reduction results of the NLMF approach presented in the comparative analysis of chapter 2, the nonlocal pixel information is also incorporated to evaluate the gradient of eight connected neighboring pixels with an adaptive gray variance to present another denoising approach. Accordingly, in this chapter, two different approaches are presented in which one is based on the NSST and nonlinear adaptive diffusion filtering approach (NSST-NADF) and another is based on nonlocal information (NL) based NADF using the NSST decomposition (NSST-NLNADF).

The remaining part of this chapter is arranged as follows. The next section describes a brief idea of the NSST thresholding and ADF approaches that are utilized to present the proposed NSST-NADF and NSST-NLNADF methods. The performance of the proposed methods is also analyzed for both the speckle and Gaussian noise reduction. Many efforts have been made to estimate and compare the noise reduction and edge preservation performance with the other existing methods.

5.2 Nonsubsampled Shearlet Transform

The NSST is an extension of the ST in multidimensional and multidirectional case which combines the multiscale and direction analysis, separately. Firstly, the NSLP is used to decompose an image into low and high frequency subimage coefficients and then the direction filtering is employed to get the different subbands and different direction shearlet coefficients. Direction filtering is achieved using the shear matrix which provides many more directions. The complete mathematical formulation of the ST has been discussed in the previous chapter. The main difference between the NSST and ST is that the downsampling and upsampling are not used to implement the NSST which is fully shift invariance version of the ST. The NSLP analysis is utilized through an iterative process that is expressed as below:

$$NSLP_{m+1} = F_m s = (Ah_m^1 \prod_{a=1}^{m-1} Ah_a^0)s \tag{5.1}$$

where s refers to an original image, $NSLP_{m+1}$ is the detail coefficients at $m+1^{th}$ and Ah_a^0 and Ah_m^1 refer to the lowpass and highpass filters, respectively.

As mentioned above, the NSLP and shearing filters (ShF) are utilized to provide the multiscale and multidirectional decomposition. At each level of the NSLP decomposition, one high frequency and one low frequency subimages are produced and further the low frequency subband is decomposed, iteratively. At the decomposition level m, an image is decomposed into $m+1$ subbands with the same size of the source image in which one is the

low frequency subband and others m are the high frequency subband images. Shearing filter is also used to decompose the high frequency subimages using the NSST decomposition without sub-sampling that satisfy the shift invariance property. Using the ShF at level K, the high frequency subband images are obtained from the NSLP at each decomposition level and 2^K directional subband image coefficients are produced with the same size as the source images. Three level NSST decomposition is shown in Figure 5.1 which illustrates the NSLP and its corresponding directional decomposition. In the present work, three level $m = 3$ decomposition is used and the number of shearing directions is taken to be 8, 8, 4 from finer to coarser level decomposition of an image. An example of three level NSST decomposition of a zone plate image is also shown in Figure 5.2.

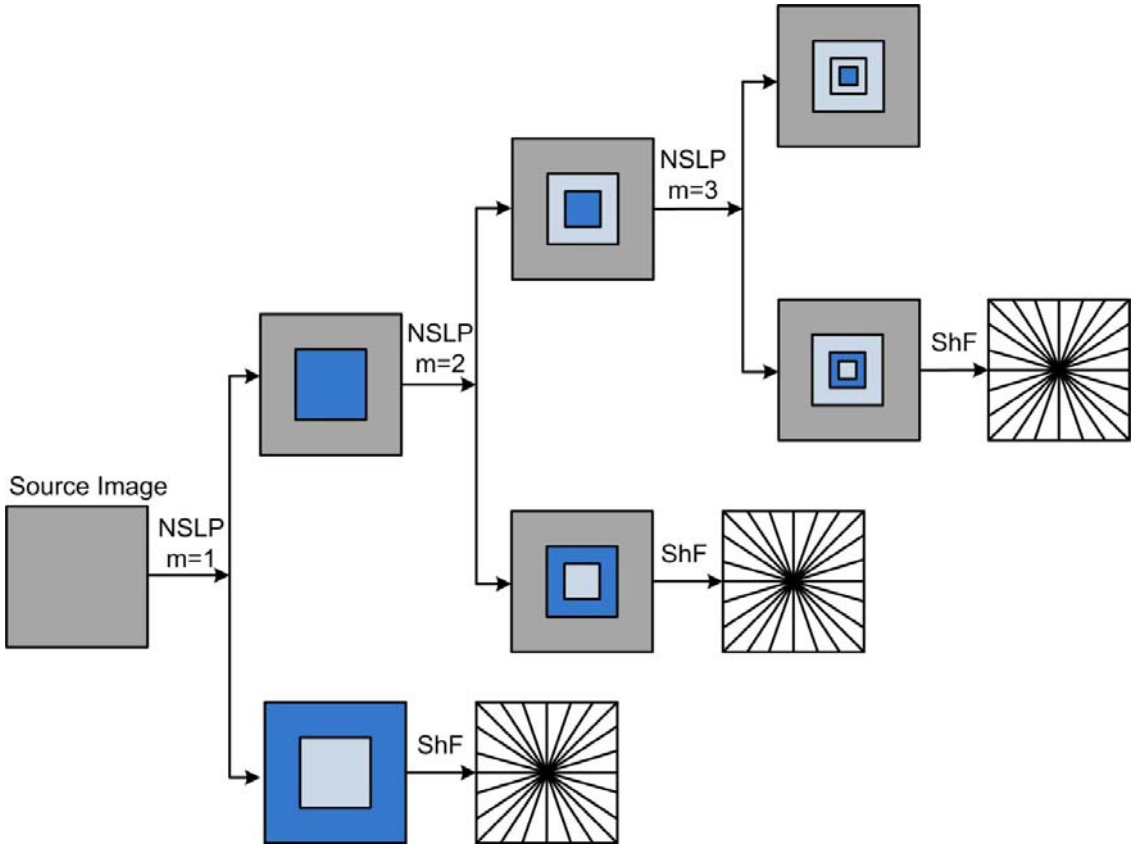

Figure 5.1 Three level multiscale and multidirectional decomposition of the NSST

5.3 NSST Thresholding

The NSST thresholding is the same as thresholding used with the ST and CVT. A summary of the algorithm is as follows:

Step 1: Apply the circular shifts on the noisy image $s(x, y)$.

$$s'(x, y) = circular\_shift\big(s(x, y), [x_{shift}, y_{shift}]\big) \tag{5.2}$$

The number of shifts depends on the length of the input vector scale.

Step 2: Perform the multiscale decomposition of the shifted copies of an image using the NSST to obtain the noisy NSST coefficients.

$$s^{NSST}(x, y) = NSST\big(s'(x, y)\big) \tag{5.3}$$

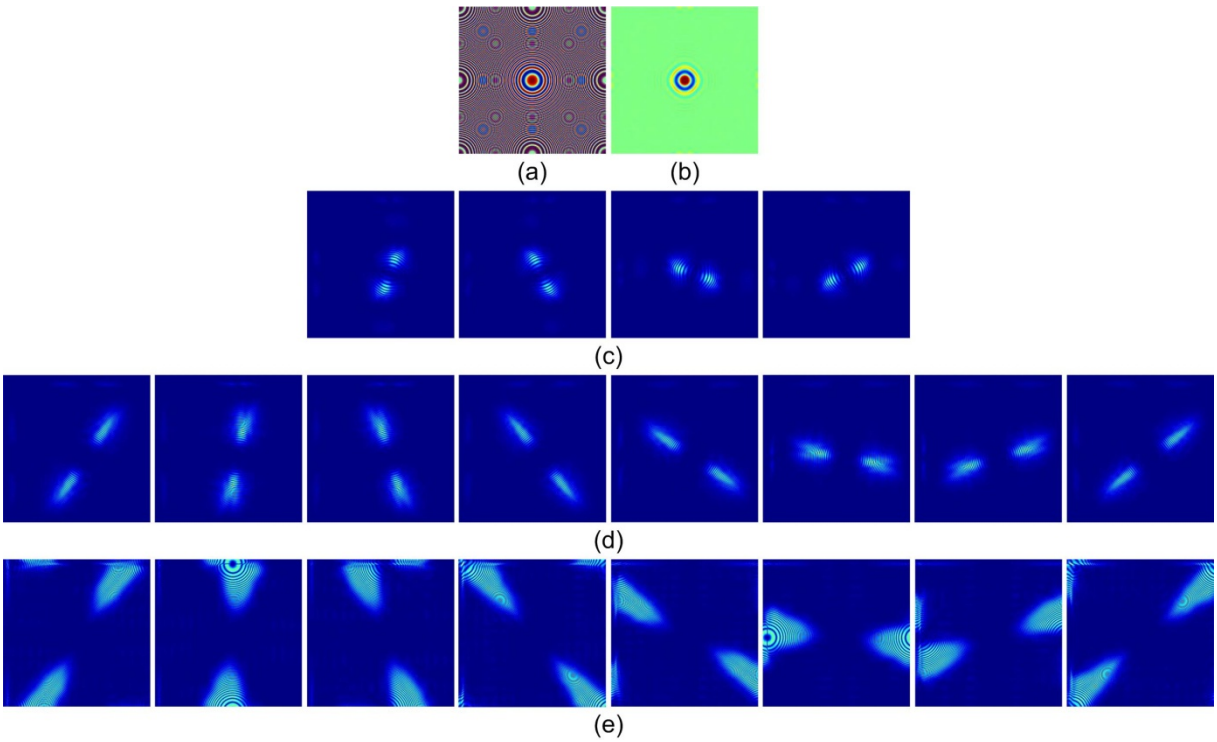

Figure 5.2 NSST decomposition of (a) Original zoneplate image (b) Approximate NSST component. The detail NSST components at (c) scale 3 (d) scale 2 (e) scale 1

Step 3: Apply the thresholding scheme on high frequency NSST coefficients $\left(s_\gamma^{NSST}(x,y)\right)$ to get the threshold coefficients.

$$\hat{s}_\gamma^{NSST}(x,y) = \Theta_{thr}\left(s_\gamma^{NSST}(x,y)\right) = \begin{cases} s_\gamma^{NSST}(x,y), & \left|s_\gamma^{NSST}(x,y)\right| \geq \beta\sigma\sigma_\gamma \\ 0\,, & \text{otherwise} \end{cases} \quad (5.4)$$

where $\hat{s}_\gamma^{NSST}(x,y)$ is the estimator of the unknown noiseless coefficients using hard thresholding, σ is the standard deviation of the noisy image, and σ_γ is the standard deviation of the noisy subband at each scale decomposed using the NSST. The noise variance of each subband is estimated from the noisy NSST coefficients using Monte Carlo techniques [225].

$$\sigma_\gamma = \frac{1}{L_\gamma}\sqrt{\sum_{x=1}^{L_\gamma}\sum_{y=1}^{L_\gamma} s_\gamma^{NSST}(x,y)s_\gamma^{NSST^\star}(x,y)} \quad (5.5)$$

where $s_\gamma^{NSST^\star}(x,y)$ is the complex conjugate of $s_\gamma^{NSST}(x,y)$ and L_γ refers to the length of subband at $\gamma = 1,2,3,\ldots,K-1\text{th}$ scale. For each high frequency NSST subbands, the scale dependent parameter β is computed using $= \sqrt{\log\left(L_\gamma\right)}$.

Step 4: Invert the multiscale decomposition to reconstruct the denoised image.

$$\hat{s}'(x,y) = NSST^{-1}\left(\hat{s}_\gamma^{NSST}(x,y)\right) \quad (5.6)$$

Step 5: Perform the inverse shift and resulting denoised image are shifted back to the original position and average the translated results to get the approximated image.

$$\hat{s}(x,y) = circular\_shift\left(\hat{s}'(x,y), \left[-x_{shift}\,, -y_{shift}\,\right]\right) \quad (5.7)$$

5.4 Anisotropic Diffusion

Anisotropic diffusion is modelled by Perona and Malik (PM) for defining a scale space image [186]. This model is an extension of the heat equation that is based on the PDE. Let $s(x, y; t)$ is an image with coordinates (x, y) at time t, and the continuous anisotropic diffusion is defined as

$$\frac{\partial s(x,y;t)}{\partial t} = div[g(x, y; t)\nabla s(x, y; t)] \quad (5.8)$$

where div is the divergence operator, g is the diffusion coefficient and ∇ refers to a gradient operator with respect to space variables. The diffusion model becomes isotropic, if g is a constant parameter. If g is a function of directional parameters, the diffusion model becomes anisotropic. They also suggested two well known diffusion coefficients considered as below:

$$g(f) = 1/\left[1 + \left(\frac{f}{\lambda}\right)^2\right] \quad (5.9)$$

$$g(f) = exp\left[-\left(\frac{f}{\lambda}\right)^2\right] \quad (5.10)$$

where $f = |\nabla s|$ and the parameter λ serves as a threshold of gradient size. Instead of having many computational and theoretical properties, there is one serious problem with the diffusion method. It is very sensitive to the noise which may introduce large oscillations in the gradient. Furthermore, the PM method cannot differentiate between true edges and noises. Another problem is that staircasing effects arise around smooth edges [128]. To provide the solution of this problem, Catte et al. [46] proposed that a Gaussian kernel G_σ is convolved with the images to reduce the effect of noise. It is very sensitive to the number of diffusion iteration by considering only the gradient information of the pixel. Normally, large gradient values are treated as edges but sometimes the important details along with edges may have low gradient magnitude [53]. Therefore, the gray level variance is incorporated along with the gradient of pixels to evaluate the diffusion coefficients using nonlocal information around the center pixel. In the PM method, the derivative term (∇s) is calculated using a template of four closest neighbors of the pixel (x, y). This term can be evaluated more accurately by considering the large number of neighboring pixels within a template. Moreover, eight nearest neighboring pixels are used within 3×3 template to evaluate the gradient term and the adaptive gray variance is also included along with the gradient to estimate the diffusion coefficients. In the NSST-NLNADF approach, the nonlocal information around the center pixel is estimated based on non local means theory [37, 69].

5.5 Proposed Nonlinear Adaptive Diffusion in NSST Domain Based Noise Filtering

In the proposed methods, the NSST thresholding and modified nonlinear anisotropic diffusion equations are utilized to increase the noise reduction performance. As mentioned in the NSST thresholding approach, the high frequency coefficients are thresholded and the low

frequency approximation coefficients remain unchanged. It preserves more edges than the WT and CVT, but it also adds some unwanted fuzzy edges in the homogeneous region like others. In order to solve this problem, coarser (approximation) NSST coefficients are processed with the modified diffusion model. The process flow of the proposed method is shown in Figure 5.3.

Implementation steps

Let $s(x,y)$ be an observed noisy image and the implementation steps of the proposed model are as follows:

Step 1: Perform the NSST to an image $s(x,y)$ at K different scales. Let $s_K^{NSST}(x,y)$ represent the approximation coefficients at K^{th} coarser scale and $\left(s_\gamma^{NSST}(x,y)\right)$ denote the detail subband coefficients of the image, where $\gamma = 1, 2, 3, \dots, K-1$.

Step 2: Apply the thresholding function $\Theta_{thr}(\cdot)$ to each detail coefficients $\left(s_\gamma^{NSST}(x,y)\right)$ of the NSST decomposition and evaluate the modified coefficients $\left(\hat{s}_\gamma^{NSST}(x,y) = \Theta_{thr}\left(s_\gamma^{NSST}(x,y)\right)\right)$ for each scale from 1 to K-1.

Step 3: Now the coarser scale approximation NSST coefficients are processed using the modified nonlinear diffusion model. Let $c(x,y;t) = s_K^{NSST}(x,y;t)$ be the coarser approximation NSST coefficients at coordinates (x,y) and iteration t. The discrete implementation of the anisotropic diffusion in Eqn. (5.8) using four nearest neighbor is given as,

$$c(x,y;t+1) = c(x,y;t) + \tau \begin{bmatrix} g_E(x,y;t)\nabla_{\mathrm{E}}c(x,y;t) \\ +g_W(x,y;t)\nabla_{\mathrm{W}}c(x,y;t) \\ +g_N(x,y;t)\nabla_{\mathrm{N}}c(x,y;t) \\ +g_S(x,y;t)\nabla_{\mathrm{S}}c(x,y;t) \end{bmatrix} \tag{5.11}$$

where $0 \le \tau \le 1/4$ and E, W, N and S refer to east, west, north and south, respectively. The gradient (∇_{j}) is evaluated as nearest neighbor differences as follows:

$$\left.\begin{aligned} \nabla_{\mathrm{E}}c(x,y;t) &= \frac{c(x+1,y;t)-c(x,y;t)}{d} \\ \nabla_{\mathrm{W}}c(x,y;t) &= \frac{c(x-1,y;t)-c(x,y;t)}{d} \\ \nabla_{\mathrm{N}}c(x,y;t) &= \frac{c(x,y+1;t)-c(x,y;t)}{d} \\ \nabla_{\mathrm{S}}c(x,y;t) &= \frac{c(x,y-1;t)-c(x,y;t)}{d} \end{aligned}\right\} \tag{5.12}$$

Here, d represents a spatial step size between two consecutive pixels in horizontal and vertical direction in the image.

(a) In the first stage of diffusion model, all the eight nearest neighbors are used to calculate the derivative term in 3×3 template. Figure 5.4 shows the neighborhood pixel representation in 3×3 template. The derivation term is calculated in two groups.

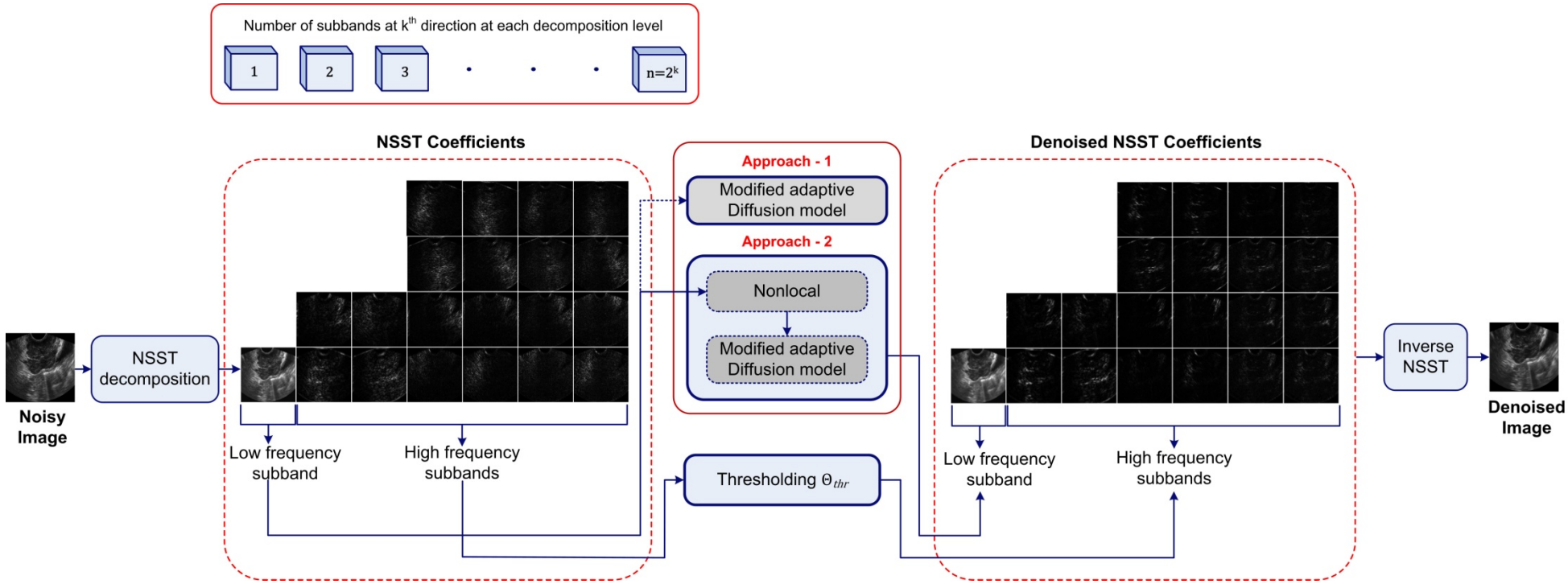

Figure 5.3 Process flow of the proposed NSST-NADF and NSST-NLNADF approaches

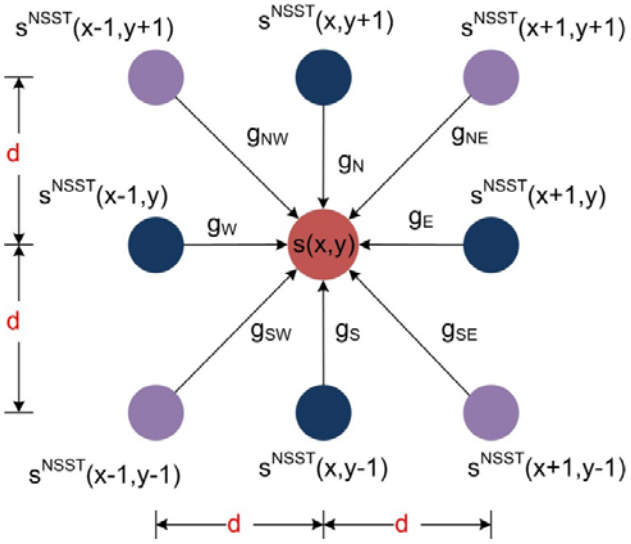

Figure 5.4 Discrete computational approach to evaluate the diffusion coefficient

(i) *For NSST-NADF (approach-1)*

In the first group, we consider only those neighboring pixels which have a distance d from the center pixel $s_K^{NSST}(x,y;t)$ as shown in the Eqn. (5.12), while in the second group, the pixels which have the distance $d\sqrt{2}$ from the center pixel are computed as follows:

$$\left.\begin{aligned}\nabla_{\mathrm{NE}}c(x,y;t) &= \frac{c(x+1,y+1;t)-c(x,y;t)}{d\sqrt{2}}\\ \nabla_{\mathrm{NW}}c(x,y;t) &= \frac{c(x-1,y+1;t)-c(x,y;t)}{d\sqrt{2}}\\ \nabla_{\mathrm{SE}}c(x,y;t) &= \frac{c(x+1,y-1;t)-c(x,y;t)}{d\sqrt{2}}\\ \nabla_{\mathrm{SW}}c(x,y;t) &= \frac{c(x-1,y-1;t)-c(x,y;t)}{d\sqrt{2}}\end{aligned}\right\} \tag{5.13}$$

(ii) *For NSST-NLNADF (approach-2)*

In the first group, we consider only those neighboring pixels which have a distance d from the center pixel $c(x,y)$ as shown in Figure 5.4 which are modified by replacing c with the nonlocal information around the current pixels c^{NL} at the iteration t. It can be expressed as [37, 261]

$$c^{NL}(x) = \sum_{y\in s}\omega(x,y)c(y) \tag{5.14}$$

$$\omega(x,y) = \frac{1}{Z(x)}exp\left(\frac{-\alpha(x,y)}{h^2}\right) \tag{5.15}$$

$$\alpha(x,y) = \kappa_a^G\left\|c\big(N(x)\big) - c\big(N(y)\big)\right\|^2 \tag{5.16}$$

$$Z(x) = \sum_y exp\left(\frac{-\beta(x,y)}{h^2}\right) \tag{5.17}$$

$$\beta(x,y) = \kappa_a^G\left\|\Big(c\big(N(x)\big) - c\big(N(y)\big)\Big)\Big(\nabla c\big(N(x)\big) - \nabla c\big(N(y)\big)\Big)\right\|^2 \tag{5.18}$$

where $c^{NL}(x)$ and $c(y)$ refer to the denoised image and noisy image, respectively. The x and y are the image pixel counts and s is the set of all the image pixels. The $\omega(x,y)$ is the similarity between the pixels x and y satisfying the condition $0 \le \omega(x,y) \le 1$ and

$\sum_y \omega(x,y) = 1$, κ_a^G is a Gaussian kernel, $a > 0$ represents the standard deviation. $c(N(x))$ and $c(N(y))$ are the intensity gray level vectors where $N(x)$ and $N(y)$ denote the square neighborhood of a fixed size centered at pixels x and y, respectively, ∇c denotes the gradient operation and the parameter h acts as a degree of filtering. Now Eqn. (5.12) is modified as

$$\left.\begin{aligned}
\nabla_{\mathrm{E}} c^{NL}(x,y;t) &= \frac{c^{NL}(x+1,y;t)-c^{NL}(x,y;t)}{d} \\
\nabla_{\mathrm{W}} c^{NL}(x,y;t) &= \frac{c^{NL}(x-1,y;t)-c^{NL}(x,y;t)}{d} \\
\nabla_{\mathrm{N}} c^{NL}(x,y;t) &= \frac{c^{NL}(x,y+1;t)-c^{NL}(x,y;t)}{d} \\
\nabla_{\mathrm{S}} c^{NL}(x,y;t) &= \frac{c^{NL}(x,y-1;t)-c^{NL}(x,y;t)}{d}
\end{aligned}\right\} \tag{5.19}$$

In the second group, the pixels which have the distance $d\sqrt{2}$ from the center pixel are computed as follows:

$$\left.\begin{aligned}
\nabla_{\mathrm{NE}} c^{NL}(x,y;t) &= \frac{c^{NL}(x+1,y+1;t)-c^{NL}(x,y;t)}{d\sqrt{2}} \\
\nabla_{\mathrm{NW}} c^{NL}(x,y;t) &= \frac{c^{NL}(x-1,y+1;t)-c^{NL}(x,y;t)}{d\sqrt{2}} \\
\nabla_{\mathrm{SE}} c^{NL}(x,y;t) &= \frac{c^{NL}(x+1,y-1;t)-c^{NL}(x,y;t)}{d\sqrt{2}} \\
\nabla_{\mathrm{SW}} c^{NL}(x,y;t) &= \frac{c^{NL}(x-1,y-1;t)-c^{NL}(x,y;t)}{d\sqrt{2}}
\end{aligned}\right\} \tag{5.20}$$

(b) *For NSST-NADF and NSST-NLNADF (approach-1 and 2)*

In the second stage, gray level variance is incorporated with gradient to calculate the diffusivity term. This gray level variance is estimated at each pixel of the approximation coefficients $s_K^{NSST}(x,y;t)$ in block size 3×3 and normalized it. After incorporating the variance (Var_b) and gradient in the diffusion equations, Eqns (5.9) and (5.10) become as

$$g(f, Var_b) = \frac{1}{1+\left(\frac{f \cdot Var_b}{\lambda}\right)^2} \tag{5.21}$$

$$g(f, Var_b) = exp\left[-\left(\frac{f \cdot Var_b}{\lambda}\right)^2\right] \tag{5.22}$$

where $f = \left|\nabla_{\mathrm{j}'} c^{NL}(x,y;t)\right|$ and $j' = E, W, N, S, NE, NW, SE, SW$ which indicate the east, west, north, south, north-east, north-west, south-east and south-west direction, respectively from the center pixels in 3×3 template as shown in Figure 5.4 .

(c) *For NSST-NADF (approach-1)*

By incorporating the above formulations, the modified nonlinear anisotropic diffusion model is given as,

$$s_K^{NSST}(x,y;t+1) = s_K^{NSST}(x,y;t) + \tau \begin{bmatrix} g_E(x,y;t)\nabla_{\mathrm{E}} s_K^{NSST}(x,y;t) + g_W(x,y;t)\nabla_{\mathrm{W}} s_K^{NSST}(x,y;t) \\ +g_N(x,y;t)\nabla_{\mathrm{N}} s_K^{NSST}(x,y;t) + g_S(x,y;t)\nabla_{\mathrm{S}} s_K^{NSST}(x,y;t) \\ +g_{NE}(x,y;t)\nabla_{\mathrm{NE}} s_K^{NSST}(x,y;t) + g_{NW}(x,y;t)\nabla_{\mathrm{NW}} s_K^{NSST}(x,y;t) \\ +g_{SE}(x,y;t)\nabla_{\mathrm{SE}} s_K^{NSST}(x,y;t) + g_{SW}(x,y;t)\nabla_{\mathrm{SW}} s_K^{NSST}(x,y;t) \end{bmatrix} \tag{5.23}$$

(d) *For NSST-NLNADF (approach-2)*

By incorporating the above formulations, the modified nonlinear anisotropic diffusion model is given as,

$$c^{NL}(x,y;t+1) = c^{NL}(x,y;t) + \tau \begin{bmatrix} g_E(x,y;t)\nabla_{\mathrm{E}} c^{NL}(x,y;t) \\ +g_W(x,y;t)\nabla_{\mathrm{W}} c^{NL}(x,y;t) \\ +g_N(x,y;t)\nabla_{\mathrm{N}} c^{NL}(x,y;t) \\ +g_S(x,y;t)\nabla_{\mathrm{S}} c^{NL}(x,y;t) \\ +g_{NE}(x,y;t)\nabla_{\mathrm{NE}} c^{NL}(x,y;t) \\ +g_{NW}(x,y;t)\nabla_{\mathrm{NW}} c^{NL}(x,y;t) \\ +g_{SE}(x,y;t)\nabla_{\mathrm{SE}} c^{NL}(x,y;t) \\ +g_{SW}(x,y;t)\nabla_{\mathrm{SW}} c^{NL}(x,y;t) \end{bmatrix} \quad (5.24)$$

Step 4: Finally, a filtered image $s(x,y)$ is obtained after taking the inverse NSST transform on the processed subimages from step 2 and 3.

5.6 Experimentation

To investigate the denoising performance of the proposed methods, three experiments having different objectives are performed on the same dataset as given below:

Experiment 1: Analysis and evaluation of the denoising performance of the proposed NSST-NADF approach.

1.1: Denoising of test images corrupted by multiplicative speckle noise.

1.2: Denoising of test images corrupted by additive Gaussian noise.

1.3: Denoising of real US medical images for speckle reduction.

Experiment 2: Analysis and evaluation of the denoising performance of the proposed NSST-NLNADF approach.

2.1: Denoising of test images corrupted by multiplicative speckle noise.

2.2: Denoising of test images corrupted by additive Gaussian noise.

2.3: Denoising of real US medical images for speckle reduction.

Experiment 3: Comparative analysis and evaluation of the proposed approaches.

3.1: Comparison of the proposed approaches with others for the test images degraded by speckle noise.

3.2: Comparison of the proposed approaches with others for the test images degraded by Gaussian noise.

3.3: Comparison of the proposed NSST-NADF and NSST-NLNADF methods with others for speckle reduction in real US images.

5.7 Results and Discussions

5.7.1 Analysis and evaluation of the proposed NSST-NADF approach

To validate the objective of this experiment, it is further decomposed into three different sub-experiments as listed below:

1.1: *Denoising of test images corrupted by multiplicative speckle noise* - To assess the performance of the NSST-NADF approach, same kidney, fetus and phantom images as shown in previous chapters are utilized. The denoised kidney images are shown in Figure 5.5. From the visual analysis of the results presented in Figure 5.5, it is clear that the proposed NSST-NADF approach is able to provide better visual quality of kidney image than the others such as the ADF, NLMF, TI-WT, CSCVT and CSST methods. These subjective outcomes of kidney images are also validated by evaluating the performance measures as discussed in chapter 2. The performance measures obtained by the NSST-NADF approach for three different noise levels ($\sigma = 0.1, 0.2$ and 0.3) are listed in Table 5.1. From the results mentioned in Table 5.1, it is observed that the proposed NSST-NADF approach achieves better speckle reduction performance by producing higher PSNR (28.55, 27.64 and 27.12) and SNR (17.93, 17.02 and 16.50) for all three noise levels. With higher values of the SNR and PSNR, it also gains larger FOM (0.7976, 0.7914 and 0.7556) and EKI (0.5276, 0.4619 and 0.4538) values that indicate superior performance of the NSST-NADF than the others. Similarly, from the visual results of the denoised fetus and phantom images illustrated in Figure 5.6 and Figure 5.7, respectively, it is observed that the proposed NSST-NADF approach produces most similar results as the original images and the results produced by the NSST-NADF approach are better than the existing methods. The quantitative results produced by the denoising methods for the fetus images are presented in Table 5.2. The results mentioned in Table 5.2 show that the proposed NSST-NADF approach produces higher SNR, PSNR, SSIM, FOM and EKI values than the other existing methods.

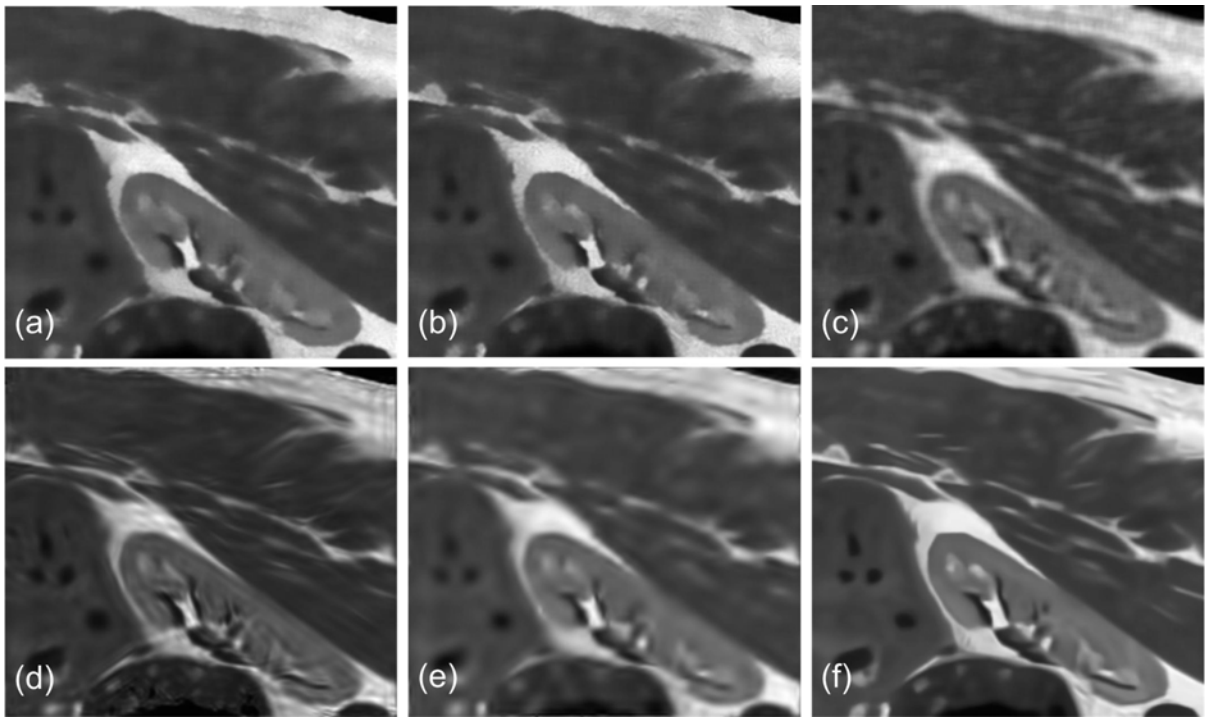

Figure 5.5 Denoised kidney images produced by the (a) ADF (b) NLMF (c) TI-WT (d) CSCVT (f) CSST (f) Proposed NSST-NADF

Table 5.1 Image quality measures obtained by the proposed NSST-NADF and other methods for kidney image degraded by speckle noise

Noise level	Methods	PSNR	SNR	SSIM	FOM	EKI
$\sigma = 0.1$	ADF	21.74	11.11	0.7610	0.3831	0.3181
	NLMF	28.37	17.75	0.7829	0.6785	0.4827
	TI-WT	27.48	16.86	0.7412	0.5484	0.4319
	CSCVT	26.77	16.15	0.7666	0.5460	0.4340
	CSST	27.54	16.92	0.7603	0.6258	0.4567
	Proposed NSST-NADF	28.55	17.93	0.8259	0.7976	0.5276
$\sigma = 0.2$	ADF	20.79	10.17	0.7190	0.3776	0.3041
	NLMF	27.37	16.75	0.7797	0.6652	0.4519
	TI-WT	27.31	16.69	0.7391	0.5364	0.4307
	CSCVT	26.57	15.95	0.7633	0.5663	0.4318
	CSST	27.28	16.66	0.7548	0.6074	0.4349
	Proposed NSST-NADF	27.64	17.02	0.7892	0.7914	0.4619
$\sigma = 0.3$	ADF	20.46	9.84	0.6974	0.3851	0.3011
	NLMF	26.20	15.58	0.7612	0.6584	0.4236
	TI-WT	26.91	16.29	0.7353	0.5457	0.4218
	CSCVT	26.27	15.65	0.7407	0.5828	0.4193
	CSST	27.05	16.43	0.7560	0.5962	0.4231
	Proposed NSST-NADF	27.12	16.50	0.7625	0.7556	0.4538

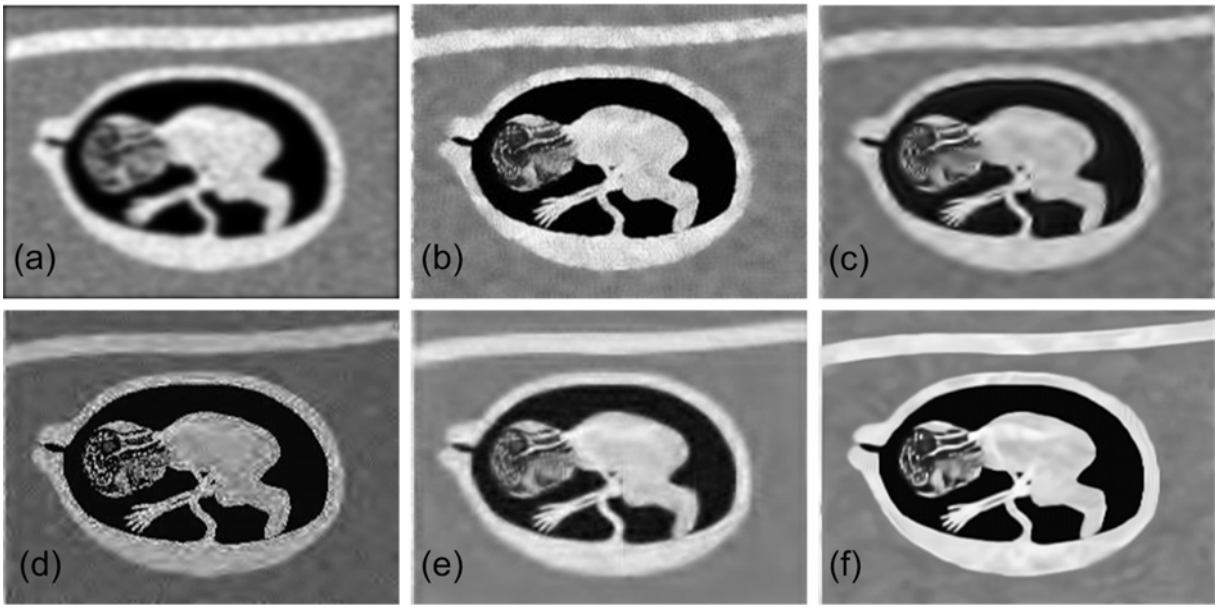

Figure 5.6 Denoised fetus images produced by the (a) ADF (b) NLMF (c) TI-WT (d) CSCVT (f) CSST (f) Proposed NSST-NADF

Similarly, Table 5.3 presents the performance measures for the denoised phantom images produced by the proposed NSST-NADF and other approaches. From all the results mentioned in Table 5.3, it is observed that the proposed NSST-NADF approach is capable to

Table 5.2 Image quality measures obtained by the proposed NSST-NADF and other methods for fetus image degraded by speckle noise

Noise level	Methods	PSNR	SNR	SSIM	FOM	EKI
$\sigma = 0.1$	ADF	17.06	12.08	0.5925	0.6121	0.3572
	NLMF	19.56	14.57	0.6800	0.8654	0.6336
	TI-WT	18.31	13.32	0.6077	0.8474	0.3785
	CSCVT	18.03	13.04	0.6381	0.8258	0.4277
	CSST	18.80	13.81	0.6490	0.8369	0.4387
	Proposed NSST-NADF	20.70	15.71	0.6820	0.9172	0.6792
$\sigma = 0.2$	ADF	15.72	10.73	0.5375	0.5037	0.3246
	NLMF	18.13	13.14	0.6369	0.8453	0.5454
	TI-WT	17.40	12.41	0.5758	0.7524	0.3579
	CSCVT	17.15	12.16	0.6164	0.7276	0.4089
	CSST	17.75	12.76	0.5764	0.7854	0.4192
	Proposed NSST-NADF	19.22	14.23	0.6383	0.8995	0.5897
$\sigma = 0.3$	ADF	15.58	10.59	0.4978	0.4447	0.3092
	NLMF	17.91	12.92	0.5752	0.8267	0.4541
	TI-WT	16.50	11.51	0.5445	0.7128	0.3167
	CSCVT	16.38	11.39	0.5816	0.7086	0.3730
	CSST	16.82	11.83	0.5095	0.7382	0.3879
	Proposed NSST-NADF	18.43	13.45	0.6050	0.8914	0.5474

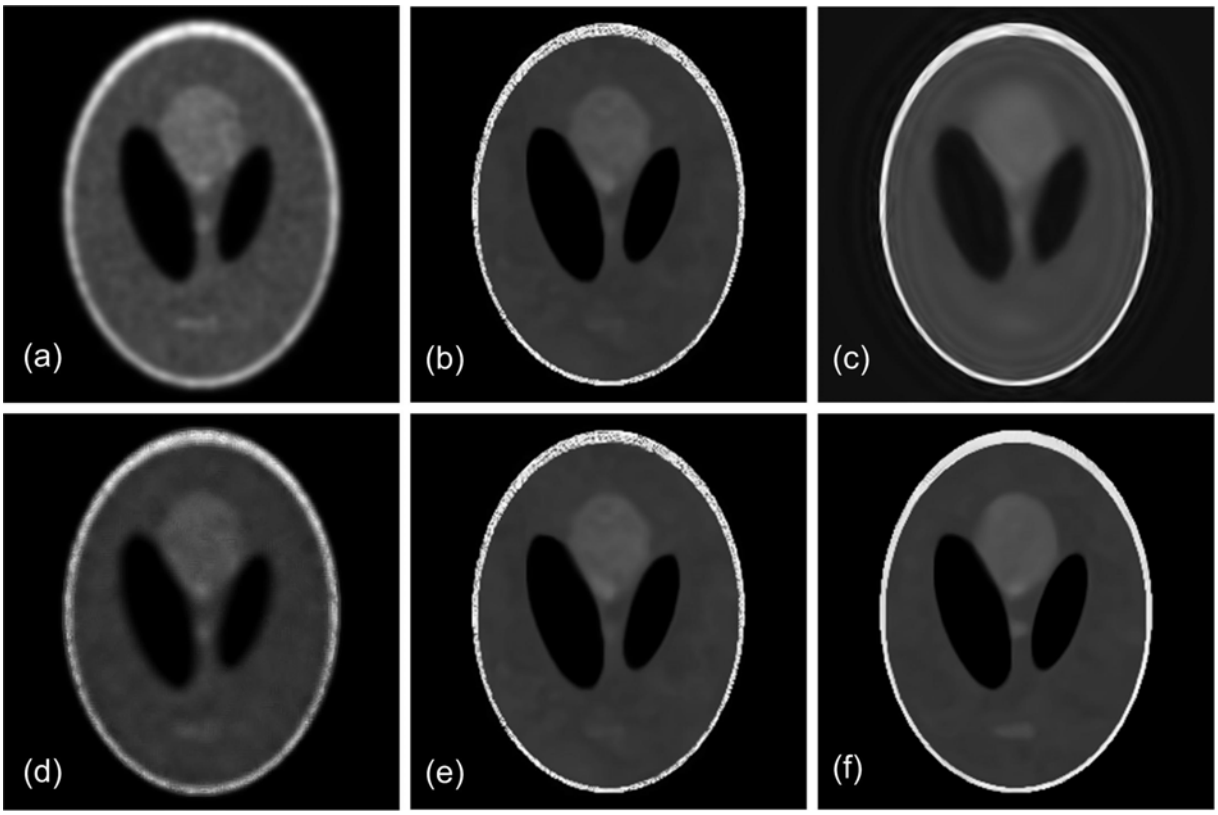

Figure 5.7 Denoised phantom images produced by the (a) ADF (b) NLMF (c) TI-WT (d) CSCVT (f) CSST (f) Proposed NSST-NADF

Table 5.3 Image quality measures obtained by the proposed NSST-NADF and other methods for phantom image degraded by speckle noise

Noise level	Methods	PSNR	SNR	SSIM	FOM	EKI
$\sigma = 0.1$	ADF	21.98	9.81	0.7650	0.4311	0.7381
	NLMF	27.31	15.14	0.8492	0.7424	0.7933
	TI-WT	24.71	12.54	0.7920	0.6292	0.5930
	CSCVT	25.01	12.84	0.7970	0.6494	0.6121
	CSST	25.55	13.39	0.8365	0.9135	0.6850
	Proposed NSST-NADF	27.59	15.42	0.8498	0.9187	0.8211
$\sigma = 0.2$	ADF	21.12	8.95	0.7451	0.4601	0.5159
	NLMF	24.69	12.53	0.8135	0.6231	0.6326
	TI-WT	23.64	11.47	0.7680	0.5134	0.5600
	CSCVT	24.12	11.95	0.7923	0.4688	0.5799
	CSST	24.44	12.27	0.7974	0.8235	0.6267
	Proposed NSST-NADF	25.01	12.84	0.8205	0.8734	0.6768
$\sigma = 0.3$	ADF	19.98	7.81	0.7305	0.4267	0.3945
	NLMF	23.14	10.97	0.7829	0.5387	0.6180
	TI-WT	23.12	10.95	0.7529	0.4687	0.5312
	CSCVT	23.38	11.22	0.7813	0.4435	0.5521
	CSST	23.48	11.31	0.7823	0.8116	0.5397
	Proposed NSST-NADF	23.51	11.34	0.7871	0.8698	0.6424

provide better PSNR and SNR values with higher edge preserving parameters like EKI. Moreover, at higher noise level, it achieves competitive values of these parameters, but still higher than others.

1.2: *Denoising of test images corrupted by additive Gaussian noise* - To perform this experiment and investigate the robustness of the proposed NSST-NADF approach, three different images such as Lena, girl and boat images presented in chapter 2 are considered. The denoised results corresponding to all three different images are shown in Figure 5.8, Figure 5.9 and Figure 5.10, respectively. From the visual assessment of the denoised images presented in these figures, it is observed that the proposed NSST-NADF approach produces better results by preserving more edges than the other methods as mentioned above. It does not only able to remove the fuzzy edges that are introduced during the CSCVT and CSST process, but also helps to preserve the edges that are lost during the ADF and NLMF approach. To analyze the denoising performance and validate the visual results of Lena, girl and boat images, the quantitative analysis is performed by evaluating the performance indices such as the PSNR, SNR, SSIM and EKI. The quantitative results corresponding to Lena, girl and boat images are listed in Table 5.4 for different levels of Gaussian noise. From the results shown in Table 5.4, it is observed that the proposed NSST-NADF approach gains approx 29.5-32.9%, 0.42-3.24%, 1.48-4.89%, 2.41-3.87% 0.11-0.36%

Figure 5.8 Denoised Lena images produced by the (a) ADF (b) NLMF (c) TI-WT (d) CSCVT (f) CSST (f) Proposed NSST-NADF

Figure 5.9 Denoised girl images produced by the (a) ADF (b) NLMF (c) TI-WT (d) CSCVT (f) CSST (f) Proposed NSST-NADF

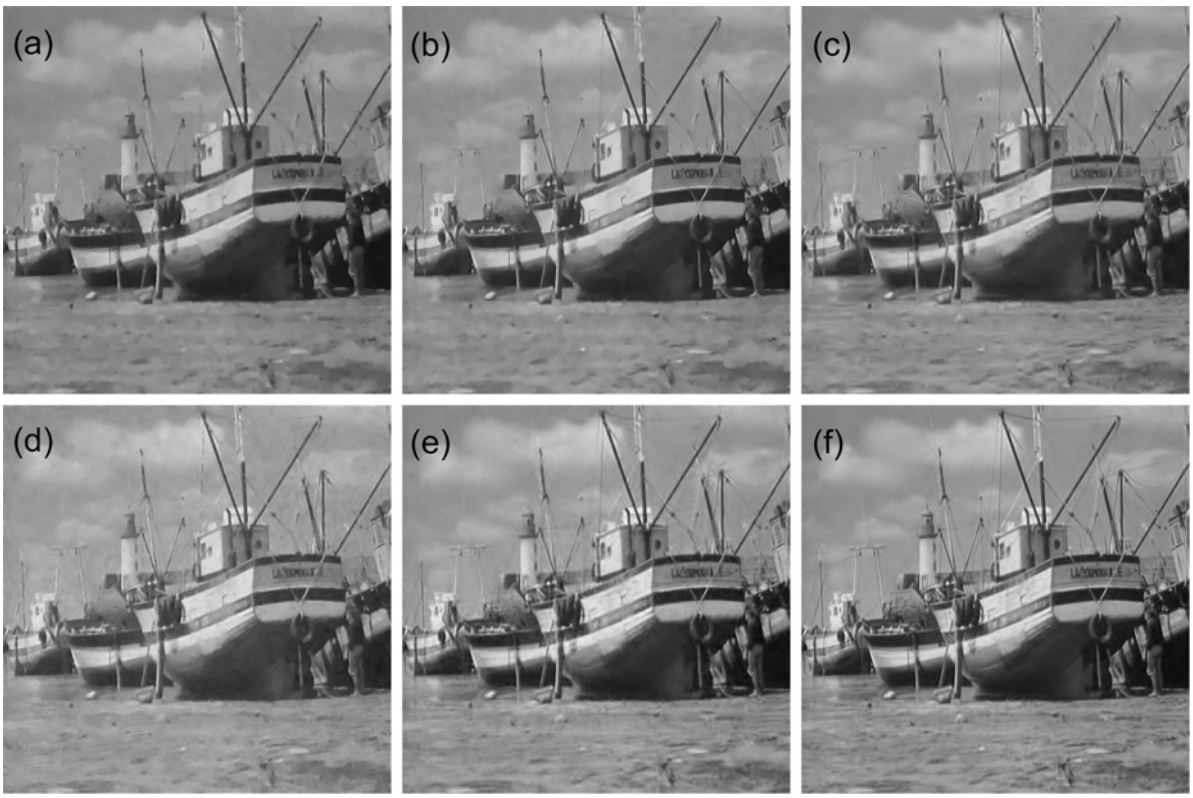

Figure 5.10 Denoised boat images produced by the (a) ADF (b) NLMF (c) TI-WT (d) CSCVT (f) CSST (f) Proposed NSST-NADF

higher PSNR and approx 38.65-41.82%, 0.47-3.96%, 1.76-6.06%, 2.88-4.78%, 0.1-0.4% higher SNR values than ADF, NLMF, TI-WT, CSCVT and CSST methods for Lena image. Besides this, the proposed approach also produces higher EKI values than ADF (approx 44.69%, 63.42% and 79.85%), NLMF (1.2%, 5.17% and 16.48%), TI-WT (3.69%, 15.33% and 31.2%), CSCVT (2.83%, 4.63% and 6.19%) and CSST (0.46%, 2.55% and 5.81%) for $\sigma_n = 10$, 20 and 30, respectively. Higher EKI values indicate that the proposed NSST-NADF approach is able to effectively preserve more edges in case of higher noise level as compared to others. Similarly, in case of girl image, the proposed approach achieves higher EKI values than ADF (19.91%, 30.35% and 47.41%), NLMF (0.93%, 2.21% and 15.48%), TI-WT (2%, 13.64% and 32.98%), CSCVT (2.53%, 4.31% and 9.11%) and CSST (0.71%, 2.33% and 8.99%) and higher SSIM values than the ADF (2.91%, 6.12% and 5.59%), NLMF (0.35%, 0.5% and 1.21%), TI-WT (0.52%, 1.34% and 2.23%), CSCVT (1.06%, 1.93% and 2.69%), CSST (1.05%, 0.35% and 0.93%), for all three different noise levels, respectively. It also improves noise suppression performance by providing higher PSNR and SNR values. In case of the boat images, the proposed approach also produces similar results as produced in the case of Lena and girl images. It achieves approx 117%, 28.49%, 45.69%, 26.27%, 25.11% higher EKI, 19.93%, 5.15%, 3.53%, 4%, 1.44% higher SSIM values with 35.71%, 2.95%, 4.11%, 3.97% and 0.79% SNR values than the ADF, NLMF, TI-WT, CSCVT and CSST methods, respectively, for $\sigma_n = 30$. It indicates better noise reduction with more edge preservation produced by the proposed NSST-NADF method than the other methods.

Table 5.4 Image quality measures obtained by the proposed NSST-NADF and other methods for Lena, girl and boat images corrupted by Gaussian noise

Images	Noise level	Metrics	ADF	NLMF	TI-WT	CSCVT	CSST	NSST-NADF
Lena image	$\sigma_n = 10$	PSNR	26.82	35.52	35.15	34.83	35.63	35.67
		SNR	21.16	29.87	29.49	29.17	29.98	30.01
		SSIM	0.9105	0.9600	0.9609	0.9569	0.9643	0.9646
		EKI	0.5908	0.8447	0.8244	0.8313	0.8509	0.8548
	$\sigma_n = 20$	PSNR	25.09	32.13	31.53	31.66	32.65	32.69
		SNR	19.43	26.47	25.88	26.01	26.99	27.04
		SSIM	0.8333	0.9203	0.9204	0.9178	0.9300	0.9347
		EKI	0.4729	0.7348	0.6701	0.7386	0.7536	0.7728
	$\sigma_n = 30$	PSNR	23.85	29.91	29.44	29.73	30.77	30.88
		SNR	18.19	24.26	23.78	24.07	25.12	25.22
		SSIM	0.8060	0.8802	0.8833	0.8805	0.8932	0.9035
		EKI	0.3970	0.6130	0.5442	0.6724	0.6748	0.7140
Girl image	$\sigma_n = 10$	PSNR	27.02	34.17	33.73	33.42	34.02	34.36
		SNR	22.47	29.61	29.18	28.87	29.47	29.81
		SSIM	0.9201	0.9436	0.9420	0.9370	0.9371	0.9469
		EKI	0.6152	0.7309	0.7232	0.7195	0.7325	0.7377
	$\sigma_n = 20$	PSNR	25.23	32.04	31.24	31.27	32.14	32.32
		SNR	20.68	27.49	26.68	26.72	27.59	27.77
		SSIM	0.8617	0.9098	0.9023	0.8971	0.9112	0.9144
		EKI	0.5249	0.6694	0.6021	0.6559	0.6686	0.6842
	$\sigma_n = 30$	PSNR	23.96	30.41	29.63	29.83	30.84	30.97
		SNR	19.41	25.86	25.07	25.28	26.29	26.42
		SSIM	0.8419	0.8784	0.8696	0.8657	0.8808	0.8890
		EKI	0.4590	0.5859	0.5088	0.6201	0.6208	0.6766
Boat image	$\sigma_n = 10$	PSNR	24.79	33.31	33.26	32.71	33.32	33.58
		SNR	19.45	27.97	27.92	27.37	27.98	28.24
		SSIM	0.8549	0.948	0.954	0.9488	0.9568	0.9597
		EKI	0.5358	0.8659	0.8523	0.8495	0.8613	0.9089
	$\sigma_n = 20$	PSNR	23.33	29.82	29.36	29.49	30.01	30.25
		SNR	17.99	24.48	24.02	24.15	24.66	24.91
		SSIM	0.7838	0.8816	0.894	0.8893	0.9056	0.9133
		EKI	0.4162	0.7662	0.7021	0.7445	0.7521	0.8417
	$\sigma_n = 30$	PSNR	22.31	27.71	27.47	27.49	28.19	28.37
		SNR	16.97	22.37	22.12	22.15	22.85	23.03
		SSIM	0.7247	0.8265	0.8395	0.8357	0.8568	0.8691
		EKI	0.3761	0.6363	0.5612	0.6475	0.6535	0.8176

1.3: *Denoising of real US medical images for speckle reduction* - To assess the performance of the proposed NSST-NADF approach on real US images, same US images as used in the previous chapters are considered. All the US images are processed by all aforementioned denoising methods and the visual results of prostate, splenic cyst and multiple liver masses US images are shown in Figure 5.11, Figure 5.12 and Figure 5.13, respectively. From the subjective analysis of the prostate US images, it is observed that the denoised image obtained by the proposed NSST-NADF approach is better than ADF, NLMF and TI-WT method. The CSST method produces some competitive results to the proposed approach in terms of edge preservation, but the proposed approach is still able to suppress more noise than the CSST method. In case of splenic cyst US images, the similar pattern is followed by the CSST and proposed method that the noise reduction is more in case of NSST-NADF approach, but the splenic cyst image, processed by the NLMF and CSCVT approach and shown in Figure 5.12 (b) and (d), respectively, suffers from the loss of edge information. Similarly, in case of multiple liver masses US images, the CSCVT adds some extra edges in the denoised image and the ADF and NLMF suffer from the loss of some edge information. Besides this, the proposed NSST-NADF approach is still able to remove the noise as much as possible. To support the subjective analysis, the MVR values are also evaluated for the proposed method and others. Figure 5.14 shows the bar graph of MVR values estimated for the two different regions marked on the four US images illustrated in Figure 2.21. From the

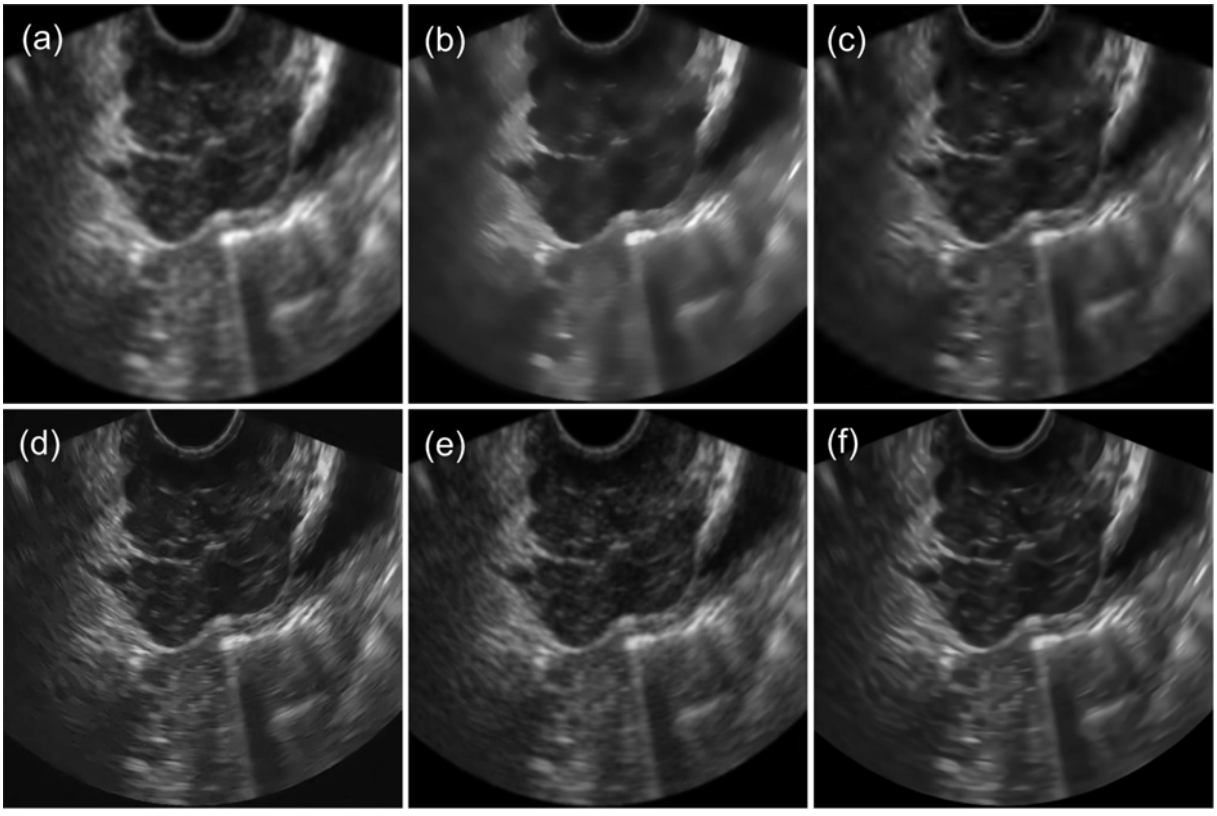

Figure 5.11 Prostate ultrasound image processed by the (a) ADF (b) NLMF (c) TI-WT (d) CSCVT (f) CSST (f) Proposed NSST-NADF

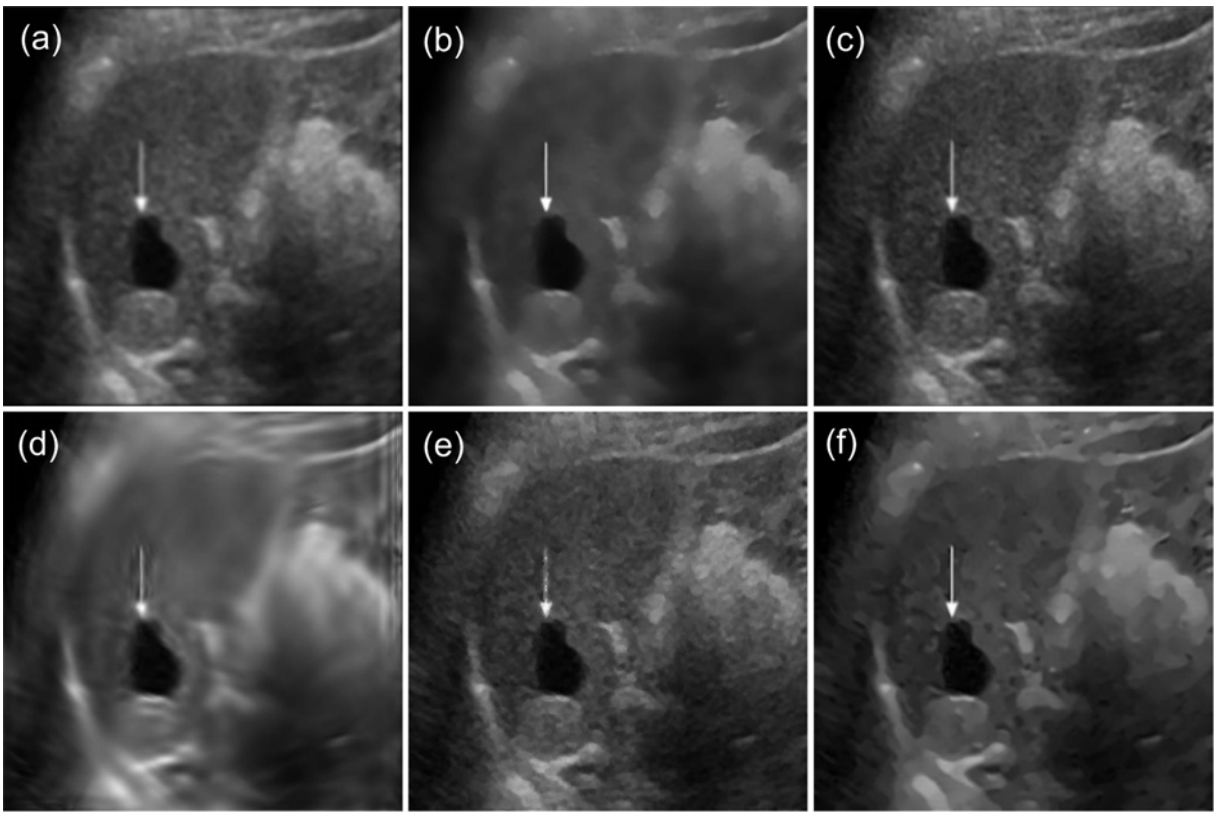

Figure 5.12 Splenic cyst ultrasound image processed by the (a) ADF (b) NLMF (c) TI-WT (d) CSCVT (f) CSST (f) Proposed NSST-NADF

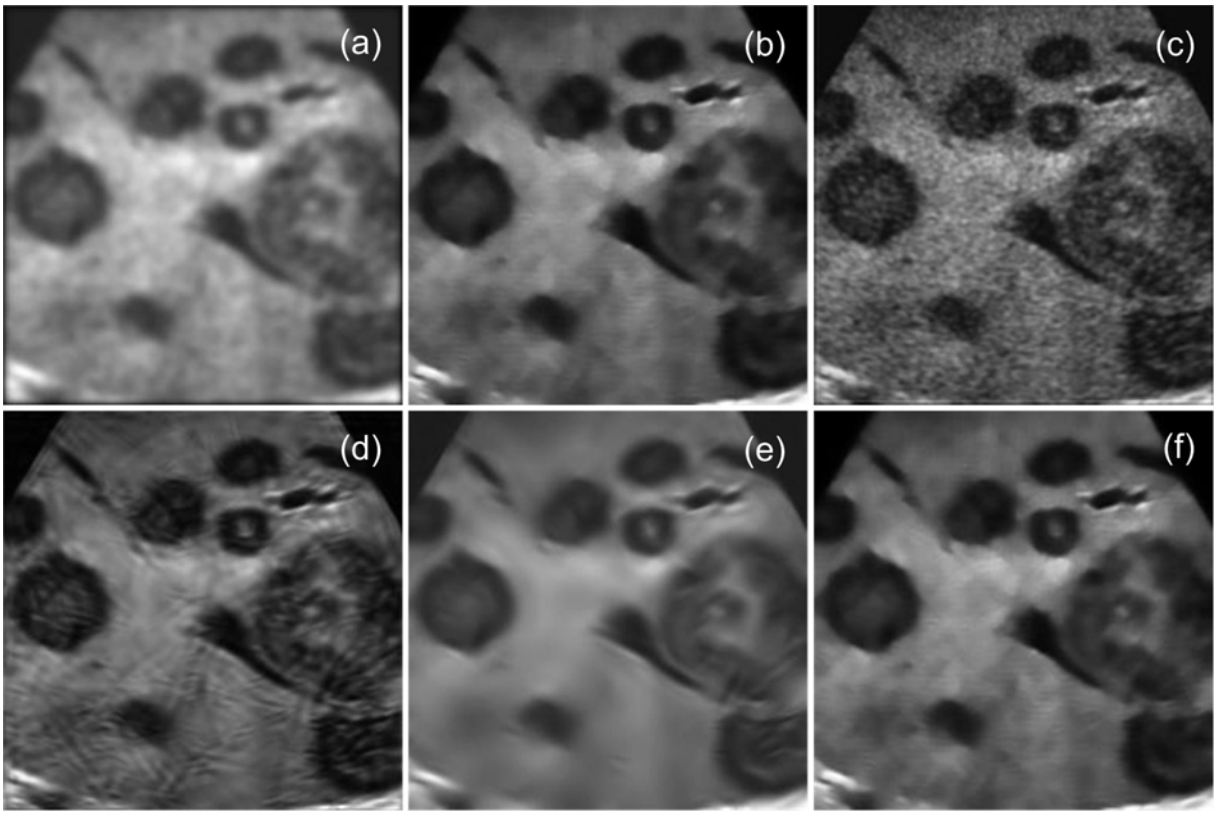

Figure 5.13 Multiple liver masses ultrasound image processed by the (a) ADF (b) NLMF (c) TI-WT (d) CSCVT (f) CSST (f) Proposed NSST-NADF

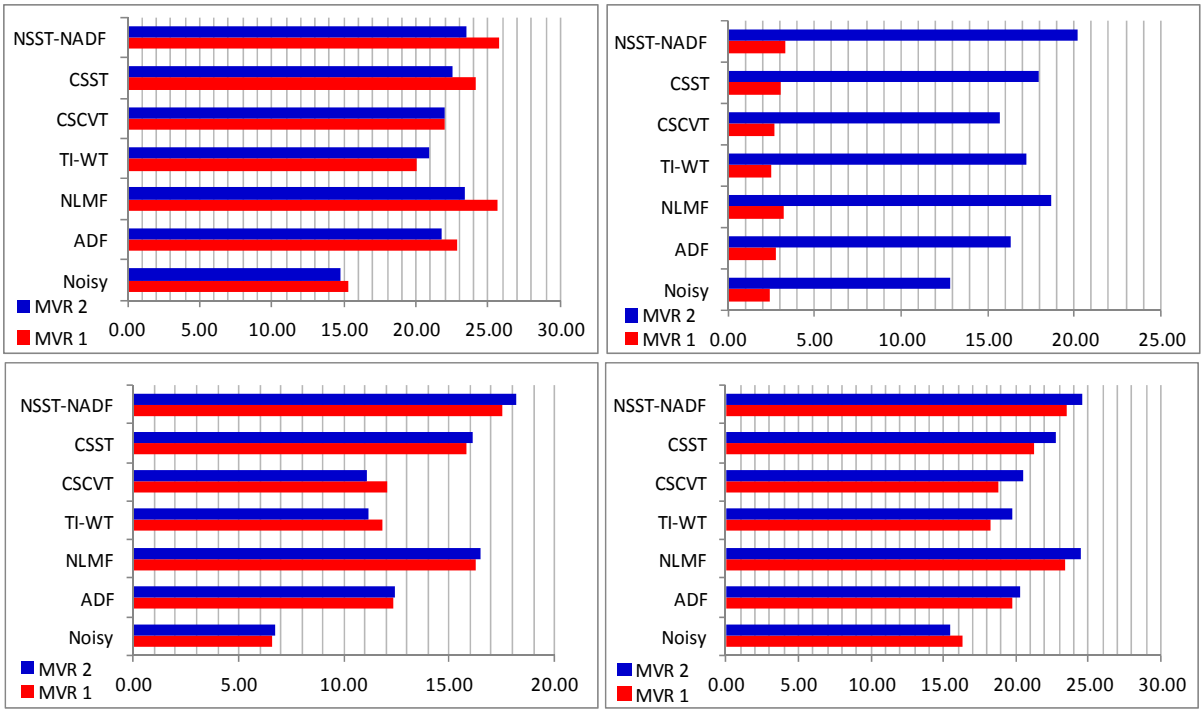

Figure 5.14 Plot of MVR values obtained by the NSST-NADF approach with other existing methods for two image regions

results presented in Figure 5.14, it is observed that the MVR values estimated by the proposed NSST-NADF approach are better than the ADF, NLMF, TI-WT, CSCVT and CSST methods for all the US images. It also indicates better speckle reduction performance provided by the proposed NSST-NADF approach. Similar to the previous chapters, another investigation is further considered to evaluate the MVR values for the 50 different US images in which 100 measurements i.e. two different regions on each of them are taken. For all the methods, the averaged MVR values (mean ± standard deviation) are listed in Table 5.5. From the MVR results, it is clearly observed that the NSST-NADF gains the higher mean value of MVR than the others which depicts the superiority of the proposed NSST-NADF approach to provide an effective speckle reduction performance.

Table 5.5 Performance comparison of the proposed NSST-NADF approach with others in terms of the averaged MVR values over 100 different regions obtained on 50 different ultrasound images

Methods	Noisy	ADF	NMLF	TI-WT	CSCVT	CSST	NSST-NADF
MVR	14.04 ± 3.04	18.26 ± 4.23	21.51 ± 4.13	18.16 ± 3.14	18.22 ± 4.57	20.94 ± 3.88	21.95 ± 4.26

5.7.2 Analysis and evaluation of the proposed NSST-NLNADF approach

2.1: *Denoising of test images corrupted by multiplicative speckle noise* - In order to validate the results obtained by the proposed NSST-NLNADF approach, the denoised images corresponding to simulated kidney, fetus and phantom images that are degraded by multiplicative speckle noise characterized by different noise variance $0.1, 0.2$ and 0.3, respectively, are shown in Figure 5.15. From the visual results presented in Figure 5.15, it is

observed that the kidney, fetus and phantom images processed by the proposed NSST-NLNADF approach achieve good visual quality of images with the preservation of more edges compared to others. It is supported by the quantitative results which are mentioned in Table 5.6. From these quantitative results, it is clearly observed that the proposed NSST-NLNADF approach gains higher PSNR (30.32, 28.72 and 27.91), SNR (19.7, 18.10 and 17.29), SSIM (0.8929, 0.8790 and 0.8703) and EKI values (0.5614, 0.4806 and 0.4637) than ADF, NLMF, CSST methods for the kidney images. The proposed NSST-NLNADF approach

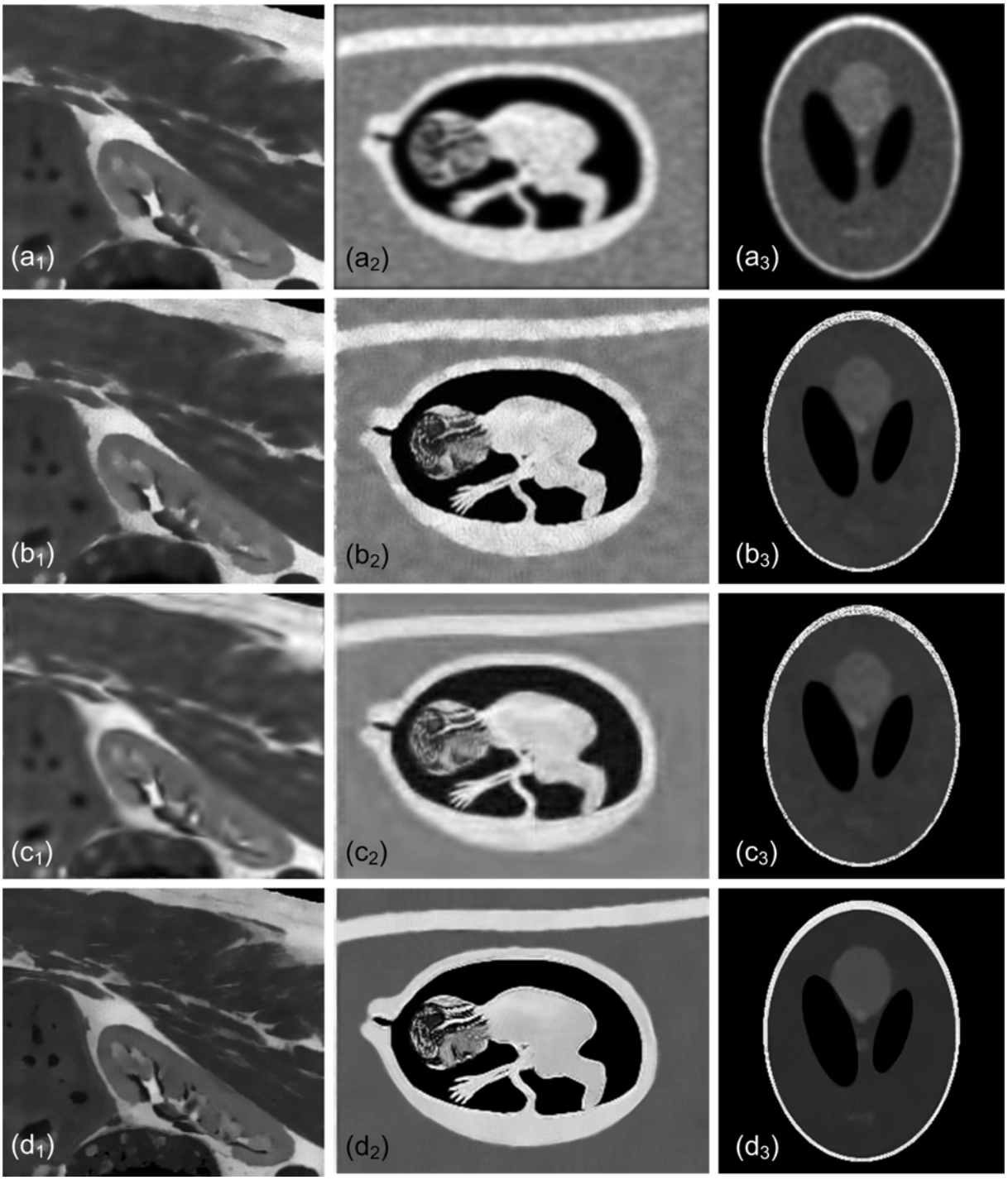

Figure 5.15 Visual denoising performance obtained by the (a) ADF (b) NLMF (c) CSST (d) Proposed NSST-NLNADF. Here 1, 2 and 3 refer to kidney, fetus and phantom images, respectively

Table 5.6 Image quality measures obtained by the ADF, NLMF, CSST and proposed NSST-NLNADF approaches for speckled test images

Images	Noise Level	Metrics	Denoising methods			
			ADF	NLMF	CSST	Proposed NSST-NLNADF
Kidney image	$\sigma = 0.1$	PSNR	21.74	28.37	27.54	30.32
		SNR	11.11	17.75	16.92	19.70
		SSIM	0.7610	0.7829	0.7603	0.8929
		EKI	0.3181	0.4827	0.4567	0.5614
	$\sigma = 0.2$	PSNR	20.79	27.37	27.28	28.72
		SNR	10.17	16.75	16.66	18.10
		SSIM	0.7190	0.7797	0.7548	0.8790
		EKI	0.3041	0.4519	0.4349	0.4806
	$\sigma = 0.3$	PSNR	20.46	26.20	27.05	27.91
		SNR	9.84	15.58	16.43	17.29
		SSIM	0.6974	0.7612	0.7560	0.8703
		EKI	0.3011	0.4236	0.4231	0.4637
Fetus image	$\sigma = 0.1$	PSNR	17.06	19.56	18.80	20.89
		SNR	12.08	14.57	13.81	15.90
		SSIM	0.5925	0.6800	0.6490	0.6851
		EKI	0.3572	0.6336	0.4387	0.7176
	$\sigma = 0.2$	PSNR	15.72	18.13	17.75	19.34
		SNR	10.73	13.14	12.76	14.35
		SSIM	0.5375	0.6369	0.5764	0.6398
		EKI	0.3246	0.5454	0.4192	0.6671
	$\sigma = 0.3$	PSNR	15.58	17.91	16.82	18.59
		SNR	10.59	12.92	11.83	13.60
		SSIM	0.4978	0.5752	0.5095	0.6270
		EKI	0.3092	0.4541	0.3879	0.5922
Phantom image	$\sigma = 0.1$	PSNR	21.98	27.31	25.55	28.90
		SNR	9.81	15.14	13.39	16.73
		SSIM	0.7650	0.8492	0.8365	0.8399
		EKI	0.7381	0.7933	0.6850	0.8624
	$\sigma = 0.2$	PSNR	21.12	24.69	24.44	25.62
		SNR	8.95	12.53	12.27	13.45
		SSIM	0.7451	0.8135	0.7974	0.8219
		EKI	0.5159	0.6326	0.6267	0.8075
	$\sigma = 0.3$	PSNR	19.98	23.14	23.48	24.32
		SNR	7.81	10.97	11.31	12.15
		SSIM	0.7305	0.7829	0.7823	0.7989
		EKI	0.3945	0.6180	0.5397	0.7278

also achieves higher PSNR (19.32%, 3.8% and 10.52%), SNR (28.42%, 5.26% and 14.96%), SSIM (25.95%, 9.01% and 23.06%) and EKI (91.53%, 30.41% and 52.67%) than the ADF, NLMF and CSST methods, respectively in case of the fetus image corrupted by speckle noise of $\sigma = 0.3$. The main focus of the proposed NSST-NLNADF approach is toward more edge preservation with the noise suppression as much as possible. Besides this, in the case of phantom image, the proposed NSST-NLNADF approach gains better edge preservation performance by obtaining higher EKI values approx (16.84%, 56.52% and 84.49%), (8.71%, 27.65% and 17.77%) and (25.9%, 28.85% and 34.85%) than the ADF, NLMF and CSST methods, respectively. It also shows better noise suppression results by providing higher PSNR (21.72%, 5.1% and 3.58%) and SNR (55.57%, 10.76% and 7.43%) than the ADF, NLMF and CSST methods, respectively, in case of higher noise level $\sigma = 0.3$. Finally, it is seen that the proposed NSST-NLNADF approach outperforms the others not only in terms of speckle reduction but also in edge preservation.

2.2: *Denoising of test images corrupted by additive Gaussian noise* - In order to analyze the robust performance of the proposed NSST-NLNADF approach, the denoised images corresponding to noisy Lena, girl and boat images are shown in Figure 5.16. It is visualized in Figure 5.16 that the denoised Lena, girl and boat images produced by the proposed NSST-NLNADF approach have more edges as compared to the others, including ADF and NLMF approaches and reduced extra edges introduced by the CSST approach. Moreover, the subjective analysis is also supported by the objective analysis after evaluating the performance indices. From the quantitative results mentioned in Table 5.7, it is observed that the proposed NSST-NLNADF approach achieves higher PSNR from ADF (approx 33.56%, 32.2% and 30.4%), NLMF (approx 0.84%, 3.24% and 3.98%) and CSST method (approx 0.53%, 1.59% and 1.07%) for Lena image degraded by the different noise levels $\sigma_n = 10, 20$ and 30, respectively. From the higher PSNR values obtained by the proposed method, it is interpreted that the NSST-NLNADF approach shows better improvement in noise reduction performance in case of higher noise level compared to the NLMF and CSST approaches. Besides improved noise reduction performance, it gains approx 45.5-91.89%, 1.76-24.27% and 1.02-12.89% higher EKI values in comparison to the ADF, NLMF and CSST methods, respectively. In case of girl image, the NSST-NLNADF approach gains higher PSNR (29.84%, 2.3% and 0.88%), SNR (36.84%, 2.71% and 1.03%), SSIM (7.15%, 2.7% and 2.42%) and EKI (48.95%, 16.69% and 10.13%) than the ADF, NLMF and CSST methods, respectively, for the noise level $\sigma_n = 30$. Furthermore, in case of the boat image degraded by the noise level $\sigma_n = 30$, the proposed NSST-NLNADF approach produces higher PSNR (27.57%, 2.71% and 0.96%), SNR (36.24%, 3.35% and 1.18%), SSIM (21.06%, 6.15% and 2.39%) and EKI (118%, 28.96% and 25.57%) than the ADF, NLMF and CSST methods, respectively.

Figure 5.16 Visual denoising performance obtained by the (a) ADF (b) NLMF (c) CSST (d) Proposed NSST-NLNADF. Here 1, 2 and 3 refer to Lena, girl and boat images, respectively

Moreover, it is concluded from both the subjective and objective analysis of the results obtained by the proposed NSST-NLNADF approach that it is able to produce better quality images with more edge preservation compared to the other methods.

Table 5.7 Image quality measures obtained by the ADF, NLMF, CSST and proposed NSST-NLNADF approaches for the test images degraded by Gaussian noise

Images	Noise Level	Metrics	Denoising methods			
			ADF	NLMF	CSST	Proposed NSST-NLNADF
Lena image	$\sigma_n = 10$	PSNR	26.82	35.52	35.63	35.82
		SNR	21.16	29.87	29.98	30.16
		SSIM	0.9105	0.9600	0.9643	0.9688
		EKI	0.5908	0.8447	0.8509	0.8596
	$\sigma_n = 20$	PSNR	25.09	32.13	32.65	33.17
		SNR	19.43	26.47	26.99	27.52
		SSIM	0.8333	0.9203	0.9300	0.9387
		EKI	0.4729	0.7348	0.7536	0.7859
	$\sigma_n = 30$	PSNR	23.85	29.91	30.77	31.10
		SNR	18.19	24.26	25.12	25.44
		SSIM	0.8060	0.8802	0.8932	0.9181
		EKI	0.3970	0.6130	0.6748	0.7618
Girl image	$\sigma_n = 10$	PSNR	27.02	34.17	34.02	34.71
		SNR	22.47	29.61	29.47	30.16
		SSIM	0.9201	0.9436	0.9371	0.9457
		EKI	0.6152	0.7309	0.7325	0.7466
	$\sigma_n = 20$	PSNR	25.23	32.04	32.14	32.65
		SNR	20.68	27.49	27.59	28.10
		SSIM	0.8617	0.9098	0.9112	0.9194
		EKI	0.5249	0.6694	0.6686	0.6974
	$\sigma_n = 30$	PSNR	23.96	30.41	30.84	31.11
		SNR	19.41	25.86	26.29	26.56
		SSIM	0.8419	0.8784	0.8808	0.9021
		EKI	0.4590	0.5859	0.6208	0.6837
Boat image	$\sigma_n = 10$	PSNR	24.79	33.31	33.32	33.80
		SNR	19.45	27.97	27.98	28.46
		SSIM	0.8549	0.9480	0.9568	0.9661
		EKI	0.5358	0.8659	0.8613	0.9138
	$\sigma_n = 20$	PSNR	23.33	29.82	30.01	30.96
		SNR	17.99	24.48	24.66	25.61
		SSIM	0.7838	0.8816	0.9056	0.9152
		EKI	0.4162	0.7662	0.7521	0.8530
	$\sigma_n = 30$	PSNR	22.31	27.71	28.19	28.46
		SNR	16.97	22.37	22.85	23.12
		SSIM	0.7247	0.8265	0.8568	0.8773
		EKI	0.3761	0.6363	0.6535	0.8206

2.3: *Denoising of real US medical images for speckle reduction* - In this section, the speckle reduction performance of the proposed approach is assessed on the real US images as used in the previous chapters. The outcomes of the experiments performed on the prostate, splenic cyst and multiple liver masses US images are shown in Figure 5.17. The quantitative

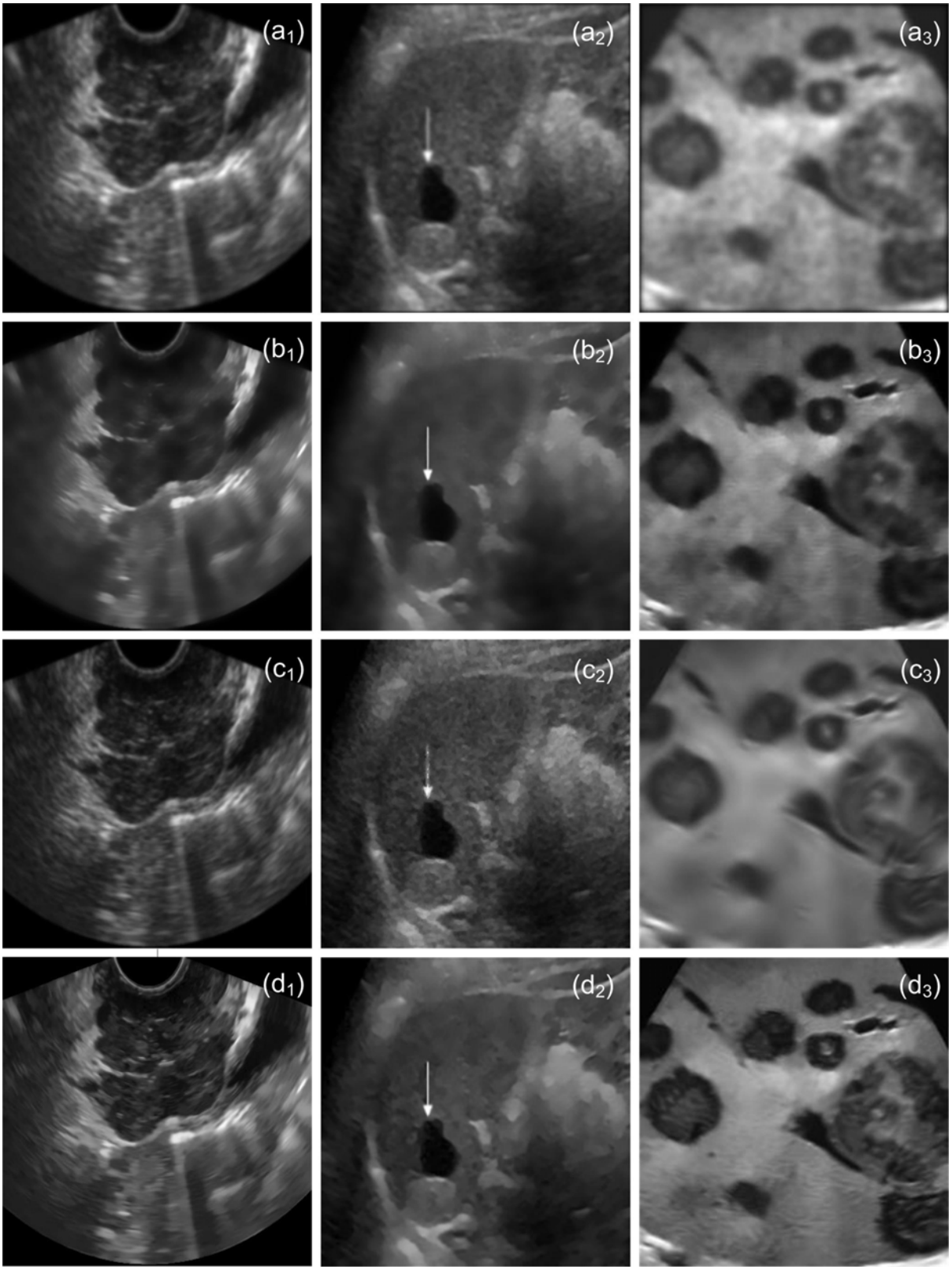

Figure 5.17 Visual speckle reduction performance obtained by the (a) ADF (b) NLMF (c) CSST (d) Proposed NSST-NLNADF

assessment is also performed by evaluating the MVR values for all the US images. The MVR is used to estimate the speckle level in the US images over different selected image regions and shown in Figure 5.18. From the results mentioned in Figure 5.18, it is clearly observed that the proposed NSST-NLNADF approach outperforms the others exhibited in terms of larger MVR values. Moreover, the averaged MVR value obtained by the proposed NSST-NLNADF approach is 22.42 with a standard deviation of 4.12, which is also higher than the proposed NSST-NADF approach and other existing methods.

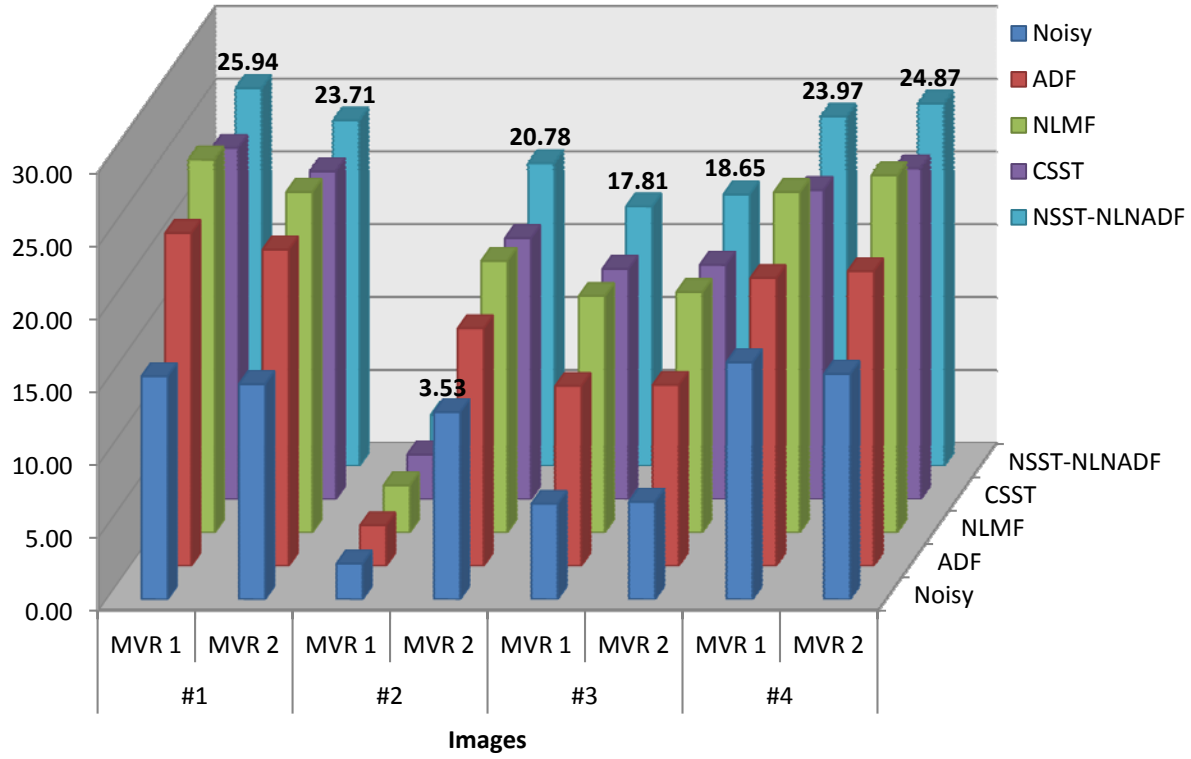

Figure 5.18 Plot for MVR values estimated for real ultrasound images with two selected image regions

5.7.3 Comparative analysis and evaluation of the proposed approaches

In order to investigate the performance of both the proposed NSST-NADF and NSST-NLNADF approaches, three different subsequent objectives are considered as follows:

3.1: *Comparison of the proposed methods with others for the test images degraded by speckle noise* - In this section, a detailed comparison of the performance of both the proposed NSST-NADF and NSST-NLNADF approaches with various different methods is presented for aforementioned three test images which are utilized to analyze the performance of these methods. The following denoising methods used for such purpose are given below:

Method 1: The AWMF approach as discussed in chapter 2.

Method 2: The WF approach as discussed in chapter 2 with 5×5 square window.

Method 3: The Kuan filter as described in [139]

Method 4: The LHMAF as described in [170, 210] with 5×5 square neighborhood window and 15 iterations.

Method 5: The MHOPNF approach as described in [12, 210] and chapter 2 with a square neighborhood of 3×3.

Method 6: Fourth order PDE filter (FOPDEF) as described in [269] with 250 iterations, $k = 0.5$ and time step $\Delta t = 0.25$.

Method 7: The speckle reducing anisotropic diffusion (SRAD) approach as discussed in [266] with second diffusivity equation, 35 averaged iterations and $\tau = 0.2$.

Method 8: Nonlinear complex diffusion (NCDF) approach as discussed in [100] with $\theta = \pi/30$ and $\kappa = 20$.

Method 9: Improved adaptive complex diffusion (INCDF) as described in [20] with $\tau_{max} = 10s$, $\kappa_{min} = 2$, $\kappa_{max} = 28$, and $\theta = \pi/30$.

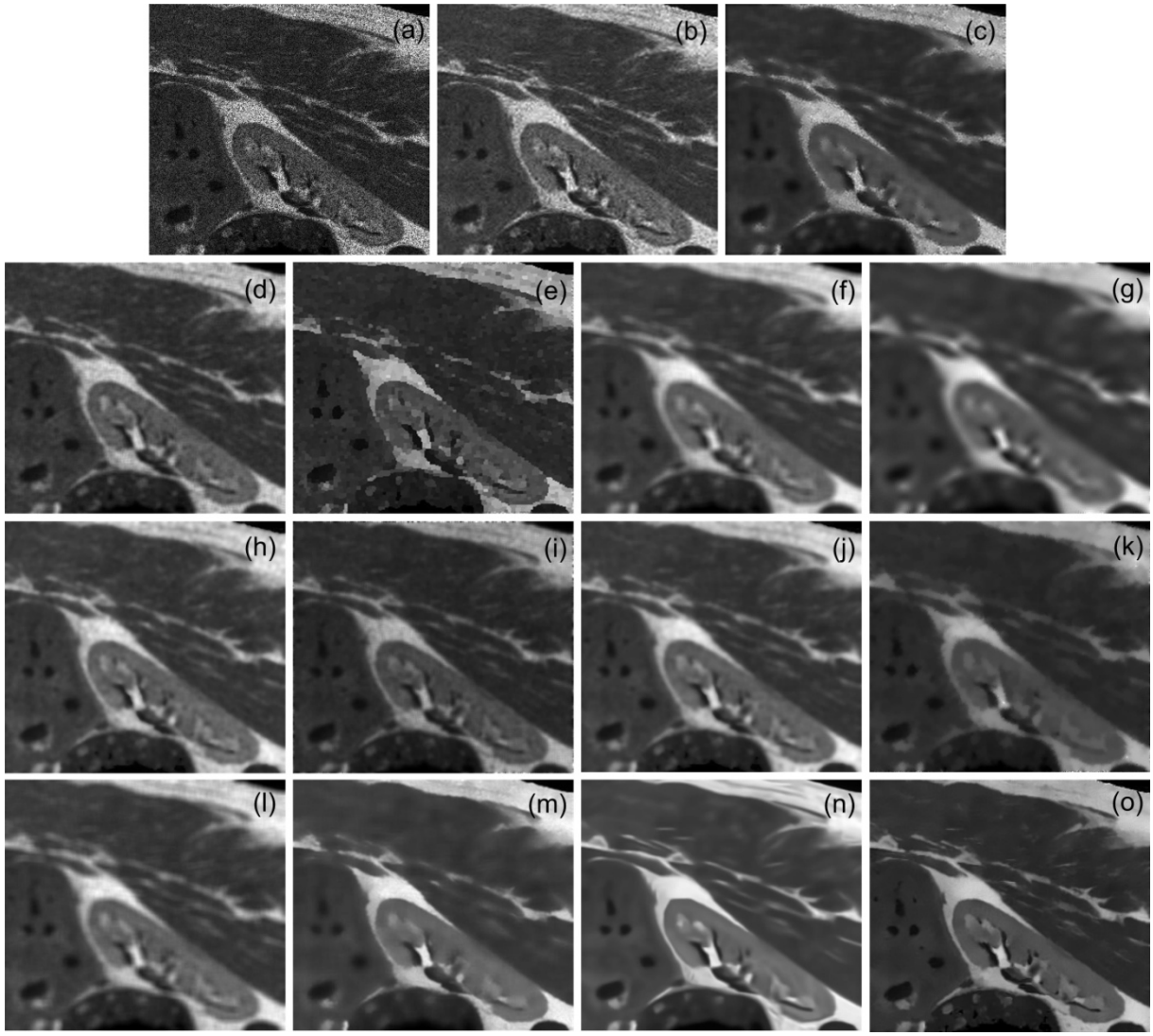

Figure 5.19 Comparative visual performance of (a) Kidney image corrupted by speckle noise and processed by the (b) AWMF (c) WF (d) Kuan (e) LHMAF (f) MHOPNF (g) FOPDEF (h) SRAD (i) NCDF (j) INCDF (k) SBF (l) SRBF (m) TVF (n) Proposed NSST-NADF (o) Proposed NSST-NLNADF

Method 10: The squeez box filter (SBF) as described in [232] with 7×7 square window and 500 iterations.

Method 11: The speckle reducing bilateral filter (SRBF) as described in [229] with $\sigma_d = 1.8$ and $\sigma_r = 2\sigma$.

Method 12: A nonlinear total variation approach (TVF) as discussed in the chapter 2.

Method 13: The proposed NSST-NADF approach as discussed in this chapter.

Method 14: The proposed NSST-NLNADF approach as discussed in this chapter.

To perform this experiment, same kidney, fetus and phantom images are used as testing images degraded by three different noise levels. The outcomes of the kidney and fetus images are presented in Figure 5.19 and Figure 5.20, respectively. From these figures, it is observed that the proposed NSST-NLNADF approach provides better quality of images by suppressing a sufficient amount of speckle noise as compared to the others. Besides the proposed approaches, diffusion based methods and the TVF approach are able to suppress considerable amount of noise, but at the cost of losing the edges or blurring the images. Figure 5.21 shows the visual results of the phantom images denoised by all the methods as mentioned above. From the visual results of phantom image, it is observed that the proposed

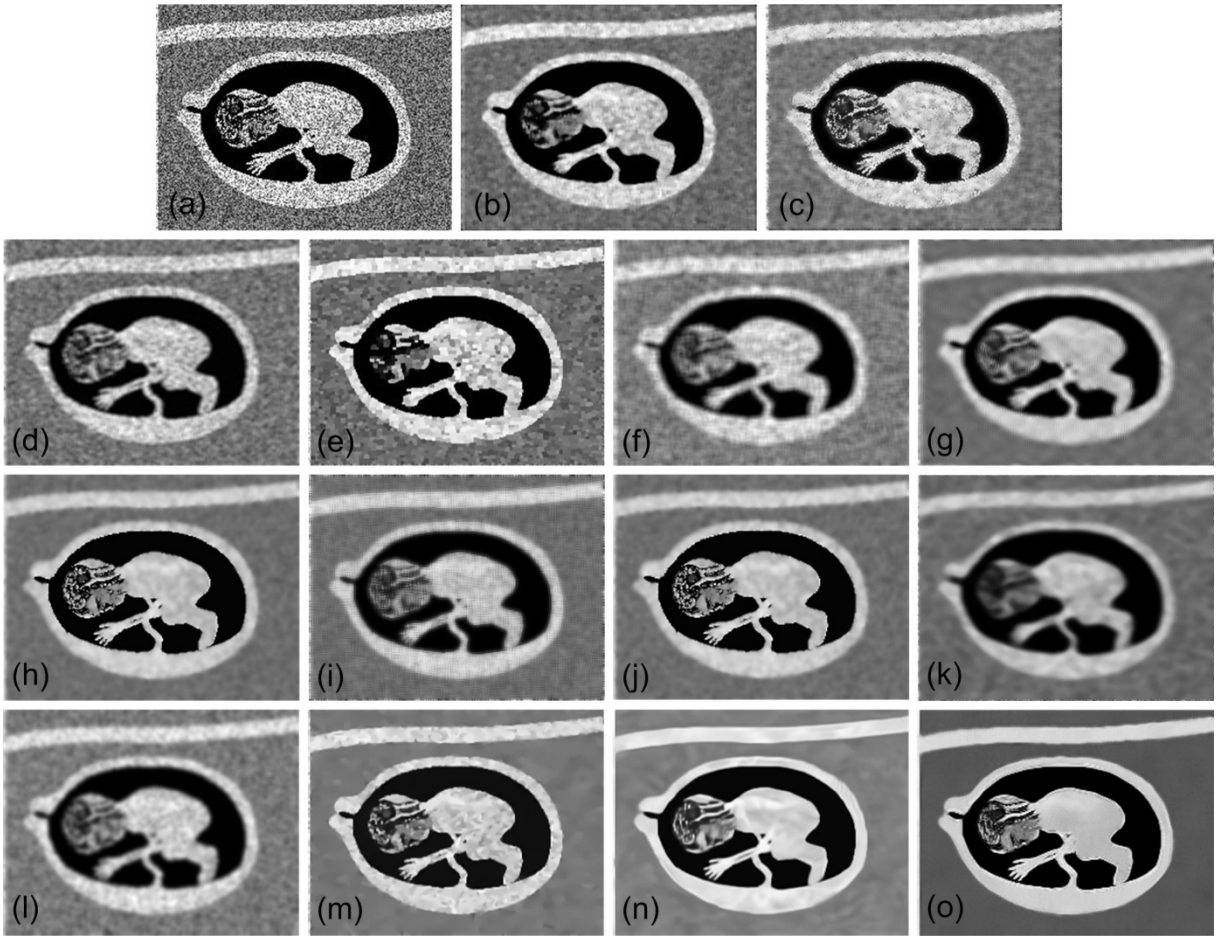

Figure 5.20 Comparative visual performance of (a) Fetus image corrupted by speckle noise and processed by the (b) AWMF (c) WF (d) Kuan (e) LHMAF (f) MHOPNF (g) FOPDEF (h) SRAD (i) NCDF (j) INCDF (k) SBF (l) SRBF (m) TVF (n) Proposed NSST-NADF (o) Proposed NSST-NLNADF

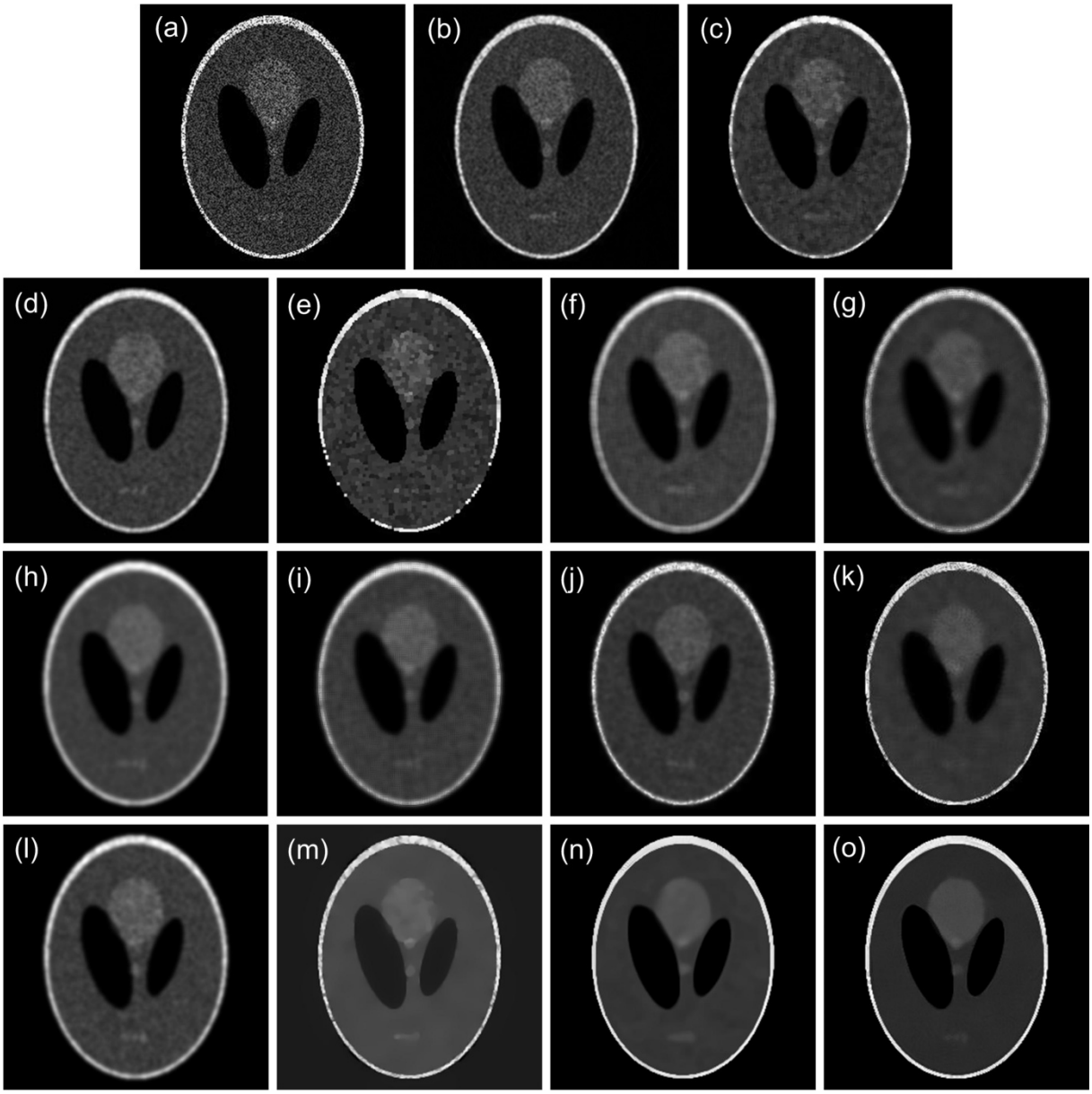

Figure 5.21 Comparative visual performance of (a) Phantom image corrupted by speckle noise and processed by the (b) AWMF (c) WF (d) Kuan (e) LHMAF (f) MHOPNF (g) FOPDEF (h) SRAD (i) NCDF (j) INCDF (k) SBF (l) SRBF (m) TVF (n) Proposed NSST-NADF (o) Proposed NSST-NLNADF

NSST-NLNADF approach produces better quality image than the proposed NSST-NADF approach and other existing methods by preserving more edges with speckle reduction. The TVF approach is also capable to suppress a considerable amount of the speckle. For the quantitative comparison that supports all the visual results presented above, the results are listed in Table 5.8 for all three images degraded by the different noise levels. From the quantitative results, it is observed that the proposed NSST-NLNADF approach gains approx 33.22-41.75%, 44.24-51.22%, 38.83-44.09%, 54.45-57.18%, 42.81-47.97%, 20.67-26.6%, 13.04-17.25%, 18.34-20.22%, 11.68-14.29%, 12.68-15.59%, 12.4-16.39%, 9.37-17.29% and 2.91-6.2% higher PSNR values and 67.38-82.92%, 97.83-108%, 75.6-97.6%, 127.2-132.9%, 90.93-99.59%, 38.21-47.79%, 22.89-29.27%, 32.6-34.8%, 20.31-24.74%, 22.2-26.2%, 21.67

Table 5.8 Performance comparison between the proposed approaches and others for the test images such as kidney, fetus and phantom images corrupted by speckle noise

Metrics	$\sigma = 0.1$				$\sigma = 0.2$				$\sigma = 0.3$			
Methods	PSNR	SNR	SSIM	EKI	PSNR	SNR	SSIM	EKI	PSNR	SNR	SSIM	EKI
Kidney image												
AWMF	21.39	10.77	0.7376	0.4388	20.69	10.07	0.7068	0.4209	20.95	10.33	0.6896	0.3260
AWF	20.05	9.44	0.7119	0.4058	19.76	9.14	0.6937	0.3899	19.35	8.74	0.6792	0.3187
Kuan	21.84	11.22	0.7596	0.3333	20.03	9.41	0.6770	0.3150	19.37	8.75	0.6103	0.3046
LHMAF	19.29	8.67	0.7406	0.3235	18.55	7.94	0.7151	0.3177	18.07	7.44	0.6822	0.3177
MHOPNF	20.49	9.87	0.7435	0.3301	20.11	9.48	0.7161	0.3235	19.19	8.57	0.6847	0.3226
FOPDEF	23.95	13.33	0.7323	0.3734	23.15	12.54	0.7249	0.3293	23.13	12.51	0.7208	0.3291
SRAD	25.86	15.24	0.7197	0.4598	25.04	14.42	0.6944	0.3332	24.69	14.07	0.6873	0.3211
NCDF	25.22	14.61	0.6869	0.4277	24.27	13.65	0.6368	0.3139	23.54	12.92	0.6256	0.3024
INCDF	26.84	16.22	0.7286	0.4962	25.13	14.51	0.7531	0.3234	24.99	14.37	0.7197	0.4029
SBF	26.23	15.61	0.7438	0.3719	25.42	14.81	0.7371	0.3397	24.77	14.14	0.7123	0.3242
SRBF	26.05	15.43	0.7186	0.4685	25.11	14.49	0.7114	0.3284	24.83	14.21	0.7045	0.3387
TVF	25.85	15.23	0.6747	0.4149	25.65	15.03	0.6527	0.4036	25.52	14.90	0.6331	0.3931
Approach-1	28.55	17.93	0.8259	0.5276	27.64	17.02	0.7892	0.4619	27.12	16.50	0.7625	0.4538
Approach-2	30.32	19.70	0.8929	0.5614	28.72	18.10	0.8790	0.4806	27.91	17.29	0.8703	0.4637
Fetus image												
AWMF	16.89	11.90	0.5382	0.5408	14.42	9.43	0.4485	0.4321	14.52	9.53	0.4005	0.3287
AWF	16.93	11.93	0.6691	0.5014	13.98	9.01	0.5762	0.5538	11.11	6.13	0.5009	0.3360
Kuan	17.12	12.13	0.4722	0.3580	16.22	11.23	0.3945	0.2944	15.17	10.18	0.3536	0.2754
LHMAF	15.21	10.22	0.5249	0.3334	12.89	7.91	0.4345	0.3120	10.79	5.81	0.3804	0.2952
MHOPNF	15.73	10.75	0.5635	0.3451	13.29	8.31	0.5110	0.2975	10.82	5.83	0.4732	0.2773
FOPDEF	17.63	12.64	0.6573	0.4603	16.39	11.41	0.6200	0.3540	15.82	10.81	0.5344	0.3188
SRAD	18.33	13.34	0.6286	0.3828	16.66	11.67	0.5512	0.3866	15.39	10.40	0.4445	0.3625
NCDF	17.63	12.64	0.5683	0.3337	16.11	11.12	0.4789	0.3498	15.56	10.57	0.4334	0.3131
INCDF	18.69	13.71	0.6381	0.4714	16.85	11.86	0.5893	0.4066	15.94	10.95	0.5079	0.3863
SBF	17.95	12.97	0.6482	0.4072	16.79	11.80	0.6194	0.3646	16.34	11.36	0.5613	0.3154
SRBF	18.58	13.60	0.6157	0.3758	16.72	11.75	0.5689	0.3951	16.54	11.55	0.4763	0.3609
TVF	17.84	12.85	0.5854	0.3696	17.01	12.02	0.5631	0.3531	16.13	11.14	0.5325	0.3105
Approach-1	20.70	15.71	0.6820	0.6792	19.22	14.23	0.6383	0.5897	18.43	13.45	0.6050	0.5474
Approach-2	20.89	15.90	0.6851	0.7176	19.34	14.35	0.6398	0.6671	18.59	13.60	0.6270	0.5922
Phantom image												
AWMF	21.71	9.55	0.7590	0.5327	20.75	8.58	0.7264	0.4738	20.02	7.86	0.6222	0.2413
AWF	22.23	10.06	0.7563	0.4696	21.18	9.01	0.6718	0.4208	20.19	8.02	0.6954	0.3775
Kuan	21.62	9.45	0.7039	0.4476	20.27	8.09	0.6418	0.3391	19.82	7.65	0.6062	0.2978
LHMAF	21.51	9.33	0.7553	0.3729	19.85	7.67	0.6827	0.3334	18.71	6.55	0.6282	0.3177
MHOPNF	22.67	10.49	0.7367	0.7034	20.54	8.37	0.7266	0.5361	19.13	6.95	0.7143	0.4341
FOPDEF	22.43	10.26	0.7760	0.5911	22.07	9.91	0.7614	0.5779	21.81	9.64	0.7599	0.4505
SRAD	22.74	10.57	0.8035	0.5995	22.31	10.14	0.7855	0.5939	22.10	9.92	0.7686	0.5909
NCDF	23.23	11.06	0.7726	0.6998	22.74	10.57	0.7079	0.6086	22.25	10.08	0.6636	0.5376
INCDF	24.52	12.35	0.8224	0.6932	23.68	11.51	0.8071	0.6470	23.06	10.88	0.7718	0.5857
SBF	24.41	12.24	0.7967	0.5872	22.41	10.26	0.7911	0.5603	21.89	9.71	0.7834	0.5389
SRBF	23.59	11.41	0.7865	0.6885	22.93	10.76	0.7389	0.6123	22.41	10.23	0.7104	0.5469
TVF	25.86	13.69	0.6883	0.6452	24.07	11.9	0.6944	0.5878	23.20	11.03	0.6986	0.5354
Approach-1	27.59	15.42	0.8498	0.8211	25.01	12.84	0.8205	0.6768	23.51	11.34	0.7871	0.6424
Approach-2	28.90	16.73	0.8399	0.8624	25.62	13.45	0.8219	0.8075	24.32	12.15	0.7989	0.7278

-27.67%, 16.04-29.35% and 4.79-9.87% higher SNR values than the methods 1-13, respectively, for kidney image. The proposed NSST-NLNADF approach also achieves approx 14.18-42.24%, 23.26-45.5%, 52.23-68.44%, 45.96-73.54%, 43.74-70.07%, 40.9-50.35%, 22.1-44.41%, 31.26-53.34%, 13.14-48.61%, 41.48-50.95%, 19.83-46.35%, 17.96-35.31% and 2.18-6.41% higher EKI values than the methods 1-13, respectively. In case of fetus image, the proposed NSST-NLNADF approach also outperforms the NSST-NADF approach by achieving higher PSNR (0.92%, 0.62%, 0.87%), SNR (1.21%, 0.84%, 1.12%), SSIM (0.45%, 0.23%, 3.64%) and EKI (5.65%, 13.13%, 8.18%) for different noise levels $\sigma = 0.1, 0.2$ and 0.3, respectively. From these results, it is also observed that the proposed NSST-NLNADF approach outperforms other existing methods in terms of noise suppression and edge preservation performance by achieving higher PSNR, SNR, SSIM and EKI values. Moreover, in case of phantom images, the proposed NSST-NLNADF approach achieves higher PSNR (4.75%, 2.44% and 3.45%) and SNR (8.5%, 4.75% and 7.14%), than the NSST-NADF approach for the different noise levels $\sigma = 0.1, 0.2$ and 0.3, respectively. With higher SNR/PSNR values, it also gains larger EKI values approx 5.03%, 19.31% and 13.29% than the NSST-NADF approach for the different noise levels. Furthermore, it also indicates from the results that the proposed NSST-NADF approach outperforms the other existing methods, but the proposed NSST-NLNADF approach shows its superiority in terms of speckle reduction and edge preservation over the NSST-NADF approach and other existing methods which is also illustrated by higher FOM values shown in Figure 5.22.

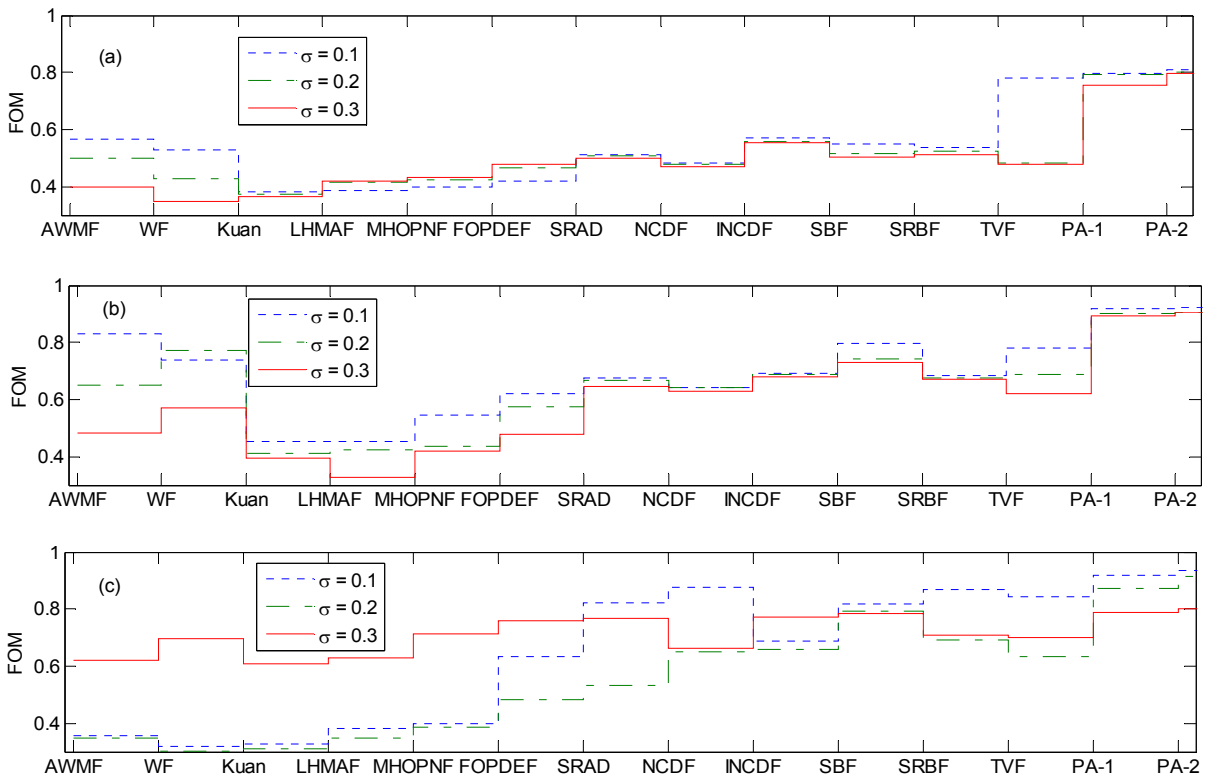

Figure 5.22 Comparative FOM values obtained for (a) Kidney (b) Fetus (c) Phantom images. Here, PA-1 and PA-2 refer to the NSST-NADF and NSST-NLNADF approaches, respectively

3.2: *Comparison of the proposed methods with others for the test images degraded by Gaussian noise* - In this experiment, other comparative results are analyzed for the standard test images such as Lena, girl and boat image degraded by additive Gaussian noise of different noise levels. For such purpose, the denoised Lena images are shown in Figure 5.23. From these visual results, it is observed that the proposed NSST-NADF and NSST-NLNADF approaches are able to produce better quality of images by retaining more edges compared to others. In case of Gaussian noise, diffusion based methods are not able to produce good quality images, but the TVF method produces better results than diffusion based methods. In case of girl image, the denoised images are shown in Figure 5.24 from which, it is observed that the proposed approaches are still able to produce better denoised images as compared to the original images.

Figure 5.23 Comparative visual performance of (a) Lena image corrupted by Gaussian noise and processed by the (b) AWMF (c) WF (d) Kuan (e) LHMAF (f) MHOPNF (g) FOPDEF (h) SRAD (i) NCDF (j) INCDF (k) SBF (l) SRBF (m) TVF (n) NSST-NADF (o) NSST-NLNADF

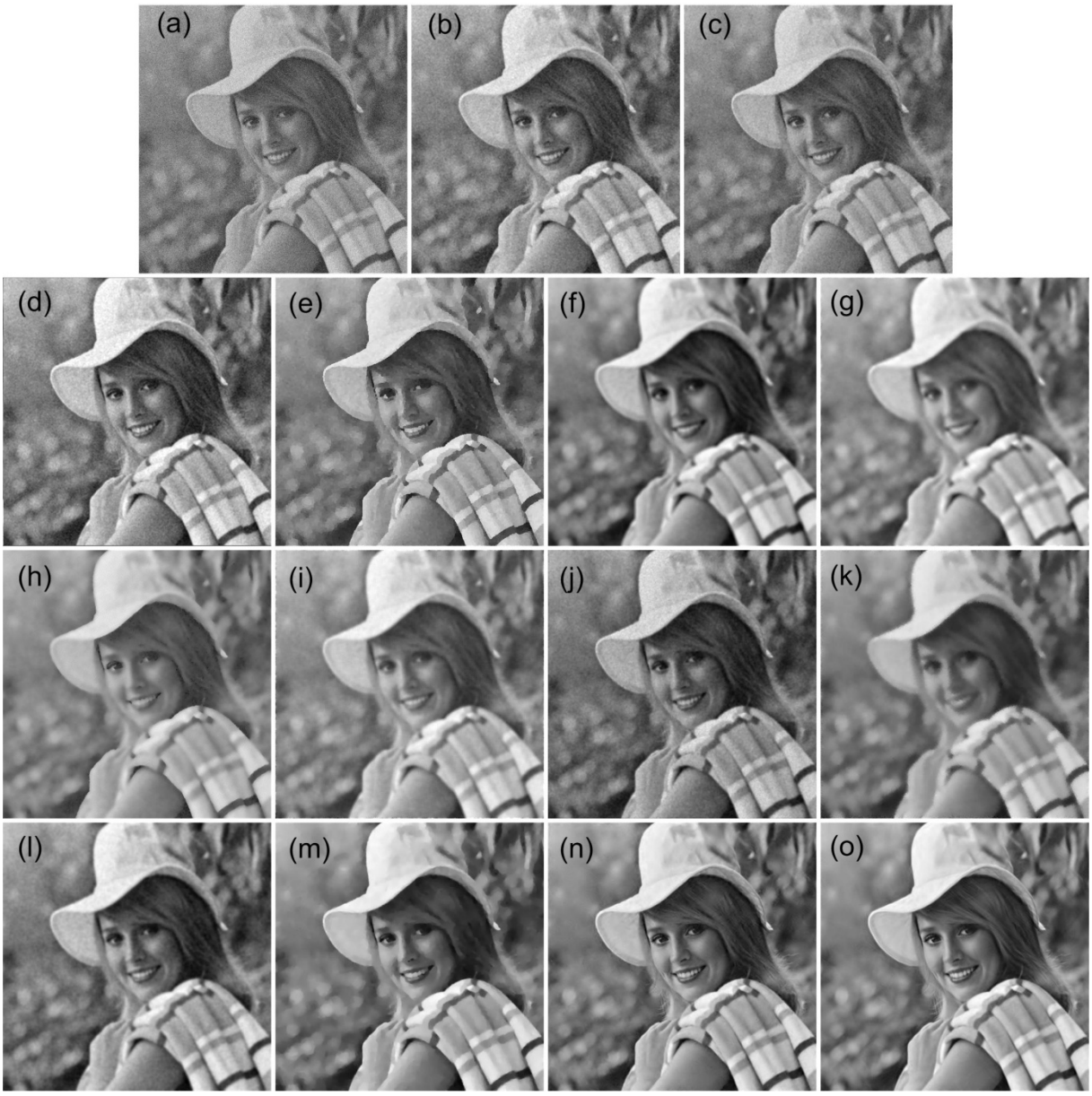

Figure 5.24 Comparative visual performance of (a) Girl image corrupted by Gaussian noise and processed by the (b) AWMF (c) WF (d) Kuan (e) LHMAF (f) MHOPNF (g) FOPDEF (h) SRAD (i) NCDF (j) INCDF (k) SBF (l) SRBF (m) TVF (n) Proposed NSST-NADF (o) Proposed NSST-NLNADF

Similar results are obtained in the case of boat image illustrated in Figure 5.25. From the visual results shown in Figure 5.25, it is observed that the proposed methods outperform the diffusion based methods and others in terms of edge preservation performance. The quantitative results estimated and listed in Table 5.9 also support the subjective analysis of aforementioned results. From the quantitative results presented in Table 5.9, it is clearly seen that the proposed NSST-NADF approach improves the noise suppression and edge preservation performance by providing higher SNR/PSNR and SSIM/EKI values compared to others for all the images, while the proposed NSST-NLNADF approach outperforms the NSST-NADF method and other existing methods. Furthermore, the proposed NSST-

NLNADF approach achieves higher PSNR (0.42%, 1.47% and 0.71%), SNR (0.5%, 1.78% and 0.87%), SSIM (0.44%, 0.43% and 1.62%) and EKI (0.56%, 1.7% and 6.69%) values than the proposed NSST-NADF approach for Lena images degraded with different noise levels $\sigma_n = 10, 20$ and 30. In case of girl and boat images, the NSST-NLNADF approach gains approx 0.45-1.02%, 0.32-2.35% higher PSNR and 0.53-1.17%, 0.39-2.81% higher SNR values, respectively, than the NSST-NADF approach. With higher PSNR and SNR values, the NSST-NLNADF approach is also able to provide higher EKI value approx (1.21%, 1.93% and 1.05%) and (0.54%, 1.34% and 0.37%) for girl and boat images, respectively. Furthermore, the proposed methods suppress both the speckle and Gaussian noise of different levels, while preserving the edges supported by the quantitative results.

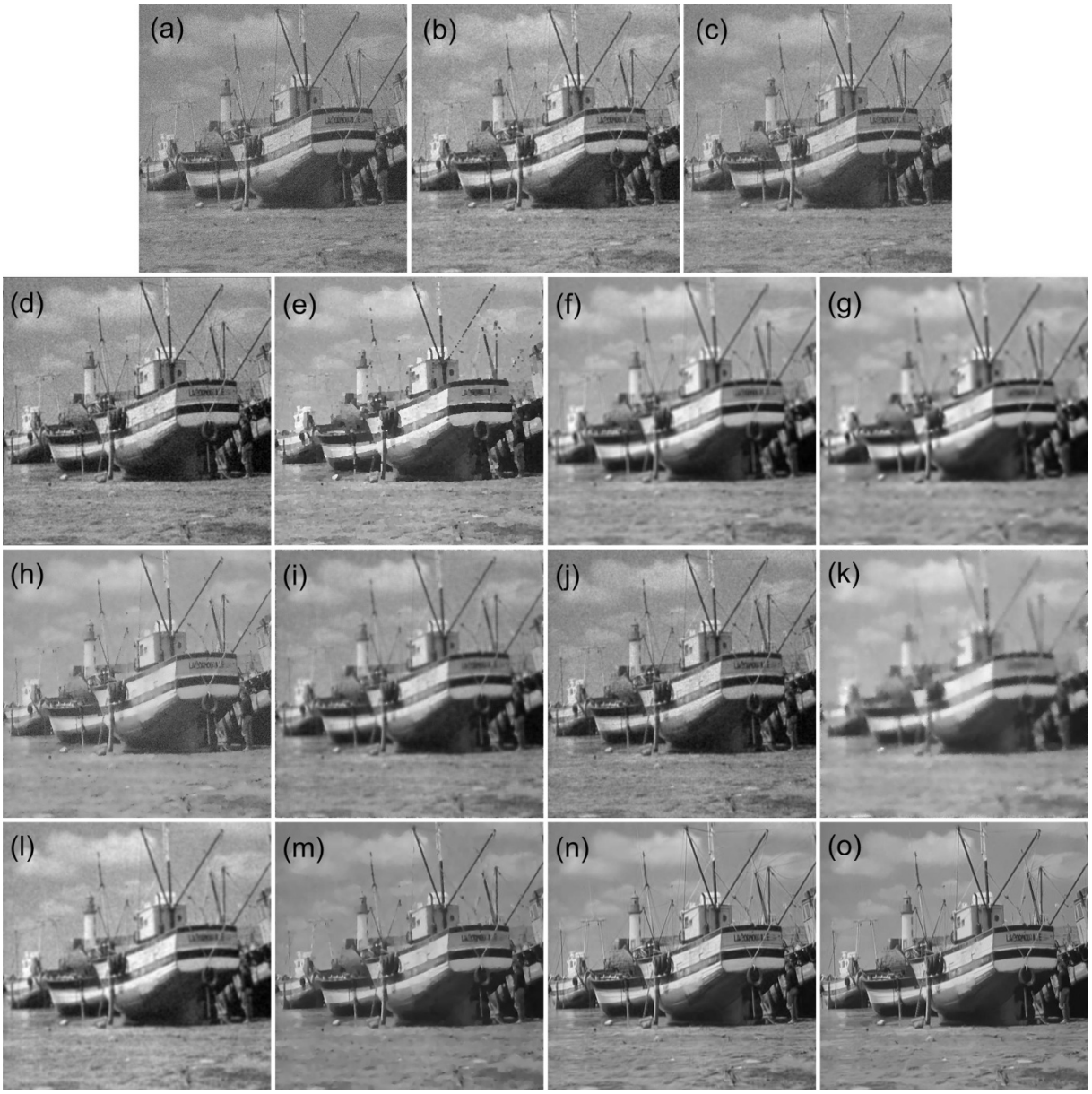

Figure 5.25 Comparative visual performance of (a) Boat image corrupted by Gaussian noise and processed by the (b) AWMF (c) WF (d) Kuan (e) LHMAF (f) MHOPNF (g) FOPDEF (h) SRAD (i) NCDF (j) INCDF (k) SBF (l) SRBF (m) TVF (n) Proposed NSST-NADF (o) Proposed NSST-NLNADF

Table 5.9 Performance comparison between the proposed approaches and others for the test images such as Lena, girl and boat images corrupted by Gaussian noise

Metrics	$\sigma_n = 10$				$\sigma_n = 20$				$\sigma_n = 30$			
Methods	PSNR	SNR	SSIM	EKI	PSNR	SNR	SSIM	EKI	PSNR	SNR	SSIM	EKI
Lena image												
AWMF	32.42	26.77	0.9265	0.6336	28.49	22.83	0.8032	0.4319	25.62	19.97	0.6815	0.3002
AWF	33.04	27.38	0.9439	0.6582	29.13	23.47	0.8265	0.5236	25.81	20.15	0.7026	0.3532
Kuan	28.15	22.49	0.9091	0.5900	26.47	20.81	0.8191	0.4600	24.82	19.26	0.7324	0.3515
LHMAF	27.01	21.35	0.8708	0.4346	25.85	20.20	0.7773	0.3854	24.54	18.88	0.6830	0.3340
MHOPNF	27.56	21.90	0.8724	0.5750	27.32	21.67	0.8207	0.4599	26.98	21.33	0.7986	0.4360
FOPDEF	27.35	21.69	0.8648	0.6023	26.87	21.22	0.8600	0.6121	26.10	20.45	0.8160	0.6081
SRAD	27.82	22.17	0.8963	0.2914	23.85	18.20	0.8397	0.3338	21.89	16.23	0.7992	0.3396
NCDF	27.75	22.09	0.8826	0.4791	26.90	21.25	0.8654	0.3198	25.70	20.04	0.8348	0.2199
INCDF	30.75	25.09	0.9369	0.6292	29.71	24.06	0.8717	0.5371	27.79	22.13	0.7735	0.4641
SBF	25.52	19.86	0.8014	0.4589	22.82	17.16	0.7493	0.4274	20.85	15.19	0.7059	0.3953
SRBF	31.17	25.51	0.9099	0.6295	29.06	23.41	0.8006	0.5936	28.13	22.47	0.6756	0.3552
TVF	29.99	24.33	0.8767	0.7216	29.98	24.33	0.8837	0.6863	29.45	23.79	0.8751	0.6520
Approach-1	35.67	30.01	0.9646	0.8548	32.69	27.04	0.9347	0.7728	30.88	25.22	0.9035	0.7140
Approach-2	35.82	30.16	0.9688	0.8596	33.17	27.52	0.9387	0.7859	31.10	25.44	0.9181	0.7618
Girl image												
AWMF	32.12	27.56	0.8244	0.5483	28.44	23.89	0.7091	0.3794	25.59	21.04	0.6858	0.2616
AWF	33.24	28.69	0.8391	0.6601	28.99	24.44	0.7314	0.4702	25.69	21.13	0.7074	0.3252
Kuan	27.63	23.08	0.9077	0.5833	26.22	21.67	0.7464	0.4920	24.64	20.09	0.6407	0.4086
LHMAF	28.41	23.86	0.8818	0.4337	26.83	22.28	0.7924	0.3885	25.18	20.63	0.7008	0.3360
MHOPNF	28.70	24.15	0.8872	0.6133	28.34	23.79	0.8686	0.6003	27.82	23.26	0.8391	0.5696
FOPDEF	29.27	24.72	0.8718	0.6275	28.64	24.09	0.8816	0.5528	27.78	23.23	0.8477	0.5878
SRAD	21.35	16.79	0.8656	0.3391	20.39	15.85	0.8188	0.3144	19.58	15.03	0.7770	0.3072
NCDF	29.43	24.87	0.8999	0.5552	28.24	23.69	0.8854	0.3775	26.67	22.12	0.8555	0.2786
INCDF	31.49	26.94	0.9358	0.6708	30.16	25.61	0.8786	0.6046	28.01	23.45	0.7837	0.4485
SBF	22.02	17.47	0.8265	0.5275	19.51	14.96	0.7702	0.4771	19.44	14.89	0.7047	0.4743
SRBF	31.03	26.48	0.9197	0.6492	30.29	25.74	0.8126	0.5894	29.49	24.94	0.6834	0.3584
TVF	30.55	25.99	0.8660	0.6806	30.73	26.18	0.8769	0.6406	30.17	25.62	0.8684	0.6075
Approach-1	34.36	29.81	0.9469	0.7377	32.32	27.77	0.9144	0.6842	30.97	26.42	0.8890	0.6766
Approach-2	34.71	30.16	0.9457	0.7466	32.65	28.10	0.9194	0.6974	31.11	26.56	0.9021	0.6837
Boat image												
AWMF	29.68	24.33	0.9238	0.5696	27.09	21.75	0.8236	0.4034	24.79	19.45	0.7165	0.2835
AWF	32.14	26.79	0.9455	0.6774	28.37	23.02	0.8549	0.5925	25.36	20.01	0.7450	0.4212
Kuan	24.71	19.37	0.8541	0.4950	23.47	18.13	0.7525	0.3992	22.26	16.92	0.6787	0.3382
LHMAF	24.99	19.64	0.8219	0.4167	24.29	18.94	0.7464	0.3727	22.51	17.17	0.6653	0.3229
MHOPNF	25.51	20.17	0.8248	0.4656	25.40	20.05	0.7887	0.4568	23.24	17.90	0.7323	0.4387
FOPDEF	24.70	19.36	0.8366	0.5439	24.31	18.97	0.8318	0.5303	23.77	18.43	0.8214	0.5635
SRAD	26.47	21.12	0.8314	0.5590	23.55	18.19	0.7934	0.4865	21.16	15.82	0.7348	0.4056
NCDF	25.43	20.09	0.8132	0.4899	24.95	19.61	0.8033	0.3371	24.21	18.87	0.7829	0.2488
INCDF	28.46	23.12	0.9186	0.7201	27.92	22.58	0.8698	0.6534	26.58	21.23	0.7877	0.5156
SBF	22.38	17.04	0.6509	0.3384	20.87	15.53	0.5909	0.3096	19.47	14.12	0.5479	0.2889
SRBF	30.62	25.28	0.8528	0.7105	26.04	20.69	0.8300	0.4658	25.84	20.50	0.7143	0.4519
TVF	27.48	22.14	0.8079	0.6637	27.43	22.09	0.8203	0.6395	27.12	21.77	0.8223	0.6084
Approach-1	33.58	28.24	0.9597	0.9089	30.25	24.91	0.9133	0.8417	28.37	23.03	0.8691	0.8176
Approach-2	33.80	28.46	0.9661	0.9138	30.96	25.61	0.9152	0.8530	28.46	23.12	0.8773	0.8206

3.3: *Comparison of the proposed NSST-NADF and NSST-NLNADF methods with others for speckle reduction in real US images* - In this experiment, a detailed comparative analysis is presented for the visual results of real US images used as similar in previous chapters and processed by all the fourteen denoising methods as mentioned above. The processed prostate, splenic cyst and multiple liver masses US images are presented in Figure 5.26. From these visual results, it is indicated that the proposed approaches are able to produce better quality US images by preventing from edge loss and suppressing the speckle as much as possible. Generally the diffusion based methods and TVF are also able to suppress a good amount of speckle available in the US images. Moreover, in case of the liver US image, the SRAD shows better noise suppression than others, but at the cost of more edge loss. Besides the diffusion based methods, the SRBF method is also capable to suppress the noise and retains more edges than the diffusion based approach. Moreover, the subjective analysis of the visual results processed by all denoising methods is validated by estimating the MVR values for different image regions marked on real US images.

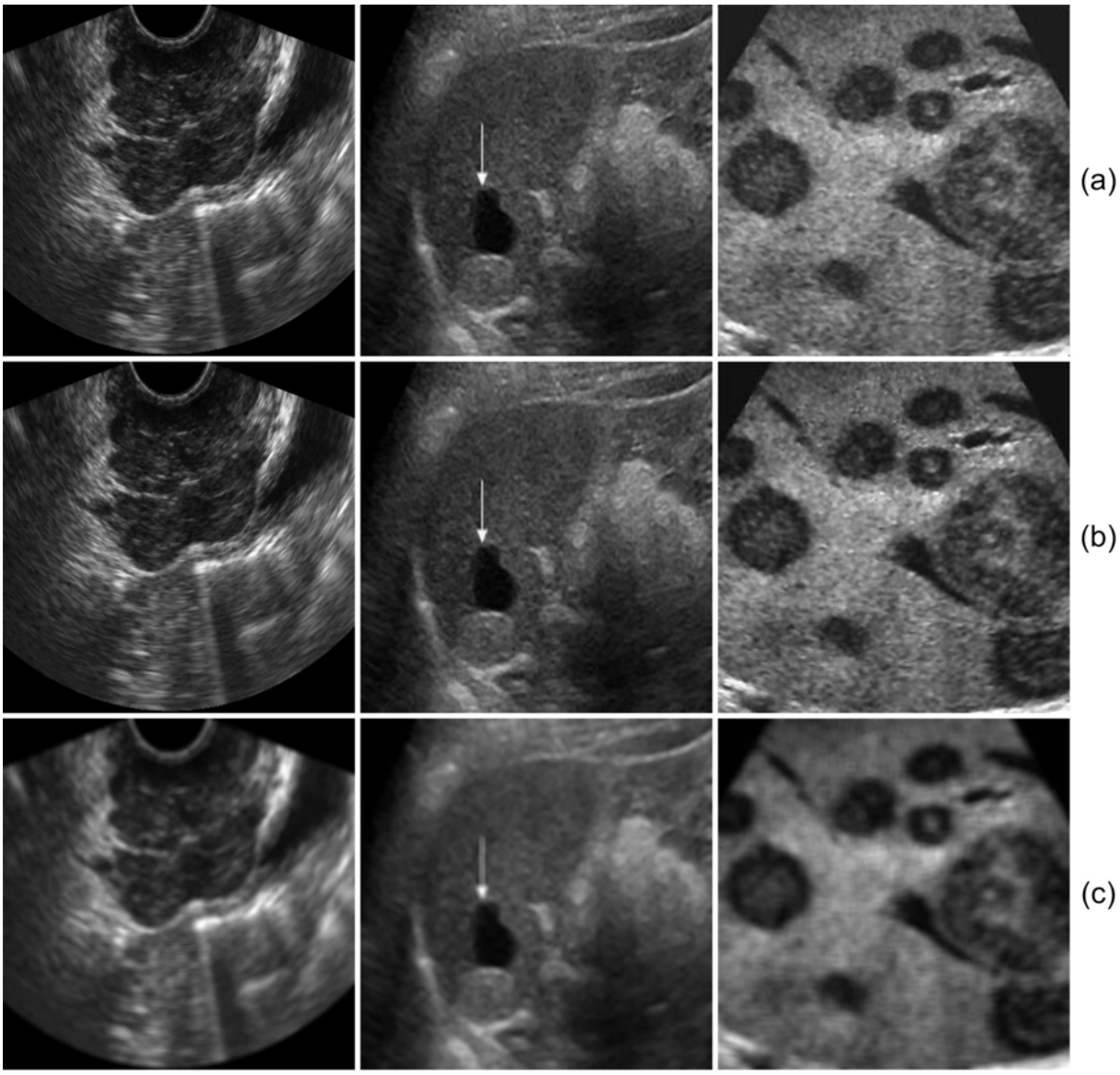

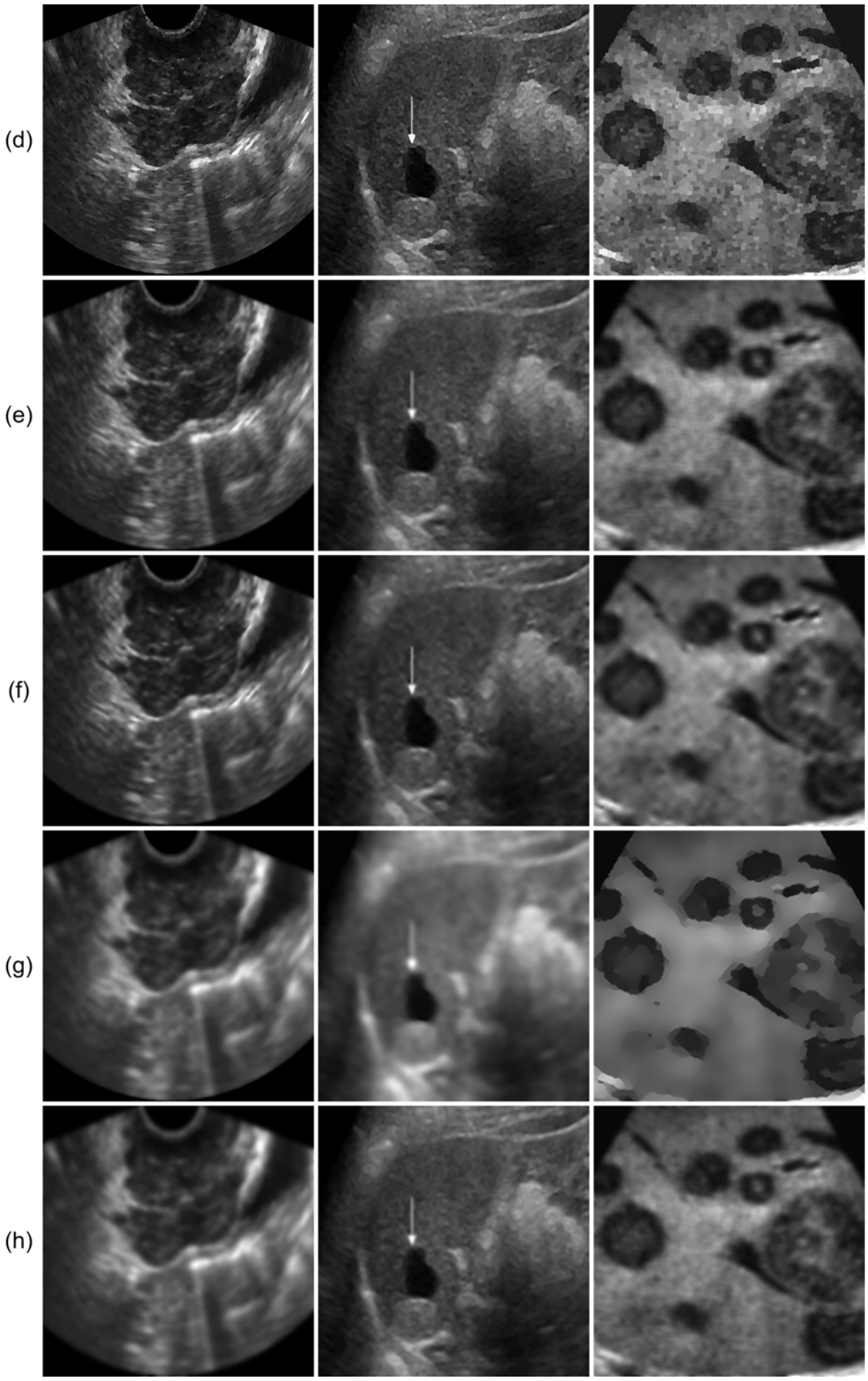
(d)
(e)
(f)
(g)
(h)

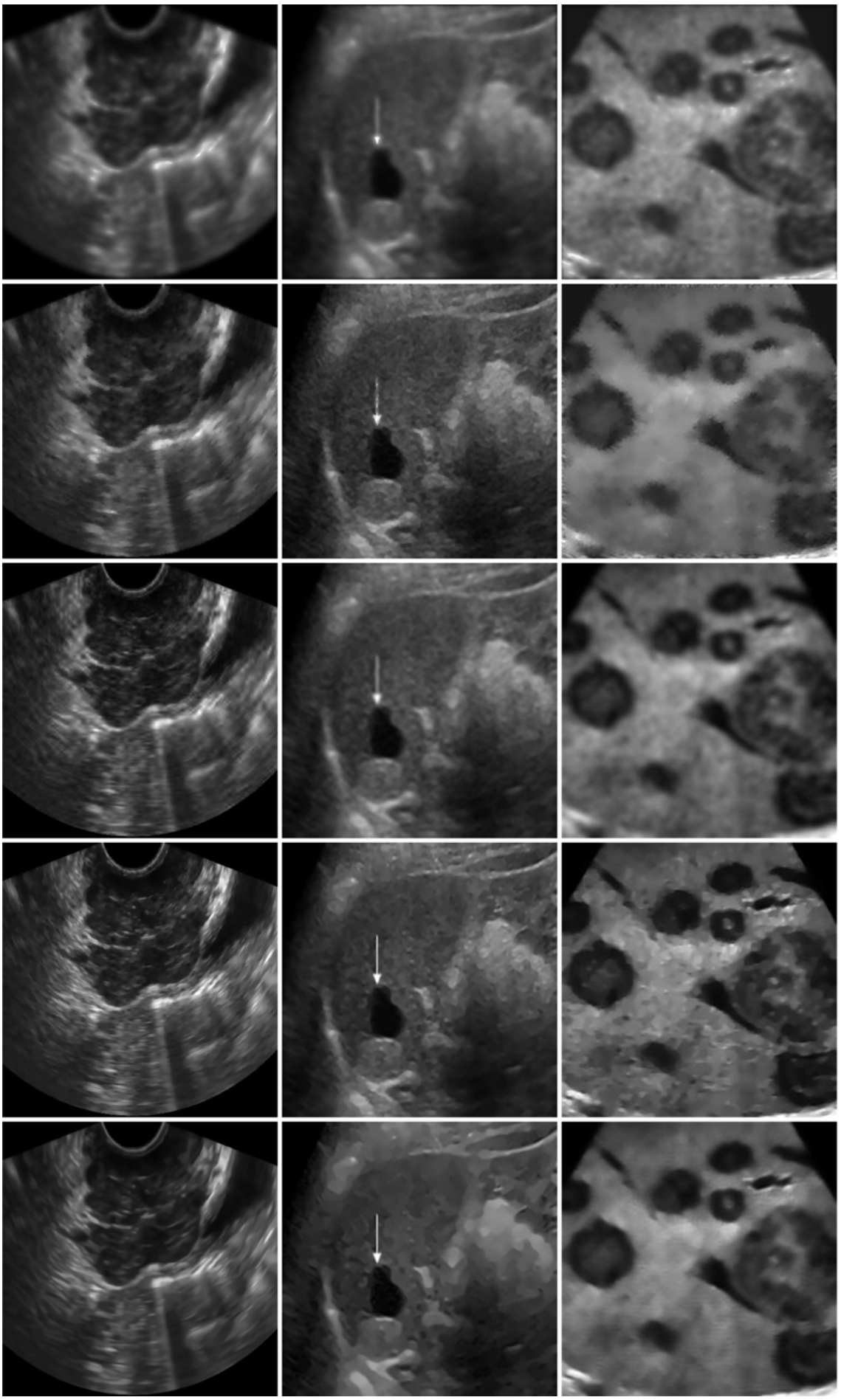
(i)
(j)
(k)
(l)
(m)

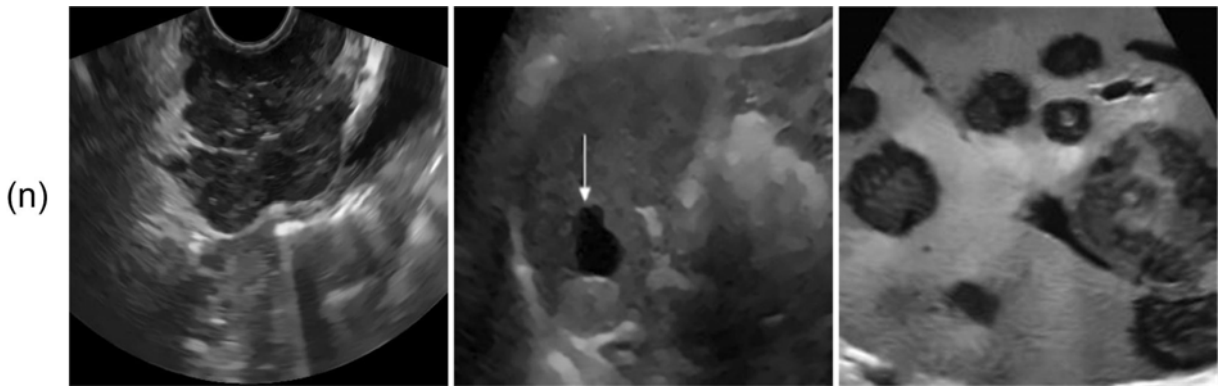

Figure 5.26 Comparative visual performance of prostate, splenic cyst and multiple liver masses ultrasound images processed by the (a) AWMF (b) WF (c) Kuan (d) LHMAF (e) MHOPNF (f) FOPDEF (g) SRAD (h) NCDF (i) INCDF (j) SBF (k) SRBF (l) TVF (m) Proposed NSST-NADF (n) Proposed NSST-NLNADF

Figure 5.27 shows the four different bar graphs of the estimated MVR values as MVR 1 and MVR 2 for both the regions defined as region 1 and region 2, respectively and for the aforementioned denoising methods. From the MVR values presented in the bar graphs, it is observed that the proposed NSST-NADF and NSST-NLNADF gain higher MVR values than others. Moreover, the proposed NSST-NLNADF approach exhibits the superiority by providing the highest MVR value among all the other methods, which is clearly shown in the Figure 5.27 (a)-(d). Further, Table 5.10 shows the MVR values (mean ± standard deviation) estimated for all hundred measurements performed on fifty different US images in which two

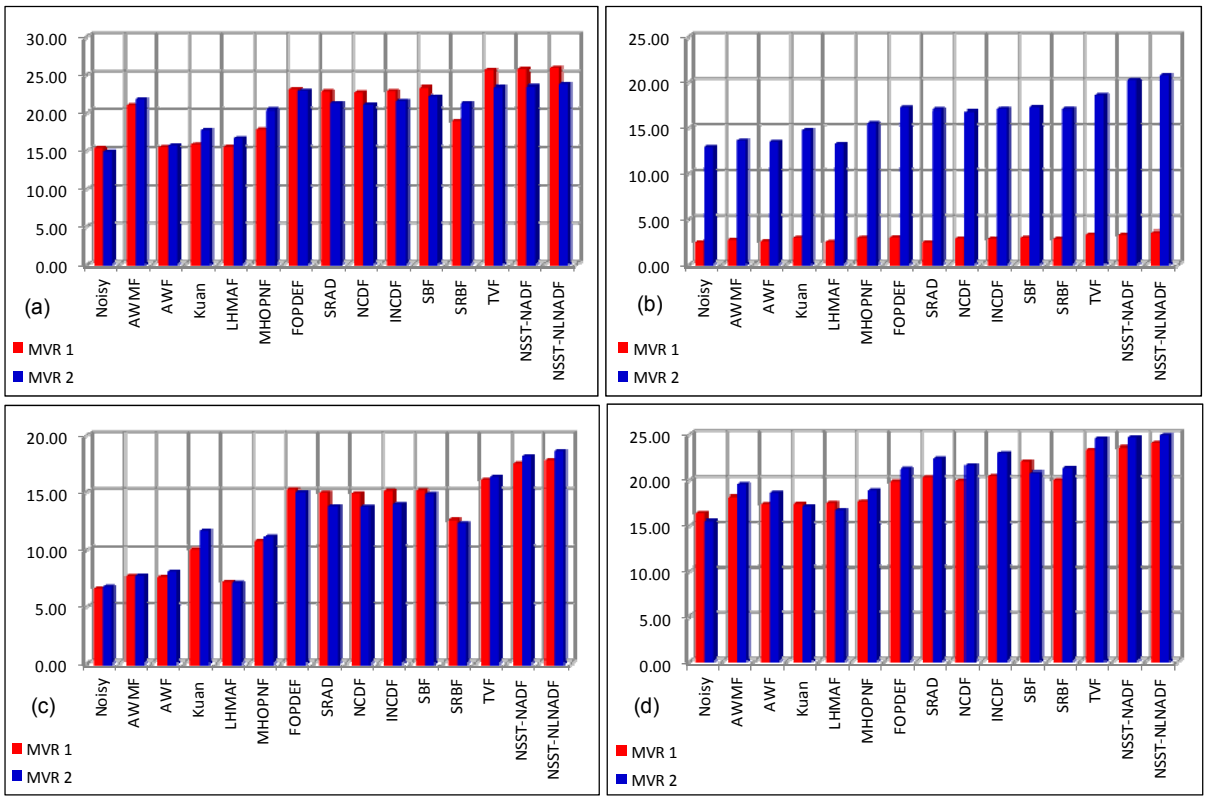

Figure 5.27 Comparison between MVR values obtained from the different denoising methods for two images regions illustrated in Figure 2.21

Table 5.10 Performance comparison of the proposed NSST-NADF and NSST-NLNADF approaches with others using the averaged MVR values over 100 different image regions marked on 50 different ultrasound images

S. No.	Methodology	MVR
1	Noisy	14.04 ± 3.04
2	AWMF	16.27 ± 4.69
3	AWF	15.64 ± 3.42
4	Kuan	16.56 ± 4.98
5	LHMAF	15.19 ± 3.46
6	MHOPNF	16.70 ± 3.49
7	FOPDEF	19.27 ± 4.46
8	SRAD	19.45 ± 3.97
9	NCDF	19.32 ± 3.69
10	INCDF	21.05 ± 3.15
11	SBF	20.12 ± 4.87
12	SRBF	19.69 ± 3.23
13	TVF	21.45 ± 4.95
14	Proposed NSST-NADF	21.95 ± 4.26
15	Proposed NSST-NLNADF	22.42 ± 4.12

measurements at two different image regions are considered for each image. The results listed in Table 5.10 exhibit the superiority of the proposed NSST-NADF approach in the effective speckle reduction compared to other existing methods. Moreover, the proposed NSST-NLNADF approach outperforms the other proposed NSST-NADF method.

5.8 Summary

In this chapter, two different denoising methods are presented in the NSST domain using nonlinear adaptive diffusion filtering (NADF) with and without nonlocal (NL) information and named as NSST-NADF and NSST-NLNADF. The proposed methods are also adapted for both the speckle and Gaussian noise. In the proposed methods, the NSST has several advantages over the other transformation techniques. The NSST also provides the multiscale and direction analysis of the noisy images. In NSST-NADF approach, the noise components are suppressed by applying modified adaptive diffusion on low frequency approximation coefficients and thresholding provides the modified coefficients which improve the denoising efficiency with better edge preservation. Furthermore, in the NSST-NLNADF approach, the NL information and adaptive gray level variance are incorporated in the modified diffusion equations within the large number of connecting neighborhood to effectively preserve more edges.

The noise suppression abilities of the proposed methods and others using several US images and standard test images have also been compared here. Experimental results show an improved denoising performance obtained by the NSST-NLNADF compared to the NSST-NADF approach. Furthermore, a detailed comparative study presented at the end of this

chapter, exhibits the superiority of the proposed approaches over other existing methods, including the TVF and NLMF methods that also produce competitive noise reduction performance to all the proposed RTNLF-1, RTNLF-2 and RBAF methods presented in the previous chapters for both the case of low/high noise levels. Finally, it is concluded that the proposed NSST-NLNADF approach ensures an improvement in noise reduction and preservation of more edges, thus providing the processed images with better visual quality.

CHAPTER 6: HYBRID EDGE-BASED ACTIVE CONTOUR METHOD WITH KERNEL FUZZY CLUSTERING

This chapter presents a hybrid segmentation approach for ultrasound medical images by utilizing both the features of kernel fuzzy clustering with spatial constraints and edge-based active contour model using distance regularized level set function. This chapter starts with a brief idea of the different segmentation methods followed by the methodology used in the proposed approach. In the proposed segmentation approach, the results obtained by the kernel fuzzy clustering is utilized not only to initialize the curve that moves toward the estimated object's boundaries, but also helps to estimate the parameters, which are responsible for controlling the level set evolution. The performance of the proposed approach used for segmentation of ultrasound medical images is discussed in both the subjective and objective manner and a comparative study has also been presented in the last section of this chapter for investigating the segmentation performance obtained by the proposed approach.

6.1 Introduction

Segmentation of medical images plays an important role in several applications such as visualization, quantitative analysis and image guided intervention and surgery [177]. Segmentation is a process of partitioning the given image into distinct regions that have specific clinical meanings. It is a very crucial approach to extract the boundaries of a particular region of interest and visualize the human tissues during the clinical diagnosis. Among the medical images obtained from different imaging modalities, the US imaging is most widely used for the diagnosis of several living organs. However, the accurate segmentation that provides the meaningful information is still a very challenging problem because of the poor quality of US images, which needs manual intervention further. Moreover, in order to achieve better segmentation performance, mostly approaches require an expert/radiologist to manipulate the several controlling parameters used in a particular segmentation approach. Furthermore, an accurate and automatic extractions of the region or the object boundaries are in a great need for the US images.

In past years, several algorithms have been presented in the literature as presented in chapter 1 from which it is observed that latest research work on the US image segmentation is concentrated on an active contour model (ACM) approach and its different modified variants [48, 64-66, 221, 236, 275, 276, 278, 279]. The performance of the traditional ACM approaches are based on the appropriate initialization of contour and choosing the appropriate controlling parameters used in the curve evolution. Thus, it is a very tedious job that is also time consuming, experience and knowledge dependent. By considering all these consequences, this chapter introduces a hybrid edge-based active contour model (EBACM) used for segmentation of the US medical images using the kernel fuzzy c-means clustering (KFCM). In this segmentation approach, the fuzzy membership function from the KFCM with spatial constraints clustering is employed not only to initialize the curve but also to evaluate

the contour propagation controlling parameters. The KFCM clustering is able to provide better results by incorporating the kernel induced distance in place of the Euclidean distance like conventional fuzzy c-means clustering [222].

The rest part of this chapter is structured as follows. The next section provides a brief idea of the different segmentation methods, including clustering and ACM methods that are employed to present the proposed hybrid segmentation approach using the EBACM and KFCM approaches and named as the EBACM-KFCM approach. After that, the proposed segmentation approach is also discussed and its implementation steps are also mentioned in the section. The performance of the EBACM-KFCM approach is also analyzed with both the synthetic noisy images and real US images and explained. Many efforts have been made to evaluate and compare the segmentation performance with other existing methods in terms of different performance measures discussed in the subsequent sections.

6.2 Classification of Segmentation Methods

Image segmentation is an important step for quantitative and qualitative analysis of the medical images and the accurate segmentation provides meaningful information in the diagnosis process. Segmentation process divides an image into its constituent subregions or objects by grouping together neighborhood pixels based on some predefined criterion. The complete segmentation results are the set of disjoint regions corresponding uniquely with objects in the input image. Most of the segmentation techniques are either based on discontinuity or similarity criterion. Segmentation methods based on the discontinuities are edge-based and those based on similarity are thresholding, region growing, region merging and splitting, and watershed [215, 241]. Some of the image segmentation methods are also discussed in brief as presented below:

6.2.1 Thresholding based segmentation

In thresholding approach, the partitioning of the object from the background of an image is performed by selecting the proper range of gray scales [117]. In thresholding approaches, threshold value has an important role that is usually selected from the image histogram. It is said that all pixels whose values (gray intensity, color, or other relevant feature) lie between two values of threshold belongs to one region. The different regions of an image are partitioned by delineating peaks, valleys and/or shapes in its corresponding intensity histogram [241]. The histogram thresholding does not require any prior information regarding the image to be segmented. This approach is very convenient and easy for segmentation. However, the accurate segmentation may not be achieved because of the presence of high noise level and texture type contents into the images. Furthermore, the region boundaries obtained by such type of techniques may give the false interpretation of the object shape.

A common thresholding algorithm is Otsu's method. In this thresholding approach, the distribution pattern of the pixels is analyzed based on the concept that the pixels in each class or cluster should be as similar as possible. It means that the variance inside each class should be minimized. Otsu defined the within-class variance as the weighted sum of the variances of each cluster. Minimizing within-class variance is equivalent to maximizing between-class variance. This method is most widely employed in literature and its result is robust and satisfactory. The problem gets severe in case of multimodal histograms with no sharp or well defined boundaries [4, 59]. It is often difficult to define functional and statistical measures only on the basis of gray level value.

6.2.2 Edge-based segmentation

Edges, lines and points carry a lot of information about the various regions in the image [4]. Though, the edges and lines are both formed where there are abrupt changes in the intensity of the pixels. Basically, the idea underlying most edge-detection techniques is the computation of a local derivative (gradient) operator. This gradient vector of an image $s(x, y)$, is obtained by the partial derivatives $\partial s/\partial x$ and $\partial s/\partial y$ at every pixel location. There are several edge detection techniques having different characteristics that can be used to detect the edges [90]. A wide variety of edge detector operators that usually are named after their inventors, exist in the literature. The most common are Prewitt [103, 193], Sobel [103, 219], Laplace [103, 192] and Canny [42, 103]. A critical disadvantage of the gradient operation is that the derivative enhances the noise. As a second-order derivative, the Laplacian method is even more sensitive to noise. An alternative is the convolution of an image with the Gaussian smoothing function which is known as Laplacian of Gaussian. Sobel operators have the advantage of providing both a derivative and a smoothing effect. The canny edge detector is based on the extreme of first derivative of the Gaussian operator applied to an image. The operator first smoothens the image to eliminate noise and then finds high gradient regions.

Mostly, edge detection by the gradient evaluation process is able to provide better results only in those images that have sharp intensity transition and relatively low noise. Due to its sensitivity to noise, some smoothing operation is generally required as pre-processing, and the smoothing effect consequently blurs the edge information. However, the computational cost is relatively lower than the other segmentation methods because the computation can be done by a local filtering operation, i.e. convolution of an image with a kernel. However, the principal limitation of the edge detection methods is also its dependence on the information contained in the local neighborhood of the image. Generally, the edge detection methods do not consider model based information embedded in an image [4]. In most of the cases, these edge detection techniques ignore the higher order organization which may be meaningfully presented in the image [4].

The goal of the edge-based segmentation methods is to connect the relevant edges in such a way that the object boundaries are produced. Because the edges are not always connected and are not always showing the object's boundaries, the image's objects which are resulted from edge detection could not be an appropriate segmentation result. It is also often difficult to identify and classify the spurious edges [215]. Therefore, the edge detection process is considered as a pre-processing step in such cases.

6.2.3 Region-based segmentation

The complement of the edge-based segmentation method is known as region-based segmentation [233]. Region-based segmentation looks for the similarity of pixels within a sub-region-based on a desired property such as intensity, color, and texture. It is based on the principle that neighboring pixels within a particular region of an image have similar characteristics. The criterion is to detect the regions that satisfy predefined homogeneity criteria. Region-based segmentation method is of two types such as split and merge approach, and region growing approach [103].

Region growing process [8, 86, 87] makes a group of pixels, or sub-regions into larger regions based on a predefined criteria. The goal of region growing is to use image characteristics to map individual pixels in an input image to sets of pixels called regions. The region growing method starts from pixel level and in each step unifies similar pixels one by one and continues till no similar character pixel is left to add. Region growing technique gives good results where borders are difficult to detect and to generate better results in noisy image [215].

The region growing approach relies on a homogeneity criterion. This is based on finding parts of images which are homogeneous for a given set of properties. Region-based methods always provide closed contour regions and make use of relatively large neighborhoods for decision-making. Users select a point, which is known as 'seed', and a region grows out from this seed until some stopping growth criteria are met. This is a basic limitation of the region growing process that needs manual intervention to select seed point and to formulate the stopping criterion. Besides this, there is a fundamental problem of selecting the seed point and suitable properties to grow the regions. Selecting initial seeds can be often based on the nature of applications or images. Unlike gradient and Laplacian edge detection methods, the borders of the regions found by region growing are perfectly thin and connected. It is also sensitive to noise that cause holes in a segmented region or between two distinct regions to be connected.

Split and merge process [55] begins with entire image, the image is divided into small regions, and in each step, heterogeneous region is divided into four rectangular smaller regions and so on till all regions are homogeneous. Now, the merging process starts and in this process all the similar neighboring homogeneous regions are unified. Because of

subsequent division of the segments into quarters, the boundaries produced by the split technique tend to be squarish and artificial [215].

6.2.4 Watershed transform based segmentation

Watershed transform [115] is one of the methods based on region-based segmentation. The watershed transform is derived from the field of mathematical morphology. It is a powerful tool for image segmentation. The watershed transform has been widely used in many fields of image processing, including medical image segmentation due to the number of advantages that it possesses. It also produces a complete division of the image in separate regions, even if the contrast is poor and thus avoids the need for any kind of contour joining. The watershed segmentation embodies many concepts of the approaches such as detection of discontinuities and region processing. It provides more stable segmentation results including continuous segmented boundaries. Watershed transformation is built by the implementation of the flooding process on a grayscale image.

The watershed transform approach utilizes region as well as contour information to segment the image by considering it as three dimensional topographic surfaces in which two are the spatial dimension and the third one being a particular specific attribute such as intensity or gradient. Based on this concept, an image is partitioned into two different sets such as catchment basins and the watershed lines, either by flooding the topographic surface from its minima or prevent from merging of the waters coming from the different sources. While simulating this process for image segmentation, two approaches may be used: either by finding basins first and then watersheds by taking a set complement or by computing a complete partition of the image in basins and subsequently find watersheds by boundary detection. To be more specific, the expression of watershed transform denotes labelling of the image such that all points of a given catchment basin have same unique label. In practice, it is noted that the watershed transform does not apply to the original image, rather it is applied to its morphological gradient [22, 241].

The main advantages of the watershed approach are its simplicity to implement and less computational complexity. It is also capable to produce connecting boundaries, if the weak boundaries or low contrast regions exist [241]. However, the main drawback of the watershed approach is over segmentation because of the presence of noise irregularities in the images.

6.2.5 Hybrid segmentation

The hybrid segmentation method combines edge and region-based segmentation techniques and provides more accurate segmentation of the images. One can extract the features of both the region growing and edge-based segmentation methods by combining the strengths of these two distinct methods. For example, region joining decision is based not

only on pixel or neighborhood similarity but also on already extracted edges and completion of these edges [23, 62].

The morphological watershed segmentation is another type of hybrid technique. The watershed method is applied to the gradient of the image. This gradient of the image can be viewed as topography with boundaries between regions as ridges. There are several hybrid segmentation techniques that exist in literature providing better segmentation results [8, 26, 114, 195, 201, 286, 287].

6.2.6 Clustering based segmentation

Clustering techniques are most widely used to partition the image pixels into different clusters [15, 116, 150, 222]. It is used to group similar data points into a same cluster iteratively by minimizing its objective functions based on the Euclidean distance of the pixel to its cluster centroids. The results of the clustering methods would be better with the lower cost value. The K-means clustering is a common clustering based segmentation technique where each pixel is iteratively allocated to the nearest cluster center position and the location of cluster centroid is estimated. After each iteration, the value of objective function reduces until the cluster configuration converges at a stable point where it has a local minimum. In K-means clustering, every object is limited to one and only one of K clusters. In contrast, a fuzzy c-means (FCM) clustering [24, 63] has been widely used for the medical image segmentation and provides better results. In the FCM, every pixel may belong to more than one cluster with the specified degree of membership. The standard FCM objective function for partitioning an image into the different cluster is given as [24]

$$J_p^{FCM}(\mu, v) = \sum_{i=1}^{L}\sum_{j=1}^{C}\mu_{j,i}^{p}\left\|s_i - v_j\right\|^2 \tag{6.1}$$

The membership functions are subject to the following constraints

$$\sum_{j=1}^{C}\mu_{j,i} = 1\,, \mu_{j,i} \in [0,1], \sum_{i=1}^{L}\mu_{j,i} > 0 \tag{6.2}$$

where $s = (s_1, s_2, s_3, \ldots, s_L)$, L is the total number of the pixels, $\mu_{j,i}$ is the membership of the pixel s_i in the j^{th} cluster and v_j is the j^{th} cluster centroid. $\|(\cdot)\|$ is the norm of a matrix and p is a weighted exponent on each fuzzy membership that controls the amount of fuzziness of the final segmentation.

The membership functions and cluster centroids are updated using the following equations by minimizing the $J_p^{FCM}(\mu, v)$

$$\mu_{j,i} = \frac{1}{\sum_{k=1}^{C}\left(\frac{\left\|s_i - v_j\right\|}{\left\|s_i - v_k\right\|}\right)^{2/p-1}},\ i = 1, 2, 3, \ldots, L \text{ and } j = 1, 2, 3, \ldots, C \tag{6.3}$$

$$v_j = \frac{\sum_{i=1}^{L}\mu_{ji}^{p}s_i}{\sum_{i=1}^{L}\mu_{ji}^{p}} \tag{6.4}$$

A summary of the FCM is as follows:

Step 1: Set the number of the clusters (C) and termination criterion > 0 i.e maximum number of iterations.

Step 2: Initialize the value of a fuzzy clustering matrix.

Step 3: Set the loop counter $l_c = 0$.

Step 4: Compute the cluster centroid (v_j) and evaluate the value of the cost function (J).

Step 5: Now, compute the membership values in the matrix for each pixel and each cluster.

Step 6: If the cost function value between successive iteration < termination criterion (ε) then STOP, otherwise set l_c=l_c+1 and return to step 4.

The main drawback of the FCM clustering based segmentation is that it is very sensitive to noise and affects the segmentation accuracy also. Since, it does not include the spatial information of the pixels. To eliminate the limitations of conventional FCM, several researchers [9, 63, 150, 222] tried to incorporate local spatial information of the pixel into the cost function of standard FCM clustering approach and provides better results than the conventional FCM. Firstly, Ahmed et al. [9] proposed the objective function of the FCM_S by including the spatial information that is also robust to noise. The objective function of the FCM_S algorithm is given as

$$J_p^{FCM\_S}(\mu, v) = \sum_{i=1}^{L}\sum_{j=1}^{\mathrm{C}} \mu_{j,i}^{p}\left\|s_i - v_j\right\|^2 + \frac{\alpha}{L_N}\sum_{i=1}^{L}\sum_{j=1}^{\mathrm{C}} \mu_{j,i}^{p}\sum_{n\in L_i}\left\|s_n - v_j\right\|^2 \tag{6.5}$$

The membership functions are subject to the following constraints

$$\sum_{j=1}^{C}\mu_{j,i} = 1\,, \mu_{j,i} \in [0,1], \sum_{i=1}^{L}\mu_{j,i} > 0 \tag{6.6}$$

where L_i represents the set of the neighbors within a window around s_i and L_N is its cardinality. The parameter α is also included in the cost function to control the effect of the neighborhood term.

The membership functions and cluster centroids are updated using the following equations by minimizing the $J_p^{FCM\_S}(\mu, v)$

$$\mu_{j,i} = \frac{1}{\sum_{k=1}^{C}\left(\frac{\left\|s_i - v_j\right\|^2 + \frac{\alpha}{L_N}\sum_{n\in L_i}\left\|s_n - v_j\right\|^2}{\left\|s_i - v_k\right\|^2 + \frac{\alpha}{L_N}\sum_{n\in L_i}\left\|s_n - v_k\right\|^2}\right)^{1/p-1}}\,,\ i = 1, 2, 3, \ldots, L \text{ and } j = 1, 2, 3, \ldots, C \tag{6.7}$$

$$v_j = \frac{\sum_{i=1}^{L}\mu_{ji}^{p}\left(s_i + \frac{\alpha}{L_N}\sum_{n\in L_i} s_n\right)}{(1+\alpha)\sum_{i=1}^{L}\mu_{ji}^{p}} \tag{6.8}$$

However, it takes more computation time than the conventional FCM because of the incorporation of additional spatial constraints and calculating the neighborhood term in each step. To overcome this problem, two different variants of the FCM_S are introduced [222] and named as FCM_X = FCM_S1 and FCM_S2 that make simpler to compute the neighborhood term by mean filtered and median filtered image, respectively. The cost function of the FCM_X can be written as follows:

$$J_p^{FCM\_X}(\mu, v) = \sum_{i=1}^{L}\sum_{j=1}^{C}\mu_{j,i}^{p}\left\|s_i - v_j\right\|^2 + \alpha\sum_{i=1}^{L}\sum_{j=1}^{C}\mu_{j,i}^{p}\left\|X - v_j\right\|^2 \quad (6.9)$$

and the membership functions and cluster centroids are updated by the equations as given below:

$$\mu_{j,i} = \frac{1}{\sum_{k=1}^{C}\left(\frac{\left\|s_i - v_j\right\|^2 + \alpha\left\|X - v_j\right\|^2}{\left\|s_i - v_k\right\|^2 + \alpha\left\|X - v_k\right\|^2}\right)^{1/p-1}}, \; i = 1, 2, 3, \ldots, L \text{ and } j = 1, 2, 3, \ldots, C \quad (6.10)$$

$$v_j = \frac{\sum_{i=1}^{L}\mu_{ji}^{p}(s_i + \alpha X)}{(1+\alpha)\sum_{i=1}^{L}\mu_{ji}^{p}} \quad (6.11)$$

where X refers to the s_i^{Mean} and s_i^{Median} for implementing the FCM_S1 and FCM_S2 approaches, respectively. The s_i^{Mean} and s_i^{Median} are the average and median of the neighboring pixels within a window around s_i, respectively. Cheng and Zhang [222] also extended the FCM to the kernel induced FCM (KFCM) with KFCM_S and its two different variants as KFCM_X = KFCM_S1 and KFCM_S2 (named as kernelized FCM with spatial constraints or spatial constrained KFCM). In the KFCM, the Euclidean distance is replaced $\left\|s_i - v_j\right\|^2$ by the kernel induced distance function $\left\|\Psi(s_i) - \Psi(v_j)\right\|^2$, where Ψ is a nonlinear map from the data space into the feature space with the corresponding kernel K. The objective function of a KFCM_X is given as

$$J_p^{KFCM\_X}(\mu, v) = \sum_{i=1}^{L}\sum_{j=1}^{C}\mu_{j,i}^{p}\left(1 - K\left(s_i, v_j\right)\right) + \alpha\sum_{i=1}^{L}\sum_{j=1}^{C}\mu_{j,i}^{p}\sum_{n\in L_i}\left(1 - K\left(X, v_j\right)\right) \quad (6.12)$$

The membership functions are subject to the following constraints

$$\sum_{j=1}^{C}\mu_{j,i} = 1\,, \mu_{j,i} \in [0,1], \sum_{i=1}^{L}\mu_{j,i} > 0 \quad (6.13)$$

where $K\left(s_i, v_j\right) = \exp\left(-\frac{\left\|s_i - v_j\right\|^2}{\sigma^2}\right)$, $\sigma^2 = \frac{1}{L}\sum_{i=1}^{L}\left\|(s_i) - \left(\frac{1}{L}\sum_{i=1}^{L}s_i\right)\right\|^2$, $S = (s_1, s_2, s_3, \ldots, s_L)$ and $\|(\cdot)\|$ refers to the norm of a matrix.

Thus, by minimizing the cost function $J_p^{KFCM\_X}(\mu, v)$ of the KFCM_X, the membership function $\mu_{j,i}$ and centroid v_j are updated iteratively and these are given by

$$\mu_{j,i} = \frac{1}{\sum_{k=1}^{C}\left(\frac{\left[1 - K\left(s_i, v_j\right)\right] + \alpha\left[1 - K\left(X, v_j\right)\right]}{\left[1 - K(s_i, v_k)\right] + \alpha\left[1 - K(X, v_k)\right]}\right)^{1/p-1}} \quad (6.14)$$

$$v_j = \frac{\sum_{i=1}^{L}\mu_{ji}^{p}\left(K\left(s_i, v_j\right)s_i + \alpha K\left(X, v_j\right)X\right)}{\sum_{i=1}^{L}\mu_{ji}^{p}\left(K\left(s_i, v_j\right) + \alpha K\left(X, v_j\right)\right)} \quad (6.15)$$

where X refers to the s_i^{Mean} and s_i^{Median} for implementing the KFCM_S1 and KFCM_S2 approaches, respectively. The s_i^{Mean} and s_i^{Median} are the average and median of the neighboring pixels within a window around s_i, respectively. In the present study, the KFCM_S1 and KFCM_S2 approaches are employed to evaluate the performance of the proposed segmentation methods, separately, by segmenting the image at initial stage.

6.3 Active Contour Based Segmentation

Active contour refers to the dynamic curves or surfaces that move within the image domain to capture the desired object's boundaries. The motion of the curve initiated by any user is driven by the combination of two forces such as internal and external forces that also achieve a minimal energy state when the curve/surface reaches the estimated boundaries of an object. Active contour models have been extensively used in handling a variety of image understanding problems such as image segmentation, shape recovery and visual tracking. The existing active contour model can be classified as parametric active contour and geometric active contour models. The parametric active contours [61, 133] are represented explicitly as parameterized curves in a Lagrangian framework, while the geometric active contours [45, 161] are represented implicitly as level sets of a two dimensional function that evolves in Eulerian framework.

6.3.1 Parametric active contour models

Parametric active contour model or snake model introduced by Kass et al. [133] has been widely used for several image processing applications, especially to locate the object's boundaries. This active contour is an evolving contour around the object that moves from its initial position toward the desired actual boundaries of the object based on the energy minimization model. The contour curve is parameterized as $C(i) = [x(i), y(i)]$, where $0 \leq i \leq 1$ refers to the arc length of the contour C. In this approach, the curve evolution is controlled by minimizing the energy associated with the current contour as the sum of the internal and external energies in the spatial domain. The mathematical formulation of the energy function is given as

$$E = \int_0^1 \frac{1}{2}(\alpha|C'(i)|^2 + \beta|C''(i)|^2)ds + \int_0^1 E_{ext}\big(C(i)\big)di \tag{6.16}$$

where α and β refer to the weighting parameters, which are responsible to control the tension and rigidity of the contour, respectively. The first integrating term refers to the internal energy function that determines the regularity of the contour, while the external energy term E_{ext} is defined on image domain (Ω) so that the desired features would have lower values. The external energy derived from image features and used to extract the contour of the desired object's boundaries is given by $E_{ext}(x, y) = -|\nabla(s(x, y))|^2$ or $E_{ext} = -|\nabla(G_\sigma(x, y) * s(x, y))|^2$, where ∇ denotes a gradient operator and $G_\sigma(x, y)$ is a two-dimensional Gaussian function with the standard deviation (σ). At the minima, the contour must satisfy the Euler-Langrange equation.

$$\underbrace{\alpha C''(i) - \beta C''''(i)}_{F_{int}} - \underbrace{\nabla E_{ext}}_{F_{ext}} = 0 \tag{6.17}$$

where F_{int} and F_{ext} refer to the internal and external forces, respectively. The contour C is treated as a function of time and the Eqn. (6.17) can be solved as

$$\frac{\partial C(i,t)}{\partial t} = \alpha C''(i,t) - \beta C''''(i,t) - \nabla E_{ext} \quad (6.18)$$

where $C(i,0) = C_0(i)$ is the initial contour. A numerical solution of the Eqn. (6.18) on discrete grid can also be achieved using a finite difference approach. Despite their popularity, the conventional parametric snake models have two major drawbacks as small capture range and the difficulties associated with topological changes such as merging and splitting of the evolving curve. A number of methods have been proposed to address the capture range problem including the distance potential forces [67], pressure forces [68], multiresolution methods [146] and Gradient Vector Flow (GVF) [61, 134].

6.3.2 Geometric active contour models

The geometric active contours have been introduced by Caselles et al. [45] and Malladi et al. [161]. These models have also been known as geodesic active contour (GAC) [45] and conformal active contour model [135]. These models are based on curve evolution theory and level set method [179, 212]. The basic idea is to represent the active contours as the zero level set function (LSF), and to evolve the LSF according to a partial differential equation. Osher and Sethian [180] introduced the mathematical formulation of a level set theory to implement the active contour. In the mathematical level set formulation of an active contour model, the contour is represented by $C = \{(x,y)|\emptyset(x,y) = 0\}$, and evolution of this contour is expressed by the zero LSF $\emptyset(t,x,y)$ at time t.

The evolution of the LSF $\emptyset(x,y)$ is shown in Figure 6.1 (a) and the propagation of the corresponding contour is presented in Figure 6.1 (b). As the LSF $\emptyset(x,y)$ increases from its initial stage, the corresponding set of contours C, i.e. the red contour propagates toward outside. With this definition, the evolution of the contour is equivalent to the evolution of the LSF, i.e. $\partial C/\partial t = \partial\emptyset(x,y)/\partial t$. The advantage of using the zero level is that a contour can be defined as a border between the positive and negative area, so the contours can be identified by just checking the sign of $\emptyset(x,y)$.

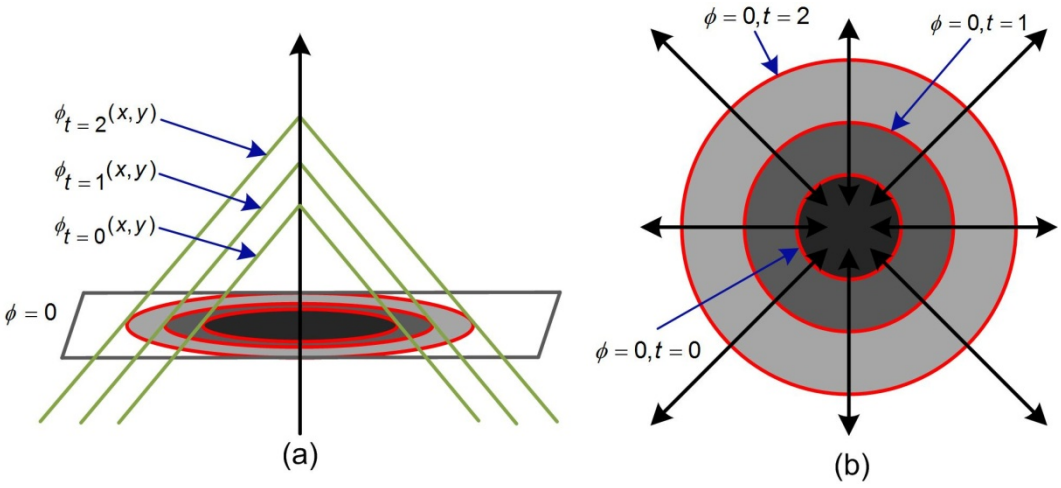

Figure 6.1 Level set evolution and the corresponding contour propagation (a) Topological view of the LSF (b) The changes on the zero level set [180]

The evolution equation of the level set function ∅ is represented in the following form

$$\frac{\partial \emptyset}{\partial t} = F|\nabla \emptyset|,\ \emptyset_0(x,y) = \emptyset(0,x,y) \tag{6.19}$$

where F denotes the speed function that controls the motion of active contour, $|\nabla \emptyset|$ denotes the normal direction and $\emptyset_0$ represents the initial contour. There are also several advantages of the geometric active contour over the traditional parametric active contour. For instance, the level set method exhibits the elastic behavior in terms of movement of the curve by evolving the LSF rather than directly moving the curve [245]. It can efficiently handle the topological changes which is also an important advantage of the geometric active contour.

For the image segmentation, geometric active contour models can be classified into two categories viz. (a) Edge-based active contour model (EBACM) and (b) Region-based active contour model (RBACM). The EBACM is closely related to the edge-based segmentation that uses the several edge detection operators, usually based on the image gradient to attract the contour toward the desired boundaries of an object. On the other hand, the RBACM is able to identify the object of interest using the region descriptor to control the curve evolution. A brief description of the EBACM approach is given in the next section that is also employed to implement the proposed segmentation method, while the RBACM approach utilized in another proposed segmentation approach will be described in the next chapter.

6.4 Edge-Based Active Contour using DRLSE Approach

Edge-based active contour methods (EBACM) are closely related to the edge-based segmentation. Mostly the EBACM consists of two different parts such as the regularity part and the edge detection part that are used to estimate the shape of the curves and to attract the contour toward the edges, respectively. Previously, Osher and Sethian [180] addressed on motion of the active contour that is also controlled by the speed function F represented in the form as

$$F = div\left(\frac{\nabla \emptyset}{|\nabla \emptyset|}\right) \tag{6.20}$$

Thus, the Eqn. (6.19) is represented as

$$\frac{\partial \emptyset}{\partial t} = |\nabla \emptyset|\left(div\left(\frac{\nabla \emptyset}{|\nabla \emptyset|}\right)\right) \tag{6.21}$$

Next popular EBACM based mean curvature motion is presented by Caselles et al. [44] and given by

$$\frac{\partial \emptyset}{\partial t} = g|\nabla \emptyset|\left(div\left(\frac{\nabla \emptyset}{|\nabla \emptyset|}\right) + \alpha\right) \tag{6.22}$$

where α refers to an inflation force that is able to push the curve toward the object, when the curvature becomes null or negative. $g = 1/[1 + |G_\sigma(x,y) * I(x,y)|^2]$ is the edge function used to stop level set evolution near the estimated object's boundary, where g vanishes. Here, G_σ

is the smoothing Gaussian function with standard deviation (σ). Latter, Caselles et al. [45] introduced another EBACM approach. It starts with the minimization of energy functional defined on parameterized contours by which the curve evolution equations are derived in the Lagrangian formulation. By embedding the contour into the LSF, the Lagrangian formulation can be reformulated in terms of the LSF in the following Eulerian formulation.

$$\frac{\partial \emptyset}{\partial t} = |\nabla \emptyset| \left(div \left(g \frac{\nabla \emptyset}{|\nabla \emptyset|} \right) + \alpha g \right) \quad (6.23)$$

This formulation is known as the GAC model in which the extra stopping term αg makes the contour converge to the object boundary more accurately and has better performance in presence of weak edges.

In traditional active contour methods, the LSF $(\emptyset)$ can develop socks, very sharp/flat shapes during the evolution, which makes further computation highly inaccurate. To avoid this problem, a common numerical scheme is used to initialize the LSF as a signed distance function before the evolution and then re-initialize the function $\emptyset$ as a signed distance function periodically during the evolution [185].

$$\frac{\partial \emptyset}{\partial t} = sign(\emptyset_0)(1 - |\nabla \emptyset|) \quad (6.24)$$

where $\emptyset_0$ is the function to be re-initialized. If $\emptyset_0$ is not smooth or much steeper on one side of the interface than the others, the zero level set of the resulting function $\emptyset$ can be moved incorrectly from that of the original function. In practice, the evolving LSF can deviate greatly from its estimated position within a small number of iteration steps, especially when the time step used in the discretized evolution equation is not small enough. Therefore, the re-initialization process has become an important solution for maintaining a stable curve evolution process and ensuring the better segmentation results. For such purpose, many researchers have tried to re-initialize the regularity of the LSF and make it stable [179, 185, 212, 248]. In order to solve re-initialization problem, Li et al. [64] proposed a new variational formulation for the GAC with a penalty term that drives the level set function to be close to the signed distance function. This method completely eliminates the periodic re-initialization process of the level set function during the evolution. However, some unwanted side effects are produced on the level set function because of the penalty term. Furthermore, Li et al. [65] extended their previous method to distance regularized level set evolution (DRLSE) by incorporating the new distance regularization term with two well potential function and external energy term that force the motion of contour toward the expected position. The variational formulation is given as,

$$E_{Total}(\emptyset) = \mu R(\emptyset) + E_{ext}(\emptyset) \quad (6.25)$$

where the overall energy $E_{Total}(\emptyset)$ consists of two parts: $R(\emptyset)$ refers the regularization term which forces $\emptyset$ to automatically approach the signed distance function during the evolution of the LSF and the parameter $\mu > 0$ is the weighting coefficient of the regularization term.

$E_{ext}(\emptyset)$ refers to the external energy that forces the zero LSF to the expected position. The external energy for the function $\emptyset(x, y)$ is defined as

$$E_{ext}(\emptyset) = \lambda L(\emptyset) + \alpha A(\emptyset) \tag{6.26}$$

where the first term and second term called as the contour length term and artificial balloon force term, respectively correspond to the gradient flows of the energy function. The first term drives the zero level set contour toward the estimated boundaries of an object while the second term is responsible to increase the moving speed of the contour. The parameter $\lambda > 0$ is a weighting coefficient of the contour length to control the smoothness of contour during curve evolution and the weighting coefficients α can be positive or negative depending upon the relative position of initial contour. The energy functional terms are defined as

$$\left.\begin{aligned} L(\emptyset) &\triangleq \int_{\Omega} g\delta_{\varepsilon}(\emptyset)|\nabla\emptyset|dx \\ A(\emptyset) &\triangleq \int_{\Omega} gH_{\varepsilon}(-\emptyset)\, dx \end{aligned}\right\} \tag{6.27}$$

where g, $\delta_{\varepsilon}(x)$ and $H_{\varepsilon}(x)$ are the edge indicator functions, Dirac delta function and Heaviside function, respectively. All these functions are defined as

$$g \triangleq \frac{1}{1+|\nabla G_{\sigma} * I|^2} \tag{6.28}$$

$$\delta_{\varepsilon}(x) = \begin{cases} 0, & |x| > \varepsilon \\ \frac{1}{2\varepsilon}\left[1 + \cos\left(\frac{\pi x}{\varepsilon}\right)\right], & |x| \le \varepsilon \end{cases} \tag{6.29}$$

$$H_{\varepsilon}(x) = \begin{cases} 0, & x < -\varepsilon \\ 1, & x > \varepsilon \\ \frac{1}{2}\left[1 + \frac{x}{\varepsilon} + \frac{1}{\pi}\sin\left(\frac{\pi x}{\varepsilon}\right)\right], & |x| \le \varepsilon \end{cases} \tag{6.30}$$

where I is the original image and g is the smoothed image obtained by convolving the Gaussian kernel (G_{σ}) with standard deviation (σ). The ε is a constant parameter that regularizes the Dirac delta function. In this study, the parameter $\varepsilon = 1.5$ is taken as described in [65]. The regularization term $R(\emptyset)$ for level set model is defined as

$$R(\emptyset) \triangleq \int_{\Omega} p(|\nabla\emptyset|)dx \tag{6.31}$$

where $p(|\nabla\emptyset|)$ is the potential function for the regularization term $R(\emptyset)$. A double well potential function is written as

$$p(s) = \begin{cases} \frac{1}{2}(s-1)^2, & s \ge 1 \\ \frac{1}{4\pi^2}(1 - \cos(2\pi s)), & s \le 1 \end{cases} \tag{6.32}$$

Using first derivative

$$p'(s) = \begin{cases} s - 1 & s \ge 1 \\ \frac{\sin(2\pi s)}{2\pi} & s \le 1 \end{cases} \tag{6.33}$$

Thus, the total energy function is approximated by

$$E_{Total}(\emptyset) = \mu \int_{\Omega} p(|\nabla\emptyset|) + \lambda \int_{\Omega} g\delta_{\varepsilon}(\emptyset)|\nabla\emptyset|dx + \alpha \int_{\Omega} gH_{\varepsilon}(-\emptyset)\, dx \tag{6.34}$$

The Eqn. (6.34) minimized by solving the gradient flow can be defined as

$$\frac{\partial \emptyset}{\partial t} = \mu div\left[\left(\frac{p'(|\nabla \emptyset|)}{|\nabla \emptyset|}\right)\nabla \emptyset\right] + \lambda \delta_{\varepsilon}(\emptyset) div\left[g\frac{\nabla \emptyset}{|\nabla \emptyset|}\right] + \alpha g \delta_{\varepsilon}(\emptyset) \quad (6.35)$$

The Eqn. (6.35) refers to the EBACM with the DRLSE formulation. On the right side of DRLSE model, the first term is the distance regularization energy while the second and third terms are the gradient flows of the different energy function as described in Eqn. (6.27). In this formulation, the LSF $\emptyset_0(x, y)$ is initialized as

$$\emptyset_0(x, y) = \begin{cases} -c_0, & (x, y) \in \Omega_0 \\ c_0, & otherwise \end{cases} \quad (6.36)$$

where $c_0 > 0$ is a constant and Ω_0 is a region of interest in the given image domain Ω. The discretization of Eqn. (6.35) can be expressed in the following iteration form.

$$\emptyset_{t+1}(x, y) = \emptyset_t(x, y) + \tau \frac{\partial \emptyset_t(x,y)}{\partial t} \quad (6.37)$$

where τ is the time step of level set evolution. For maintaining the stable level set evaluation, the time step parameter τ and penalty term μ must satisfy the condition $(\tau\mu < 1/4)$.

6.5 Proposed Hybrid Edge-Based Active Contour Method with KFCM Clustering

In the proposed hybrid edge-based active contour model using the KFCM clustering (EBACM-KFCM) approach, both the features of the KFCM with spatial constraints clustering KFCM_X (KFCM_S1 and KFCM_S2) and the EBACM using DRLSE model are merged to formulate two algorithms for the segmentation of US medical images. The proposed method starts with the KFCM_S1 and KFCM_S2 clustering methods, individually, for the purpose of initial segmentation. At this stage, it generates spurious blobs and outliers in the image. Thus, the morphological operations such as erosion and dilation have been used to suppress such effects and to recover the object of interest.

After that, the results of the KFCM_X = KFCM_S1 and KFCM_S2 are utilized to initialize the DRLSE formulation based active contour model and to evaluate the controlling parameters also which have a responsibility of accurate contour propagation. Let, the region of interest in the result of fuzzy clustering be expressed as I_R and $\mu_m^{KFCM\_X}$ as the membership function for the KFCM_X method. Now, the initializing function of the level set model can be given as

$$\emptyset_0(x, y) = (4I_R - 2)\varepsilon \quad (6.38)$$

where ε is a constant parameter which regularizes the Dirac delta function [64, 65, 179] and I_R refers to the binary image obtained using the following equation as given below:

$$I_R = \begin{cases} 0, & \mu_m^{KFCM\_X} < T \\ 1, & \mu_m^{KFCM\_X} \geq T \end{cases} \quad (6.39)$$

where $T \in [0,1]$ refers to the adjustable threshold value that is used to control the size of the contour.

The proposed automatic segmentation algorithm has both the property of autoinitialization of the LSF and autoconfiguration of several controlling parameters using the KFCM_S1 and KFCM_S2 clustering, individually. This also helps to control the parameter values used in the DRLSE model, which are provided manually and changed for every image data. In the EBACM model mentioned in Eqns. (6.35) and (6.37), it is prime requirement to estimate all the four parameters such as regularization term coefficient (μ), coefficient of the contour length (λ), balloon force (α) and time step parameter (τ). All these controlling parameters are estimated from the results of the KFCM_X clustering. The balloon force (α) should be large and it depends on its sign either positive (means to shrink toward the object boundary) or negative (means to expand toward the object boundary). The balloon force is estimated using the result obtained by the KFCM_X model

$$\alpha = -2\left(\mu_{\mathrm{m}}^{\mathrm{KFCM\_X}} - 0.5\right) \tag{6.40}$$

For the DRLSE approach, the weighting coefficient of the regularization term (μ) is evaluated by estimating the length and area of the initial LSF that is also the result of the KFCM_X method. The area and length of the contour produced by the KFCM_S1 and KFCM_S2, individually, estimated using the Dirac delta and Heaviside function are given as below:

$$Length = \int_{\Omega} \delta(\emptyset_0) dxdy \tag{6.41}$$

$$Area = \int_{\Omega} H(\emptyset_0) dxdy \tag{6.42}$$

where the Heaviside function $H(\emptyset_0)$ is

$$H(\emptyset_0) = \begin{cases} 0, & \emptyset_0 < 0 \\ 1, & \emptyset_0 \geq 1 \end{cases} \tag{6.43}$$

The time step parameter (τ) is calculated by

$$\tau = \frac{Area}{Length} \tag{6.44}$$

For the stable and accurate curve evolution, the multiplication of time step parameter (τ) and weighting coefficient of the regularization term (μ) should be less than 1/4 [64, 65]. Based on the experimental results, the coefficient of the regularizing term (μ) is evaluated as

$$\mu = 0.2/\tau \tag{6.45}$$

Thus, the weighting coefficient of the contour length is estimated as

$$\lambda = 0.1\tau \tag{6.46}$$

Therefore, the mathematical formulation of the EBACM approach using DRLSE can be given as below:

$$\frac{\partial \emptyset}{\partial t} = \mu div\left[\left(\frac{p\prime(|\nabla\emptyset|)}{|\nabla\emptyset|}\right)\nabla\emptyset\right] + \lambda\delta_{\varepsilon}(\emptyset) div\left[g\frac{\nabla\emptyset}{|\nabla\emptyset|}\right] - 2g\left(\mu_{\mathrm{m}}^{\mathrm{KFCM\_X}} - 0.5\right)\delta_{\varepsilon}(\emptyset) \tag{6.47}$$

Now, Eqns. (6.37) and (6.47) refer to the formulation of EBACM using DRLSE approach used for the segmentation purpose.

Implementation Steps

For the automated segmentation of US medical images and implementing the above aspects, the proposed algorithm is formulated as follows:

Step 1: Start with the given US image.

Step 2: Apply the KFCM_X clustering algorithm on the given input image.

a) Set the number of the clusters (C), p and termination criterion > 0. In the present work, the parameters such as $p = 2$ and termination criterion $= 0.001$ are taken based on the experimental results. The parameter (C) is considered according to the images and their region of interest.

b) Compute the average and median value of the neighboring pixel for the KFCM_X = KFCM_S1 and KFCM_S2, respectively.

c) Initialize the value of fuzzy clustering matrix and set the loop counter $l_c = 0$.

d) Compute the cluster centroid using Eqn. (6.15) and evaluate the value of the objective function (J).

e) Now, compute the membership values in the matrix using Eqn (6.14) for each pixel and for each cluster.

f) If the cost function value between successive iteration < termination criterion, then STOP, otherwise set l_c=l_c+1 and go to step d.

Step 3: Select the region of interest in the result of KFCM_X = KFCM_S1 and KFCM_S2 obtained from step 2 and evaluate the initial level set function using Eqn. (6.38).

Step 4: Estimate the smooth image (g) by convolving the original image and a Gaussian low pass filter of size 8×8 with the standard deviation of 0.5 using Eqn. (6.28)

Step 5: Compute the value of the time step parameter τ and regularization parameter μ using Eqns. (6.44) and (6.45), respectively.

Step 6: Compute the weighting coefficient of contour length λ using Eqn. (6.46).

Step 7: Now, the balloon force coefficient is estimated using Eqn. (6.40).

Step 8: Apply the EBACM with DRLSE evolution using Eqns. (6.47) and (6.37).

6.6 Evaluation Criterion

For the quantitative evaluation and analysis of the segmentation performance obtained by the different segmentation methods, several validation parameters are used such as the true positive (TP) [244], false positive (FP) [244], accuracy (ACC) [50], jaccard similarity index (JSI) [244], dice coefficient (DC) [240] and Hausdorff distance (HD) [124, 244].

(a) *True positive* (TP) *ratio*: The TP value denotes the pixels that become visible in both the binary mask of the segmented region generated by manual and computerized segmentation method. The TP is defined as

$$TP = \frac{|S_M \cap S_T|}{|S_M|} \tag{6.48}$$

where S_M indicates the manually segmented ground truth binary mask and S_T denotes the binary mask of the region segmented by the computerized method. The higher value of the TP ratio means the more overlapping area between the real and segmented region.

(b) *False positive* (FP) *ratio*: The FP value denotes the pixels that become visible in the segmented region generated by the test method, but it does not appear in the ground truth binary mask. When the FP takes lower value, fewer incorrect regions are covered by the segmented region. The FP ratio is given as

$$FP = \frac{|S_M \cup S_T - S_M|}{|S_M|} \tag{6.49}$$

(c) *Accuracy* (ACC): The ACC means the proportion of the pixels contained within the correctly extracted region obtained by the test method out of all the pixels of manually delineated region. The segmentation accuracy is given as below:

$$ACC = \frac{TP+TN}{TP+FP+TN+FN} \tag{6.50}$$

where TP, FP, TN, FN represent the true positive, false positive, true negative and false negative values, respectively.

(d) *Jaccard similarity index* (JSI): The JSI is used as a statistical measure of similarity between the regions delineated by manual and computerized method and it is given as

$$JSI = \frac{|S_M \cap S_T|}{|S_M \cup S_T|} \tag{6.51}$$

If the value of the JSI metric is higher, it signifies that the more segmented region match to the manual segmentation.

(e) *Dice Coefficient* (DC): The DC value is utilized to measure the similarity of the extracted region using test segmentation algorithms and manually delineated. The DC is defined as follows:

$$DC = 2 \times \frac{|S_M \cap S_T|}{|S_M + S_T|} \tag{6.52}$$

The values of dice coefficient should be close to unity that insures the exact overlapping of the segmented and manually delineated region.

(f) *Hausdorff distance* (HD): Finally, the HD values are utilized as a measure of the structural difference between two objects. It is given as the maximum of the Euclidean distance between the least distant point pair in the structures [206]. For the two contours R and S, the HD index is estimated as follows:

$$HD(R,S) = max\left\{\sup_{x \in R} \inf_{y \in S} d(x,y), \sup_{x \in S} \inf_{y \in R} d(x,y)\right\} \tag{6.53}$$

where sup and inf refer to supremum and infimum operators, respectively and $d(x,y)$ denotes the Euclidean distance between two points x and y. Therefore, the HD provides the

upper limit of the object misalignment between the contour of the extracted and manual delineated boundaries. The lower HD values indicate better segmentation performance with respect to the manual delineation.

6.7 Experimentation

To analyze the segmentation capability of the proposed methods introduced earlier, different objective measures are used. Here, the segmentation performance of two different proposed approaches-1 and 2 named as the EBACM-KFCM_S1 and EBACM-KFCM_S2, respectively, are investigated. The proposed approach-1 and 2 signify that the results of the KFCM_S1 and KFCM_S2 clustering methods are employed to initialize the LSF and to control the several contour evolution controlling parameters used in the EBACM approach, respectively. To assess the segmentation performance of the proposed approaches and other existing methods, two different experiments are conducted on both the synthetic test images including noisy images and several real US medical images.

Experiment 1: To analyze and evaluate the segmentation performance of the proposed EBACM-KFCM_S1 and EBACM-KFCM_S2 approaches applied to the synthetic test images and present a comparative analysis of the proposed and other existing methods, qualitatively and quantitatively.

Experiment 2: To analyze and evaluate the segmentation performance on the real US images processed by both the proposed approach-1 and 2 and demonstrate a comparison between the segmentation results provided by the proposed approaches and other existing methods.

6.8 Results and Discussions

Experiment 1: *Analysis and evaluation for the segmentation performance of the synthetic test images* - In order to validate the experimental objective, several test images synthesized using the MATLAB are considered, in which two of them are presented to analyze the segmentation performance of the proposed EBACM-KFCM_S1 and EBACM-KFCM_S2 approaches. For the first synthetic image of size 118 × 134 pixels, Figure 6.2 (a) and (c) show segmented images with the red contour mark on the estimated object boundaries that are extracted by the proposed approach-1 and 2, respectively. From Figure 6.2 (a) and (c), it can be observed that the proposed approaches are able to successfully detect the object's boundaries. Moreover, the proposed EBACM-KFCM_S2 approach provides more accurate results by extracting the boundaries than the EBACM-KFCM_S1 approach. Furthermore, it is clearly demonstrated by the plot of final LSF as shown in Figure 6.2 (b) and (d) corresponding to Figure 6.2 (a) and (c), respectively.

In order to evaluate the performance of the proposed approach-1 and 2 against noise, another synthetic noisy image of size 101 × 99 pixels is considered. Its segmentation results

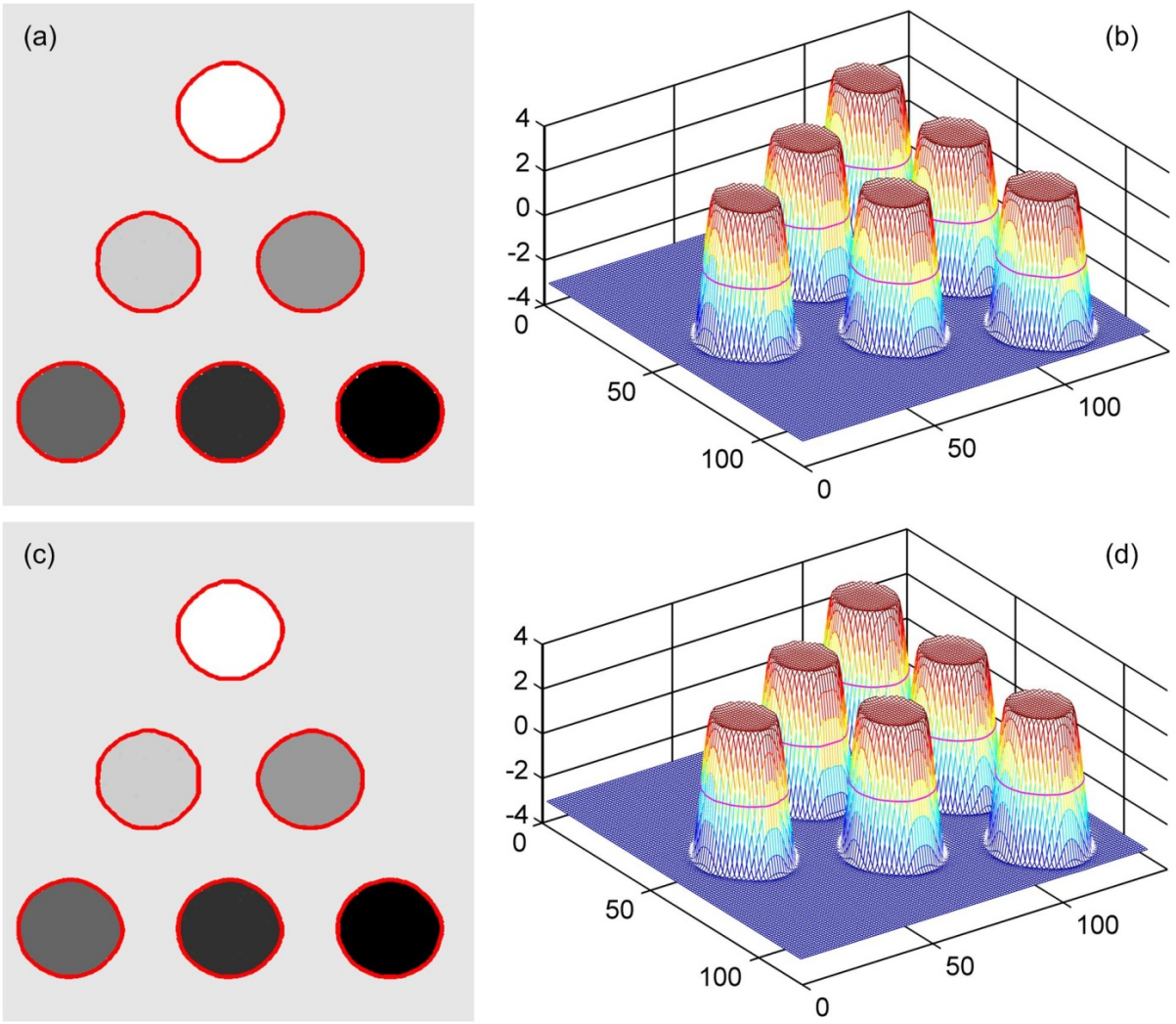

Figure 6.2 Segmentation results of the synthetic image-1 (SI-1) produced by the (a) Proposed EBACM-KFCM_S1 approach (c) Proposed EBACM-KFCM_S2 approach. (b) and (d) represent the three dimensional display of the final LSF of a and c, respectively

produced by the proposed EBACM-KFCM_S1 and EBACM-KFCM_S2 are shown in Figure 6.3 (a) and (c), respectively, and their corresponding final LSF are also shown in Figure 6.3 (b) and (d), respectively. From both the results, it can be observed that the proposed methods are still able to successfully extract the estimated objects' boundaries.

Furthermore, to assess the superiority of the proposed segmentation approaches, their results were compared with the results obtained by the FCM_S1 method, FCM_S2 method, KFCM_S1 method, KFCM_S2 method, GAC method [45, 182], ACMRSF method [48, 66], and EBACM method [64, 65]. For the comparative analysis of the segmentation results obtained by aforementioned methods, the segmented images of both the synthetic test images are presented in Figure 6.4 (b)-(j) and Figure 6.5 (b)-(j), respectively. From these results, it is observed that the proposed method is able to successfully extract the estimated region and boundaries of the object. The subjective outcomes of the proposed and other methods are also supported by the six different performance measures. These quantitative outcomes are listed in Table 6.1 for both the synthetic images (SI-1 and SI-2).

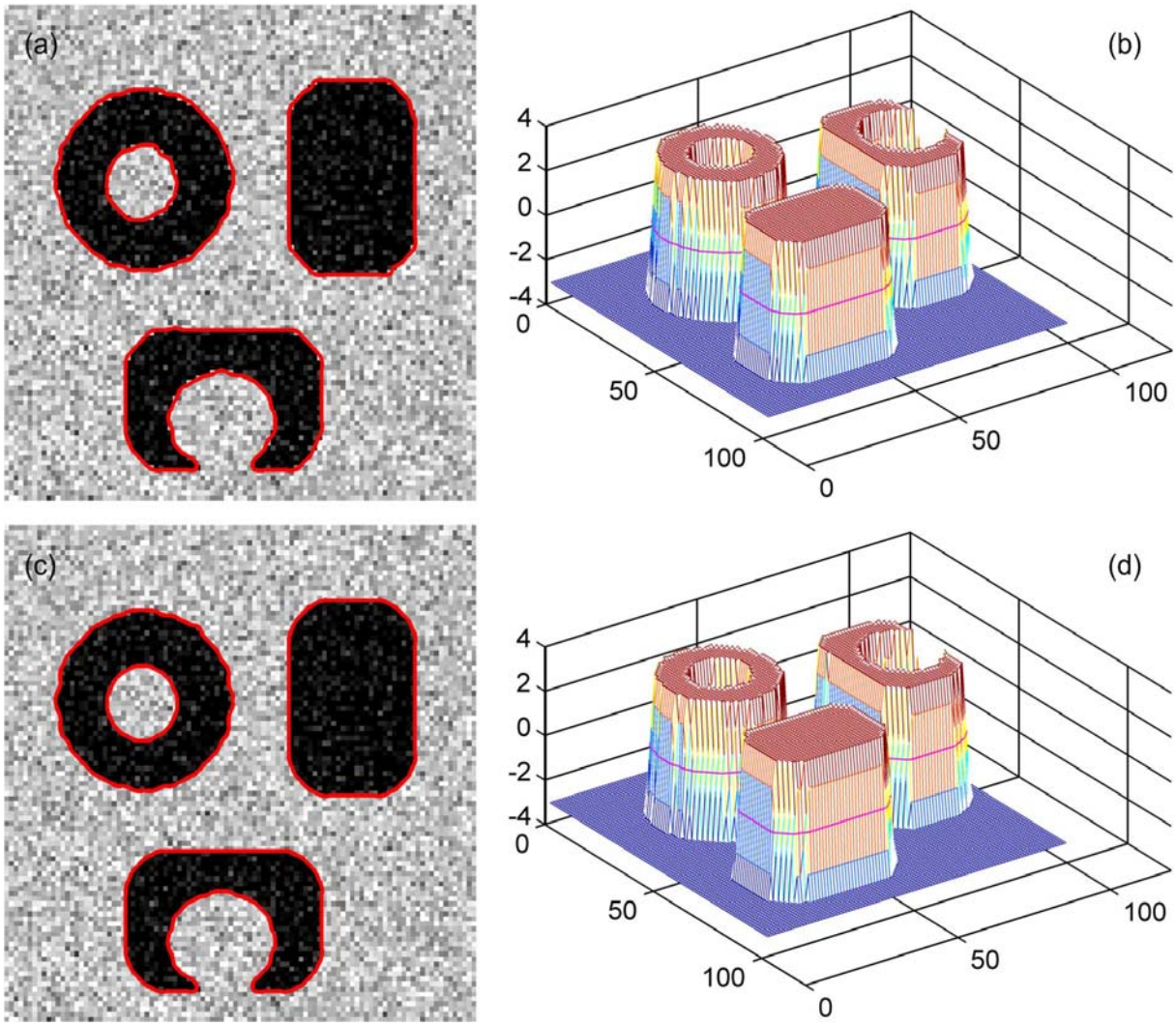

Figure 6.3 Segmentation results of the noisy synthetic image-2 (SI-2) produced by the (a) Proposed EBACM-KFCM_S1 approach (c) Proposed EBACM-KFCM_S2 approach. (b) and (d) represent the three dimensional display of the final LSF of a and c, respectively

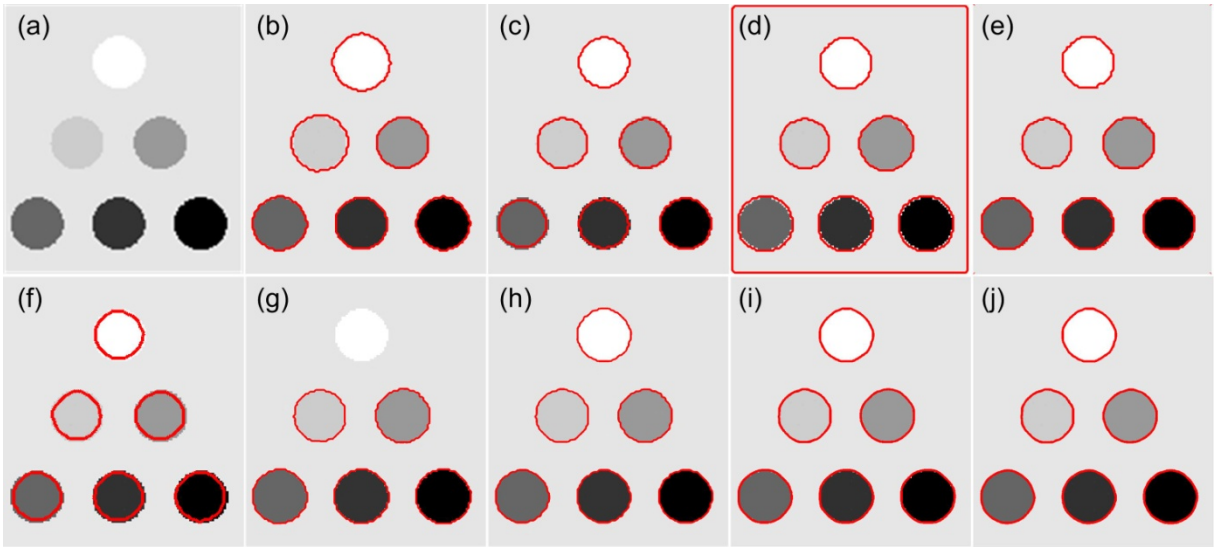

Figure 6.4 Segmentation results for the synthetic test image-1 (a) Original image. Results obtained by (b) FCM_S1 (c) FCM_S2 (d) KFCM_S1 (e) KFCM_S2 (f) GAC (g) ACMRSF (h) EBACM (i) Proposed EBACM-KFCM_S1 (j) Proposed EBACM-KFCM_S2

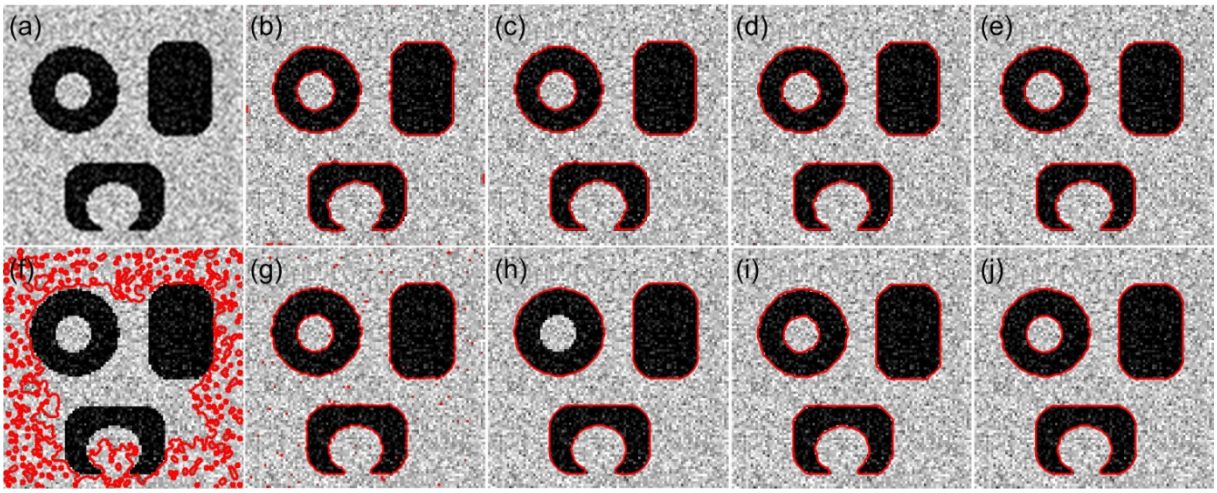

Figure 6.5 Segmentation results for the synthetic test image-2 (a) Original image. Results obtained by (b) FCM_S1 (c) FCM_S2 (d) KFCM_S1 (e) KFCM_S2 (f) GAC (g) ACMRSF (h) EBACM (i) Proposed EBACM-KFCM_S1 (j) Proposed EBACM-KFCM_S2

The results mentioned in Table 6.1 show that the proposed methods gain approx 98% segmentation accuracy which obviously outperforms the others. The other measures such as JSI and DC obtained by the proposed methods also achieve higher values than others. It indicates more similar region extracted by the proposed approach-1 and 2 than the other methods.

Table 6.1 Performance measures obtained by various segmentation methods for the synthetic test images illustrated in Figure 6.4 and Figure 6.5

Methods	Images	TP	FP	ACC	JSI	DC	HD
FCM_S1	SI-1	96.3029	2.2958	97.0036	94.1416	96.9824	3
	SI-2	99.0883	7.6586	95.7148	92.0393	95.8546	2.8284
FCM_S2	SI-1	98.2707	6.2016	96.0346	92.5323	96.1213	3
	SI-2	95.1131	1.2188	97.4471	94.9054	97.3861	3
KFCM_S1	SI-1	94.0072	0.1193	96.9439	93.8952	96.8515	3
	SI-2	94.7848	2.2247	96.2801	92.7221	96.2236	2.8284
KFCM_S2	SI-1	95.4681	0.3578	97.5552	95.1277	97.5030	2.2361
	SI-2	95.7330	1.4376	97.6477	95.3159	97.6018	3
GAC	SI-1	94.0072	24.359	84.8241	75.5934	86.1005	4.899
	SI-2	90.1167	24.225	57.8957	51.6946	68.1561	6.5574
ACMRSF	SI-1	90.6977	1.6100	94.5438	89.2606	94.3256	3
	SI-2	97.1554	10.685	93.2349	87.7759	93.4901	5.7082
EBACM	SI-1	97.2570	2.8026	97.2272	94.6056	97.2208	3.4641
	SI-2	97.4836	1.5317	97.9759	96.0129	97.9659	3
Proposed approach-1 (EBACM-KFCM_S1)	SI-1	96.2456	0.3287	97.7244	95.9831	97.9212	2.6458
	SI-2	97.5930	1.1670	98.2130	96.4672	98.2018	3
Proposed approach-2 (EBACM-KFCM_S2)	SI-1	96.2135	0.2087	98.0024	96.0131	97.9660	2.2361
	SI-2	97.5930	1.1306	98.2312	96.5020	98.2199	3

The TP ratio obtained by the proposed methods is also high (approx 97%), but sometimes the proposed method exhibits lower TP values than others. This is because of the blurry regions around the boundaries that become very difficult to be differentiated with the real boundaries. Moreover, these blurry regions are also marked by an expert at the time of manual segmentation. In the results mentioned in Table 6.1, some methods have higher TP values than the proposed methods. However, these methods also gain higher FP values which indicate their inaccurate segmentation results. Besides it, the proposed methods also exhibit the abilities of accurately extracting the region of interest by achieving the lowest values of the Hausdorff distance. Moreover, the box plots of all six metric evaluations for all the synthetic test images are presented in Figure 6.6. In each box plot, the top and bottom of each rectangular box indicate the 25th and 75th percentile, respectively, with the median shown inside the box. It is clearly seen from Figure 6.6 that the median of the TP, JSI, ACC, DC and FP, HD values evaluated by the proposed approach-2 are highest and lowest, respectively. This also indicates the superiority of the proposed approach-1 and 2 over the others in terms of the successful extraction of the objects of interest. Moreover, the proposed EBACM-KFCM_S2 approach outperforms the EBACM-KFCM_S1 approach and others.

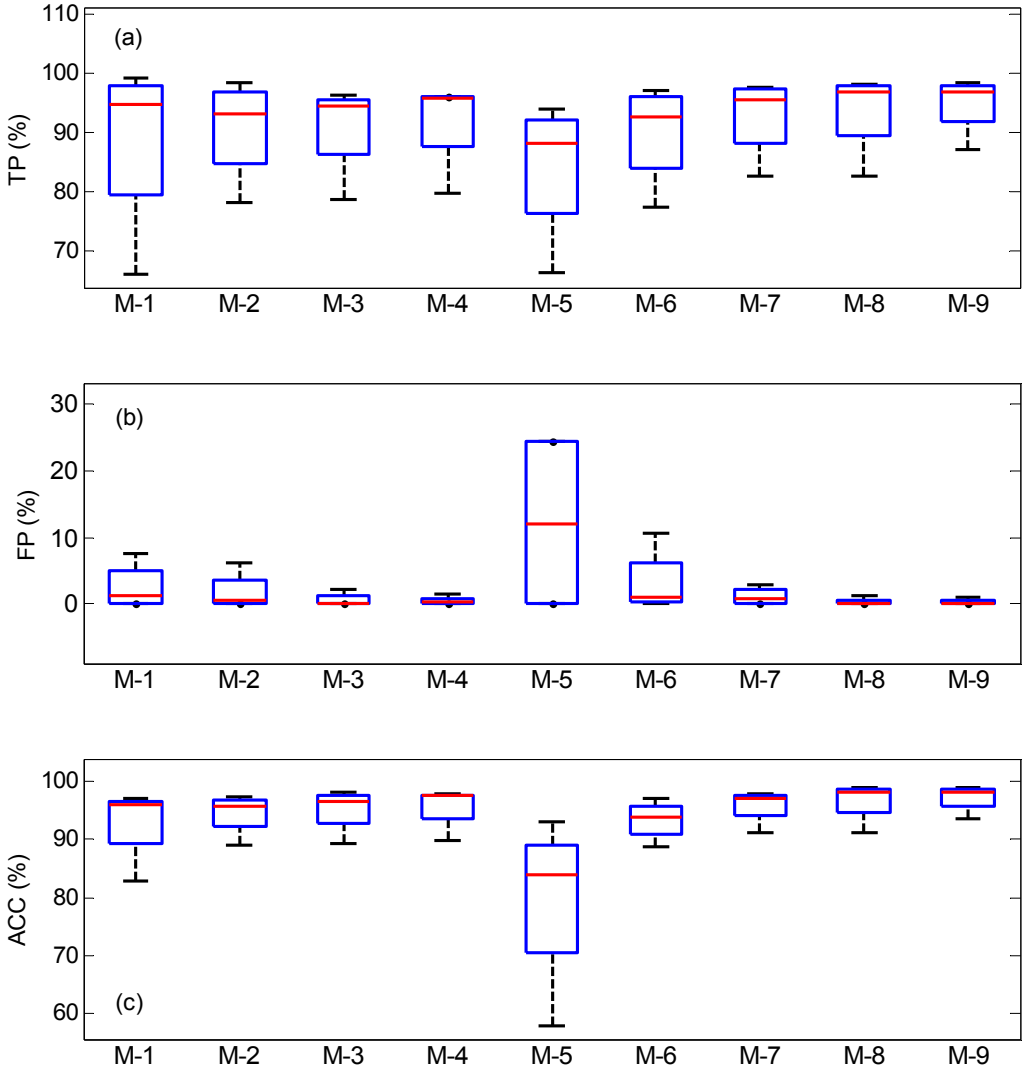

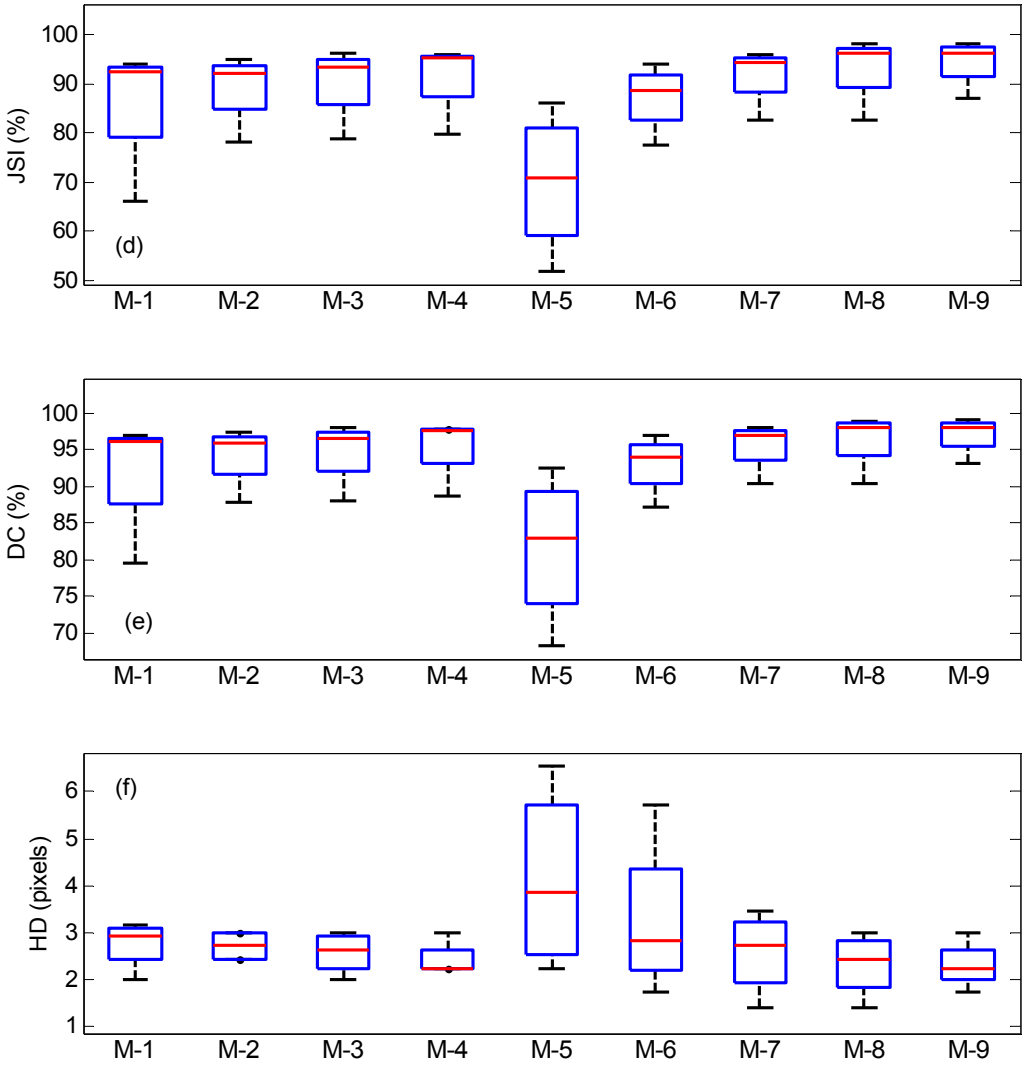

Figure 6.6 Box plot of the TP, FP, ACC, JSI, DC and HD measurements of all synthetic test images processed by the proposed EBACM-KFCM_S1 (M-8), EBACM-KFCM_S2 (M-9) and others, where M-1, M-2, M-3, M-4, M-5, M-6 and M-7 refer to the FCM_S1, FCM_S2, KFCM_S1, KFCM_S2, GAC, ACMRSF and EBACM methods, respectively

Further, the processing time taken by all the segmentation methods individually, are also evaluated. For such purpose, all the experiments have been performed using MATLAB 7.10 and PC having Intel® core™ i7-2600 CPU @ 3.40 GHz processor and 4 GB RAM on windows 8 Pro. The details of averaged processing time and number of iterations to extract the regions of all the images are listed in Table 6.2. All the results are produced on the same machine. From the results mentioned in Table 6.2, it can be observed that the proposed methods do not take too much time and require less number of iterations as compared to others. The proposed approach-1 and 2 take lower averaged iteration as 30 and 20, respectively, than the GAC (275), ACMRSF (175), EBACM (35) methods. Therefore, the processing time required to achieve the outcomes produced by the proposed approach-1 and 2 becomes lower (1.6818 and 1.5594, respectively) than others. By visualizing the results, it is clearly observed that the GAC and EBACM methods take higher computational

time to provide the segmented image. Finally, it can be concluded that the proposed approaches are able to produce better segmentation results with higher accuracy than other existing methods, but not at the cost of higher iteration values and computation time.

Table 6.2 Comparative performance of the segmentation approaches with the averaged iterations and computational time for all the synthetic test images

Methods	Averaged resolution	Averaged computational time, s	Averaged iterations
FCM_S1	94 × 95	0.3049	25
FCM_S2	94 × 95	0.1998	7
KFCM_S1	94 × 95	0.4252	27
KFCM_S2	94 × 95	0.3351	18
GAC	94 × 95	20.171	275
ACMRSF	94 × 95	2.5843	175
EBACM	94 × 95	5.8896	35
Proposed approach-1	94 × 95	1.6818	30
Proposed approach-2	94 × 95	1.5594	20

Experiment 2: *Analysis and evaluation for the segmentation performance of real US images* - In order to investigate the segmentation performance of the proposed EBACM-KFCM_S1 and EBACM-KFCM_S2 approaches and to present comparative analysis, fifty different US images are considered. For the present analysis, these US images were acquired from the image database (http://www.ultrasoundcases.info, http://radiologyinfo.org/en/photocat/ and http://ultrasonics.bioengineering.illinois.edu). In the present study, the segmentation results of ten different US images are presented in a qualitative manner. Figure 6.7 shows a comparison of the segmentation results of left ventricle US image obtained by the aforementioned segmentation methods. Figure 6.7 (a) shows the manual delineated region. From Figure 6.7 (i) and (j), it is observed that the proposed approaches accurately segment the object's boundaries. Figure 6.7 (b)-(h) presents the extracted region boundaries provided by the FCM_S1, FCM_S2, KFCM_S1, KFCM_S2, GAC, ACMRSF and EBACM, respectively. From these results, it can be observed that only FCM_S2, KFCM_S1, KFCM_S2, ACMRSF and proposed approach-1 and 2 are able to properly extract the boundary of the region of interest. Moreover, the proposed EBACM-KFCM_S1 and EBACM-KFCM_S2 approaches outperform all the other methods. Moreover, for ensuring the superiority of the proposed methods by providing better segmentation results, a comparative view of the different US images processed by aforementioned segmentation methods are presented in Figure 6.8 and Figure 6.9. The segmentation results of five different US images are illustrated in Figure 6.8. The image shown in first row is an US image of the left ventricle and another US image of splenic cyst is shown in the second row. The image shown in third row refers to the US image of benign tumor and last two images are the US images of liver metastases. In

addition, in Figure 6.9, four different US images are shown in the first column. The image in first row shows the US image of the brain showing dilated ventricles indicating too much fluid (hydrocephalus). The next image refers to the US image of benign cyst and last two images are the US images of multiple liver masses. Their manually delineated images are shown in both the Figure 6.8 (a) and Figure 6.9 (a) The outcomes of these different US images segmented by similar aforementioned methods are presented in Figure 6.8 (b)-(j) and Figure 6.9 (b)-(j). From these results, it can be clearly observed that the proposed methods precisely segment the region and object boundaries. Moreover, the segmentation results obtained by the proposed methods are approximately similar to that of the manually delineated region as compared to others.

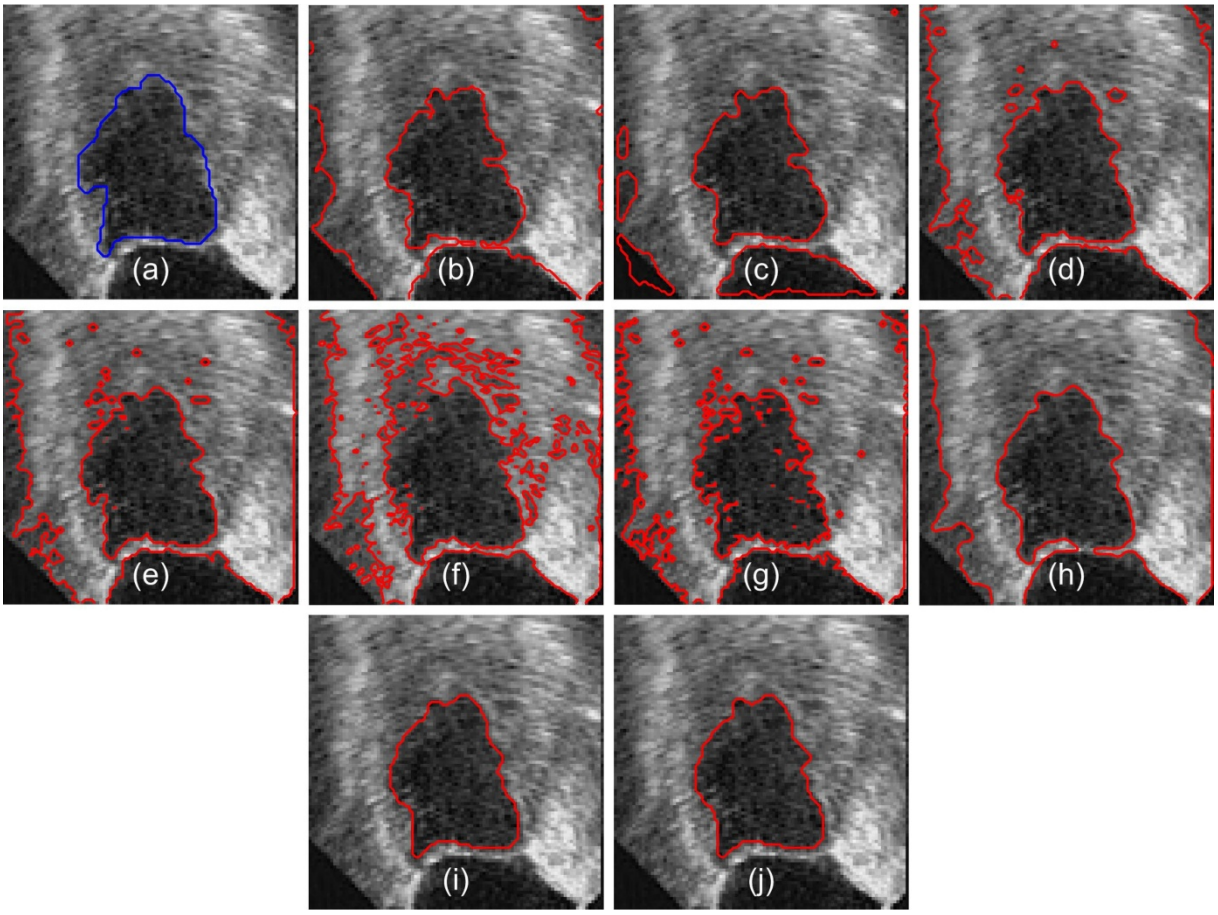

Figure 6.7 Segmentation results obtained by (a) Manually segmented ultrasound image (b) FCM_S1 (c) FCM_S2 (d) KFCM_S1 (e) KFCM_S2 (f) GAC (g) ACMRSF (h) EBACM (i) Proposed EBACM-KFCM_S1 (j) Proposed EBACM-KFCM_S2

Besides all these subjective evaluations of all the US images, different quantitative analysis has also been done in terms of the different performance metrics as mentioned above. Their corresponding quantitative results are listed in Table 6.3, which shows the averaged performance measures such as the TP, FP, ACC, JSI and DC evaluated for all the US images. From these results, it is observed that the proposed methods obviously outperform the other existing methods. The proposed approach-1 and 2 gain approx 4.22-4.71%, 3.24-3.73%, 2.63-3.1%, 0.22-0.71% 5.13-5.62%, 5.26-5.76% and 1.7-2.2% higher TP

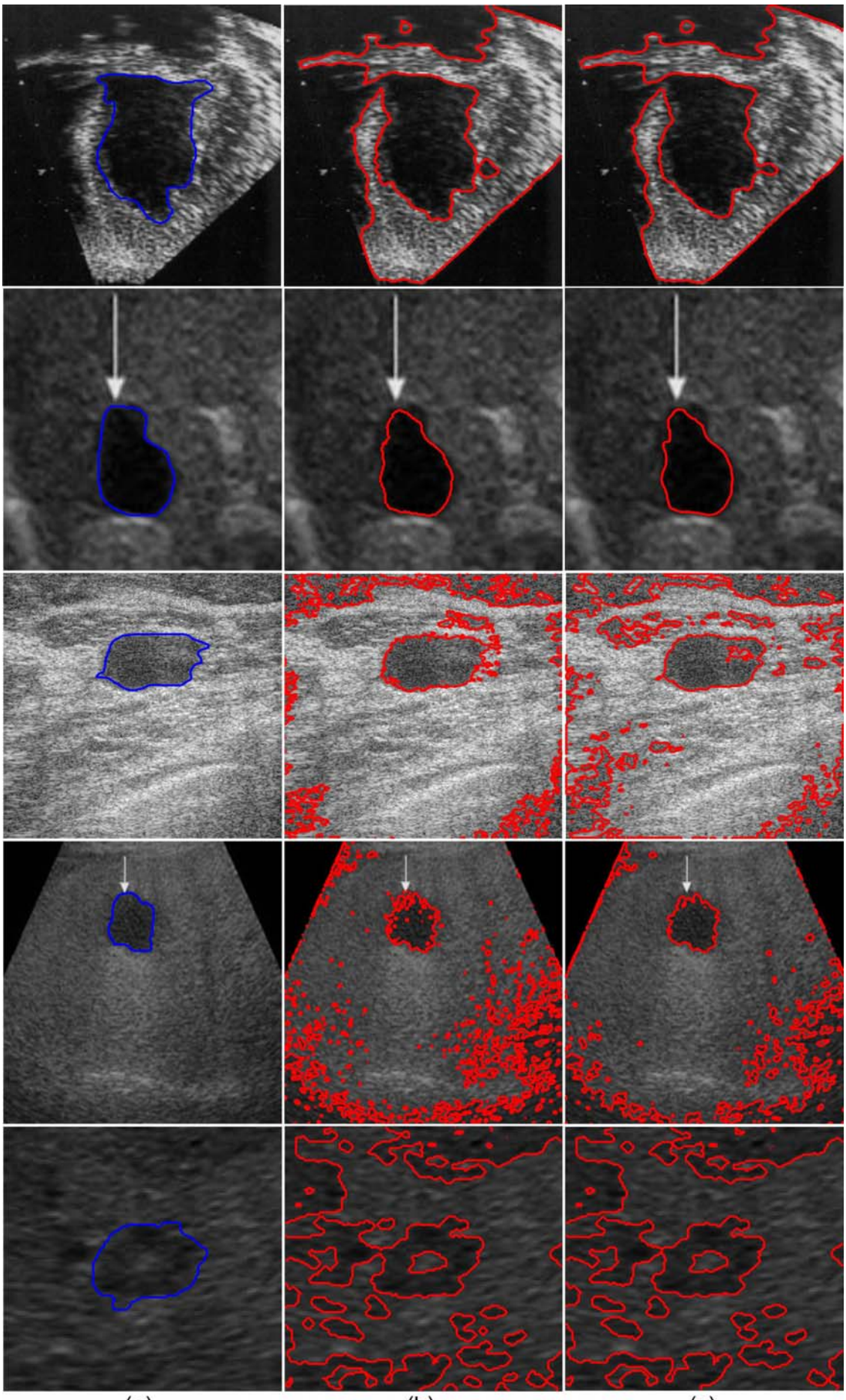

(a) (b) (c)

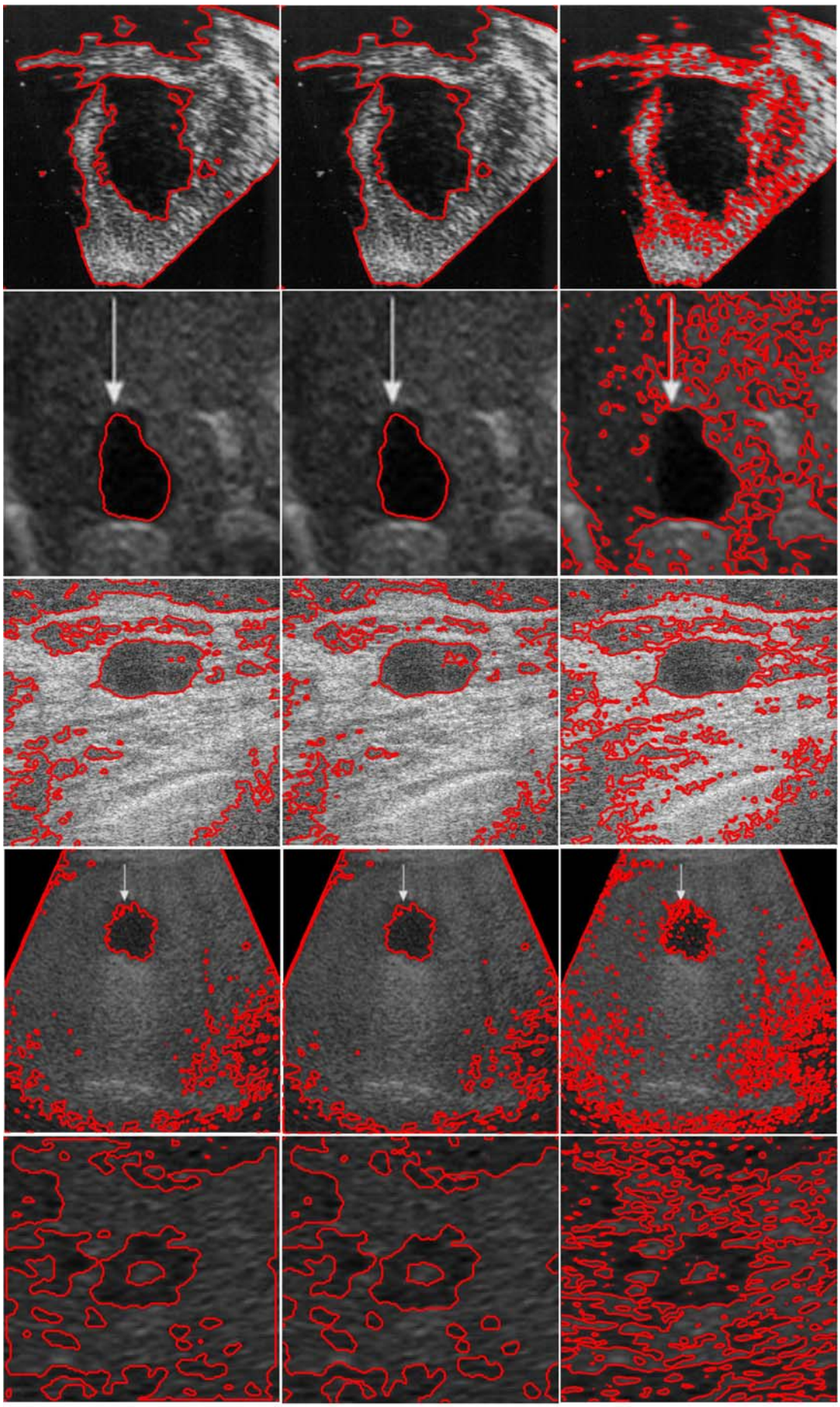

(d) (e) (f)

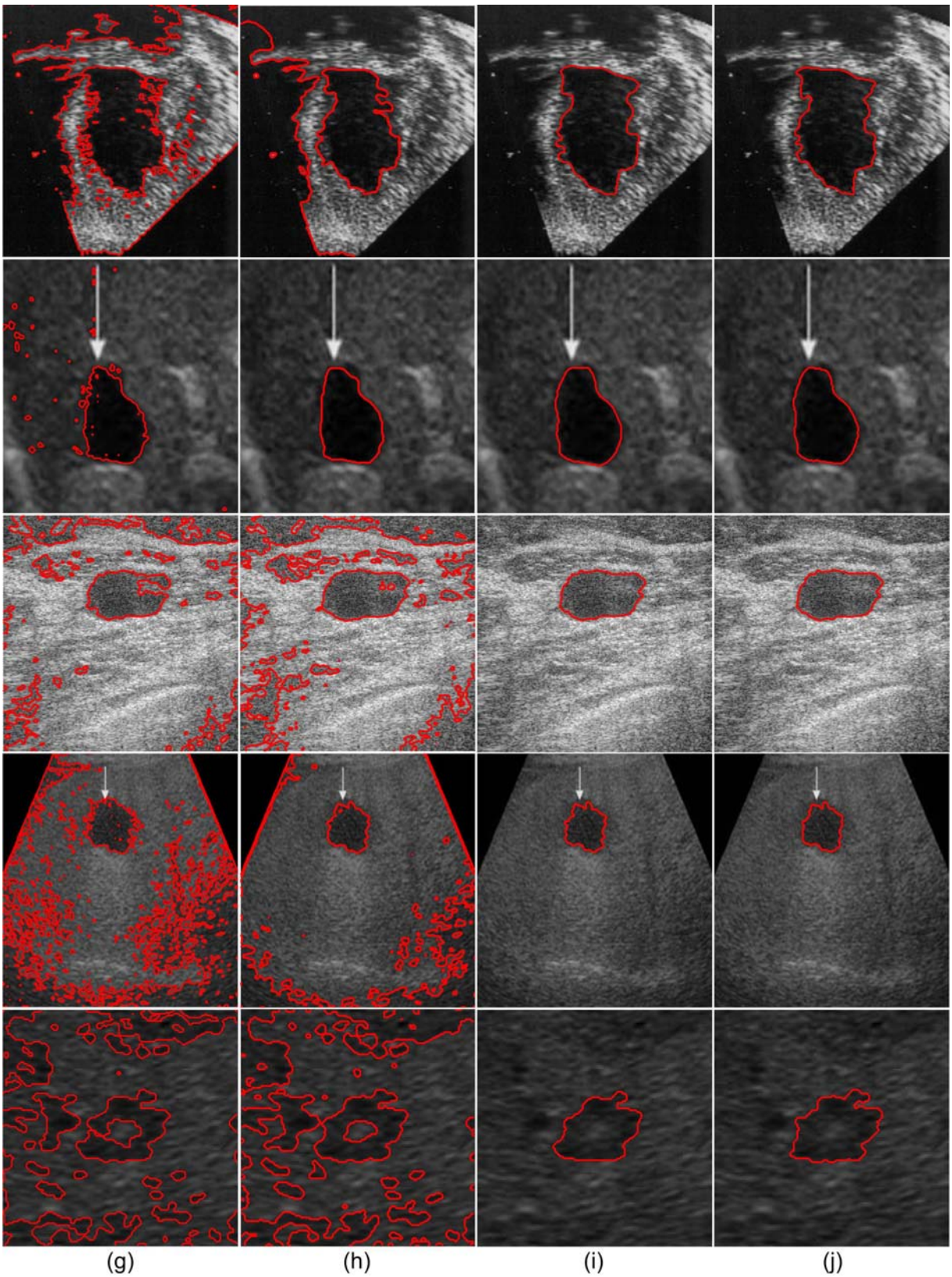

Figure 6.8 Comparative visual analysis of the segmentation results of different ultrasound images obtained by the (a) Manual (b) FCM_S1 clustering (c) FCM_S2 clustering (d) KFCM_S1 clustering (e) KFCM_S2 clustering (f) GAC method (g) ACMRSF method (h) EBACM method (i) Proposed EBACM-KFCM_S1 method (j) Proposed EBACM-KFCM_S2 method

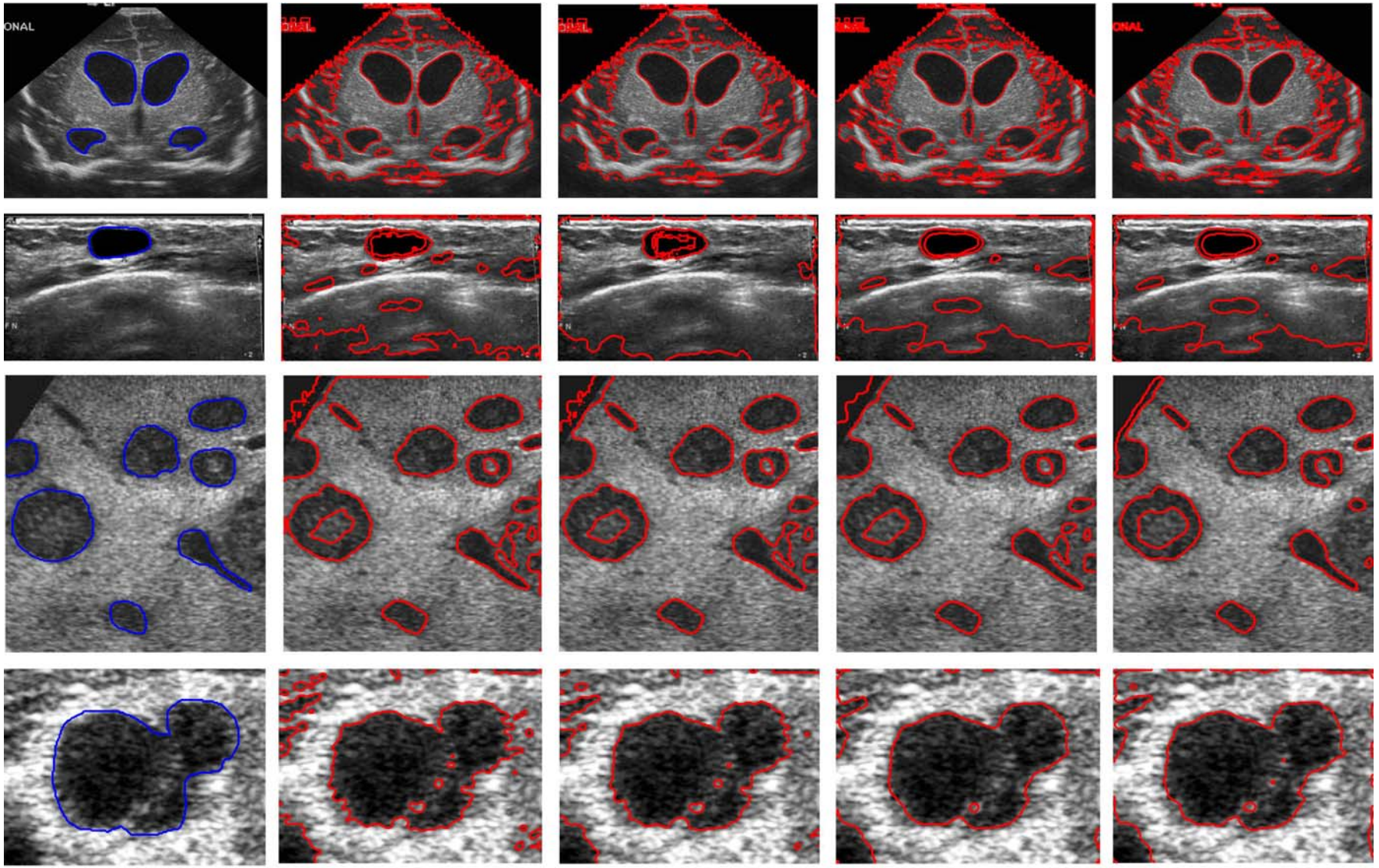

(a) (b) (c) (d) (e)

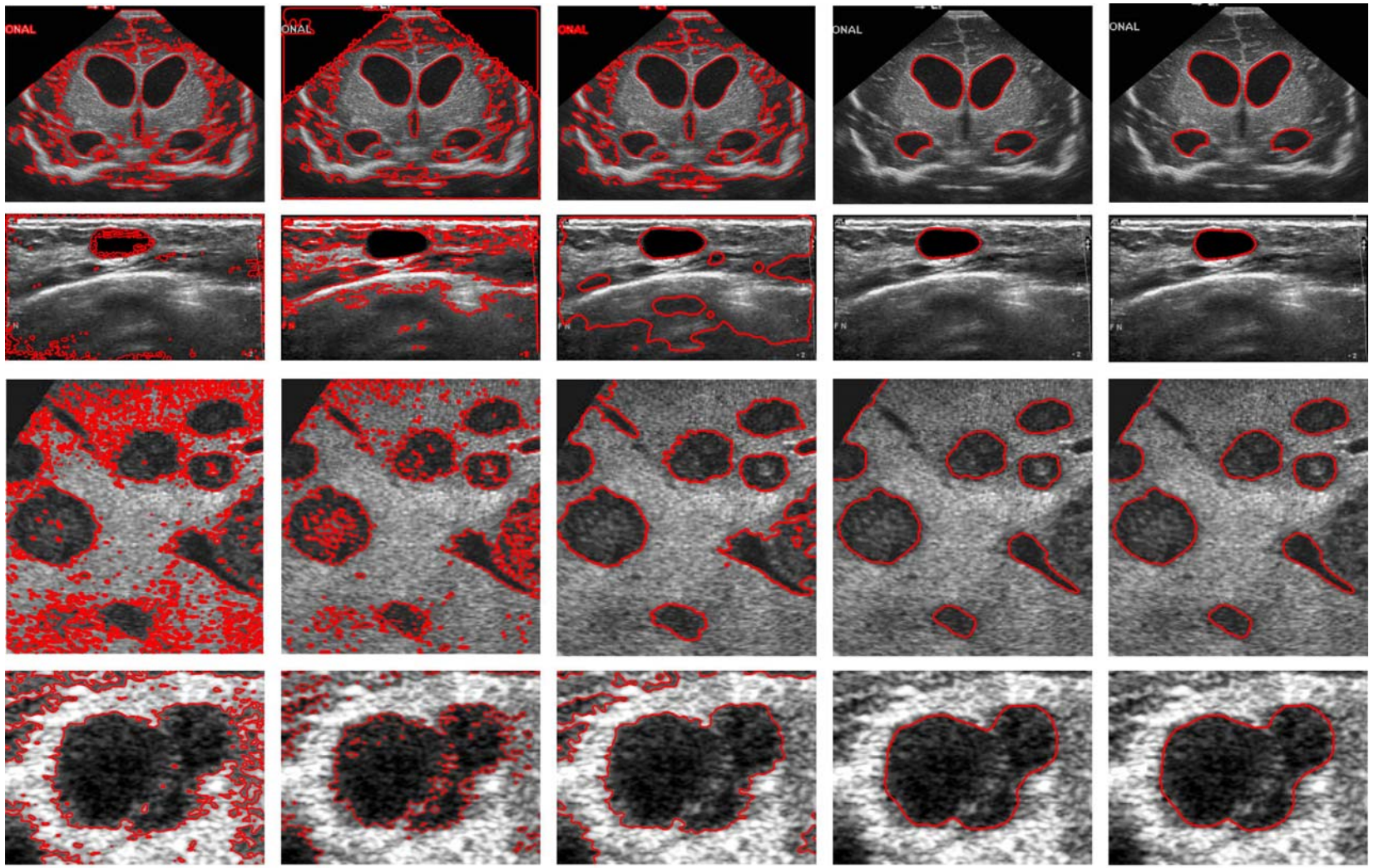

Figure 6.9 Comparative segmentation performance obtained by (a) Manual (b) FCM_S1 clustering (c) FCM_S2 clustering (d) KFCM_S1 clustering (e) KFCM_S2 clustering (f) GAC method (g) ACMRSF method (h) EBACM method (i) Proposed EBACM-KFCM_S1 method (j) Proposed EBACM-KFCM_S2 method

Table 6.3 Comparison of the averaged performance measures (TP, FP, ACC, JSI and DC) obtained by the different segmentation approaches for all the ultrasound images

Methods	TP (AVG ± STD)	FP (AVG ± STD)	ACC (AVG ± STD)	JSI (AVG ± STD)	DC (AVG ± STD)
FCM_S1	0.8905 ± 0.0360	0.1184 ± 0.0906	0.9071 ± 0.0271	0.8445 ± 0.0394	0.9126 ± 0.0239
FCM_S2	0.8989 ± 0.0384	0.1061 ± 0.0846	0.9110 ± 0.0275	0.8496 ± 0.0312	0.9155 ± 0.0248
KFCM_S1	0.9043 ± 0.0572	0.0562 ± 0.0371	0.9141 ± 0.0236	0.8577 ± 0.0364	0.9225 ± 0.0231
KFCM_S2	0.9260 ± 0.0290	0.0588 ± 0.0396	0.9236 ± 0.0180	0.8626 ± 0.0383	0.9260 ± 0.0253
GAC	0.8828 ± 0.0156	0.3164 ± 0.2476	0.8332 ± 0.0902	0.7658 ± 0.0919	0.8626 ± 0.0316
ACMRSF	0.8817 ± 0.0656	0.0963 ± 0.0533	0.8927 ± 0.0439	0.8101 ± 0.0532	0.8909 ± 0.0545
EBACM	0.9124 ± 0.0498	0.0661 ± 0.0224	0.9231 ± 0.0174	0.8581 ± 0.0377	0.9227 ± 0.0246
PA-1	0.9281 ± 0.0342	0.0361 ± 0.0226	0.9291 ± 0.0144	0.8675 ± 0.0328	0.9288 ± 0.0164
PA-2	0.9325 ± 0.0363	0.0322 ± 0.0167	0.9315 ± 0.0171	0.8763 ± 0.0335	0.9326 ± 0.0189

* PA-1: Proposed approach-1 (EBACM-KFCM_S1)
* PA-2: Proposed approach-2 (EBACM-KFCM_S2)

values than the FCM_S1, FCM_S2, KFCM_S1, KFCM_S2, GAC, ACMRSF, EBACM methods, respectively. It ensures that more overlapping area is obtained by the proposed methods compared to the others. The proposed method also exhibits an improvement in the segmentation accuracy by 1.98-2.68%, 0.59-1.9% than the FCM and KFCM clustering methods. Moreover, the accuracy of the proposed methods is increased by 11.79%, 4.34% and 0.9 -1.09% from GAC, ACMRSF and EBACM methods, respectively. The higher values of the JSI and DC obtained by the proposed methods assure more similarity between the region extracted by the computerized segmentation method and marked manually. They gain approx 2.1-3.76%, 0.56-2.16%, 13.28-14.42%, 7.08-8.17% and 1.09-2.12% higher values of the JSI and 1.45-2.3%, 0.3-1.2%, 7.67-8.23% 4.25-7.79% and 0.66-1.18% more DC values as compared to FCM_X, KFCM_X, GAC, RSF and LSE methods, respectively. Finally, the proposed methods also provide the lowest FP values that show the incorrect detection of the estimated region of interest. The averaged FP values obtained by the proposed methods are decreased by approx 69.51-72.80%, 65.97-69.65%, 35.76-42.70%, 38.60-45.23%, 88.59-89.82%, 62.51-66.56%, 45.38-51.28% from the FCM_S1, FCM_S2, KFCM_S1, KFCM_S2, GAC, ACMRSF and EBACM methods, respectively.

Furthermore, the Hausdorff distance is also evaluated for each US image segmented by all the aforementioned segmentation approaches. Table 6.4 illustrates the HD metric (average ± standard deviation) obtained by each method. The averaged HD values listed in Table 6.4 indicate the superiority of the proposed approach-1 and 2 over the other methods by achieving the lowest HD values. Moreover, the proposed EBACM-KFCM_S2 approach also outperforms the proposed approach-1. This is also illustrated by the quantitative results mentioned in both the Table 6.3 and Table 6.4. The computational time taken by all the segmentation approaches is evaluated for the US images. For such comparison, the

averaged computational time in seconds and averaged number of iterations taken by the individual segmentation methods are presented in Table 6.5. All the experiments are performed on the same machine as mentioned in previous experiment. From Table 6.5, it is concluded that the proposed methods take less number of iterations and comparatively less computation time as compared to the other methods.

Table 6.4 Hausdorff distance obtained by the various segmentation methods for all the ultrasound images

Methods	HD
FCM_S1	4.5742 ± 0.8436
FCM_S2	4.2630 ± 0.6562
KFCM_S1	3.3482 ± 1.4896
KFCM_S2	3.6338 ± 0.9897
GAC	6.9969 ± 3.0891
ACMRSF	4.8472 ± 1.4808
EBACM	3.5790 ± 1.3367
Proposed approach-1	3.0125 ± 0.7155
Proposed approach-2	2.9615 ± 0.7653

Table 6.5 Comparative performance of the segmentation approaches with the averaged number of iterations and computational time for all the ultrasound images

Methods	Averaged resolution	Averaged computational time, s	Averaged iterations
FCM_S1	294 × 310	0.5265	35
FCM_S2	294 × 310	0.4916	38
KFCM_S1	294 × 310	1.3451	39
KFCM_S2	294 × 310	2.2393	48
GAC	294 × 310	141.26	1250
ACMRSF	294 × 310	15.448	242
EBACM	294 × 310	13.378	100
Proposed approach-1	294 × 310	4.3159	24
Proposed approach-2	294 × 310	5.4439	20

6.9 Summary

The US image segmentation is a very difficult task because of its poor quality of images. Several algorithms have been presented in literature, but most of the methods require a manual intervention to initialize the curve and to set the different parameters used in these methods. Manual tracing is a time consuming process and does not provide the accurate results. Therefore, in this chapter, two hybrid approaches using edge-based active contour model initialized by the KFCM_S1 and KFCM_S2 clustering, individually, are presented for the segmentation of US medical images. These proposed approaches initiate with the result of KFCM_X clustering, which is responsible for successfully extracting the

estimated object boundaries by initializing the curve during the DRLSE process and evaluating the several controlling parameters. The DRLSE approach also helps to eliminate the re-initialization of the level set function in the EBACM approach. In addition to this, it eliminates the manual requirement and decreases the processing time. Experiments were carried out on both the several synthetic images and ultrasound images to make the subjective evaluation. From both the objective and subjective evaluation, it is concluded that the proposed methods are more robust and accurate to segment the required region of interest in the US images by ensuring an improvement in the segmentation accuracy.

CHAPTER 7: HYBRID REGION-BASED ACTIVE CONTOUR METHOD WITH GAUSSIAN KERNEL FUZZY CLUSTERING

This chapter presents another hybrid segmentation approach for the ultrasound medical images by utilizing the features of the Gaussian kernel fuzzy c-means clustering and region-based active contour model driven by region scalable fitting energy function. This chapter starts with a brief idea of the region-based active contour models and Gaussian kernel fuzzy clustering method. In the proposed approach, the results of the Gaussian kernel fuzzy clustering is utilized to initialize the curve and to estimate the several controlling parameters used in the region-based active contour model. The segmentation performance obtained by the proposed approach are discussed qualitatively and quantitatively. A comparative analysis is also presented to investigate the segmentation performance of the proposed and other approaches.

7.1 Introduction

In the previous chapter, it has been mentioned that the existing active contour models can be classified into two major classes: edge-based models and region-based models. The EBACM rely on the edge detector function that depends on the image gradient to stop the contour evolution on the desired object's boundaries [291]. These models can detect objects only with edges defined by the gradient. In practice, the discrete gradients are bounded and thus the stopping function will hardly approach to zero at the edges. Therefore, the evolving contour may pass through the boundary of the desired object, especially in noisy images or when the boundary of the object is too weak [44, 161]. On the other hand, region-based models aim to identify each region of interest by using some region descriptors, e.g., intensity, color, and texture, to guide the motion of active contour. The RBACM approach has shown some attractive characteristics such as the unrestricted position of the initial contour, the automatic detection of interior boundaries, and reasonable segmentation due to global energy minimization. Region-based active contours evolve deformable shapes based on two factors: energy minimization based on statistical properties that pursue the uniformity within each region and curvature motion motivated by the LSF that also keeps the regularity of the active contours.

In this chapter, a hybrid segmentation approach for US medical images is proposed that utilizes the features of RBACM approach and Gaussian kernel fuzzy c-means (GKFCM) clustering. In this segmentation approach, the intensity information in the local regions (as against the global regions in conventional RBACM approach) is used to guide the motion of contour toward the desired object. The proposed segmentation approach presents two different fitting functions that locally approximate the average image intensities on the two sides of contour. In this method, the fuzzy membership function is also incorporated into the data fitting functions to accurately segment the region of interest with higher accuracy. Furthermore, the fuzzy membership function from the GKFCM is utilized not only to initialize

the contour, but also to estimate the contour propagation controlling parameters. The RSF formulation that is responsible for attracting the contour toward the object boundaries, overcomes the requirement of the re-initialization process. In this way, it enhances the convergence speed of the contour propagation. The GKFCM clustering is also able to provide better results by adding a new term (η_j) used to control the effect of neighboring term for each cluster.

The remaining part of this chapter is structured as follows. The next two sections describe a brief idea of the RBACM and GKFCM approaches that are utilized to present a proposed hybrid segmentation approach and named as the RBACM-GKFCM. After that, the proposed segmentation approach is discussed and its implementation steps are also given in this section. This is further followed by the different experiments performed to evaluate the segmentation performance of the proposed method. A comparative analysis of the results obtained by the different segmentation methods represented in terms of objective and subjective manner is also discussed in the results and discussion section.

7.2 Gaussian Kernel Fuzzy Clustering

Fuzzy clustering is used to arrange a similar data points into a same cluster, iteratively by optimizing its cost function, which is based on the Euclidean distance of the pixels from the centroids of the different cluster. As mentioned in the previous chapter, the FCM is used to provide good results for medical image segmentation. However, it is very sensitive to noise that also affects the segmentation accuracy. Therefore, the different variants of the FCM such as the FCM_S1, FCM_S2, KFCM_S, KFCM_S1 and KFCM_S2 clustering methods have been introduced by the researchers [9, 222]. The main limitation of the FCM and KFCM based clustering is that the parameters of these methods heavily affect the final clustering results. In order to overcome the limitations of these methods, clustering method is concentrated on the Gaussian kernel fuzzy c-means clustering (GKFCM) that is modified by Yang and Tsai [260]. Several quantitative evaluations have been performed and shown that the two different variants of the GKFCM with spatial constraints known as the GKFCM_X = GKFCM_S1 and GKFCM_S2 perform better than others. Similar to the KFCM clustering, the Euclidean distance $\|s_i - v_j\|^2$ is replaced by the kernel induced distance function $\|\Psi(\mathrm{s_i}) - \Psi(\mathrm{v_j})\|^2$, where Ψ is a nonlinear map from the data space into the feature space with the corresponding kernel. The objective function of the GKFCM is a special case of the KFCM of the parameter of $\alpha = \eta_j$. In the present work, the GKFCM_X clustering approach is utilized as the initial stage in the implementation of the proposed approach. The objective function of the GKFCM_X is given below:

$$J_p^{GKFCM\_X}(\mu, v) = \sum_{i=1}^{L}\sum_{j=1}^{\mathrm{C}} \mu_{j,i}^{p}\left(1 - K\left(s_i, v_j\right)\right) + \sum_{i=1}^{L}\sum_{j=1}^{\mathrm{C}} \eta_j \mu_{j,i}^{p}\left(1 - K\left(X, v_j\right)\right) \qquad (7.1)$$

The fuzzy membership functions are subject to the following constraints

$$\sum_{j=1}^{C} \mu_{j,i} = 1\,,\ \mu_{j,i} \in [0,1],\ \sum_{i=1}^{L} \mu_{j,i} > 0 \tag{7.2}$$

where $K(s_i, v_j) = \exp\left(-\frac{\|s_i - v_j\|}{\sigma^2}\right)$, $\sigma^2 = \frac{1}{L}\sum_{i=1}^{L} \left\|(s_i) - \left(\frac{1}{L}\sum_{i=1}^{L} s_i\right)\right\|^2$, $S = (s_1, s_2, s_3, \dots, s_L)$, $\mu_{j,i}$ is the membership of the pixel s_i in the j^{th} cluster and v_j is the centroid of the j^{th} cluster. $\|(\cdot)\|$ is the norm of a matrix and p is a weighted exponent on each fuzzy membership that controls the amount of fuzziness of the final segmentation. The term η_j is used to control the effect of the neighboring term for each cluster and is evaluated as given below:

$$\eta_j = \frac{\min_{j' \neq j}\left(1 - K(v_{j'}, v_j)\right)}{\max_k\left(1 - K(v_k, s^{Mean})\right)} \tag{7.3}$$

Thus, by minimizing the cost function $J_p^{GKFCM\_X}(\mu, v)$ of the GKFCM_X, the membership function and centroid are updated iteratively using the following equations.

$$\mu_{j,i} = \frac{1}{\sum_{k=1}^{C}\left(\frac{[1 - K(s_i, v_j)] + \eta_j[1 - K(X, v_j)]}{[1 - K(s_i, v_k)] + \eta_j[1 - K(X, v_k)]}\right)^{1/p-1}} \tag{7.4}$$

$$v_j = \frac{\sum_{i=1}^{L} \mu_{ji}^{p}\left(K(s_i, v_j)s_i + \eta_j K(X, v_j)X\right)}{\sum_{i=1}^{L} \mu_{ji}^{p}\left(K(s_i, v_j) + \eta_j K(X, v_j)\right)} \tag{7.5}$$

where X represents the s_i^{Mean} and s_i^{Median} for implementing GKFCM_S1 and GKFCM_S2, respectively. The s_i^{Mean} and s_i^{Median} are the average and median values of the neighboring pixels within a window around s_i, respectively. Thus, in the present work, both the GKFCM_S1 and GKFCM_S2 clustering methods are used to initialize the LSF used for curve evolution in the RBACM-RSF approach, individually.

7.3 Region-Based Active Contour Models

Mumford and Shah [169] addressed the image segmentation problem as a variational problem to find an optimal piecewise-smooth approximation $F(x, y)$ of a given image $I(x, y)$ and a set of boundaries C, such that the approximation $F(x, y)$ varies smoothly within the connected components of the subsets excluding the boundaries. They proposed the solution of the variational segmentation problem by minimizing the global energy function as given below:

$$E_{MS}(F, C) = \int_{\Omega} |I(x, y) - F(x, y)|^2 dxdy + \int_{\Omega/C} |\nabla F(x, y)|^2 \, dxdy + \upsilon|C| \tag{7.6}$$

where $|C|$ is the length of the contour. In practice, it is difficult to minimize the Eqn. (7.6) due to unknown contour C of lower dimension. This type of region-based segmentation method relies on the homogeneity of the object to be segmented. This assumption is often violated in medical images due to the motion of organs, presence of noise or acquisition artifacts. Based on the Mumford and Shah segmentation model, Chan and Vese (CV) [48, 49, 242] introduced an active contour approach naming it as the CV model, where the function $F(x, y)$

mentioned in Eqn. (7.6) is a piecewise constant function. They successfully solved the minimization problem by using the LSF that utilizes the global image statistic inside and outside the evolving curve rather than the gradients on the boundaries. They proposed the following energy function as given below:

$$E_{CV} = \lambda_1 \int_{outside(C)} |I(x,y) - C_1|^2 dxdy + \lambda_2 \int_{inside(C)} |I(x,y) - C_2|^2 dxdy + \upsilon \cdot \text{Area}\big(\text{inside}(C)\big) + \mu \cdot \text{Length}(C) \quad (7.7)$$

where $\mu \geq 0,\ \upsilon \geq 0,\ \lambda_1, \lambda_2 > 0$ are the fixed parameters.

The first two terms in above Eqn. (7.7) are called the global fitting energy terms.

$$F_1(\text{C}) + F_2(\text{C}) = \int_{outside(C)} |I(x,y) - C_1|^2 dxdy + \int_{inside(C)} |I(x,y) - C_2|^2 dxdy \quad (7.8)$$

where the terms outside(C) and inside(C) represent the regions outside and inside the variable contour C, respectively. The optimal constants C_1 and C_2 that minimize the above global fitting energy are the averages of intensities in the entire regions outside(C) and inside(C), respectively. From Figure 7.1, it can be easily seen that if contour C is outside the object then $F_1(C) > 0$ and $F_2(C) \approx 0$. If contour C is inside the object then $F_1(C) \approx 0$ and $F_2(C) > 0$. If the contour C is inside and outside the object, then $F_1(C) > 0$ and $F_2(C) > 0$. Finally, the fitting energy term is minimized if $C = C_0$, i.e. if the contour C is on the boundary of the object.

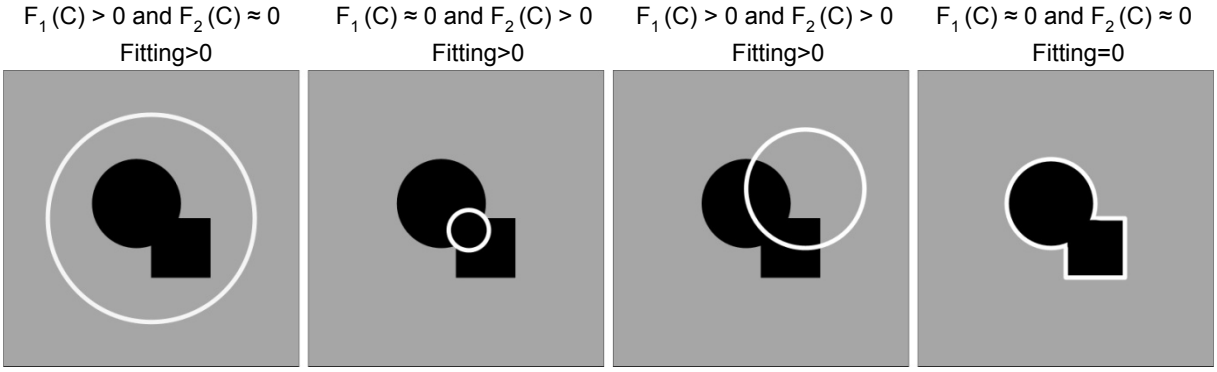

Figure 7.1 All possible cases in the position of contour [48]

The energy function in Eqn. (7.7) can be represented by a level set formulation and then the energy minimization problem can be converted to solve a level set evolution equation as

$$\frac{\partial \emptyset}{\partial t} = \delta_\varepsilon(\emptyset)\left[\mu div\left(\frac{\nabla \emptyset}{|\nabla \emptyset|}\right) - \nu - \lambda_1 (I(x,y) - C_1)^2 - \lambda_2 (I(x,y) - C_2)^2\right] \quad (7.9)$$

where constants C_1 and C_2 are the averages of the intensities in the entire regions outside(C) and inside(C), respectively and are represented as a function of $\emptyset$.

$$C_1(\emptyset) = \frac{\int_\Omega I(x,y) H\big(\emptyset(x,y)\big) dxdy}{\int_\Omega H\big(\emptyset(x,y)\big) dxdy} \quad (7.10)$$

$$C_2(\emptyset) = \frac{\int_\Omega I(x,y)\left(1-H(\emptyset(x,y))\right)dxdy}{\int_\Omega \left(1-H(\emptyset(x,y))\right)dxdy} \quad (7.11)$$

The CV model mostly works better for those images where the intensities in each region either inside(C) or outside(C) are always constant. However, it leads to poor segmentation for image with intensity inhomogeneity. The segmentation performance of the CV model is affected by the placement of initial contour. Different results may be obtained on the same image by selecting different initial contour. Thus, the proper initialization of a contour in the CV model is still a challenging problem to provide accurate segmentation results.

A simultaneous and parallel effort to the work of Chan-Vese, Tsai et al. [238] proposed a reformulation of the Mumford Shah model from a curve evolution perspective, using a gradient flow formulation and a level set framework implementation. In order to overcome the limitations of the CV model, Li et al. [66] proposed a RBACM model using the new variational LSF, which works on the RSF energy and level set regularization term. The RSF energy function is defined in terms of the two fitting functions that are shown to be the averages of local image intensities on the two sides of the contour. In the resulting curve evolution that minimizes the associated energy function, intensity information in local regions at a certain scale is used to compute the two fitting functions and thus guide the motion of contour toward the estimated object boundaries. Because of the presence of level set regularization term in this formulation, the regularity of the LSF is preserved to ensure accurate curve evolution and it also avoids re-initialization procedure [66]. The overall energy function can be written as

$$E_{Total}(\emptyset) = E_{RSF}(\emptyset) + E_R(\emptyset) \quad (7.12)$$

where E_{Total} is the overall energy, E_{RSF} refers to the RSF energy which is defined as

$$E_{RSF}(C, F_1, F_2) = \sum_{i=1}^{2} \lambda_i \int_{\Omega_i} K(x-y)|I(y) - F_i(x)|^2 \, dy \quad (7.13)$$

where λ_1 and λ_2 are two positive constants, $F_1(x)$ and $F_2(x)$ are two different fitting functions that approximate the average image intensities in $x \in \Omega$ and $K(a) = \left(1/\sqrt{2\pi}\sigma\right).exp\left(-\frac{|a|^2}{2\sigma^2}\right)$ is defined as a Gaussian kernel function with its standard deviation σ. Another term present in Eqn. (7.12), $E_R(\emptyset)$ is a combination of level set regularization term $P(\emptyset)$ and contour length term $L(\emptyset)$. The formulation of the term $E_R(\emptyset)$ can be written as

$$E_R(\emptyset) = \mu P(\emptyset) + \nu L(\emptyset) \quad (7.14)$$

where $P(\emptyset) = \frac{1}{2}\int(|\nabla\emptyset| - 1)^2 dx$ and $L(\emptyset) = \int \delta_\varepsilon(\emptyset)|\nabla\emptyset| \, dx$, where δ_ε denotes to Dirac delta function with a constant parameter ε which is responsible to regularize the Dirac delta function. It is estimated as

$$\delta_\varepsilon(\phi) = \frac{1}{\pi}\left(\frac{\varepsilon}{\varepsilon^2+\phi^2}\right) \quad (7.15)$$

Now, the Eqn. (7.12) can be written as

$$E_{Total}(\emptyset, F_1, F_2) = \int_{\Omega} E_{RSF}(\emptyset, F_1 F_2) + \mu \frac{1}{2} \int_{\Omega} (|\nabla \emptyset| - 1)^2 dx + \nu \int_{\Omega} \delta_{\varepsilon}(\emptyset) |\nabla \emptyset| \, dx \quad (7.16)$$

The Eqn. (7.16) minimized by solving the gradient flow is given as [66]

$$\frac{\partial \emptyset}{\partial t} = -\delta_{\varepsilon}(\emptyset)(\lambda_1 e_1 - \lambda_2 e_2) + \mu \left[\nabla^2 \emptyset - div\left(\frac{\nabla \emptyset}{|\nabla \emptyset|}\right)\right] + \nu \delta_{\varepsilon}(\emptyset) div\left[\frac{\nabla \emptyset}{|\nabla \emptyset|}\right] \quad (7.17)$$

where

$$\begin{cases} e_1(x) = \int_{\Omega_1} K(x-y) \, |I(y) - F_1(x)|^2 dy \\ e_2(x) = \int_{\Omega_2} K(x-y) \, |I(y) - F_2(x)|^2 dy \end{cases} \quad (7.18)$$

In the above formulation mentioned in Eqn. (7.17) consists three different terms. The first term $-\delta_{\varepsilon}(\emptyset)(\lambda_1 e_1 - \lambda_2 e_2)$ denotes the data fitting term that is utilized to propagate the contour toward the estimated object boundaries. The second term $\mu \left[\nabla^2 \emptyset - div\left(\frac{\nabla \emptyset}{|\nabla \emptyset|}\right)\right]$ is the contour regularity term that is responsible to maintain the regularity of the LSF with its weighting coefficient (μ) named as regularization coefficient. Lastly, the third term $\nu \delta_{\varepsilon}(\emptyset) div\left[\frac{\nabla \emptyset}{|\nabla \emptyset|}\right]$ named as the contour length term is able to provide the smoothness on the zero LSF controlled by its controlling parameter (ν). In Eqn. (7.18), F_1 and F_2 refer to the weighted averages of the intensities within a neighboring region of x, whose size is proportional to the scale parameter (σ) and are given as

$$F_1 = \frac{K_{\sigma}(x) * \left[M_1^{\varepsilon}(\emptyset(x)) I(x)\right]}{K_{\sigma}(x) * M_1^{\varepsilon}(\emptyset(x))} \quad (7.19)$$

$$F_2 = \frac{K_{\sigma}(x) * \left[\left(M_2^{\varepsilon}(\emptyset(x))\right) I(x)\right]}{K_{\sigma}(x) * \left(M_2^{\varepsilon}(\emptyset(x))\right)} \quad (7.20)$$

where K_{σ} refer to the Gaussian kernel function and is defined similarly as used in Eqn. (7.13). The Heaviside function H in the above formulation is approximated by the smooth function H_{ε} is given by

$$H_{\varepsilon}(x) = \frac{1}{2}\left[1 + \frac{2}{\pi} arctan\left(\frac{x}{\varepsilon}\right)\right] \quad (7.21)$$

and $M_1^{\varepsilon}(\emptyset) = H_{\varepsilon}(\emptyset)$, $M_2^{\varepsilon}(\emptyset) = 1 - H_{\varepsilon}(\emptyset)$. In this formulation, the level set function $\emptyset_0(x, y)$ is initialized as given below:

$$\emptyset_0(x, y) = \begin{cases} -c_0, & (x, y) \in \Omega_0 - \partial\Omega_0 \\ 0, & (x, y) \in \partial\Omega_0 \\ c_0, & (x, y) \in \Omega - \Omega_0 \end{cases} \quad (7.22)$$

where $c_0 > 2\varepsilon$ is a constant, Ω_0 is a region of interest in the given image domain Ω and $\partial\Omega_0$ is the boundary of the Ω_0. The discretization of Eqn. (7.17) can be given as

$$\emptyset_{t+1}(x, y) = \emptyset_t(x, y) + \tau \frac{\partial \emptyset_t(x,y)}{\partial t} \quad (7.23)$$

where τ is the time step of level set evolution.

7.4 Proposed Hybrid Region-Based Active Contour Method with GKFCM Clustering

The segmentation performance of the active contour based models are subjected to appropriate contour initialization and optimal configuration of the contour propagation controlling parameters that also require extensive manual intervention. In the proposed approach, the GKFCM_X clustering and the RBACM model driven by the RSF energy are utilized to formulate two hybrid approaches for segmenting the US images. The proposed approaches start with the GKFCM_S1 and GKFCM_S2 clustering methods, individually. The results of the GKFCM_S1 and GKFCM_S2 are then individually employed to initialize the LSF that moves toward the object's boundaries. The results of the GKFCM_X also help to evaluate the several controlling parameters that control the accurate curve evolution. Let, the region of interest in the result of fuzzy clustering be expressed as I_R and $\mu_m^{GKFCM\_X}$ as the membership function for the GKFCM_X method. Now, the initializing function of the level set model can be given as

$$\emptyset_0(x,y) = (4I_R - 2)\varepsilon \tag{7.24}$$

where ε is a constant parameter which regularizes the Dirac delta function [66, 179] and I_R refers to an image obtained using the following equation as given below:

$$I_R = \begin{cases} 0, & \mu_m^{GKFCM\_X} < T \\ 1, & \mu_m^{GKFCM\_X} \geq T \end{cases} \tag{7.25}$$

where $T \in [0,1]$ refers to the adjustable threshold value that is used to control the size of the contour and $\mu_m^{GKFCM\_X}$ is the membership function for the GKFCM_X method.

The proposed hybrid segmentation approach has a property of autoinitialization of the LSF and autoconfiguration of the different contour propagation controlling parameters using the GKFCM_S1 and GKFCM_S2 clustering methods, individually. This also helps to control the parameter values used in the level set evolution that are provided manually and changing for every image data. In the RBACM approach driven by the RSF energy function mentioned in Eqns (7.17) and (7.23), it is a prime requirement to compute all four different parameters such as regularization term coefficient (μ), time step parameter (τ), coefficient of the contour length (v) and other two parameters λ_1 and λ_2. All these parameters are estimated using the results of the GKFCM_X clustering method. Firstly, the time step parameter (τ) is estimated by estimating the area and the length of the initial LSF and is given as

$$\tau = \frac{Area}{Length} = \frac{\int_\Omega H(\emptyset_0)dxdy}{\int_\Omega \delta(\emptyset_0)dxdy} \tag{7.26}$$

where $H(\emptyset_0) = \begin{cases} 0, & \emptyset_0 < 0 \\ 1, & \emptyset_0 \geq 1 \end{cases}$ and now, the coefficient of the regularization term is evaluated as 0.2 times of the inverse of time step parameter based on successive experiments with the different values [65, 66, 147, 275]. This is because of the requirement of product of the time step parameter and weighting coefficient of the regularization term to be less than 1/4 for the

stable and accurate curve evolution. The coefficient of regularizing term is evaluated as

$$\mu = 0.2/\tau \tag{7.27}$$

In the proposed approach, for achieving the smooth contour, the value of weighting coefficient of the contour length (v) is estimated by

$$v = 0.1\tau \tag{7.28}$$

The other two parameters λ_1 and λ_2 refer to the weights of two integral expressed in Eqn (7.17) that are used to force the contour toward object boundaries either inside or outside the contour. Thus, the values of the coefficients λ_1 and λ_2 is estimated as follows:

$$\lambda_1 = \lambda_2 = \frac{1}{2}\left(1 - 2\mu^{\text{GKFCM\_X}}\right) \tag{7.29}$$

Therefore, the mathematical formulation of the RBACM approach using the RSF energy can be given as below

$$\frac{\partial \emptyset}{\partial t} = \left(-\frac{1}{2}\delta_\varepsilon(\emptyset)\left(1 - 2\mu^{\text{GKFCM\_X}}\right)(e_1 - e_2)\right) + \mu\left(\nabla^2\emptyset - div\left(\frac{\nabla\emptyset}{|\nabla\emptyset|}\right)\right) + \frac{0.02}{\mu}\left(\delta_\varepsilon(\emptyset)div\left(\frac{\nabla\emptyset}{|\nabla\emptyset|}\right)\right) \tag{7.30}$$

Now, the Eqns. (7.30) and (7.23) refer to a formulation of the RBACM using RSF energy approach.

Implementation Steps

For a proposed hybrid segmentation approach and implementing the above aspects, the algorithm is formulated by the following implementation steps.

Step 1: Start with the given ultrasound image (I).

Step 2: Perform the GKFCM_X clustering algorithm on the given input image.

a) Set the number of the cluster (C), p and the termination criterion > 0. In the present study, the parameters such as $p = 2$ and termination criterion $=$ 0.001 are taken based on the experimental results. The parameter (C) is considered according to the images and their region of interest.

b) Compute the average and median values of the neighboring pixel for GKFCM_X (GKFCM_S1 and (GKFCM_S2), respectively.

c) Compute the value of the η_j using Eqn. (7.3).

d) Initialize the value of a fuzzy clustering matrix and set the loop counter $l_c = 0$.

e) Compute the cluster centroids using Eqn. (7.5) and evaluate the corresponding cost function of GKFCM_S1 and GKFCM_S2, respectively.

f) Now, evaluate the membership values in the matrix using Eqn. (7.4) for each pixel and each cluster.

g) If the value of the cost function between successive iteration < termination criterion, then STOP. Otherwise, set l_c=l_c+1 and go to step e.

Step 3: Set the region of interest in the results of the GKFCM_X obtained from the step 2 and initialize the LSF using Eqn. (7.24).

Step 4: Now, we evaluate the controlling parameters that are provided manually and changed for every image data in the conventional ACM model. The time step parameter (τ) and weighting coefficient of the regularization term (μ) are estimated using Eqns. (7.26) and (7.27), respectively.

Step 5: Compute the weighting coefficient of the contour length v using Eqn. (7.28).

Step 6: Evaluate the values of the coefficients λ_1 and λ_2 using Eqn. (7.29).

Step 7: Finally, apply the RBACM driven by RSF energy using the Eqns. (7.30) and (7.23).

7.5 Experimentation

In order to evaluate the segmentation performance obtained by the proposed approaches and other methods, different experiments are performed. To perform such experiments, same data sets as used in the previous chapter are considered. The performance of the proposed methods are investigated on both the test images synthesized using MATLAB and real US images. Here, the segmentation results are obtained by the two different proposed approaches-1 and 2 named as RBACM-GKFCM_S1 and RBACM-GKFCM_S2, respectively. The proposed approach-1 and 2 signify that the results of the GKFCM_S1 and GKFCM_S2 clustering methods are employed, individually, to initialize the LSF. To assess the segmentation results provided by the proposed and other existing methods, two different experiments are conducted as given below:

Experiment 1: Analysis and evaluation of the segmentation results obtained by the proposed RBACM-GKFCM_S1 and RBACM-GKFCM_S2 methods applied to the synthetic test images and demonstration of a comparison between the segmentation results provided by the proposed and other approaches.

Experiment 2: Analysis and evaluation of the segmentation results on the real US images processed by both the proposed approaches and presentation of comparative analysis of the proposed and other existing methods in term of both the subjective and objective manner.

Moreover, the results obtained by the proposed methods are also compared with some related segmentation approaches such as the FCM_S1 [222], FCM_S2 [222], GKFCM_S1 [260], GKFCM_S2 [260], GAC model [45, 182], ACMRSF approach [48, 66], RBACM-SFCM approach [26] and EBACM approach [64, 65]. For the comparative analysis, same performance measures discussed in chapter 5 are utilized. The detailed discussion of all the segmentation results obtained by all these methods is presented in the next section.

7.6 Results and Discussions

Experiment 1: *Analysis and evaluation for the segmentation results of synthetic test images* - In order to investigate the performance of the proposed approach-1 and 2, three different test images including the noisy image are considered. The segmentation results of all the three different test images provided by the proposed RBACM-GKFCM_S1 and

RBACM-GKFCM_S2 approaches are shown in Figure 7.2 (a) and (c), respectively. For first two synthetic images of size 77 × 59 pixels, and 84 × 84 pixels, Figure 7.2 (a) and (c) show the segmentation results marked with red contour on the estimated boundaries of objects that are extracted by the proposed approach-1 and 2, respectively. From Figure 7.2 (a) and (c), it can be observed that the proposed approaches are able to provide accurate results by extracting the object boundaries. Moreover, it is clearly demonstrated by the plot of the final LSF shown in Figure 7.2 (b) and (d) correspond to Figure 7.2 (a) and (c), respectively. These results also show that the proposed methods are able to accurately segment the object boundaries. Furthermore, another noisy image of size 101 × 99 pixels is taken to investigate the effectiveness of the proposed methods against the noise. The third row of the Figure 7.2 (a) and (c) present their segmented results obtained by the proposed approach-1 and 2, respectively, for the noisy synthetic image. Their final LSF is also shown in the Figure 7.2 (b) and (d). From these segmentation results, it is observed that the proposed approaches are still able to accurately extract the estimated object's boundaries.

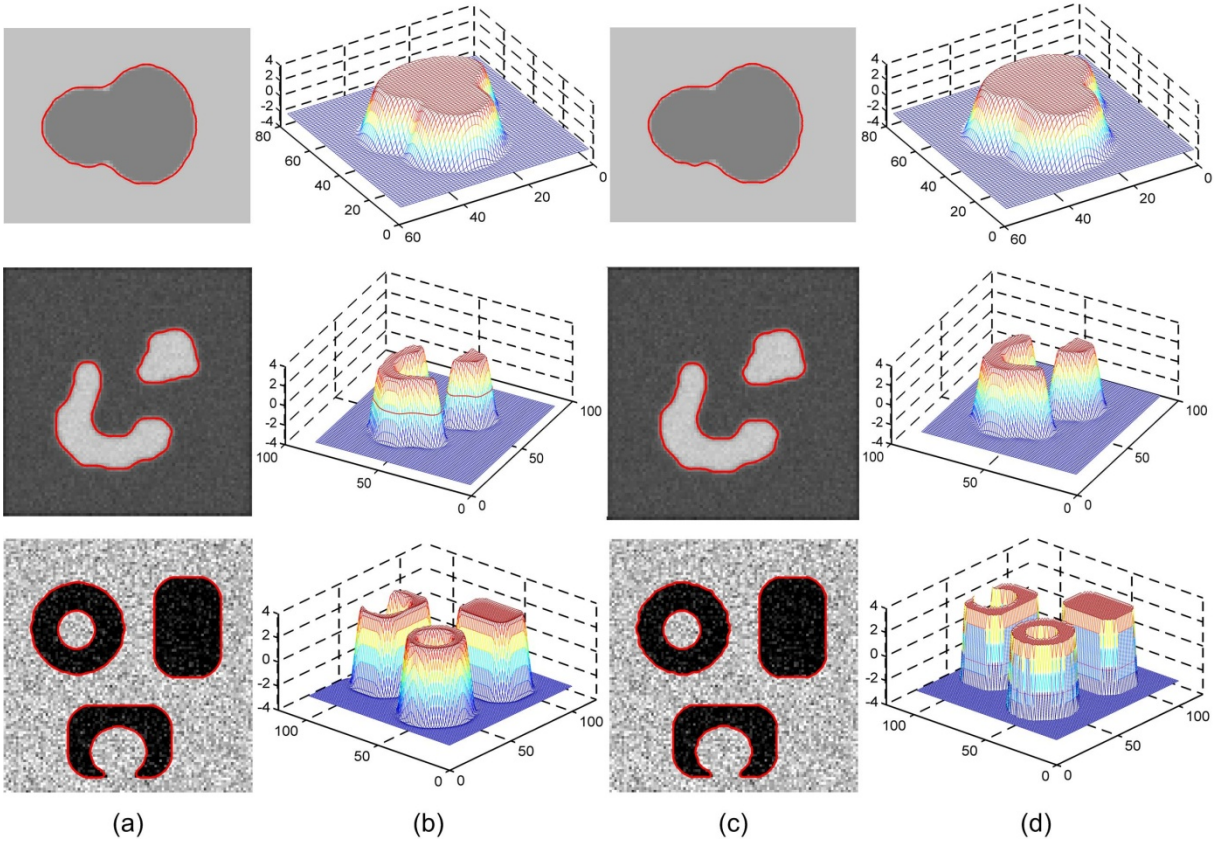

Figure 7.2 Segmentation results of the synthetic test images produced by (a) Proposed RBACM-GKFCM_S1 approach (c) Proposed RBACM-GKFCM_S2 approach. (b) and (d) represent three dimensional display of the final LSF of a and c, respectively

Moreover, the segmentation results obtained by the proposed methods are compared with aforementioned methods. For such comparative analysis, two different synthetic images out of several test images are taken as shown in Figure 7.3 (a) and Figure 7.4 (a). Their corresponding segmentation results are shown in Figure 7.3 (b)-(k) and Figure 7.4 (b)-(k).

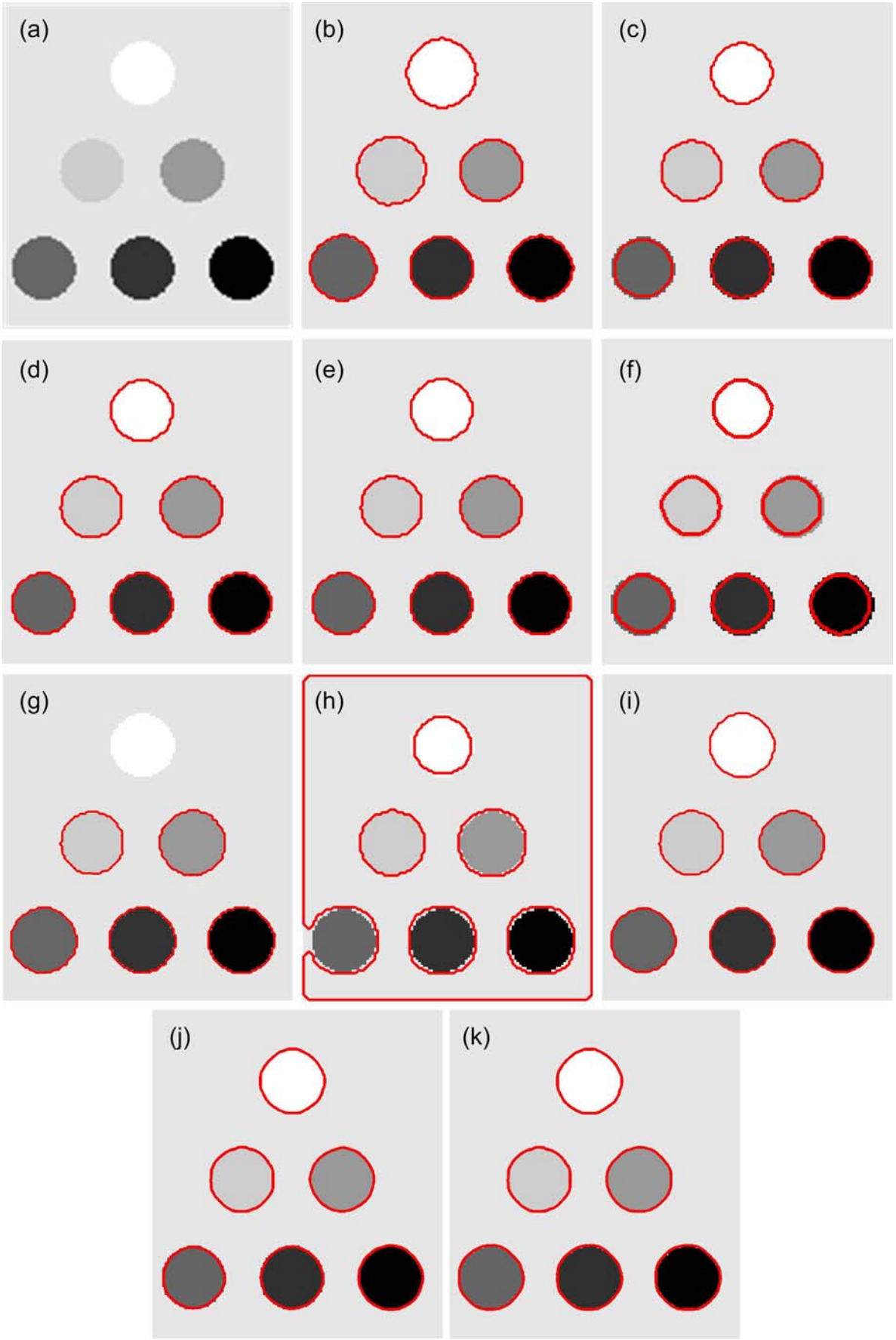

Figure 7.3 Performance comparison of the synthetic image-1 (a) Original image. Results obtained by (b) FCM_S1 (c) FCM_S2 (d) GKFCM_S1 (e) GKFCM_S2 (f) GAC (g) ACMRSF (h) RBACM-SFCM (i) EBACM (j) RBACM-GKFCM_S1 (k) RBACM-GKFCM_S2

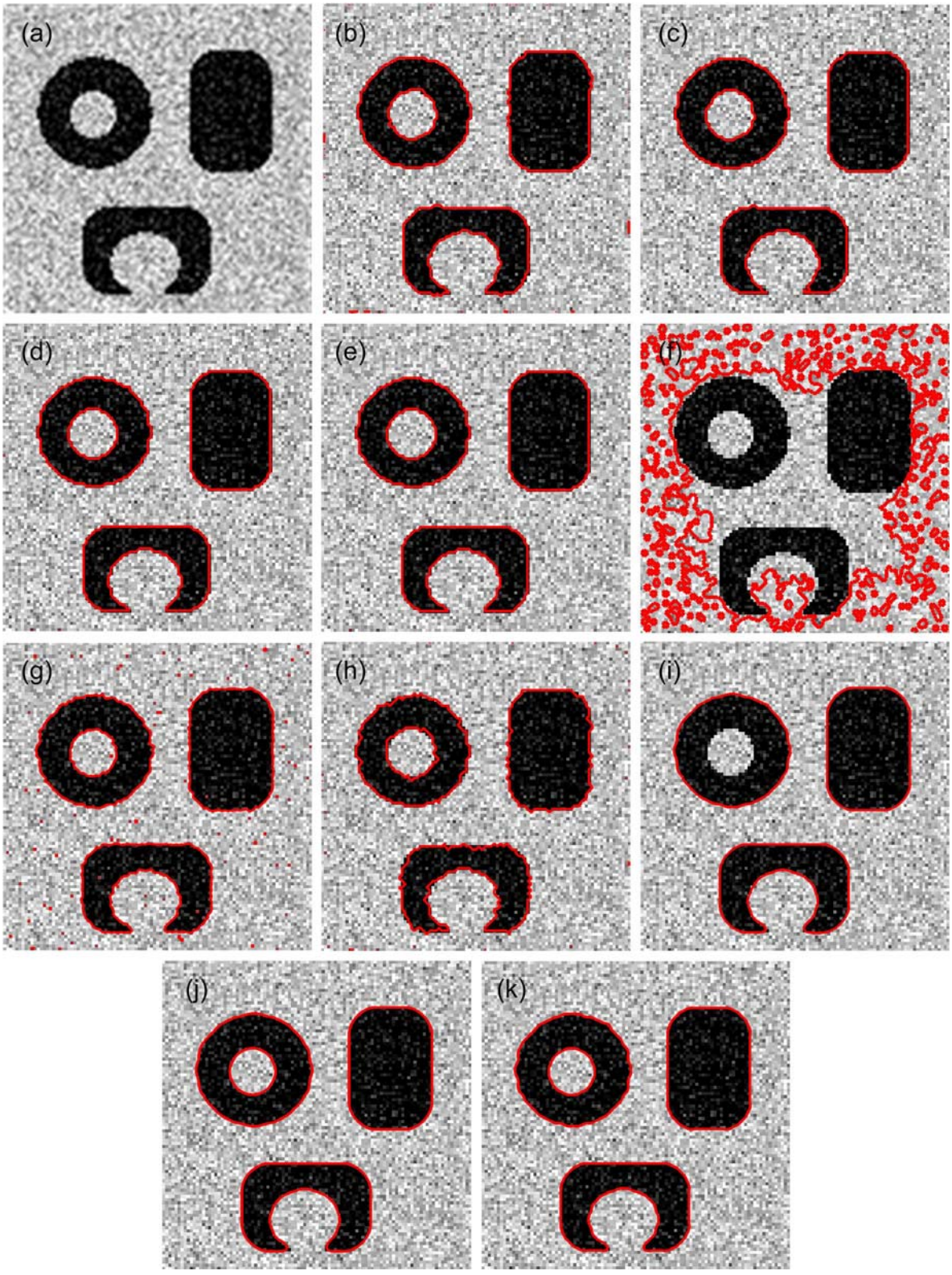

Figure 7.4 Performance comparison of the synthetic image-2 (a) Original image. Results obtained by (b) FCM_S1 (c) FCM_S2 (d) GKFCM_S1 (e) GKFCM_S2 (f) GAC (g) ACMRSF (h) RBACM-SFCM (i) EBACM (j) RBACM-GKFCM_S1 (k) RBACM-GKFCM_S2

The segmented images shown in Figure 7.3 and Figure 7.4 also present that the proposed approaches provide better results than others. The proposed RBACM-GKFCM_S1 approach is much better than the RBACM-GKFCM_S2 by successfully extracting the

estimated region and objects boundaries. These qualitative results are also supported by the quantitative results using all six performance measures used in the chapter 6. The averaged performance measures (average (STD)) such as the TP ratio (%), FP ratio (%), ACC (%), JSI (%), DC (%) and HD are listed in Table 7.1. From the results mentioned in Table 7.1, it is observed that the proposed approaches gain approx 95-96% higher averaged segmentation accuracy than the others. The other measures such as the JSI and DC gain higher values for the proposed methods. This indicates more similar region extracted by the proposed methods than the others. The proposed approaches also achieve higher TP ratio (approx 92-93%), but sometimes a lower value of the TP ratio may be exhibited for the proposed method compared to some other methods. This is because of the blurry regions around the object boundaries that become very difficult to be differentiated with the real boundaries. Since, these blurry regions are also marked by an expert at the time of manual segmentation, sometimes the TP ratio becomes higher than the proposed methods. However, these methods also show their inaccurate segmentation results indicated by higher FP values. Besides it, the proposed methods exhibit the ability of accurately detecting the object of interest by gaining the lowest HD values.

Table 7.1 Averaged performance measures obtained by the different segmentation methods for all synthetic test images

Methods	TP	FP	ACC	JSI	DC	HD
FCM_S1	88.5713 (5.2673)	2.5674 (1.5430)	93.0019 (3.6933)	86.1958 (3.5021)	92.1279 (5.4266)	2.7477 (0.5168)
FCM_S2	90.7154 (5.8466)	1.8551 (0.9541)	94.5552 (2.7345)	89.2289 (7.5362)	94.1774 (4.3695)	2.7159 (0.3283)
GKFCM_S1	91.5110 (6.0950)	0.0572 (0.0461)	95.6019 (1.9674)	91.2071 (5.9365)	95.2605 (3.5248)	2.6124 (0.4837)
GKFCM_S2	91.3984 (6.1717)	0.0481 (0.0386)	95.5253 (1.9899)	91.0534 (5.9812)	95.1743 (3.5622)	2.5454 (0.6011)
GAC	84.1650 (12.3110)	12.1461 (4.0252)	79.7470 (15.2026)	69.9560 (14.6357)	81.6513 (10.4125)	4.1302 (1.9803)
ACMRSF	89.9492 (7.7889)	3.1921 (1.0412)	93.3785 (3.5023)	87.1338 (7.0434)	93.0084 (4.1165)	3.2715 (1.7100)
RBACM-SFCM	93.0288 (4.3238)	8.2423 (3.5138)	93.6432 (3.3766)	89.1189 (6.2907)	94.0451 (3.4655)	3.1847 (1.1932)
EBACM	92.7708 (6.0105)	1.0836 (0.3545)	95.6686 (3.0137)	91.7403 (5.1842)	95.6083 (3.1719)	2.5820 (0.8821)
Proposed approach-1	92.2195 (6.0065)	0.3314 (0.1934)	95.7547 (2.7646)	91.7714 (5.6932)	95.7556 (3.2819)	2.4491 (0.5793)
Proposed approach-2	93.3782 (4.8368)	0.2352 (0.1533)	96.4984 (2.4030)	93.0224 (4.7909)	96.3360 (2.6333)	2.1771 (0.7233)

Moreover, the proposed RBACM-GKFCM_S2 approach achieves higher TP, ACC, DC, JSI values and lower FP and HD values than the proposed RBACM-GKFCM_S1 approach. For a better representation of results, the performance measures obtained for all the synthetic test images are presented by box plot shown in Figure 7.5. From Figure 7.5, it can also be observed that the median of the TP, JSI, ACC, DC and FP, HD values obtained by the proposed method are highest and lowest, respectively. It also indicates the superiority of the proposed methods compared to others in terms of the successful extraction of the region of interest.

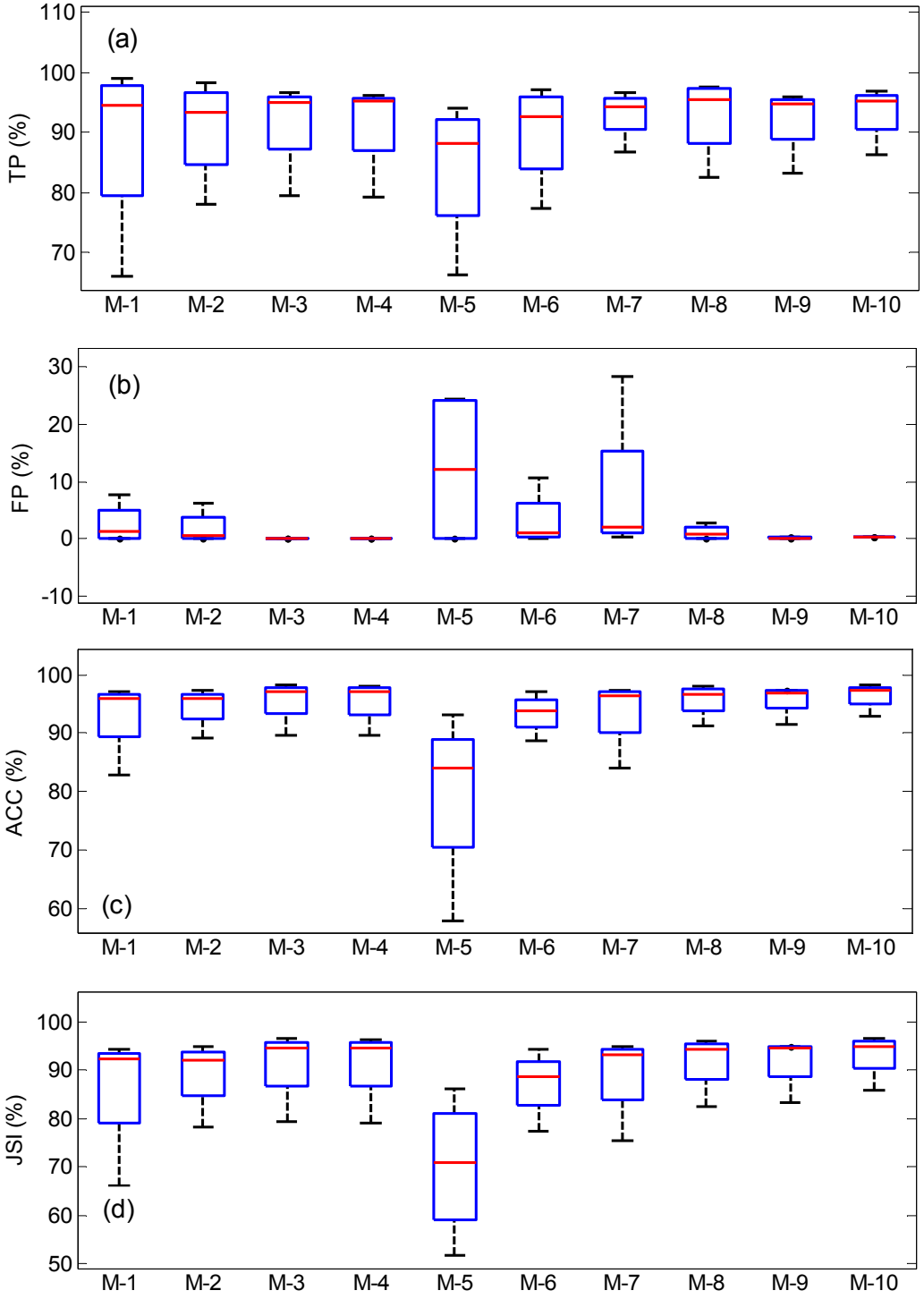

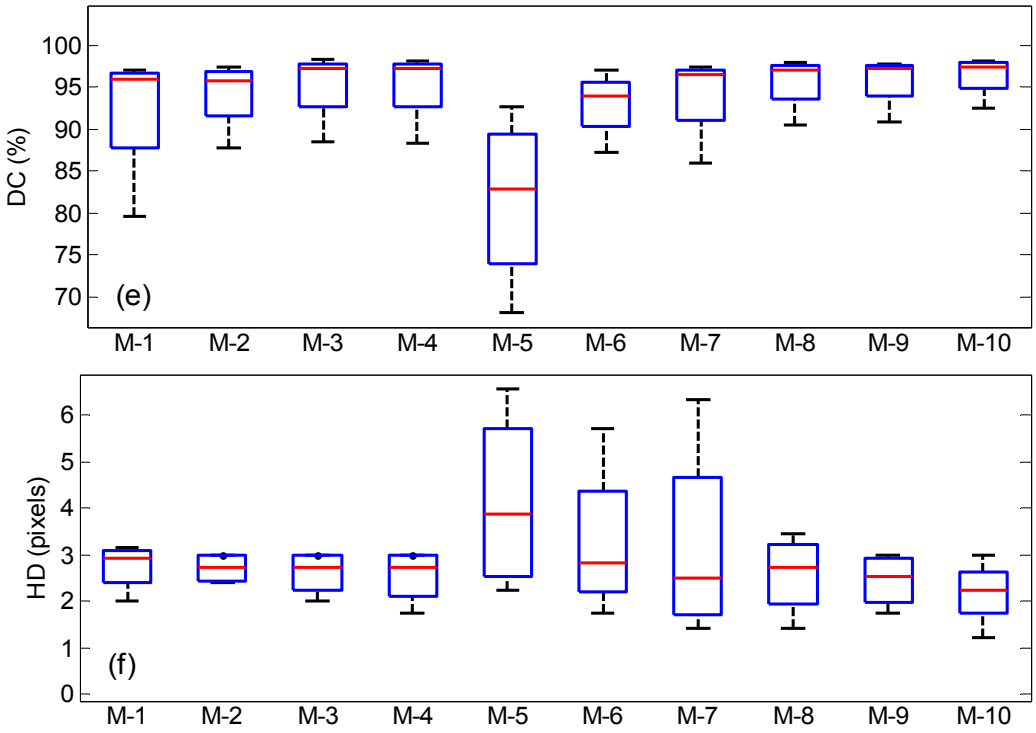

Figure 7.5 Box plot of the TP, FP, ACC, JSI, DC and HD measurements for all synthetic test images processed by the proposed RBACM-GKFCM_S1 (M-9) and RBACM-GKFCM_S2 (M-10) and others, where M-1, M-2, M-3, M-4, M-5, M-6, M-7 and M-8 refer to the FCM_S1, FCM_S2, GKFCM_S1, GKFCM_S2, GAC, ACMRSF, RBACM-SFCM, EBACM methods, respectively

Furthermore, the computation time for all the segmentation methods has also been evaluated. The details of the processing time and averaged number of iterations to extract the regions for all images are listed in Table 7.2. All the results are produced on the same machine as mentioned in the previous chapter. From the results, it can be observed that the proposed approaches take less time and less number of iterations compared to the others.

Table 7.2 Comparative performance of the segmentation approaches with the averaged number of iterations and computational time for all the synthetic test images

Methods	Averaged resolution	Averaged iterations	Averaged computational time, s
FCM_S1	94 × 95	25	0.3049
FCM_S2	94 × 95	7	0.1998
GKFCM_S1	94 × 95	30	0.2262
GKFCM_S2	94 × 95	15	0.1607
GAC	94 × 95	275	20.171
ACMRSF	94 × 95	175	2.5843
RBACM-SFCM	95 × 95	50	2.3871
EBACM	94 × 95	35	10.889
Proposed approach-1	94 × 95	45	1.6671
Proposed approach-2	94 × 95	30	1.4995

Experiment 2: *Analysis and evaluation for the segmentation performance of real US images* - In order to investigate the segmentation performance of the proposed methods and to present a comparison with other aforementioned methods, same dataset has been utilized as in the previous chapter. The results of two left ventricle US images are shown in Figure 7.6 (a) and Figure 7.7 (a), respectively. Figure 7.6 (b) and Figure 7.7 (b) present the manually delineated region of both the left ventricle US images. The outcomes of both the US images segmented by all methods such as the FCM_S1, FCM_S2, GKFCM_S1, GKFCM_S2, GAC, ACMRSF, RBACM-SFCM, EBACM, proposed RBACM-GKFCM_S1 and proposed RBCAM-GKFCM_S2 are presented in Figure 7.6 (c)-(l) and Figure 7.7 (c)-(l), respectively. From these results, it is observed that the proposed methods precisely segment the region and object boundaries. Moreover, the segmentation results obtained by the proposed methods are approximately similar to that of the manually delineated region when compared with the others. Furthermore, to illustrate the superiority of the proposed approach-1 and 2 for providing the better segmentation results, a comparative view of segmented US images obtained by aforementioned methods are presented in Figure 7.8 and Figure 7.9. For such comparison, the US images used as similar in the previous chapter (presented in Figure 6.8 and Figure 6.9) are considered. Their segmentation results of four different US images are also shown in Figure 7.8 in which first is the US image of splenic cyst as shown in the first row and another US image of benign tumor shown in the second row. Last two images are of the US images of liver metastases. Moreover, in the Figure 7.9, all four different images shown in the four rows refer to the US image of the brain, benign cyst and multiple liver masses. Their manually delineated regions are also shown in the previous chapter. Their segmented images produced by aforementioned segmentation methods are shown in Figure 7.8 and Figure 7.9. From these results, it can be easily observed that the proposed approaches are able to produce better results than other methods and extract the region as similar to the manually delineated region of the US image.

Besides the visual analysis of the segmented US images, several quantitative analysis have also been done in terms of the performance measures. Their corresponding quantitative results are mentioned in Table 7.3 that presents the averaged performance measures such as TP (%), FP (%), ACC (%), JSI (%) and DC (%) values for all US images utilized to perform the experiment. From the results listed in Table 7.3, it can be observed that the proposed approach-1 (RBACM-GKFCM_S1) and 2 (RBACM-GKFCM_S2) obviously outperform the other existing algorithms. Moreover, the proposed methods 1 and 2 achieve approx 4.27-5.73%, 3.29-4.74%, 0.7-2.1%, 0.6-1.96%, 5.18-6.65%, 5.31-6.78%, 9.29-10.82% and 1.76-3.19% higher TP ratio than FCM_S1, FCM_S2, GKFCM_S1, GKFCM_S2, GAC, ACMRSF, RBACM-SFCM and EBACM method, respectively. These results ensure that the more overlapping area is obtained by the proposed method compared to the other

methods. The proposed methods also reveal an improvement in the segmentation accuracy by 2.6-3.16%, 0.96-1.13% than the FCM and GKFCM clustering methods.

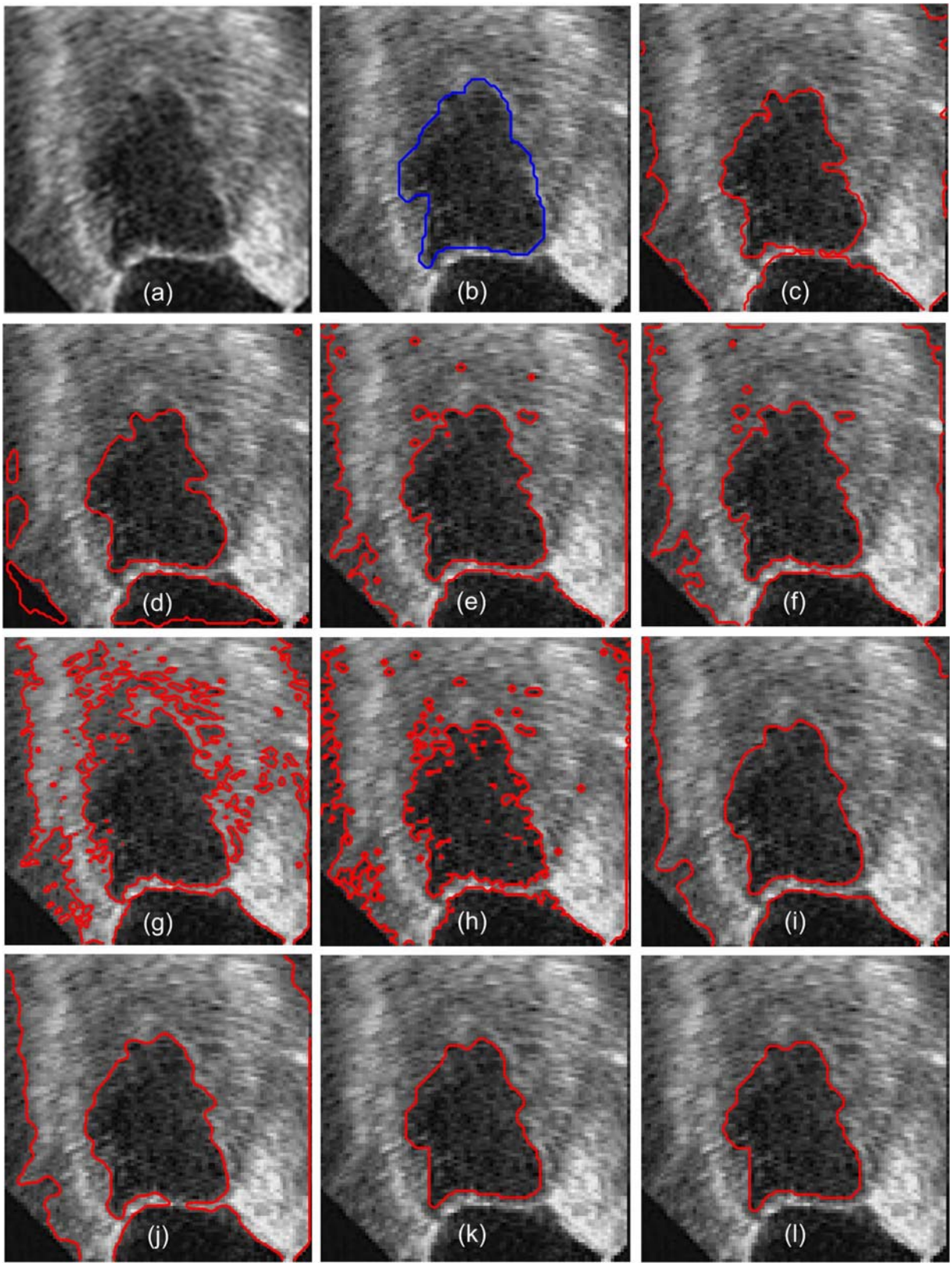

Figure 7.6 (a) Original ultrasound image-1. Segmentation results obtained by (b) Manual (c) FCM_S1 (d) FCM_S2 (e) GKFCM_S1 (f) GKFCM_S2 (g) GAC (h) ACMRSF (i) RBACM-SFCM (j) EBACM (k) Proposed RBACM-GKFCM_S1 (l) Proposed RBACM-GKFCM_S2

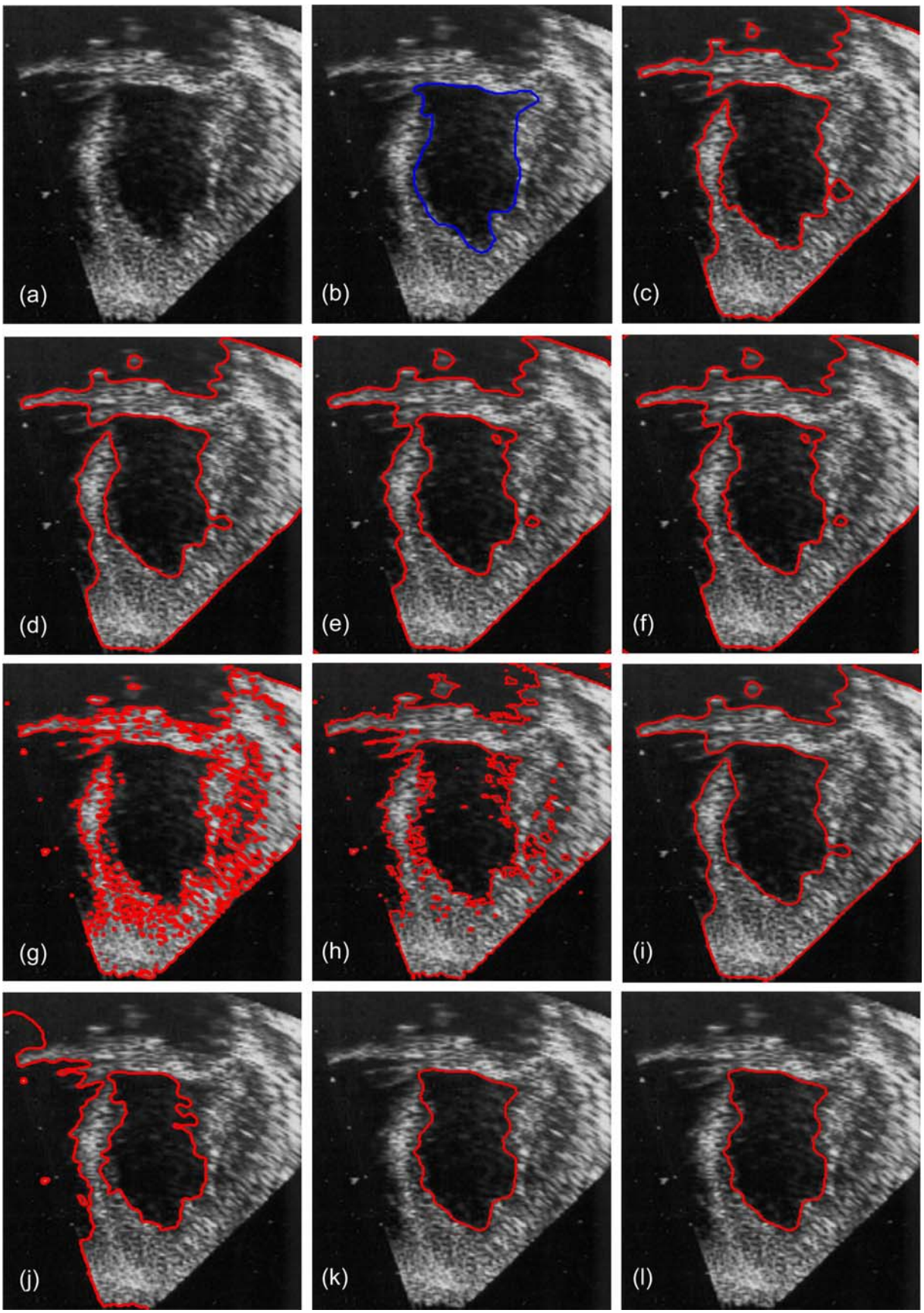

Figure 7.7 (a) Original ultrasound image-2. Segmentation results obtained by (b) Manual (c) FCM_S1 (d) FCM_S2 (e) GKFCM_S1 (f) GKFCM_S2 (g) GAC (h) ACMRSF (i) RBACM-SFCM (i) EBACM (k) Proposed RBACM-GKFCM_S1 (l) Proposed RBACM-GKFCM_S2

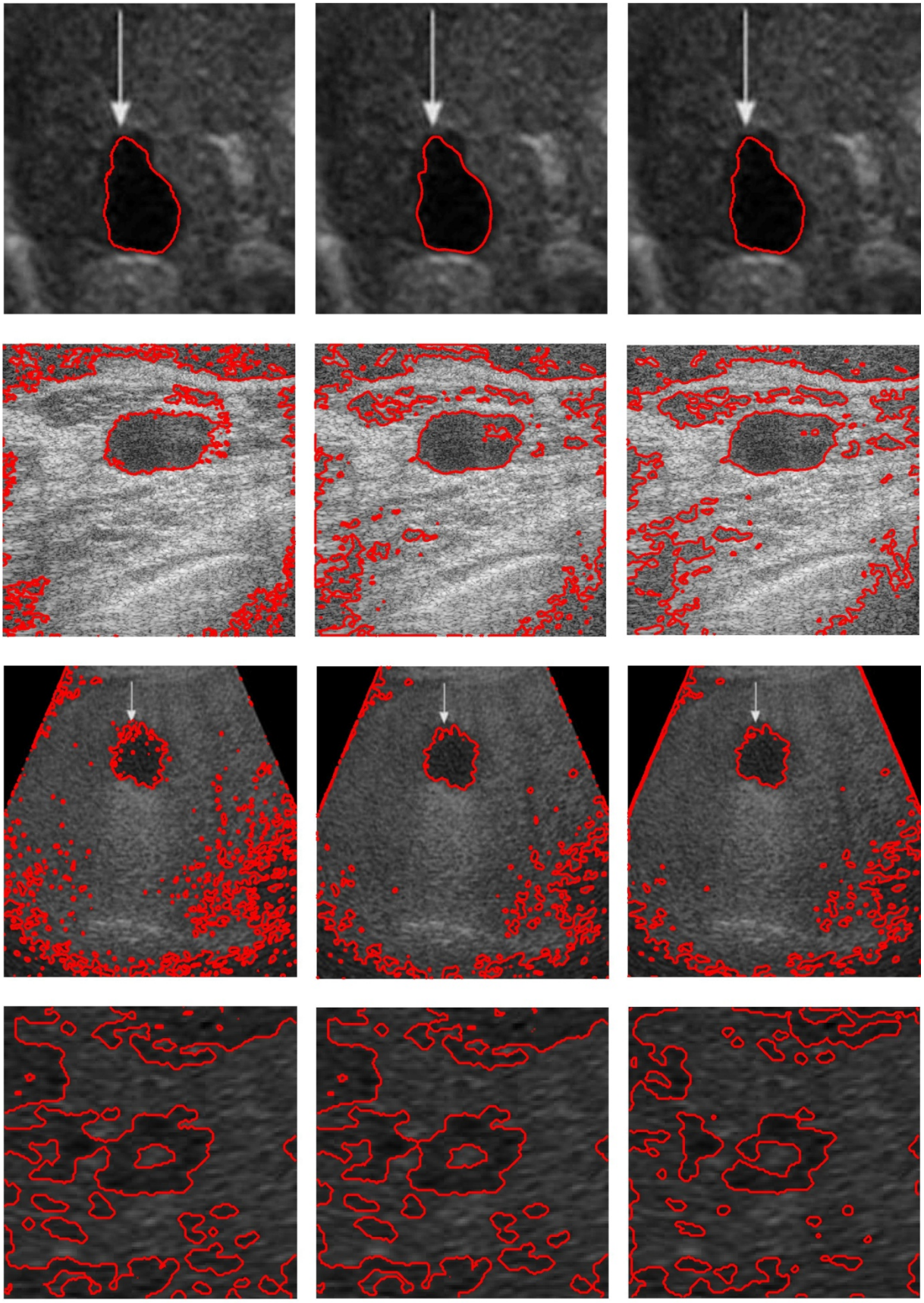

(a) (b) (c)

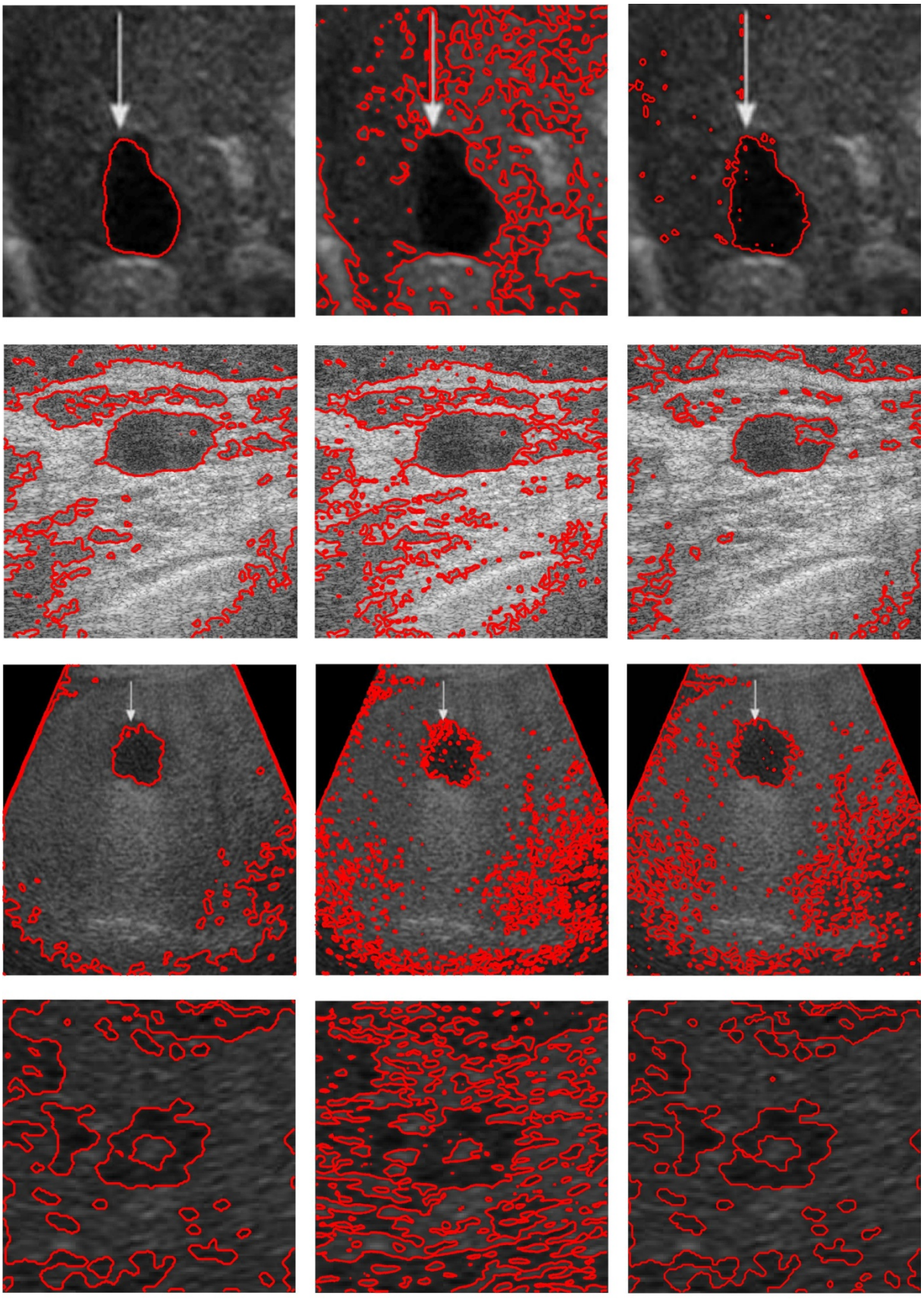

(d) (e) (f)

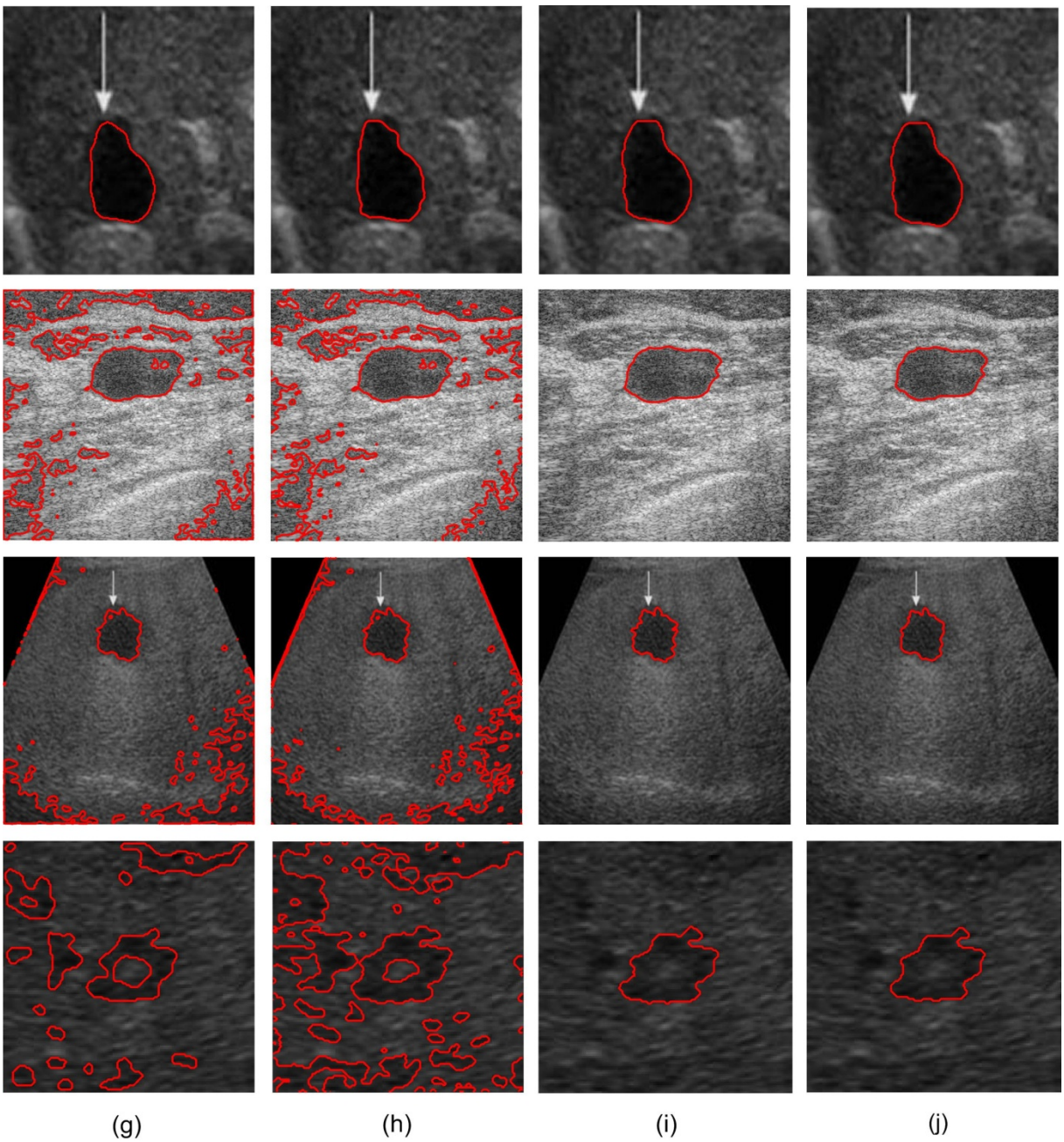

Figure 7.8 Comparative visual analysis of the segmentation results of different ultrasound images obtained by (a) FCM_S1 (b) FCM_S2 (c) GKFCM_S1 (d) GKFCM_S2 (e) GAC (f) ACMRSF (g) RBACM-SFCM (h) EBACM (i) Proposed RBACM-GKFCM_S1 (j) Proposed RBACM-GKFCM_S2

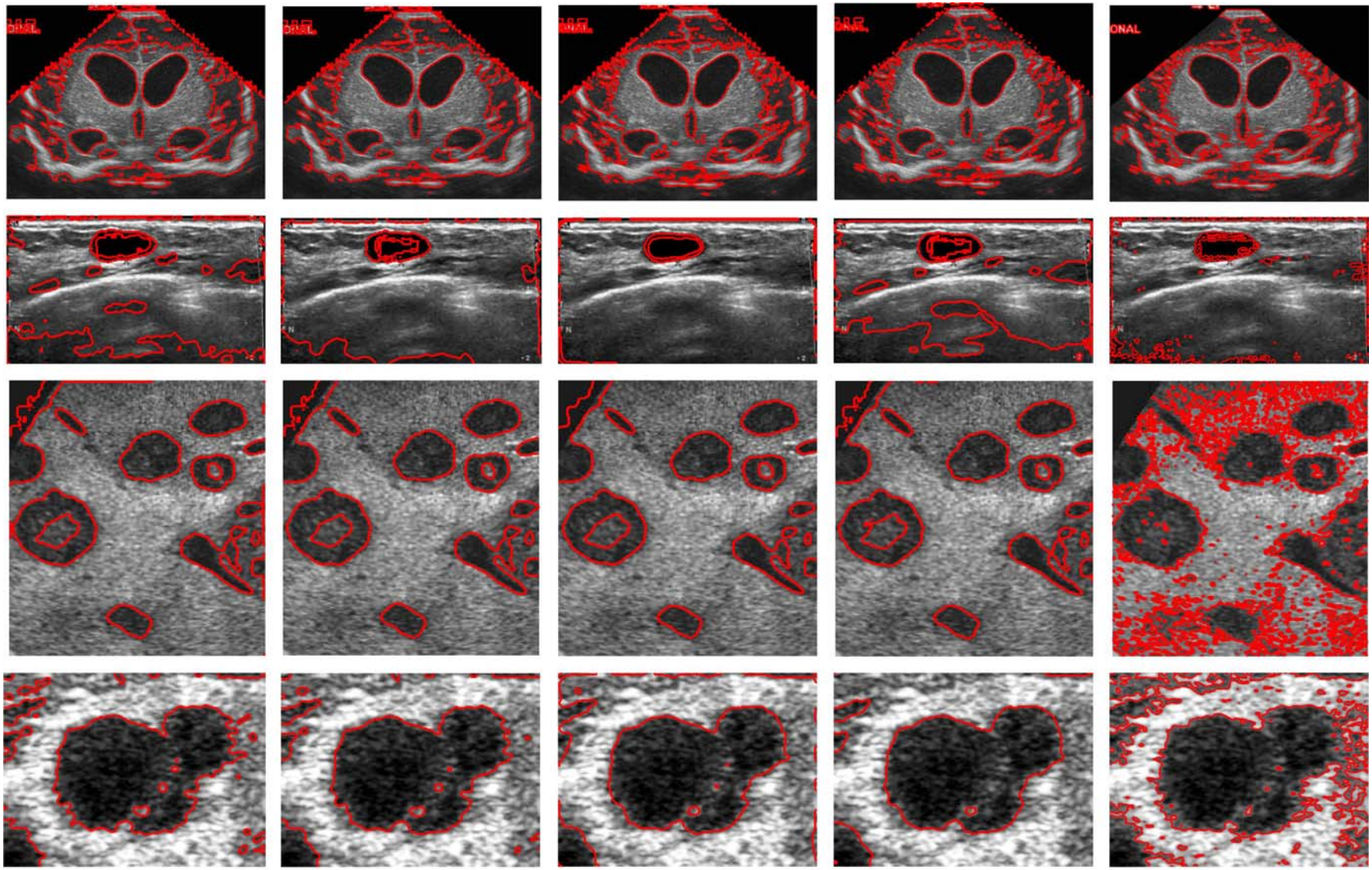
FCM_S1
FCM_S2
GKFCM_S1
GKFCM_S2
GAC

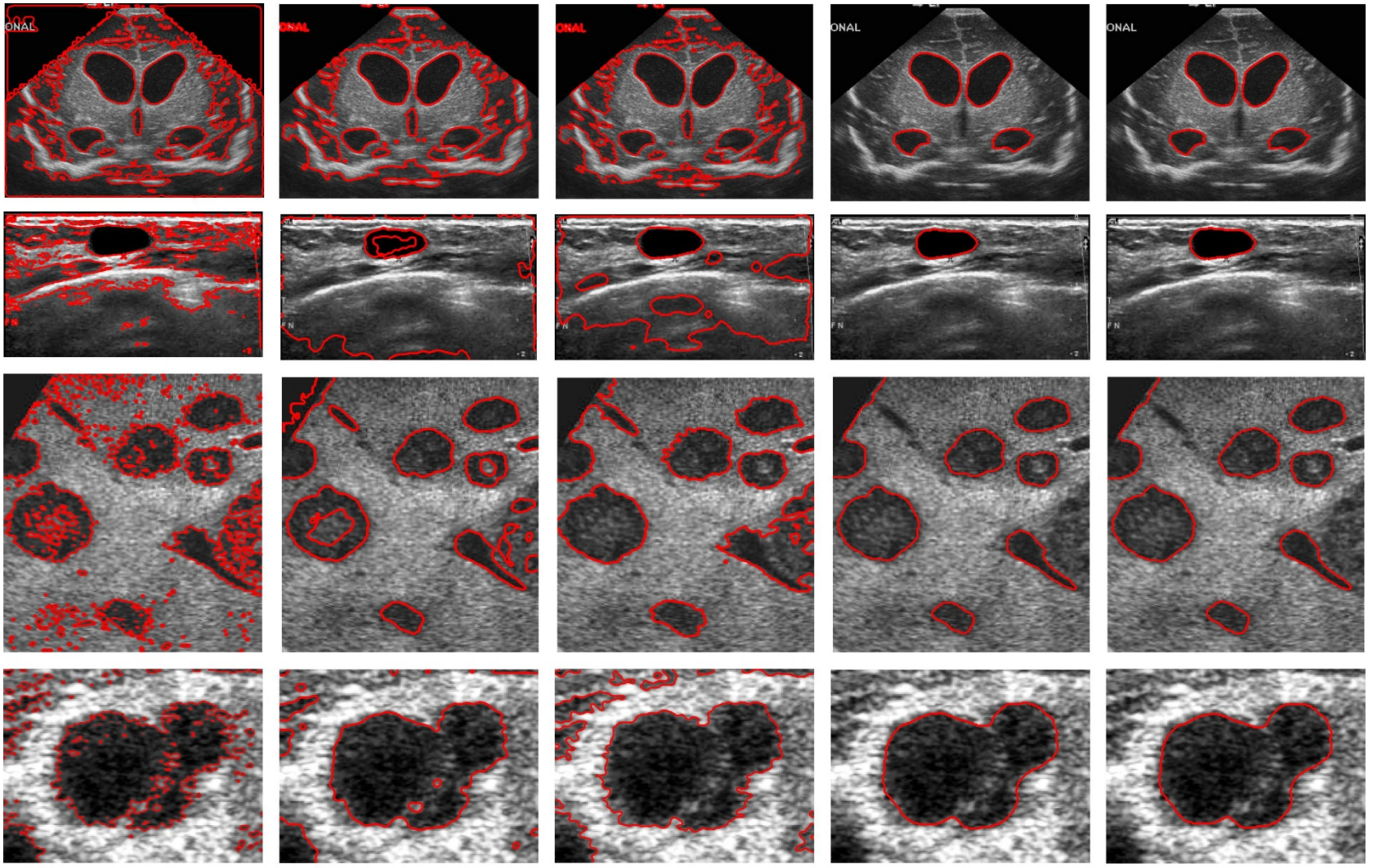

Figure 7.9 Comparative segmentation performance obtained by the different methods

Table 7.3 Averaged performance measures (TP, FP, ACC, JSI and DC) obtained by the different segmentation methods for all the ultrasound images

Methods	TP	FP	ACC	JSI	DC
FCM_S1	0.8905 ± 0.0360	0.1184 ± 0.0906	0.9071 ± 0.0271	0.8445 ± 0.0394	0.9126 ± 0.0239
FCM_S2	0.8989 ± 0.0384	0.1061 ± 0.0846	0.9110 ± 0.0275	0.8496 ± 0.0312	0.9155 ± 0.0248
GKFCM_S1	0.9221 ± 0.0329	0.0476 ± 0.0541	0.9258 ± 0.0261	0.8588 ± 0.0463	0.9234 ± 0.0271
GKFCM_S2	0.9234 ± 0.0326	0.0484 ± 0.0538	0.9253 ± 0.0311	0.8679 ± 0.0576	0.9266 ± 0.0345
GAC	0.8828 ± 0.0156	0.3164 ± 0.2476	0.8332 ± 0.0902	0.7658 ± 0.0919	0.8626 ± 0.0316
ACMRSF	0.8817 ± 0.0656	0.0963 ± 0.0533	0.8927 ± 0.0439	0.8101 ± 0.0532	0.8909 ± 0.0545
RBACM-SFCM	0.8496 ± 0.1464	0.0535 ± 0.0679	0.9007 ± 0.0677	0.8113 ± 0.1316	0.8899 ± 0.0522
EBACM	0.9124 ± 0.0498	0.0661 ± 0.0224	0.9231 ± 0.0174	0.8581 ± 0.0377	0.9227 ± 0.0246
PA-1	0.9285 ± 0.0460	0.0331 ± 0.0385	0.9347 ± 0.0244	0.8760 ± 0.0436	0.9334 ± 0.0249
PA-2	0.9345 ± 0.0409	0.0319 ± 0.0358	0.9358 ± 0.0246	0.8772 ± 0.0443	0.9345 ± 0.0253

* PA-1: Proposed approach-1 (RBACM-GKFCM_S1)

* PA-2: Proposed approach-2 (RBACM-GKFCM_S2)

Moreover, the accuracy of the proposed methods is raised by approx 12.31%, 4.83%, 3.9% and 1.26-1.38% from the GAC, ACMRSF, RBACM-SFCM and EBACM methods, respectively. It gains approx 3.11-3.87%, 0.93-2.14%, 14.6%, 8.13-8.28%, 7.97-8.12 % and 2.09-2.23% higher values of the JSI and 1.96-2.40%, 0.73-1.20%, 8.21-8.34%, 4.89%, 4.8-5.1% and 1.16-1.28% higher DC values compared to the FCM, KFCM, GAC, ACMRSF, RBACM-SFCM and EBACM methods, respectively. The higher values of the JSI and DC produced by the proposed methods assure more similarity between the region extracted by the computerized segmentation method and manually. Finally, the proposed approaches also get the lowest FP values that define the incorrect extraction of the region of interest in comparison to the manual delineated region. The averaged FP values obtained by the proposed methods are decreased by approx 72.04-73.06%, 68.8-69.93%, 30.46-32.98%, 31.61-34.09%, 89.54-89.92%, 65.63-66.87%, 38.13-40.7% and 49.92-51.74% from the FCM_S1, FCM_S2, GKFCM_S1, GKFCM_S2, GAC, ACMRSF, RBACM-SFCM and EBACM methods, respectively.

In addition, to further investigate the performance of the proposed segmentation approaches, Hausdorff distance is evaluated for each US image processed by all the aforementioned segmentation methods. Table 7.4 illustrates the averaged HD metric (average ± STD) obtained by each method. These results indicate the superiority of the proposed approach-1 and 2 by obtaining the smallest HD values. Moreover, the RBACM-GKFCM_S2 also has lower HD value than the RBACM-GKFCM_S1 approach.

Furthermore, the averaged resolution, iteration and computational time taken by all the segmentation approaches are compared and listed in Table 7.5 from which it is concluded that the proposed approaches also take less number of iterations with higher speed compared to the other methods. All the computations are performed on the same machine as mentioned in the previous chapter.

Table 7.4 Hausdorff distance obtained by the various segmentation methods for all the ultrasound images

Methods	HD
FCM_S1	4.5742 ± 0.8436
FCM_S2	4.2630 ± 0.6562
GKFCM_S1	3.2424 ± 1.0615
GKFCM_S2	3.2585 ± 1.1061
GAC	6.9969 ± 3.0891
ACMRSF	4.8472 ± 1.4808
RBACM-SFCM	4.3482 ± 1.1641
EBACM	3.5790 ± 1.3367
Proposed approach-1	2.8658 ± 1.2053
Proposed approach-2	2.5206 ± 1.2507

Table 7.5 Comparative performance of the segmentation approaches with the averaged number of iterations and computational time for all the ultrasound images.

Methods	Averaged resolution	Averaged computational time, s	Averaged iterations
FCM_S1	294 × 310	0.5265	35
FCM_S2	294 × 310	0.4916	38
GKFCM_S1	294 × 310	1.5064	39
GKFCM_S2	294 × 310	1.8986	48
GAC	294 × 310	141.26	1250
ACMRSF	294 × 310	15.448	242
RBACM-SFCM	295 × 310	2.6215	100
EBACM	294 × 310	13.378	100
Proposed approach-1	294 × 310	2.1137	24
Proposed approach-2	294 × 310	2.9411	20

7.7 Summary

The accurate segmentation of a particular region of interest in the US image is one of the vital tasks because of the poor quality of images. In this chapter, two hybrid segmentation approaches for the US images are proposed that utilize both the features of the RBACM driven by the RSF energy and the GKFCM_X clustering method. These hybrid segmentation methods initiate with the results of the GKFCM_X method that is responsible for successfully extracting the estimated object boundaries by initializing the curve during level set evolution and for evaluating the several controlling parameters also. Besides this, it eliminates the requirement of manual tracing and decreases the computation time also. Several experiments have been performed on both the synthetic and real ultrasound images. From both the subjective and objective evaluation, it is concluded that the proposed methods provide better performance compared to the others. It does not only ensure an improvement in the segmentation performance by correctly identifying the estimated boundaries, but exhibits the improved performance in terms of the processing speed also.

CHAPTER 8: CONCLUSIONS AND SCOPE FOR FUTURE WORK

This chapter presents the conclusions based on the performance of all the proposed denoising and segmentation methods discussed in the previous chapters. The conclusion based on the comparative analysis among all the proposed denoising and segmentation approaches illustrated in Appendix A and B, respectively, is also presented here. The chapter also suggests several possible directions of the present work to be investigated in the future.

8.1 Conclusions

This thesis has focused on the edge preserved noise reduction in the US images and segmentation of these images. The major objectives of this study has been to design and develop the effective methods to improve the visual perception of the images by suppressing the noise and extract (segment) a particular region from the US images that may be used for further analysis. Besides despeckling of the US medical images, attention has also been given to develop more generalized algorithms so that they can be applied not only to suppress multiplicative speckle noise, but also to additive noise like Gaussian noise (which is inherently observed in most of the images).

Accurate segmentation of the US images is a very difficult task due to the presence of noise in the images. Thus, six denoising approaches such as the MBRT, RTNLF-1, RTNLF-2, RBAF, NSST-NADF and NSST-NLNADF have been developed to enhance the quality of the US images, while four segmentation methods such as the EBACM-KFCM_S1, EBACM-KFCM_S2, RBACM_GKFMC_S1 and RBACM-GKFCM_S2 have also been developed to provide accurate segmentation.

Based on the experimental results, distinct conclusions have been drawn at various stages of the present work, which are summarized as below:

8.1.1 Evaluation of the existing denoising approaches

Among two different category viz, spatial and transform domain, it has been observed that many researchers are working on diffusion, total variation, nonlocal mean filtering from the spatial domain categories on one side and wavelet, ridgelet and curvelet based approaches from the transform domain on the other side. Thus, a comparative analysis of existing denoising methods like the AWMF, WF, MHOPNF, ADF, SRAD, NCDF, TVF, NLMF, TI-WT, ridgelet, curvelet and shearlet based approaches have been carried out on the several test images and US images. As noise suppression and edge preservation are conflicting parameters, this comparative evaluation is performed keeping these two aspects in mind. Based on the analysis, another M-band ridgelet based thresholding (MBRT) approach has also been proposed to fulfil the requirement of denoising with edge preservation. A comparative analysis of all the existing methods and proposed method is also presented. The conclusions drawn from this comparison are presented below:

On the basis of quantitative analysis, it has been observed that the NLMF and shearlet based approach produce better speckle noise reduction performance in case of low and high noise level, respectively by providing higher PSNR and SNR values. Besides better speckle noise reduction, the MBRT approach is able to provide better edge preservation performance by achieving higher EKI values compared to the other methods. It is also observed from the experimental results that the image processed by the transform based approaches such as ridgelet, curvelet and shearlet produce a better visual appearance compared to aforesaid methods. However, it also produces some visual distortion by introducing some fuzzy edges near the original edges and in the homogeneous region of images. Moreover, the diffusion based and TVF approaches also show a considerable improvement in terms of noise suppression and edge preservation. However, as the noise level available in the image increased, the denoising performance deteriorated due to loss of edge information with the noise residual. The TVF approach also introduces some staircasing effect in the denoised images and the diffusion approaches exhibit the maximum amount of blurring effect which is verified by lower EKI values. Further, the proposed MBRT approach produces higher performance measures than wavelet, ridgelet and curvelet based approaches in terms of both the noise suppression and edge preservation. The shearlet and proposed MBRT methods have less distortion than the curvelet.

8.1.2 Proposed ripplet domain nonlinear filtering approach

The efforts in the previous section have been made to evaluate and analyze the performance of existing and the proposed MBRT approach applied to all the US and test images. To preserve more edges and to overcome the limitation of curvelet, two different ripplet domain nonlinear filtering approaches such as the RTNLF-1 and RTNLF-2 have been proposed that utilize both the features of nonlinear bilateral filter (NLBF) and two thresholding approaches such as NeighShrink and BlockShrink. Quantitative analysis of the experimental results using the various performance measures shows that the proposed RTNLF-1 and 2 approaches are able to reduce the noise in a better way than the other methods without distorting the information.

From the comparative evaluation and analysis shown in Table A.1 (in appendix A), it is observed that the proposed approach RTNLF-1 gains approx (4.46%, 4.52%, 1.24%), (7.18%, 7.61%, 2.14%), (1.43%, 3.73%, 2.74%), (5.57%, 7.75% and 13.83%) and (22.18%, 14.31%, 17.46%), higher averaged PSNR, SNR, SSIM, FOM and EKI values (for different noise levels as $\sigma = 0.1, 0.2$ and 0.3, respectively), respectively, than the proposed MBRT method. It indicates better denoising performance provided by the proposed RTNLF-1 approach. Moreover, the proposed method RTNLF-2 approach outperforms both the MBRT and RTNLF-1 method. The proposed RTNLF-2 approach also achieves approx (6.35%, 5.84%, 3.48%), (10.25%, 9.84%, 6.02%), (3.68%, 4.53%, 3.13%), (6.28%, 8.80%, 14.71%),

(24.87%, 17.77, 19.58%) higher averaged PSNR, SNR, SSIM, FOM and EKI values (for different noise levels similar as above), respectively, than the MBRT approach, while the approx 1.81-2.21%, 2.07-3.8%, 0.38-2.22%, 0.67-0.98% and 1.81-3.03% higher PSNR, SNR, SSIM, FOM and EKI values are achieved by the proposed RTNLF-2 approach as compared to the RTNLF-1 approach. Further, the proposed RTNLF-2 method provides the US images with better perceptual quality than the others and it is validated by analyzing the evaluated MVR values shown in Table A.2 i.e. 22.17 higher than the MBRT (21.12) and the proposed RTNLF-1 approach (21.98). Thus, from the observation, it is clear that the proposed methods show a significant improvement in terms of enhancement of image quality and detectability.

8.1.3 Proposed remnant approach for adaptive fusion based noise filtering

Based on the comparative analysis shown in chapter 2 and 3, it is observed that the TVF approach also produces the competitive results than the above mentioned methods. However, the edge information is lost during the TVF process. Besides the TVF approach, curvelet and shearlet based approach also provide better edge preservation, but they suffer from serious issues as mentioned above. Thus, the RBAF approach based on the adaptive fusion process which is utilized to fuse three different images processed by the (a) TVF approach, (b) CSST approach, separately and (c) edge structured information extracted by noise residual of the TVF method and further processed by the CSST approach, has been proposed. The proposed RBAF approach is able to overcome the limitation of TVF, CVT and ST methods, i.e. it helps to reduce the fuzzy edges and staircase effects from the test and US images. From the quantitative analysis of the experimental results shown in chapter 4, it is observed that the proposed RBAF approach shows an improved noise suppression performance than the MBRT and RTNLF approaches by achieving higher PSNR and SNR by approx (3.07-6.91%, and 5.29-11.17%) and (0.45-2.35% and 0.73-3.72%), respectively. Sometimes, the RTNLF-2 approach outperforms the RBAF approach by producing higher performance measures in case of test images, while for the US images, the RBAF approach produces much better denoised images with better visual quality than the proposed MBRT, RTNLF approaches. This is also verified by Table A.2 that shows higher averaged MVR value (22.23) produced by the RBAF approach as compared to the MBRT (21.12), RTNLF-1 and 2 (21.98 and 22.17, respectively). Thus, it is concluded that the proposed RBAF approach helps to remove the noise as much as possible without loss of edge information.

8.1.4 Proposed nonsubsampled shearlet domain noise filtering approach using nonlinear adaptive diffusion equations

The efforts in the earlier chapters were focused on the improvement in noise reduction performance with better edge preservation. These efforts have been successful to

considerable extent resulting in more usefulness of the approaches, while improving or maintaining the qualitative performance. Thus, two approaches such as the NSST-NADF and NSST-NLNADF approaches are proposed, considering the merits of the ADF and NLMF approaches as shown in chapter 2. However, these methods suffer from the loss of edge information in the denoised images. To overcome this limitation and better representation of edges, these approaches are utilized to modify the diffusion equations by incorporating the adaptive gray variance with the gradient information of a large size, i.e. eight connected neighboring pixels in the NSST-NADF approach, while nonlocal pixel information is incorporated to evaluate the adaptive gray variance within the same neighborhood in the NSST-NLNADF approach. The NSST also overcomes shift invariance problem of the ST as mentioned in the literature.

From the results shown in Table A.1, it is observed that the proposed NSST-NLNADF approach outperforms all the other proposed methods in both the terms either in noise suppression or in edge preservation. This approach is also suitable for both additive and multiplicative noise corrupted images. The NSST-NLNADF approach achieves higher PSNR (7.08-10.3%, 2.7-5.76%, 1.42-3.7%, 2.25-3.89% and 2.52-4.26%), SNR(12.2-16.7 %, 4.41-9.85%, 2.3-5.83%, 3.66-6.56% and 4.11-6.67%), SSIM (6.04-9.25%, 4.3-6.34%, 2.27-5.94%, 1.7-6.03% and 2.5-6.57%), FOM (5.3-17%, 2.7-2.82%, 1.8-1.99%, 0.98-2.58% and 1.11-2.56%) and EKI (29.91-21.5%, 2.41-4.89%, 0.59-1.81%, 8.69-18.64% and 5.59-8.52%) than the other proposed MBRT, RTNLF-1, RTNLF-2, RBAF and NSST-NADF approaches. Sometime in case of lower noise level, the RTNLF-1 and 2 approaches provide better edge preservation by obtaining higher EKI values for the test image datasets. Besides the superiority of the NSST-NLNADF approach, in case of high level of speckle noise ($\sigma = 0.3$), the proposed NSST-NADF approach also shows better noise reduction by providing higher SNR (7.64%, 5.39%, 1.52% and 2.23%) and PSNR (4.41%, 3.14%, 0.91% and 1.31%) than the proposed MBRT, RTNLF-1, RTNLF-2 and RBAF methods, while the RTNLF-1 and 2 methods outperform the NSST-NADF approach in terms of edge preservation performance. Moreover, based on the comparative MVR analysis shown in Table A.2, it is observed that the higher averaged MVR value (22.42) achieved by the proposed NSST-NLNADF approach shows its superiority over the other proposed MBRT (21.12), RTNLF-1 (21.98), RTNLF-2 (22.17), RBAF (22.23) and NSST-NADF (21.95). In view of the above conclusions, it is finally stated that the work on denoising methods presented in the thesis contributed significantly toward the state-of-art of denoising of the US images.

8.1.5 Proposed hybrid edge-based active contour method with KFCM

Most of the segmentation methods used for extracting the boundaries of a region or object of interest in the US images are thresholding and active contour based approaches. All of these require extensive manual intervention. Thus, in this part of the thesis, two hybrid

EBACM with the KFCM_S1 and KFCM_S2 clustering approaches, i.e. EBACM-KFCM_S1 and EBACM-KFCM_S2, are proposed that utilize both the features of EBACM using distance regularized level set evolution and KFCM approaches.

These proposed EBACM-KFCM_S1 and EBACM-KFCM_S2 segmentation methods use kernel fuzzy clustering to initialize the counter, which propagates toward the desired object's boundaries against the manual initialization in case of traditional active contour methods. The proposed methods estimate the contour propagation controlling parameters automatically from the results of KFCM_S1 and KFCM_S2, individually. From the subjective analysis, it is found that the segmented regions extracted by the proposed approaches are close to the manually delineated region. Experimental results shown in Table B.1 illustrate that the proposed EBACM-KFCM_S1 (92.91%, 86.75%, 92.88%) shows a significant improvement in terms of averaged segmentation ACC, JSI and DC values, respectively, on the US images as compared to the FCM_S1 (90.71%, 84.45%, 91.26%), FCM_S2 (91.1%, 84.96%, 91.55%), KFCM_S1 (91.41%, 85.77%, 92.25%), KFMC_S2 (92.36%, 86.26%, 92.60%), GAC (83.32%, 76.58%, 86.26%), ACMRSF (89.27%, 81.01%, 89.09%) and EBACM (92.31%, 85.81%, 92.27%) methods. It also takes much less time to segment the images than the others. Moreover, the proposed EBACM-KFCM_S2 approach also outperforms the proposed EBACM-KFCM_S1 approach by achieving higher averaged ACC (93.15%), JSI (87.63%) and DC (93.26%) against the 92.91%, 86.75% and 92.88%, respectively. Thus, it is concluded from these results that the proposed segmentation methods outperform all other state-of-art methods in terms of accurate extraction of the object boundaries of interest.

8.1.6 Proposed hybrid edge-based active contour method with GKFCM

In the last part of this work, two efficient hybrid region-based segmentation methods, i.e. RBACM-GKFCM_S1 and RBACM-GKFCM_S2 are proposed using the Gaussian kernel fuzzy clustering. These proposed segmentation methods utilize the features of the RBACM approach driven using the RSF energy function and the GKFCM. Because of incorporating the fuzzy membership function, the proposed methods are able to overcome the problem of contour initialization and to estimate the curve evolution controlling parameters. These proposed approaches start with the GKFCM and then the results of the clustering approach are utilized for initializing the curve applied to the RBACM approach. It is observed that the proposed approaches use the intensity information in local regions of the image to propagate the contour toward the object's boundary as against the global region of RBACM approach.

From the quantitative evaluation and analysis of the experimental results shown in chapter 7, it is observed that the proposed RBACM-GKFCM_S1 and RBACM-GKFCM_S2 approaches outperform the other existing methods mentioned in chapter 7. Further, another comparative analysis is presented among all the proposed segmentation approaches and

listed in Table B.1. Based on these results, it is observed that the proposed RBACM-GKFCM_S1 approach gains higher averaged ACC, JSI, DC and lower HD values (93.47%, 87.60%, 93.34% and 2.8658) against the EBACM-KFCM_S1 (92.91%, 86.75%, 92.88% and 3.0125) and EBACM-KFCM_S2 (93.15%, 87.63%, 93.26% and 2.9615). These results show the superiority of the proposed RBACM-GKFCM_S1 over the other existing methods, while the second proposed RBACM-GKFCM_S2 outperforms the RBACM-GKFCM_S1 approach by providing higher performance measures (93.58%, 87.72%, 93.45%) against the ACC, JSI and DC (93.47%, 87.60% and 93.34%), respectively, estimated by the RBACM-GKFCM_S1.

Finally, it is stated that the developed methods such as MBRT, RTNLF-1, RTNLF-2, RBAF, NSST-NADF and NSST-NLNADF for denoising of the US images and the EBACM-KFCM_S1, EBACM-KFCM_S2, RBACM-GKFCM_S1 and RBACM-GKFCM_S2 used for the segmentation of the US medical images contributed significantly toward the state-of-art of denoising and segmentation of the US images and synthetic images, too.

8.2 Scope for the Future Work

Although the present work could contribute in the area of the noise reduction and segmentation, following suggestions are made for future work in this area:

(1) The proposed denoising work resulted in the preservation of more edges, which may be utilized to improve the performance of several image processing tasks such as segmentation, registration, classification and fusion.

(2) In this study, the present segmentation methods use Gaussian kernel fuzzy clustering to initialize the contour. The performance of these proposed approaches may be analyzed by the other initialization technique such as thresholding.

(3) The research work was carried out on 2D US images as 3D datasets were not available. In future, a 3D model may be developed.

(4) The performance and efficiency of the proposed methods may be analyzed on image datasets acquired from the different medical imaging modalities.

(5) After extracting the particular abnormalities in the US images, based on its both imaging features and anatomical locations, a classification system may be developed.

(6) The denoised images obtained by the proposed methods may be validated by the expert radiologists by implementing on large database.

(7) It would still be a wonderful idea to develop an expert system that may assist the radiologists in taking decisions.

International Journals

[1] Deep Gupta, R.S. Anand and Barjeev Tyagi, " A hybrid segmentation method based on Gaussian kernel fuzzy clustering and region based active contour model for ultrasound medical images," *Biomedical Signal Processing and Control*, *Elsevier*, vol. 16, pp. 98-112, 2015.

[2] Deep Gupta, R.S. Anand and Barjeev Tyagi, "Speckle filtering of ultrasound images using a modified nonlinear diffusion model in nonsubsampled shearlet domain," *IET Image Processing*, 2014, doi: 10.1049/iet-ipr.2014.0330.

[3] Deep Gupta, R.S. Anand and Barjeev Tyagi, "Despeckling of ultrasound medical images using nonlinear adaptive anisotropic diffusion in nonsubsampled shearlet domain," *Biomedical Signal Processing and Control*, *Elsevier,* vol. 14, pp. 55-65, 2014.

[4] Deep Gupta, R.S. Anand and Barjeev Tyagi, "Ripplet domain non-linear filtering for speckle reduction in ultrasound medical images," *Biomedical Signal Processing and Control*, *Elsevier,* vol. 10, pp. 79-91, 2014.

[5] Deep Gupta, R.S. Anand and Barjeev Tyagi, "Despeckling of ultrasound images of bone fracture using M-band ridgelet transform," *Optik-International Journal for Light and Electron Optics*, *Elsevier,* vol. 125, no. 3, pp 1417-1422, 2014.

[6] Deep Gupta, R.S. Anand and Barjeev Tyagi, "Edge preserved enhancement of medical images using adaptive fusion based denoising by shearlet transform and total variation algorithm," *Journal of Electronic Imaging, SPIE,* vol. 22, no. 4, pp.1-16, 2013.

[7] Deep Gupta, R.S. Anand and Barjeev Tyagi, "Despeckling of ultrasound medical images using ripplet domain non-linear filtering," *Signal, Image and Video Processing, Springer,* 2013, doi 10.1007/s11760-013-0540-4.

[8] Deep Gupta, R.S. Anand and Barjeev Tyagi, "A hybrid segmentation using kernel fuzzy clustering and distance regularized level set approach for ultrasound medical images," IET Image Processing, (Under review).

Book Chapter

[9] Deep Gupta, R.S. Anand and Barjeev Tyagi, "Despeckling of ultrasound images of bone fracture using RADWT based non-linear filtering," *Lecture Notes in Electrical Engineering*, ed: Springer Netherlands. pp. 697-711, 2014, BOOK ISBN: 978-94-007-6817-8.

International Conferences

[10] Deep Gupta, R.S. Anand and Barjeev Tyagi, "Enhancement of medical ultrasound images using multiscale discrete shearlet transform based thresholding," in *Proceedings: IEEE International Symposium of Electronic, System and Design*, pp. 286-290, Dec. 19-22, 2012, BESU Howrah, India.

[11] Deep Gupta, R.S. Anand and Barjeev Tyagi, " Enhancement of medical ultrasound images using non-linear filtering based on rational-dilation wavelet transform," in *Proceedings: International Conference on Signal Processing and Imaging Engineering*, pp. 615-620, Oct.24-26, 2012, San Francisco, USA.

[1] Abd-Elmoniem, K.Z., Youssef, A.B.M., and Kadah, Y.M., "Real-time speckle reduction and coherence enhancement in ultrasound imaging via nonlinear anisotropic diffusion," *IEEE Transactions on Biomedical Engineering,* vol. 49, no. 9, pp. 997-1014, 2002.

[2] Abdel-Dayem, A. and El-Sakka, M., "Carotid artery ultrasound image segmentation using fuzzy region growing," in *Image Analysis and Recognition*. vol. 3656, M. Kamel and A. Campilho, Eds., ed: Springer Berlin Heidelberg, pp. 869-878, 2005.

[3] Abrahim, B.A. and Kadah, Y., "Speckle noise reduction method combining total variation and wavelet shrinkage for clinical ultrasound imaging," In *Proceedings: 1st Middle East Conference on Biomedical Engineering*, pp. 80-83, 2011.

[4] Acharya, T. and Ray, A.K., "Image segmentation," in *Image Processing*, ed: John Wiley & Sons, Inc., pp. 131-156, 2005.

[5] Achim, A., Bezerianos, A., and Tsakalides, P., "Novel bayesian multiscale method for speckle removal in medical ultrasound images," *IEEE Transactions on Medical Imaging,* vol. 20, no. 8, pp. 772-783, 2001.

[6] Achim, A., Tsakalides, P., and Bezerianos, A., "SAR image denoising via Bayesian wavelet shrinkage based on heavy-tailed modeling," *IEEE Transactions on Geoscience and Remote Sensing,* vol. 41, no. 8, pp. 1773-1784, 2003.

[7] Acton, S.T., "Deconvolutional speckle reducing anisotropic diffusion," In *Proceedings: IEEE International Conference on Image Processing*, pp. 5-8, 2005.

[8] Adams, R. and Bischof, L., "Seeded region growing," *IEEE Transactions on Pattern Analysis and Machine Intelligence,* vol. 16, no. 6, pp. 641-647, 1994.

[9] Ahmed, M.N., Yamany, S.M., Mohamed, N., Farag, A.A., and Moriarty, T., "A modified fuzzy c-means algorithm for bias field estimation and segmentation of MRI data," *IEEE Transactions on Medical Imaging,* vol. 21, no. 3, pp. 193-199, 2002.

[10] Aili, W., Ye, Z., Shaoliang, M., and Mingji, Y., "Image denoising method based on curvelet transform," In *Proceedings: 3rd IEEE Conference on Industrial Electronics and Applications*, pp. 571-574, 2008.

[11] Aja-Fernández, S. and Alberola-López, C., "On the estimation of the coefficient of variation for anisotropic diffusion speckle filtering," *IEEE Transactions on Image Processing,* vol. 15, no. 9, pp. 2694-2701, 2006.

[12] Ali, S.M. and Burge, R.E., "New automatic techniques for smoothing and segmenting SAR images," *Signal Processing,* vol. 14, no. 4, pp. 335-346, 1988.

[13] Alzubi, S., Islam, N., and Abbod, M., "Multiresolution analysis using wavelet, ridgelet, and curvelet transforms for medical image segmentation," *Journal of Biomedical Imaging,* vol. 2011, pp. 1-4, 2011.

[14] Anand, C.S. and Sahambi, J.S., "Wavelet domain non-linear filtering for MRI denoising," *Magnetic Resonance Imaging,* vol. 28, no. 6, pp. 842-861, 2010.

[15] Arakeri, M. and Reddy, G.R.M., "Efficient fuzzy clustering based approach to brain tumor segmentation on MR images," in *Computational Intelligence and Information Technology*. vol. 250, V. Das and N. Thankachan, Eds., ed: Springer pp. 790-795, 2011.

[16] Awate, S.P., "Adaptive, nonparametric Markov models and information-theoretic methods for image restoration and segmentation," School of Computing, The University of Utah, 2006.

[17] Aysal, T.C. and Barner, K.E., "Rayleigh-maximum-likelihood filtering for speckle reduction of ultrasound images," *IEEE Transactions on Medical Imaging,* vol. 26, no. 5, pp. 712-727, 2007.

[18] Bamber, J.C. and Daft, C., "Adaptive filtering for reduction of speckle in ultrasonic pulse-echo images," *Ultrasonics,* vol. 24, no. 1, pp. 41-44, 1986.

[19] Basak, K., Mahadevappa, M., and Dutta, P.K., "Multiscale noise-adaptive homomorphic filtering based speckle denoising in laser speckle imaging," In *Proceedings: IEEE 4th National Conference on Computer Vision, Pattern Recognition, Image Processing and Graphics*, pp. 1-5, 2013.

[20] Bernardes, R., Maduro, C., Serranho, P., Araújo, A., Barbeiro, S., and Cunha-Vaz, J., "Improved adaptive complex diffusion despeckling filter," *Optics Express,* vol. 18, no. 23, pp. 48-59, 2010.

[21] Bernstein, R., "Adaptive nonlinear filters for simultaneous removal of different kinds of noise in images," *IEEE Transactions on Circuits and Systems,* vol. 34, no. 11, pp. 1275-1291, 1987.

[22] Beucher, S. and Meyer, F., "The morphological approach to segmentation: the watershed transformation," *Optical Engineering,* vol. 34, pp. 433-433, 1992.

[23] Beveridge, J.R., Griffith, J., Kohler, R.R., Hanson, A.R., and Riseman, E.M., "Segmenting images using localized histograms and region merging," *International Journal of Computer Vision,* vol. 2, no. 3, pp. 311-347, 1989.

[24] Bezdek, J.C. and Pal, S.K., *Fuzzy Models for Pattern Recognition*, IEEE press. New York, 1992.

[25] Bhadauria, H.S. and Dewal, M., "Medical image denoising using adaptive fusion of curvelet transform and total variation," *Computers & Electrical Engineering,* vol. 39, no. 5, pp. 1451-1460, 2013.

[26] Bhadauria, H.S. and Dewal, M.L., "Intracranial hemorrhage detection using spatial fuzzy c-mean and region-based active contour on brain CT imaging," *Signal, Image and Video Processing,* vol. 8, no. 2, pp. 357-364, 2014.

[27] Bhoi, N. and Meher, S., "Total variation based wavelet domain filter for image denoising," In *Proceedings: 1st International Conference on Emerging Trends in Engineering and Technology*, pp. 20-25, 2008.

[28] Bhuiyan, M.I.H., Ahmad, M.O., and Swamy, M.N.S., "Spatially adaptive thresholding in wavelet domain for despeckling of ultrasound images," *IET Image Processing,* vol. 3, no. 3, pp. 147-162, 2009.

[29] Bhutada, G.G., Anand, R.S., and Saxena, S.C., "Fast adaptive learning algorithm for sub-band adaptive thresholding function in image denoising," *International Journal of Computational Intelligence Studies,* vol. 1, no. 3, pp. 227-241, 2010.

[30] Bhutada, G.G., Anand, R.S., and Saxena, S.C., "Edge preserved image enhancement using adaptive fusion of images denoised by wavelet and curvelet transform," *Digital Signal Processing,* vol. 21, no. 1, pp. 118-130, 2011.

[31] Bhutada, G.G., Anand, R.S., and Saxena, S.C., "Image enhancement by wavelet-based thresholding neural network with adaptive learning rate," *IET Image Processing,* vol. 5, no. 7, pp. 573-582, 2011.

[32] Bhutada, G.G., Anand, R.S., and Saxena, S.C., "PSO-based learning of sub-band adaptive thresholding function for image denoising," *Signal, Image and Video Processing,* vol. 6, no. 1, pp. 1-7, 2012.

[33] Black, M.J., Sapiro, G., Marimont, D.H., and Heeger, D., "Robust anisotropic diffusion," *IEEE Transactions on Image Processing,* vol. 7, no. 3, pp. 421-432, 1998.

[34] Boukerroui, D., Baskurt, A., Noble, J.A., and Basset, O., "Segmentation of ultrasound images—multiresolution 2D and 3D algorithm based on global and local statistics," *Pattern Recognition Letters,* vol. 24, no. 4–5, pp. 779-790, 2003.

[35] Bourne, R., "Image quality," in *Fundamentals of Digital Imaging in Medicine*, ed: Springer London, pp. 87-108, 2010.

[36] Brownrigg, D., "The weighted median filter," *Communications of the ACM,* vol. 27, no. 8, pp. 807-818, 1984.

[37] Buades, A., Coll, B., and Morel, J.-M., "A non-local algorithm for image denoising," In *Proceedings: IEEE Computer Society Conference on Computer Vision and Pattern Recognition*, pp. 60-65, 2005.

[38] Cai, T.T. and Silverman, B.W., "Incorporating information on neighbouring coefficients into wavelet estimation," *Sankhyā: The Indian Journal of Statistics, Series B,* pp. 127-148, 2001.

[39] Cai, T.T. and Zhou, H.H., "A data-driven block thresholding approach to wavelet estimation," *Annals of Statistics,* vol. 37, no. 2, pp. 569-595, 2009.

[40] Calderero, F. and Marques, F., "Region merging techniques using information theory statistical measures," *IEEE Transactions on Image Processing,* vol. 19, no. 6, pp. 1567-1586, 2010.

[41] Candès, E., Demanet, L., Donoho, D., and Ying, L., "Fast discrete curvelet transforms," *Multiscale Modeling & Simulation,* vol. 5, no. 3, pp. 861-899, 2006.

[42] Canny, J.F., "Finding edges and lines in images," *Massachusetts Inst. of Techical Report,* vol. 1, 1983.

[43] Cardinal, M.H., Meunier, J., Soulez, G., Maurice, R.L., Therasse, E., and Cloutier, G., "Intravascular ultrasound image segmentation: a three-dimensional fast-marching method based on gray level distributions," *IEEE Transactions on Medical Imaging,* vol. 25, no. 5, pp. 590-601, 2006.

[44] Caselles, V., Catté, F., Coll, T., and Dibos, F., "A geometric model for active contours in image processing," *Numerische Mathematik,* vol. 66, no. 1, pp. 1-31, 1993.

[45] Caselles, V., Kimmel, R., and Sapiro, G., "Geodesic active contours," *International Journal of Computer Vision,* vol. 22, no. 1, pp. 61-79, 1997.

[46] Catté, F., Lions, P., Morel, J., and Coll, T., "Image selective smoothing and edge detection by nonlinear diffusion," *SIAM Journal on Numerical Analysis,* vol. 29, no. 1, pp. 182-193, 1992.

[47] Chambolle, A., "An algorithm for total variation minimization and applications," *Journal of Mathematical Imaging and Vision,* vol. 20, no. 1, pp. 89-97, 2004.

[48] Chan, T.F. and Vese, L.A., "Active contours without edges," *IEEE Transactions on Image Processing,* vol. 10, no. 2, pp. 266-277, 2001.

[49] Chan, T.F. and Vese, L.A., "A level set algorithm for minimizing the Mumford-Shah functional in image processing," In *Proceedings: IEEE Workshop on Variational and Level Set Methods in Computer Vision*, pp. 161-168, 2001.

[50] Chang, R.-F., Wu, W.-J., Moon, W., and Chen, D.-R., "Automatic ultrasound segmentation and morphology based diagnosis of solid breast tumors," *Breast Cancer Research and Treatment,* vol. 89, no. 2, pp. 179-185, 2005.

[51] Chang, S.G., Bin, Y., and Vetterli, M., "Adaptive wavelet thresholding for image denoising and compression," *IEEE Transactions on Image Processing,* vol. 9, no. 9, pp. 1532-1546, 2000.

[52] Chang, S.G., Bin, Y., and Vetterli, M., "Spatially adaptive wavelet thresholding with context modeling for image denoising," *IEEE Transactions on Image Processing,* vol. 9, no. 9, pp. 1522-1531, 2000.

[53] Chao, S.-M. and Tsai, D.-M., "An improved anisotropic diffusion model for detail- and edge-preserving smoothing," *Pattern Recognition Letters,* vol. 31, no. 13, pp. 2012-2023, 2010.

[54] Chen, C.-M., Chou, Y.-H., Chen, C.S.K., Cheng, J.-Z., Ou, Y.-F., Yeh, F.-C.*, et al.*, "Cell-competition algorithm: A new segmentation algorithm for multiple objects with irregular boundaries in ultrasound images," *Ultrasound in Medicine & Biology,* vol. 31, no. 12, pp. 1647-1664, 2005.

[55] Chen, C.-M., Chou, Y.-H., Han, K.-C., Hung, G.-S., Tiu, C.-M., Chiou, H.-J.*, et al.*, "Breast lesions on sonograms: computer-aided diagnosis with nearly setting-independent features and artificial neural networks 1," *Radiology,* vol. 226, no. 2, pp. 504-514, 2003.

[56] Chen, G., Bui, T., and Krzyżak, A., "Image denoising with neighbour dependency and customized wavelet and threshold," *Pattern Recognition,* vol. 38, no. 1, pp. 115-124, 2005.

[57] Chen, X., Deng, C., and Wang, S., "Shearlet-based adaptive shrinkage threshold for image denoising," In *Proceedings: International Conference on E-Business and E-Government*, pp. 1616-1619, 2010.

[58] Chen, X., Sun, H., and Deng, C., "Image denoising algorithm using adaptive shrinkage threshold based on shearlet transform," In *Proceedings: 4th International Conference on Frontier of Computer Science and Technology*, pp. 254-257, 2009.

[59] Cheng, H., Shan, J., Ju, W., Guo, Y., and Zhang, L., "Automated breast cancer detection and classification using ultrasound images: A survey," *Pattern Recognition,* vol. 43, no. 1, pp. 299-317, 2010.

[60] Cheng, S., Qiguang, M., and Pengfei, X., "A novel algorithm of remote sensing image fusion based on shearlets and PCNN," *Neurocomputing,* vol. 117, no. 6, pp. 47-53, 2013.

[61] Chenyang, X. and Prince, J.L., "Snakes, shapes, and gradient vector flow," *IEEE Transactions on Image Processing,* vol. 7, no. 3, pp. 359-369, 1998.

[62] Chu, C.-C. and Aggarwal, J.K., "The integration of image segmentation maps using region and edge information," *IEEE Transactions on Pattern Analysis and Machine Intelligence,* vol. 15, no. 12, pp. 1241-1252, 1993.

[63] Chuang, K.-S., Tzeng, H.-L., Chen, S., Wu, J., and Chen, T.-J., "Fuzzy c-means clustering with spatial information for image segmentation," *Computerized Medical Imaging and Graphics,* vol. 30, no. 1, pp. 9-15, 2006.

[64] Chunming, L., Chenyang, X., Changfeng, G., and Fox, M.D., "Level set evolution without re-initialization: a new variational formulation," In *Proceedings: IEEE Conference on Computer Vision and Pattern Recognition*, pp. 430-436 vol. 1, 2005.

[65] Chunming, L., Chenyang, X., Changfeng, G., and Fox, M.D., "Distance regularized level set evolution and its application to image segmentation," *IEEE Transactions on Image Processing,* vol. 19, no. 12, pp. 3243-3254, 2010.

[66] Chunming, L., Chiu-Yen, K., Gore, J.C., and Zhaohua, D., "Minimization of region-scalable fitting energy for image segmentation," *IEEE Transactions on Image Processing,* vol. 17, no. 10, pp. 1940-1949, 2008.

[67] Cohen, L.D., "On active contour models and balloons," *CVGIP: Image Understanding,* vol. 53, no. 2, pp. 211-218, 1991.

[68] Cohen, L.D. and Cohen, I., "Finite-element methods for active contour models and balloons for 2-D and 3-D images," *IEEE Transactions on Pattern Analysis and Machine Intelligence,* vol. 15, no. 11, pp. 1131-1147, 1993.

[69] Coupe, P., Hellier, P., Kervrann, C., and Barillot, C., "Nonlocal means-based speckle filtering for ultrasound images," *IEEE Transactions on Image Processing,* vol. 18, no. 10, pp. 2221-2229, 2009.

[70] Crouse, M.S., Nowak, R.D., and Baraniuk, R.G., "Wavelet-based statistical signal processing using hidden Markov models," *IEEE Transactions on Signal Processing,* vol. 46, no. 4, pp. 886-902, 1998.

[71] Dabov, K., Foi, A., Katkovnik, V., and Egiazarian, K., "Image denoising by sparse 3-D transform-domain collaborative filtering," *IEEE Transactions on Image Processing,* vol. 16, no. 8, pp. 2080-2095, 2007.

[72] Dabov, K., Foi, R., Katkovnik, V., and Egiazarian, K., "BM3D image denoising with shape-adaptive principal component analysis," In *Proceedings: Workshop on Signal Processing with Adaptive Sparse Structured Representations*, 2009.

[73] Deledalle, C.-A., Denis, L., and Tupin, F., "Iterative weighted maximum likelihood denoising with probabilistic patch-based weights," *IEEE Transactions on Image Processing,* vol. 18, no. 12, pp. 2661-2672, 2009.

[74] Dhawan, A.P., *Medical Image Analysis*, Wiley New York, 2003.

[75] Dhawan, A.P., Huang, H., and Kim, D.-S., *Principles and Advanced Methods in Medical Imaging and Image Analysis*, World Scientific. Singapore, 2008.

[76] Djemal, K., "Speckle reduction in ultrasound images by minimization of total variation," In *Proceedings: IEEE International Conference on Image Processing*, pp. 357-360, 2005.

[77] Do, M.N. and Vetterli, M., "The finite ridgelet transform for image representation," *IEEE Transaction on Image Processing,* vol. 12, no. 1, pp. 16-28, 2003.

[78] Do, M.N. and Vetterli, M., "The contourlet transform: an efficient directional multiresolution image representation," *IEEE Transactions on Image Processing,* vol. 14, no. 12, pp. 2091-2106, 2005.

[79] Donoho, D.L., "De-noising by soft-thresholding," *IEEE Transactions on Information Theory,* vol. 41, no. 3, pp. 613-627, 1995.

[80] Donoho, D.L. and Johnstone, I.M., "Adapting to unknown smoothness via wavelet shrinkage," *Journal of the American Statistical Association,* vol. 90, no. 432, pp. 1200-1224, 1995.

[81] Donoho, D.L., Johnstone, I.M., Kerkyacharian, G., and Picard, D., "Wavelet shrinkage: asymptopia?," *Journal of the Royal Statistical Society. Series B (Methodological),* pp. 301-369, 1995.

[82] Donoho, D.L. and Johnstone, J.M., "Ideal spatial adaptation by wavelet shrinkage," *Biometrika,* vol. 81, no. 3, pp. 425-455, 1994.

[83] Easley, G.R. and Labate, D., "Image processing using shearlets," *Shearlets,* pp. 283-325, 2012.

[84] Easley, G.R., Labate, D., and Colonna, F., "Shearlet-based total variation diffusion for denoising," *IEEE Transactions on Image Processing,* vol. 18, no. 2, pp. 260-268, 2009.

[85] Easley, G.R., Labate, D., and Lim, W.-Q., "Sparse directional image representations using the discrete shearlet transform," *Applied and Computational Harmonic Analysis,* vol. 25, no. 1, pp. 25-46, 2008.

[86] Fan, J., Yau, D.K., Elmagarmid, A.K., and Aref, W.G., "Automatic image segmentation by integrating color-edge extraction and seeded region growing," *IEEE Transactions on Image Processing,* vol. 10, no. 10, pp. 1454-1466, 2001.

[87] Fan, J., Zeng, G., Body, M., and Hacid, M.-S., "Seeded region growing: an extensive and comparative study," *Pattern Recognition Letters,* vol. 26, no. 8, pp. 1139-1156, 2005.

[88] Fan, Z., Yang Mo, Y., Koh Liang, M., and Yongmin, K., "Nonlinear diffusion in laplacian pyramid domain for ultrasonic speckle reduction," *IEEE Transactions on Medical Imaging,* vol. 26, no. 2, pp. 200-211, 2007.

[89] Fan, Z., Yang Mo, Y., Yongmin, K., Lichen, Z., and Koh Liang, M., "Multiscale nonlinear diffusion and shock filter for ultrasound image enhancement," In *IEEE Computer Society Conference on Computer Vision and Pattern Recognition*, pp. 1972-1977, 2006.

[90] Farag, A.A., "Edge-based image segmentation," *Remote Sensing Reviews,* vol. 6, no. 1, pp. 95-121, 1992.

[91] Felzenszwalb, P.F. and Huttenlocher, D.P., "Efficient graph-based image segmentation," *International Journal of Computer Vision,* vol. 59, no. 2, pp. 167-181, 2004.

[92] Fodor, I.K. and Kamath, C., "Denoising through wavelet shrinkage: an empirical study," *Journal of Electronic Imaging,* vol. 12, no. 1, pp. 151-160, 2003.

[93] Foi, A., Katkovnik, V., and Egiazarian, K., "Pointwise shape-adaptive DCT for high-quality denoising and deblocking of grayscale and color images," *IEEE Transactions on*

Image Processing, vol. 16, no. 5, pp. 1395-1411, 2007.

[94] Forouzanfar, M., Moghaddam, H., and Gity, M., "A new multiscale Bayesian algorithm for speckle reduction in medical ultrasound images," *Signal, Image and Video Processing,* vol. 4, no. 3, pp. 359-375, 2010.

[95] Forouzanfar, M. and Moghaddam, H.A., "Ultrasound speckle suppression using heavy-tailed distributions in the dual-tree complex wavelet domain," In *Proceedings: International Waveform Diversity and Design Conference*, pp. 65-68, 2007.

[96] Frost, V.S., Stiles, J.A., Shanmugan, K.S., and Holtzman, J., "A model for radar images and its application to adaptive digital filtering of multiplicative noise," *IEEE Transactions on Pattern Analysis and Machine Intelligence,* vol. PAMI-4, no. 2, pp. 157-166, 1982.

[97] Fukuda, S. and Hirosawa, H., "Smoothing effect of wavelet-based speckle filtering: the Haar basis case," *IEEE Transactions on Geoscience and Remote Sensing,* vol. 37, no. 2, pp. 1168-1172, 1999.

[98] Gao, G., "Image denoising by non-subsampled shearlet domain multivariate model and its method noise thresholding," *Optik - International Journal for Light and Electron Optics,* vol. 124, no. 22, pp. 5756-5760, 2013.

[99] Gao, H.-Y., "Wavelet shrinkage denoising using the non-negative garrote," *Journal of Computational and Graphical Statistics,* vol. 7, no. 4, pp. 469-488, 1998.

[100] Gilboa, G., Sochen, N., and Zeevi, Y.Y., "Image enhancement and denoising by complex diffusion processes," *IEEE Transactions on Pattern Analysis and Machine Intelligence,* vol. 26, no. 8, pp. 1020-1036, 2004.

[101] Goel, P., Sinha, H.P., and Singh, H., "Ultrasonic image denoising using multiscale ridgelet transform with hard and neighcoeff thresholding," *International Journal of Computer & Communication Technology,* vol. 2, no. 7, pp. 65-70, 2011.

[102] Gong, L., Ng, L., Pathak, S.D., Tutar, I., Cho, P.S., Haynor, D.R.*, et al.*, "Prostate ultrasound image segmentation using level set-based region flow with shape guidance," In *Proceedings: Medical Imaging*, pp. 1648-1657, 2005.

[103] Gonzalez, R.C. and Woods, R.E., *Digital Image Processing*, Prentice-Hall India, 2001.

[104] Goodman, J.W., "Some fundamental properties of speckle," *Journal of the Optical Society of America,* vol. 66, no. 11, pp. 1145-1150, 1976.

[105] Guo, H., Odegard, J.E., Lang, M., Gopinath, R.A., Selesnick, I.W., and Burrus, C.S., "Wavelet based speckle reduction with application to SAR based ATD/R," In *Proceedings: IEEE International Conference Image Processing*, pp. 75-79, 1994.

[106] Guo, K., Kutyniok, G., and Labate, D., "Sparse multidimensional representations using anisotropic dilation and shear operators," in *Wavelets and Splines* G. Chen and M. J. Lai, Eds., ed Nashville, TN: Nashboro Press, pp. 189-201, 2006.

[107] Guo, K. and Labate, D., "Optimally sparse multidimensional representation using shearlets," *SIAM journal on mathematical analysis,* vol. 39, no. 1, pp. 298-318, 2007.

[108] Guofang, X., Brady, M., Noble, J.A., and Yongyue, Z., "Segmentation of ultrasound B-mode images with intensity inhomogeneity correction," *IEEE Transactions on Medical Imaging,* vol. 21, no. 1, pp. 48-57, 2002.

[109] Gupta, D., Anand, R., and Tyagi, B., "Enhancement of medical ultrasound images using non-linear filtering based on rational-dilation wavelet transform," In *Proceedings: World Congress on Engineering and Computer Science*, 2012.

[110] Gupta, D., Anand, R.S., and Tyagi, B., "Enhancement of medical ultrasound images using multiscale discrete shearlet transform based thresholding," In *Proceedings: IEEE International Symposium on Electronic System Design*, pp. 286-290, 2012.

[111] Gupta, S., Chauhan, R.C., and Sexana, S.C., "Wavelet-based statistical approach for speckle reduction in medical ultrasound images," *Medical and Biological Engineering and Computing,* vol. 42, no. 2, pp. 189-192, 2004.

[112] Hajiaboli, M.R., "An anisotropic fourth-order diffusion filter for image noise removal," *International Journal of Computer Vision,* vol. 92, no. 2, pp. 177-191, 2011.

[113] Hao, X., Gao, S., and Gao, X., "A novel multiscale nonlinear thresholding method for ultrasonic speckle suppressing," *IEEE Transactions on Medical Imaging,* vol. 18, no. 9, pp. 787-794, 1999.

[114] Haris, K., Efstratiadis, S.N., Maglaveras, N., and Katsaggelos, A.K., "Hybrid image segmentation using watersheds and fast region merging," *IEEE Transactions on Image Processing,* vol. 7, no. 12, pp. 1684-1699, 1998.

[115] Haris, K., Efstratiadis, S.N., Maglaveras, N., and Pappas, C., "Hybrid image segmentation using watersheds," In *Proceedinds: Visual Communications and Image Processing*, pp. 1140-1151, 1996.

[116] Hassan, M., Chaudhry, A., Khan, A., and Kim, J.Y., "Carotid artery image segmentation using modified spatial fuzzy c-means and ensemble clustering," *Computer Methods and Programs in Biomedicine,* vol. 108, no. 3, pp. 1261-1276, 2012.

[117] Henstock, P.V. and Chelberg, D.M., "Automatic gradient threshold determination for edge detection," *IEEE Transactions on Image Processing,* vol. 5, no. 5, pp. 784-787, 1995.

[118] Hou, B., Zhang, X., Bu, X., and Feng, H., "SAR image despeckling based on nonsubsampled shearlet transform," *IEEE Journal of Selected Topics in Applied Earth Observations and Remote Sensing,* vol. 5, no. 3, pp. 809-823, 2012.

[119] Hu, Q., He, X., and Zhou, J., "Multi-scale edge detection with bilateral filtering in spiral architecture," In *Proceedings: Pan-Sydney Area Workshop on Visual Information Processing*, pp. 29-32, 2004.

[120] Huang, Q.-H., Lee, S.-Y., Liu, L.-Z., Lu, M.-H., Jin, L.-W., and Li, A.-H., "A robust graph-based segmentation method for breast tumors in ultrasound images," *Ultrasonics,* vol. 52, no. 2, pp. 266-275, 2012.

[121] Huang, Q., Bai, X., Li, Y., Jin, L., and Li, X., "Optimized graph-based segmentation for ultrasound images," *Neurocomputing,* vol. 129, pp. 216-224, 2014.

[122] Huang, T., Yang, G., and Tang, G., "A fast two-dimensional median filtering algorithm," *IEEE Transactions on Acoustics, Speech and Signal Processing,* vol. 27, no. 1, pp. 13-18, 1979.

[123] Huang, Y.-L. and Chen, D.-R., "Watershed segmentation for breast tumor in 2-D sonography," *Ultrasound in Medicine & Biology,* vol. 30, no. 5, pp. 625-632, 2004.

[124] Huttenlocher, D.P., Klanderman, G.A., and Rucklidge, W.J., "Comparing images using the Hausdorff distance," *IEEE Transactions on Pattern Analysis and Machine Intelligence,* vol. 15, no. 9, pp. 850-863, 1993.

[125] İşcan, Z., Kurnaz, M.N., Dokur, Z., and Ölmez, T., "Ultrasound image segmentation by using wavelet transform and self organizing neural network," *Neural Information Processing-Letters and Reviews,* vol. 10, no. 8-9, pp. 183-191, 2006.

[126] Izzetoglu, M., Devaraj, A., Bunce, S., and Onaral, B., "Motion artifact cancellation in NIR spectroscopy using Wiener filtering," *IEEE Transactions on Biomedical Engineering,* vol. 52, no. 5, pp. 934-938, 2005.

[127] Ji, Z., Chen, Q., Sun, Q.-S., and Xia, D.-S., "A moment-based nonlocal-means algorithm for image denoising," *Information Processing Letters,* vol. 109, no. 23, pp. 1238-1244, 2009.

[128] Jianwei, M. and Plonka, G., "Combined curvelet shrinkage and nonlinear anisotropic diffusion," *IEEE Transactions on Image Processing,* vol. 16, no. 9, pp. 2198-2206, 2007.

[129] Kang, J., Min, L., Luan, Q., Li, X., and Liu, J., "Novel modified fuzzy c-means algorithm with applications," *Digital Signal Processing,* vol. 19, no. 2, pp. 309-319, 2009.

[130] Kannan, S.R., Sathya, A., Ramathilagam, S., and Devi, R., "Novel segmentation algorithm in segmenting medical images," *Journal of Systems and Software,* vol. 83, no. 12, pp. 2487-2495, 2010.

[131] Kapoor, A., Pandey, P., and Biswas, K., "Fuzzy rule based document image segmentation for component labeling," In *Proceedings: 3rd National Conference on Computer Vision, Pattern Recognition, Image Processing and Graphics*, pp. 11-14, 2011.

[132] Karaman, M., Kutay, M.A., and Bozdagi, G., "An adaptive speckle suppression filter for medical ultrasonic imaging," *IEEE Transactions on Medical Imaging,* vol. 14, no. 2, pp. 283-292, 1995.

[133] Kass, M., Witkin, A., and Terzopoulos, D., "Snakes: Active contour models," *International Journal of Computer Vision,* vol. 1, no. 4, pp. 321-331, 1988.

[134] Kichenassamy, S., Kumar, A., Olver, P., Tannenbaum, A., and Yezzi, A., "Gradient flows and geometric active contour models," In *Proceedings: 5th International Conference on Computer Vision*, pp. 810-815, 1995.

[135] Kichenassamy, S., Kumar, A., Olver, P., Tannenbaum, A., and Yezzi, A., Jr., "Conformal curvature flows: From phase transitions to active vision," *Archive for Rational Mechanics and Analysis,* vol. 134, no. 3, pp. 275-301, 1996.

[136] Kivanc Mihcak, M., Kozintsev, I., Ramchandran, K., and Moulin, P., "Low-complexity image denoising based on statistical modeling of wavelet coefficients," *IEEE Signal Processing Letters,* vol. 6, no. 12, pp. 300-303, 1999.

[137] Krinidis, S. and Chatzis, V., "A robust fuzzy local information c-means clustering algorithm," *IEEE Transactions on Image Processing,* vol. 19, no. 5, pp. 1328-1337, 2010.

[138] Krissian, K., Westin, C.F., Kikinis, R., and Vosburgh, K.G., "Oriented speckle reducing anisotropic diffusion," *IEEE Transactions on Image Processing,* vol. 16, no. 5, pp. 1412-1424, 2007.

[139] Kuan, D.T., Sawchuk, A., Strand, T.C., and Chavel, P., "Adaptive restoration of images with speckle," *IEEE Transactions on Acoustics, Speech and Signal Processing,* vol. 35, no. 3, pp. 373-383, 1987.

[140] Kuan, D.T., Sawchuk, A.A., Strand, T.C., and Chavel, P., "Adaptive noise smoothing filter for images with signal-dependent noise," *IEEE Transactions on Pattern Analysis and Machine Intelligence,* vol. PAMI-7, no. 2, pp. 165-177, 1985.

[141] Labate, D., Lim, W.-Q., Kutyniok, G., and Weiss, G., "Sparse multidimensional representation using shearlets," In *Proceedings: SPIE*, pp. 254-262, 2005.

[142] Lee, J.-S., "Digital image enhancement and noise filtering by use of local statistics," *IEEE Transactions on Pattern Analysis and Machine Intelligence,* vol. PAMI-2, no. 2, pp. 165-168, 1980.

[143] Lee, J.-S., "Speckle analysis and smoothing of synthetic aperture radar images," *Computer Graphics and Image Processing,* vol. 17, no. 1, pp. 24-32, 1981.

[144] Lee, J.-S., "Speckle suppression and analysis for synthetic aperture radar images," *Optical Engineering,* vol. 25, no. 5, pp. 636-643, 1986.

[145] Lee, M.-S., Yen, C.-L., and Ueng, S.-K., "Speckle reduction with edges preservation for ultrasound images: using function spaces approach," *IET Image Processing,* vol. 6, no. 7, pp. 813-821, 2012.

[146] Leroy, B., Herlin, I., and Cohen, L., "Multi-resolution algorithms for active contour models," in *Lecture Notes in Control and Information Sciences*. vol. 219, M.-O. Berger,

R. Deriche, I. Herlin, J. Jaffré, and J.-M. Morel, Eds., ed: Springer Berlin Heidelberg, pp. 58-65, 1996.

[147] Li, B.N., Chui, C.K., Chang, S., and Ong, S.H., "Integrating spatial fuzzy clustering with level set methods for automated medical image segmentation," *Computers in Biology and Medicine,* vol. 41, no. 1, pp. 1-10, 2011.

[148] Li, P.-C. and O'Donnell, M., "Elevational spatial compounding," *Ultrasonic Imaging,* vol. 16, no. 3, pp. 176-189, 1994.

[149] Li, Y., Chen, R.-m., and Liang, S., "A new image denoising method based on shearlet shrinkage and improved total variation," *Intelligent Science and Intelligent Data Engineering,* pp. 382-388, 2012.

[150] Liew, A.W.C., Leung, S.H., and Lau, W.H., "Fuzzy image clustering incorporating spatial continuity," *IEE Proceedings - Vision, Image and Signal Processing,* vol. 147, no. 2, pp. 185-192, 2000.

[151] Lim, W.-Q., "The discrete shearlet transform: A new directional transform and compactly supported shearlet frames," *IEEE Transactions on Image Processing,* vol. 19, no. 5, pp. 1166-1180, 2010.

[152] Liu, G., Zeng, X., Tian, F., Li, Z., and Chaibou, K., "Speckle reduction by adaptive window anisotropic diffusion," *Signal Processing,* vol. 89, no. 11, pp. 2233-2243, 2009.

[153] Liu, S., Shi, M., Hu, S., and Xiao, Y., "Synthetic aperture radar image de-noising based on shearlet transform using the context-based model," *Physical Communication,* 2014.

[154] Liu, X., Liu, J., Xu, X., Chun, L., Tang, J., and Deng, Y., "A robust detail preserving anisotropic diffusion for speckle reduction in ultrasound images," *BMC Genomics,* vol. 12, no. Suppl 5, p. S14, 2011.

[155] Loizou, C.P., Pattichis, C.S., Christodoulou, C.I., Istepanian, R.S.H., Pantziaris, M., and Nicolaides, A., "Comparative evaluation of despeckle filtering in ultrasound imaging of the carotid artery," *IEEE Transactions on Ultrasonics, Ferroelectrics and Frequency Control,* vol. 52, no. 10, pp. 1653-1669, 2005.

[156] Long, C., Chen, C.L.P., and Mingzhu, L., "A multiple-kernel fuzzy C-means algorithm for image segmentation," *IEEE Transactions on Systems, Man, and Cybernetics, Part B: Cybernetics,* vol. 41, no. 5, pp. 1263-1274, 2011.

[157] Loupas, T., McDicken, W.N., and Allan, P.L., "An adaptive weighted median filter for speckle suppression in medical ultrasonic images," *IEEE Transactions on Circuits and Systems,* vol. 36, no. 1, pp. 129-135, 1989.

[158] Lutz, H.T. and Soldner, R., "Basic physics of ultrasound," in *WHO Manual of Diagnostic Ultrasound*. vol. 1, H. Lutz and E. Buscarini, Eds., 2 ed: Gutenberg Press Ltd., 2011.

[159] Ma, J. and Fenn, M., "Combined complex ridgelet shrinkage and total variation minimization," *SIAM Journal on Scientific Computing,* vol. 28, no. 3, pp. 984-1000, 2006.

[160] Maduro, C., Serranho, P., Santos, T., Rodrigues, P., Cunha-Vaz, J., and Bernardes, R., "OCT noise despeckling using 3D nonlinear complex diffusion filter," in *Technologies for Medical Sciences*. vol. 1, R. M. Natal Jorge, J. M. R. S. Tavares, M. Pinotti Barbosa, and A. P. Slade, Eds., ed: Springer Netherlands, pp. 141-157, 2012.

[161] Malladi, R., Sethian, J.A., and Vemuri, B.C., "Shape modeling with front propagation: a level set approach," *IEEE Transactions on Pattern Analysis and Machine Intelligence,* vol. 17, no. 2, pp. 158-175, 1995.

[162] Manjón, J.V., Carbonell-Caballero, J., Lull, J.J., García-Martí, G., Martí-Bonmatí, L., and Robles, M., "MRI denoising using non-local means," *Medical Image Analysis,* vol. 12, no. 4, pp. 514-523, 2008.

[163] Marshall, S., "New direct design method for weighted order statistic filters," *Proceedings: IEE Vision, Image and Signal Processing,* vol. 151, no. 1, pp. 1-8, 2004.

[164] Mateo, J.L. and Fernández-Caballero, A., "Finding out general tendencies in speckle noise reduction in ultrasound images," *Expert Systems with Applications,* vol. 36, no. 4, pp. 7786-7797, 2009.

[165] Miao, Q.-g., Shi, C., Xu, P.-f., Yang, M., and Shi, Y.-b., "A novel algorithm of image fusion using shearlets," *Optics Communications,* vol. 284, no. 6, pp. 1540-1547, 2011.

[166] Michailovich, O.V. and Tannenbaum, A., "Despeckling of medical ultrasound images," *IEEE Transactions on Ultrasonics, Ferroelectrics and Frequency Control,* vol. 53, no. 1, pp. 64-78, 2006.

[167] Mittal, D., "Extraction and classification of diagnostic features from ultrasound liver images," PhD Thesis, Electrical Engineering Department, IIT Roorkee, 2011.

[168] Mittal, D., Kumar, V., Saxena, S., Khandelwal, N., and Kalra, N., "Enhancement of the ultrasound images by modified anisotropic diffusion method," *Medical & Biological Engineering & Computing,* vol. 48, no. 12, pp. 1281-1291, 2010.

[169] Mumford, D. and Shah, J., "Optimal approximations by piecewise smooth functions and associated variational problems," *Communications on Pure and Applied Mathematics,* vol. 42, no. 5, pp. 577-685, 1989.

[170] Nagao, M. and Matsuyama, T., "Edge preserving smoothing," *Computer Graphics and Image Processing,* vol. 9, no. 4, pp. 394-407, 1979.

[171] Nasholm, S.P., "Ultrasound beams for enhanced image quality," Department of Circulation and Medical Imaging, Faculty of Medicine, Norwegian University of Science and Technology, 2008.

[172] Nasholm, S.P., Hansen, R., Masoy, S.E., and Standal, O., "Reverberation suppression using SURF as an alternative to second harmonic," In *Proceedings: IEEE Ultrasonic Symposium*, 2006.

[173] Nasri, M. and Nezamabadi-pour, H., "Image denoising in the wavelet domain using a new adaptive thresholding function," *Neurocomputing,* vol. 72, no. 4–6, pp. 1012-1025, 2009.

[174] Nezamoddini-Kachouie, N., Fieguth, P., and Jernigan, E., "BayesShrink ridgelets for image denoising," in *Image Analysis and Recognition*, A. Campilho and M. Kamel, Eds., ed: Springer Berlin Heidelberg, pp. 163-170, 2004.

[175] Nguyen, T. and Wu, Q.M.J., "A fuzzy logic model based Markov random field for medical image segmentation," *Evolving Systems,* vol. 4, no. 3, pp. 171-181, 2013.

[176] Nikpour, M. and Hassanpour, H., "Using diffusion equations for improving performance of wavelet-based image denoising techniques," *IET Image Processing,* vol. 4, no. 6, pp. 452-462, 2010.

[177] Noble, J.A. and Boukerroui, D., "Ultrasound image segmentation: a survey," *IEEE Transactions on Medical Imaging,* vol. 25, no. 8, pp. 987-1010, 2006.

[178] O'Donnell, M. and Silverstein, S.D., "Optimum displacement for compound image generation in medical ultrasound," *IEEE Transactions on Ultrasonics, Ferroelectrics, and Frequency Control,* vol. 35, no. 4, pp. 470-476, 1987.

[179] Osher, S. and Fedkiw, R., *Level set methods and dynamic Implicit surfaces*, Springer Verlag. New York, 2003.

[180] Osher, S. and Sethian, J.A., "Fronts propagating with curvature-dependent speed: Algorithms based on Hamilton-Jacobi formulations," *Journal of Computational Physics,* vol. 79, no. 1, pp. 12-49, 1988.

[181] Pal, N.R. and Pal, S.K., "A review on image segmentation techniques," *Pattern Recognition,* vol. 26, no. 9, pp. 1277-1294, 1993.

[182] Paragios, N. and Deriche, R., "Geodesic active contours and level sets for the detection and tracking of moving objects," *IEEE Transactions on Pattern Analysis and Machine Intelligence,* vol. 22, no. 3, pp. 266-280, 2000.

[183] Pei, S.-C., Lei, C.-L., and Shih, F., "Recursive order-statistic soft morphological filters," In *Proceedings: IEE Vision, Image and Signal Processing*, pp. 333-342, 1998.

[184] Peng, B., Zhang, L., and Zhang, D., "A survey of graph theoretical approaches to image segmentation," *Pattern Recognition,* vol. 46, no. 3, pp. 1020-1038, 2013.

[185] Peng, D., Merriman, B., Osher, S., Zhao, H., and Kang, M., "A PDE-based fast local level set method," *Journal of Computational Physics,* vol. 155, no. 2, pp. 410-438, 1999.

[186] Perona, P. and Malik, J., "Scale-space and edge detection using anisotropic diffusion," *IEEE Transactions on Pattern Analysis and Machine Intelligence,* vol. 12, no. 7, pp. 629-639, 1990.

[187] Pham, D.L. and Prince, J.L., "An adaptive fuzzy C-means algorithm for image segmentation in the presence of intensity inhomogeneities," *Pattern Recognition Letters,* vol. 20, no. 1, pp. 57-68, 1999.

[188] Phelippeau, H., Talbot, H., Akil, M., and Bara, S., "Shot noise adaptive bilateral filter," In *Proceedings: IEEE 9th International Conference on Signal Processing*, pp. 864-867, 2008.

[189] Pizurica, A. and Philips, W., "Estimating the probability of the presence of a signal of interest in multiresolution single- and multiband image denoising," *IEEE Transactions on Image Processing,* vol. 15, no. 3, pp. 654-665, 2006.

[190] Portilla, J., Strela, V., Wainwright, M.J., and Simoncelli, E.P., "Image denoising using scale mixtures of Gaussians in the wavelet domain," *IEEE Transactions on Image Processing,* vol. 12, no. 11, pp. 1338-1351, 2003.

[191] Prasad, Y. and Biswas, K.K., "Fuzzy rough based regularization in Generalized Multiple Kernel Learning," *Computers & Mathematics with Applications,* vol. 66, no. 10, pp. 1770-1781, 2013.

[192] Pratt, W.K., *Digital Image Processing*, John Wiley and Sons New York, 2006.

[193] Prewitt, J.M., "Object enhancement and extraction," *Picture Processing and Psychopictorics,* vol. 10, no. 1, pp. 15-19, 1970.

[194] Qiao, Y.-L., Song, C.-Y., and Zhao, C.-H., "M-band ridgelet transform based texture classification," *Pattern Recognition Letters,* vol. 31, no. 3, pp. 244-249, 2010.

[195] Qin, L., You, J., Zhang, D., and Bhattacharya, P., "A multiscale approach to retinal vessel segmentation using gabor filters and scale multiplication," In *Proceedings: IEEE International Conference on Systems, Man and Cybernetics*, pp. 3521-3527, 2006.

[196] Qin, S., Yang, C., Tang, B., and Tan, S., "The denoise based on translation invariance wavelet transform and its applications," In *Proceedings: A Conference on Structural Dynamics*, pp. 783-787, 2002.

[197] Quistgaard, J.U., "Signal acquisition and processing in medical diagnostic ultrasound," *IEEE Signal Processing Magazine,* vol. 14, no. 1, pp. 67-74, 1997.

[198] Rabbani, H., "Image denoising in steerable pyramid domain based on a local Laplace prior," *Pattern Recognition,* vol. 42, no. 9, pp. 2181-2193, 2009.

[199] Rabbani, H., Vafadust, M., Abolmaesumi, P., and Gazor, S., "Speckle noise reduction of medical ultrasound images in complex wavelet domain using mixture priors," *IEEE Transactions on Biomedical Engineering,* vol. 55, no. 9, pp. 2152-2160, 2008.

[200] Rajan, J. and Kaimal, M.R., "Speckle reduction in images with WEAD and WECD," in *Computer Vision, Graphics and Image Processing*, P. Kalra and S. Peleg, Eds., ed: Springer Berlin Heidelberg, pp. 184-193, 2006.

[201] Rastgarpour, M., Shanbehzadeh, J., and Soltanian-Zadeh, H., "A hybrid method based on fuzzy clustering and local region-based level set for segmentation of inhomogeneous medical images," *Journal of Medical Systems,* vol. 38, no. 8, pp. 1-15, 2014.

[202] Renbo, X., Weijun, L., Jibin, Z., and Lun, L., "An optimal initialization technique for improving the segmentation performance of Chan-Vese model," In *Proceedings: IEEE International Conference on Automation and Logistics*, pp. 411-415, 2007.

[203] Roy, S., Sinha, N., and Sen, A., "Fuzzy soft thresholding based hybrid denoising model," in *Advances in Digital Image Processing and Information Technology*. vol. 205, D. Nagamalai, E. Renault, and M. Dhanuskodi, Eds., ed: Springer Berlin Heidelberg, pp. 1-10, 2011.

[204] Rudin, L.I., Osher, S., and Fatemi, E., "Nonlinear total variation based noise removal algorithms," *Physica D: Nonlinear Phenomena,* vol. 60, no. 1, pp. 259-268, 1992.

[205] Saad, A.S., "Speckle reduction of ultrasound images using wavelets analysis," In *Proceedings: 1st Jordanian European International Conference on Medical Informatics and Biomedical Engineering*, pp. 51-54, 2006.

[206] Sachdeva, J., Kumar, V., Gupta, I., Khandelwal, N., and Ahuja, C.K., "A novel content-based active contour model for brain tumor segmentation," *Magnetic Resonance Imaging,* vol. 30, no. 5, pp. 694-715, 2012.

[207] Saevarsson, B.B., Sveinsson, J.R., and Benediktsson, J.A., "Time invariant curvelet denoising," In *Proceedings: Nordic Signal Processing Symposium*, pp. 117-120, 2004.

[208] Salinas, H.M. and Fernandez, D.C., "Comparison of PDE-based nonlinear diffusion approaches for image enhancement and denoising in optical coherence tomography," *IEEE Transactions on Medical Imaging,* vol. 26, no. 6, pp. 761-771, 2007.

[209] Sanches, J.M., Nascimento, J.C., and Marques, J.S., "Medical image noise reduction using the Sylvester-Lyapunov equation," *IEEE Transactions on Image Processing,* vol. 17, no. 9, pp. 1522-1539, 2008.

[210] Seabra, J. and Sanches, J., "Ultrasound speckle/despeckle image decomposition for tissue analysis," in *Recent Advances in Ultrasound Imaging and Its Application*, J. M. Sanches, A. F. Laine, and J. S. Suri, Eds., ed: Springer US, pp. 73-95, 2012.

[211] Sengar, R.S., Upadhyay, A.K., Singh, M., and Gadre, V.M., "Segmentation of two dimensional electrophoresis gel image using the wavelet transform and the watershed transform," In *Proceedings: IEEE National Conference on Communications*, pp. 1-5, 2012.

[212] Sethian, J.A., *Level Set Methods and Fast Marching Methods*, Cambridge University Press. U.K., 1999.

[213] Shao, D., Liu, P., and Liu, D.C., "Characteristic matching-based adaptive fast bilateral filter for ultrasound speckle reduction," *Pattern Recognition Letters,* vol. 34, no. 5, pp. 463-469, 2013.

[214] Shrimali, V., "Segmentation and interpretation of ultrasound medical images," PhD Thesis, Electrical Engineering Department, IIT Roorkee, 2008.

[215] Shrimali, V., Anand, R., and Kumar, V., "Current trends in segmentation of medical ultrasound B-mode images: A review," *IETE Technical Review,* vol. 26, no. 1, pp. 8-17, 2009.

[216] Simon, M.P., Bhutada, G.G., and Anand, R.S., "A comparative analysis of diffusion-based and wavelet-based approaches for despeckling of ultrasound medical images," *International Journal of Biomedical Engineering and Technology,* vol. 7, no. 2, pp. 174-193, 2011.

[217] Singh, M. and Singh, S., "Spatial texture analysis: a comparative study," In *Proceedings: 16th International Conference on Pattern Recognition*, pp. 676-679, 2002.

[218] Smith, S.M. and Brady, J.M., "SUSAN—a new approach to low level image processing," *International Journal of Computer Vision,* vol. 23, no. 1, pp. 45-78, 1997.

[219] Sobel, I., "Neighborhood coding of binary images for fast contour following and general binary array processing," *Computer Graphics and Image Processing,* vol. 8, no. 1, pp. 127-135, 1978.

[220] Solbo, S. and Eltoft, T., "Homomorphic wavelet-based statistical despeckling of SAR images," *IEEE Transactions on Geoscience and Remote Sensing,* vol. 42, no. 4, pp. 711-721, 2004.

[221] Solem, J.E., Overgaard, N.C., and Heyden, A., "Initialization techniques for segmentation with the Chan-Vese model," In *Proceedings: 18th International Conference on Pattern Recognition*, pp. 171-174, 2006.

[222] Songcan, C. and Daoqiang, Z., "Robust image segmentation using FCM with spatial constraints based on new kernel-induced distance measure," *IEEE Transactions on Systems, Man, and Cybernetics, Part B: Cybernetics,* vol. 34, no. 4, pp. 1907-1916, 2004.

[223] Stankwitz, H.C., Dallaire, R.J., and Fienup, J.R., "Nonlinear apodization for sidelobe control in SAR imagery," *IEEE Transactions on Aerospace and Electronic Systems,* vol. 31, no. 1, pp. 267-279, 1995.

[224] Starck, J.-L., Murtagh, F., Candes, E.J., and Donoho, D.L., "Gray and color image contrast enhancement by the curvelet transform," *IEEE Transactions on Image Processing,* vol. 12, no. 6, pp. 706-717, 2003.

[225] Starck, J.L., Candes, E.J., and Donoho, D.L., "The curvelet transform for image denoising," *IEEE Transactions on Image Processing,* vol. 11, no. 6, pp. 670-684, 2002.

[226] Steffen, P., Heller, P.N., Gopinath, R.A., and Burrus, C.S., "Theory of regular M-band wavelet bases," *IEEE Transactions on Signal Processing,* vol. 41, no. 12, pp. 3497-3511, 1993.

[227] Sun, Q., Hossack, J.A., Tang, J., and Acton, S.T., "Speckle reducing anisotropic diffusion for 3D ultrasound images," *Computerized Medical Imaging and Graphics,* vol. 28, no. 8, pp. 461-470, 2004.

[228] Sun, T., Gabbouj, M., and Neuvo, Y., "Center weighted median filters: some properties and their applications in image processing," *Signal Processing,* vol. 35, no. 3, pp. 213-229, 1994.

[229] Tang, J., Guo, S., Sun, Q., Deng, Y., and Zhou, D., "Speckle reducing bilateral filter for cattle follicle segmentation," *BMC Genomics,* vol. 11, no. Suppl 2, p. S9, 2010.

[230] Tasdizen, T., "Principal neighborhood dictionaries for nonlocal means image denoising," *IEEE Transactions on Image Processing,* vol. 18, no. 12, pp. 2649-2660, 2009.

[231] Tauber, C., Batatia, H., and Ayache, A., "A robust speckle reducing anisotropic diffusion," In *Proceedings: International Conference on Image Processing*, pp. 247-250, 2004.

[232] Tay, P.C., Acton, S.T., and Hossack, J.A., "Ultrasound despeckling using an adaptive window stochastic approach," In *Proceedings: IEEE International Conference on Image Processing*, pp. 2549-2552, 2006.

[233] Thakur, A. and Anand, R.S., "A local statistics based region growing segmentation method for ultrasound medical images," *International Journal of Signal Processing,* vol. 1, no. 2, pp. 141-6, 2004.

[234] Thakur, A. and Anand, R.S., "Image quality based comparative evaluation of wavelet filters in ultrasound speckle reduction," *Digital Signal Processing,* vol. 15, no. 5, pp. 455-465, 2005.

[235] Thijssen, J. and Oosterveld, B., "Texture in tissue echograms. Speckle or information?," *Journal of Ultrasound in Medicine,* vol. 9, no. 4, pp. 215-229, 1990.

[236] Tian, Y., Duan, F., Zhou, M., and Wu, Z., "Active contour model combining region and edge information," *Machine Vision and Applications,* vol. 24, no. 1, pp. 47-61, 2013.

[237] Tomasi, C. and Manduchi, R., "Bilateral filtering for gray and color images," In *Proceedings: 6th International Conference on Computer Vision*, pp. 839-846, 1998.

[238] Tsai, A., Yezzi, A., Jr., and Willsky, A.S., "Curve evolution implementation of the Mumford-Shah functional for image segmentation, denoising, interpolation, and magnification," *IEEE Transactions on Image Processing,* vol. 10, no. 8, pp. 1169-1186, 2001.

[239] Vanithamani, R. and Umamaheswari, G., "Wavelet based despeckling of medical ultrasound images with bilateral filter," In *Proceedings: IEEE Region 10 Conference TENCON*, pp. 389-393, 2011.

[240] Vansteenkiste, E., Pizurica, A., and Philips, W., "Improved segmentation of ultrasound brain tissue incorporating expert evaluation," In *Proceedings: 27th Annual IEEE International Conference of the Engineering in Medicine and Biology Society*, pp. 6480-6483, 2005.

[241] Vantaram, S.R. and Saber, E., "Survey of contemporary trends in color image segmentation," *Journal of Electronic Imaging,* vol. 21, no. 4, pp. 1-28, 2012.

[242] Vese, L. and Chan, T., "A multiphase level set framework for image segmentation using the Mumford and Shah model," *International Journal of Computer Vision,* vol. 50, no. 3, pp. 271-293, 2002.

[243] Wagner, R.F., Smith, S.W., Sandrik, J.M., and Lopez, H., "Statistics of speckle in ultrasound B-scans," *IEEE Transactions on Sonics and Ultrasonics,* vol. 30, no. 3, pp. 156-163, 1983.

[244] Wang, W., Zhu, L., Qin, J., Chui, Y.-P., Li, B.N., and Heng, P.-A., "Multiscale geodesic active contours for ultrasound image segmentation using speckle reducing anisotropic diffusion," *Optics and Lasers in Engineering,* vol. 54, pp. 105-116, 2014.

[245] Wang, X.-F., Huang, D.-S., and Xu, H., "An efficient local Chan–Vese model for image segmentation," *Pattern Recognition,* vol. 43, no. 3, pp. 603-618, 2010.

[246] Wang, Z.-h., Wang, J.-q., Zhao, D.-g., and Fu, W., "Image fusion based on shearlet and improved PCNN," *Laser & Infrared,* vol. 2, p. 023, 2012.

[247] Wang, Z., Bovik, A.C., Sheikh, H.R., and Simoncelli, E.P., "Image quality assessment: From error visibility to structural similarity," *IEEE Transactions on Image Processing,* vol. 13, no. 4, pp. 600-612, 2004.

[248] Weber, M., Blake, A., and Cipolla, R., "Sparse finite elements for geodesic contours with level-sets," in *Computer Vision* vol. 3022, T. Pajdla and J. Matas, Eds., ed: Springer Berlin Heidelberg, pp. 391-404, 2004.

[249] Wells, P.N.T., "Absorption and dispersion of ultrasound in biological tissue," *Ultrasound in Medicine & Biology,* vol. 1, no. 4, pp. 369-376, 1975.

[250] Wells, P.N.T., "Current status and future technical advances of ultrasonic imaging," *IEEE Engineering in Medicine and Biology,* vol. 19, no. 5, pp. 14-20, 2000.

[251] Wu, H.-M. and Lu, H.H.-S., "Iterative sliced inverse regression for segmentation of ultrasound and MR images," *Pattern Recognition,* vol. 40, no. 12, pp. 3492-3502, 2007.

[252] Xia Jun, J., Ni, L., and Miao, Y., "A new digital implementation of ridgelet transform for images of dyadic length," In *Proceedings: 3rd International Conference on Information Technology and Applications*, pp. 613-616, 2005.

[253] Xiang, Y., Sahay, R.R., and Kankanhalli, M.S., "Hazy image enhancement based on the full-saturation assumption," In *Proceedings: IEEE International Conference on Multimedia and Expo Workshops*, pp. 1-4, 2013.

[254] Xie, J., Jiang, Y., Tsui, H.-T., and Heng, P.-A., "Boundary enhancement and speckle reduction for ultrasound images via salient structure extraction," *IEEE Transactions on Biomedical Engineering,* vol. 53, no. 11, pp. 2300-2309, 2006.

[255] Xu, C. and Prince, J.L., "Snakes, shapes, and gradient vector flow," *IEEE Transactions on Image Processing,* vol. 7, no. 3, pp. 359-369, 1998.

[256] Xu, J., Yang, L., and Wu, D., "Ripplet: A new transform for image processing," *Journal of Visual Communication and Image Representation,* vol. 21, no. 7, pp. 627-639, 2010.

[257] Xuli, Z., Laine, A.F., and Geiser, E.A., "Speckle reduction and contrast enhancement of echocardiograms via multiscale nonlinear processing," *IEEE Transactions on Medical Imaging,* vol. 17, no. 4, pp. 532-540, 1998.

[258] Yang, D., Wang, L., Hei, X., and Gong, M., "An efficient automatic SAR image segmentation framework in AIS using kernel clustering index and histogram statistics," *Applied Soft Computing,* vol. 16, pp. 63-79, 2014.

[259] Yang, J., Wang, Y., Xu, W., and Dai, Q., "Image and video denoising using adaptive dual-tree discrete wavelet packets," *IEEE Transactions on Circuits and Systems for Video Technology,* vol. 19, no. 5, pp. 642-655, 2009.

[260] Yang, M.-S. and Tsai, H.-S., "A Gaussian kernel-based fuzzy c-means algorithm with a spatial bias correction," *Pattern Recognition Letters,* vol. 29, no. 12, pp. 1713-1725, 2008.

[261] Yang, M., Liang, J., Zhang, J., Gao, H., Meng, F., Xingdong, L.*, et al.*, "Non-local means theory based Perona–Malik model for image denoising," *Neurocomputing,* vol. 120, no. 23, pp. 262-267, 2013.

[262] Yang, R., Yin, L., Gabbouj, M., Astola, J., and Neuvo, T., "Optimal weighted median filtering under structural constraints," *IEEE Transactions on Signal Processing,* vol. 43, no. 3, pp. 591-604, 1995.

[263] Yap, M.H., Edirisinghe, E., and Bez, H., "Processed images in human perception: A case study in ultrasound breast imaging," *European Journal of Radiology,* vol. 73, no. 3, pp. 682-687, 2010.

[264] Yi, S., Labate, D., Easley, G.R., and Krim, H., "Edge detection and processing using shearlets," In *Proceedings: 15th IEEE International Conference on Image Processing*, pp. 1148-1151, 2008.

[265] Yonggang, S. and Karl, W.C., "A fast level set method without solving PDEs," In *Proceedings: IEEE International Conference on Acoustics, Speech, and Signal Processing*, pp. 97-100, 2005.

[266] Yongjian, Y. and Acton, S.T., "Speckle reducing anisotropic diffusion," *IEEE Transactions on Image Processing,* vol. 11, no. 11, pp. 1260-1270, 2002.

[267] Yongjian, Y. and Acton, S.T., "Edge detection in ultrasound imagery using the instantaneous coefficient of variation," *IEEE Transactions on Image Processing,* vol. 13, no. 12, pp. 1640-1655, 2004.

[268] Yongsheng, P., Birdwell, J.D., and Djouadi, S.M., "Efficient implementation of the Chan-Vese models without solving PDEs," In *Proceedings: IEEE 8th Workshop on Multimedia Signal Processing*, pp. 350-354, 2006.

[269] You, Y.L. and Kaveh, M., "Fourth-order partial differential equations for noise removal," *IEEE Transactions on Image Processing,* vol. 9, no. 10, pp. 1723-1730, 2000.

[270] Yousif, O. and Ban, Y., "Improving urban change detection from multitemporal SAR images using PCA-NLM," *IEEE Transactions on Geoscience and Remote Sensing,* vol. 51, no. 4, pp. 2032-2041, 2013.

[271] Yu, C., Zhang, C., and Xie, L., "A multiplicative Nakagami speckle reduction algorithm for ultrasound images," *Multidimensional Systems and Signal Processing,* vol. 23, no. 4, pp. 499-513, 2012.

[272] Yu, H., Zhao, L., and Wang, H., "Image denoising using trivariate shrinkage filter in the wavelet domain and joint bilateral filter in the spatial domain," *IEEE Transactions on Image Processing,* vol. 18, no. 10, pp. 2364-2369, 2009.

[273] Yu, J., Tan, J., and Wang, Y., "Ultrasound speckle reduction by a SUSAN-controlled anisotropic diffusion method," *Pattern Recognition,* vol. 43, no. 9, pp. 3083-3092, 2010.

[274] Yu, J., Wang, Y., and Shen, Y., "Noise reduction and edge detection via kernel anisotropic diffusion," *Pattern Recognition Letters,* vol. 29, no. 10, pp. 1496-1503, 2008.

[275] Yuan, J., "Active contour driven by region-scalable fitting and local Bhattacharyya distance energies for ultrasound image segmentation," *IET Image Processing,* vol. 6, no. 8, pp. 1075-1083, 2012.

[276] Yuan, J., "Active contour driven by local divergence energies for ultrasound image segmentation," *IET Image Processing,* vol. 7, no. 3, pp. 252-259, 2013.

[277] Zhang, J., Wang, C., and Cheng, Y., "Comparison of despeckle filters for breast ultrasound images," *Circuits, Systems, and Signal Processing,* pp. 1-24, 2014.

[278] Zhang, K., Song, H., and Zhang, L., "Active contours driven by local image fitting energy," *Pattern Recognition,* vol. 43, no. 4, pp. 1199-1206, 2010.

[279] Zhang, K., Zhang, L., Song, H., and Zhou, W., "Active contours with selective local or global segmentation: A new formulation and level set method," *Image and Vision Computing,* vol. 28, no. 4, pp. 668-676, 2010.

[280] Zhang, M. and Gunturk, B., "A new image denoising method based on the bilateral filter," In *Proceedings: IEEE International Conference on Acoustics, Speech and Signal Processing*, pp. 929-932, 2008.

[281] Zhang, M. and Gunturk, B.K., "Multiresolution bilateral filtering for image denoising," *IEEE Transactions on Image Processing,* vol. 17, no. 12, pp. 2324-2333, 2008.

[282] Zhang, X.-P., "Thresholding neural network for adaptive noise reduction," *IEEE Transactions on Neural Networks,* vol. 12, no. 3, pp. 567-584, 2001.

[283] Zhang, X., Feng, X., and Wang, W., "Two-direction nonlocal model for image denoising," *IEEE Transactions on Image Processing,* vol. 22, no. 1, pp. 408-412, 2013.

[284] Zhang, X. and Li, D., "À trous wavelet decomposition applied to image edge detection," *Geographic Information Sciences,* vol. 7, no. 2, pp. 119-123, 2001.

[285] Zhang, X., Zhang, Q., and Jiao, L., "Image denoising with non-local means in the shearlet domain," In *Proceedings: International Workshop on Multi-Platform/Multi-Sensor Remote Sensing and Mapping*, pp. 1-5, 2011.

[286] Zhang, Y., Wu, S., Yu, G., and Wang, D., "A hybrid image segmentation approach using watershed transform and FCM," In *Proceedings: 4th International Conference on Fuzzy Systems and Knowledge Discovery*, pp. 2-6, 2007.

[287] Zheng, H. and Hellwich, O., "Discrete regularization for perceptual image segmentation via semi-supervised learning and optimal control," In *Proceedings: IEEE International Conference on Multimedia and Expo*, pp. 1982-1985, 2007.

[288] Zhong, T., Tagare, H.D., and Beaty, J.D., "Evaluation of four probability distribution models for speckle in clinical cardiac ultrasound images," *IEEE Transactions on Medical Imaging,* vol. 25, no. 11, pp. 1483-1491, 2006.

[289] Zhou, D. and Cheng, W., "Image denoising with an optimal threshold and neighbouring window," *Pattern Recognition Letters,* vol. 29, no. 11, pp. 1694-1697, 2008.

[290] Zhou, D. and Shen, X., "Image denoising using block thresholding," In *Proceedings: Congress on Image and Signal Processing*, pp. 335-338, 2008.

[291] Zhu, G., Zhang, S., Zeng, Q., and Wang, C., "Boundary-based image segmentation using binary level set method," *Optical Engineering,* vol. 46, no. 5, pp. 1-3, 2007.

APPENDIX – A

Table A.1 Averaged PSNR, SNR, SSIM, FOM and EKI values evaluated for all the proposed denoising approaches applied on the test images

Noise level	Methods	PSNR	SNR	SSIM	FOM	EKI
σ = 0.1	MBRT	24.21 ± 4.05	14.95 ± 1.81	0.7601 ± 0.1048	0.8424 ± 0.0813	0.5875 ± 0.1669
	RTNLF-1	25.29 ± 4.09	16.03 ± 1.28	0.7709 ± 0.0893	0.8893 ± 0.0883	0.7178 ± 0.2005
	RTNLF-2	25.75 ± 4.29	16.49 ± 1.38	0.7881 ± 0.0898	0.8953 ± 0.0867	0.7336 ± 0.1920
	RBAF	25.88 ± 4.64	16.62 ± 2.48	0.7925 ± 0.0938	0.8789 ± 0.0749	0.6567 ± 0.1801
	NSST-NADF	25.61 ± 4.28	16.35 ± 1.37	0.7859 ± 0.0908	0.8778 ± 0.0695	0.6760 ± 0.1468
	NSST-NLNADF	26.70 ± 5.08	17.44 ± 1.99	0.8060 ± 0.1080	0.8875 ± 0.0688	0.7138 ± 0.1505
σ = 0.2	MBRT	22.88 ± 3.86	13.62 ± 2.17	0.7211 ± 0.1177	0.7895 ± 0.0354	0.5435 ± 0.1273
	RTNLF-1	23.91 ± 4.11	14.65 ± 2.02	0.7479 ± 0.0953	0.8507 ± 0.0567	0.6213 ± 0.1258
	RTNLF-2	24.22 ± 4.08	14.96 ± 1.99	0.7538 ± 0.0974	0.8589 ± 0.0573	0.6401 ± 0.1309
	RBAF	24.02 ± 4.69	14.76 ± 2.42	0.7584 ± 0.0964	0.8579 ± 0.0627	0.5726 ± 0.1109
	NSST-NADF	23.96 ± 4.31	14.70 ± 2.13	0.7493 ± 0.0974	0.8548 ± 0.0564	0.5761 ± 0.1081
	NSST-NLNADF	24.56 ± 4.78	15.30 ± 2.47	0.7802 ± 0.1249	0.8746 ± 0.0637	0.6517 ± 0.1640
σ = 0.3	MBRT	22.05 ± 3.94	12.79 ± 2.59	0.7006 ± 0.1289	0.7354 ± 0.0179	0.4943 ± 0.1218
	RTNLF-1	22.32 ± 3.78	13.06 ± 2.29	0.7198 ± 0.0973	0.8371 ± 0.0735	0.5806 ± 0.1269
	RTNLF-2	22.81 ± 3.79	13.56 ± 2.44	0.7225 ± 0.0980	0.8436 ± 0.0685	0.5911 ± 0.1270
	RBAF	22.72 ± 4.89	13.46 ± 2.64	0.7219 ± 0.0931	0.8388 ± 0.0680	0.5012 ± 0.0619
	NSST-NADF	23.02 ± 4.37	13.76 ± 2.59	0.7182 ± 0.0988	0.8389 ± 0.0730	0.5479 ± 0.0943
	NSST-NLNADF	23.61 ± 4.70	14.35 ± 2.65	0.7654 ± 0.1251	0.8604 ± 0.0576	0.5946 ± 0.1321

Table A.2 Comparative MVR analysis for all proposed denoising approaches applied on the ultrasound images

Methods	MBRT	RTNLF-1	RTNLF-2	RBAF	NSST-NADF	NSST-NLNADF
MVR	21.12 ± 4.93	21.98 ± 3.93	22.17 ± 4.33	22.23 ± 3.98	21.95 ± 4.26	22.42 ± 4.12

APPENDIX – B

Table B.1 Averaged performance measures (TP, FP, ACC, JSI, DC and HD) evaluated for all the proposed segmentation approaches applied on the ultrasound images

Metrics (AVG ± STD)	EBACM-KFCM_S1	EBACM-KFCM_S2	RBACM-GKFCM_S1	RBACM-GKFCM_S2
TP	0.9281 ± 0.0342	0.9325 ± 0.0363	0.9285 ± 0.0460	0.9345 ± 0.0409
FP	0.0361 ± 0.0226	0.0322 ± 0.0167	0.0331 ± 0.0385	0.0319 ± 0.0358
ACC	0.9291 ± 0.0144	0.9315 ± 0.0171	0.9347 ± 0.0244	0.9358 ± 0.0246
JSI	0.8675 ± 0.0328	0.8763 ± 0.0335	0.8760 ± 0.0436	0.8772 ± 0.0443
DC	0.9288 ± 0.0164	0.9326 ± 0.0189	0.9334 ± 0.0249	0.9345 ± 0.0253
HD	3.0125 ± 0.7155	2.9615 ± 0.7653	2.8658 ± 1.2053	2.5206 ± 1.2507